Tests and characterization of gamma cameras for medical applications

Mattia Fontana

N° d'ordre NNT : xxx

THÈSE DE DOCTORAT DE L'UNIVERSITÉ DE LYON
opérée au sein de
l'Université Claude Bernard Lyon 1

École Doctorale ED52
Physique et Astrophysique de Lyon

Spécialité de doctorat :
Discipline : Physique médicale

Soutenue publiquement le 14/12/2018, par :
Mattia Fontana

Tests and characterization of gamma cameras for medical applications

Test et caractérisation de caméras gamma pour le médical

Devant le jury composé de :

Llosá Gabriela, Professeur associée, IFIC - Institut de Fisica Corpuscolar, Paterna, Espagne
Rapporteure

Thirolf Peter, Professeur associé, Fakultät für Physik der LMU München - Lehrstuhl für Experimentalphysik - Medizinishce Physik, Garching, Allemagne
Rapporteur

Augier Corinne, Professeur, IPNL - Institut de Physique Nucléaire de Lyon, France
Examinatrice

Cerello Piergiorgio, Chercheur, INFN - Istituto Nazionale di Fisica Nucleare, sezione di Torino, Italie
Examinateur

Morel Christian, Professeur, CPPM - Centre de Physique de Particules de Marseille - Aix-Marseille Université, Marseille, France
Examinateur

Rafecas Magdalena, Professeur, Institut für Medizintechnik - Universität zu Lübeck, Allemagne
Examinatrice

Testa Étienne, Maître de conférences, IPNL - Institut de Physique Nucléaire de Lyon, France
Directeur de thèse

Létang Jean Michel, Maître de conférences, CREATIS - Centre de Recherche en Acquisition et Traitement de l'Image pour la Santé, Lyon, France
Co-directeur de thèse

Dauvergne Denis, Directeur de Recherche CNRS, LPSC - Laboratoire de Physique Subatomique et de Cosmologie de Grenoble, France
Invité

Tests and characterization of gamma cameras for medical applications

PhD Candidate

MATTIA FONTANA

Thesis directors

ÉTIENNE TESTA and JEAN MICHEL LÉTANG

Université Claude Bernard
Lyon 1
Physics departement
Doctoral school ED52:
Physics and Astrophysics

Defended on December the 14th
2018

Abstract

The application of nuclear and particle physics techniques in the field of medical diagnosis and pathology treatment is nowadays well-established in the clinical routine. In particular, elementary particles are the basis of several medical imaging techniques (Positron Emission Tomography (PET), Single Photon Emission Computed Tomography (SPECT), Computed Tomography (CT) scans, etc.), as well as of treatment methods, mainly concerning cancer, which causes about 9 millions deaths per year all over the world.

In this context, ion beam therapy is a promising technique in cancer treatment because of the ion defined range and favorable dose delivery features with respect to standard photon radiotherapy. Strict and precise treatment planning and monitoring are now key points for the method development and full exploitation. In particular, with the aim of optimizing the ion treatment effectiveness, the ion range monitoring is mandatory: different solutions have been explored, but an online treatment check is still a challenge. The ion beam treatment monitoring can be performed by means of secondary charged or neutral particles. In this context, the detection of the Prompt-Gammas (PGs) emitted during treatments has proven its potential in the ion range control in real time. Since the first evidence of the existing correlation between the emitted gamma profile fall-off and the Bragg peak position, several groups are involved in research activities in order to develop and optimize instruments and methods with the aim of improving this monitoring technique. Among the others, collimated and Compton cameras are being investigated for this application. The same detectors can also be employed in nuclear medicine for the detection of the radioactive elements decay products.

A collaboration of 4 laboratories in France, called *Contrôle en Ligne de l'hadronthérapie par Rayonnements Secondaires* (CLaRyS), is involved in the parallel development of two composite detectors for ion beam monitoring and nuclear medicine applications, and this thesis is carried out within this collaboration with the detectors clinical trial as final aim.

The development project started a few years ago and is now at the final stage. The two cameras have been designed according to simulation studies, and the different components are now under tests. The collimated camera is composed of a multi-slit tungsten mechanical collimator, set in front of an absorber composed of 30 Bismuth Germanium Oxide - $Bi_{12}GeO_{20}$ (BGO) blocks, for a total size of $210\times175\times30$ mm^3; each block presents a streaked structure with a 8×8 pseudo-pixel matrix and the signal is read-out by 4 Photo-Multipliers (PMs). A $\sim$3 ns time resolution can be achieved on average for the prompt-gamma detection. The same absorber is part of the Compton camera, in addition to a scatterer section composed of 7 Double-sided Silicon Strip Detectors (DSSDs), $96\times96\times2$ mm^3 each.

With the collimated camera, the parallel emitted photons are selected by the collimator and a mono-dimensional emission profile can be reconstructed. The Compton camera has a more efficient detection technique, thanks to the absence of a mechanical collimation system, and could potentially lead to three-dimensional information via the reconstruction of the Compton cones. These features make it suitable for the application in nuclear medicine, in particular as an alternative to the present SPECT collimated cameras, allowing for accurate and efficient image reconstructions with the usage of high energy gamma sources, which should reduce

image blurring effects due to attenuation in the patient and the total released dose with respect to the present clinical routine.

Concerning the monitoring of ion beam therapy treatments, an additional detector component is needed to temporally and spatially tag the incoming beam ions and help rejecting background events (mostly due to neutrons) which strongly affects the prompt-gamma yield. A scintillating fiber tagging hodoscope, which can be coupled to both collimated and Compton camera, is under development: it is composed of 2 perpendicular planes of 128 scintillating fibers, read-out from both sides by 8 multi-anode (64 channels) PMs by Hamamatsu.

This thesis work consists in the critical evaluation, characterization and tuning of the different components, together with the associated electronics, and of the complete detector systems on beam. In parallel, simulation studies can improve the detection techniques and optimize the detector structure, as well as pave the way for further applications.

This manuscript is divided into three parts. Part I introduces the thesis rationale. After a general introduction devoted to the thesis context in chapter 1, an overview of the state of the art of the gamma detection techniques applied in medicine and the employed gamma detection systems is given in chapter 2. Part II consists of four chapters and describes my personal work. Chapter 3 focuses on the two cameras developed by the CLaRyS collaboration; the camera components are described in details, and all the characterization measurements performed during the three years of my PhD thesis are explained. Chapters 4 and 5 present the simulation studies I performed with the aim of investigating the potential of the developed detectors for the application in ion beam therapy monitoring and nuclear medicine, respectively. Chapter 6 is dedicated to the description of the tests performed on proton beams for the detector/electronics characterization measurements. In Part III I summarize and discuss all the results obtained in this thesis work; furthermore, the perspectives of the project are fixed on a time-line for the next future.

Contents

List of Figures

List of Tables

Part
I

Rationale

1

Context

Contents

The application of physics concepts and techniques to the field of health-care is nowadays well-established in the clinical routine. Even if physical techniques have been used in medicine from the earliest time (Duck 2014), the discipline today known as "medical physics", emerged and developed in the past century thanks to the increasing knowledge and use of ionizing radiations both for diagnosis and disease treatment. In the late 19^{th} century, the x-ray discovery by Röntgen, the radioactivity discovery by Henri Becquerel, and the radium and radioactive isotopes studies by Pierre and Marie Curie paved the way to the whole medical physics practice of the next century, where x-ray imaging and radiotherapy were soon established. Only three weeks after the discovery of the x-rays, Robert Jones and Oliver Lodge imaged with x-rays a boy's hand (Cantor 1988), officially starting the diagnostic application of such a radiation. Following the first successes, more attention was given to radio-protection and dosimetry studies, and the investigations focused on new ways to use radioactive tracers for imaging purpose; this finally led to the birth of nuclear medicine, with the clinical use of the radioisotope Iodine-131 (^{131}I) in 1939 (Kereiakes 1987). Nuclear medicine rapidly gained importance in the diagnosis clinical panorama, also thanks to the introduction of new detectors, such as the Anger camera introduced in the '60s, and new imaging techniques, such as the detection of photons from positron annihilation (Positron Emission Tomography (PET)). Moreover, several alternative methods were proposed or implemented for diagnosis (Magnetic Resonance Imaging (MRI), ultrasounds, etc.). In parallel, x-rays were soon employed also for tumor treatment: already in 1896, Emil Grubbe irradiated a woman with breast cancer (Evans 1951), and in the same year in Lyon a patient with a stomach cancer has been treated by Victor Despeignes (Despeignes 1896; Foray 2016). One year later, a skin tumor was successfully irradiated in Vienna using x-rays. Thanks to the invention of the klystron, and, later, of the so-called "magnetron", by the Varian brothers with William Webster Hansen, the radiotherapy could spread and become a clinical reality; more refined treatment techniques were then introduced with the development of commercial particle accelerators after World War 2 (Keevil 2012).

At present days, the medical physics progress strongly relies on technological development and computer science, which already revolutionized several fields of science. In particular, cancer research is now a key area for technical and technological development, concerning both diagnosis and treatment (Webb 2009). Cancer continues to be one of the major issues in the medical scenario: it is at present the second cause of death worldwide, but it is expected to surpass heart diseases and become the main killer in the next tens of years (Jemal et al. 2010; Thun et al. 2010). The last two decades saw important improvements in radiotherapy techniques and machines, with more precise dose planning and delivery, which enhanced the patient survival and strongly reduced the impact of radiations on healthy tissues. This was possible also thanks to refined imaging technologies, allowing for an accurate tumor volume definition, as well as for image-guided treatments. In this scenario, ion beam therapy, already proposed in the middle of the past century, is rapidly spreading thanks to novel beam delivery technologies, able to relatively reduce the treatment costs and allowing for a commercial diffusion of this treatment method (which is still very limited with respect to standard radiotherapy). Notwithstanding the remarkable steps forward disclosed in the last years, there is still wide room for improvements in this field, which mainly requires strong imaging basis in order to fully profit of the treatment technique potential.

The work presented in this document has been carried out in this context and mainly deals with the development of gamma imaging detectors to be applied in the field of quality assurance for ion beam treatment. Furthermore, the same detectors have been applied to the nuclear

medicine field in simulation, with the aim of assessing its possible clinical implementation for a future development of the nuclear medicine clinical routine.

In the following sections, a general overview of the two main domains of interest for this thesis work is given.

1.1 Ion beam therapy

Radiation treatment is an essential component of the tumor therapy, being the second most applied and successful kind of therapy after surgery (Schardt et al. 2010). The majority of patients with localized malignant tumors are treated with radiations (Baskar et al. 2012; Durante et al. 2009; Moding et al. 2013), applied in several fractions in different days in order to reduce the damages to normal tissues (Bentzen 2006). The most of the patients treated with radiotherapy techniques receives standard photon treatments, with x-rays coming from linear electron accelerators; a small percentage undergoes specialized gamma treatments like gamma knife irradiations, again using x-ray beams from linear electron accelerators, or brachytherapy. About 1 % of the radiotherapy patients are irradiated with charged particle beams, with the so-called ion beam therapy (Durante et al. 2016).

Ion beam therapy, or "hadrontherapy", is a cancer radiation treatment method based on light ion beams instead of photons. It was first proposed by Wilson in 1946 in a famous seminal paper (R. R. Wilson 1946); the author was asked by his director Ernest Lawrence to clarify the stopping process of protons in matter. Thanks to measurements at the Berkeley cyclotron, he highlighted the physical principles and the possible benefits driven by the implementation of such a kind of radiation in clinical treatments, with particular focus on the simple case of protons and some considerations about heavier ions, like alpha particles and carbon ions. At that time, the accelerator technologies were still under development after the invention of the cyclotron by Ernest O. Lawrence in 1930, which allowed to increase the range of charged particles in matter, in particular in cells and human tissues, and the beam energy required for treatments was about to be reached. Pioneering studies of the biomedical applications of accelerated hadron beams were performed by Cornelius Tobias in 1948 (Blakely et al. 2009) in Berkeley (USA), and the first patients have been treated almost ten years later in the same laboratory by Lawrence and Tobias (Tobias et al. 1958, 1955) with protons and, later on, with He ions (Halperin 2006). New accelerators in four continents were used to continue the quest started in Berkeley, and the experience was extended to carbon ion beams from 1994 in Japan (Heavy Ion Medical Accelerator in Chiba, Japan (HIMAC)), and Germany (Heidelberg Ion Therapy Center, Germany (HIT)).

Nowadays clinical adapted machines are well-established on the market, making ion beam therapy emerging as a wide-spread technique in the every-day cancer treatment routine all over the world. Starting from the early 2000's, many new treatment centers have been designed and built. An intense research effort has been dedicated to this field in the last decades; in addition to considerable improvements achieved in the accelerator technologies, new and refined imaging techniques allowed for important enhancement in the treatment planning, also supported by the continuous development of computer science and the growth of computing power. In parallel, the biological implications of ion irradiation has been deeply investigated (Brahme 2004; Friedrich et al. 2012; Tobias et al. 1982). Moreover, since more and

more patients are treated every year with this technique, more clinical data are at present available for further study and the connection between physicists and physicians is strongly progressing both in the research field and in treatment practice. Several advancements are expected in the next years, following the extensive research work carried out by several groups in the world. In the following section, the basic physical principles and features of this treatment method are explained, and advantages and drawbacks with respect to standard radiotherapy techniques are analyzed. After that, the need for ion range verification is discussed and detailed in order to reach the main topic for this thesis: the prompt-gamma detection.

1.1.1 Physics of ion beam therapy

The physics rationale of ion beam therapy is extensively described in all its aspects in several review, such as Belkić 2010; Bichsel 2013; Durante et al. 2016; Lomax 2009; Newhauser et al. 2015; NuPECC 2014; Schardt et al. 2010. In the following, the physical basis of this tumor treatment technique is highlighted.

Charged nuclear particle beams at relatively high energy show a characteristic depth-dose distribution in matter which makes them suitable for the application in cancer treatment as a valid alternative to standard photon therapy (x-ray or megavolt beams), bringing several advantages to the patient side. This energy deposition profile ("Bragg curve") is named for Sir William Henri Bragg, who investigated the slowing-down process of α particles in air (Bragg et al. 1904, 1905). Low-energy (x-rays) and high-energy photons traversing the patient body deposit their energy by interacting with the target atomic electrons (mainly by Compton interaction), with the deposited dose decreasing at increasing depth after a build-up region (mainly due to forward scattered Compton electrons). Even if the entrance surface (the skin for a patient) can be spared thanks to this build-up region, with a dose peak shift of a few centimeters, a high relative dose is delivered to the tissues along the whole beam path. In order to maximize the tumor volume-to-healthy tissue dose ratio, a standard photon treatment always foresees several irradiation fields from different entrance points and angles (see Figure 1.1, left). This energy deposit behavior is common to all neutral particles, as shown in the first two boxes in Figure 1.2 where the depth-dose profiles of photons at various energies and neutrons in water are presented. In contrast to neutral particles, the energy deposited per track unit increases for increasing depth for the charged ones: in the remaining four boxes of Figure 1.2 the depth-dose profile in water is shown for electrons, pions, protons and neon ions; it is characterized by an entrance low relative dose *plateau* and by a narrow high deposited dose peak at the end of the range (in the last few millimeters), called "Bragg peak". The dose peak is sharper the more massive is the particle, as clear from Figure 1.2, where the different species are sorted by increasing mass. As for protons and heavier ions, their clinical interest for the treatment of deep-seated tumors appears clearly from the above considerations: a nuclear particle beam is able to deliver a reduced dose to the healthy tissues surrounding the target volume, where the dose is concentrated. This allows for the treatment of tumor volumes close to Organs At Risk (OAR), also with limited irradiation angles with respect to photons, as shown in the right part of Figure 1.1, where the planning for a carbon ion treatment of a lung cancer with only three irradiation fields is depicted.

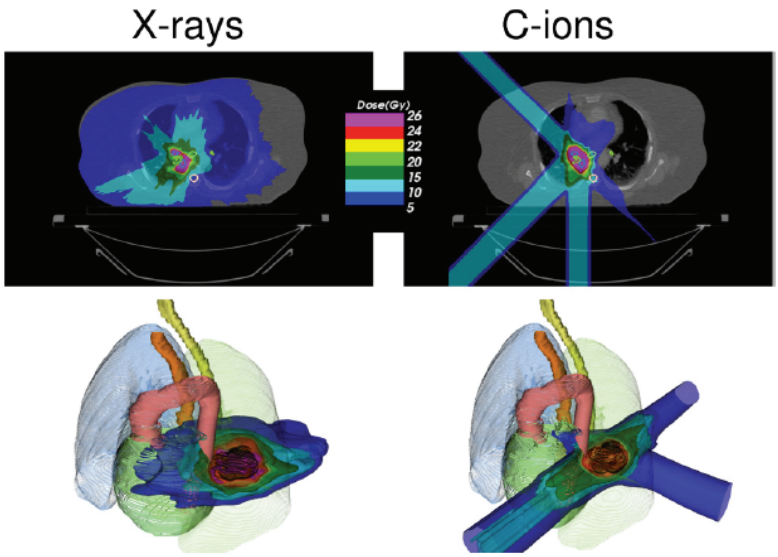

Figure 1.1: Treatment planning of lung cancer for the irradiation with x-rays (left) or carbon ions (right) (in Durante et al. 2016).

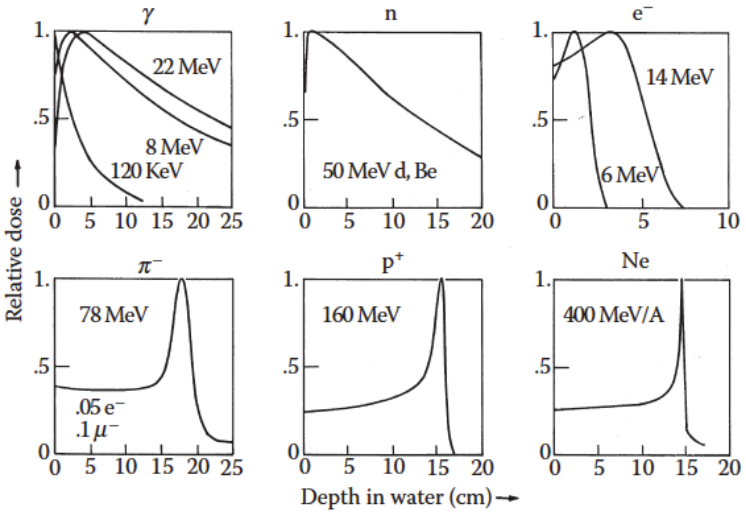

Figure 1.2: Relative dose as a function of the particle depth in water for different particle species. For photons, the reported energy in MeV corresponds to MV linac-accelerated electron induced bremmstrahlung. In Paganetti 2012a.

1.1.1.1 Charged particle interactions in matter

The charged particle interactions in matter can be described by three main mechanisms: Electromagnetic (EM) inelastic interactions with the atomic electrons, EM elastic interactions with the atomic nuclei, and nuclear reactions. In addition to the listed interactions, also Bremsstrahlung is theoretically possible, but its effect is negligible at ion energies of clinical interest. The EM inelastic interactions with atomic electrons cause an energy loss which is generally approximated with a Continuous Slowing Down Approach (CSDA) for simplicity, assuming a mono-dimensional quasi-linear ion path and an average, continuous energy loss rate. The mass difference between electrons and ions (as an example, the proton mass is 1832 times greater than that of an electron), justifies the quasi-linear approximation, while the significant cross-section for small energy transfer allows one to consider a continuous decelerating force. The elastic repulsion caused by an atomic nucleus is able to deflect the projectile ion, with an angle which depends on the target-projectile relative mass. The inelastic nuclear reactions are less frequent, but reduce the intensity of the primary beam (the primary particle is destroyed or deflected at large angle), and cause the emission of secondary nuclear fragments. A schematic view of the three main interaction mechanisms described is given in Figure 1.3 for the example case of protons, while in the following the effects of these interactions are detailed.

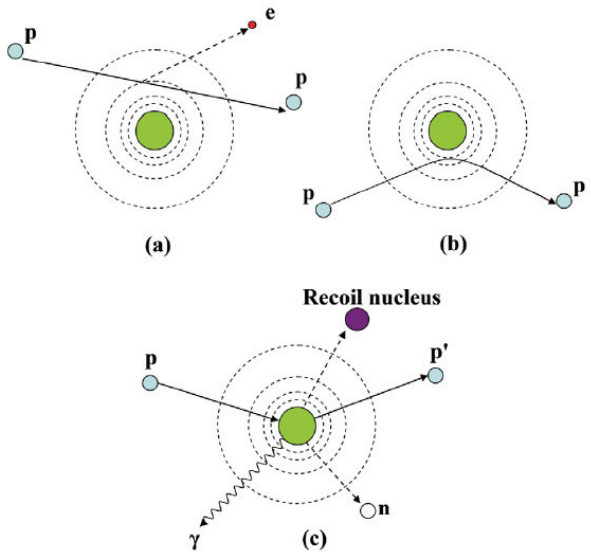

Figure 1.3: Schematic view of an example of the three main interactions mechanics of protons in matter: Coulomb (EM) interaction with atomic electrons (a), Coulomb (EM) interactions with atomic nucleus (b), nuclear reactions(c). In Newhauser et al. 2015.

EM interactions with target atomic electrons

At the primary particle velocities of clinical interest, the ion energy loss rate is dominated by inelastic collisions with the target atomic electrons and is well described by the formula attributed to Bethe (Bethe 1930) and Bloch (Bloch 1933), often referred as Bethe-Bloch formula, reported in equation 1.1 in its form independent of the mass density. This expression is also known as mass stopping power.

$$\frac{S}{\rho} = -\frac{\mathrm{d}E}{\rho \mathrm{d}x} = 4\pi N_A r_e^2 m_e c^2 \frac{z^2}{\beta^2}\frac{Z}{A}\left[\ln\frac{2m_e c^2\beta^2\gamma^2}{I} - \beta^2 - \frac{\delta}{2} - \frac{C}{Z}\right] \tag{1.1}$$

where N_A is the Avogadro's number ($6.022 \times 10^{23}\mathrm{mol}^{-1}$), r_e is the classical electron radius expressed in equation 1.2 with $\epsilon_0 = 8.854 \times 10^{-12}$ F/m the permittivity of the vacuum, $m_e c^2$ = 511 keV the mass energy of the electron, $e = 1.6 \times 10^{-19}$ C the electron charge and c the speed of light,

$$r_e = \frac{1}{4\pi\epsilon_0}\frac{e^2}{m_e c^2} = 2.181 \times 10^{-15}\mathrm{m} \tag{1.2}$$

z is the charge of the projectile, Z and A are the atomic number and mass of the target material, respectively, $\beta = v/c$ is the projectile velocity, $\gamma = (1-\beta^2)^{-1/2}$, I is the mean excitation potential of the target material. The last two terms represent corrections for high energies (δ density effect correction term) and low energies (C shell correction term) incident ions. By observing equation 1.1, it clearly emerges how the energy loss rate is proportional to the square of charge and inverse velocity of the projectile. The target material composition also plays a major role. As the logarithmic term varies slowly with the target properties, and since Z/A is also almost constant, it turns out that the linear energy loss rate is proportional to the electron density, and thus to the atomic density (to be noticed, for clinical applications, that the density in a patient can vary by almost three orders of magnitude, ranging from the air cavity in the lungs to the most dense bones). As already mentioned, the energy loss increases for decreasing ion energy due to the $1/\beta^2$ dependence at high velocities (when the projectile velocity is much larger than its orbital electron velocities, and therefore remains fully stripped), and the maximum energy-loss rate, corresponding to the Bragg peak depth, is reached at the projectile velocity expresses as

$$v_p = z^{2/3} v_0 \tag{1.3}$$

where $v_0 = e^2/\hbar$ is the Bohr velocity ($\beta = 1/137$). For velocity values below v_p, corresponding to the average orbital velocity in the Thomas-Fermi atomic model, the ion captures electrons and its charge decreases, as well as the stopping force. However, the residual range is small (a few tens micrometers), and therefore the Bragg peak is assimilated to the end of the ion path. Note that, at very small velocities, atomic elastic collisions become important in the slowing down process.

Ion range

The energy loss rate equation directly leads to the definition of the ion beam range in matter (if we neglect nuclear interactions which cause a modification of the projectile nature), which is the integral over the incident energy of the energy loss per track unit, reported in equation 1.4. This formulation assumes a mono-dimensional ion trajectory with negligible lateral scattering (mentioned above and discussed below) and uses the CSDA.

$$R(E) = \int_0^E \left(\frac{\mathrm{d}E'}{\mathrm{d}x}\right)^{-1} \mathrm{d}E' \tag{1.4}$$

where E is the ion beam incident energy. To be noticed that the range is not a deterministic value, but it is intended as an average value and defined for the whole beam, not for single incident particles, which are affected by statistical fluctuations in the energy loss, leading to the so-called "range straggling" (described by different theoretical models, such as the ones in Bohr 1915; Landau 1944; Vavilov 1957, and detailed below). The integration of the Bethe-Bloch is often a hard task, but, as realized by Bragg and Kleeman (Bragg et al. 1905), the range dependence on the incident particle energy can be practically expressed with an analytic approach as the power law in equation 1.5. This approximation directly derives from studies on alpha particles which anticipated the formulation of equation 1.1.

$$R(E) = \alpha E^p \tag{1.5}$$

where E is again the ion beam initial energy, the constant α depends on the target material and the constant p is related to the projectile energy (or velocity). The proton range can be easily scaled to other ions at the same energy per nucleon in the same material with a factor M/z^2, where M is the ion mass. The range of ions with the same specific energy scales from water to other homogeneous material with a factor of A/Z^2.

Range straggling

The ion range predicted by equations 1.4 or 1.5 is an average value, calculated by considering a smooth and continuous energy loss process and neglecting the individual ion behavior. The actual range suffers from statistical fluctuations in the projectile energy loss that broaden the Bragg peak, in the so-called "range straggling". In general, the longitudinal beam straggling can be described by an asymmetric distribution (Vavilov 1957), which is approximated to a Gaussian in the limit of many collisions, leading to the expression of the relative straggling in equation 1.6:

$$\frac{\sigma_R}{R} = (M^{-\frac{1}{2}})\phi\left(\frac{E}{Mc^2}\right) \tag{1.6}$$

The ratio of the straggling width σ_R and mean range R is then all the more reduced as the ion mass (M) increases, with ϕ a slowly varying function which depends on the target material (Rossi 1952) and E the total ion energy. According to equation 1.6, it is interesting to notice how the relative straggling for carbon ions is about 3.5 times smaller with respect to protons (e.g. 7 mm and 25 mm at 18 cm of average range for carbon ions and protons, respectively - see Durante et al. 2016). In addition to energy loss fluctuations, range straggling contributions also come from the beam initial energy distribution: the actual beam is not perfectly mono-energetic, and the energy distribution width is determined by the accelerator and the beam optics elements. This contribution has to be added (quadratic sum) to the range straggling estimate. Figures 1.6c and 1.6d show the depth-dose profiles of proton and carbon ion mono-energetic beams, respectively, at different energies in water. The effect of range straggling is clearly visible in the broadening of the Bragg peak, which is more significant for protons with respect to carbon ions, and increases for increasing range in matter.

EM interactions with target nuclei

In addition to the energy loss process considered till here, which shapes the beam in the longitudinal direction (range variations), the actual delivered dose also depends on the lateral beam profile, which derives from the size and angular divergence of the incident beam and is mainly governed, at the target level, by elastic Coulomb scattering with atomic nuclei and

by secondary particles produced by nuclear fragmentation. In case an ion passes close to a target atomic nucleus, it is elastically scattered by the repulsive electromagnetic force: the projectile loses a negligible amount of energy, so that this kind of interaction can be neglected when calculating the energy loss rate described above, but the change in its trajectory must be estimated for range and dose predictions. Starting from the single scattering model by Rutherford (Rutherford 1911), and moving to the calculation of the statistical distribution function for the scattering angle at a certain penetration depth given by Bothe 1921, a complete theory allowing for the calculation of the scattering angle probability in case of Multiple Coulomb Scattering (MCS) has been proposed by Molière (Molière 1948) (confirmed to provide good predictions thanks to a large set of proton beam spread data - see Gottschalk et al. 1993). More practical formulas were then derived afterwards (see Gottschalk 2010; Highland 1975; Lewis 1950). The Molière formulation has been then simplified for analytic calculations towards a Gaussian approximation. The Gaussian standard deviation (σ_θ) expression in equation 1.7 is given by the characteristics MCS angle θ (Highland 1975)

$$\sigma_\theta = \frac{14.1\text{MeV}}{\beta pc} Z_p \sqrt{\frac{L}{L_{\text{rad}}}}\left[1 + 0.038 \ln\left(\frac{L}{L_{\text{rad}}}\right)\right] \tag{1.7}$$

where β, p and Z_p are respectively the projectile velocity, momentum and charge, c is the speed of light, L is the material thickness and L_{rad} is the radiation length (reported for common materials in Tsai 1974) expressed in equation 1.8.

$$L_{\text{rad}}(Z) = \frac{716.4}{Z(Z+1)\ln(\frac{287}{\sqrt{Z}})}\ \text{g/cm}^3 \tag{1.8}$$

with Z the atomic number of the material. Even if the Gaussian approach is not always accurate to describe the lateral beam spread (mainly at large angles), the Molière MCS description allows to retrieve the main parameters contributing to this effect: in particular, heavier particles have narrower lateral beam spread, and the scattering effect increases at increasing ion range (but is inversely proportional to the beam energy) and for high-Z materials. A more precise model of the lateral beam spread should involve nuclear reactions and the produced secondary particles, but an analytic approach is difficult and Monte Carlo (MC)-based calculations are necessary, but still time consuming. The empirical parameterizations are still strongly based on experimental data: as an example, measurements of the lateral beam spread in a water column for different beam energies (ranges) are reported in Pedroni et al. 2005. In Figure 1.4 the lateral spread of different ions in water is plotted as a function of range for various beam energies (A) and as a function of beam energy (B) after 15 cm range in water.

Nuclear reactions

In addition to the electromagnetic interactions with electrons and nuclei which mainly govern the stopping process, primary ions impinging on a target also undergo nuclear reactions with the target nuclei which may cause the disintegration of the projectile and the target nucleus or a partial fragmentation. In general, nuclear reactions induce modifications in the beam composition and cause variations in the longitudinal and lateral beam structure which must be taken into account for the delivered physical and biological dose estimate. Moreover, this kind of reactions leads to the production of secondary particles, such as secondary protons, neutrons, hydrogen and helium isotopes and other ions (mainly with heavy ion irradiation), and gammas. In the high velocity regime (when the relative velocity in the nuclei center of mass is much larger than the nucleon Fermi velocity), the nuclear interactions occurring between

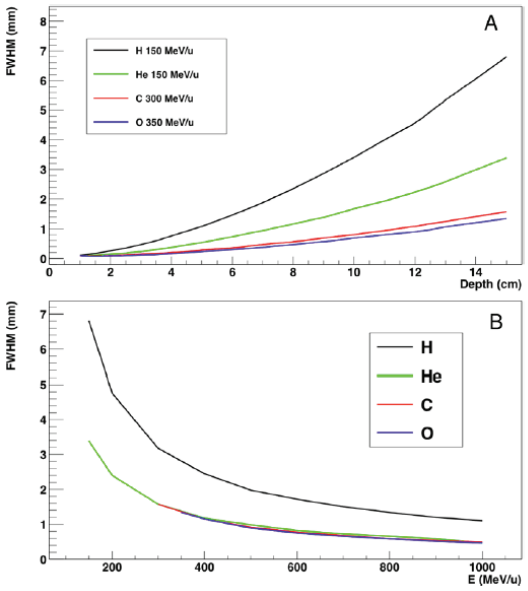

Figure 1.4: Lateral spread of different ions in water obtained with Geant4 Monte Carlo simulations. The Full Width at Half Maximum (FWHM) of the beam spot distribution is presented as a function of depth in water (A) for beams at different energies and as a function of beam energy (B) after 15 cm range in water. In Durante et al. 2016.

projectile ions and target nuclei can be described by a two-step process. At the "collision" stage, depending on the distance between projectile and target centers (impact parameter b), a variable number of nucleons is involved in the interaction and composes the reaction zone generally defined as "fireball". The so-called "spectator" nucleons are almost not affected and create projectile-like and target-like fragments ("fragmentation" process), often in excited states. After the collision, the excited fireball and fragments decay through the emission of secondary light particles, in the so-called "de-excitation" process, and the lighter fragments continue their path through the target. A schematic view of a typical nuclear reaction is given in Figure 1.5. Several models have been proposed to describe the nuclear interactions in their two steps. The Intra-nuclear Cascade (INC) model has been originally proposed by Serber and Heisenberg (Serber 1947), and later implemented in the sixties (Bertini et al. 1974), and is used to describe the collision stage. It is based on a series of two-body interactions between the incident particle and the target nucleons, which are considered quasi-free. For each nuclear interaction, the code models the complete outcome, and all produced particles are tracked until they are below a given energy threshold, in a process called "intra-nuclear cascade". Other candidates are the Quantum Molecular Dynamics (QMD), which describes each nucleon as a gaussian wave packet, and all nucleons are included in the collision, and the Boltzmann-Master-Equation (BME), which is a sophisticated model describing the thermalization of composite nuclei for low energy projectiles. The de-excitation stage can involve the so-called "evaporation" (Weisskopf 1937), where light fragments are emitted from the excited nuclei, "fission" of the excited nuclei in two fragments (for high-Z nuclei which can be only found in implants), "Fermi-breakup" of light nuclei which disassembles in smaller fragments (Fermi 1950), and gamma emission to dissipate the residual energy. The majority of the complete models for nucleus-nucleus reactions includes the previously described ones (often in simplified versions, optimized in order to minimize the calculation time) and is a variant of the so-called "abrasion-ablation" model (Hüfner et al. 1975), generally used in

transport codes. The abrasion phase describes the collision and the ablation one models the de-excitation stage; to be noticed that the ablation description is generally more adapted to peripheral collisions (high b), where the fragments are excited after the collision and decay to the ground state by emitting light particles and gamma rays.

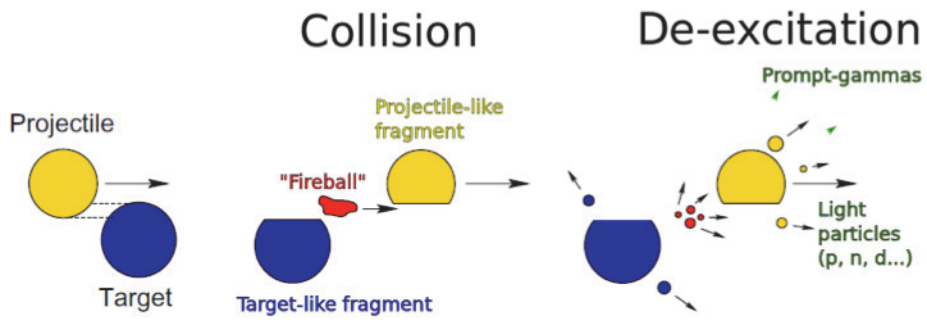

Figure 1.5: Schematic view of the nuclear reaction between a projectile and a target nucleus. The two steps are defined as "collision" and "de-excitation" processes.

Two main effects of the fragmentation processes are relevant to ion beam therapy. First, the described nuclear reactions cause a loss of primary beam particles; this effect is all the more important for increasing penetration depth. It is clear that in peripheral collisions (high b) the probability of primary ion loss is lower with respect to central collisions (small b), where projectile and target are most likely completely destroyed. Figures 1.6a and 1.6b (top panel) show the primary particle fluence loss in a proton and carbon ion beam, respectively, as a function of the depth in water. In the entrance region before the fall-off the fluence loss is caused by nuclear reactions, while close to the Bragg peak the fluence fall-off is mainly due to stopping of primary particles with zero residual energy. In addition, the range straggling effect is visible. Concerning carbon ion beams, as reported in Durante et al. 2016, during a standard treatment only 50 % of the primary ions reach the Bragg peak region for ∼20 cm range, while the others undergo fragmentation processes and are lost. Second, lower-mass and Z fragments result from the nuclear interactions in case of irradiation with ions heavier than protons (with proton beams, only secondary protons and neutrons are produced). The projectile velocity determines the velocity of the secondary fragments, which can travel with longer ranges with respect to the primaries due to their reduced mass and charge (remember the range scaling factor M/z^2): this produces a tail in the dose distribution (for ions heavier than protons). The features of this tail have been deeply studied for different primary ions species (^{10}B, ^{12}C, ^{14}N, ^{16}O, ^{20}Ne), and shell-structure effects have been verified with a non-direct relationship between proton number Z and tails extension (Schall et al. 1996). Figure 1.6d (and Figure 1.6b, bottom panel) shows the effects of nuclear reactions on the Bragg curves related to carbon ion beams at different energies stopping in water, measured in a water column (Schardt et al. 2008). With increasing primary energy and, consequently, beam penetration depth, the ratio between Bragg peak and entrance plateau dose is reduced by the decreased number of primary ions (this effect is also visible for proton beams in Figure 1.6c), while the tail after the Bragg peak is wider due to the increased number of lower-Z fragments traveling with longer range. In addition to this, the energy loss stochastic fluctuations are clearly visible in the broadening of the Bragg peak, as already described.

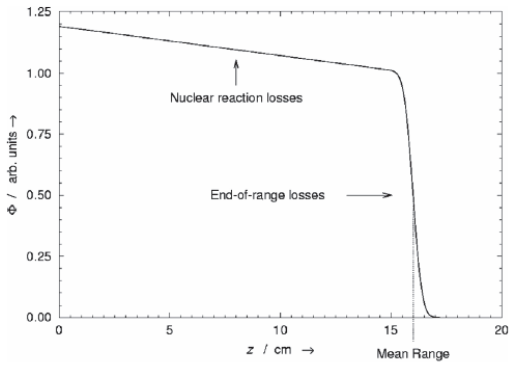

(a) Primary particle fluence loss in a proton beam as a function of the depth in water. In Newhauser et al. 2015.

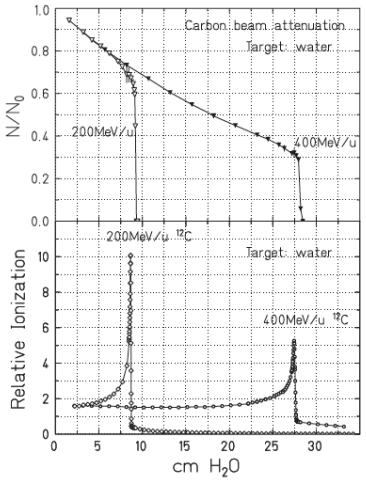

(b) Primary particle fluence loss (top panel) and corresponding Bragg peaks (bottom panel) of carbon ion beams as a function of the depth in water for two initial beam energies. In Haettner et al. 2006.

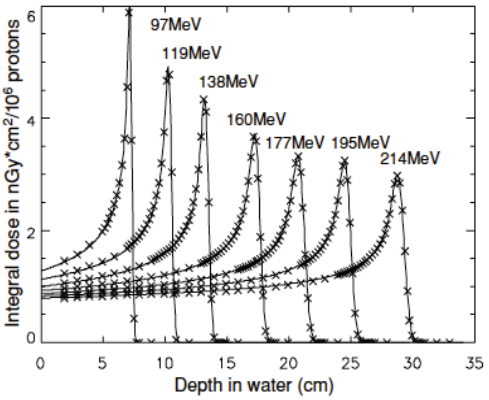

(c) Integral dose as a function of the depth in water for proton beams at 7 different energies. The crosses represent experimental points, the solid lines are the results of dose model calculations. In Pedroni et al. 2005.

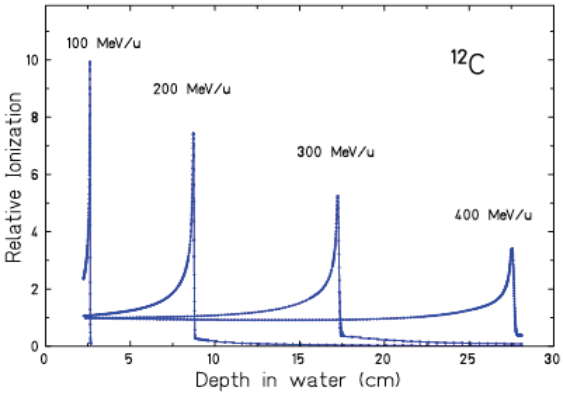

(d) Measured relative ionizations for carbon ion beams stopping in water. In Schardt et al. 2008.

Figure 1.6: Effects of nuclear interactions (first row) on proton (left column) and carbon ion (right column) beams and resulting dose distributions (bottom row).

Fragmentation processes have been deeply studied in nuclear physics and experimental data are available for many ion species at various energy (Friedländer et al. 1982). Dedicated studies for applications in radiotherapy started at Princeton (MacCabee et al. 1974) with oxygen beams and were carried out for many years at the Bevalac in Berkeley (Llacer et al. 1990, 1984b; Schimmerling et al. 1989, 1983), mainly with the neon beams used, at that time, for patient treatments. Similar studies were conducted later at the HIMAC facility (Matsufuji et al. 2003, 2005) and at GSI Helmholtz Centre for Heavy Ion Research, Germany (GSI) (Golovkov et al. 1997; Schall et al. 1996), where several ion species have been compared. Results concerning the build-up characteristics of secondary fragments, also based on carbon ion irradiation of water targets, are published in Haettner et al. 2006 and Haettner et al. 2013; in these works, 200 and 400 MeV/u ions have been used to investigate energy spectra and yields of the produced fragments at different angles and various depths along the beam path. A similar analysis has been carried out with 95 MeV/u carbon ion beam irradiation data collected at *Grand Accelerateur National d'Ions Lourds*, Caen, France (GANIL): in this case, Poly-Methyl-Metacrylate (PMMA) thick targets (5, 10, 15, 20 and 25 mm) have been used (Braunn 2010; Braunn et al. 2011). The obtained results have been compared to simulated data produced with fragmentation models implemented in Geant4 and mentioned in previous paragraphs, such as the Binary Intra-nuclear Cascade (BIC) (based on the INC) and the QMD models, showing that model improvements were still needed to reproduce the experimental data. Indeed, detailed information about fragmentation can be retrieved via Monte Carlo simulations and used to evaluate the impact on the delivered dose. As an example, in Wroe et al. 2005 the authors studied in simulation the impact of nuclear reactions in the dose delivered with proton beams in different targets, like water, tissue equivalent plastic, and International Commission on Radiological Protection (ICRP) muscle, bone and adipose. Simulations published in Grassberger et al. 2011 of 160 MeV protons in water allowed to estimate the dose contributions given by primary particles (between 90 % and more than 99 % of the total depending on the range), with the remaining fraction of dose mainly connected to secondary protons and α particles: negligible dose is given by heavier fragments. A more intense dose contribution from heavier fragments is expected for carbon ion irradiation, but an accurate Monte Carlo simulation of these processes is still a challenge. The dose deposition in the distribution tail beyond the Bragg peak has been also studied in simulation: in Francis et al. 2014, for example, the dose connected to nuclear fragments has been estimated in 36 % of the total.

As mentioned, in addition to charged fragments, nuclear interactions also produce gammas, mainly originating from atomic de-excitation processes (prompt-gammas) or from the annihilation of positrons emitted by β^+-emitter fragments (^{10}C, ^{11}C, ^{13}N, ^{14}O, ^{15}O), and neutrons, which can induce the emission of further gammas. All the secondary particles which can be absorbed by the target contribute to the total dispensed dose, while the others (with the exception of neutrons), escaping the target volume, can be exploited for non-invasive measurements of beam and target features. In particular, different techniques have been proposed and tested to measure secondary protons and gamma rays (both prompt-gammas and positron-annihilation gammas) with the aim of retrieving information about the ion range and obtain an online treatment verification. A detailed discussion about this topic will be given in section 1.1.5.

Focusing on neutrons, which are produced in large quantities and over a wide energy range, they cannot be exploited for primary ion range monitoring since their detection is not correlated with the ion path in matter (M. Testa et al. 2010). The neutron signal can be used to retrieve dosimetric information *in vivo*, as reported in Carnicer et al. 2014: the research group

at the *Centre Antoine Lacassagne*, Nice, France (CAL) studied the secondary radiation in the proton ocular treatment room as a function of the beam modulation, with a large volume ionization chamber. A strong correlation was found between the secondary ambient dose equivalent per proton dose and proton dose rate, which enables *in vivo* dosimetric verification independently of the beam monitoring system. In any case, neutrons must be modeled with care in order to evaluate the safety measures to be implemented in treatment centers (Newhauser et al. 2002), as well as the implications in the delivered dose and secondary cancer probability (Newhauser et al. 2011). The dose contribution caused by secondary neutrons strongly depends on the beam delivery system (see section 1.1.3 for the description of the beam delivery systems), as demonstrated in Gottschalk 2006. In particular, passive elements used for beam shaping have been identified as one of the main sources of secondary neutrons contributing to the total delivered dose to the patient (Yan et al. 2002), so that in modern facilities deflecting elements are set after the passive modules in order to limit the neutron flux towards the target. It is interesting to notice that the amount of produced neutrons and resulting dose is comparable for protons and carbon ion irradiation, even if the neutron yield is higher for carbon ions: this is due to the different beam intensities used in clinics for the two species, with more than a factor 20 in favour of protons. In Gunzert-Marx et al. 2008, the total dose due to secondary neutrons has been estimated for 20 Gy absorbed dose during 200 MeV/u carbon ion irradiation of a water target, and it resulted in 1 % of the total absorbed dose. Finally, if compared to photon standard radiotherapy at high acceleration voltage (about 25 MV), the neutron dose associated to ion beam therapy treatments results to be smaller, as demonstrated in recent studies (La Tessa et al. 2012; U. Schneider et al. 2015).

In the following section, the attention is focused on the biological aspects of this cancer treatment modality.

1.1.2 Biological effects of ion beam therapy

In addition to the already presented physical differences between photon radiation therapy and ion beam therapy treatments, a fundamental aspect to be addressed is the biological effect of such radiations. In the following, the main biological implications of radiation therapy are summarized with the aim of highlighting the favorable contribution given by charged particles with respect to photons and, at the same time, discuss some controversial points (Paganetti et al. 2013).

Any kind of radiation interacting and deposing energy in human tissues causes ionizations which lead to cellular and molecular effects. The effectiveness of ionizing radiation in curing cancer is based on the consequences produced by these ionizations, which can affect the double-helical DNA macro-molecules inducing various kinds of damages. In addition to this, other targets are also involved in the cell response to radiation, such as mitochondria and cellular membranes. In most of the cases, localized DNA damages, also called strand breaks, can be repaired with cellular reparation processes. In case DNA breaks are in close proximity they can originate the so-called Double-Strand Breaks (DSBs), both with direct ionizations of indirect process (such as δ-electron energy deposition and the creation of reactive chemical species). Figure 1.7a shows a schematic view of the different kinds of DNA damages induced by radiations, together with their effects in case of successful or unsuccessful reparation mechanisms. DSBs are generally harder to be repaired and lead to cellular dysfunction and loss of genetic material, resulting in cell death or in the loss of reproductive capacity. It appears clear

from this simplified presentation that not only the total absorbed dose, but also the ionization event distribution plays a major role in the determination of the radiation effectiveness (Belli et al. 1992). The absorbed dose is defined in ICRU 1980a, 1998 as

$$\mathrm{D} = \frac{\mathrm{d}\bar{\epsilon}}{\mathrm{d}m} \tag{1.9}$$

where $\mathrm{d}\bar{\epsilon}$ is the mean energy imparted by ionizing radiation to matter of mass $\mathrm{d}m$. To be precise, the imparted energy must also be defined: in the same ICRU reports we find that

$$\epsilon = R_{\mathrm{in}} - R_{\mathrm{out}} + \sum Q \tag{1.10}$$

with R_{in} and R_{out} the sum of the energies of all ionizing particles entering or leaving the volume, respectively, $\sum Q$ the sum of all changes of the rest mass energy of nuclei and elementary particles in any nuclear transformations occurred in the volume due to the ionizing radiation. As mentioned, for the same absorbed dose, the ability of killing tumor cells is linked to the nature of the delivered radiations via the ionization event distribution. It is useful here to introduce the concept of Linear Energy Transfer (LET), defined as the amount of energy deposited by a particle per track unit, directly related to the number of ionization per unit distance. In general, photons, x-rays and γ-rays are referred to as low-LET radiation, while the larger stopping power of protons and ions makes them a high-LET kind of radiation. For photon radiation, the distribution of the caused lesions is approximately random, while it is more closely related to the particle track for high-LET primaries (Lobrich et al. 1996) causing a clustering effect in radiation damage which has been verified to be effective for cell killing (Holley et al. 1996; Rydberg 1996). This is due to the nature of interactions of photons and ions in matter, already detailed in the previous section. Photons transfer energy to the cells by photo-electric or Compton interactions, with rather low cross-sections which determine a small number of ionization events and freed electrons per incident photon within the cell volume. Such freed electrons can further create secondary electrons along their path, but many photons are required to depose the prescribed dose, and the resulting ionization cluster distribution is almost homogeneous. The physical interactions of ions determine a completely different distribution of the deposited energy, localized along the ion path. The dose imparted in the radial direction is governed by a large amount of low energy electrons (Auger electrons) emitted in ion-atom interactions (also a limited amount of high-energy δ electrons are created), which are scattered by the medium atoms (electrons and nucleus) and cause secondary ionizations. The cross-section of these ionizations exhibits a maximum at about 100 eV, corresponding to a mean free path of a few nm. Given the DNA molecule size, this effect leads to a high probability of creating DSBs or correlated single-strand breaks. Cell survival studies (Blakely et al. 1984; Tobias et al. 1982) verified these theoretical considerations showing that heavy charged particles have an increased biological effectiveness compared to x-rays. These data are generally analyzed with a parameterization of the cell survival curve through a Linear-Quadratic (LQ) model (Hall et al. 2012)

Linear Energy Transfer

$$S(D) = \exp(-\alpha D - \beta D^2) \tag{1.11}$$

where S is the survival fraction, D is the absorbed dose and α and β are parameters which are experimentally determined, or obtained via radio-biological models (see section 1.1.4). The

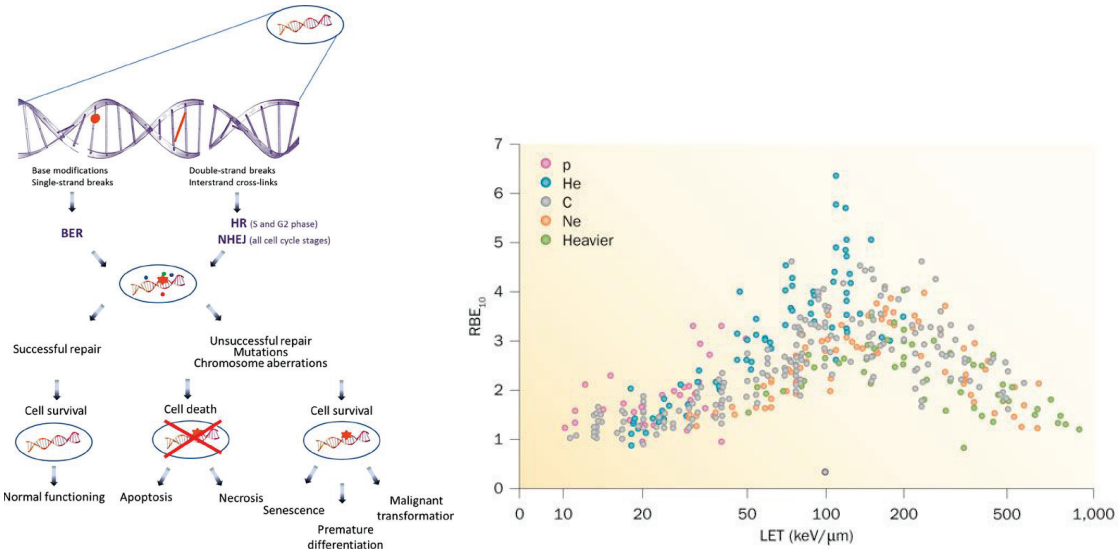

(a) Schematic representation of DNA damages caused by radiations. In Arena et al. 2014.

(b) Relative Biological Effectiveness (RBE) dependence on LET for different particle species. RBE is calculated at 10 % survival, LET values are given is keV/µm in water. Different ions are represented in different colors. Data points are extracted from the Particle Radiation Data Ensemble (PIDE) database. In Durante et al. 2016.

Figure 1.7: Ionizing radiations cause DNA damages in tissues, which are the basis for tumor radiation therapy. On the left side, the scheme presents the possible kind of damages induced by radiations on the cell DNA. The radiation effectiveness in killing cells is then related to the distribution of ionization events, which is all the more dense for high-LET primaries at low energies. The RBE is then enhanced for this kind of radiation. On the right side, the RBE is related to the LET for different ion species.

α/β ratio is linked to the radio-sensitivity of cells: the smaller it is, the larger the DNA repair capability will be. This is the rationale for fractionation in radiation therapy. Indeed, the total dose planned for the treatment of malignant cells is delivered in fractions along several days, because split doses have the advantage to spare normal tissues, with low α/β ratio, more than tumors, showing higher α/β ratio.

Relative Biological Effectiveness

Given the complex scenario presented till here, it is clear that the physical absorbed dose is not sufficient to describe the effect of the delivered radiation treatment, and weighting factors based on radiation protection data have been introduced to account for both the biological properties of ions and the response of different tissues. In order to transfer the experience from photon data to ion irradiation and to create a common evaluation parameter, the more powerful and versatile concept of RBE has been introduced. The RBE is defined as the ratio between the photon and ion doses necessary to produce the same biological effect (isoeffective dose):

$$\mathrm{RBE} = \left.\frac{D_{\mathrm{photon}}}{D_{\mathrm{ion}}}\right|_{iso} \tag{1.12}$$

where D_{photon} and D_{ion} are the absorbed dose for photon and ion irradiation. Notwithstanding the apparently simple definition, RBE results to be a very complex quantity, but for the moment the only one really used in clinics. It depends on several physical and biological parameters, such as LET, dose, dose rate, fractionation scheme, particle type, target biological features (radiosensitivity, oxygen concentration, etc.) (Durante et al. 2009). As a result, the RBE value changes along the primary ion path in matter, and is very difficult to be accurately predicted at the treatment planning stage. As an example, the dependence on LET is shown in Figure 1.7b. Although an accurate prediction is difficult to be obtained, the overall evolution of the RBE as a function of LET demonstrate a further advantageous feature of ions with respect to photons. From very low LET to approximately 100 – 200 keV/μm , the RBE increases: an overkilling effect determines then a drop at very high LET values. Thus, RBE is higher for low energetic high-LET particles, which cause larger ionization density as their velocity decrease. This effect means that in the Bragg peak region the biological effectiveness of such radiations is more pronounced with respect to the plateau entrance area, where healthy tissues are spared. The RBE enhancement for increasing LET is at present neglected in proton therapy, and a constant value of 1.1 is implemented in the clinical routine. This point is deeply discussed in the last years, and many simulation results and models have been produced to verify or propose modification to this usage (Giantsoudi et al. 2013; Giovannini et al. 2016; Guan et al. 2015; Jones 2015; McNamara et al. 2015; Sethi et al. 2014). Anyway, it is verified that a significant increase in RBE with respect to photons can only be achieved with heavier ions, as also shown by the experimental data reported in Figure 1.7b. For this reason, clinical trials have been conducted at the Lawrence Berkeley Laboratory starting from 1975 on different ion species such as He, Ne, N, O, C, Si, Ar (Castro 1995). Very heavy ions have the advantage of providing very-high LET (and so RBE) in the Bragg peak region, useful to overcome cell killing capability limitation due, for example, to cell oxygenation effects (discussed in the following) (Blakely et al. 1984). On the other side, heavy ions also show very high LET in the entrance region, which is not desirable. These results led to the implementation of carbon ion therapy, together with proton therapy, as a good comprise between radio-biological enhanced effectiveness in the target region (carbon-ion RBE ranges between 3 and 4 in the Bragg peak - see Wilkens et al. 2008) and limited LET in the entrance plateau. As outlined in previous lines, a further parameters to account for in the evaluation of the biological effects of radiations is the cell oxygen status . If compared to healthy tissues, tumor masses can grow in size producing malignant cells, and tumor core generally show lower oxygen levels. Even if the reason is not completely explained, hypoxic conditions cause an increased cell radio-resistance, probably linked to the reduction of indirect DNA damages induced by reactive chemical species. This effect is quantified via the Oxygen Enhancement Ratio (OER),

Oxygen Enhancement Ratio

$$\text{OER} = \frac{D_{\text{hypoxic}}}{D_{\text{aerobic}}} \tag{1.13}$$

with D_{hypoxic} and D_{aerobic} the absorbed dose for normal and reduced oxygen level resulting in the same clinical effect. Its value is about 3 for conventional radiation (Schardt et al. 2010), while it is reduced for ion irradiation due to the increased RBE, making them fundamental for curing tumors with hypoxic regions.

Only some of the biological aspects have been cited here, and all their clinical implications should be ideally taken into account for an accurate treatment planning. This is the reason why some of the points discussed here will be further addressed in section 1.1.4.

1.1.3 Accelerators and beam delivery

The goal of ion beam therapy is to treat deep-seated tumors with a conform dose distribution. Different ion species, hadrons and charged particles in general have been and are under study for the clinical application (neutrons, charged pions, antiprotons, helium ions – i.e. alpha particles –, heavier ions like lithium, oxygen, up to silicon ions), but only two are at present implemented for the patient treatments: protons and fully stripped carbon ions (Degiovanni et al. 2015). The ability of treating any kind of tumor at any depth in human body relies on the possibility of providing the employed particles enough energy to obtain a range of about 25 cm in soft tissues. The ions employed in treatment must be then accelerated to about 60 – 70 % of the speed of light ($\beta = 0.6 - 0.7$, see Durante et al. 2016) via different acceleration techniques and machines. This translates into maximum energy values of the order of 200 – 250 MeV and 4500 MeV (i.e. 375 MeV/u) for protons and carbon ions, respectively (Braccini 2010). In order to achieve the desired ion energy, sizable accelerators are needed and different solutions have been explored; at present, cyclotrons and synchrotrons are clinically implemented and available on the market. In the following, after a brief historical introduction, we sketch the main characteristics of the accelerators used in clinics, and we highlight the main features which are reflected in the treatment delivery. In addition to this, the beam delivery systems are described. Moreover, an overview of the main directions followed for the future acceleration and beam delivery techniques upgrade is provided.

1.1.3.1 Accelerators for ion beam therapy

Cyclotrons

The way towards the possible application of ion beams in therapy (proposed only later by Wilson - see R. R. Wilson 1946) was opened by the invention of the cyclotron by Ernest Orlando Lawrence in 1929 (Lawrence et al. 1932), which added a magnetic field to the recently proposed linear accelerator (Wideröe 1928). A cyclotron is composed of two hollow electrodes with a frequency-alternating voltage applied between them, which accelerates the charged particles at each revolution. The circular trajectory is obtained thanks to a fixed vertical magnetic field. A scheme of the main components of a cyclotron is sketched in Figure 1.8.

Nuclear physics saw a paramount development thanks to this invention, but also in the medical field the impact was remarkable. Already in 1935, Lawrence produced the first cyclotron-originated radionuclides, then used for radiotracing, diagnosis and treatment. The first cyclotron-based treatment was performed with fast neutrons (i.e. with kinetic energies between a few MeV and a few tens of MeV) in 1938, following a paper by Gordon Locher who underlined the therapeutic potentialities of neutrons (Locher 1936); the neutrons were produced by bombarding a beryllium target with cyclotron-accelerated deuterons (Stone et al. 1940). The unfavorable depth-dose distribution of neutrons and the difficulties linked to their collimation finally led to abandon the neutron treatments in 1948 (Stone 1948) and move towards proton-beam treatments in the 50's: neutrons were revised in 1965 by Catterall in London (Catterall et al. 1971) and are still used today in Boron Neutron Capture Therapy (BNCT) techniques (Barth et al. 2005; Nedunchezhian et al. 2016). As already mentioned in section 1.1, the first proton therapy treatment was conducted by Cornelius Tobias, and John Lawrence with the Lawrence cyclotron in 1954 (Tobias et al. 1958, 1955). Between 1954 and 1974, more than 100 patients were treated in Berkeley with cyclotron-accelerated protons. In parallel, in 1957 the first tumor was irradiated with protons at the Uppsala cyclotron in

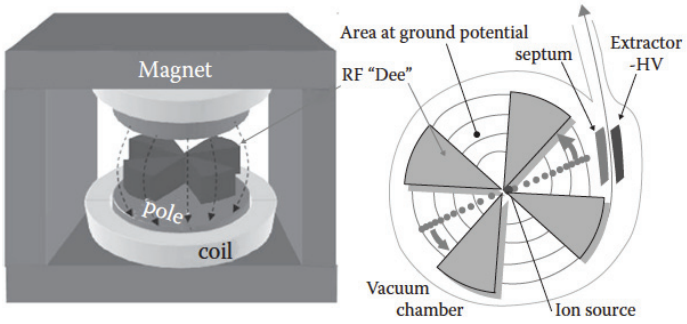

Figure 1.8: Schematic view of the main components of a cyclotron accelerator. On the left side the magnet is sketched together with the radio-frequency elements ("Dees"), which are also shown on the section depicted on the right side, with the ion source in the center. In Paganetti 2012a.

Sweden (B. Larsson 1962), and an intensive proton therapy program, led by Robert Wilson, was started in Harvard with a new-built cyclotron (R. Wilson 2004). Following these first experiences, new physics laboratories decided to set up proton beams for therapy (USSR, Japan, Switzerland), until the creation of the first hospital-based center, built at the Clatterbridge Oncology Center in the United Kingdom, which started operating in 1989 with a 62.5 MeV cyclotron. This historical overview shows how the cyclotron technology has soon spread all over the world, not only in research centers, but also for therapy purpose. The present cyclotron machines, which are now commercially available by different providers, still rely on the same accelerating principle as the first Lawrence system, but the technology has greatly advanced. In particular, the vertical magnetic fields in charge of bending the particles on a spiral trajectory has been improved, giving the beam the desired transverse compactness. Moreover, the beam extraction efficiency has been improved, and multiple extractions are now possible to supply different transport lines. Moreover, synchro-cyclotrons are a solution compatible with hadrontherapy applications. Based on the cyclotron accelerating principle, a synchro-cyclotron presents a variable frequency for the alternating voltage which is used to compensate for relativistic effects when the accelerated ions approach the speed of light. Such a solution has the advantage of allowing for the creation of more compact systems with high magnetic fields, and is at present exploited for commercial accelerators by the main providers.

Synchrotrons

In addition to cyclotrons and synchro-cyclotrons, other accelerating machines initially developed for fundamental research have been translated to medical applications and are nowadays knowing a large diffusion: the synchrotrons. While the cyclotron present a fixed-value magnetic field, so that the radius of the beam trajectory increases during the acceleration process, in the synchrotron the trajectory radius is kept constant thanks to the variation of the bending magnetic field. The boost is provided by radio-frequency cavities, based on the same principle as the one composing linear accelerators: the radio-frequency increases to follow the particle revolution speed, and this acceleration principle allows to overcome the cyclotron energy limitation, as well as to obtain beam at different energies by tuning the extraction process. The invention is based on the independent ideas of Vladimir Veksler (Veksler 1944) and Ed-

win McMillan (McMillan 1945): the latter both coined the name of the machine in its letter, and constructed the first electron synchrotron in 1945 in Berkeley. Some years later, the first proton synchrotron was designed in 1952 by Sir Marcus Oliphant, who already published a preliminary sketch of the machine in 1943 (Oliphant 1943). As for the cyclotron case, several years have been required to see the construction of the first hospital-based hadrontherapy facility using a synchrotron. The first center was built at Loma Linda University in California, were a 7-m-diameter synchrotron constructed by Fermilab was installed and started treating patients in 1990. The center has been a pioneer in the field also for the presence of three 10-m-diameter rotating gantries. After the clinical studies performed at the University of Tsukuba, in Japan, between 1983 and 2000, with the treatment of about 700 patients with synchrotron proton beams, a second hospital-based center was built and equipped with an Hitachi synchrotron and two rotating gantries. Since the first use of synchrotrons for treatment purpose, several improvements have been achieved in the accelerator technology to better adapt its features to the hadrontherapy needs. In particular, the beam size can be now reduced with strong focusing optics, and the beam energy can be varied on a single spill basis (1 – 2 s). At present, all the hadrontherapy facilities in operation are based on circular accelerators (cyclotrons and synchrotrons): proton beams are produced with both the solutions, while only synchrotron-produced carbon-ion beams are used. In Figure 1.9 the size of different accelerators design is compared (CABOTO is still at the design stage, the Ion Beam Applications, Belgium (IBA) / ARCHADE superconducting carbon cyclotron in France is under design, while HIT, *Centro Nazionale di Adroterapia Oncologica*, Italy (CNAO) and the SIEMENS accelerator are at present in operation).

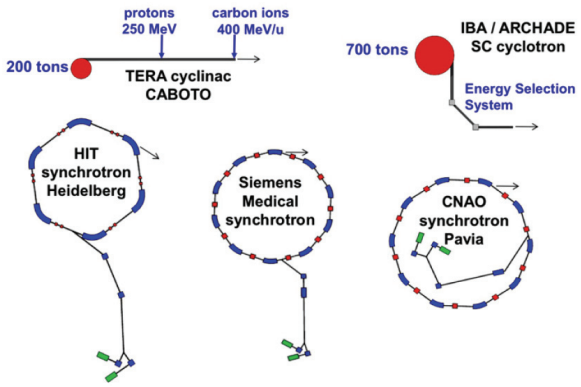

Figure 1.9: Comparison of the size of various ion accelerators for hadrontherapy. CABOTO is a cyclinac studied by the TERA Foundation; the superconducting cyclotron, designed by IBA, will be installed in Caen, France, within the ARCHADE project; HIT and CNAO are in operation in Heidelberg, Germany and Pavia, Italy, respectively; the SIEMENS synchrotron is installed in Marburg and Shangai. In Amaldi et al. 2010a.

Novel acceleration approaches

In the past years, novel approaches have been proposed to improve the present accelerators and beam features, mainly for what concerns the beam quality and the machine size and cost. It is worth to mention the Fixed Field Alternating Gradient (FFAG) accelerator, which combines the fixed magnetic field and variable radio-frequency with separated sector magnets (Sheehy 2017). This approach allows for the production of higher intensity beams with respect to

synchro-cyclotrons, and for the variation of the extracted beam energy at high repetition rate. Some designs have been proposed for hadrontherapy applications in the last decade (Antoine et al. 2009; Peach et al. 2010), but the present machine size still limits its spread in treatment centers. Furthermore, linear acceleration approach has been proposed since 1991 in both "all-linac" (Hamm et al. 1991; Lennox 1991) and "cyclinac" (Amaldi 2009) solutions. In addition to the compactness, the main advantage of linacs is the possibility to continuously vary the output beam energy on a pulse to pulse basis; moreover, there is neither the need for complex injection or extraction systems, such the ones used in synchrotrons, nor the need of an energy passive modulation technique as the one used in cyclotrons (see section 1.1.3.3). An extended description of linear accelerators for hadrontherapy is given in Amaldi et al. 2009. Following the first successful prototypes tested by the TERA Foundation and the Italian *Istituto Nazionale di Fisica Nucleare*, Italy (INFN) in the last twenty years (Amaldi et al. 2004; Ronsivalle et al. 2011), the *Conseil Européen pour la Recherche Nucléaire*, Geneva, Switzerland (CERN) spin-off company Advanced Oncotherapy (A.D.A.M.) is proposing a commercial solution called Linac for Image Guided HadronTherapy (LIGHT). A further solution can be given by the Dielectric Wall Accelerator (DWA) (Caporaso et al. 2009), where the acceleration tube is made of High Gradient Insulator disks alternated with conducting elements. A laser pulse is used to activate the switching units connected to these conducting modules. Very interesting thanks to a reduced size, this acceleration scheme still suffers beam focusing issues; moreover, it presents very short pulses which force a very precise selection of the number of ion per pulses at the source level. Finally, the electric field needed for reducing the machine size till 2 – 2.5 m is of the order of 100 MV/m; this challenging value has not been achieved yet, even if a prototype is under study at the Lawrence Livermore National Laboratory, USA (LLNL), with promising results (Hettler et al. 2013; Zografos et al. 2013). Another attractive technique is the so-called "laser driven" acceleration, based on the use of short and powerful laser pulses irradiating a thin target, with the generation of a plasma field (Tajima et al. 2009). The electrons emerging from this plasma are able to induce a strong electric field which accelerates the protons (or ions). Again, this solution would allow for the creation of very compact systems, with relatively simple and light beam optics, but some issues are still under study to be solved; in particular, the accelerated beam has an almost continuous energy spectrum which forces to implement energy selection solutions to be adapted to treatment purposes.

1.1.3.2 Beam time structure

A particle beam can be described by a set of quantifying parameters which relates to single particle properties or to a collection of particles. In addition to the beam energy (which should be defined as an energy spectrum), beam current (which describes the beam intensity as the flux of particles per time unit) and emittance (transverse size and momentum), it is worth to describe in details what is defined as time structure. A basic distinction is made between continuous beams and bunched beams. Whenever particles are accelerated by means of radio-frequency varying fields, the accelerating machine output is a bunched beam, composed of bunches with fixed time length. Concerning the acceleration systems employed to produce clinical beams, synchrotron and cyclotrons (or synchro-cyclotrons) present strongly different time structures. In order to give an overall description of the typical time features of synchrotron- and cyclotron-produced beams, it is possible to distinguish between micro- and macro-structure. The macro-structure describes cycles of beam acceleration and extraction, the latter characterized by an internal micro-structure. By comparing the two cited kinds of accelerators, it is possible to approximate the cyclotron-produced beams as continuous, with a

macro-structure characterized by sub-millisecond periods (depending on the specific machine) and approximately 10 % duty cycle (fraction of period with active ion delivery). Synchrotrons produce pulses which are separated in periods of several seconds, with duty cycles similar to the ones of cyclotrons (10^{-1} on average). For synchro-cyclotrons, the duty cycle is approximately 10^{-3}. Each accelerator pulse (for both cyclotrons and synchrotrons), corresponding to one extraction cycle, contains several micro-bunches, creating the micro-structure. For cyclotrons, micro-bunches duration is in the ns scale, while a synchrotron micro-bunch can last several tens of ns. The period separating micro-bunches varies in the range of tens of ns for cyclotrons till hundreds of ns for synchrotron beams.

Table 1.1 shows the orders of magnitude for the beam time structure for some particle accelerators used in the clinical routine. The differences between synchrotrons, cyclotrons and synchro-cyclotrons are evident. In addition, the beam typical intensity is reported.

Table 1.1: Orders of magnitude of main time structure parameters for some accelerators used in clinics. Reproduce from Krimmer et al. 2017b.

		Synchrotron		**Cyclotron C230 IBA**	**Cyclotron Varian**	**Synchro-cyclotron S2C2 IBA**
		^{12}C	Protons			
Typical intensity (ions/s)		10^7	10^9	10^{10}	10^8 – 10^{10}	$\sim 10^{10}$
Macrostruct.	Period (s)	1 – 10			/	10^{-3}
	Duty cycle	10^{-1}			10^{-1}	10^{-3}
Microstruct.	Bunch width	20 – 50		1 – 2	0.5	8
	Period (ns)	100 – 200		10	14	16
	Ions/bunch	2 – 5	200 – 500	200	2 – 200	4000

An accurate knowledge of the beam time structure is of utmost importance for the optimization of the interface to the beam delivery systems (see section 1.1.3.3), for the treatment planning, as well as for treatment monitoring purpose. The design of detectors able to exploit the emission of secondary particles to retrieve beam range and dose information must account for the beam time structure in order to evaluate the best solution to deal with signal background, counting rate and read-out channel occupancy. This topic will be further discussed in section 1.1.5 where the sources of uncertainties affecting ion beam therapy treatment are described and the detection monitoring solutions are presented. In particular, for the specific case of Prompt-Gamma (PG) detection (one of the main topic of this thesis work), a complete overview is given in chapter 2.

1.1.3.3 Beam delivery systems

Once accelerated, the high-energetic ions must be delivered to the patient in order to be conform to the treatment specification, focusing the provided dose on the Planned Target Volume (PTV). As described and detailed in section 1.1.1, the beam range can be varied by modulating the primary particle energy with the aim of covering the whole tumor volume. The Bragg curve obtained with a mono-energetic beam is called “pristine Bragg curve”, and can

be used to irradiate a section of the target volume at a given depth. The superposition of several pristine Bragg curve is necessary to deliver the prescribed dose to the tumor, which has been previously modeled in three dimensions. In particular, the beam energy spectrum has to be spread in order to increase the axial dimension of the peak region, in the so-called Spread-Out Bragg Peak (SOBP). At the same time, the beam fluence must be adapted to avoid over-irradiation of the entrance region. An example of SOBP is given in Figure 1.10. Note that the distal spot has a significantly higher fluence than proximal ones, since there is no contribution of higher energy particles. This is true for single field treatments , while for several field treatments different spot fluence structures can be used. This will have an influence on the sensitivity of the method used to control the position of the distal part of the SOBP, as discussed in section 1.1.5.

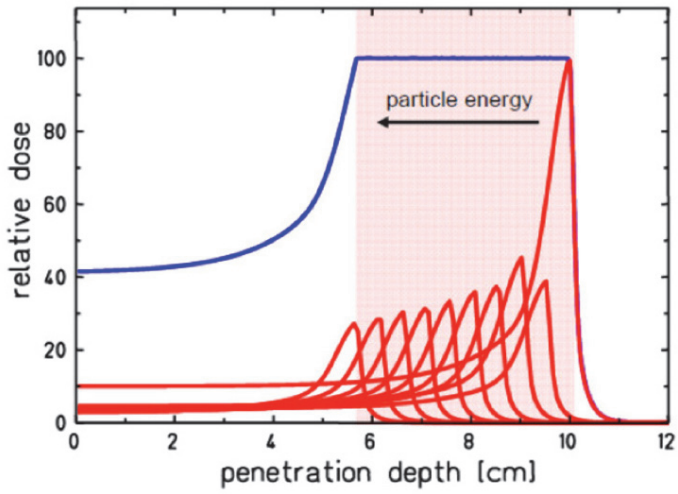

Figure 1.10: Example of SOBP. The target region is highlighted and the discrete pristine peaks composing the SOBP are sketched in red. In Durante et al. 2016.

All the described tasks are in charge of the beam delivery system, which must be optimized to interface with the accelerator and to the patient by transporting the beam to the treatment area and adjusting its features to obtain the desired dose distribution. The delivery systems implemented in clinics are based on two main strategies: passive beam modulation and active scanning. For an extensive presentation of this topic, refer to Gottschalk et al. 2008. The technique must be chosen according to the accelerator machine: it is important to remind that cyclotrons provide fixed energy beams with pulses separated by tens of nanoseconds, while in a conventional synchrotron the energy can be varied cycle by cycle, with short pulses generally separated by 1 – 2 s dead-time (see section 1.1.3.2).

Passive beam shaping

The passive beam delivery approach generally applies to cyclotron-produced beams, and its principle is sketched in Figure 1.11. The beam extracted from the accelerator is fixed in size and energy, and is first broadened by scattering devices. Afterwards, a range modulator (generally a rotating wheel) is used to spread out the mono-energetic Bragg peak with the aim of covering the whole target thickness. The wheel periodically inserts material of varying thickness into the beam line, resulting in a range modulation with the desired features. The obtained SOBP can be shifted as a whole thanks to the addition of range shifters of fixed thickness. After the energy (range) adaptation, the beam is shaped according to the PTV

definition with collimators (often multi-leaf) and compensators, which are specific to each patient and irradiation port.

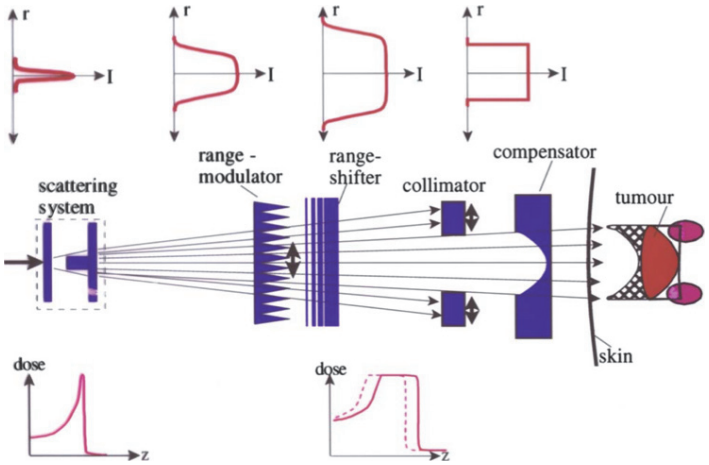

Figure 1.11: Schematic view of a fully passive beam delivery system. In Schardt et al. 2010.

The passive beam delivery technique presents three main disadvantages with respect to the active delivery described in the following. First, the structure of the created SOBP is fixed and the depth-dose can only be tailored to the distal end of the target volume and not to the proximal end, given the fact that the SOBP can only be shifted towards the entrance region. This feature automatically leads to a considerable dose given to normal tissues outside the target volume, in particular in the proximal part, as illustrated by the hatched region in Figure 1.11. Second, the amount of material inserted in the beam line causes nuclear interactions which lead to the creation of secondary high-LET fragments (mainly neutrons), affecting the dose delivered to the entrance region. Third, each collimator/compensator are specifically designed for each patient irradiation port, which leads to complex and costly manufacturing for such devices. The main asset of passive beam delivery is that the whole target volume is irradiated at once, which leads to shorter irradiation times. This last point is quite important for the irradiation of large PTVs.

Active beam scanning

When the beam is produced with a synchrotron, the possibility to switch the energy from pulse to pulse makes feasible an active target scanning and beam range adaptation. Active beam delivery is also possible with cyclotron-accelerated beams, but the beam energy is modulated with degrading passive elements, and a spectrometer is needed for energy selection, at the cost of an important intensity reduction. The active beam delivery systems exploit the electrical charge of the accelerated particles to deflect the beam laterally through magnets and perform a scan of the defined treatment field. A schematic view of an example of active delivery system is provided in Figure 1.12. The target volume is divided into iso-energetic layers which are irradiated sequentially by deflecting the beam with dipoles in order to fully cover a grid of pre-defined voxels.

Even though this approach is demanding from the accelerator performance point of view, it brings several advantages with respect to a passive one: there is no need for patient specific equipment like collimators and compensators, and any volume can be in principle covered with a conformal dose; the dose can be adapted on a single voxel basis; the material in the

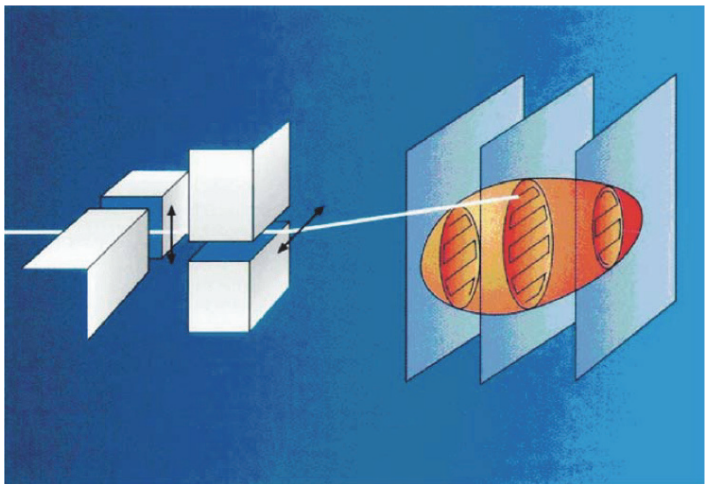

Figure 1.12: Schematic view of a fully active beam delivery system. In particular, here the GSI raster scanning system is depicted. In Schulz-Ertner et al. 2006.

beam line close to the patient is minimized so that the production of secondary particles is strongly reduced. With such a delivery system, the term Intensity-Modulated Particle Therapy (IMPT) has been introduced, in analogy to the Intensity-Modulated RadioTherapy (IMRT) techniques applied in standard photon radiotherapy. Indeed, the IMRT exploits multi-leaf collimators to tailor the beam to the target, so that it results to be similar to ion passive delivery systems. In photon therapy, the beam modulation on a single spot basis is possible with cyber-knife machines (Srivastava et al. 2015). The first so-called "spot-scanning" system was introduced at National Institute of Radiological Sciences, Japan (NIRS), already in the early 80's (Kanai et al. 1983). This first experience was soon followed by a pilot project of spot-scanning at Paul Scherrer Institut, Villigen, Switzerland (PSI) (Pedroni et al. 1995) and by the realization of a fully 3D scanning beam system at GSI, where the "raster-scan" technique is implemented (Haberer et al. 1993) (with the beam moved from one voxel to the next one with no interruptions, and all points in an iso-energy slice connected together in a dense grid). Nowadays, various companies are offering commercial scanning beam system solutions, so that a rapid spread of this convenient technique is foreseen for the next years. The counterpart of the active scanning system is a relatively slow delivery of a given dose in a large tumor volume (minimum 1 ms per spot - Durante et al. 2016), which can be more rapidly covered by passive delivery approaches.

Rotating-gantries

We described till here static beam configurations, with a fixed irradiation position. In the clinical routine, in order to further improve the target volume-to-healthy tissue dose ratio, various beam penetration angles can be foreseen, similarly to standard photon therapy (even if a reduced number of different angles is required). In addition to this, deep-seated tumors close to OAR can require specific irradiation angles to be treated with the desired safety margins. In order to achieve this goal, two approaches are possible: rotate the patient or rotate the beam line. Even if the patient rotation solution has been explored in the past, several reasons are in favor of a fixed supine position, with only horizontal rotations allowed: the supine position is in compliance with the pre-treatment imaging (Computed Tomography (CT) scan) used for treatment planning (see section 1.1.4); a patient rotation necessarily leads to organ motion which is undesired; the supine position is more reproducible in the different treatment

fractions. As a consequence, rotating gantries have been developed to allow for the beam line displacement. The electron linacs employed in conventional radiotherapy are generally mounted on gantries which can rotate 360 degrees around the patient couch to select the optimum beam direction. Likewise, in hadrontherapy, rotating gantries solutions have been designed for both protons and heavier ions. In contrast to the compact gantries used in standard radiotherapy, the high beam magnetic rigidity (defined as the product of the bending radius and the required magnetic field strength, equal to the ratio of momentum to charge of the particles) is a constraint on the size of these structures for proton therapy, and, much more, for heavier ion therapy. In general, the beam is first deflected away from the extraction axis, and then bent back to the patient direction with several dipoles. Moreover, quadrupoles are use to optimize the beam focusing before the treatment room. A scheme of a standard gantry design is given in Figure 1.13a. As already mentioned in section 1.1.3.1, the first gantry for protons was installed at the Loma Linda University Medical Center in 1990, followed in 1996 by the first one in Europe at PSI in 1996, which also included an upstream scanning system (Pedroni et al. 1995). At present most of proton therapy centers are equipped with at least one rotating gantry. The huge dimensions imposed by the carbon ion beam rigidity (three times bigger rigidity for 5000 MeV carbon ions with respect to 200 MeV protons) limited the implementation of such a technology in carbon therapy centers, while different technical solutions have been explored. As an example, at HIMAC, in a single treatment room the beam can be delivered to the patient via an horizontal and a vertical line, for the sequential treatment from different angles. The first rotating gantry system for heavy ions was installed at HIT and is now in operation: the diameter is of 13 m, for a total weight of about 700 tons (see Figure 1.13b).

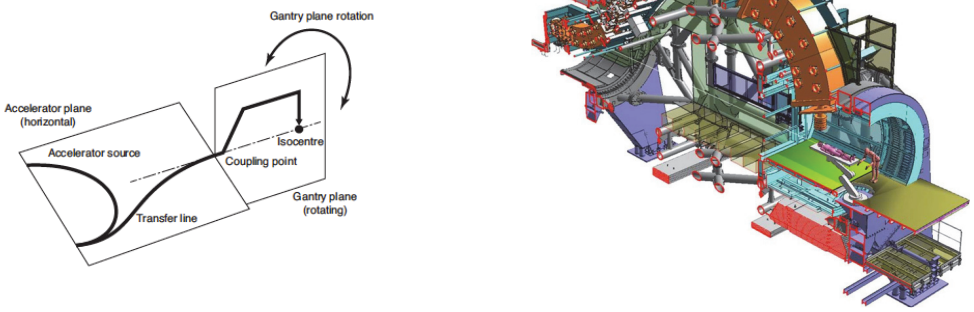

(a) Schematic design of a rotating gantry installed in a particle therapy center. In Owen et al. 2014.

(b) Scheme of the HIT ion rotating gantry. In Schardt et al. 2010.

Figure 1.13: Schemes of a standard gantry design (left) and of the carbon-ion rotating gantry installed at HIT (right).

Intense research efforts are dedicated to improve the gantry technology, mainly directed towards the implementation of more compact systems equipped with superconducting magnets. A first superconducting carbon ion gantry has been recently installed at NIRS, and is approximately half size with respect to the German one (Iwata et al. 2013).

1.1.4 Treatment planning

Given the available accelerator and beam delivery system, the best possible treatment features are elaborated by the treatment planning process, which combines the clinical information about the patient with the physical an biological aspects of particle therapy. The treatment planning is always patient and disease-specific, and is based on imaging techniques providing the physicians with the data necessary to delineate the target volume and the surrounding OAR. The minimal approach is represented by a pre-treatment x-ray CT scan, providing quantitative information about the anatomical structures via photon attenuation images. As briefly outlined in the previous paragraph, it is important to record the pre-treatment images in the same conditions (patient position, fixation structures, etc.) later applied in the treatment itself. Complementary imaging devices, such as MRI and PET (Levy 2007), are often used in combination with CT to improve the target definition quality, mainly in case of proximity with OAR. In addition to the target delineation, the physicians are also in charge of the therapy prescription, which includes the total dose to be delivered to the PTV, the dose limits for the surrounding tissues, and the fraction planning. All the listed information are the input for the Treatment-Planning System (TPS) , which makes the connection between the prescribed dose distribution and the beam acceleration and delivery devices. The physicists and clinicians use the TPS to define all the treatment beam-specific features such that the clinical prescription is satisfied at the maximum extent. The software output details the beam entrance ports to be used (in terms of gantry positions, if a gantry is available), the beam ranges and intensities, the irradiation scheme in terms of dose-per-voxel, and, more generally, the expected dose distribution in the patient, which allows to quantify the Tumor Control Probability (TCP) and the probability of complications to the normal tissues. As the whole planning process is based on x-ray CT scans, providing photon beam attenuation images, a relationship between the CT values and ion Relative Stopping Power (RSP) is needed. The CT values are expressed in Hounsfield Units (HU), defined as

Treatment-Planning System

From Hounsfield units to relative stopping power

$$\text{CT value}(\vec{x}) = 1000 \times \frac{\mu(\vec{x}) - \mu_W}{\mu_W} \tag{1.14}$$

where $\vec{x}$ is the considered location, $\mu(\vec{x})$ the x-ray absorption coefficient in tissue, μ_W the one in water as reference. Water is always used as reference medium, in particular through the concept of Water-Equivalent Path Length (WEPL). There is not a functional relationship between the two quantities, and systematic studies have been carried out at PSI for protons (Schaffner et al. 1998; U. Schneider et al. 1996). For carbon ions, similar investigtions have been performed at NIRS (Kanematsu et al. 2003; Matsufuji et al. 1998) and GSI (Jäkel et al. 2001a; Rietzel et al. 2007), and experimental verification has been obtained via measurements on animal tissues. In Figure 1.14 the data of a look-up table for the conversion of HU into carbon ion WEPL are plotted in the HU range of relevant biological tissues.

The conversion factors are tabulated and implemented in the main TPSs, but several studies are still ongoing in order to optimize the calibration accuracy (as an example, see Inaniwa et al. 2018). As highlighted in several research works, this is one of the main sources of uncertainty affecting proton and carbon ion range prediction and, so, treatment precision. Possible investigated solutions to reduce systematic uncertainties in the RSP determination related to the Hounsfield unit conversion are represented by proton Computed Tomography (pCT) and dual energy x-ray CT (Yang et al. 2010). Further details will be given in section 1.1.5. In addition to the beam range determination, the TPS software must also deal with biological dose

Biological dose modeling

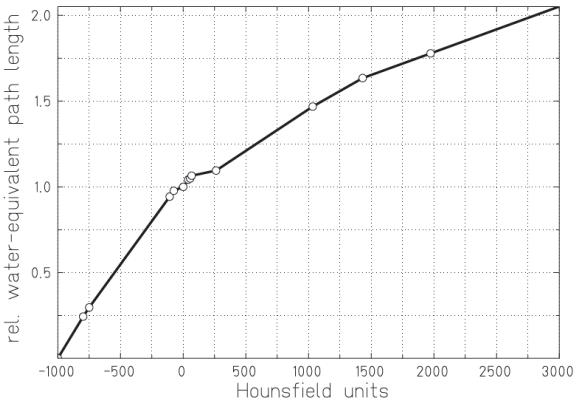

Figure 1.14: Hounsfield look-up table for carbon ion treatment planning, based on the data collected at GSI and reported in Jäkel et al. 2001a. In Rietzel et al. 2007.

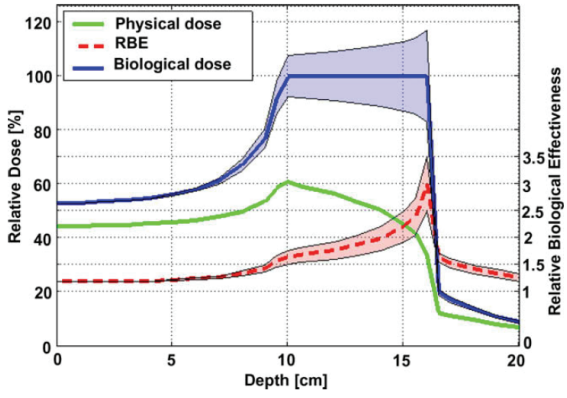

Figure 1.15: Comparison of physical (green solid line) and biological (blue solid line) dose for a 290 MeV ^{12}C ion beam with a 6 cm SOBP for a maximum RBE of 3.0. The RBE varies in the range 2.5 – 3.5 and an uncertainty band is sketched to represent the biological dose possible variation due to the selection of the RBE value (dashed-red line). In Suit et al. 2010.

calculations. Indeed, as highlighted in section 1.1.2, charged particles differ from photons in their radiobiological properties and effects. Notwithstanding the 10 – 20 % RBE variations verified for protons with varying LET along the path in the patient tissues, a practical constant value of 1.1 is generally used in clinics (ICRU 2007; Paganetti et al. 2002). This value corresponds to the average RBE at mid SOBP overall dose levels. In the distal section of the Bragg peak, a higher RBE has been verified; this effect slightly affects the dose profile fall-off in protontherapy and is not modeled in the present planning systems. As mentioned in section 1.1.2, several studies are ongoing in the last years with the aim of optimizing the biological models and applying a variable proton RBE in clinics, and the topic is still open to discussion in the expert community (Lühr et al. 2018; Paganetti 2014; Paganetti et al. 2013; Unkelbach et al. 2018; Willers et al. 2018). A different approach must be applied to heavy ions (carbon ions in particular), given the much stronger dependence of their RBE on the various parameters listed in section 1.1.2. Focusing on carbon ions, treatment plans are generally optimized using the so-called RBE-weighted dose, calculated according to verified models based on experimental data. In Figure 1.15, the physical and biological doses absorbed during a carbon ion beam irradiation with a SOBP are compared and the RBE variation along the beam path is also reported, together with the estimated uncertainties which also affect the RBE-weighted dose evaluation. For this purpose, two main models are nowadays implemented in clinical practice. On one side, the Japanese centers use a model developed at NIRS, based on in vitro cell killing experiments on human salivary glands and neutron irradiation experience gathered at HIMAC, as well as on the application of the LQ model (Matsufuji et al. 2007). Recently, a modified Microdosimetric Kinetic Model (MKM) has been introduced in order to optimize the plans to active scanning with ion beams (Inaniwa et al. 2015). On the other side, a specific biophysical model has been developed in Germany at GSI, called Local Effect Model (LEM), and it is now used in the clinical centers in Germany, Italy and China. Its main idea is to transfer known cell-survival data for photons to ions, assuming that the difference in biological efficiency arises only from a different pattern of local dose deposition along the primary beam (Jäkel et al. 2001b; Krämer et al. 2000). The two models have been verified to give comparable results, in agreement with the measured RBE, with in-vitro experiments on mice cells (Uzawa et al. 2009), while different predictions are obtained when different treatment schemes on different tissues are studied (Fossati et al. 2012; Steinsträter et al. 2012). Besides, the NanOx model (described in Cunha et al. 2017) is being developed in order to address some of the flaws of the LEM and MKM. The model is able to predict cell survival with good agreement to experimental data, and its parameters are under study for optimization (Monini et al. 2018). The definition of a common effective dose prediction method is ongoing: this will allow for comparative studies of clinical results and for an improved collaboration of the few ion treatment centers operating all over the world. These biological models are applied for the planning of active scanning carbon ion treatments, for which the target volume is previously divided into slices: the dose is then optimized for iso-range slices. In contrast, for proton passive beam delivery systems, the plan optimization is generally reduced to the study and production of the patient-specific beam modulators. In the future, biology-guided forms of proton therapy can be foreseen; the RBE variations, instead of being an issue for which corrections are needed to the treatment planning, could be used to the treatment effectiveness advantage. Focusing on the possible direction of improvements in the future of treatment planning , the research efforts are concentrated in the last years also on another fundamental topic: the treatment of moving organs. It is clear that the well-defined ion range and narrow dose peak make ion treatments potentially more sensitive to inter- and intra-fractional organ motion, as highlighted in Bert et al. 2008; Engelsman et al. 2013; Phillips et al. 1992 and Thörnqvist et al. 2013, as an example. Concerning the organ displacement between following fractions, it can be corrected by more

Treatment of moving organs

frequent imaging scans, ideally a new one before every treatment fraction, in order to adapt the treatment planning to weight variations, target size modifications and similar anatomical effects. The organ movement caused by the respiratory cycle requires more complex strategies to be taken into account for the treatment plan and delivery. The respiratory motion patterns are genarally complex and not regular, involving translational and rotational displacements. Several strategies to mitigate the effect of organ motion are being investigated, some of them directly coming from the experience acquired in IMRT. As well summarized in Schardt et al. 2010, among these strategies it is worth to mention rescanning of repainting techniques, based on the average effect of several irradiations with reduced beam fluence on the same iso-range slices; gating techniques, which aim to correlate the irradiation active time to a continuous monitoring of the respiration cycle; tracking, which requires a 3D compensation of the target motion in real-time, particularly adapted for scanning techniques. A further step will be the real time monitoring of moving organs by means of external markers linked to biomechanical modelling of internal organs (Manescu et al. 2013). Some of the cited techniques, or combinations of them, are being tested and are now at the validation stage, but there is still wide room for improvements towards the application of 4D treatment planning (Bert et al. 2017; Graeff et al. 2013). Further information about this topic can be found in a recent review by Kubiak (Kubiak 2016). Range predictions, biological modeling and organ motion are only some of the sources of uncertainties affecting the planning and delivery of ion therapy treatment, detailed in section 1.1.5; for this reason, safety margins are applied in clinics for the definition of the irradiation target volume and the quantification of the planned dose. In the actual clinical routine, the PTV is a geometrical extension of the so-called Clinical Target Volume (CTV) and is delineated in order to account for treatment uncertainties. Safety margins are also applied in standard x-ray therapy (McKenzie et al. 2000), where under- or over-shooting errors have limited effects with respect to ion beam therapy. As highlighted in Albertini et al. 2011, the application of safety margins is useful to improve the treatment plan robustness in case low dose gradients are applied, while the effect results marginal for highly modulated IMPT. At present, in order to account for the overall effects of all sources of uncertainties in the range prediction (MCS, beam energy straggling, imaging tools accuracy and calibration, biological effects, patient positioning and organ motions), margins up to 3.5 % + 3 mm can be applied around the CTV (Paganetti 2012b), mainly based on Monte Carlo or analytic dose calculations which result in clinically compatible predictions.

Safety margins

In the following paragraph, the uncertainties related to ion therapy treatment are discussed in details, with particular care devoted to possible clinical solutions.

1.1.5 Ion beam therapy uncertainties and treatment monitoring

Heavy charged particles are suitable for cancer radiation therapy given the better achievable dose conformity and the reduced energy deposit in tissues surrounding the target with respect to standard photon treatment techniques. These advantageous features directly derive from the nature of ion interactions in matter, described in section 1.1.1, which determines a depth dose profile characterized by a finite range and a energy deposit (dose) peak (Bragg peak). In order to accurately predict the ion range and, more generally, the dose distribution delivered during a clinical treatment, all the possible ion interactions in matter must be considered. This prediction is associated with important uncertainties due to imaging precision, patient setup, anatomical variations and motions, beam delivery system accuracy, dose calculation approximations and biological considerations (Paganetti 2012b). Ideally speaking, a perfect

knowledge of the beam and target structure and perfect evaluation of all the parameters involved in the dose determination would result in the optimal way to treat a deep-seated tumor, with a reduced dose delivered to the surrounding healthy tissue (even close to OAR) with limited fields of irradiation, and a dose accurately concentrated to the tumor volume. The actual clinical routine must face limitations in beam production and control as well as in patient composition evaluation, which causes the need for approximated treatment planning and the setup of treatment safety margins (see section 1.1.4), limiting the full exploitation of this treatment technique potential. In this section, an overview of the different sources of uncertainties affecting ion therapy treatments is given, and the solutions, already implemented or under study, are presented, with particular attention focused on ion range monitoring techniques, main topic for this thesis. All the mentioned sources of uncertainties associated to hadrontherapy treatment converge in a significant spread in the beam effective range with respect to the predicted one. Treatment planning systems are able to accurately model range straggling and MCS broadening along the beam path in water (Hong et al. 1996), but the prediction accuracy has limitations when translated to patients. As highlighted in Schlegel et al. 2008, a precise determination of the primary ion penetration depth is essential in order to rely on particle therapy treatments, much more than for standard photon treatments. The reason is schematically presented in Figure 1.16.

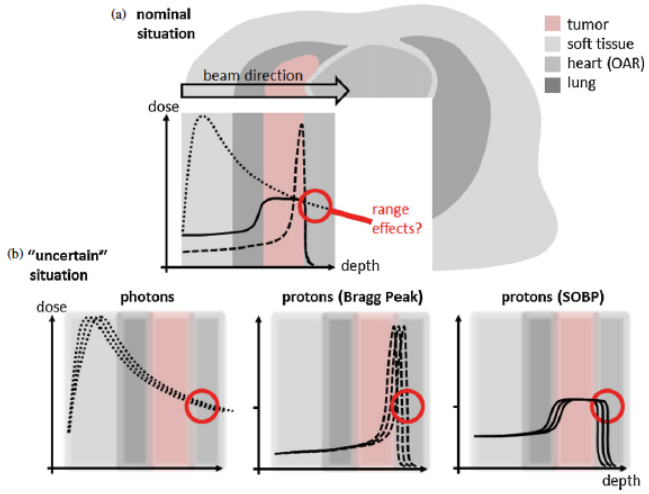

Figure 1.16: Schematic view of the potential benefit due to the depth-dose features of protons as compared to photons (a) and influence of range uncertainties on photon irradiation and proton pristine and spread-out Bragg peaks. In Knopf et al. 2013.

In the top panel of Figure 1.16 the ideal treatment configuration is shown, with the pristine Bragg peak located at the distal limit of the PTV (dashed line) and the SOBP covering the whole tumor volume (solid line); the two proton irradiation methods are compared to the photon dose profile (dotted line), which releases the maximum of the dose in the entrance region and it is not capable of sparing the tissues surrounding the tumor volume, before and beyond the tumor in the beam direction. In the bottom line of the same figure, the effect of range uncertainties are represented: from left to right, in case of photon dose profile shifts, the modification in the dose delivered to healthy tissues is relatively limited, the main effect being a shift in the dose maximum in the entrance region; for a mono-energetic Bragg peak, a shift in the peak position can result in both an under-irradiation of malignant tissues and a dose maximum located in soft healthy tissues; the same effect is present for the SOBP, with the

only advantage of a reduced under-irradiation of the tumor region. It is clear from this simple case how the extremely sharp dose gradient provided by heavy charged particles must be accurately controlled in order to fully profit of its beneficial effect in treating cancer. As mentioned, an exact range calculation is extremely difficult to be obtained in human tissues. As described in section 1.1.4, the treatment planning is at present based on a pre-treatment CT scan which is generally acquired only before the first treatment fraction. The CT image accuracy is indeed the first source of uncertainty in range calculation . The limitations in the imaging precision (mainly due to image noise - see Chvetsov et al. 2010) and the reconstruction artefacts (which can be important in presence of metal implants as verified in Jäkel et al. 2007; Newhauser et al. 2007) already affect the reference data set. Small but not negligible effects are also related to the CT resolution (España et al. 2011a). The obtained CT data must be then converted from x-ray attenuation values (HU) related to water to relative ion stopping power (see section 1.1.4). The conversion is based on calibration curves (U. Schneider et al. 1996; W. Schneider et al. 2000), generally obtained with CT scans of tissue phantom materials with known density and elemental composition. These curves are affected by uncertainties, to be added to the fact that the actual conversion is dependent on the material composition: same x-ray attenuation values can correspond to different relative stopping powers, or vice versa. In addition to this, the conversion may depend on the specific CT scanner, as shown in Ainsley et al. 2014. Several studies have highlighted the magnitude of such uncertainties, which varies, for example, in the range 1 – 2 % from soft tissues to bones for protons (Schaffner 1998), which is translated in range possible discrepancies of 1 – 3 mm. Specific studies have also been conducted on animal fresh tissues in order to optimize the CT calibration for carbon ion treatments (Rietzel et al. 2007). In total, uncertainties of the order of 3 % are generally considered to take into account the described imaging limitations (Moyers et al. 2001). It has been proven that dual-energy CT can improve material composition information (Bazalova et al. 2008; Hünemohr et al. 2014; Wohlfahrt et al. 2018; Yang et al. 2010) and the resulting range uncertainties can be reduced, in particular for carbon ion therapy (Hünemohr et al. 2014). A possible solution to further reduce the errors related to the HU values conversion is the implementation of direct density measurements techniques, where the treatment beam is also used for imaging purposes giving direct access to stopping power data. This possibility was discussed since the late sixties (Koehler 1968), and the technological advancements (mainly in data acquisition systems and detection techniques) recently allowed to obtain promising results in the last years. In addition to the advantageous removal of the data conversion stage, the so-called ion radiography brings other benefits to the treatment side, with the possibility of performing position verification with fast scans just before the treatment delivery (U. Schneider et al. 1995), as well as on the patient side, given the reduced dose necessary for a complete scan with respect to standard x-ray CT (U. Schneider et al. 1995). Further details about this imaging technique are given in the dedicated section 1.1.5.1. Till here the uncertainties directly coming from the treatment planning process have been described, and can be considered as systematic errors, reproduced unchanged for every delivered fraction of the treatment. Conversely, stochastic uncertainties emerge at the treatment delivery level and affect the planned range with random variations. The majority of treatment planning system operating in clinics are based on analytical calculations relying on WEPL data, not able to account for complex geometries. In presence of tissue inhomogeneities, MCS causes what is generally referred to as a degradation in the distal fall-off of Bragg peaks (Urie et al. 1986), in particular in proximity of high-density gradients. Accurate modeling of MCS is then strictly required for correct range predictions (Schuemann et al. 2014). The patient anatomical configuration plays a major role not only on a single fraction basis, but also in different fractions. Conventional fractionation schemes foresee treatments which can last for several weeks; the patient

CT uncertainty

MCS range degradation

Patient anatomy changes

anatomical characteristics can experience significant changes, such as tumor mass reduction, weight loss or gain (Albertini et al. 2008), modifications in the filling of internal cavities. It is clear that such variations introduce further shifts in the predicted ion range, which can be different from fraction to fraction. Moreover, in different fractions, slight differences in the delivered ion energy are possible, with small but not negligible effects. Moving on but always referring to static anatomy issues, the patient setup in the treatment room is another source of uncertainty which can cause discrepancies between the planned and the delivered dose distribution, as shown for example in Fattori et al. 2014. Furthermore, in particular for the treatment of tumors in the thorax, organ motion is an important source of dose delivery errors. Focusing on lung cancers, which are already difficult to be precisely targeted due to the low lung density (3 times lower than water), the respiratory motions are hard to be modeled and cause an overall blurring of the dose distribution and severe local range variations due to the high-density gradient between dense tumor tissues and low-density lung tissue. Important research efforts are devoted to the optimization of the treatment of moving organs, as explained in section 1.1.4. In particular, for active scanning delivery techniques, potentially powerful if synchronized with the movements of the target areas, an interplay effect involving beam and organ motion can affect the dose homogeneity and must be minimized (Dowdell et al. 2013; Grassberger et al. 2015). To conclude the list of source of uncertainties affecting ion beam therapy treatment planning and delivery, it is worth to mention the contribution of biological effects. For protons, a generic constant RBE value is generally used in clinics to relate proton dose to photon dose, while it has been verified how the biological effectiveness varies along the beam path, in particular at varying LET. In SOBP, the increasing LET at decreasing primary residual energy is compensated by a reduction of the proton fluence, in order to obtain an homogeneous dose distribution. The increase in LET causes an increase in the RBE which is not considered and results in a shift in the biologically effective range, estimated in $\sim$1 – 2 mm (Paganetti et al. 2000; J. B. Robertson et al. 1975; Wouters et al. 1996). Heavier ion therapy planning systems already account for RBE variations to prescribe a conformal dose distribution, but the prediction process is not error-free. Moreover, the dose distribution delivered with heavy ion irradiation is also characterized by a tail beyond the Bragg peak caused by the nuclear interaction fragments; a correct prediction of the nuclear interaction channel becomes significant, and it is at present not accurate enough to point the beam towards critical structures and fully profit of the narrow dose peak. The optimization of treatment planning system has focused, in the past years, on Monte Carlo-based dose plans, which can reduce the listed uncertainties, and rely on the continuous progress of physical and biological modeling. A complete overview about this topic is given in Paganetti 2012b for the case of protons. In table 1.2, originally presented in Paganetti 2012b and here reported with the modifications which can be found in Durante et al. 2016, the sources of uncertainties in the proton range are reported with an estimate of their relative contribution with and without the application of Monte Carlo optimization techniques.

Organ motion dose blurring

Biological effects

As mentioned in section 1.1.4, the current approach to deal with range uncertainties directly comes from standard x-ray radiation therapy and involves the setting of margins around the target volume. The margins are generally determined analytically and result to be larger in the distal end of the target volume to account for range shifts, while smaller margins are applied laterally to include beam penumbra uncertainties. The field arrangement is another applied mitigation of the problem (Lomax et al. 2001), in particular in proximity of OAR. For example, lateral fields can be used instead of distal ones. Notwithstanding the several solutions used, *in vivo* verification of the delivered range is still a pressing desire in the clinical community. Standard imaging devices are commonly used to monitor photon therapy treatments,

Table 1.2: Estimated magnitude of range uncertainties separated for the various sources, and potential benefit provided by Monte Carlo simulations. The estimates are based on data in (Bednarz et al. 2010; Bischel et al. 1992; Chvetsov et al. 2010; España et al. 2010; ICRU 1980b; Kumazaki et al. 2007; Matsufuji et al. 1998; Paganetti et al. 2000; J. B. Robertson et al. 1975; Sawakuchi et al. 2008; Schaffner et al. 1998; Urie et al. 1986; Wouters et al. 1996). Table reproduced from Durante et al. 2016.

Source of range uncertainty in the patient	**Range uncertainty w/o Monte Carlo (% or mm)**	**Range uncertainty with Monte Carlo (% or mm)**
Independent of dose calculation:		
Measurement uncertainty in water for commissioning	$\pm$ 0.3 mm	$\pm$ 0.3 mm
Compensator design	$\pm$ 0.2 mm	$\pm$ 0.2 mm
Beam reproducibility	$\pm$ 0.2 mm	$\pm$ 0.2 mm
Patient setup	$\pm$ 0.7 mm	$\pm$ 0.7 mm
Dose calculation:		
Biology	+ $\sim$ 0.8 %	+ $\sim$ 0.8 %
CT images and calibration	$\pm$ 0.5 %	$\pm$ 0.5 %
CT conversion to tissue (excluding I-values)	$\pm$ 0.5 %	$\pm$ 0.2 %
CT grid size	$\pm$ 0.3 %	$\pm$ 0.3 %
Mean excitation energy (I-values) in tissues	$\pm$ 1.5 %	$\pm$ 1.5 %
Range degradation: complex in-homogeneities	- 0.7 %	$\pm$ 0.1 %
Range degradation: local lateral in-homogeneities	$\pm$ 2.5 %	$\pm$ 0.1 %
Total (excluding biology and lateral in-homogeneities)	2.7 % $\pm$ 1.2 mm	2.4 % $\pm$ 1.2 mm
Total (excluding biology)	4.6 % $\pm$ 1.2 mm	2.4 % $\pm$ 1.2 mm

where the delivered beam is not stopped in the patient. On the contrary, ion beams do not exit the patient body, so that monitoring techniques can only be based on secondary radiation or indirect measurements. An exception is represented by implanted devices, proposed for the dose and range measurements, briefly discussed in section 1.1.5.5. As highlighted in Parodi 2015, the monitoring should be ideally in three-dimensions on-line, time-resolved and in real-time, in order to allow for a prompt detection of severe deviations between prescribed and delivered dose, and eventually for the interruption of the beam delivery. A number of different approaches have been proposed in the last years, and significant research efforts are dedicated to this specific point by several groups all over the world. In particular, nuclear reactions products are deeply investigated as a source of information about the beam range. The developed techniques have to be adapted to the present clinical routine, so that the beam features (clinical intensity, time structure, size) and treatment plan characteristics (kind of beam delivery, spot size, irradiation intensity per spot, etc.) must be considered. In the following sections, after a paragraph devoted to charged particle CT, the main techniques implemented for ion range monitoring purpose or at present under study are described, and the current available or future instrumentation is presented. In chapter 2, the attention will be focused on the detection of PGs, central topic of this thesis, and a detailed overview of the state of the art of this particular monitoring techniques is provided.

1.1.5.1 Ion radiography and tomography

Given the considerable contribution of x-ray HUs conversion to ion stopping power to the treatment planning uncertainties, the best solution to overcome this limitation relies in avoiding this conversion step. This can be obtained by directly using high-energy ions to perform patient imaging scan. After the original proposal delineated in the Cormack seminal paper in 1963 (Cormack 1963), the first studies with protons date back to 1968 (Koehler 1968), and at the beginning of the seventies the feasibility of this techniques to obtain high contrast images was demonstrated (Cookson 1974; Cormack et al. 1976; Steward et al. 1973). After the first pioneering studies, the developments were almost abandoned in favor of other imaging techniques, in particular x-ray based, providing better spatial resolution with simpler machines (Kramer et al. 1977). As a consequence of the present widespread of hadrontherapy and the multiplication of treatment centers, several research groups showed a renewed interests in the field, and various development projects are ongoing in Europe and USA with promising results guaranteed by the significant technological advancements occurred in the last years. To date, most of the experimental efforts have been and are being devoted to proton-based imaging (reviewed for example in Bucciantonio et al. 2015; Poludniowski et al. 2015), but pioneering imaging experiments with heavier ions were already carried out in the late seventies and eighties (Chu et al. 1993; Tobias et al. 1977). In recent years, many research groups in Japan and Europe are working on carbon-ion imaging prototypes to be applied in the existing carbon therapy centers. An overview of the ongoing research in the field of proton and ion imaging is given at the end of this section. The radiography technique is based on ion beams applied to the patient at higher energy with respect to the treatment ones, which must traverse the body and can be detected on exit to directly retrieve the residual range. In Figure 1.17a the design of a standard detection system for ion radiography is sketched. The Most Likely Path (MLP) through the patient (phantom) is estimated thanks to two thin tracking detector stages, measuring the primary particle trajectories both entering and exiting the target. The second tracker is followed by a range or energy detector, which measure by complete absorption the residual range or energy of the primary ion. Thanks to

the coincidence detection of entrance and exit coordinates and residual energy/range of each primary particle, a density two-dimensional map of the target area can be obtained.

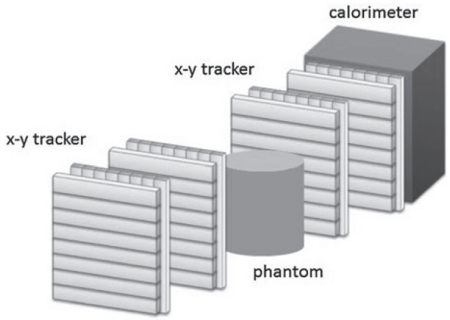

(a) Schematic view of standard ion CT detector design. Each primary incoming particle is tracked before the interaction in the patient and at the exit, and its residual energy is absorbed and measured by a calorimeter. In Mattiazzo et al. 2015.

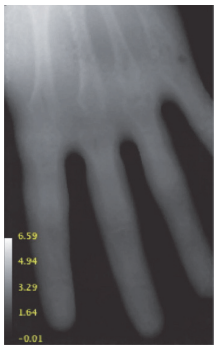

(b) Proton CT image of an hand phantom. In Plautz et al. 2014.

Figure 1.17: Proton and heavier ion radiography and CT are under study in the last years as promising techniques for optimizing the treatment planning performance in hadrontherapy. A standard detector design is sketched in the left panel, while the first image of an hand phantom is reported in the right one.

As mentioned, since all the primary incident particles must completely pass through the target for a residual energy measurements, the beam energy must be higher than the one applied for radiotherapy treatments. In the case of protons, standard clinical accelerators can provide beam at a maximum energy of 230 – 250 MeV (the projected range of 250 MeV protons in water is $\sim$ 38 cm - see National Institute of Standards and Technology (NIST) tables at Berger et al. 2018), not enough to pass in all directions through the hip region of a typical adult, and far short of the shoulder-to-shoulder distance through a human male. Such energies are anyway sufficient for scanning the head or the lung region for most patients (Johnson 2017). The optimal beam conditions for radiography have already been pointed out for protons in one of the first studies about this topic (Moffett et al. 1975). At that time, small pencil beams were preferred, with low intensity and limited energy spread. In reality, the beam can be also passively spread to cover the whole detector aperture, or a scanning technique can be used as suggested in the original papers. In addition to the first highlighted advantage of this technique, which provides direct access to stopping power data, there are other factors determining its convenience with respect to x-ray imaging. A dosimetric advantage with respect to x-rays has been already proven in 1975 (Moffett et al. 1975), and a reduction of imaging dose by a factor 10 to 20 has been reported in U. Schneider et al. 1995. Recent results showed, for equal density resolution, 50 – 100 times lower image exposure for protons with respect to x-rays (U. Schneider et al. 2004). Moreover, the low dose enables one to perform proton imaging scans before each treatment fraction: this is potentially very useful for positioning optimization (the scan is performed under the same geometrical conditions as the treatment) and for the detection of anatomical changes, which cannot be included in the present treatment planning, based on a single CT scan performed before the beginning of the whole treatment cycle. However, it must be considered that ion radiographies are performed in the same treatment room and couch, limiting the patient flow. Moreover, a major limita-

tion of proton radiography techniques is represented by a poor spatial resolution due to MCS, already highlighted in the first publications (Koehler 1968; Moffett et al. 1975). Several small angle deflections produce uncertainties in the reconstructed trajectories (Penfold et al. 2009; U. Schneider et al. 2004, 1995). Heavier ions are less affected by MCS in the target, so that better spatial resolution with respect to protons can be achieved, but they suffer from substantial nuclear spallation and the projectile and target fragmentation can add background to the final image (Parodi 2014). The helium ions, which already have the advantage of requiring much less energy than carbon ions in order to fully penetrate a phantom, behave more like protons within the phantom, but with significantly reduced scattering and increased spatial resolution. Helium, indeed, appears to be the optimum compromise, even if it is not implemented in clinics for tumor treatments at present. With the increasing diffusion of heavy-ion therapy centers, anyway, we can expect a further development of this field in the next years (Parodi 2014). The described ion transmission imaging method provides two-dimensional information, but it can be extended into 3D with the rotation of the system around the target (or the patient rotation) and the application of tomographic reconstruction. The so-called ion-CT makes use of optimized Filtered Back-Projection (FBP) methods or Algebraic Reconstruction Techniques (ARTs) to obtain 3D patient images by combining various data sets from different angles. At present, ion transmission imaging for both radiography and tomography is not yet clinically implemented, but a number of research groups conducts instrumental development campaigns to produce prototypes to be tested in clinics. Although the basic design is common, with tracker and absorber components, different technological solutions are being explored. The first prototype designed for this purpose, after the first trial conducted at the early stage of this research field, was studied at PSI; it was based on a pair of Multi Wire Proportional Chambers (MWPCs) as tracker, followed by a Sodium Iodide (NaI) 7.5 mm diameter crystal for the energy measurement (U. Schneider et al. 1995). The detector was later upgraded to overcome rate and size limitations, with the use of scintillating fiber hodoscopes instead of MWPCs and plastic scintillator tiles to substitute the mono-block NaI crystal (Pemler et al. 1999). Similar scintillating-fiber trackers have been used by the OFFSET collaboration for its prototype (Lo Presti et al. 2014). The same author recently presented a beam monitoring and radiography prototype (QBeRT) with upgraded read-out system, providing enhanced results (Gallo et al. 2016; Lo Presti et al. 2016). The TERA Foundation at CERN has been involved for several years in the development of detectors to be applied in the quality assurance for hadrontherapy. Within the Advanced QUality Assurance (AQUA) project (Amaldi et al. 2010b), proton radiography instruments were developed and tested on clinical beams, starting from 2009. The first prototype, based on Gas Electron Multiplier (GEM) detectors (Sauli 1997) for tracking and plastic scintillator layers for the calorimeter, had an active area of 10×10 cm^2 (Amaldi et al. 2011), then extended to 30×30 cm^2 for the second version of the machine, with similar detection technologies but improved rate acceptance capabilities thanks to new read-out systems (Bucciantonio 2015; Bucciantonio et al. 2013). A complete, wide surface proton CT system has been proposed by an American collaboration of the Northern Illinois University (NIU) and the Fermi National Accelerator Laboratory (FNAL) (Naimuddin et al. 2016). It is based on 0.5 mm diameter scintillating fibers read out by SiPM, for an active area of 24×20 cm^2. Alternative, more expensive designs include silicon-strip detectors for proton tracking, such as the one in development in Italy by the PRIMA collaboration, with eight layers of silicon sensors and a calorimeter composed of a 2×7 array of Cerium-activated yttrium aluminum garnet (YAG:Ce) crystals, 3×3 cm^2 section and 10 cm length each (Scaringella et al. 2013). The experience of a collaboration of the Loma Linda University (LLU) and the University of California and Santa Cruz (UCSC) started with a small prototype with slow acquisition (Sadrozinski et al. 2011), based on doped Cesium Iodide (CsI) crystal to measure the residual range, then ex-

tended to a larger one (Johnson et al. 2016), sufficient for a human head scan, which already provided advanced results. The "Phase-II Scanner" is based on two silicon-strip detector modules for the tracking section and five polystyrene-based scintillator segments for the range measurements. In Figure 1.17b a proton CT image of an head phantom obtained with the first generation detector is shown. A similar system has also been studied in simulation by a group in Korea (C. Y. Lee et al. 2016). The same tracking detectors are used in a Japanese collaboration project; the group developed a slow-acquisition and small aperture prototype and already planned an upgrade to a ten times larger system with increased acquisition rate capabilities (Saraya et al. 2014). The British collaboration Proton Radiotherapy Verification and Dosimetry Application (PRaVDA) tested a first prototype of a proton CT system entirely based on silicon detectors (Taylor et al. 2015, 2016). An alternative and simpler approach has been investigated with a system using a stack of 40 nuclear emulsion plates which records the proton tracks then reconstructed off-beam (Braccini et al. 2010); the results are interesting, even if such a solution is not suitable for real-time imaging. Even if the majority of the research efforts are devoted to proton application of the radiography/tomography technique, some tests has been made also for heavier ions. At NIRS, a combination a fluorescent screen viewed by a Charge-Coupled Device (CCD) camera and rotational range shifters has been investigated (Abe et al. 2002), together with a more conventional system composed of scintillating fibers for tracking and a thick plastic absorber (Shinoda et al. 2006). At HIT, studied setups involved silicon flat panel detector (Telsemeyer et al. 2012) or a range telescope consisting of a stack of parallel plate Ionization Chambers (ICs) with 3 mm thick plastic absorbers, and single beam spot-based radiographies have been performed (Rinaldi et al. 2013). All the listed systems produced promising results (Parodi 2014).

1.1.5.2 Positron Emission Tomography

PET is one of the most extensively studied techniques for ion beam range verification in particle therapy. The idea, initially mentioned in pion therapy (Goodman et al. 1986), dates back to the 1970s (Bennett et al. 1975; Knopf et al. 2013), and consists in detecting the secondary 511 keV photons emerging from the patient as product of the annihilation of positrons emitted by isotopes generated by the beam nuclear interactions (see section 1.1.1.1). The detection in time coincidence of such gamma rays can be used to reconstruct a three dimensional distribution of positron emitters in the patient, which correlates to the beam range. The ion range verification by means of PET is extensively described in section 2.2.1.

1.1.5.3 Prompt-gamma detection

An alternative way to access valuable information about the Bragg peak position of both proton and carbon ion beams in human tissue is represented by the detection of high-energy photons promptly emitted as a by-product of nuclear interactions (see section 1.1.1). For many years, this kind of radiation was investigated as a source of background in PET-based monitoring system (Parodi et al. 2005), mainly because the produced photon energy is too high to be detected with standard devices like Single Photon Emission Computed Tomography (SPECT) cameras (Kraan 2015). The idea of using prompt-gamma radiation to obtain a direct and instantaneous verification of the beam stopping position in tissues was first proposed by Stichelbaut and Jongen at the 39th Particle Therapy Co-Operative Group (PTCOG) meeting in

2003 (Stichelbaut et al. 2003). Experimental verification of the correlation between prompt-gamma profiles and Bragg peak position has been presented for protons and carbon ions (Min et al. 2006; É. Testa et al. 2008) few years later, and the method is nowadays deeply studied as a promising solution for online range verification in clinical conditions. The research efforts involve imaging and time or energy resolved techniques, for which several detection solutions are being developed and tested. In section 2.2.2 the prompt-gamma detection physical principle for range verification and the state of the art of this research field are presented. The details of the detection solution under development by the CLaRyS collaboration, within which this thesis has been conducted, are presented in chapter 3 and chapter 6 (dedicated to the detector beam tests); the simulation results of the clinical application of the Compton camera for proton and carbon ion range verification are illustrated and discussed in chapter 4.

1.1.5.4 Interaction Vertex Imaging

As described in section 1.1.5.1, high-energy traversing ion beams can be used for radiography and tomography purposes in order to increase the accuracy of stopping power measurements for treatment planning. The detection of protons can also be used as a treatment monitoring technique, if secondary protons produced in nuclear collisions are considered. This ion range control modality has been proposed less than a decade ago (Amaldi et al. 2010b; Dauvergne et al. 2009) and is generally referred to as Interaction Vertex Imaging (IVI). The charged particles created during fragmentation processes in the target can be energetic enough to exit the patient and are most likely forward directed; thanks to a detector located downstream from the patient, their trajectories can be then reconstructed and extrapolated back to the production point. The principle is similar to vertex identification problems in fixed target particle physics experiments. The comparison of the obtained distribution with the one simulated at the treatment planning stage provides a means of controlling the ion range. In addition, the amount of emerging charged particles can be, in principle, correlated to the dose. Given the larger amount of protons generated by carbon irradiation with respect to proton ones (Gunzert-Marx et al. 2008), this method is more suitable for carbon ion therapy monitoring. A feasibility study has been presented in Henriquet et al. 2012; the authors investigated the possible implementation of such a control in carbon ion therapy with Geant4 simulations. The modeled detector is composed of two pairs of 50 μmthick pixelized Complementary Metal Oxide Semiconductor (CMOS) trackers, placed at an angle of 30 degrees with respect to the beam direction, and two methods have been tested, one based on the coincidence of two protons emitted from the same vertex, the second relying on the incident carbon ion trajectory determined by a beam hodoscope in coincidence with single secondary proton detection. The study showed the possibility of achieving millimetric precision on the Bragg peak position in the ideal case of homogeneous targets with pencil beams of 2×10^5 carbon ions. Experimental tests have been conducted at HIT with a similar setup involving hybrid-pixel detector with CMOS readout, and with higher statistics the accuracy in the beam range monitoring was found to be 1 – 3 mm (Gwosch et al. 2013). In the experimental studies reported in Agodi et al. 2012 and Piersanti et al. 2014, PMMA targets have been irradiated with mono-energetic carbon-ion beams at different energies, and secondary protons have been measured with systems placed at 60 and 90 degrees with respect to the beam direction; the results have been compared to FLUKA predictions, and reasonable agreement has been verified. The detector developed by the TERA Foundation at CERN (Bucciantonio 2015) has been also proposed as a solution for IVI, but it has never been tested for this purpose. Recently, the method was tested in clinical conditions with measurements performed at HIT; the resolution of the Bragg peak position was found to

be about 4 – 5 mm in an homogeneous PMMA phantom with 10^6 incident carbon ions and a tracker of 1×2 cm^2 (Finck et al. 2017). The IVI method could therefore monitor the Bragg peak position with a promising resolution in clinical conditions, but further efforts are needed to improve Monte Carlo predictions of the angular distribution of the fragments, as well as to increase acceptance and efficiency of the employed detectors.

1.1.5.5 Other techniques

Point measurements

The detection of secondary radiations emerging from the patient body during particle therapy is not the only available channel for measuring the ion stopping position and, more generally, verify the treatment delivery. The dose delivered in photon and electron treatments have been measured *in vivo* with diodes and thermo-luminescence dosimeters, as reviewed in Essers et al. 1999, and implantable devices with wireless readout have been introduced in standard radiotherapy (Black et al. 2005; Scarantino et al. 2008) and investigated for proton range verification. The main challenge is the positioning of the detector, which strongly influences the measurement of the steep dose distal fall-off of ion beams, and two solutions have been proposed by the same author to overcome this issue. The residual range of the irradiation beam can be retrieved at each position via its time dependence, which is unique at every point in depth (Lu 2008b). This method, proposed for passively scattered beams but also applicable to actively scanned ones, has been tested with a small IC, and sub-millimeter precision for the determination of the proton range at a specific position in water has been proven (even if in ideal conditions). The second proposed method relies on the delivery of a pair of complementary fields, with sloped depth dose profiles (Lu 2008a). The ratio between the two measured distributions can verify the radiological path length. As the previous one, this approach has been experimentally tested, in this case with a commercial implantable dosimeter (Lu et al. 2010), and dose ratios have been measured with a relative uncertainty of 1 – 3 %. Notwithstanding the valuable obtained results, the applicability of both solutions is strongly limited by the need of implanting devices in the patient, ideally close or within the tumor, which is often not possible. In any case, possible improvements are still being studied recently (Toltz et al. 2017). An alternative way to measure the range with simple detectors in one dimension is the so-called "range probe" (Mumot et al. 2010; Watts et al. 2009). This concept relies on the direct measurement of the Bragg peak of single high-energy pencil beams passing through the patient, in a sort of simplified mono-dimensional version of proton radiography discussed in section 1.1.5.1, and can in principle both validate the range *in vivo* and verify patient positioning errors with low additional dose.

MRI imaging

MRI imaging has also been considered as a way to observe delivered dose distributions. The application of such a technique is made possible by the changes induced by radiations in tissues, and it has been investigated mainly for spine patients (Gensheimer et al. 2010), but the accuracy was not sufficient to verify the ion range. However, the high spatial resolution achievable with commercial scanners is a good point in favor of further investigations.

Acoustic imaging

The improvement of ultrasound imaging techniques determined in the last years a renewed interest on its application to ion range verification. It has been demonstrated that iono-acoustic detectable signals are produced by the localized dose deposition of ion beams (Tada et al. 1991), which induces local temperature increases and, thus, a pressure wave (Parodi et al. 2015); these pulses have been already measured in 1995 in a proton therapy treatment (Hayakawa et al. 1995). A schematic view of the detection principle is presented in Figure 1.18a. Recently, tests on proton beam have been performed at the CAL, in Nice, with mono-energetic beams in the energy range 145 – 227 MeV (Lehrack et al. 2017); as the author stated, the method as been been proven to be a cost-effective, fast and

accurate way to obtain quality control measurements in proton therapy, with sub-millimeter range determination accuracy (the results have been compared to reference data collected with an IC). However, it has been highlighted how the synchro-cyclotron offered ideal condition for the application of iono-acoustic measurements, thanks to the delivered intense and short (microsecond) bunches. Signal-to-Noise Ratio (SNR) is an additional problem at the present development stage, but it has to be pointed out that iono-acoustics offers a method not only to locate the Bragg peak, but also to correlate it with an ultrasound tumor image; the research effort is so clearly justified, and improvements are expected in the next years. To be noticed, anyway, that the iono-acoustics probes can be used only with soft tissues, so that their application, for example in head-and-neck treatment monitoring seems not feasible. In addition to the deeply investigated techniques based on secondary particles generated by nuclear reactions (PET and PGs), there are also bremsstrahlung photons coming from secondary electrons generated during ion deceleration. The basic principle is explained in Yamaguchi et al. 2012, where the author highlights that the dependence of the bremmstrahlung photon energy spectrum on the incident beam energy provides a method to control the beam range. In particular, secondary electron bremmstrahlung dominates at low ion energies, close to the Bragg peak, and its energy spectrum allows one to retrieve the correlated Bragg peak position. A complete experimental confirmation has been provided with measurements performed in Japan in different centers (HIMAC among them) with carbon ion beams and a Cadmium Telluride (CdTe) detector, involving also background estimates. This technique provides in principle an overall better sensitivity with respect to PG detection and PET, and completely avoids the wash-out effects which affect positron emitter activity measurements, and has been developed in the last years. As secondary electron bremmstrahlung cross section scales as Z^2, this method is potentially advantageous for carbon ions. In particular, mono-energetic carbon ion beams have been recently imaged with a pinhole gamma camera (Yamaguchi et al. 2018), but the clinical necessary resolution in detecting range shifts has not been achieved yet. In addition, given the low energy of the emitted Bremsstrahlung photons, this technique is intrinsically limited to superficial tumor treatment control.

Bremsstrahlung imaging

Also water luminescence effects have been verified during the irradiation with proton pencil beams, and are under investigation as a promising solution for range and field width estimations (Komori et al. 2018). As mentioned, the listed methods have been proposed as alternatives with respect to the more investigated detection of secondary emitted photons, both from positron annihilation and prompt-emission. These two techniques are anyway the most advanced ones, and also hybrid systems are under investigation to obtain a combination of their main advantages and a potential reduction of the identified drawbacks. The so-called "3-γ" imaging concept has been explored in France and Germany. The French group combined a standard full ring PET scanner with a Time Projection Chamber (TPC) filled with liquid xenon for the Compton measurement (Oger et al. 2012), but the detector application is limited to nuclear medicine examinations in its present design. The German group focused on multiple Compton camera heads for the detection in coincidence of positron annihilation photons and de-excitation rays for nuclear medicine applications; such a system can be adapted to perform combined detection of 511 keV photons from β^+ emission and PGs, as already highlighted in (Lang et al. 2014). A conceptual detector design for such an application is shown in Figure 1.18b. Another interesting simulation study applying this "whole-gamma imaging" concept in nuclear medicine is reported in (Yamaya et al. 2017).

Water luminescence

Hybrid systems

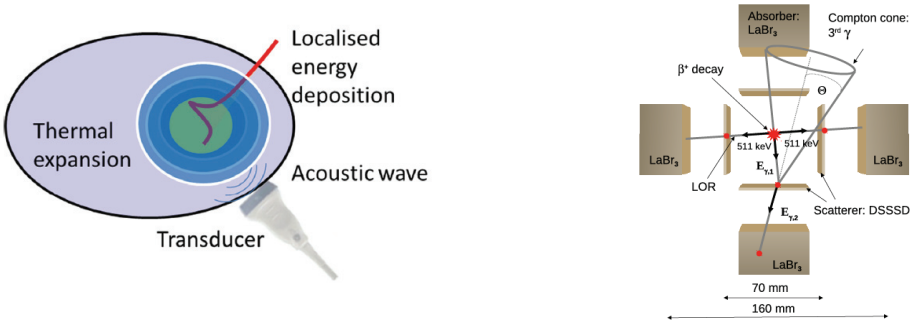

(a) Schematic view of the basic principle of iono-acoustic waves detection for ion range verification. In Parodi et al. 2015.

(b) Conceptual design of the 3-γ detection system proposed in Lang et al. 2014, composed of multiple Compton camera arms for the detection of correlated PET and de-excitation gammas or PET and prompt photons produced in nuclear interactions during particle therapy treatments. In Lang et al. 2014.

Figure 1.18: Alternative methods for *in vivo* range verification of ion beam therapy include the detection of iono-acoustic waves produced by the localized dose deposited by the energetic ion beams, whose principle is sketched on the left side, and hybrid systems for 3-photon detection, which can be applied to both nuclear medicine diagnostics and hadrontherapy monitoring, as the one sketched on the right side.

1.2 Nuclear medicine

Nuclear medicine is a medical specialty which makes use of particle physics concepts (in addition to medical, biological and chemical knowledge) and instrumentation to study physiological processes and perform non-invasive diagnostic examinations and disease treatments. More specifically, nuclear medicine groups all the medical techniques which foresee the use of chemical compounds containing a radioactive isotope; this radio-pharmaceutical is given to the patient (or mixed to patient samples, for example blood) orally, by injection or by inhalation, and the isotope decay products are used to deliver a treatment dose, for example to cancerous tissues, or for imaging purposes, in case the emitted particles can exit the body and be detected by radiation detectors. This thesis focuses on the development of gamma detectors, originally designed for the application in particle therapy; the following sections are devoted to delineate the context in which the studied detectors can be applied for diagnostics, and simulation results of such an application are reported in chapter 5.

Some hints about the historical origins of this medical fields have been given in the introduction of this chapter. The use of radioactive isotopes for medical purposes has been investigated since 1920, at the beginning only theoretically, then, since 1940, attempts have been undertaken at imaging radio-nuclide concentration in the human body. The first scan of a radio-nuclide activity in the body was obtained with a very slow planar scanner introduced by Ben Cassen at the beginning of the fifties (Blahd 1996), and less than 10 years later Hal Anger developed the first gamma camera, introducing the approach still followed for the modern detectors (Anger 1958). The Anger scintillation camera is a planar physically collimated detector

which produced two-dimensional projection images of the radio-isotope activity without scanning. The Anger camera, if rotated around the patient, can also be used for tomography, with reconstruction algorithms able to reproduce the three-dimensional emission distribution from two-dimensional multiple-angle slices. The method to reconstruct images from projections had been published by Radon in 1917 (Radon 1917), and then applied in CT and nuclear medicine after 1970. Iterative reconstruction methods were also being investigated, but their application started in the eighties when more computing power became available. The tomographic translation of the Anger gamma camera determined the birth of SPECT imaging: together with PET, SPECT is still the basis of present diagnostic nuclear medicine. The idea of detecting photon pairs produced by positron annihilation is also attributed to Anger, but the first dedicated PET system was built by Ter-Pogossian and colleagues in the 1970s, and employed for phantom and animal studies (Ter-Pogossian 1983; Ter-Pogossian et al. 1975). Soon afterwards, Phelps, Hoffman and colleagues built the first whole-body PET-scanner (Hoffmann et al. 1976). In the next sections, the physics of radioactive decays is briefly reminded to introduce the detailed discussion of PET and SPECT techniques, including a short historical overview, the presentation of the imaging principle and an overview of state-of-the-art machines.

1.2.1 Radiotracers

Nuclear medicine imaging techniques are based on radio-tracers. A tracer is a chemical compound which transports an unstable isotope (radio-nuclide); this molecule is designed to be involved in specific metabolic processes and, thus, to concentrate in the volume to be targeted for imaging purpose. The γ-rays emitted by the radio-nuclide can be measured as a function of position and time, providing anatomical and metabolic information. In the following, the main physical aspects of radioactive decays are briefly recalled.

As mentioned, a radio-nuclide is an unstable isotope of a chemical element which decays towards a stable atomic configuration and loses energy by emitting radiation in the form of particles and electromagnetic rays. The decay can involve several steps, if the resulting "daughters" are still unstable, and the process continues until a stable nuclide is reached. Some general features of radioactive decay processes can be detailed mathematically without regard to a specific mechanism. In particular, the decay rate of a sample of radioactive nuclides depends on the nuclides population N, according to a decay constant noted as λ, as expressed by equation 1.15.

$$\frac{\mathrm{d}N}{\mathrm{d}t} = -\lambda N \tag{1.15}$$

On one hand, the decay constant λ is specific of each nuclide, and reflects its degree of instability. The decay rate, on the other hand, is a representation of the sample activity, which is measured in the Internation System of units (SI) in Becquerel (1 Bq = 1 disintegration per second) and its multiples, even if an older and still used unit is the curie (Ci) (1 Ci = 3.7×10^{10} disintegrations per second). The solution of the differential equation in 1.15 gives the number of parent atoms N at any time t, or the activity by multiplying both side by λ:

$$N = N_0 e^{-\lambda t}$$
$$A = A_0 e^{-\lambda t} \tag{1.16}$$

with N_0 and A_0 the original number of parent atoms and the original activity, respectively. Following these first expressions, the physical half-life $T_{1/2}$ of a radioactive nuclide is the time required for the decay of half of the atoms in a sample; its mathematical form is reported in equation 1.17.

$$T_{1/2} = \frac{\ln 2}{\lambda} = \frac{0.693}{\lambda} \tag{1.17}$$

Several decay modes exist, and they can be divided into three main categories: emission of nucleons (protons and neutrons), emission or capture of electrons, emission of photons. In particular, five main decay channels have been identified (see Figure 1.19b):

- α-decay;
- electron emission – β^--decay;
- electron capture (electron captured from the inner shells of the atom);
- positron emission – β^+-decay;
- isomeric transition: gamma emission and internal conversion (electron emission).

In Figure 1.19a the decay scheme of a generic nuclide ${}^{A}_{Z}X$ is depicted (A is the atomic mass, Z the number of protons); the α-decay produces ${}^{A-4}_{Z-2}P$, electron capture and positron emission equivalently generate ${}^{A}_{Z-1}Q$, while ${}^{A}_{Z+1}R$ originates from electron emission and can be created in a metastable configuration ${}^{A}_{Z+1}R^*$ which then decays to the stable state via isomeric transition with the emission of a photon.

α-decay

The α-decay is the spontaneous emission of an α particle (i.e. a helium nucleus, consisting of two protons and two neutrons), typically from heavy nuclides ($A > 150$). It was discovered by Marie and Pierre Curie in 1898 (Curie et al. 1898) and first described by Rutherford one year later (Rutherford 1899), who also identified the α particles as helium nuclei, together with Boltwood in 1911 (Boltwood et al. 1911). The decay can be described by equation 1.18. Often it is followed by the emission of characteristic x-ray or gammas, accompanied by competing processes of internal conversion and Auger electron emission. The produced α particles have energies in the 2 – 10 MeV range and are not used for imaging purposes, given the very limited range in tissues (about 100 μm). This characteristic makes such a decay appropriate for therapy, even if the very short decay time is a limiting factor. Only the α-decay of a few high-Z elements is actually used, for example, for tumor irradiation in the so-called "internal radiotherapy" or "brachytherapy" (Dahiya 2016; Suntharalingam et al. 2005).

$${}^{A}_{Z}X \rightarrow {}^{A-4}_{Z-2}Y + {}^{4}_{2}\mathrm{He} + \text{energy} \tag{1.18}$$

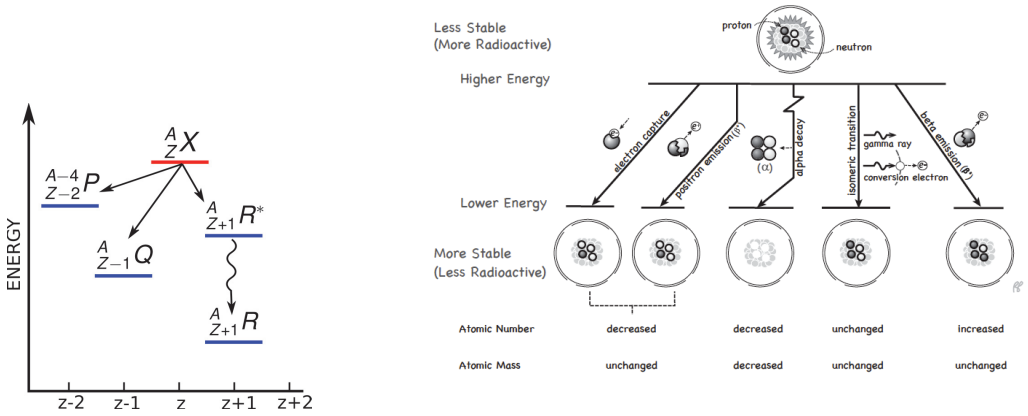

(a) Radioactive decay scheme. In Hendee et al. 2002

(b) Schematic view of the radioactive decays. In Powsner et al. 2013.

Figure 1.19: The various radioactive decay channels are schematized in (a) for a generic isotope ${}^{A}_{Z}\mathrm{X}$. A more detailed scheme, describing the decay processes and products, is given in (b).

Electron emission

The decay via emission of an electron (β^-- or negatron-decay) can be seen as the conversion of a neutron in a proton and an electron-anti-neutrino pair, as in the generic reaction reported in equation 1.19.

$$\begin{aligned} {}^{A}_{Z}X \rightarrow {}^{A}_{Z+1}Y + e^- + \overline{\nu} + \text{energy} \\ n \rightarrow p + e^- + \overline{\nu} \end{aligned} \tag{1.19}$$

This decay channel pertains to nuclei with a N/Z ratio (with N the number of neutrons) too high for stability and results in nucleus with Z increased by one, N decreased by one and so the same atomic mass A (isobaric transition) but a different chemical element. β^--decay pathways are characterized by specific maximum energies $E_{\max}$ for the emitted electron, with an average value of approximately 1/3 $E_{\max}$; the remaining energy is carried away by the anti-neutrino. This results in poly-energetic energy spectra for the emitted electrons. The difference in the energy released during decay and the one possessed by the emitted electron threatened the energy conservation law for years. In 1930, in a letter, Wolfgang Pauli suggested that a second particle was emitted during the decay, explaining the energy, momentum and angular momentum conservation. The name neutrino was attributed to such a particle by Enrico Fermi. Any possible excess energy in the nucleus after the decay (metastable state) is emitted as gamma rays or internal conversion electrons. As for the α particle case, electrons have limited range in matter, thus release dose to the tissues, and have no diagnostic value (but they are used in brachytherapy), but metastable states deriving from β^--decays are pure sources of γ-rays and are so employed for imaging. One of the most diffused tracers is a metastable daughter of ^{99}Mo, the ^{99m}Tc; it decays in stable ^{99}Tc (half life = 6 hours) by emitting a 140 keV photon.

Positron emission

On the other side of the "nuclide stability line", neutron-poor radionuclides (with low N/Z ratio) tend to decay by the emission of a positron (β^+ decay) and to increase the neutron

number by one. As shown by equation 1.20, the net result is the conversion of a proton into a neutron with the ejection of a neutrino, in addition to the positron. As in the previous case, the transition is isobaric because the total number of nucleons is unchanged.

$$\begin{aligned} {}^{A}_{Z}X &\rightarrow {}^{A}_{Z-1}Y + e^{+} + \nu + \text{energy} \\ p &\rightarrow n + e^{+} + \nu \end{aligned} \tag{1.20}$$

The emission of positrons was discovered in 1933 by Irene Curie and her husband Frederic Joliot, in bombardments of aluminium by α particles (Leone et al. 2010). Even if the reaction principle is similar to β^{-}-decay, an important difference resides in the behavior of the decay product. Both electron and positron undergo energy deposition processes by excitation and ionization, but if electrons can be captured by atoms (or absorbed in free electron bands) when they come to rest, positrons react with their antiparticle (electron) by annihilation. The entire rest mass of the particle pair is converted to energy and emitted as two back-to-back 511 keV photons for conservation laws. The annihilation takes place in a time window of about 1 ns after the β^{+}-decay, and within a few millimeter of the decay site (depending on the medium). This kind of reaction is the basis of one of the most diffused nuclear medicine imaging techniques, the PET, discussed in section 2.3.1. An example of a positron emitter used in imaging is ^{18}F, with a half-life of 109 minutes. To be noticed that, as for β^{-}-decay, the daughter nucleus can further emit photons to lower its energetic level, which can be used in combined imaging techniques (three-γ imaging). The N/P ratio of neutron deficient nuclides can also be increased via Electron Capture (EC) reactions ; the nucleus can capture an orbital electron and convert a proton into a neutron, with the consequent emission of a neutrino. This phenomenon is described by equation 1.21.

EC

$$\begin{aligned} {}^{A}_{Z}X + e^{-} &\rightarrow {}^{A}_{Z-1}Y + \nu + \text{energy} \\ p + e^{-} &\rightarrow n + \nu \end{aligned} \tag{1.21}$$

Most electrons are captured from the K shell, more uncommon are the capturing processes involving L shell or even shells farther from the nucleus. As a result of the capture, a vacancy is created and filled by an electron from an higher-energy shell. This transition leads to a reduction of the atomic rest energy, and the release of characteristic x-rays and/or Auger electrons. As with other modes of decay, further γ-rays can be emitted if the daughter nucleus is left in an excited state after the capture process. An example of electron capture decay is represented by ^{201}Tl, which decays to ^{201}Hg with the emission of K-x-rays of 69 – 83 keV (98 % abundance) and photons of 135 and 167 keV in 10 % total abundance. Many nuclei decay by both electron capture and positron emission, as for example the ^{22}Na. As mentioned for the previously described decay modes , often the daughter nucleus is formed in an excited state, which is still unstable. The transition towards a condition of stability entails an internal atomic re-arrangement and the emission of γ-rays at characteristic energies. In general, such a transition is almost instantaneous, but some excited states can persist for longer periods, with half-lives which range on several orders of magnitude, between 10^{-6} s and hundreds of years. The decay of this kind of nuclei, called metastable or isomeric, is called isomeric transition, and only results in the γ-ray emission with no emission or capture of other particles by the nucleus. A complementary pathway for the energy release is represented by the interaction of

Isomeric transition - γ-decay

the nucleus with an atomic electron; this process is called Internal Conversion (IC), and the involved electron is ejected. This emission is further followed by x-rays and Auger electron emission, so that the atom can resume a stable state. The isomeric transition is described by equation 1.22, where the letter m indicates the metastable state.

$$ {}^{Am}_{Z}X \rightarrow {}^{A}_{Z}X + \text{energy} \tag{1.22} $$

To be noticed that no radioactive nuclide decays solely by an isomeric transition, which is always preceded by another decay mode. In addition to the already mentioned decay of ^{99m}Tc, deriving from the previous decay of ^{99}Mo, also ^{60}Co decays in excited ^{60}Ni nuclei which then reach the ground energy state by isomeric transition with the emission of 1.17 and 1.33 MeV photons. In table 1.3 some of the radioisotopes typically used for imaging and therapy are listed with their half-life and common uses.

Table 1.3: Commonly-used radioisotopes for the clinical imaging and therapy routine. Table adapted from Ruth 2009.

Application	Radioisotope	Half-life	Details
Imaging	Technetium-99m	6 h (from ^{99}Mo 66 h)	Used to image the almost all the body, skeleton and heart muscle in particular.
	Cobalt-57	272 d	Used as marker to estimate organ size and for *in vitro* diagnostic kits.
	Gallium-67	78 h	Used for tumor imaging and localization of inflammatory lesions.
	Indium-111	67 h	Used for specialist diagnostic studies and colon transit studies.
	Iodine-123	13 h	Used for diagnosis of thyroid function.
	Krypton-81m	13 s (from ^{8}1Rb 4.6 h)	Used in gas status for images of pulmonary ventilation and in general for lung applications.
	Rubidium-82	65 h	Convenient PET agent for myocardial perfusion imaging.
	Thallium-201	73 h	Used for diagnosis of coronary artery disease and other heart studies.
	Carbon-11	20.4 m	
	Nitrogen-13	9.97 m	Positron emitters used in PET for studying brain physiology and pathology.
	Oxygen-15	2 m	They also have a significant role in cardiology.
	Fluorine-18	110 m	
Therapy	Bromine-77	2.4 d	Auger electrons decay mode.
	Palladium-103	17.5 d	Auger electrons decay mode.
	Rhenium-186	90.6 h	β^--decay mode.
	Astatine-211	7.2 h	α-decay mode.

Radionuclide production

Although many naturally occurring radioactive nuclides exist, all of those commonly administrated to patients in nuclear medicine tracers are produced artificially in order to fit the clinical requirements. Artificial induced radioactivity was introduced by the already mentioned Irene Curie and his husband, who bombarded aluminum targets with α particles (Leone et al. 2010). Nowadays, most radionuclides are produced with cyclotrons and nuclear reactors, and radionuclide generators are used to "store" short-life isotopes. In general, β^- emitters are produced by bombarding stable nuclei with neutrons from nuclear reactors, while β^+-decay nuclides are produced with bombardment with protons, helium ions, deuterons or tritons accelerated with cyclotrons (see section 1.1.3.1 for the description of the cyclotron). In other cases, radionuclides are produced as by-products of fission in nuclear reactors, or as decay product of other isotopes produced with one of the listed methods. In the cyclotron-based production, the accelerated ions collide with the target nuclei causing nuclear reactions, presented in section 1.1.1.1. As explained, fragmentation processes can create radioactive nuclei, such as β^+ emitters, employed in PET diagnostics. In general, cyclotron facilities must be in close proximity to the hospital where the produced radionuclides will be administrated because of their short half-life. ^{18}F, created with this technique as product of nuclear reactions with ^{18}O, is an exception in this sense, with an half-life of 109 minutes. In nuclear reactors, two techniques are exploited: nuclear fission and neutron activation. The absorption of neutrons from nuclear reactors can induces fission processes in heavy nuclei, which split in lighter (often unstable) ones. Its long half-life makes ^{235}U the most widely used fissile element; when

it absorbs a neutron, the resulting state of ^{236}U is unstable and in most cases it promptly splits into its fission fragments. For example, ^{99}Mo has already been mentioned as the parent nucleus for the production of ^{99m}Tc and derives by the fission of uranium. Another widely used nuclide produced with fission procedure is the ^{131}I. The creation of the fission fragments is very often accompanied by the emission of secondary neutrons which can be used to create other nuclides by neutron activation. Stable nuclei, indeed, can capture neutrons and produce, in most cases, β^- emitters, as the ^{32}P or the ^{50}Cr. In some cases, the sample activity reached with such a production technique is not sufficient, because stable nuclei are still present among the parent atoms, and so fission mechanisms are preferred. The last mechanism involves radionuclide generators, particularly interesting for short half-life nuclides. In order to solve the supply problem for short-living isotopes, the sample is often prepared with the longer-living parent nuclide (the so-called "generator"), which then decays in the desired one continually providing it. This is for example the case of the most important radio-nuclide used in a variety of application, ^{99m}Tc, result of the decay of ^{99}Mo.

Radiotracer features

Once produced, the radioactive nuclei must be attached to appropriate substances providing the desired biological properties, for example to be preferentially absorbed in the target region. The final product, ready to be administrated to the patient, is called "radiotracer". For diagnostics, the selected radioisotope half-life should be short enough so that a considerable part of the decays occurs during the examination time; any radiation released after the end of the examination is a source of useless dose to the patient. The dose delivered after the end of the treatment can be reduced if the biological excretion, guaranteed by the tracer characteristics, is rapid. Always focusing on diagnosis, the optimal decay scheme is the pure γ-decay, with an isomer as radionuclide; anyway, the amount of produced non-penetrating radiation should be minimized. The exception is represented by β^+ emitters, resulting in the positron annihilation 511 keV photons exploited by PET techniques. In addition to this, the produced photon energy must be considered: nowadays, the majority of scintillation cameras are optimized for energies close to 140 keV (main emission of ^{99m}Tc), which is a compromise among patient attenuation, spatial resolution and detection efficiency. Photons at lower energies are largely attenuated and increase the patient dose without contributing to the image formation. High-energy photons escape the body and deliver a minimal dose to the patient, but the present machines have poor detection efficiency in that energy range, and the physical collimators are not optimized; both these factors result in image quality degradation. High-energy photons can be used if new detector solutions are explored, like the one presented in chapter 5. For therapy non-penetrating radiation are requested and must be maximized, and correlated photon emission can be in principle used for dosimetric verification, in the so-called theranostics approach (Yordanova et al. 2017). From the biological point of view, "hot spots" (in which the tracer is more concentrated than in other regions) are desired for therapy, while for diagnosis it is possible to profit from both "hot" and "cold spots". Several mechanisms can be implemented in order to concentrate the radiotracer in the target area. Localized administration of the radiotracer in the target region is the first option, while with active transport techniques, the tracer is concentrated into specific organ against concentration gradients thanks to cellular metabolic processes. The glucose metabolism is also exploited, for example for the Fluoro-Deoxy-Glucose (FDG) tracer used in 85 % of the PET clinical practice. The tracer size is fundamental in techniques based on the phagocytosis by specialized cells or on traps in specific organs. Very large molecules (20 – 40 μm diameter) can concentrate in capillaries with smaller diameter. An irregular diffusion through tissue membrane can also be used to identify lesions if specific tracers are employed. Chemotaxis (the movement of a cell in response to chemical stimulus) can also promote the migration and accumulation of radiotracers, for

example as part of an overall inflammatory response. Moreover, some radio-pharmaceuticals are produced with specific characteristics which provide them high affinity to bind to receptor sites, for example in tumors. Finally, the blood flux can be used for blood specific studies.

The choice of the radiotracer depends on the specific organ or region of the body to be examined and on the chosen detection technique. As already detailed, on one side PET aims to detect the two back-to-back photons produced by the annihilation of a positron emitted by the radio-isotope and an electron of the patient body. On the other side, SPECT detects single photons, and the spatial localization is given by mechanical collimation systems. In both cases, tomographic reconstruction is foreseen to obtain three-dimensional images.

The physical basis, historical development and present status of these two techniques are detailed in section 2.3. In addition, the theranostics approach, aiming to perform combined diseases radiation treatment and diagnosis and/or verification imaging, is also addressed in section 2.3.3.

2

Gamma detection in medicine

Contents

As described in chapter 1, the detection of gamma photons plays a role of utmost importance in medical physics, for what concerns both the monitoring of ion beam therapy treatments and the nuclear medicine examination techniques.

Ion beam therapy is rapidly emerging as a valuable cancer treatment technique and a superior alternative to photon radiotherapy for specific clinical indications. The narrow dose peak at the end of the ion range allows for targeted delivery of high dose to the tumor while sparing healthy surrounding tissues. However, since such a treatment technique is highly sensitive to dose prediction and delivery uncertainties, online range monitoring solutions are necessary. Over- and under-shooting effects potentially lead to severe damages to healthy tissues and/or treatment inefficiency, and thus have to be controlled in real-time. The research effort in this field mainly focuses on the non-invasive detection of primary by-products of beam-tissue nuclear interactions: photons from electron-positron annihilation and prompt gammas are most extensively studied for this purpose.

In nuclear medicine diagnostics, radioactive tracers are injected in the patient body and the gamma rays, products of the tracer isotope decay, exiting the patient are detected to retrieve physiological and anatomical information. Positrons are emitted by β^+-decaying isotopes, and the two back-to-back photons generated by their annihilation with patient electrons are detected in time coincidences in Positron Emission Tomography (PET) techniques. On the other hand, Single Photon Emission Computed Tomography (SPECT) exploits single photons emitted by γ-decaying isotopes with collimated detectors.

The research work presented in this thesis focuses on the development of gamma cameras for the detection of prompt gamma rays to tackle the challenge of real-time range monitoring during particle therapy treatments. In addition, the developed prototype design has been tested for application in nuclear medicine SPECT-like examinations. In this chapter, after a brief introduction about the photon interaction channels in matter, the main techniques based on gamma detection developed in the two mentioned fields are described, and the state-of-the-art of gamma detectors employed for these two purposes is sketched.

2.1 Photon interactions in matter

In penetrating an absorbing medium, photons may experience various interactions with the atoms of the medium, involving either the nuclei or the orbital electrons. The interactions with nuclei may be direct photon-nucleus collisions or interactions between the photon and the electrostatic field of the nucleus (pair production). On the other hand, the photon-orbital electron interactions can involve either loosely bound electrons (binding energy E_B small in comparison with the photon energy $h\nu$ - $E_B \ll h\nu$) or tightly bound electrons (binding energy comparable to, or slightly smaller than the photon energy - $E_B \lesssim h\nu$). All these processes are characterized by a partial or complete energy transfer of the gamma-ray photon, and two different outcomes are possible:

- Photon disappears (i.e. is completely absorbed) and its energy is transferred to light charged particles (electron and positrons);
- Photon is scattered and two results are possible:

– the resulting photon has the same energy as the incident photon and no light charged particle is released in the interaction;

– the resulting scattered photon has a lower energy than the incident photon and the energy excess is transferred to a light charged particle (electron).

We focus here on the interaction channels which play an important role in radiation measurements:

- photoelectric absorption;
- Compton scattering;
- pair production.

Photoelectric absorption

In case the photon interacts with an absorber atom and completely disappears by transferring all its energy to the target, the interaction mechanism is called photoelectric absorption. In the interaction an orbital electron is ejected with kinetic energy E_K corresponding to the difference between the incident photon energy $h\nu$ and the electron binding energy E_B, as reported in equation 2.1. The ejected orbital electron is generally referred to as "photoelectron". A schematic view of the photoelectric absorption mechanism is shown in Figure 2.1.

$$E_K = h\nu - E_B \tag{2.1}$$

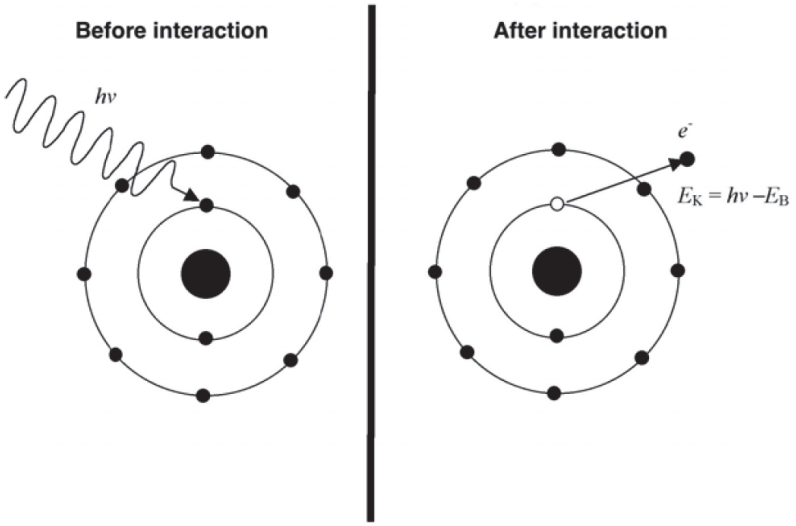

Figure 2.1: Schematic diagram of the photoelectric effect. A photon with energy $h\nu$ interacts with a K-shell electron, which is ejected as photoelectron with kinetic energy E_K. In Podgorsak 2010.

The interaction is with the atom as a whole, and cannot take place with free electrons for conservation of energy and momentum constraints, although the whole photon energy is trans-

ferred to an atomic electron in one of the atom bound shells (tightly bound electron). Energy and momentum cannot be conserved simultaneously in a photon-free electron interaction: the momentum conservation requires a third object (the atom) involved in the interaction which must absorb the extra momentum. When the photon energy exceeds the K-shell binding energy of the absorber, about 80 % of all photoelectric absorption interactions occur with the K-shell electrons. If the energy transferred to the photoelectron is not below the binding energy threshold, it can be sufficient to raise it to a higher orbit, in a process of excitation. As a result of the photoelectric absorption, in addition to the ejected photoelectron, the absorber atom has a vacancy in one of its bound shells. This vacancy is quickly filled through capture of a free electron of the medium and/or rearrangement of electrons from other shells at higher energy level. Therefore, depending on the involved shells, one or more characteristics x-ray photons (fluorescent photons) may also be generated. Such photons are generally reabsorbed close to the original atom site through a further photoelectric absorption involving less tightly bound shells. In some fraction of the cases, the emission of an Auger electron may substitute for the characteristic x-ray in carrying away the atomic excitation energy. As the fluorescent photons, Auger electrons are generally reabsorbed very near the site of the original interaction. The photoelectric process is the predominant mode of interaction for gamma rays of relatively low energy, and it is also enhanced for absorber materials of high atomic number Z. Even if a single analytic expression for the probability of photoelectric absorption over all ranges of photon energy E_γ and Z, the probability (σ_{PE}) dependence on these two parameters can be approximated as shown in equation 2.2, where n varies in the range [4,5] depending on the photon energy (4 for relatively low photon energies, 5 in the relativistic region) (Knoll 2000).

$$\sigma_{PE} \propto \frac{Z^n}{E_\gamma^{3.5}} \tag{2.2}$$

In Figure 2.6 the cross section for the photoelectric absorption is compared to the one of the other photon interaction mechanisms for a copper absorber as a function of the photon energy. It exhibits a characteristic saw-tooth structure in which the sharp discontinuities arise whenever the photon energy coincides with the binding energy of a particular electron shell. Except for the K shell, all other shells have a fine energy structure which reflect in the cross section curve.

Compton scattering

An interaction of a photon of energy $h\nu$ with an orbital electron of an atom is called Compton scattering in honor of Arthur Compton who made the first measurements of photon-"free electron" scattering in 1923 (Compton 1923). Compton earned the Nobel prize for his discovery in 1927. In Compton scattering, the incoming gamma-ray photon is deflected through an angle θ with respect to its original direction, while transferring a portion of its energy to the electron, referred to as "recoil electron". In theoretical studies of such an interaction mechanism, an assumption is made that the photon interacts with a free and stationary electron. As a result of the interaction, the photon, which had an initial energy $h\nu$, continues traveling in the new direction (angle θ with respect to the incident direction) with reduced energy $h\nu'$, and the recoil electron is ejected from the atom with a kinetic energy E_K and a direction with an angle ϕ with respect the photon incident direction. A schematic view of the interaction is given in Figure 2.2. The expression that relates the energy transfer and the scattering angle for any given interaction can be derived by writing simultaneous equations for the conservation of energy and momentum. The obtained relationship is presented in equation 2.3, with the

notation described above and m_0c^2 the rest-mass energy of the electron (511 keV). From the same calculation the kinetic energy of the recoil electron is also obtained from the expression in equation 2.4.

$$h\nu' = \frac{h\nu}{1 + \frac{h\nu}{m_0c^2}(1 - \cos(\theta))} \tag{2.3}$$

$$E_K = h\nu \frac{\frac{h\nu}{m_0c^2}(1 - \cos(\theta))}{1 + \frac{h\nu}{m_0c^2}(1 - \cos(\theta))} \tag{2.4}$$

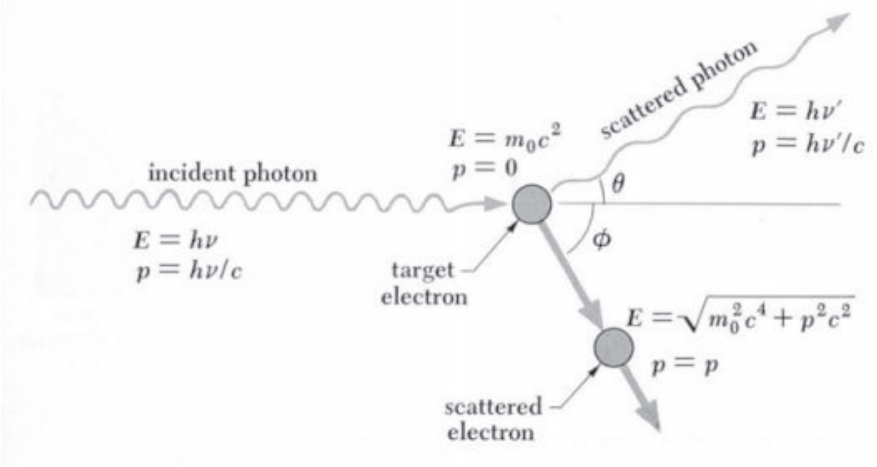

Figure 2.2: Schematic view of the Compton scattering principle. Image from https://universe-review.ca/R15-12-QFT10.htm.

From equation 2.3 it emerges how small scattering angles correspond to little energy transfers, and the other way around. In particular, for $\theta = 0$, no energy is transferred to the electron and the interaction becomes a classical Thomson scattering. For $\theta > 0$ the energy of the scattered photon saturates at high values of the incident photon energy; the larger is the scattering angle, the lower is the saturation value of $h\nu'$ for $h\nu \to \infty$. The relationship between the photon energy before and after the interaction is shown in Figure 2.3a for various scattering angles θ between 0 ° (forward scattering) and π (back-scattering). The scattering angle θ and the recoil electron angle ϕ are related by equation 2.5.

$$\cot(\phi) = \left(1 + \frac{h\nu}{m_0c^2}\right) \tan\left(\frac{\theta}{2}\right) \tag{2.5}$$

This relationship shows that for a given θ, the higher is the incident photon energy $h\nu$, the smaller is the recoil electron angle ϕ. In Figure 2.3b the scattering and recoil angle dependence is plotted for different values of $\epsilon = h\nu/m_0c^2$.

The probability of Compton scattering per atom of the absorber depends on the number of electrons available as scattering targets and therefore linearly increases with the atomic number Z. In Figure 2.6 the probability energy dependence is shown for a copper target and

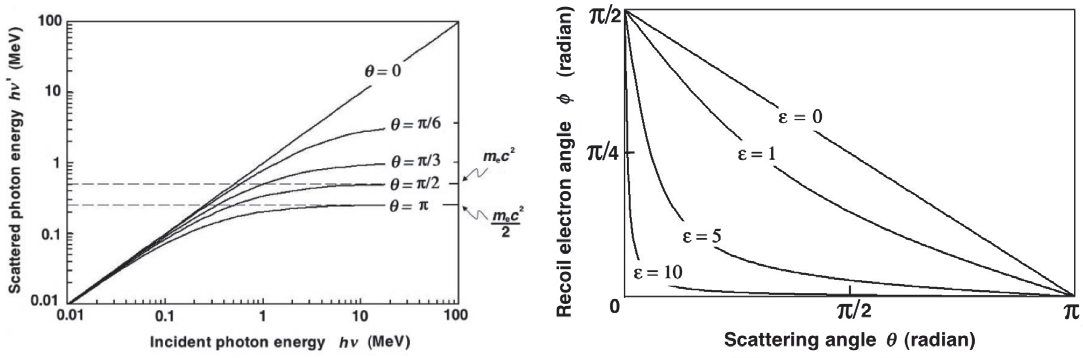

(a) Scattered photon energy against the incident photon energy for various Compton scattering angles in the range from 0 ° to π.

(b) Relationship between the electron recoil electron ϕ and the photon Compton scattering angle θ for various values of $\epsilon = h\nu/m_0c^2$.

Figure 2.3: In Podgorsak 2010

compared to the other interaction channels probability. The differential cross section, or angular distribution of scattered gamma rays, is predicted by a formula derived by Oskar Klein and Yoshio Nishina in 1929, and reported in equation 2.6 (Klein et al. 1929).

$$\frac{d\sigma}{d\Omega} = Zr_e\left(\frac{1}{1+\epsilon(1-\cos(\theta))}\right)^2\left(\frac{1+\cos^2(\theta)}{2}\right)\left(1+\frac{\epsilon^2(1-\cos(\theta))^2}{(1+\cos^2(\theta)[1+\epsilon(1-\cos(\theta))])}\right) \quad (2.6)$$

where r_e is the classical electron radius expressed in equation 1.2. The distribution is shown graphically in Figure 2.4 and illustrates the strong tendency for forward scattering at high values of the gamma-ray energy. At low incident photon energies the probability for forward scattering and back-scattering are equal and twice as large as the probability for side scattering. As the incident photon energy increases, the scattering becomes increasingly more forward peaked and back-scattering rapidly diminishes.

As mentioned, the Compton cross section and energy transfer are calculated with the assumption of free electrons, but at very low incident photon energies such an assumption breaks down and the electronic binding energy E_B affects the Compton interaction: the closer is the photon energy $h\nu$ to E_B, the larger is the deviation of the atomic cross section from the one calculated with the Klein-Nishina formula. Various theories have been developed to account for electronic binding energy effects and apply corrections on the Compton atomic cross sections (Bergstrom et al. 1997). It is worth to notice that for a given absorber Z, the binding energy correction is more significant at lower photon energies, and for a given initial energy $h\nu$, the binding energy correction is more significant at higher atomic number Z. The described binding energy effect is also referred to as "Doppler broadening" (DuMond 1928, 1929).

Pair production

If the photon incident energy exceeds twice the rest-mass energy of and electron $2m_ec^2 = 1.02$ MeV, the production of an electron-positron pair in conjunction with a complete absorption of the photon becomes energetically possible. In practice, as shown in Figure 2.6, the probability of such an interaction mechanism, referred to as pair production, remains very low until the gamma-ray energy approaches several MeV and therefore pair production is predominantly confined to high-energy photons. For $h\nu > 2m_ec^2$, the interaction can lead to a

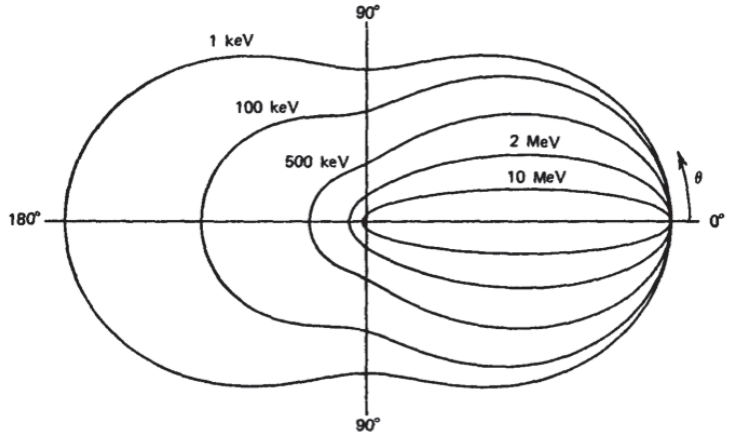

Figure 2.4: Polar plot of the number of photons (incident from the left side) Compton scattered into a solid angle unit at the scattering angle θ, for the different indicated incident photon energies. In Knoll 2000.

momentum transfer to the target body (either the atomic nucleus or an electron). When such an extra momentum is absorbed by the atomic nucleus, the recoil energy, as a result of the relatively large nuclear mass, is exceedingly small and the effect is described as the standard pair production: the incident gamma-ray disappears and is replaced by an electron-positron pair. When the pair production occurs in the field of an orbital electron of the atom, it picks up the extra momentum and the recoil energy may be significant and determine the ejection of the orbital electron; in this case, the photon is absorbed and three particles leave the interaction site, two electrons and a positron, in the so-called "triplet production". A schematic representation of these two effects is given in Figure 2.5.

The total kinetic energy transferred to the charged particles is the difference between the photon incident energy and twice the rest-mass energy of the positron-electron pair. In both cases, because the positron will annihilate after slowing down in the absorbing medium, two annihilation photons are normally produced as secondary products of the interaction. No simple expression exists for the probability of pair production per nucleus, but its magnitude varies approximately as the square of the absorber atomic number Z, and it rises sharply with the photon energy around the threshold region and then increases slowly according to a logarithmic function.

The relative importance of the three described interaction processes for different absorber materials (Z) and gamma-ray energies ($h\nu$) are illustrated in Figure 2.7. Three areas are defined by the two solid lines in the plot, which indicates the energy/Z values for which the two neighboring effects have equivalent probability.

If we now consider a photon beam interacting with a target, all the mentioned interaction processes remove gamma-ray photons from the beam either by absorption or by scattering away from the beam direction, and can be characterized by a fixed probability of occurrence

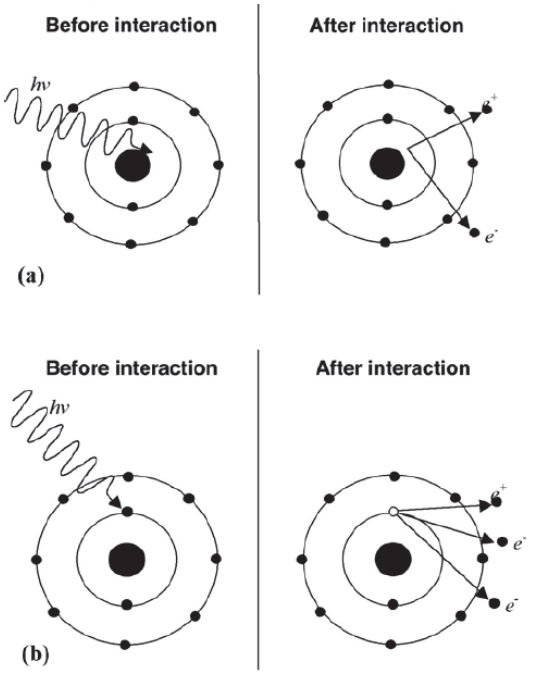

Figure 2.5: Schematic representation of pair production (a) in the Coulomb field of a nucleus and triplet production (b) in the Coulomb field of an orbital electron. In Podgorsak 2010.

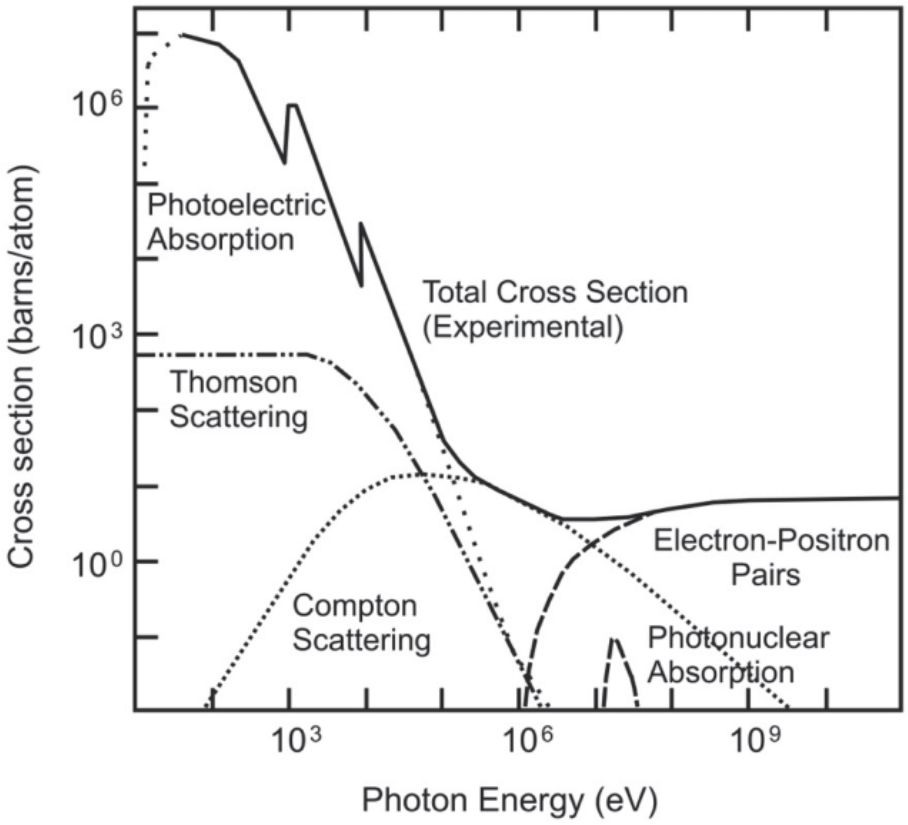

Figure 2.6: Cross sections of the photoelectric absorption, Thomson scattering, Compton scattering, pair production (electron-positron pairs), and photo-nuclear absorption for a copper absorber as a function of the photon energy energy. In Hermanss 2013.

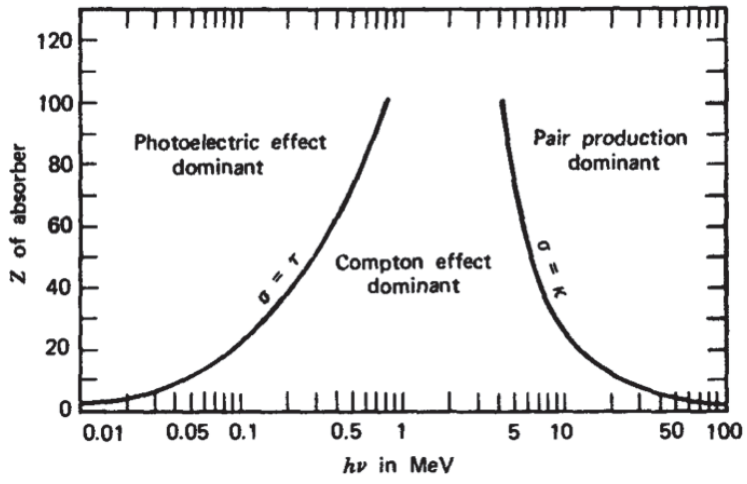

Figure 2.7: Relative importance of the three major types of photon interaction in matter. The lines show the values of Z and $h\nu$ for which the two neighboring effects are just equal. In Knoll 2000.

per unit path length in the absorber. The number of transmitted photons I can be then expresses in terms of the number of incident photons in the beam I_0 as a function of the "linear attenuation coefficient" μ and the absorber thickness t, as shown by equation 2.7.

$$\frac{I}{I_0} = e^{-\mu t} \tag{2.7}$$

where $\mu = N\sigma$ with N the volume density of target atoms and σ the total interaction cross section (photoelectric + Compton + pair production). The average distance traveled by the a photon of the beam in the absorber before an interaction takes place is called "mean free path" λ, and is the reciprocal of the linear attenuation coefficient. In solids, for common gamma-ray energies, λ can vary in the range between few millimeters to tens of centimeters. A more widely used parameter is the "mass attenuation coefficient" μ_ρ, which normalize the linear attenuation coefficient to the absorber density ρ (equation 2.8).

$$\mu_\rho = \frac{\mu}{\rho} \tag{2.8}$$

If the mass attenuation coefficient is used, the convenient concept of mass thickness is also introduced, corresponding to the product of the absorber thickness t by its density ρ and generally measured in mg/cm^2. For compound and mixtures, the mass attenuation coefficient is approximated by a summation of a weighted average of its constituent, as expressed in equation 2.9.

$$\mu_\rho = \sum_i w_i \frac{\mu_i}{\rho} \tag{2.9}$$

with w_i the proportion by weight of the i-th constituent, and μ_i/ρ its mass attenuation coefficient. The attenuation coefficients have specific values for a given photon energy $h\nu$ and absorber atomic number Z, and are tabulated on the National Institute of Standards and Technology (NIST) database according to the calculations in Seltzer 1993.

2.2 Ion range monitoring with secondary gamma rays

Among the secondary radiations produced during particle therapy treatments, gamma rays are probably the most extensively studied for range verification purposes. Gamma rays are emitted in relaxation processes of nuclei excited by nuclear interactions (Prompt-Gammas (PGs)) and as result of the annihilation of positrons produced by beam-induced positron emitting isotopes or in pair creations generated by PGs. In all cases, the emission profiles correlate to the ion path in matter, and the profile fall-off allows to locate the Bragg peak position.

In the following, the developed methods exploiting these two ion range signatures are described.

2.2.1 Range verification with Positron Emission Tomography

As explained in section 1.1.1.1, the fragmentation processes involving target nuclei during proton therapy irradiation and both projectile and target nuclei in case of heavier ion beam therapy, can produce radioactive isotopes. In particular, β^+ emitting fragments are of significant interest for range verification purpose. Table 2.1 shows the main reaction channels and relative isotopes produced along a proton beam path in tissue. More details about the most relevant reaction channels and their characteristics (energy threshold, isotope decay constant, maximal kinetic energy of the emitted positrons), can be found in Oelfke et al. 1996. Additional channels and isotopes are produced during carbon ion irradiation, given the possible projectile activation.

Table 2.1: Proton-nuclear reaction channels and relative positron emitters produced in human tissues. Table reproduced from España et al. 2011b.

Target	Nuclear reaction channel	β^+ isotopes	Half-life
C	^{12}C(p, pn)^{11}C, ^{12}C(p, p2n)^{10}C	^{10}C, ^{11}C	19.29 s, 20.33 min
N	^{14}N(p, 2p2n)^{11}C, ^{14}N(p, pn)^{13}N, ^{14}N(p,n)^{14}O	^{13}N (^{11}C, ^{14}O)	9.96 min
O	^{16}O(p, pn)^{15}O, ^{16}O(p, 3p3n)^{11}C, ^{16}O(p,2p2n)^{13}N, ^{16}O(p,p2n)^{14}O, ^{16}O(p,3p4n)^{10}C	^{14}O, ^{15}O, (^{11}C, ^{13}N)	70.61 s, 122.24 s
P	^{31}P(p, pn)^{30}P	^{30}P	2.50 min
Ca	^{40}Ca(p, 2pn)^{38}K	^{38}K	7.64 min

Figure 2.8 (top) shows the concept of the PET detection technique. The emitted positrons annihilate with human tissue electrons after traveling few mm distances, and 511 keV back-to-back photons are produced and can be detected in coincidence with PET machines. The spatial distribution of the β^+ decay points can be then obtained via the reconstruction of the

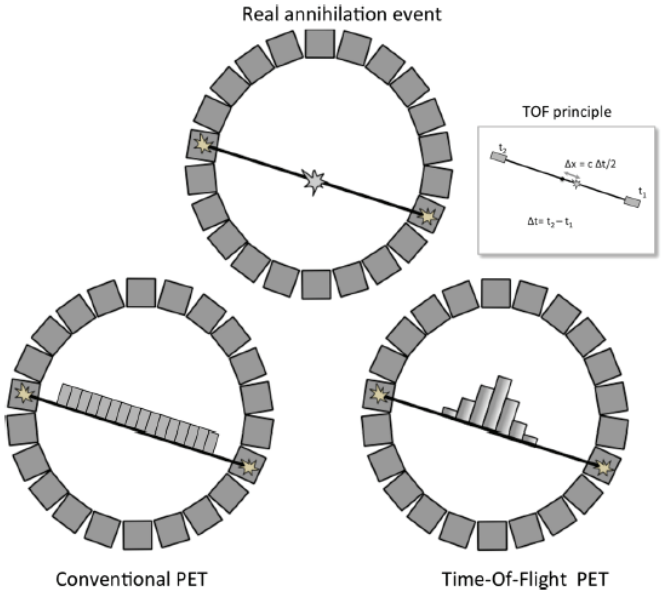

Figure 2.8: Schematic representation of the PET technique principle. In the top figure, a standard real annihilation event is presented, while in the bottom line the principle of conventional and Time-Of-Flight (TOF)-PET are compared. In Vandenberghe et al. 2016.

so-called "lines of response" connecting the two detected photons, and it correlates, even if not directly, to the dose profile. Figure 2.9 shows the one-dimensional β^+ activity profiles along the beam axis for various incident beam types impinging on a Poly-Methyl-Metacrylate (PMMA) target. The positron emitter distribution dependence on the beam nature clearly emerges from these profiles, but a form of indirect correlation with the dose profile distal edge is always verified. In particular, a remarkable difference exists between light ions (protons, ^{3}He and ^{7}Li), for which the induced activity is almost only due to target residuals, and heavier ones (^{12}C and ^{16}O), with a considerable contribution also coming from projectile fragmentation sub-products, which concentrate near the end of the range, explaining the activity peak. The investigation of the correlation between delivered dose and β^+ detected activity must face several issues, as highlighted in Parodi 2018, mainly connected to the difficulty to retrieve quantitative information from PET images and to wash-out effects. Long-lived positron emitters, indeed, can be transported away from the production point by blood flow and metabolic processes, affecting the precision of the obtained images. This effect has been deeply studied experimentally at Heavy Ion Medical Accelerator in Chiba, Japan (HIMAC) with rabbit tissues and Anger-type scintillation cameras (Mizuno et al. 2003; Tomitani et al. 2003), and, more recently, at GSI Helmholtz Centre for Heavy Ion Research, Germany (GSI) with ^{12}C beams (Fiedler et al. 2008a). A reduction of a factor up to 1.5 in the precision of the range determination due to wash-out processes is reported, and a correlation between biological half-life and local dose has been verified and used in simulation to improve the quality of PET images. Although several research efforts have been dedicated to improve the precision of the dose recovery from β^+-emitter distributions (Parodi et al. 2006, 2010, 2007), the only feasible solution for the monitoring of dose delivery is the comparison of measured distributions to simulated ones (Pönisch et al. 2004). These Monte Carlo simulations are based on the planning Computed Tomography (CT) scan, the irradiation scheme, the detector geometry, the imaging procedure; deviations in the delivered dose caused by patient positioning or anatomical modifications can be detected, mainly because they are reflected in changes in

the maximum particle range in the target tissues. Thus, the main quality criterion of the PET monitoring method is the precision in the measurement of range shifts with respect to the predicted ones (Fiedler et al. 2010). The accuracy of the reference simulated activity distribution has advanced in the past years, but it is still limited by the lack of underlying cross-sectional data, the not perfect knowledge of the elemental composition of the patient and the complex prediction of metabolic wash-out processes. Complementary imaging modalities can give fundamental contributions to the simulation predictions: for example, the use of supplemental Magnetic Resonance Imaging (MRI) data has been proposed to better analyze local wash-out effects. In addition to this, the implementation of hybrid PET-CT systems, preferably with dual-energy CT, would improve the conversion of CT information to the material composition needed for the PET simulations (Landry et al. 2013).

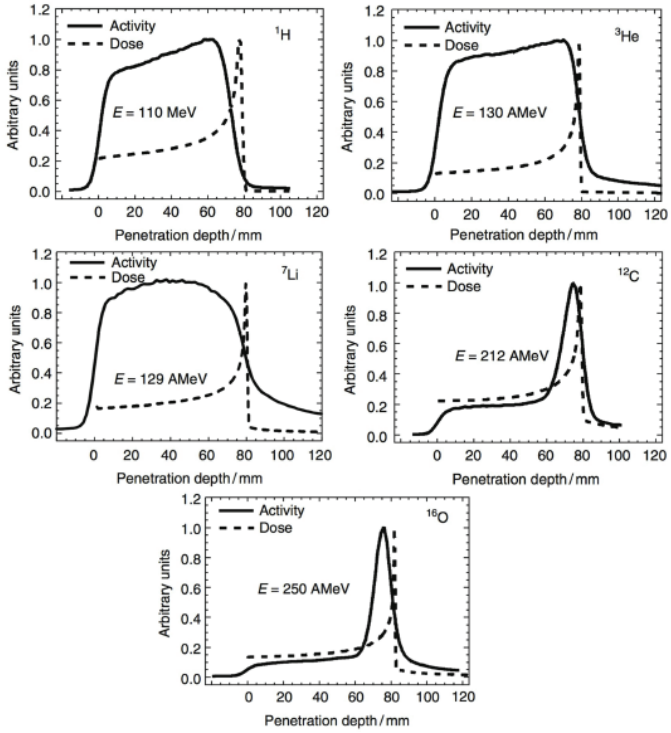

Figure 2.9: β^+ activity profiles for various ion beams impinging on a PMMA thick target. The depth-dose profiles are also shown in dashed lines for comparison. In Fiedler et al. 2012.

The PET data acquisition can be performed following three main strategies:

- In-beam data acquisition: the PET system is integrated in the beam delivery system and the data acquisition is performed during or immediately after irradiation in the treatment room. In synchrotron facilities, a further solution is represented by acquisitions in the time between different spills, while for cyclotrons data-taking during beam extraction has been explored and seems feasible (Kraan et al. 2014). On one hand, this method is advantageous because it allows detecting short-lived isotopes, thus increasing the available statistics, and reducing the effects of biological processes. Moreover, the patient position does not change with respect to the treatment. On the other hand, the integration of PET scanners in the treatment site can be costly and cause limitations on the detector geometry affecting detection efficiency and, consequently, image quality. The scanner should not be directly exposed to the beam in order to avoid damage

and activation of active modules and electronics, and at the same time it should allow enough degrees of freedom for the patient table. The need of an opening for the beam portal typically results in the choice of planar dual-head configurations.

- In-room data acquisition: the installation of commercial full-ring PET scanners in the treatment room, but not directly on the beam line, allows the so-called "in-room" data acquisitions quickly after the end of the treatment irradiation. This solution leads to longer treatment room occupation, because some minutes of imaging time are required to gain enough statistics, but allows the use of commercial machines, less expensive and more efficient than custom integrated scanners designed for in-beam applications. Moreover, patient positioning issues are minimized by the limited movements and signal wash-out is reduced.

- Off-line data acquisition: if the patient has to be transported out of the treatment room for the PET scan, the implemented strategy is classified as "off-line". The limited cost and treatment occupation time are probably the only advantages of this method, which suffers from relevant signal decay and wash-out processes given the long time between the end of the irradiation and the beginning of the PET scan. Off-line images predominantly show activity from isotopes whose half-life is comparable or longer than the transportation and setup time, thus it is mainly restricted to ^{11}C (half-life longer than 20 minutes), produced in relatively small amount in proton therapy, more abundant in carbon treatments. The reduced number of available decays requires longer acquisition time with respect to in-beam and in-room solutions, which further enhance the effect of metabolic processes. The patient re-positioning issues also contribute to the image quality degradation.

A schematic view of the three PET acquisition modalities is presented in Figure 2.10a. As mentioned in the three data acquisition modality description, the counting statistics is one of the fundamental parameters to be studied for the design of PET monitoring solutions. It can be estimated as the integral of the decay curve shown in Figure 2.10b, where the time intervals corresponding to the three acquisition strategies are separated. The curve is based on measurements performed at GSI during therapeutic irradiation with carbon ions; an in-beam solution has been adopted, with 40 s additional data taking time after the irradiation. The in-room selected window lasts 3 minutes, and for the off-line case, long-time measurements of one patient have been used (Fiedler et al. 2008b). If 100 % is assigned to the number of registered true events in the in-beam condition, 50 % is estimated for the in-room solution and 58 % for the off-line data taking (Shakirin et al. 2011). It is then clear that off-line solutions are severely challenged by the extremely low signal, considerably lower with respect to the standard application of the employed commercial scanners (down to average activity values of few tens of Bq/ml (Bauer et al. 2013)). The scanner geometry is another fundamental parameter to be considered: as mentioned, the chosen data-acquisition strategy determines the scanner design. In-room and off-line solutions can make use of commercial full-ring systems, with a complete field of view. In addition to this, modern combined PET-CT scanners enable an accurate co-registration of treatment and imaging position, so that the unavoidable patient movement due to transportation and repositioning can be partially corrected. The geometrical constraints imposed by in-beam integrated solutions cause reduced efficiency and restricted field-of-view, which are reflected in image artefacts (Crespo et al. 2006), particularly significant in the imaging of large tumor objects. Improvement can be provided by TOF-PET detectors (Crespo et al. 2007; Surti et al. 2011), as discussed below. In Parodi 2015 the au-

thor highlights how the first historical attempts to implement PET particle therapy monitoring, described in the following, have not relied on optimized instrumentation for the specific application. Anyway, the promising results obtained by several groups encouraged dedicated investigations which are leading to substantial improvements of such a technique in the past years. In particular, the application of gamma detectors with depth-of-interaction capability, also studied for standard diagnostics applications, has demonstrated its effectiveness in correcting parallax artefacts in the reconstructed images; improvements in data acquisition and synchronization with the accelerator radio-frequency offer the possibility of including the signal detected during the beam-on time for in-beam solutions, thus increasing the counting statistics and reducing the acquisition time; new adapted geometries, such as the Japanese OpenPET system (Tashima et al. 2012; Yamaya et al. 2008), recently finalized in its upgraded version (Yamaya 2017), offer higher-efficiency alternatives to standard dual-head systems. It is worth to dedicate particular attention to the already mentioned TOF-PET, deeply studied in the past years, which already demonstrated improved imaging capabilities with respect to standard scanners. The measurement of the detection time of each of the two photons helps, through the calculation of the arrival time difference, in restricting the emission point along the reconstructed line of response and thus also in rejecting part of accidentals. In standard PET, the three-dimensional reconstruction relies on the superposition of several lines of response and on filtered back-projection algorithms. The time information adds a second dimension to the line of response reconstruction, with the localization of the interaction point in a few cm along the line, depending on the detector time resolution. For example, a coincidence timing resolution of 600 ps Full Width at Half Maximum (FWHM) translates to a position uncertainty of 9 cm FWHM. In Figure 2.8 (bottom line), the TOF-PET principle is sketched and compared to the conventional PET detection scheme. The potential benefits of TOF information in PET image reconstruction were already understood since the early stage of its development for diagnosis purpose, and the first TOF-PET systems were built already in the 1980s in the US (Gariod et al. 1982). They were based on Cesium Fluoride (CsF) or Barium Fluoride (BaF_2) scintillators, the best available at the time in terms of time resolution, but their spatial performance and sensitivity were poor with respect to conventional PET scanners. The improvements in scintillating material as well as in Photo-Multiplier (PM) performance and reliability allowed for the first commercial proposal of a TOF-PET scanner only in 2006, by Philips (Surti et al. 2007). The development of TOF-PET machines is strongly connected to their application in diagnosis, and further details will be given in section 2.3.1. As for particle therapy monitoring application, the TOF technique applied to PET can be used to partially reverse the effects caused by non-complete angles of in-beam data collection (Crespo et al. 2006), and in general to improve the image quality. Various groups are developing detector solutions for clinical implementation of such a technique; some of them have already been tested on beam with promising results. They will be described in more details in the following, after a brief historical overview of the PET application in particle therapy quality assurance.

As emerges from the above paragraphs, PET is probably the most extensively studied technique for online beam range verification and is at present the only method clinically implemented (Yamaya 2018). The first published proposal of using PET for range verification in particle therapy dates back to 1975 (Bennett et al. 1975). In the following years, further suggestions were connected to pion (Goodman et al. 1986; Shirato et al. 1989) and neutron therapy (Vynckier et al. 1989), but the actual clinical implementation was pioneered in the context of heavy ion therapy at Lawrence Berkeley Laboratory (LBL) (Chatterjee et al. 1981; Llacer et al. 1979). The original idea was to verify the correctness of ^{20}Ne ion therapy treat-

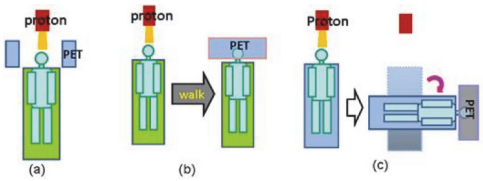

(a) Schematic view of the three PET configurations for the application in ion range monitoring. Form left to right: in-beam, off-line and in-room PET. In Zhu et al. 2013.

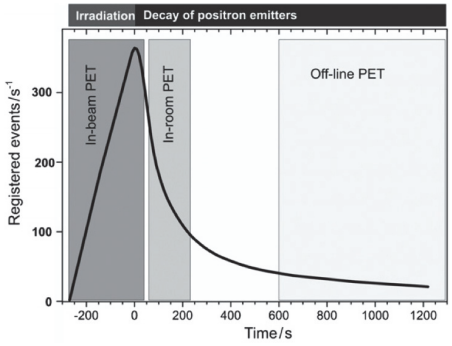

(b) PET registered events as a function of time corresponding to the measurement of one field during irradiation and up to 20 minutes after irradiation. The time intervals corresponding to in-beam, in-room, and off-line PET measurements are highlighted. In Shakirin et al. 2011.

Figure 2.10: The application of the PET technique to the monitoring of ion range in particle therapy includes three possible modalities: in-beam, in-room and off-line PET, represented in the scheme in (a). The amount of registered events depends on the created positron emitter half-life, and thus on the implemented modality, as shown by the histogram in (b).

ment plans by delivering a low dose β^+ emitting ion beam (e.g. ^{19}Ne) prior to the treatment and measuring its range via PET imaging of the emitted photons; before the regular treatment with stable beams. Pilot experiments were conducted with a planar PET camera based on two blocks of Bismuth Germanium Oxide - $Bi_{12}GeO_{20}$ (BGO) crystals, including measurements in a live dog (Llacer et al. 1984a). The experimental data showed interesting results, even if the use of a passive beam shaping system determined a significant activation of the BGO camera (mainly due to neutrons) and, thus, a substantial noise level. Analog investigations using radioactive ion beams (^{15}O, ^{17}F, ^{19}Ne) were carried out in the nineties at GSI with various PET cameras (Pawelke et al. 1996), and further developments of this technique were obtained at the HIMAC facility (Iseki et al. 2004; Kitagawa et al. 2006), where a dedicated line was set up for radioactive beam based treatments (Kanazawa et al. 2002; Urakabe et al. 2001). The "autoactivation" process (Tobias et al. 1971) described above (i.e. the production of radioactive nuclei in the target by incident beam of stable ions) makes anyway possible the implementation of PET monitoring techniques on standard high-energy beams, and the first clinical implementation of such technique was launched at GSI in 1997, after the tests with radioactive beams mentioned above and fragmentation studies conducted with ^{12}C, ^{16}O, ^{20}Ne beams on a PMMA target (Enghardt et al. 1992). An in-beam PET system was designed and installed into the treatment room and has been employed routinely for monitoring the irradiation of more than 440 patients (mainly suffering from head-and-neck cancer), with data acquisitions performed in the pause of pulsed beam delivery. This experience proved how PET is a valuable tool for particle therapy quality assurance (Enghardt et al. 2004). In parallel to these developments in Germany, an off-line solution was implemented at National Institute of Radiological Sciences, Japan (NIRS) with a commercial full-ring volumetric scanner, but it was not used in clinics.

As previously explained, notwithstanding the lacking peak structure in the activity profile (see Figure 2.9), also proton irradiation therapy can be monitored by PET scanners. Various detailed studies investigated its feasibility and performance in the nineties (Litzenberg et al. 1992, 1999; Oelfke et al. 1996; Paans et al. 1993). Two groups worked in parallel on clinical studies of PET monitoring in proton therapy. In Japan, a dual-head PET scanner has been installed at the National Cancer Center, Kashiwa (Nishio et al. 2006): it is based on high-resolution BGO detector components and integrated in the proton gantry. The measurements are collected immediately after irradiation (in-room solution), mainly due to the considerable radiation background during the continuous beam delivery and the passive beam shaping. The satisfactory results led to the implementation of a daily PET workflow, which allowed the research group to follow the anatomical changes of the patient during the treatment progress and correct the treatment planning. The test of this method included 48 patients suffering from head-and-neck, liver, lung, prostate and brain tumors (Nishio et al. 2010). In the US, at the Massachusetts General Hospital (MGH), Boston, a pilot clinical study was performed with an off-line solution which made use of a commercial full-ring scanner (Parodi et al. 2007). The PET scan was performed about 20 minutes after proton irradiation. The off-line approach has been deeply studied in the same context in those years, and compared to in-beam PET solutions in cyclotron and synchrotron based scenarios (Knopf et al. 2011; Parodi et al. 2008). The advantage in terms of available statistics for in-beam solutions has been measured: the ratios between the amount of physical decays available for in-beam and off-line detection range from 40 % to 60 % for cyclotron-based facilities, to 65 % to 110 % (carbon ions) and 94 % to 166 % (protons) at synchrotron-based facilities (Parodi et al. 2008). The in-room solution has also been explored at the same institution, with an acquisition time reduced to less than 5 minutes thanks to the higher sensitivity with respect to the off-line modality (Zhu et al. 2011). At Heidelberg Ion Therapy Center, Germany (HIT), in Germany, both an in-beam (Sommerer et al. 2009), and an off-line solution (Bauer et al. 2013) have been tested, while alternative off-line solutions have been implemented in Japan (Hishikawa et al. 2002) and US (Hsi et al. 2009). With the aim of extending the field of view and thus enhancing the sensitivity of in-beam PET designs, Japanese researchers proposed the already mentioned OpenPET as a new geometrical solution. Its first-generation prototype is composed of two complete rings, with the beam port between the two (Yamaya et al. 2008, 2009) and the possible implementation of an integrated CT. A more efficient geometry has been proposed some years later, consisting of a single-ring which can provide an accessible and observable open space with higher sensitivity and reduced number of detectors compared to the previous generation one (Tashima et al. 2012). The ring is cut at a slant angle in order to be disposed at a certain angle with respect to the beam line, but maintain parallel detector modules orientation. A similar solution was proposed in Crespo et al. 2006, but with a conventional PET ring with an oblique orientation with respect to the beam direction ("slant PET"). A small prototype of single-ring OpenPET was produced, consisting of 4 layers (16×16 array) of Zr-doped GSO scintillators with a size of 2.8×2.8×7.5 mm^3 read out by H8500 Hamamatsu PMs (Tashima et al. 2016), and tested at HIMAC with radioactive ^{11}C beam. The prototype can operate in open and closed mode, the second only adapted for acquisition in beam-off condition, and easily arranged in the two configurations. The tests, performed in the two modes, the spatial resolution and sensitivity were 2.6 mm and 5.1 % for the open mode and 2.1 mm and 7.3 % for the closed one. A rapid transformation to a closed arrangement is foreseen by the authors immediately after irradiation in order to minimize the decrease of resolution and sensitivity. After these encouraging results, a full-size whole-body version of the single-ring OpenPET has been recently completed (Yamaya 2017). Extensive studies about PET monitoring have been and are being carried out also in Italy. An in-beam prototype consisting of two planar heads made of Lutetium-Yttrium

OxyorthoSilicate - $Lu_{2(1-x)}Y_{2x}SiO_5$ (LYSO) crystals (Vecchio et al. 2009), 5×5 cm^2 active area, has been tested at the proton therapy center CATANA, in Catania, equipped with a 62 MeV beam line for ocular tumor treatments (Cirrone et al. 2003). The measurements validated the detector design (Attanasi et al. 2008), which has been called DoPET and also compared to the in-beam system installed at GSI with simultaneous measurements of β^+ activity induced in a PMMA target (Attanasi et al. 2009), showing improved spatial resolution mainly due to the smaller crystals. The field of view of the first prototype was a major issue, so that an extended version with 10×10 cm^2 active area per head has been realized and tested by the Italian collaboration at *Centro Nazionale di Adroterapia Oncologica*, Italy (CNAO) (Kraan et al. 2015; Rosso et al. 2013) and in Catania (Camarlinghi et al. 2014; Sportelli et al. 2014). The comparison of the results with Monte Carlo simulated data showed good agreement; for treatment-like data taking, the ability of the system to give valuable feedback on particle range on homogeneous targets within 2 minutes after irradiation has been demonstrated, but the data collected during beam-on time were not satisfactory. In the context of PET data taking during beam-on time, several studies have been performed concerning short-lived isotopes, which has to be included in the total activity evalutation in case of in-spill acquisitions. Already mentioned in the DoPET related publications, they have been deeply studied experimentally. Defined as positron emitters with half-life below 19 s, the ones significant for *in vivo* PET monitoring have been identified in Dendooven et al. 2015: in particular, the author concludes that the contribution to the β^+ activity given by ^{12}N isotopes in the first tens of seconds after irradiation can potentially lead to real-time range verification of proton therapy with the implementation of optimized detectors, providing equal or superior information with respect to PG detection (see sections 1.1.5.3 and 2.2.2). A proof-of-principle experiment for the detection of such isotopes has been performed at the KVI-CART cyclotron with 90 MeV protons and a PET system based on LYSO crystals coupled to digital Silicon Photo-Multipliers (SiPMs) (Buitenhuis et al. 2017). A range shift of 5 mm could be measured with 3 mm accuracy using the ^{12}N activity profile. Another PET prototype based on SiPMs is the one developed by the Italian Innovative Solutions for Dosimetry in Hadrontherapy (INSIDE) collaboration (Marafini et al. 2015), and described in (Bisogni et al. 2017). The design is based on fast pixelated Lutetium Fine Silicate (LFS) scintillators coupled one-to-one to SiPMs. The readout electronics has been developed to accept the count rate expected from synchrotron beams during the spill phase (Rolo et al. 2013). The whole system also includes a charged particle tracker ("dose profiler"), and its design has been studied for the installation on the CNAO beam line, where it has been tested and is at present in operation. The first characterization tests performed with PMMA and anthropomorphic phantoms demonstrated the capability of the system to operate in both beam-on and -off condition, and the comparison between in-spill and interspill data showed a substantial agreement in terms of distal fall-off. The results were also in agreement with Monte Carlo simulated data. In December 2016, the INSIDE PET was also tested during a patient treatment, and the possibility of online monitoring of proton therapy in clinical conditions has been demonstrated (Ferrero et al. 2018). For carbon ion irradiation, in-spill measurements have not been satisfactory due to the large amount of random coincidences, but at treatment end, or at most 20 s afterwards, the range measurement has been verified to be reliable within 1–2 mm, when comparing both different experimental sessions and data with simulations (Pennazio et al. 2018). Digital photon counters have been the basis for the development of TOF-PET prototypes, attractive solution for improved spatial reconstruction capabilities in both full-ring and dual head solutions. Within the European project ENVISION, two different configurations have been explored for in-beam TOF-PET imaging: one of them relies on LYSO crystal read out by SiPM, and a TOF resolution of 235 ps Coincidence Resolution Time (CRT) FWHM have been obtained (Morrocchi et al. 2012). The alternative solution

involved low-cost gas detectors (multigap Resistive Plate Chamber (RPC)), but it was less performing in terms of time resolution (Watts et al. 2013). Another small prototype based on LYSO crystal and digital photo-sensors, presented in (Degenhardt et al. 2012), has been tested for TOF application in clinical conditions at HIT with protons. The acquisitions were performed in the pauses between spills or after irradiation, providing relevant information for a future development of a clinical size detector (Cambraia Lopes et al. 2016).

The development of an in-beam PET detector is also the objective of the *Laboratoire de Physique de Clermont*, France (LPC) *Application et Valorisation des Interactions Rayonnements-Matière* (AVIRM) research group. The prototype, called *Détecteur Pixélisé de Grande Acceptance* (DPGA) (French) or Large Area Pixelized Detector (LAPD) (English), is composed of 240 identical $13\times1\times315$ mm^3 LYSO crystals glued to PMs, assembled in groups of four ("quartets") with similar gain PMs for the read-out on a custom Front-End (FE) board (Montarou et al. 2016). The system has been first tested in a hospital in Clermont-Ferrand with a PMMA phantom and Fluoro-Deoxy-Glucose (FDG) injected radiotracer (some tenth of MBq of activity), and then with proton beams at HIT, in a reduced-size version. These first tests have been used to validate and characterize the detector, but limited acquisition rate capabilities have been verified with the preliminary VERSABUS Module Eurocard (VME)-based solution. The prototype is now installed at the *Centre Antoine Lacassagne*, Nice, France (CAL) in Nice, on the 65 MeV line, and the new acquisition system based on Micro Advanced Telecommunications Computing Architecture (μ-TCA) is at the test stage.

PET is at present the only applied solution for ion range monitoring in clinical conditions (Yamaya 2018), and, as described, the research is ongoing to provide real-time control capabilities with improved image quality. Its principle can also be applied to hybrid systems, investigated in the last years and briefly mentioned in section 1.1.5.5, including the detection of β^+ activity in combination with PGs (see sections 1.1.5.3 and chapter 2.2.2) or additional single photon emission. This implementation will probably imply compromises in the individual technique performance, but their complementary information can open new perspectives for *in vivo* ion range verification.

2.2.2 Ion range monitoring with prompt-gamma radiation

As introduced in chapter 1, the high ballistic precision of particle therapy is advantageous because it provides high dose selectivity while sparing the healthy tissues surrounding the tumors, but at the same time it makes such a cancer care modality quite sensitive to any source of uncertainty and deviation with respect to the treatment planning: patient mis-positioning, organ motion or anatomical variations between fractions (such as tumor shrinking, weight loss, cavity filling). A reduction of the safety margins presently applied to the Planned Target Volume (PTV) to account for such uncertainties would be only possible with the availability of a real-time range monitoring system. As the primary beam stops inside the patient, the range control can be based on secondary radiations issued from nuclear reactions. In particular, the work presented in this thesis is focused on range monitoring techniques relying on the detection of PG rays.

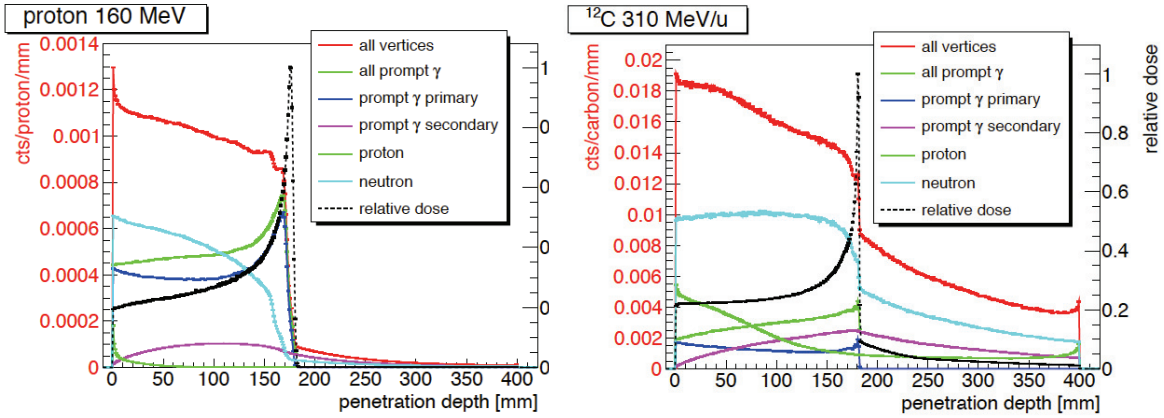

(a) 160 MeV protons. **(b)** 310 MeV/u carbon ions.

Figure 2.11: Emission vertices of secondary particles emerging from a cylindrical water target (15 cm diameter, 40 cm length) irradiated by a 160 MeV proton beam (a) and a 310 MeV/u carbon ion beam (b). An energy lower threshold of 1 MeV has been applied. In Krimmer et al. 2017b.

2.2.2.1 Prompt-gamma emission during particle therapy

The PG range monitoring techniques rely on the emission of photons due to the relaxation of excited nuclei within about one nanosecond after the nuclear interaction. The PGs are emitted in the whole solid angle around the patient and in a wide energy range (from some hundreds of keV up to 10 MeV). Such a prompt radiation has been demonstrated to be correlated to the ion range for both protons and carbon ions. It can be exploited via single photon detection systems to provide a real-time feedback in case of major deviations of the measured range with respect to the planned one, and eventually trigger a treatment emergency stop.

PG spatial features

Figure 2.11 shows the distribution of emission vertices of secondary radiation emitted by a homogeneous water phantom (cylinder of 15 cm diameter and 40 cm length) in the beam direction, together with the dose profile. The simulated data have been obtained by irradiating the phantom with 160 MeV protons (Figure 2.11a) and 310 MeV/u carbon ions (Figure 2.11a), having the same expected range in water. All the secondary particle vertex distributions are correlated to the primary ion range, and in particular PGs appear as the best candidates for range monitoring purpose, given the significant emitted statistics. Also neutrons are produced in considerable fraction, mainly in carbon ion irradiation, but the spatial information about their production vertex is hardly retrievable. The correlation between longitudinal PG and dose profiles can be exploited for "imaging" monitoring approaches lo locate the Bragg peak position. Physically and electronically collimated prototypes, used to access the spatial information carried by the emitted photons, will be described in following sections. In addition to the spatial information, also energy and timing PG specific features can be used as tools to retrieve the Bragg peak position with the so-called "non-imaging techniques". The wide energy spectrum of the produced PG rays depends on the composition of the target material, and it is characterized by discrete lines. In Figure 2.12a, the PG energy spectrum is shown for the simulated irradiation of Polyethylene (PE), PMMA and water targets with a 160 MeV proton beam. The discrete spectroscopic lines are clearly visible: in particular, three lines

PG energy distribution

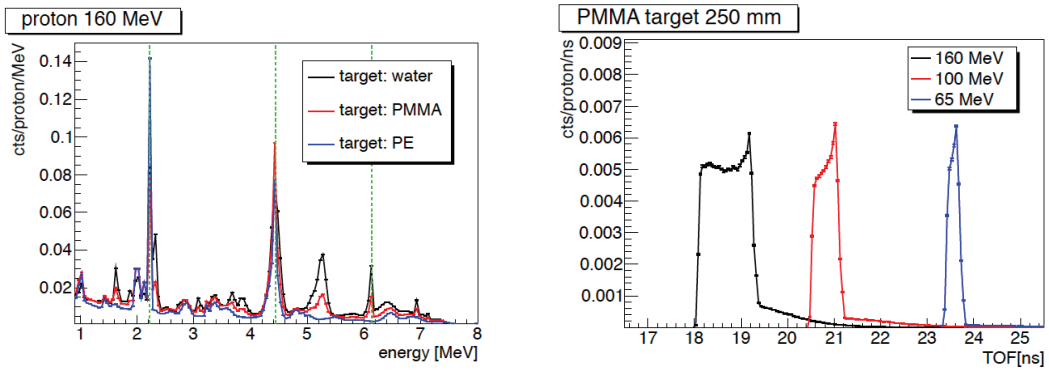

(a) Simulated PG energy spectra resulting from the irradiation of PE, PMMA and water targets (cylinders 15 cm diameter, 25 cm length) with 160 MeV protons. The vertical lines highlight specific spectroscopic transitions.

(b) Simulated TOF spectra of PGs emerging from a PMMA cylindrical target (cylinders 15 cm diameter, 25 cm length) for 65, 100 and 160 MeV proton beam irradiation.

Figure 2.12: In Krimmer et al. 2017b.

are highlighted, corresponding to the de-excitation of ^{16}O (6.13 MeV), ^{12}C (4.44 MeV), and to the neutron capture by hydrogen (binding energy of deuterium = 2.22 MeV). The latter is not correlated to the primary particle range. The comparison of the measured PG energy spectrum to the expected one can be used to access information about the material traversed by the primary beam and estimate the proton range: such a technique is referred to as Prompt Gamma Spectroscopy (PGS) (Verburg et al. 2014), and will be further discussed in following sections. To be noticed that the PG yields are not only depending on the traversed material composition, but also on the beam energy; a global enhancement is observed as the energy decreases (Krimmer et al. 2017b).

PG TOF distribution

As mentioned, also time information can be used for range monitoring purposes. Figure 2.12b shows the TOF distribution of PGs emerging from a PMMA target (15 cm diameter, 25 cm length) irradiated with 65, 100 and 160 MeV proton beams. The influence of proton energy (range) on the spectrum peak position, width and integral is clear, and is the basic idea for two proposed monitoring techniques: Prompt Gamma Timing (PGT), which is based on the TOF spectrum peak position and width (Golnik et al. 2014), and Prompt Gamma Peak Integral (PGPI), additionally exploiting the TOF spectrum integral to verify beam position and total dose, thus approaching *in vivo* dosimetry (Krimmer et al. 2017a).

All monitoring techniques based on PGs must commonly deal with some specific PG features. As a starting point, PG production yields must be considered when designing monitoring prototypes. Specific measurements are needed for particle therapy, with defined beam energies, targets and irradiation fields, even if some data of PG production by proton and carbon ions are available in the literature for general nuclear physics and astrophysics purposes (Dyer et al. 1981; Kiener et al. 1998). In Pinto et al. 2015 the authors studied the absolute PG production yields in ten single-slit experiments with the irradiation of PMMA and water targets with proton and carbon ion beams, and the results are shown in Figure 2.13 for proton (left) and carbon ion beams (right) and summarized in table 2.2, reproduced from the same publication. The detection energy threshold was set to 1 MeV.

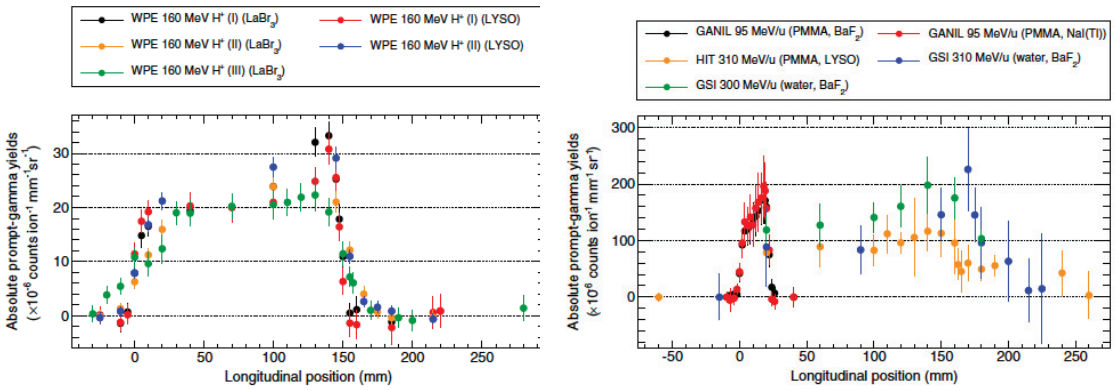

(a) 160 MeV protons. 3 data sets have been obtained with Lanthanum Bromide ($LaBr_3$) detector, 2 with LYSO detector.

(b) Carbon ions at various energies. PMMA and water targets have been employed, and the PG detection has been performed with BaF_2, LYSO and Sodium Iodide doped with Thallium (NaI(Tl)) detectors.

Figure 2.13: Absolute PG yields profiles for 160 MeV proton beams (a) and carbon ion beams at various energies (95 MeV/u at *Grand Accelerateur National d'Ions Lourds*, Caen, France (GANIL), 310 MeV/u at HIT and 300 MeV/u at HIT) (b) irradiating PMMA and water targets. The detection energy threshold was set to 1 MeV. In Pinto et al. 2015.

Table 2.2: Absolute PG yields (for PGs with energy higher than 1 MeV) measured in the first point after the PG profile entrance rise. The energy range shows the energy range of the primary particles inside the Field Of View (FOV) of the measurement point estimated in simulation. Table reproduced from Pinto et al. 2015.

Material	Energy range (MeV/u)	Ion species	Absolute yield [$\times 10^{-6}$ counts ion^{-1}mm^{-1}sr^{-1}]
PMMA	[77 – 90]	Carbon ions	$124 \pm 0.7_{\text{stat}} \pm 30_{\text{sys}}$
PMMA	[272 – 310]	Carbon ions	$79 \pm 2_{\text{stat}} \pm 23_{\text{sys}}$
Water	[264 – 292]	Carbon ions	$112 \pm 1_{\text{stat}} \pm 22_{\text{sys}}$
PMMA	[139 – 156]	Protons	$16 \pm 0.07_{\text{stat}} \pm 1_{\text{sys}}$

The comparison of PG yields for proton and carbon ion beam irradiation with the same range in water, i.e. 160 MeV protons and 310 MeV/u carbon ions, shows a value approximately five times greater for the latter with respect to the former. Such an increased emission is due to the contribution of both projectile and target nuclei, while only the target nuclei can emit PGs in proton irradiation. For carbon ions irradiation at different energies, an increased PG emission has been verified for the lowest energy ions, as expected from published cross sections. Moreover, if comparing the PMMA and water targets for the same primary ion features, water results in an enhanced prompt photon emission. Other experimental results are reported in Agodi et al. 2012, 2013: the authors measured PG yields of 80 MeV/u carbon ions impinging on a PMMA target considering the full ion range, while in Pinto et al. 2015 the results are normalized to the path length unit (1 mm). The found yield is $(2.32 \pm 0.01_{\text{stat}} \pm 0.15_{\text{sys}}) \times 10^{-3}$ counts ion^{-1}sr^{-1}, which is compatible to the results in Pinto et al. 2015 if the proper normalization is considered. Higher energy carbon ion beams (220 MeV/u) and PMMA targets have been employed to produce the results presented in Mattei et al. 2015. More recently, the same authors studied the prompt photon production of ^{4}He, ^{12}C and ^{16}O beams interacting in PMMA target at HIT, showing good agreements with the aforementioned results (for carbon ions), and providing additional information about new ion species (Mattei et al. 2017). Furthermore, detailed information about specific PG spectroscopic lines are reported in Verburg et al. 2013, 2014, and have been recently published in Kelleter et al. 2017.

In order to summarize the present knowledge about PG production and give reference values for clinical applications, as reported in Krimmer et al. 2017b, a rough estimate of the PG yields (for PGs with energy higher then 1 MeV) per projectile for 15 cm range in water is 0.05 per proton and about 0.3 per carbon ion. These yields results to be similar to the one of the total amount of β^+ emitters (Pinto et al. 2015; Robert et al. 2013). However, secondary radiation attenuation is another fundamental parameter to be considered, since only a fraction of the emitted photons will be able to emerge from the patient body and, at the same time, keep the information on the creation vertex. The higher energies of prompt photons (1 – 10 MeV) with respect to positron annihilation ones (511 keV) lead to an improved transmission through the patient body (factor 5), thus an increased expected detection rate (Moteabbed et al. 2011). The available PG statistics for beam range monitoring can be assessed by considering the absolute yields measurements presented above (including attenuation considerations) and the average clinical beam intensities. In particular, 10^{10} protons per second and $10^{[7-8]}$ carbon ions per second are typical clinical values. For a monitoring on a single spot basis, which is highly desirable, the most important spot (generally in the distal region of the PTV) can be chosen as reference: the number of incident ions in such a spot is approximately 10^8 and 10^6 for protons and carbon ions, respectively (Grevillot et al. 2012; Krämer et al. 2000). For these kinds of spots, in the whole solid angle, about 10^7 (for protons) and 10^5 (for carbon ions) PG rays are emitted in the spot duration. This number is then reduced by the detection device efficiency and FOV.

2.2.2.2 Simulation of prompt-gamma emission and detection

The general objective of PG control of particle therapy treatment is the ion range on-line monitoring, which is performed via a comparison between measured and predicted PG distributions, in accordance with the treatment planning. The prediction of PG emission profiles relies on simulations, which are based on the experimental data described in the previous paragraph, and must include the prediction of the detector response. Precision and accuracy

of the physical models and the reference data are crucial in the simulation process, also given the complex dependency of PG yields to parameters such as beam features (ion species, energy, spatial distribution) and target composition.

Monte Carlo simulation is generally time consuming (Dedes et al. 2015; Robert et al. 2013; Schumann et al. 2015), and several approaches are being studied to reduce the calculation time and allow for direct translation to clinics. Graphics Processing Unit (GPU)-oriented implementations highly improve the simulation efficiency, and some solutions have been successfully tested. Clinically acceptable dose calculation accuracy has been achieved with few tens of seconds of calculation time required, but electron and neutron transport have been disabled in the code described in Qin et al. 2017. With respect to standard Monte Carlo codes, an improvement in efficiency of three orders of magnitude is reported for the clinical validation of the gPMC (GPU-based Monte Carlo (MC) code for proton dose calculation) in Giantsoudi et al. 2015. Alternative approximate methods are based on the Variance Reduction Technique (VRT), already implemented, for example, for in-beam PET predictions (Sommerer et al. 2009). It has been shown that computation time can be reduced by about three orders of magnitude with respect to standard MC codes (El Kanawati et al. 2015; Huisman et al. 2016). A full three-dimensional PG map can be obtained in about two hours on a single core computer; this makes the clinical implementation possible, even if further improvements are still needed. As a general remark, it must be noticed that MC tool-kits have not been conceived for the energy range of interest in particle therapy, thus a fine tuning of the model parameters is necessary. The comparison of different MC codes often results in large differences in the PG simulated yields (Bohlen et al. 2010; Schumann et al. 2015; Verburg et al. 2012), and the hadronic models still have to be improved, ideally with the availability of differential cross-sections and PG yields further measurements in the clinical energy range (Newhauser et al. 2015). However, substantial enhancement have been achieved in the Quantum Molecular Dynamics (QMD) model (Dedes et al. 2014), and quantitative characterization of PG emission yields have been performed (Pinto et al. 2016; Schumann et al. 2015).

In addition to MC-based approaches, also the implementation of analytic models is efficient (Russo et al. 2016; Sterpin et al. 2015), even if they are based on pre-computed PG profiles obtained with MC calculations, thus they suffer from the aforementioned uncertainties. However, the comparison of simulated and measured PG profiles shows a very good agreement in Sterpin et al. 2015 (calculation performed with the MCNPX MC tool, and PG detection was performed with the knife-edge camera described in section 2.2.3.3 and in Perali et al. 2014). Finally, the pre-computation of PG profiles is not required by filtering approaches, which make use of the dose distribution maps, available form the treatment planning, and directly get the expected PG distribution (Kroniger et al. 2015).

2.2.3 PG ion range monitoring devices: state of the art

The detection of PG rays for particle therapy monitoring has been proposed already in 2003 (Stichelbaut et al. 2003), and since then several approaches have been investigated by developing adapted detection devices. The specificity of particle therapy range control techniques based on PGs requires the design of dedicated detectors, adapted to a wide photon energy spectrum and able to cope with the background level expected during particle therapy treatments. Standard medical imaging cameras, like the Anger cameras employed for SPECT examinations, cannot be adapted to such requirements. The explored solutions to create clini-

cal prototypes can be classified, as proposed in Krimmer et al. 2017b and already mentioned in this chapter, in imaging devices, based on the spatial information provided by each collected prompt photon, and non-imaging ones, which exploit integrated prompt photon yields. In table 2.3, reproduced from Krimmer et al. 2017b, the main features exploited by the developed modalities are summarized.

Table 2.3: Characteristics of the PG monitoring modalities. The star symbol represents mandatory measurements, the star in brackets means auxiliary but not mandatory measurements. Table reproduced from Krimmer et al. 2017b.

PG features	Imaging systems		Non-imaging systems		
	Physical collimation	Electronic collimation	PG timing (PGT)	PG peak integral (PGPI)	PG spectroscopy (PGS)
Position	⋆	⋆			
Energy	(⋆)	(⋆)	(⋆)	(⋆)	⋆
TOF	(⋆)	(⋆)	⋆	⋆	(⋆)

In the following sections, the state of the art of the various PG monitoring modalities is presented following the proposed classification.

2.2.3.1 Non-imaging prototypes

Non-imaging PG monitoring solutions are based on the integrated measurement of time or energy resolved photon spectra, and exploit the indirect relation between the characteristics of such spectra and the primary ion range to verify the conformity of the delivered treatment to the planned one. The objective of such techniques is not to retrieve spatial information from the collected photons, thus less demanding detectors are required with respect to imaging solutions, and the footprint in the treatment room is minimized, as well as the device cost.

PGT

As the primary ion beams interacting in the patient during treatments cause nuclear excitation and, thus, the emission of prompt photons, the width of the PG-TOF spectrum can be correlated to the ion range. Such a monitoring method has been first proposed in 2014 by Golnik and colleagues (Golnik et al. 2014) and tested with 150 MeV protons at the AGOR cyclotron, KVI-CART. The proton beam irradiated a homogeneous graphite target (10×10×30 cm^3, density 1.7 g cm^{-3}), with an expected range of 10.3 cm; the target has been set in three different positions (20 mm between each position), and the gamma detection has been performed with a Cerium doped Gadolinium Aluminium Gallium Garnet (GAGG:Ce) cylindrical detector. The setup is shown on the left side of Figure 2.14, and the resulting spectra are shown on the right side.

The shift of the average spectrum position, corresponding to the target shift, is clearly visible.In the same work, the authors also present the results of the irradiation with the same proton beam (150 MeV) of PMMA target at increasing thickness, from 5 to 15 cm. The detection has been performed with the same GAGG:Ce detector. The resulting TOF spectra are shown in Figure 2.15.

The beam expected range was 13.6 cm, so that it stopped in the target only for 14 and 15 cm

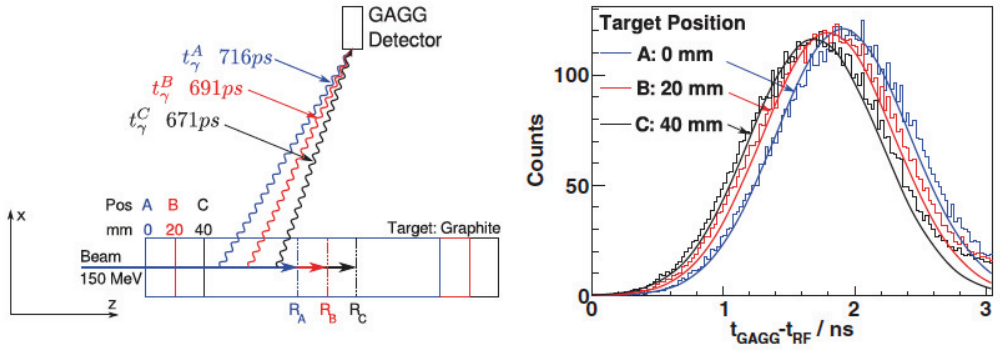

Figure 2.14: (Left) Setup for the irradiation of a graphite target with 150 MeV proton beams. The target was set in three different positions, with successive 20 mm shifts. (RIght) Resulting PG-TOF spectra; the photon measurements has been performed with a GAGG:Ce cylindrical detector. The experimental data are normalized to 10^9 incident protons. In Golnik et al. 2014.

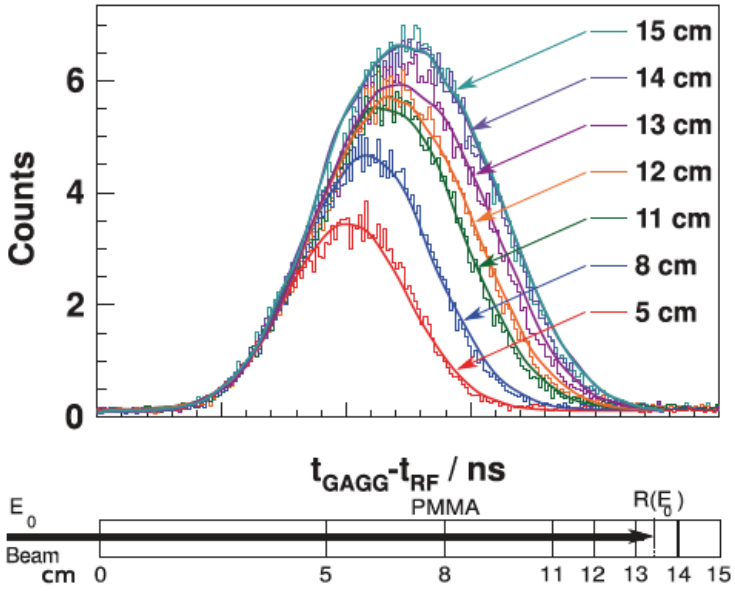

Figure 2.15: Comparison of experimental and modeled PG-TOF profiles obtained with the irradiation of PMMA targets with increasing thickness. The PG detection is performed with a GAGG:Ce detector. In Golnik et al. 2014.

thick PMMA blocks. Figure 2.15 shows the good agreement between simulated (solid lines) and experimental data (histograms), and the shift and broadening of the PG-TOF spectra with the increasing target thickness. Similar results have been also obtained by simulating proton beams at increasing energies, from 50 to 230 MeV, corresponding to a range change in the range [2 – 17] cm. Simulation studies also included the irradiation of heterogeneous targets, and the experimental clinical verification was performed at the proton treatment center in Essen, equipped with an Ion Beam Applications, Belgium (IBA) C230 cyclotron, with several phantoms and detectors. The range variations in a stacked PMMA target, as well as the effect of air cavities and bone inserts have been verified, and the PGT-based range verification showed the ability to detect 5 mm range shifts in heterogeneous targets for clinically relevant doses, but the strong influence of the accelerator Radio-Frequency (RF) signal stability has also been highlighted (Hueso-González et al. 2015b). The TOF measurement was actually based on the accelerator RF signal, and a phase variation on the time-scale of hours caused shifts in the TOF spectrum equivalent to the one provoked by the shift of the target of a few centimeters. The author pointed out the need for a beam monitoring system to provide the time reference for the TOF measurement; such a beam monitor has been developed and tested to characterize the bunch structure of the clinical C230 cyclotron of the Oncoray center in Dresden (Petzoldt et al. 2016). In Figure 2.16 the authors show the ability of this monitoring method to detect range shifts due to target in-homogeneity for decreasing amount of primary protons: shifts due to bone and air inserts in a homogeneous PMMA can be detected for primary statistics down to 10^8 primary protons, with increasing uncertainty for decreasing number of primaries.

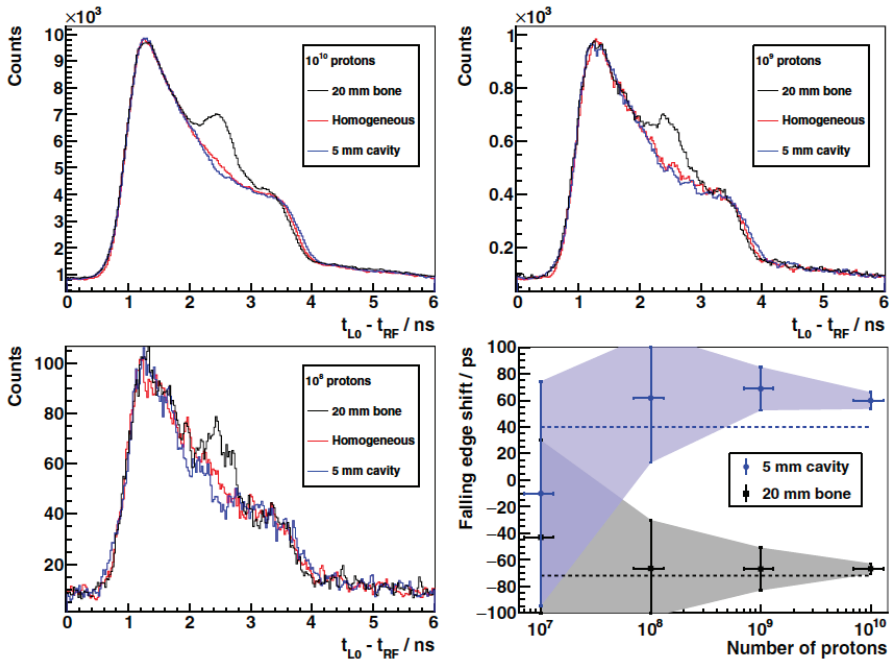

Figure 2.16: First three panels: PGTOF spectra obtained with the 230 MeV proton irradiation of a homogeneous PMMA target and two targets with air and bone inserts are compared for increasing number of primary protons. The PG detection is performed with a $LaBr_3$ detector (L0). The bottom right panel shows the shift of the spectra falling edge with respect to the homogeneous target case as a function of the number of incident protons. In Hueso-González et al. 2015b.

It has been estimated in Pausch et al. 2016 that 10^4 detected PG rays are needed to reveal a 5 mm range shift, with a bunch width of 2 ns. This is a fundamental requirement to be taken into account when designing a prototype for this application, together with the expected data throughput, which is significant given the absence of collimation system. However, with energy selected gamma rays of several MeV, a timing resolution of 200 ps has been obtained with optimized detector configurations (Cerium Bromide ($CeBr_3$) scintillators coupled to compact U100 energy and timing spectrometer specifically developed for this application), and throughput rates of about 600 kcps (kilo counts per second) have been handled Pausch et al. 2016.

The time resolved measurement of PG rays is also exploited in the PGPI monitoring method. PGPI
The integral of the PG peak in the TOF spectrum measured with various detectors located at different positions around the target is used to control the ion range. After preliminary studies at the in Arronax cyclotron in Nantes, experimental tests have been performed at the CAL in Nice, following previous results published in Carnicer et al. 2012 and obtained with the same accelerator. 65 MeV protons at an intensity of 3×10^9 protons per second have been used to irradiate a homogeneous PMMA target, and the PG rays have been collected with $LaBr_3$ scintillators read-out with a dedicated card developed at the *Institut de Physique Nucléaire de Lyon*, France (IPNL). The accelerator RF signal or a beam monitoring system have to be used to provide the time reference for the TOF measurement. For this first study, the data have been synchronized to the positions of the modulator wheel used for passive beam delivery, provided via a photosensor. In Figure 2.17 the PG spectra collected for two different positions of the modulator (corresponding to the maximum thickness and the hole) are shown (Krimmer et al. 2017a). The integral is calculated after background subtraction and the selection of the TOF proper window for the PG selection, and compared for different detectors in various positions. The ratios of the integrals measured in different positions show few percent variations in the PG emission rate, corresponding to few millimeter range deviations, with simple and quick analytic data processing.

In the case of 65 MeV protons, such a method has been verified to be able to detect 3 mm range shifts in PMMA for 10^8 incident protons. In addition, the authors also highlight that absorption in the target can determine similar effects on the PG spectra, so that with the combination of signals from several detectors placed around the target, its position can be retrieved (Krimmer et al. 2017a).

As an alternative to time-resolved measurements, spectroscopic PG analysis can provide indi- PGS
rect information about the ion range in matter through the direct estimate of the target composition. Initial studies on the PG energy spectra have been performed in simulation and with experimental measurements with germanium detectors (Polf et al. 2009a,b), and the relative content of specific oxygen and carbon isotopes in a target could be identified via quantitative analysis of the related spectroscopic lines (Polf et al. 2013). This principle was then developed by Verburg, preliminarily in simulation (Verburg et al. 2012), then experimentally with a shielded cerium doped $LaBr_3$ detector: the composition of the target could be retrieved by the energy spectrum obtained with a single detector placed close to the end of the ion range (see Figure 2.18), and at the same time the residual proton range could be estimated (Verburg et al. 2013, 2014). To do so, the energy dependence of the differential cross sections is accurately modeled, and the data are compared to such models. The method is adapted to both measuring the residual ion range, with an obtained accuracy of 1 mm, and to detecting relative range shifts, with a precision below half a millimeter for 5×10^8 delivered protons.

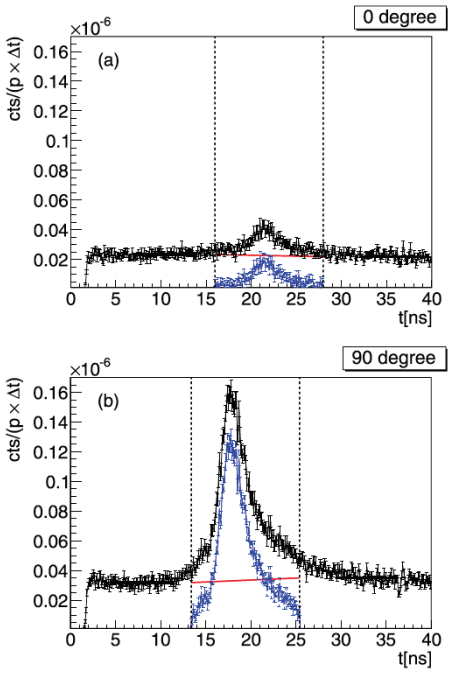

Figure 2.17: TOF spectra measured for two positions of the modulator wheel, corresponding to the maximum thickness (0 °) and the hole (90 °). An energy threshold of 1 MeV has been applied for the gamma detection. After background subtraction (red line), the integral is calculated in the range delimited by the vertical dashed lines. In Krimmer et al. 2017b.

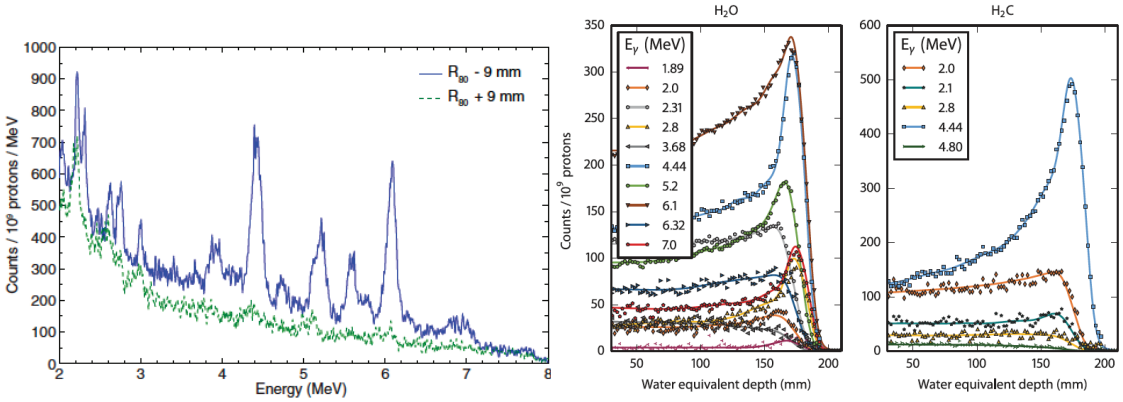

(a) Energy spectrum of PG rays integrated in a 2 ns time window, measured 9 mm before and after the position of the 80 % of the dose fall-off level in water.

(b) Discrete PG spectroscopic lines along 165 MeV proton beam stopped in water and polyethylene. The lines model the experimental data.

Figure 2.18: In Verburg et al. 2013 (left) and Verburg et al. 2014 (right).

A full-scale clinical prototype based on eight $LaBr_3$ scintillators and an enhanced collimator design has been recently developed (Hueso-González et al. 2018). The prototype has been tested with phantom on a proton Pencil Beam Scanning (PBS) gantry, and satisfactory performance has been obtained for a clinical beam current of 2 nA incident on the phantoms. 1.1 mm precision in the measurement of the absolute proton range is stated, and tests on a ground-truth anthropomorphic head phantom (Wohlfahrt et al. 2018) are foreseen for final validation.

Non-imaging devices represent cost-effective solutions for range verification in particle therapy, and an extended clinical application of these methods can be expected in the next future.

2.2.3.2 Imaging prototypes

With respect to non-imaging detection systems, imaging prototypes are more complex since the objective is the direct measurement of the spatial information carried by the prompt photons about their emission point. Collimation strategies are needed to retrieve spatial information, and the devices developed for particle therapy monitoring applications can be divided into mechanically and "electronically" collimated cameras. In addition to this, image reconstruction methods are needed, and are briefly presented in section 2.4.

2.2.3.3 Mechanical collimation

Collimated cameras provide direct information about the ion range, thus ensuring increased robustness with respect to non-imaging techniques. Mechanical collimation systems are intended to select the photons approaching the detector according to their direction, by absorbing or scattering away the undesired ones. The spatial distribution of the PG emission points is directly retrieved along the beam path in matter, according to the specific camera FOV. The design is somehow similar to Anger cameras employed in nuclear medicine, but the collimator design has to be adapted to the PG energy range, and the selection is generally made on a single dimension, parallel to the beam direction. As for Anger cameras, the collimator is generally coupled to high-density scintillator detectors read-out by photo-sensors. Several collimator geometries, with various degrees of complexity, have been tested since the beginning of the investigation of PG as a tool for particle therapy range monitoring. In the first PG studies, which allowed to verify the correlation of the emission profile to the distal fall-off region, simple scintillator detectors have been placed behind parallel slit collimators (Min et al. 2006, 2007). The collimator is also effective in capturing fast neutrons, thus reducing neutron background contamination, more pronounced with carbon-ion beams. In this case, TOF information has been used during measurements performed by the IPNL group at GANIL, in addition to the mechanical parallel slit collimation (É. Testa et al. 2009, 2008).

Multi-slit collimators

Parallel multi-slit configurations represent an improvement of such first approaches, but will require multiple or position sensitive detectors. As for Anger cameras, the presence of a passive selection system always imposes a trade-off between detection efficiency and spatial resolution, and dedicated simulation studies have been performed by the already cited groups to

optimize multi-slit collimator designs (Min et al. 2012; Pinto et al. 2014). The collimator studied in Pinto et al. 2014 is available at the IPNL and composes, together with a BGO-detector array, the collimated camera under development by the CLaRyS collaboration, object of this thesis work and described in details in chapter 3. The first tests on beam of a basic camera configuration has been recently performed at the CAL in Nice with 65 MeV proton beams, and the results are presented in chapter 6.

Pinhole / Knife-edge cameras

Alternative designs include pinhole and knife-edge cameras. The pinhole design is directly derived from classical optics, and consists in a thick collimator with a tiny hole, allowing for two-dimensional imaging. The concept is adapted for the detection of PG rays, and the collimator must be customized for the PG energy range. Kim and colleagues designed via MC simulations and constructed a pinhole camera based on thallium-doped Cesium Iodide (CsI) scintillation detectors, which has been tested with 50 MeV proton beams irradiating a water target (J.-W. Kim 2009). The camera aperture was located in proximity to the expected end point of the proton range, and 1 mm proton range variations could be detected in water. Such a collimation strategy strongly impacts the detection efficiency; for range monitoring, mono-dimensional imaging in the beam direction is sufficient, and the pinhole aperture can be extended to a knife-edge configuration, a single slit perpendicular to the beam direction and parallel to the detector plane (Bom et al. 2012). A knife-edge camera prototype has been optimized via MC simulations and developed (Smeets et al. 2012); the tests performed on 100 and 160 MeV proton beams showed few millimeters standard deviation in the range estimate for numbers of protons that correspond to doses in water at the Bragg peak as low as 15 cGy at 100 MeV and 25 cGy at 160 MeV, assuming pencil beams with a Gaussian profile of 5 mm sigma at target entrance. Following these first studies, a second prototype with LYSO scintillation slabs and SiPMs have been constructed by IBA. With such a device, shown in Figure 2.19, experimental studies have been performed with 100, 160 and 230 MeV protons on a homogeneous PMMA target, with beam currents at the nozzle exit of several nA. If compared to simulation expectations, the measured PG profiles were consistent and a precision of 2σ in retrieving 4 mm range shifts has been reported for 0.5×10^8, 1.4×10^8 and 3.4×10^8 protons at 100, 160 and 230 MeV, respectively, with a PG energy selection in the range 3 – 6 MeV (Perali et al. 2014). An extensive experimental study has also been performed to assess the camera performance in presence of target in-homogeneity, by using tissue equivalent inserts in a PMMA target to mimic ribs, lung air cavities and skin (adipose tissue). In most of the considered cases, the detectability of 2 mm shifts has been verified with approximately 2.6×10^{11} delivered protons, but the system failed in detecting range shifts in close proximity to large density gradients (for example, near air cavities or low density lung tissue) (Priegnitz et al. 2015). The beam must stop more than 7 mm after the cavity to detect range variations.

The described study only included in-homogeneity in the beam direction, but laterally in-homogeneous targets can lead to range mixing which further complicate the range detection. As highlighted in Priegnitz et al. 2016, in such cases the detection of range deviations strongly depends on the target composition. The combination of range deviation detection with an analysis of the slope of the distal edge of the measured PG profile is proposed by the authors to identify the origin of the range deviation if it is due to range mixing, because range mixed PG profiles exhibit less steep distal slopes with respect to beams traversing laterally homogeneous targets. In a further study aiming to test the clinical applicability of the knife-edge camera, it has been showed that 2 – 5 mm range shifts can be detected also for passive beam delivery, with the proper neutron background rejection based on non-collimated data acquisitions with water targets (Priegnitz et al. 2016). The LYSO-SiPM detector composing the knife-edge camera

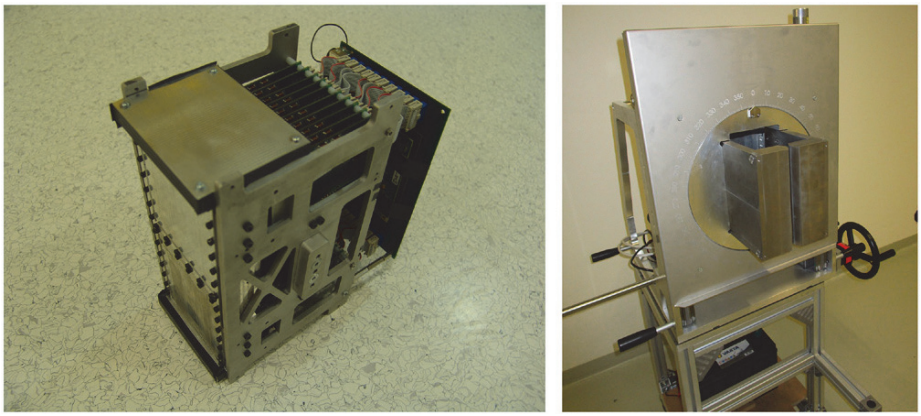

Figure 2.19: LYSO slabs of the knife-edge camera (left) and complete camera with the knife-edge-shaped slit collimator mounted on a trolley. In Priegnitz et al. 2015.

have been also tested with the IPNL multi-slit collimator (see chapter 3 and Pinto et al. 2014), and comparison measurements of the two configuration have been performed at the West German Proton Therapy Center Essen (WPE) with a C230 IBA cyclotron and a PBS-dedicated nozzle. A PMMA target has been exposed to 100, 160 and 230 MeV proton beams, and PG profiles have been collected with the two collimator setups. The knife-edge-shaped collimator was found to be better adapted to the used camera device, because twice less protons were needed to reach a given precision in the range measurement (Smeets et al. 2016). However, it must be noticed that the slit width used for the multi-slit camera was not comparable to the one of the knife-edge camera, thus degrading the multi-slit camera efficiency. The obtained result was expected, and compatible configurations have not been experimentally compared yet. All the presented study led to the first clinical implementation of the system and, more generally, of a PG-based monitoring device (Richter et al. 2016). The knife-edge camera has been used to monitor an head-and-neck tumor treatment with passive beam delivery, with the setup shown in Figure 2.20a. In Figure 2.20b the PG profiles obtained for three iso-energy layers of the treatment, corresponding to three steps of the modulator wheel, are shown. The capability to derive spatial information of the proton range during a real treatment has been demonstrated.

A second IBA prototype has also been tested with PBS, during 6 brain tumor treatment fraction over three weeks. Although some limitations have been identified, mainly related to the camera positioning, the possibility of spot-by-spot proton range verification has been demonstrated, with a precision of the shift retrieval depending on the number of protons in each spot. The capability of detecting range shifts below the range uncertainty margin applied in the treatment plan was also confirmed (Xie et al. 2017).

A two-dimensional collimated imaging solution has been designed and realized by Ready and colleagues (Ready 2016; Ready et al. 2016). It consists of a 4×4 array of Cerium-doped Lutetium OxyorthoSilicate - $Lu_2SiO_5(Ce)$ (LSO) crystals placed behind an arrangement of knife-edge slit collimators. Experimental tests have been performed by irradiating PMMA targets with a 50 MeV proton beam at currents up to 2 nA, and PG rays have been selected in the energy range 2 – 7 MeV. The two-dimensional PG emission distributions have been recon-

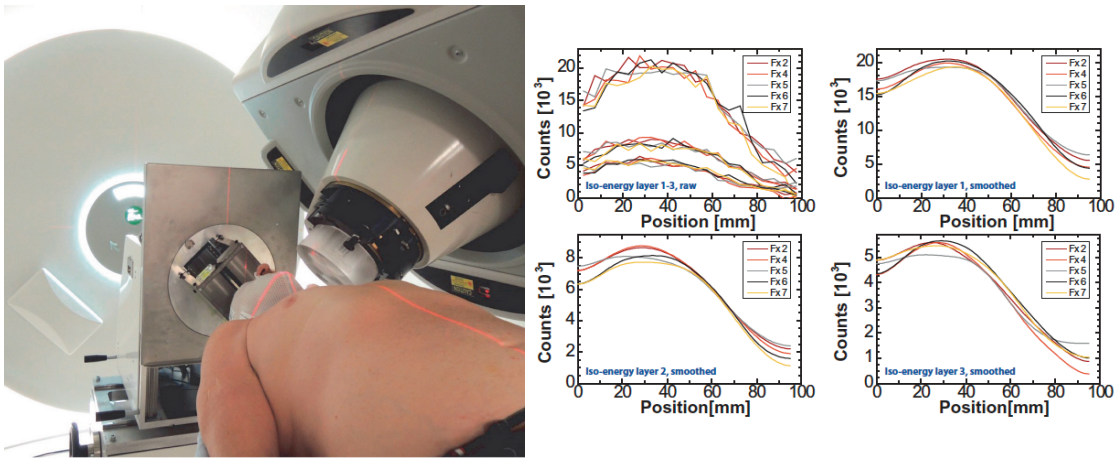

(a) Application of the knife-edge camera for the monitoring of the treatment of an head-and-neck tumor.

(b) PG net profiles collected during the first three iso-energy layers, corresponding to three different positions of the modulator wheel. In the first panel, the net profiles are shown. The other three panels show the Gaussian smoothed profiles of the three layers separated.

Figure 2.20: In Richter et al. 2016.

structed via Maximum Likelihood Expectation Maximization (MLEM) algorithm and range shifts of approximately 3 mm could be detected for 10^8 delivered protons.

2.2.3.4 Electronic collimation: Compton cameras

One of the main disadvantages of the previously described imaging system is the limited detection efficiency due to the presence of a physical collimator. In order to design imaging devices with higher statistics, the mechanical collimation has to be replaced by a so-called "electronic" collimation, which is based on Compton kinematics. In the PG energy range the Compton effect is dominant, as shown in Figure 2.7, thus can be exploited in combination with at least one more interaction to perform a sort of "photon tracking". Originally designed for astrophysics applications, the potential of Compton cameras for medical imaging has been soon recognized (Singh 1983; Todd et al. 1974) and then directly translated to the ion beam therapy monitoring domain. Such a gamma detection system is generally composed of two sections: a scatterer and an absorber. The scatterer is dedicated to the gamma Compton-scattering, and should be designed to optimize the Compton scattering probability in the prompt gamma energy range, while reducing the so-called Doppler broadening effect due to electron binding and motion (Ordonez et al. 1997) (see section 2.1); in most cases, this leads to the choice of a light material (low Z), segmented in several subsections. On the other hand, heavier materials may be used to improve photon detection efficiency. The absorber finally intends to capture the Compton scattered photons via photoelectric effect and is often composed of segmented high-Z scintillating materials. Slightly different Compton camera configurations can also achieve Compton electron tracking in the scattering detector, which results in additional information for the reconstruction. From the interaction points and the deposited

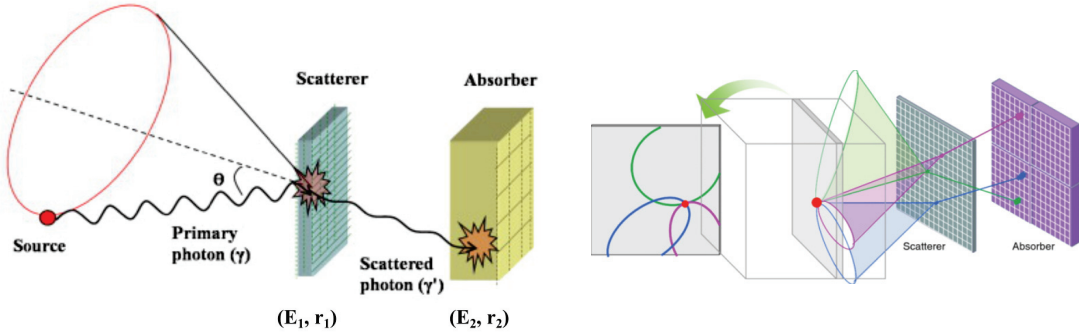

(a) Schematic view of the Compton camera detection principle for a standard camera setup.

(b) Schematic view showing a conventional Compton camera setup and reconstructed cones.

Figure 2.21: Adapted from Seo et al. 2010 (left) and in S. M. Kim et al. 2013 (right).

energies in the scatterer and the absorber, the emission point of the incident photon can be constraint to the surface of a cone via Compton kinematics, as shown in Figure 2.21 for standard camera setups. Analytic or iterative algorithms use these cones to create the image of the prompt gamma emission distribution, with intrinsic three dimensional capability (Kuchment et al. 2016; McKisson et al. 1994; Wilderman et al. 1998).

The Compton interaction position in the scatterer provides the apex of the cone, and the cone axis is given by the line connecting the interaction positions in scatterer and absorber. The cone aperture is then calculated via equation 2.10, where E_1 is the energy deposited in the scatterer, and E_2 is the energy deposited in the absorber. It is to be noticed that this relationship assumes that the initial photon energy (E_0) corresponds to $E_1 + E_2$; this means that full absorption of the photons is required for the application in PG detection, since the energy of the incident photon is not known *a priori*.

$$\cos\theta = 1 - \frac{m_e c^2 E_1}{E_2(E_1 + E_2)} \tag{2.10}$$

with $m_e c^2 = 511$ keV.

If at least three Compton interactions are collected in the camera, the full photon energy absorption is not necessary for the cone reconstruction, as explained in (Kurfess et al. 2000). The incident photon energy (E_0) can be calculated analytically as in equation 2.11, where E_{1c} and E_{2c} are the energy deposited in the two Compton scattering interactions and θ_{2c} is the Compton scattering angle related to the second interaction.

$$E_0 = E_{1c} + \frac{1}{2}\left(E_{2c} + \sqrt{E_{2c}^2 + \frac{4E_{2c}m_e c^2}{1-\cos\theta_{2c}}}\right) \tag{2.11}$$

However, the correct ordering of events is required, and limiting the data collection to multiple

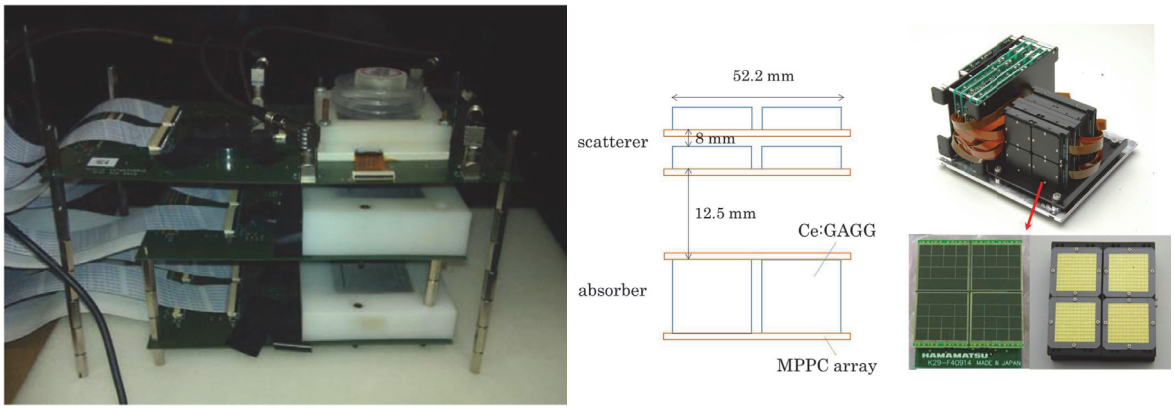

(a) Picture of the MACACO Compton prototype in a laboratory setup.

(b) Schematic representation and picture of an handheld Compton camera based on GAGG:Ce scintillators.

Figure 2.22: In Solevi et al. 2016 (left) and in Kishimoto et al. 2015 (right).

scattered events leads to an efficiency reduction of at least an order of magnitude (Roellinghoff et al. 2011).

Several research groups have developed or are developing Compton camera prototypes, following different strategies, concepts and employing various detector types, such as scintillators, semiconductors and gaseous detectors, as well as their combination. The application is not limited to the medical field; prototypes have been also developed for industrial monitoring, homeland security and nuclear inspections (Martin et al. 1994; McKisson et al. 1994). The field is in continuous progress, and in the following the state-of-the art of the prototypes already tested or under construction is presented.

Scintillators

Three layers of monolithic $LaBr_3$ crystals (27.2×26.8 mm^2 and 32×36 mm^2 section and 5 and 10 mm thickness respectively) compose a Compton camera prototype developed in Valencia and called MACACO (see Figure 2.22a), successfully used to reconstruct point-like sources (Llosá et al. 2016) and able to detect range shifts within 10 mm for 150 MeV proton beam (beam current 9×10^7 protons/s) impinging on a water target (Solevi et al. 2016). The final device followed preliminary prototypes based on a single $LaBr_3$ coupled to SiPMs (Llosá et al. 2012) and on the combination of $LaBr_3$ and LYSO crystals (Llosá et al. 2013).

A handheld Compton camera prototype based on GAGG:Ce scintillators has been developed (Kishimoto et al. 2015). The prototype is shown in Figure 2.22b. This device was originally designed to measure radioactive isotopes such as ^{137}Cs, that were released during and after the Fukushima nuclear disaster in 2011. The device showed a spatial resolution in the reconstruction of point-like source emissions below 7 mm (Kishimoto et al. 2015). Its application to particle range monitoring has been tested with 70 MeV protons on water, PMMA and $Ca(OH)_2$ targets: significant uncertainties in the determination of the Bragg peak position determined the planning of an improved performance version of the system (Taya et al. 2016).

Semiconductors and scintillators

With the aim of maximizing the ratio between Compton and photoelectric absorption probabil-

ities in the scatterer and, at the same time, reducing the Doppler broadening effects, semiconductor detectors have been considered in several prototypes, coupled to high-Z scintillators for the absorber. The Compton camera developed by the CLaRyS collaboration, main object of this thesis, is based on this idea and employs 7 Double-sided Silicon Strip Detectors (DSSDs) for the scatterer stack, coupled to an array of BGO blocks as absorber (Fontana et al. 2018; Krimmer et al. 2015). A beam tagging hodoscope based on scintillating fibers is also included in the development program (Krimmer et al. 2014). A complete description of the camera components and the present status of the development is given in chapter 3. The most recent results obtained in simulation studies concerning the application of this prototype to particle therapy range monitoring and nuclear medicine are presented in chapter 4 and chapter 5, respectively. The 2 mm thick silicon planes chosen for the scatterer section have been optimized to maximize the probability of stopping the Compton recoil electron within the same layer where the photon Compton interaction took place. As mentioned, the tracking of the Compton recoil electron gives additional information for the event reconstruction stage; the direction of the incident photon can be confined from the full cone to an arch (Frandes et al. 2010). The possible exploitation of this imaging advantage is explored in the prototype developed in Munich by Thirolf and colleagues. The design concept is similar to the one proposed by the CLaRyS collaboration: a monolithic cerium-doped $LaBr_3$ scintillator crystal, 50×50×30 mm^3, used as absorber, is coupled to six DSSD layers 50×50×0.5 mm^3. The reduced thickness allows for the tracking of the recoil electron, with an increased escape probability. The absorber scintillator is read out via a 256-fold segmented multianode PM; an energy resolution of 3.8 % FWHM has been reported at 662 keV, with a timing resolution of 270 ps (Thirolf et al. 2016). An algorithm based on the k-nearest neighbor method is implemented for the position reconstruction (Dam et al. 2011), and its Categorical Average Pattern (CAP) version has been verified to provide the best results (Aldawood et al. 2017). The algorithm is based on pre-determined spatially dependent detector response, and has been recently further improved with artifact correction capabilities; the new Categorical Gaussian Distributed Replacement (CGDR) algorithm has been used to obtain a spatial resolution below 3 mm at 1.3 MeV (Liprandi et al. 2017). A further electron-tracking Compton prototype based on a Silicon-On-Insulator (SOI) pixel detector and a GAGG:Ce detector has been developed and is described in Yoshihara et al. 2017. It has been conceived for the localization of contamination nuclides inside the Fukushima Daiichi Nuclear Power Plant in Japan, and two dimensional imaging of a ^{137}Cs source has been demonstrated. The application of such an imaging device in nuclear medicine has been suggested by the authors, and its implementation in the monitoring on therapeutic beam range is not excluded. Various Compton camera prototypes make use of Cadmium Zinc Telluride (CZT) as alternative to silicon detectors. In Kormoll et al. 2011 the design study of a Compton camera composed of a CZT detector as scatterer (20×20×5 mm^3, 16 strips per plane) and a streaked LSO crystal as absorber (52.7×52.7×20 mm^3) is presented. The scatterer section showed a time resolution of 2.8 ns FWHM, while a 0.6 ns resolution was reported as a result of tests performed with bremsstrahlung photons (up to 13 MeV) at the ELBE electron accelerator in Germany (Hueso-González et al. 2014). The same authors presented a direct comparison of LSO and BGO detectors for the detection of photons in the PG energy range (Hueso-González et al. 2015a); although less performing than LSO, BGO is an interesting alternative given the absence of internal radioactivity which reduces the amount of fake events contributing to the background (random coincidences). Moreover, its much lower price makes it suitable for commercial devices. In addition to the CLaRyS collaboration prototype which includes BGO blocks for the absorber section, a Compton camera coupling three BGO crystals (52.7×52.7×20 mm^3) and a CZT-based scatterer has been tested with 4.44 MeV photons (Golnik et al. 2016). The BGO crystals have been calibrated in energy on a single pixel-basis, with a method presented

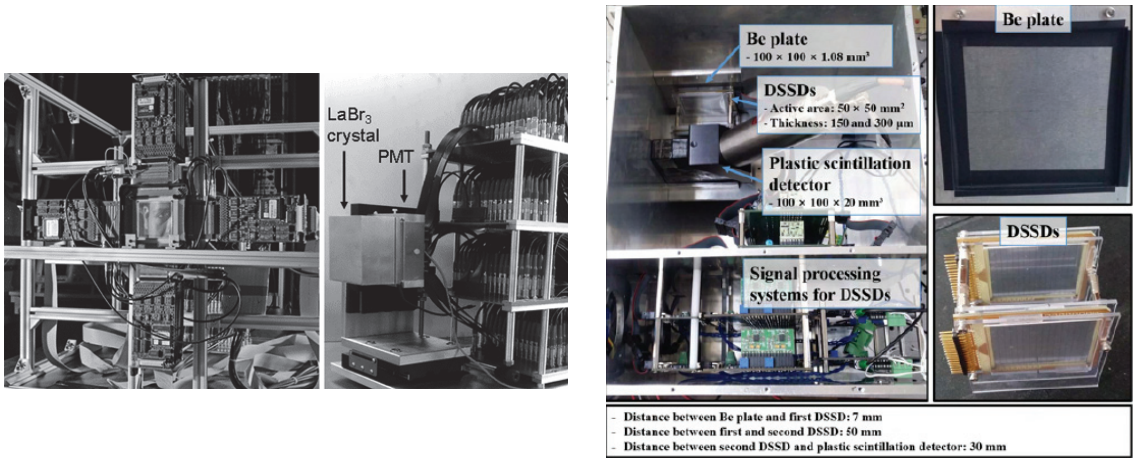

(a) Layout of the Munich electron tracking Compton camera.

(b) Components of the GEVI prototype.

Figure 2.23: In Thirolf et al. 2016 (left) and in H. R. Lee et al. 2017 (right).

in (Hueso-González et al. 2015a), and an energy resolution of 27 % FWHM has been found. Such a method has been refined and extended for the characterization measurements published in (Fontana et al. 2018) and described in chapter 3 for the CLaRyS BGO blocks. A different approach has been first studied in simulation by Kim and colleagues, referred to as Gamma Electron Vertex Imaging (GEVI) (C. H. Kim et al. 2012a,b), and then translated into a prototype. The concept relies on the passive conversion of PG rays to electrons, that are then tracked. The developed prototype consists of a 1 mm thick beryllium plate to convert the incident photons into electrons; the electron tracker is then composed of two DSSD layers, 50×50 mm^2 surface, 150 and 300 μm thick, respectively. The kinetic energy of the electrons is then collected by a plastic-scintillator calorimeter (H. R. Lee et al. 2017). A ^{90}Sr source has been employed to test the electron detection performance, replacing the beryllium converter; a spatial resolution of 16 mm FWHM for the reconstruction of the point-like source has been obtained. With the converter, photons from a ^{60}Co source have been used, and the obtained spatial resolution was 35 mm FWHM. The present prototype is equipped with an acquisition system with limited rate acceptance, and tests with 45 MeV protons impinging on a PMMA target showed a very low sensitivity of 4×10^{-8} (H. R. Lee et al. 2017).

Semiconductors only

Compton cameras completely based on semiconductor detectors have also been explored. Simulations studies have been published in (Peterson et al. 2010) and present the design optimization of a three-stage Compton camera based on germanium detectors. In addition, different materials have been investigated (D. Robertson et al. 2011), and the influence of Doppler broadening has been analyzed in details (Mackin et al. 2013). Following the simulation results, a prototype only based on CZT detectors has been constructed, named Polaris-J Compton Camera: it consists of four pixelated detectors with 20×20 mm^2 surface for 10 and 15 mm thickness (McCleskey et al. 2015). The camera showed an absolute efficiency in detecting gammas from a ^{60}Co source of 2.2×10^{-5} and 5.8×10^{-7} for double and triple scatter events, respectively. Clinical proton beams of 114 and 150 MeV on a water target have been used to test the feasibility of range verification, and 3 mm range shifts could be detected with one-dimensional profile analysis for approximately 1.7×10^{10} delivered protons (Polf et al. 2015). The experimental setup is shown in Figure 2.24a.

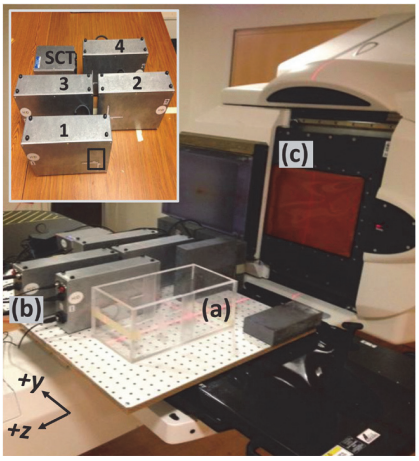

(a) Experimental setup for the beam tests of the Polaris-J Compton camera (b) with a water target (a). The box in the top left side shows a close up view of the four CZT detector stages.

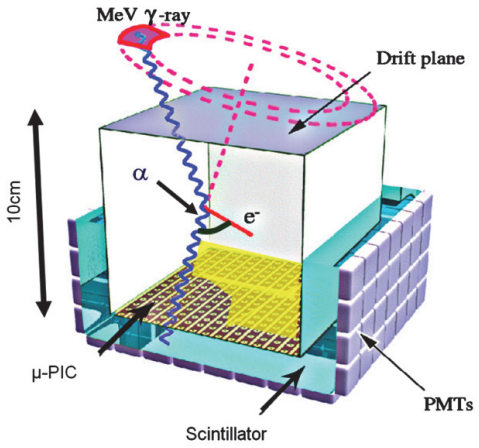

(b) Schematic view of the prototype and operation principle of the ETCC.

Figure 2.24: In Polf et al. 2015 (left) and in (right).

Gaseous detectors

Gaseous detectors can also be applied to Compton imaging. An electron tracking Compton camera (ETCC) has been proposed by Takada and colleagues, originally for astrophysics applications in baloon experiments (Takada et al. 2011). A gaseous Time Projection Chamber (TPC) ($10\times10\times15$ cm^3, filled with 1 atm of a mixture of Argon and C_2H_6) is devoted to the electron tracking, and coupled to scintillator detectors (cerium-doped Gadolinium OxyorthoSilicate - Gd_2SiO_5 (GSO) pixel scintillator array) read out by multi-anode PMs to detect the scattered photons. A schematic view of the prototype is shown in Figure 2.24b. Such a prototype has been used for test measurements with 140 MeV proton beam stopped in a water target, with a reported efficiency of 3×10^{-6} (Kurosawa et al. 2012).

2.3 Gamma detection in nuclear medicine

The nuclear medicine diagnostics routine is mainly based on PET and SPECT. In the following sections, the basic principle of these two techniques are described. In addition to this, the theranostic approach coupling radiation therapy and diagnostic imaging with the use of custom developed agents is addressed.

2.3.1 Positron Emission Tomography

PET systems rely on the detection of annihilation gamma rays that follow positron decay of the radioisotope injected in the patient and consequent positron annihilation. The gamma rays exiting the patient body are detected in coincidence by scintillating detectors surrounding the patient, and the distribution of positron emitters is retrieved *in vivo*. Figure 2.25 shows the principle at the basis of PET imaging.

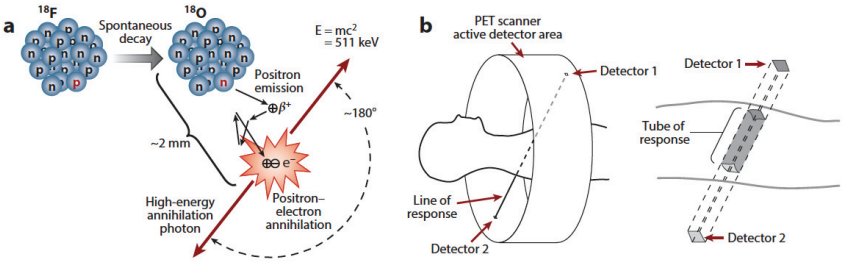

Figure 2.25: The β^+ decay of ^{18}F creates the stable isotope ^{18}O and a positron, which travels short distance (1 – 2 mm) before interacting with an electron. The consequent annihilation produces two anticollinear 511 keV photons (a). The two photons are detected by the PET scanner in time coincidence, and the two points of interaction defines a line of response, then extended to a so-called "tube of response" which accounts for the detector's elements finite dimensions (b). In Vaquero et al. 2015.

The two annihilation photons are typically detected with time coincidence windows ranging between 1 and 10 ns, depending on the specific features of the employed scanner. The spatial resolution of PET imaging is intrinsically limited by the fundamental nature of positron annihilation, if we consider that after its creation, the positron can travel a few millimeters and follow a tortuous path through the tissue (mainly due to Coulomb scattering with electrons which can occur at large angles given the fact that the rest mass of positron is the same as the one of the electron) before reaching thermal energies and annihilating. In addition to the positron range, also the fact that the positron is not fully at rest at the annihilation time leads to a limitation of the spatial resolution of PET images. Indeed, this results in an angular uncertainty in the direction of the two annihilation photons known as "noncolinearity". Moreover, significant limitations are linked to the employed detector: the coincidence detector-pair resolution is normally specified as the FWHM of the Point-Spread Function (PSF) obtained from the convolution of the two individual detector PSFs. For a detector composed of small discrete crystals, the interactions are generally assumed to take place at the center of individual crystals, and the resulting FWHM of the coincident detector PSF is one-half the crystal size. A further factor affecting PET imaging resolution is the parallax error, which results form the uncertainty of the Depth Of Interaction (DOI) of the gamma rays in the crystal. Thus, unless the DOI within a crystal can be accurately determined (dedicated designs are needed), an incorrect Line Of Response (LOR) will be assigned to the interaction. A schematic representation of the parallax error is provided in Figure 2.26a. The parallax error is all the more increased when the PET ring diameter is reduced of the thickness of the crystals is increased, as the relative thickness of the detector increases.

Figure 2.26b shows the three kinds of coincidence events that a standard PET accepts:

- true coincidences: gamma rays are detected from a single decay that have not scattered in the patient;
- scattered events: one or both gamma rays scatter within the patient;

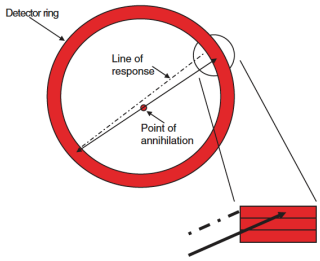

(a) Schematic view of the parallax error. The gamma ray (solid line) interacts in a crystal after penetrating one or more adjacent crystals in the detector ring. The detection electronics, if DOI information is not accessible, will incorrectly assign the LOR (dotted line) based on the front of the interaction crystal.

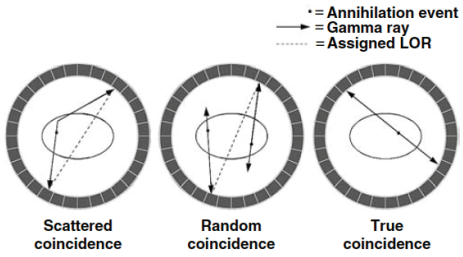

(b) The three types of coincidence events measured in a PET scanner.

Figure 2.26: In Lewellen et al. 2004.

- random coincidences: two separate decays result in the detection of only one gamma rays from each one and the two events are close enough in time to be in coincidence.

It is clear that increasing the number of true coincidences leads to less noise in the final image and allows one to reconstruct the collected data with high spatial resolution, and the effect of scattered coincidences can be corrected at the reconstruction stage, as well as the attenuation effect in the patient. The random coincidences are hardly treated, but their number can be reduced by decreasing the injected radiotracer activity.

The origin of the PET imaging modality dates back to the beginning of the 50s, when a simple brain probe was used to localize brain tumors by detecting photon coincidences with 2 opposing NaI(Tl) detectors at the MGH (Sweet 1951). In the same year, a similar approach was published on *Science* by a second research group (Wrenn et al. 1951). The development of reconstruction techniques for tomographic imaging started in the early 1960s (Kuhl et al. 1963), and in parallel to the first clinical trial for x-ray computed tomography the MGH physics group developed the Filtered Back-Projection (FBP) technique (Chesler 1971). The first ring tomograph was built in 1973 by Robertson of Brookhaven National Laboratory (BNL), and it was composed of 32 detectors disposed in a circular array (J. S. Robertson et al. 1972). One year later, the PETT I (Positron Emission Transaxial Tomography) tomograph prototype was built at the Washington University by Michael E. Phelps: such a prototype was then upgraded to a human-size system, called PET III, which included extended reconstruction not limited to the transaxial plane. The system consisted of an hexagonal array with 48 NaI(Tl) detectors, and of a gantry allowing for a 60-degree rotation. With this system, the first human PET images using the FBP algorithm were produced (Hoffmann et al. 1976), marking the beginning of modern PET development. Following the PET III development, the first commercial PET scanner, named ECAT II (Emission Computed Axial Tomograph), was designed and put on the market; it was composed of 96 NaI(Tl) crystals, and it had a dedicated computer. The

transition to commercial systems continued in the following years, and it boosted the establishment of worldwide PET research programs. Another fundamental step in the development of the PET technology was the discovery of the BGO scintillator. The first scanners were all based on NaI(Tl), difficult to manufacture because of its hygroscopic nature, and with a low density, thus limited efficiency in detecting 511 keV gamma rays. The luminescence features of BGO were first studied by Weber at the University of California (Weber et al. 1973), and Nester and Huang characterized the BGO scintillation properties in 1975 (Nestor et al. 1975). These studies leaded to the first design and construction of a BGO-based PET scanner in 1978, and right after to the commercialization of the NeuroECAT, the first commercial machine to use BGO as scintillating material. Hundreds of BGO-based tomographs have been produced since the first introduction. The availability of commercial valuable PET scanners was only one of the factors determining the spread of this imaging technique: in parallel, the development of optimized radiotracers was the second key point. Since the beginning of the PET experience and until the second half of the 1970s, the images were obtained mainly using ^{11}C-glucose, ^{15}O-water and ^{13}N-ammonia for blood flow, ^{15}O-oxygen for oxygen utilization, and ^{18}F fluoride for bone scans. In addition, successful molecular imaging probe was derived from the ^{14}C-deoxyglucose. The synthesis of ^{18}F-tagged deoxyglucose was discussed already at the beginning of the 1970s, and the Brookhaven group (Al Wolf and Joanna Fowler in particular), synthesized the first FDG (Ido et al. 1978). Refined synthesis methods were developed in the following years, also thanks to the improvements of cyclotron accelerator technology, allowing for a routine basis tracer production. Nowadays, a number of companies provide small cyclotrons with various forms of automated chemistry for producing molecular imaging probes, and FDG is still the most employed one for modern clinical PET imaging. During the 1980s, particular focus was dedicated to the detector side, with the development of the so-called “block detectors”: the new optical multiplexing scheme permitted to use many small scintillator pixels on a small number of PMs, and so provided high granularity (and spatial resolution) with a limited number of read-out channels. Since 1985, the majority of PET tomographs used some form of block detectors, which also allowed for a reduction in the scanner production cost. The introduction of this technology also increased the participation of the major imaging companies in the PET experience: in 1986, Siemens began to distribute PET scanners along with small cyclotrons for the production of radiotracers, and soon after also General Electric (GE) entered the PET market by purchasing the tomograph business from Scanditronix. PET machines and imaging techniques were soon introduced in the clinical routine and approved by the main health-care systems. In the 1980s, research efforts have been also dedicated to the introduction of DOI capabilities in the PET scanners to reduce parallax errors. A combination of NaI(Tl) and BGO crystals has been used by Karp and colleagues (Karp et al. 1987), and the different decay time constants were used to retrieve DOI information. Various techniques have been explored in the following years to develop DOI detection capabilities, such as the introduction of multiple crystal layers in the perpendicular direction (Liu et al. 2001) or the implementation of reflectors to create custom light-sharing patterns (Murayama et al. 1998). Although the research is still active on this topic, it should be considered that the effect of parallax error is small if compared with the overall resolution of the PET scanner itself. Further improvements came with the discovery and first production of LSO crystals, in 1989. BGO is very dense but has only 15 % of the light output of NaI(Tl) and relatively slow decay time (300 ns). LSO has slightly lower density and effective atomic number, but 5 times more light output than BGO. Moreover, the decay time is 7.5 times faster than BGO (Melcher et al. 1992). The high refinement cost initially discouraged the use of LSO for PET, but it soon decreased thanks to the development of cost-effective techniques, so that the first LSO-PET tomograph, microPET, was designed and fabricated in 1997 (Cherry

et al. 1997). It was designed for small animals, and commercially reproduced in 30 copies for academic programs and pharmaceutical companies. In February 1999, the first human-size LSO tomograph was delivered to the Max Planck Institute in Germany, while a combination of LSO and NaI(Tl) crystal was used for a PET-SPECT tomograph used in the Free University of Amsterdam since March 2000. In addition to the higher light output of LSO with respect to BGO, leading to better spatial and energy resolution, another major advantage of this scintillator is the fast timing, which translates in lower detector dead time and in the capability to measure the time difference between the arrivals of the two annihilation photons. This TOF measurement provides positioning information which can localize the positron annihilation within a few centimeters along the line of response. A schematic view of the TOF-PET principle is provided in Figure 2.27.

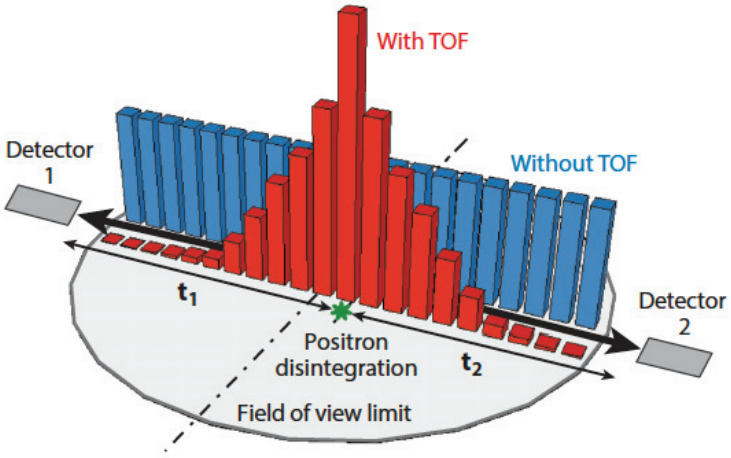

Figure 2.27: Schematic view of the information provided by TOF measurement to the PET detection. Without TOF, a flat probability is assigned to the reconstructed LOR (blue), while the measurement of the arrival time difference between the two coincident photons is translated into a distance from the LOR midpoint where the probability density function should centered (red). In Vaquero et al. 2015.

This possibility was explored already in the 1980s with fast scintillators (Lewellen et al. 1988; Ter-Pogossian et al. 1982), such as CsF and BaF_2, which were anyway not suitable for clinical PET application due to a low absorption efficiency. On the other hand, the BGO response was too slow to perform TOF. With the introduction of LSO, it was also recognized that its very good timing resolution (together with the one of the similar scintillator LYSO) could be utilized in the development of TOF-PET systems (Moses et al. 1999), overcoming the limitation of the early designs of the 1980s. In 2005 Siemens presented the results from a prototype that achieved a timing resolution of 1.2 ns, and soon after the first TOF-PET machine was launched by Philips (Philips Gemini TF) (Karp et al. 2008). Based on LYSO crystal, it provided 585 ps FWHM single timing resolution. At present, all the main PET vendors offer TOF-PET solutions with hundreds of ps timing resolution. Beyond PET detector designs using conventional PMs, the arrival of SiPMs has led to a great interest in utilizing these new photosensors to achieve improved timing resolution in TOF-PET scanners. Philips recently introduced the Vereos system, which uses digital SiPMs for signal readout from individual LYSO crystals; such a machine

provides a system coincidence timing resolution of approximately 310 ps (Miller et al. 2015). In parallel GE developed the SIGNA TOF-PET/MRI system using a detector ring based on analog SiPMs inserted in the magnet bore, thereby allowing simultaneous PET and MR imaging. The reported system coincidence timing resolution of this system is 390 – 400 ps (Levin et al. 2013). Hence, while scanners with detectors using conventional PMs are pushing closer to 400 ps timing resolution, new SiPM technology indicates that system resolution close to 300 ps is achievable with the lutetium based scintillators. With the rapid improvements of both scintillator and photosensor technology shown by recent results, a TOF resolution below 100 ps seems achievable in the next future (Lecoq 2017; Surti et al. 2016). Recent studies also investigated cost-effective solutions to achieve performance comparable to present commercial systems. In particular, a whole-body PET scanner based on plastic scintillators is being developed in Poland by the Jagiellonian University group. The J-PET is constructed with axially arranged strips of plastic scintillators, aiming to detect the annihilation photons via Compton interaction and read out on both sides by PMs. The position of interaction in the scintillator is determined from the time difference of light signal arriving on each strip end. A Time-Over-Threshold (TOT) technique is used instead of the charge measurement of standard PET systems in order to take advantage of the superior timing properties of plastic scintillators with respect to crystal detectors (LSO and BGO). Preliminary studies showed that it is possible to achieve a coincidence time resolution of about 500 ps FWHM with simple time measurements, coupled to a few millimeters spatial resolution (Niedźwiecki et al. 2017).

2.3.2 Single Photon Emission Computed Tomography

In SPECT tomographic images of the radionuclide distribution in the patient are generated from the emitted gamma photons detected as singles with collimated scintillators. Planar imaging reproduces a two-dimensional projection of the tracer distribution from a single view, while the tomographic image is obtained by the reconstruction of several slices collected from multiple camera positions. Both techniques are used in clinics: planar imaging is less demanding and only requires a single camera head, while multiple camera heads mounted on a rotating gantry are generally used for tomographic imaging, and image reconstruction is required.

Although many innovations have been made since the introduction of the first gamma camera in 1958 by Hal Anger (Anger 1958), today's clinical detectors share many of the essential features of Anger's early designs, and are often called Anger cameras. A standard SPECT gamma camera is composed of an aperture or collimator which mechanically selects photons traveling in specific directions, depending on the collimator configuration. The photons approaching the camera from directions different than those specified by the collimation system are passively absorbed. The gamma photons with the selected direction then encounter a scintillation detector coupled to photosensors. The related electronics and data acquisition system are generally optimized to impose energy threshold in order to reject undesired photons, such as those which underwent scattering in the collimator section. A schematic view of the main component of the SPECT camera is given in Figure 2.28a, while a simplified view of the collimation principle is sketched in Figure 2.28b.

The most simple photon passive selection device is the pinhole aperture, but acceptable spatial resolution can be only obtained at the expense of the system sensitivity. Improved, but always limited overall sensitivity is provided by the introduction of collimators composed of arrays

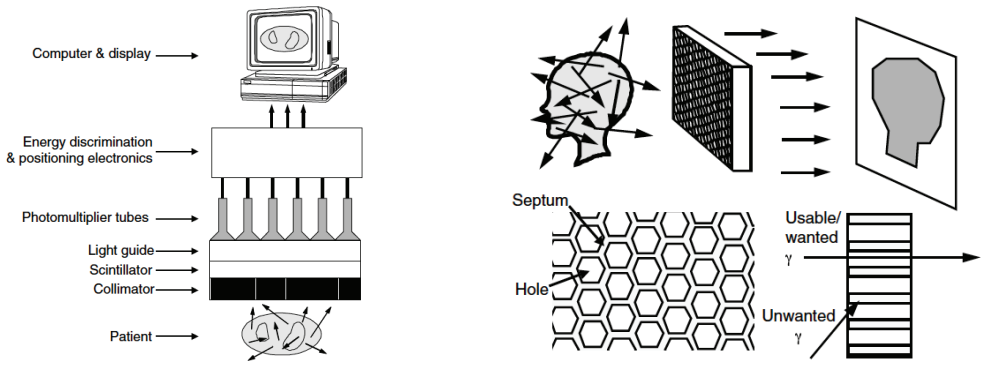

(a) Schematic view of the main components of a SPECT gamma camera.

(b) Schematic representation of the collimation principle of SPECT gamma cameras.

Figure 2.28: In Zeng et al. 2004.

of holes separated by septa. Collimator septa are composed of highly absorbing material with high atomic number and high density. Alloys of lead, tungsten and gold are the most common materials used for this purpose. Various hole shapes (circular, square, triangular or hexagonal) are used in common collimators, but the hexagonal shape is the most common because it provides the best efficiency. In addition to parallel hole patterns, also converging and diverging collimators have been developed. Converging collimators magnify an image on a camera face and thus can yield finer resolution and/or higher sensitivity images than those resulting from used of parallel-hole collimators. Converging solutions are adapted to small-size objects with respect to the camera FOV, while the image of large objects would result truncated (if part of the object is outside the FOV of the camera) or distorted (because the magnification is dependent on the distance from the collimator). The most spread parallel-hole collimators find routine use in clinics in four configurations: Low Energy High Resolution (LEHR), Low Energy General Purpose (LEGP), Medium Energy General Purpose (MEGP), and High Energy General Purpose (HEGP). Each designation is adapted to a defined gamma energy range, and thus to certain radioisotopes, and is also an indication of the trade-off between resolution and sensitivity which are affected by the septal material, the hole size and length, and the septal thickness. Collimator sensitivity is maximized by the thinnest possible septa, but thin septa can lead to septal penetration which is extremely detrimental to diagnostic performance. The aforementioned trade-off is then a crucial parameter to be considered when designing a SPECT camera, and, together with the employed scintillator and photosensor features, completely determine the overall system performance (Gunter 2004).

The origins of SPECT imaging can be identified with the invention of the Anger scintillation camera in the late 1950s (Anger 1958, 1964); previously, scans were performed by manually positioning a Geiger counter above the organ of interest, but with the Anger camera the entire organ could be scanned at one time. During the 1960s, both longitudinal and transaxial emission tomography were deeply studied. Crandall and Cassen developed a longitudinal tomographic scanner which used a highly focusing collimator placed on a large crystal-matrix detector (Crandall et al. 1966), and in 1969, Anger invented a sophisticated longitudinal tomograph that used a scanning scintillation camera (Anger 1969). Transaxial tomographs were developed by Kuhl and colleagues between 1963 and 1976, and the final prototype used discrete scintillator arrays (Kuhl et al. 1976). Discrete scintillation detectors have been

also used for other scanners in the late 1970s, but the first investigators to explore the possible implementation of an Anger camera for transaxial tomography were Paul Harper and colleagues at the University of Chicago. In the early stages, a rotatable chair was placed in front of a single head fixed Anger camera (Muehllehner et al. 1971). In 1976, Jaszczak and Keyes, independently developed a SPECT system that used an Anger camera mounted on a rotating gantry (Jaszczak et al. 1977; Keyes et al. 1977). In the following years, the first whole-body SPECT system was developed and clinically evaluated in 1978 at the Baylor College of Medicine (Jaszczak et al. 1979). During the late 1970s and the 1980s, both rotating-camera SPECT systems and stationary detector configurations were proposed and developed in Europe and US (S. A. Larsson 1980; W. L. Rogers et al. 1988), and the bases for modern machines were established. SPECT takes advantage of many years of experience and is now a well-established imaging modality in nuclear medicine. Thanks to its cost-effectiveness, such an imaging technique is widely employed in the clinical routine, and all the major medical imaging companies offer a SPECT system, generally in dual-head configuration with rotating gantry. At present, virtually all single-photon imaging in nuclear medicine relies on Anger-type cameras, relatively simple and cost-effective, but limited in sensitivity and energy acceptance given the presence of a mechanical photon selection system. Already in 1974 this limitation was addressed by Todd and Nightingale who proposed the application of Compton imaging methods to nuclear medicine (Todd et al. 1974). The Compton detection principle is described in section 2.2.3.4. It is to be noticed that for the application in nuclear medicine, the detector design is less constraint than in ion range monitoring, given the *a priori* knowledge of the incident photon energy. Starting from 1981, Singh and colleagues published a number of seminal papers that described analytical and experimental results for Compton camera composed of a pixelated germanium first detector and a standard Anger camera as second detector (Singh 1983; Singh et al. 1981, 1983). The investigation of such an imaging modality for the application in single photon detection for nuclear medicine continued in the following years. More recently, a prostate probe has been proposed and built by Llosa and colleagues, based on Compton imaging exploited by a composition of silicon sensors (4×1 cm with 256 pads) and NaI(Tl) scintillators (16×16×1.27 cm^3). The prototype has been tested with ^{57}Co and ^{133}Ba sources (Llosá et al. 2006), and a spatial resolution of 5 mm FWHM for the imaging of a point-like^{133}Ba source has been reported (Llosá et al. 2008). After a first prototype essentially developed for high-energy astrophysics observations (Takeda et al. 2007), a Japanese group optimized a Compton device based on silicon and Cadmium Telluride (CdTe) detectors for high spatial resolution, and proposed its application in nuclear medicine (Takeda et al. 2009). The prototype, then optimized for biomedical application and described in Takeda et al. 2012, consists of a 2.56×2.56-cm DSSD and four layers of pixelated CdTe detectors. The thickness of each detector is 0.5 mm. The device has been tested with rats and the resulting spatial resolution in the three dimensions was 8×8×10 mm (Suzuki et al. 2013), similar to the one of clinical SPECT systems, but poorer with respect to PET machines (Madsen 2007). However, improvements and spatial resolution similar or superior with respect to standard PET are expected. Notwithstanding the highlighted limitations, the capability of three dimensional image reconstruction in clinical condition has been verified. DSSD layers and NaI(Tl) crystals are also the basic components of a double-scattering Compton camera developed by a Korean research group. First studied in MC simulations (Seo et al. 2007), the system is composed of two identical 50×50×1.5 mm^3 silicon layers and a NaI(Tl) scintillator crystal, 3 inches diameter × 3 inches height. Preliminary tests with a point-like ^{22}Na source showed a spatial resolution of 9.0 and 4.8 mm for 511 kev and 1275 keV photons, respectively (Seo et al. 2010). The device has also been tested with gamma sources placed inside anthropomorphic phantoms: in particular, ^{22}Na and ^{137}Cs have been used, and a spatial resolution below

Compton cameras for SPECT

15 mm has been showed in both cases (Seo et al. 2011). The application of such a prototype to ion beam range verification has also been envisaged. The performance of a Compton camera based on pixelated germanium detectors have been evaluated and are presented in (Alnaaimi et al. 2011). Although the camera demonstrated the ability to image distributed sources, some limitations in acquisition and image processing time have been highlighted. The ETCC camera (Kabuki et al. 2007) presented in section 2.2.3.4 has been also tested for nuclear medicine applications with the imaging of nuclear medicine common reagents (Kabuki et al. 2009). The camera has also been used for phantom and small animal tests: in particular, the brain of mice has been imaged with FDG tracer, and the comparison with conventional PET data showed a good agreement. In addition, the camera also succeeded in imaging multiple tracers (FDG and ^{131}I isotope) (Kabuki et al. 2010). The field is still today actively explored: in particular, the availability of new high-energy tracers could provide advantages in terms of dose and spatial accuracy, but high-energy photons are hardly collimated with mechanical passive system. The electronic collimation exploited by Compton cameras can be the solution for high-sensitivity and high-resolution SPECT examinations. More details can be found in in chapter 5 of this thesis, where the described topic has been addressed with simulation studies. The presented results have been recently published in (Fontana et al. 2017a) and (Fontana et al. 2017b).

2.3.3 Theranostics

The theranostics approach in nuclear medicine couples diagnostic imaging and cancer therapy using the same molecule or at least very similar drugs, given in different dosages. For example, the combination of Iodine-131 (^{131}I) (gamma emitter) and Lutetium-177 (^{177}Lu) (beta emitter), is used for both imaging and therapy. Furthermore, different isotopes of the same elements (for example Iodine-123 (^{123}I), ^{131}I and the newer terbium isotopes - Tb) can also be used for theranostics given the multiple associated emissions (β and γ, γ rays at different energies, α and γ) (Alzahrani et al. 2012; Gerard et al. 2002; Muller et al. 2012). During the treatment, theranostics can be applied in monitoring the therapy course and estimating the potential response and eventual toxicity. The safety of high cumulative doses of radioactive agents after multiple repeated cycles is, however, a cause of concern. Anyway, remarkable improvements have been obtained in targeted therapies, which have proven to be effective with favorable safety profiles (Baum et al. 2012; Kwekkeboom et al. 2008; Strosberg et al. 2017). The diagnostic part of theranostics can be performed with both PET and SPECT machines, depending on the employed radioisotope emissions. Most therapeutic radiopharmaceuticals are labeled with β^--emitting isotopes, having a tissue penetration of only few millimeters and so adapted to spare the healthy tissues surrounding the tumor. The first theranostic radiopharmaceutical in nuclear medicine history was radioiodine, used for therapy and imaging in thyroid diseases (B. Hertz 2016). Iodine is taken up by the thyroid gland for the production of hormones, vital for the development of the brain, normal growth and metabolic balance. In 1937, Hertz developed the idea of administrating radioactive iodine in patients with thyroid diseases, and few years of preclinical studies at the Massachusetts Institute of Technology (MIT) (where the first cyclotron for medical use had been built) followed this first proposal. In 1941, the first patient was treated with radioiodine (S. Hertz et al. 1942). To date, ^{131}I is the gold standard for certain therapeutic indications, given its low cost and the advantageous combination of β^- and gamma emission. The electron radiation targets the thyroid from the inside, while the organ can be visualized using a gamma camera.

Since its first proposal, the use of theranostic agents has been consistently increasing: the

combination of targeted cancer imaging and therapy is a considerable contribution to personalized medicine and may play an important role in the future with the implementation of new chemical agents and the continuous improvement of imaging systems (Yordanova et al. 2017). For the context of this thesis it is worth to notice that, as for diagnosis SPECT, high-energy gamma emitters can be applied in theranostics, and Compton camera can be implemented for the imaging task. This point is further discussed in chapter 5.

2.4 Image reconstruction

Regardless of their specific application, imaging-related data sets have to be reconstructed in order to obtain the desired image. Nuclear medicine and PG detection devices share the basic reconstruction approaches, and dedicated algorithms have been developed for each application. In particular, image reconstruction approaches can be classified in analytic and iterative methods. Analytic algorithms are generally based on back-projections, with further steps of filtering and regularization that could be added to the reconstruction process in order to provide enhanced accuracy. In the particular case of nuclear medicine, tomographic reconstruction algorithms are used in PET and SPECT to obtain three-dimensional information. Improvements over the analytic approach are usually provided by the iterative one, able to profit from a more realistic model of the system as well as to account for image noise components. This better performance comes at the expense of algorithm complexity and calculation time. Iterative methods start from a model of the final image, generally corresponding to a regular geometric surface/volume divided into a defined number of equivalent pixels/voxels. The system is modeled in order to connect the image to the collected data: each element of the model represents the probability that the emission of a given collected gamma ray is related to a specific pixel/voxel. In order to model the data, since the gamma detection is Poisson distributed, a Poisson approach is implemented to describe in statistical terms the relationship between the value of the measurements and the expected value of the measurements. Modified Poisson statistical models and Gaussian models are also used, given the fact that after physical data corrections (attenuation, scatter, randoms, etc.) the data sets could diverge from a Poisson distribution. Once this first definition steps are accomplished, a principle governing the process iterations must be defined to converge to the "best image". The Maximum Likelihood approach is probably the most intensively studied and used, at present, in medical imaging, but alternative methods are available. Finally, an algorithm must be created to find the best image according to the defined models and iteration principle. The Expectation Maximization algorithm is the most common one, and can be adopted in several variations according to the specific application and objectives.

In the following sections, the two algorithms used during this thesis work to reconstruct the CLaRyS Compton camera data are described in more details.

2.4.1 Line-cone analytic reconstruction

The analytic reconstruction of Compton camera collected data gives, for each event, a cone surface on which the gamma emission point must lie. In the particular case of the Compton camera application in ion range monitoring, the *a priori* knowledge of the beam direction can

be included in the reconstruction point: the intersection of each reconstructed cone with the beam line results in two single points per event. The mono-dimensional distribution of the gamma emission points can be then reconstructed in the beam direction. This is the basic principle of the line-cone analytic reconstruction, which is used to reconstruct the Compton camera data; reconstructed profiles obtained with simulated data are shown in chapter 4. Alternative analytic reconstruction methods are proposed in other studies (Basko et al. 1998; Cree et al. 1994; Hirasawa et al. 2003; Maxim et al. 2009; Parra 2000).

2.4.2 Iterative reconstruction of Compton camera data

The iterative reconstruction approach allows to account for image background components and include the detector energy and spatial resolutions, and results in a three-dimensional image. Several algorithms have been proposed for the reconstruction of Compton events, based on the main points listed above (Andreyev et al. 2011; Gillam et al. 2011; Huang et al. 2018; Mackin et al. 2012; Schöne et al. 2017, 2010; Taya et al. 2017; Zoglauer et al. 2011). The data related to the CLaRyS Compton camera have been reconstructed with a List Mode-Maximum Likelihood Expectation Maximization (LM-MLEM) algorithm, a version of the MLEM method based on the list of detected events. It has been developed by the *Centre de Recherche en Acquisition et Traitement de l'Image pour la Santé*, Lyon, France (CREATIS) group, which is actively working in this field in collaboration with the IPNL (Hilaire et al. 2014; Lojacono et al. 2013; Maxim et al. 2009). The first step is to define the volume which includes the origin of the prompt gamma ray detected. This volume is divided into equal voxels and the emission intensity is assumed homogeneous for each voxel j, with a Poisson distribution of parameter λ_j (a vector of the emissions intensities of all the voxels). The algorithm is based on a system matrix T composed of the coefficients t_{ij} which represent the probability that a photon produced in the voxel j is detected in coincidence by the Compton camera as an event i. The probability for a gamma detected in coincidence to be emitted from the voxel j is denoted as s_j. The LM-MLEM algorithm starts with an initial value $\lambda_j^{(0)}$, which can be the simple back-projection reconstruction. The iterations rely on the recurrence relation in equation 2.12.

$$\lambda_j^{(l+1)} = \frac{\lambda_j^{(l)}}{s_j} \sum_{i=1}^{N_\gamma} t_{ij} \frac{1}{P_i^{(l)}}, \quad \text{with} \quad P_i^{(l)} = \sum_{k=1}^{N_v} t_{ij} \lambda_k^{(l)}, \tag{2.12}$$

where N_γ is the number of detected events and N_v is the number of voxels in the image.

For each detected photon, the coefficients in column i are calculated by taking into account the uncertainties on the angle between the source and the involved scatterer plane and the angle between the scatterer plane and the absorber involved module. The matrix elements t_{ij} are calculated as in equation 2.13.

$$t_{ij} = K(\beta_i, E_{tot}) \frac{|\cos(\theta_{V_2V_1})|}{V_2V_1^2} \int_{M \in v_j} \frac{|\cos(\theta_{V_1M})|}{V_1M^2} h_i(M) dv, \tag{2.13}$$

where β_i is the Compton scattering angle, V_1 the interaction position in the scatterer, V_2 the interaction position in the absorber, h_i the spatial kernel which models the uncertainties on

the Compton angle for each voxel M, $K(\beta_i, E_{tot})$ the differential cross section and v_j the reconstructed volume.

In order to simplify and speed up the calculation of the t_{ij} matrix, the voxels located far from the reconstructed cone are set to zero. The distance between the cone and the voxel is calculated by taking the voxel center as reference point. For each iteration, the matrix T is stored and the reconstructed image can be produced.

The algorithm has been used to reconstruct the simulated data produced to test the CLaRyS Compton prototype for particle therapy monitoring and nuclear medicine, and the results are presented in chapter 4 and chapter 5, respectively.

Part II

Thesis work

3

CLaRyS prototypes

The characterization method and the results presented in section 3.2.2 of this chapter have been published in Fontana et al. 2018.

Contents

Following the highlighted limits of ion beam therapy (see chapter 1), a collaboration of five French research institutions was established in 2010 with the aim of exploring different experimental solutions for the ion range online monitoring. The research group originally involved the *Institut de Physique Nucléaire de Lyon*, France (IPNL), the *Centre de Physique des Particules de Marseille*, France (CPPM), the *Laboratoire de Physique Subatomique et Corpuscolaire*, Grenoble, France (LPSC), the *Laboratoire de Physique de Clermont*, France (LPC) and the *Centre de Recherche en Acquisition et Traitement de l'Image pour la Santé*, Lyon, France (CREATIS). The collaboration focuses on the investigation of methods and detection solutions for the online monitoring of ion beam range during ion beam therapy treatment, and is so called *Contrôle en Ligne de l'hadronthérapie par Rayonnements Secondaires* (CLaRyS).

The main goal of the collaboration is the parallel development of three gamma detection systems to be employed for ion range online monitoring purpose in the ion beam therapy field: a Positron Emission Tomography (PET) detector called *Détecteur Pixélisé de Grande Acceptance* (DPGA), a multi-collimated gamma camera and a Compton camera.

The design and development of the PET system is managed by the LPC group, which left the collaboration in 2017, and this detection system is not treated in this thesis work.

In this chapter the two gamma cameras (multi-collimated and Compton) prototypes are described in details, and the present status of the instrumental development is presented. A complete overview of the detector development carried out in the past years is presented for the sake of completeness, and my personal contributions are listed and detailed in the final section 3.4. In the following, an entire chapter (chapter 6) is dedicated to the tests of the detectors performed with proton beams.

3.1 CLaRyS gamma camera components

The two gamma cameras under development by the CLaRyS collaboration are devoted to the detection of prompt-gamma rays emitted during ion beam treatments (see chapter 2). The design of the two cameras has been optimized by different Monte Carlo simulation studies for what concerns both the detector components and the geometrical setup.

As already mentioned, a Compton camera is usually composed of two detector sections, a scatterer and an absorber: the CLaRyS prototype respects the standard design. In the scatterer, described in section 3.1.1, the prompt-gamma incoming ray is deflected by Compton interaction and the interaction position and deposited energy are stored. The scattered photon reaches then the absorber section, where its energy is ideally totally deposited and stored, again with the interaction position. This configuration is used to provide what is usually defined as "electronic collimation", but a mechanical collimation is still an option for photon detection and localization. The scatterer section can be replaced by a mechanical collimator, described in section 3.1.2, which selects the parallel incoming photons then absorbed by the same absorber detector (a geometrical setup adaptation is possible to optimize the detection performance and will be discussed in the following). The mechanically collimated system is called multi-collimated camera, due to the collimator multi-slit structure.

As underlined in chapter 2, the prompt-gamma measurements are affected by several sources

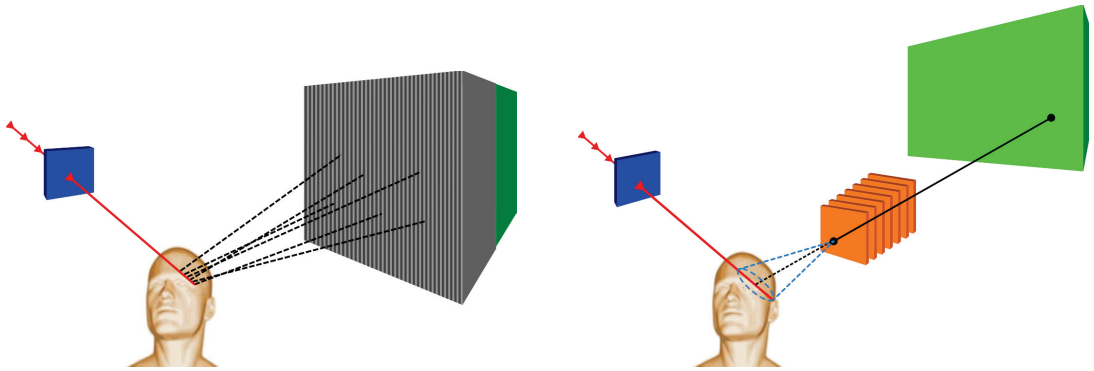

(a) Scheme of the multi-collimated camera with the beam tagging hodoscope.

(b) Scheme of the Compton camera with the beam tagging hodoscope.

Figure 3.1: Schematic view of the two CLaRyS gamma camera prototypes: the multi-collimated camera (a) and the Compton camera (b), both coupled to the beam tagging hodoscope. The ion beam is represented by the red line, and some beam bunches has been highlighted. The detection principle is also sketched for the two detectors: the tungsten collimator select the parallel incoming photons for the multi-slit collimated camera (a), while the Compton cone is reconstructed with the two interactions in scatterer and absorber in the Compton camera (b).

of background: in particular, the signals detected by the two cameras can come from secondary particles other then prompt-gammas, like photons from positron annihilation, neutrons and protons (for beam of ions heavier then protons). One of the possible solutions for background rejection is the use of Time-Of-Flight (TOF) information, requiring a further detection section dedicated to the beam tagging. A beam tagging hodoscope is being developed in parallel and can be coupled to both the gamma cameras for TOF measurements; its description is presented in section 3.1.4.

A schematic view of the two prototypes is given in Figure 3.1.

3.1.1 Scatterer

The scatterer stack is one of the components of the Compton camera prototype. Dedicated to the photon Compton scattering, its design has been studied to fulfill the camera requirements.

The Compton events reconstruction strongly relies on the measurement of the energy deposited by the photon in its Compton interaction, mandatory to properly calculate the Compton scattering angle, which is then the aperture of the resulting Compton cone. The camera accuracy is then strictly dependent on the scatterer energy resolution. At the same time, the camera efficiency is dominated by the balance between Compton interaction and photoelectric absorption probability in the scatterer detector.

Given the need for at least two interactions for a proper event reconstruction (a Compton scattering in the scatterer section and an ideally complete absorption in the absorber section, described in 3.1.3), the material choice and the geometrical configuration play a fundamental role in the camera operation. The setup must be tuned in order to define the best trade-off

between Compton and photoelectric interaction probability and to optimize, as mentioned, the detector energy resolution.

Given the fact that the Compton interaction probability linearly increases with the material atomic number (Z), while the photoelectric absorption depends on Z^n with n varying between 4 and 5 according to the photon primary energy (Knoll 2000), a low Z material is preferred to optimize the Compton probability with respect to the photoelectric one. Considering now the detector energy resolution, it must be noticed that it is strongly governed by the so-called "Doppler spread", which affects the relationship between deposited energy and Compton scattering angle. The Compton angle reconstruction formula in equation 2.3 neglects the initial recoil electron state, which is considered unbound. The energy state of the electron adds uncertainty on the reconstructed deposited energy, and so in the Compton angle calculation, with a relatively increasing contributions for decreasing incident photon energy. Given its direct dependence on the recoil electron binding energy, the "Doppler spread" is reduced for low Z materials. For a given material, the effect is larger for large scattering angles and it decreases with increasing energy of the incident photon. Following the described theoretical considerations, silicon detectors are the most coherent choice. This choice was mainly governed by the better energy resolution offered by silicon with respect to other materials (diamond, germanium, Cadmium Zinc Telluride (CdZnTe), scintillators), and it has been verified in simulation, where a silicon scatterer has been compared to competitor materials; the result are included in the Monte Carlo study presented in chapter 5.

Dedicated Monte Carlo simulation studies have been performed in order to define the most suitable geometrical configuration for the Compton camera, including the scatterer stack (Richard 2012). As a trade-off between detection efficiency and total cost, 10 layers were included in the original scatterer design. Concerning the layer size, about 10×10 cm^2 of active area in the transverse plane have been identified as the most convenient choice, also considering the absorber size (see section 3.1.3) and the distances between the detection sections required by the TOF measurements and imposed by the detector rate acceptance in clinical conditions (see appendix A). Moving to the layer thickness, its choice is governed by the definition of the camera operation. The CLaRyS Compton camera does not aim to track the Compton recoil electron, which must be then absorbed inside the same scatterer layer where the Compton interaction took place. This requirement is necessary to well reconstruct the Compton interaction angle, which needs the whole transferred energy as parameter; in addition to this, a recoil electron escaping the involved detection layer can interact in a different layer causing false coincidences which affect the camera efficiency and imaging accuracy. In order to minimize the recoil electron escape probability, relatively thick detectors are needed. On the contrary, thin layers are required to measure precisely the depth of interaction, and thus the scattering angle. A good compromise was obtained with 2 mm thick slabs.

The technological choice of the collaboration was oriented to silicon Double-sided Silicon Strip Detectors (DSSDs), provided by the Norwegian company SINTEF. A schematic view of the detector principle is given in Figure 3.2a. The silicon crystal is doped with negative (n) and positive (p) charge carriers on the two opposite sides, creating diodes which are then reverse biased. A polarization voltage is applied to the two opposite sides of the crystal, and a depletion region with no free charges is created. A ionizing particle interacting in the depletion region generates electron-hole pairs in number proportional to the deposited energy. The generated charges drift towards anode (electrons) and cathode (holes) and are converted

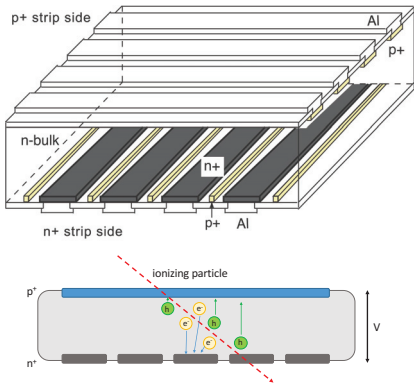

(a) Schematic view of a standard DSSD (from Takeda et al. 2008) and sketch of the signal generation. The actual implantation scheme can slightly differ from the one present on the employed detectors.

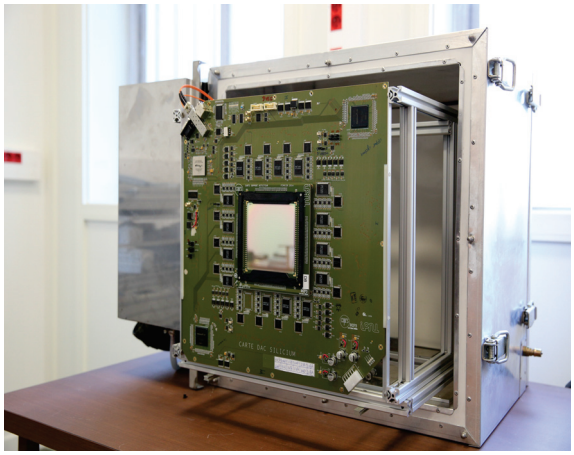

(b) Scatterer silicon layer with its Front-End (FE) card in the thermal regulated box (described in section 3.1.1.2).

Figure 3.2: Overview of the scatterer layers, with its working principle (a) and a picture of the detector connected to the Front-End (FE) card in the thermal regulated box (b).

into electrical signals. The read-out is ensured by the implanted strips, which transfer the charges outside the detection region.

Each layer has an active volume of 96×96×2 mm^3, segmented with 64 strips per detection plane. The strip pitch is 1.41 mm, for a strip width of 1.31 mm. The applied bias voltage is nominally – 750 V (applied to the p-side while the n-side is set to ground), and it is uniformly shared on the whole surface to obtain a homogeneous depletion region. A guard ring, composed of 23 strips surrounding the read-out ones on the p-side, ensures the desired voltage gradient. The more internal strip of the guard ring on the p-side is connected to the high voltage, while the n-side has a single strip for the guard ring in peripheral position and connected to the ground. The p and n read-out strips are then connected to the Front-End (FE) electronics via bonding cables.

The FE electronics card has been developed by the *Institut de Physique Nucléaire de Lyon*, France (IPNL) electronics group and is described in details in section 3.1.1.1. The silicon detector is directly plugged on the card, and the mechanical support for the scatterer stack has been studied according to the card size, as shown in Figure 3.2b.

Among the 10 received DSSDs, only 7 fulfilled the requirements imposed by the Compton camera application, mainly in terms of noise level (leakage current); 3 layers have been rejected, so that the final prototype scatterer is composed of 7 silicon planes.

The 7 selected layers have been characterized with a temporary acquisition system in terms of leakage current at different temperatures. The results of these measurements can be found in Ley 2015. The measurements enabled one to verify the producer specifications in terms of bias voltage to be applied for a complete detector depletion, as well as to identify the noisy strips and create a complete characterization database. In addition to this, they highlighted

the need to cool the detectors down with respect to the room temperature (25 °C) in order to reduce the leakage current to acceptable levels, and so reducing the total noise level, affecting the detector performance. In order to accomplish the cooling task a thermal regulated box based on cold air pump has been designed and produced. It operates as the scatterer stack mechanical support, and it is described in section 3.1.1.2.

3.1.1.1 Scatterer front-end card

As mentioned in the previous paragraph, the main requirement for the scatterer detector modules is a very good energy resolution. The desired working performance can be quantified as follows:

- 1 keV Full Width at Half Maximum (FWHM) energy resolution;
- 1.41 mm spatial resolution (corresponding to the strip pitch);
- 15 ns FWHM time resolution.

The scatterer FE card has been developed by the IPNL electronics group in order to achieve this performance. It is composed of two well separated sections, analog and digital, which must be kept separated in the card layout in order to minimize the contribution of the digital noise on the treatment of the analog signals. Moreover, in order to reduce the electronic noise, the analog section must be placed as close as possible to the detector, to minimize the signal path length.

At first, a dedicated Application-Specific Integrated Circuit (ASIC) has been designed and developed to treat the signals directly coming from the DSSD (Dahoumane et al. 2014). Each ASIC processes 8 detectors channels, so that 8 ASIC per plane are required for the read-out of a complete silicon layer. This section represents the core of the analog stage. The ASIC has been designed and tested to achieve the desired performance in terms of Equivalent Noise Charge (ENC), which must be lower than 118 electrons Root Mean Square (RMS) in order to obtain the 1 keV FWHM energy resolution, signal dynamics and accepted detection rate. The analog raw signal first passes through a Charge Sensitive Amplifier (CSA), which returns an analog amplified signal. This pulse can be further amplified with a Slow Shaper (SHS) based on a Capacitor Resistor - Resistor Capacitor (CR-RC) filter, which filters and shapes the signal in about 1 μs, or via a fast amplifier (with 15 ns shaping time). The first mode is used for a refined charge (deposited energy) measurement and can be employed for detector tests and characterization, while the second is the standard working one which allows for fast energy and time measurements. The amplified signal finally passes through a discriminator, which gives a digital output. Analog (from CSA or SHS) and digital signals are then sent to the digital stage of the card for the measurement of time, position and energy.

The digital stage is mainly composed of one Analog-to-Digital Converter (ADC) module per ASIC and two Field Programmable Gate Arrays (FPGAs). The analog signal from the ASIC is processed by the ADC, which is a 12-bit module with 8 channels, with a sampling rate of 100 Mega Sample Per Second (Msps). Each ADC returns 16 Low-Voltage Differential Signaling (LVDS) pairs (2 per channel), which are sent to the FPGAs together with two clock signals (two LVDS pairs) and the 8 digital outputs of the ASIC. So, 44 input channels of the FPGA are used

for the acquisition of 8 read-out channels (one ASIC). Two FPGAs Altera Cyclone III (Altera 2012) are installed on the card to handle the signals coming from the whole detector (128 channels, 64 per detection plane): both of them are equipped with a Time-to-Digital Converter (TDC) for the time measurement.

A third FPGA (Altera StratixII GX (Altera 2009)) is finally installed on the card to handle the processed data collection and the communication with the acquisition system, described in section 3.1.5, via a 3 Gbit/s link.

The ASIC has been developed in three versions, and the cards have been optimized during the development process and produced in its final version (shown in Figure 3.3a) in the Spring 2017. The 7 cards are now available and the development of the FPGA firmware is ongoing.

More details about the card layout, components and operating principle, as well as a description of the tests performed during the development can be found in Chen 2017 and Dahoumane et al. 2012.

3.1.1.2 Scatterer thermal regulated box

The results of the leakage current tests performed on the silicon detectors showed the need of cooling the detector down to achieve the required performance in terms of noise, which affects the spatial, time and energy resolutions. The leakage current has been studied in temperature cycles in the range – 40 – +40 °C, and an overall consistent behavior has been observed both on N and P strips of the detector. The leakage current slightly increases in the range – 40 – 0 °C, with values in the range 0 – 8 nA for the analyzed strips, and then drastically increases beyond 0 °C, with peaks of more then 80 nA at +40 °C. The complete description of the performed measurements and the detailed results can be found in Ley 2015.

A cooling system is needed for the silicon detectors operations: it must be able to keep the temperature constant and below, at least, 0 °C, preferably around – 20 °C where the leakage current is more stable in case of small temperature variations. The clinical environment limitations must be considered to design such a cooling system (portability, gas, noise level), as well as the material budget and the mechanical integration with the other camera components.

The implemented solution consists in the thermal regulated box shown in Figure 3.2b, together with one of the silicon layers. The size of the box is 490×490×300 mm^3, and the structure is composed of 2 mm of aluminum and three insulation layers of 10 mm of silica aerogel Spaceloft® (Aspen Aerogels 2011), for an equivalent thickness of 2 mm of silicon (0.7 % of interaction probability for 1 MeV photons). The cooling is performed via an electric air pump, which is able to keep the temperature inside the box at – 20 °C with a 400 W heat evacuation power. The heat power produced by the 7 silicon FE cards in operation must be verified, but the estimate confirms the effectiveness of the thermal box nominal performance. Once card and detector will be fully operational, a test will be performed to check the temperature stability inside the box and possible issues like water condensate/freezing, thermal dilatation, vibrations.

The FE cards and the silicon layers are fixed inside the box via a mechanical support designed and produced by the IPNL mechanics group. The support, which ensures a millimeter position

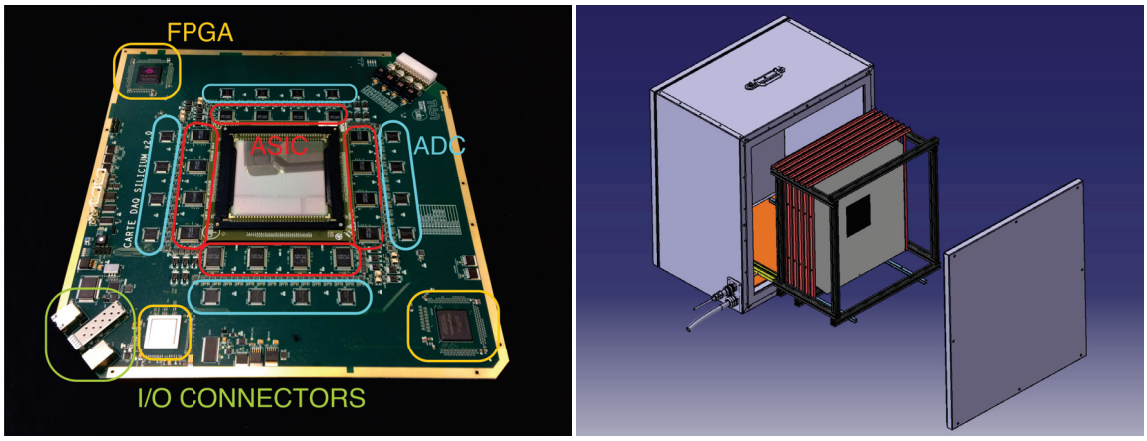

(a) Final version of the scatterer FE card with the silicon detector layer. The main components are highlighted. Three FPGAs are present on the board, one (close to the I/O connectors) used to collect and send the data processed by the other two. 8 ASICs and 8 ADC per detector plane surround the silicon detector, connected in the center of the board.

(b) Scheme of the scatterer stack thermal box and internal mechanical support.

Figure 3.3: Scatterer silicon layers equipment: final version of the FE card (a) and scheme of the detector integration in the thermal regulated box (b).

accuracy, is fixed on metal rails which allow to easily handle each detector layer. A scheme of the thermal box and the internal support is shown in Figure 3.3b.

3.1.2 Collimator

The multi-collimated camera is equipped with a multi-slit collimator, with tungsten alloy slabs (97 % tungsten, nichel and iron for the remaining components - density 18.5 g/cm^3) of 1.5×120×170 mm^3. Its design has been extensively studied in Monte Carlo simulations (Pinto et al. 2014), and it can be easily adapted to different geometrical configurations of the absorber detector and to various monitoring requirements. In particular, the distance between neighboring slabs can be modified, as well as the number of total slabs, in order to find the best trade-off between detection efficiency and spatial resolution; this depends on the distance patient-collimator, on the required extension of the field of view and on the desired monitoring time. Two identical collimators of 30×14×17 cm^3 have been produced, in order to be able to set several absorber configurations in the transverse direction (extended version along the beam axis or in the perpendicular direction). In Figure 3.4a a picture of the tungsten collimator is presented, while in Figure 3.4b we show a schematic view of a possible multi-collimated camera configuration.

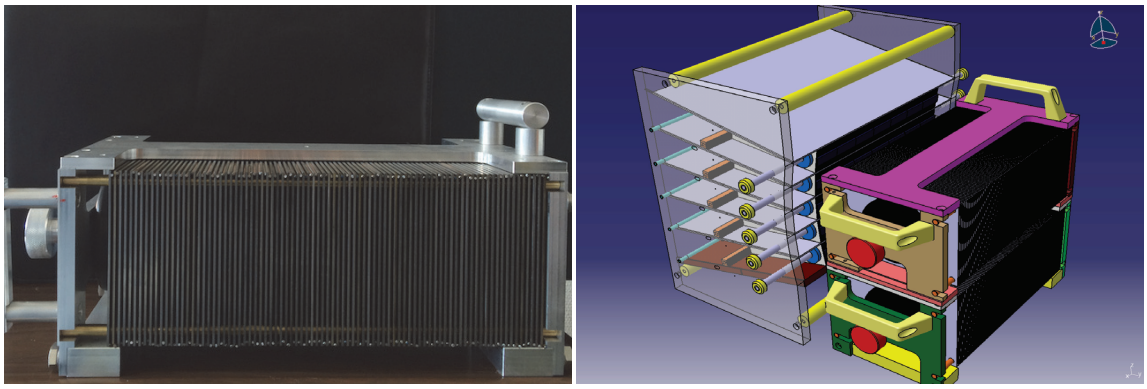

(a) Multi-slit tungsten collimator.

(b) Scheme of the multi-slit collimated camera configuration.

Figure 3.4: Tungsten collimator and its setup in the multi-slit collimated camera. Two identical collimators are available, with 1.5×120×170 mm^3 tungsten slabs and a pitch of 5.5 mm. The two tungsten multi-slit collimators are placed in front of a 6×5 Bismuth Germanium Oxide - $Bi_{12}GeO_{20}$ (BGO) block absorber setup in its mechanical support (see section 3.1.3). Both the single collimator setup (size and pitch) and the two collimators configuration can be easily modified to adapt the system to specific applications.

3.1.3 Absorber

The Compton and multi-collimated camera absorber was initially conceived as a very large surface plane composed of 96 BGO blocks recovered from a dismantled PET system HR+ by SIEMENS, documented in (Adam et al. 1997; Brix et al. 1997).

BGO is one of the most used scintillators for gamma detection applications, thanks to a fair energy resolution and an optimal gamma detection efficiency, given the high effective atomic number (75) and high density (7.12 g/cm^3) (Elftmann et al. 2015) which maximize the photo-electric probability. Moreover, the absence of internal radioactivity which characterizes other scintillator materials employed in the same field (i.e. Lutetium-Yttrium OxyorthoSilicate - $Lu_{2(1-x)}Y_{2x}SiO_5$ (LYSO), Cerium-doped Lutetium OxyorthoSilicate - Lu_2SiO_5(Ce) (LSO)), makes it suitable for low noise detectors, required by a Compton camera to reduce the amount of random coincidences, one of the main sources of background for the application in ion beam therapy monitoring (Ortega et al. 2015). As highlighted in (Hueso-González et al. 2015a), LYSO and LSO show overall better performance with respect to BGO for what concerns mainly energy and time resolution, due to an about 4 times higher light yield, but the gap is reduced for the detection of gamma rays in the prompt-gamma energy range (especially beyond 1 MeV). The limited cost of BGO with respect to LSO and the comparable performances in the prompt-gamma energy range make it an optimal solution for prompt-gamma camera prototypes, provided fast timing and spectroscopy are not the main requirements.

Each BGO block composing the gamma camera absorber has an area of 3.5×3.8 cm^2, with a thickness of 3.0 cm. The mono-block BGO crystal is streaked in a 8×8 pseudo-pixel matrix; a reflecting material is inserted between the pseudo-pixels to improve the light collection and optimize the spatial information accuracy via pixel separation. The read-out is achieved via four Photo-Multiplier (PM) tubes per block, composing a quartet, coupled to the block back surface. Thanks to the internal streaked structure of the block, the scintillation light is shared between the four PMs depending on the pseudo-pixel where the interaction takes

place (in case of multiple interactions more than one pseudo-pixel can be involved). The streaks have a different thickness according to their position in the block: they fully cover the block thickness on the block borders and they progressively shorten towards the block center, with a mono-block structure in the central block section on the entrance face. Note that the crystal dimension and streaked structure were optimized by the manufacturer for the detection of 511 keV photons, therefore it is not *a priori* obvious that such blocks could keep their performance above 1 MeV. The reconstruction of the position of interaction is done via Anger logic, i.e. with a center of gravity calculation.

The whole set of recovered blocks was supposed to undergo a "reconditioning" process, including the PM removal, the crystal back surface polishing with diamond-based abrasive tool, the single PMs gain characterization and grouping in quartets with similar gains, the final re-coupling of the PMs and block shielding.

A set of "reconditioned" blocks has been tested with the method described in section 3.2 and their performance has been compared to a set of original blocks. An overall degradation of the detection performance has been verified on all the tested "reconditioned" blocks, which showed lower amplitude output signals probably linked to a reduction of the collected scintillation light. Various correction methods have been tested, with unsatisfactory results. According to the outcome of these tests, summarized in Sandjong et al. 2017, the collaboration finally opted to adapt the camera design for the use of original, "non-reconditioned" BGO blocks.

Thirty original blocks are now available to compose the absorber detector. In addition to the already presented features, it must be noticed that the lateral faces of the original blocks, as well as the half of the PM length, are covered with a reflecting material which ensures the complete collection of the scintillation light. This is probably a component which was not well reproduced during the reconditioning process. The whole structure is then protected by a 1 mm thick aluminum foil, which also isolates from external light contamination.

Figure 3.5a shows one BGO block before the coupling to the PM quartet: the streaked structure is clearly visible, as well as the white reflecting material separating the pseudo-pixels and the one surrounding the block lateral sides. As mentioned, the same material also covers part of the photo-multiplier tubes, as shown in picture 3.5b, where the four PMs are glued to the block back surface. The described aluminum cover is visible in Figure 3.5c, while in Figure 3.5d a scheme of a block together with the related PM quartet is given. The spatial reconstruction logic is also reported in the same figure.

3.1.3.1 Absorber front-end and read-out cards

General design

A custom front-end card has been designed and produced by the LPC research group *Application et Valorisation des Interactions Rayonnements-Matière* (AVIRM) and is used for the read-out of each BGO block. The card is equipped with four voltage modulators which divide the provided high voltage on the four PM tubes. The voltage sent to each PM can be tuned via screw-potentiometers on these modules. A $\pm$ 5 V low voltage is applied to the cards as supply for the differential amplifier modules, one per PM. Differential output channels are used to send the PM signals to the read-out card, called Analog Sampling Module (ASM) board, via flat cables. A picture of the FE card is given in Figure 3.6a. To be noticed that four analog output channels have been added on some cards in order to allow laboratory tests with a signal

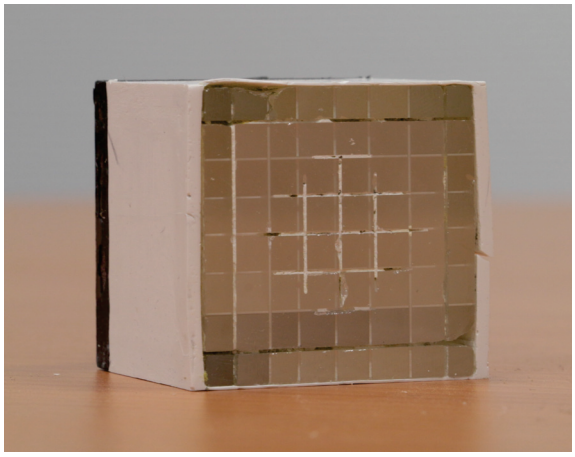

(a) BGO block with its pseudo-pixel internal structure. The block is in "poor" state after the uncoupling from the PMs.

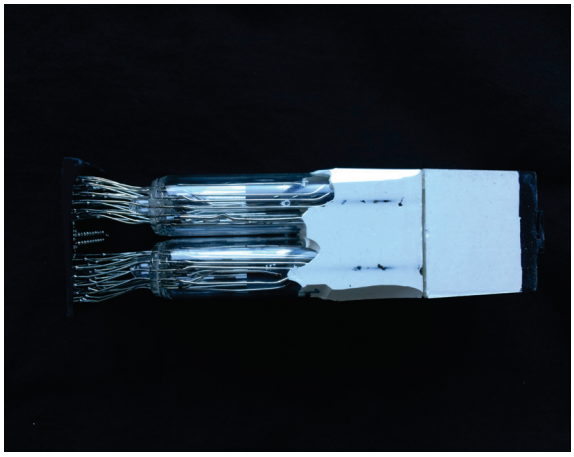

(b) BGO crystal coupled to PM quartet and covered with white reflecting material.

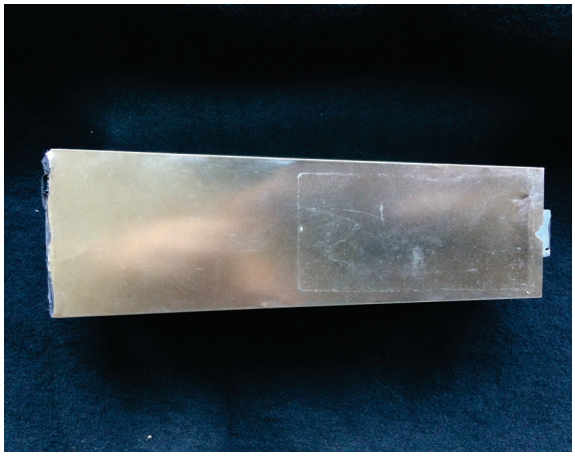

(c) BGO complete module with aluminum cover.

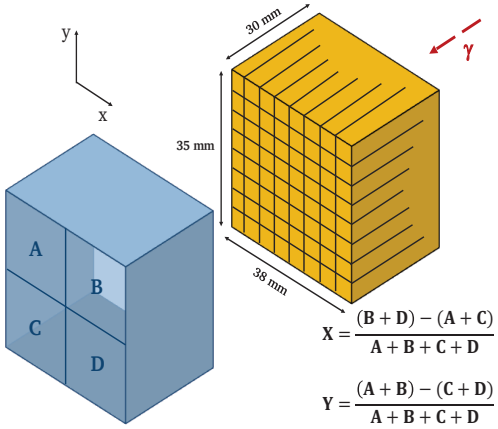

(d) Scheme of a BGO block and its spatial reconstruction logic.

Figure 3.5: Components of an absorber module and its working principle.

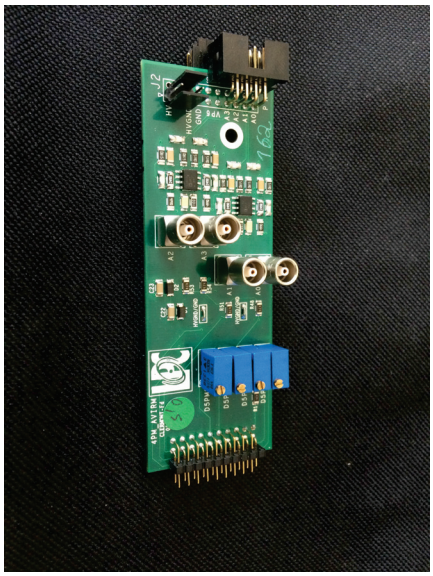

(a) FE card of the absorber BGO detectors. 4 analog outputs have been added for test purpose.

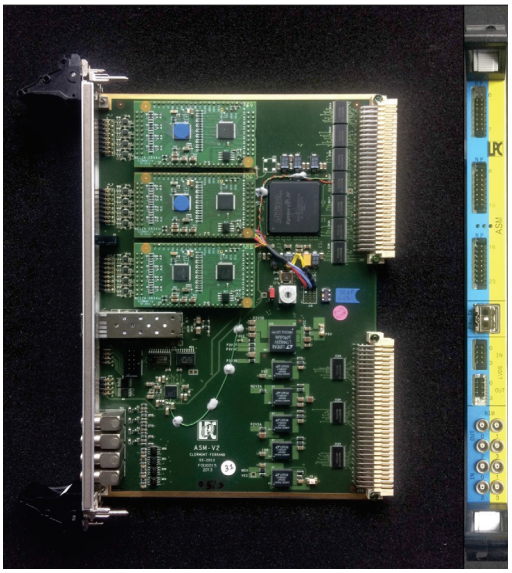

(b) ASM board of the absorber BGO detectors. Each board performs the read-out of 6 blocks.

Figure 3.6: Absorber read-out electronics: FE card (a) and ASM board (b).

treatment based on standard electronics modules, as described in section 3.2. These outputs retrieve the signal before the differential amplification stage, so that the low voltage supply is not needed for this read-out configuration.

The PM signals amplified by the FE card (differential outputs) are received by the ASM boards. Developed by the LPC AVIRM group, it is based on the VERSABUS Module Eurocard (VME) standard and designed for the application in the *Détecteur Pixélisé de Grande Acceptance* (DPGA) PET system, equipped with LYSO mono-crystals, grouped in quartets and read-out by the same FE card described above. The adaptation to the gamma camera application, so that for the BGO modules signal treatment, involves only the firmware part. Each board has 24 differential inputs and it is so able to read the signals from 6 BGO blocks; a total of 5 boards are then needed for the complete read-out of the gamma camera absorber (30 blocks). The incoming signals are treated by three intermediate cards equipped with a Domino Ring Sampler (DRS)4 chip (Ritt 2009), designed and developed at the Paul Scherrer Institut, Villigen, Switzerland (PSI), with 8 sampling channels at a maximum frequency of 5 Giga Sample Per Second (Gsps) (200 ps period) for 1024 samples, and an ADC 12 bit-20 MHz module. The sampling frequency of the DRS4 can be modified to fit with the specific application: in particular, the BGO blocks produce wider signals with respect to the LYSO crystals of the DPGA, therefore the sampling is reduced to 1 GHz for our application. A FPGA Altera Cyclone IV GX (Altera 2015) receives and handles the digital outputs of the three intermediate cards and is in charge of sending the data to the acquisition system via a 3 Gbit/s optical link. The FPGA also governs the generation of the pre-trigger signal which is sent to an auxiliary board called Trigger et HORloge (THOR) in order to start the acquisition of the gamma cameras, as detailed in section 3.1.5.

Absorber acquisition with development card

During the development of the final camera acquisition system based on the Micro Advanced Telecommunications Computing Architecture (μ-TCA) equipment, which required a dedicated

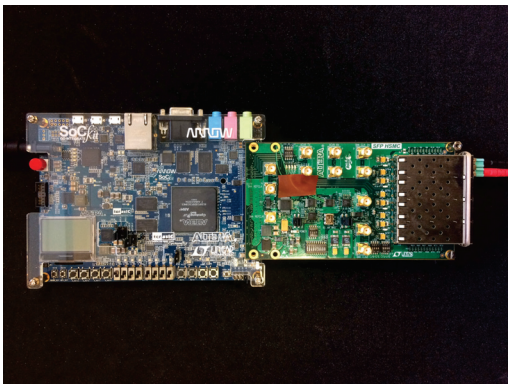

(a) Altera development card for the absorber BGO detectors.

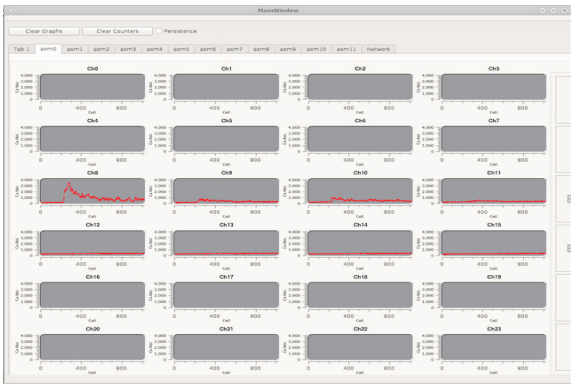

(b) Example of acquisition software interface for the absorber ASM card acquisition based on the Altera development card. The interface shows the collected raw signals from each PM of a maximum of six blocks (corresponding to 24 channels, read-out by one single ASM board).

Figure 3.7: Details of the temporary absorber acquisition based on the Altera development card.

firmware development ad testing process, a temporary acquisition system has been set for the absorber BGO blocks, mainly dedicated to the test and characterization of the ASM boards. It is based on a commercial development card, provided by Terasic (Altera University Program), equipped with an FPGA Altera Cyclone V (Terasic 2015). The FPGA card can be programmed for the needed tasks, and it is directly connected to an acquisition PC via Ethernet cable. Three High-Speed Mezzanine Card (HSMC) connectors allow for the connection to an expansion board SFP-HSMC (Terasic 2009), again by Terasic, provided with a second FPGA and with optical fiber input/output connectors for the interface to the ASM boards. A single optical input is configured for this acquisition setup, with the firmware developed by the AVIRM group in LPC and adapted at the IPNL; one single ASM card can be connected to the board, so that a maximum of 6 BGO blocks can be read-out at the same time. A picture of the development card connected to the mezzanine is given in Figure 3.7a. Figure 3.7b shows an example of the user interface and data visualization of the C++ based acquisition software developed and provided by the AVIRM group.

3.1.3.2 Absorber mechanical support

A first mechanical structure for the absorber detector was initially conceived by the LPC group in order to hold up to 100 modules, foreseen by the original camera design. The reduction of the number of available blocks caused by the “reconditioning” process failure made necessary an adaptation of such a support. The new design has been carried out by the mechanics group of the IPNL in order to be compact and flexible in terms of detection modules setup. Figure 3.8 displays both a picture and a scheme of the absorber configuration with its mechanical support. The two lateral sides are built with Poly-Methyl-Metacrylate (PMMA) boards connected by metal bars, and the BGO blocks can be arranged in up to 5 rows of variable size, ranging from 3 to 7 blocks. Each block row is supported by a thin metal foil, designed to reduce at minimum the blocks separation and to respect the original ring geometry deriving from the SIEMENS

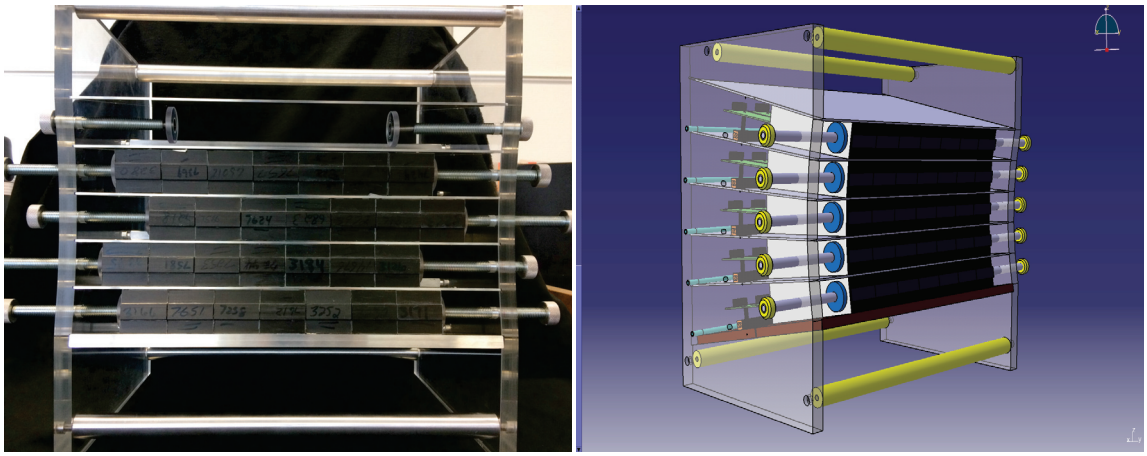

(a) Picture of the absorber detector in its mechanical support.

(b) Scheme of the absorber detector with its mechanical support.

Figure 3.8: Absorber front view with the BGO block lines arranged in the mechanical support (a). Scheme of the BGO absorber with its mechanical support (b).

PET system. The blocks composing a row are then laterally pressed via two screws on the two sides of the structure, which can also be used to adapt the relative row position horizontally. On the back side, a metal bar is added to avoid undesired movements, and the FE cards are fixed with plastic pillars. The realized support results to be versatile, compact and adapted to the prototype tests for both the Compton camera (where a squared setup is preferred) and the multi-collimated one (where the collimator geometry must be fit by the absorber geometrical configuration).

3.1.4 Beam tagging hodoscope

A beam tagging hodoscope is being developed in parallel to the two gamma cameras, mainly for background rejection and reconstruction optimization purposes. As already mentioned, the detection of prompt-gammas (with mechanical or "electronical" collimation), is affected by the presence of other secondary particles produced during the ion beam irradiation, mainly neutrons. This background source can be efficiently identified and reduced by applying TOF selection windows to the data acquisition. The TOF measurements can be performed using the accelerator radio-frequency signal as reference for cyclotron accelerators, while a direct beam detection results to be more accurate for synchrotron-based treatments. An auxiliary detector is then needed before the beam interaction in the patient.

The CLaRyS hodoscope prototype is designed to provide space and time information about the incoming primary beam, particle by particle or bunch by bunch, depending on the beam intensity and detector efficiency and rate acceptance which must be characterized. In addition to the already explained use of the time information, a space primary particle tagging can be used to improve the reconstruction accuracy and constraint the possible reconstructed emission vertex in case of analytic reconstruction approach for both the multi-collimated and Compton cameras (see chapter 2).

The detector under development is based on squared 1 mm^2 polystyrene scintillating fibers

BCF-12, 140 mm in length, provided by Saint Gobain (Saint Gobain 2017). A picture of the hodoscope on its mechanical support (detailed in the following) is presented in Figure 3.9. The fibers are arranged into two perpendicular planes for a two-dimensional spatial information: each plane is composed of 128 fibers, for a total active area (for 2D measurements in coincidence) of 128×128 mm^2. The active detector surface is completely covered with black tape, which shields from external light. The scintillation light produced in the fibers by a ionizing particle depositing energy is transported to the read-out system via FORETEC optical fibers (1.55 cm diameter, 1 m length), which are connected to the scintillating fibers thanks to a custom mechanical support and to a proper gluing process (see Figure 3.10a). Each scintillating fiber is read-out on both sides to optimize the detector efficiency and to improve the time resolution, which does not depend on the interaction position along the fiber with this configuration; the total number of read-out channels is then 512. The signal read-out is ensured by 8 multi-anode PMs Hamamatsu H8500 (Hamamatsu 2006) shown in Figure 3.10c. The optical fibers are connected to the PM anode surfaces through a plastic custom mask, shown in Figure 3.10d. The PMs are equipped with custom black boxes which operate as mechanical support and external light protection (see Figure 3.10a). In order to provide further light isolation, the whole PM boxes are covered with black tape.

The optical fibers are connected to the 8 PMs with a logic aiming to increase the maximum counting rate. 4 PMs are dedicated to the read-out of the horizontal fibers, and 4 to the vertical ones, and the neighboring fibers are connected to different PMs. An active area of 4×4 mm^2 on the two planes is then read-out by all the 8 PMs. Moreover, the two sides of the same scintillating fiber are connected on the same PM. This fiber connection logic also improves the detector robustness; in case of problem on one PM, only 1 mm each 4 mm is lost on a single plane, so that the detection of the beam is still possible on the whole active area.

Each PM is connected to a single custom FE card. The hodoscope FE cards have been developed by the IPNL electronics group: their design is described in section 3.1.4.1. 8 FE cards are then used for the read-out, and the collected data are sent to the acquisition system described in section 3.1.5.

3.1.4.1 Hodoscope front-end card

The hodoscope is designed to tag in space and time the incoming beam ions, so that the signal read-out must be optimized to provide accurate time measurements and a high detection rate acceptance, with reduced dead time and detection efficiency close to 100 %. In particular, the design requirements include a maximum counting rate acceptance of 10^8 Hz per detection plane, with a time resolution of 1 ns (Krimmer et al. 2014). The hodoscope FE card shown in Figure 3.11a has been developed by the IPNL electronics group to fulfill the listed requirements. The Hamamatsu PM is connected to the 64-channel connector (4 connectors of 16 channels each) and two custom ASICs are dedicated to the data first treatment (32 channels each).

A first version of the FE ASIC has been developed in 2012 by the group *Micro-électronique RHône AUvergne* (MICRHAU) for the read-out of 8 channels (designed for the 32+32 fiber hodoscope prototype described in section 3.1.4.3). The input part is composed of a current conveyor, and the output one has two sections: a current discriminator and a charge preamplifier for the charge measurements in test mode (Deng et al. 2012, 2013). In addition,

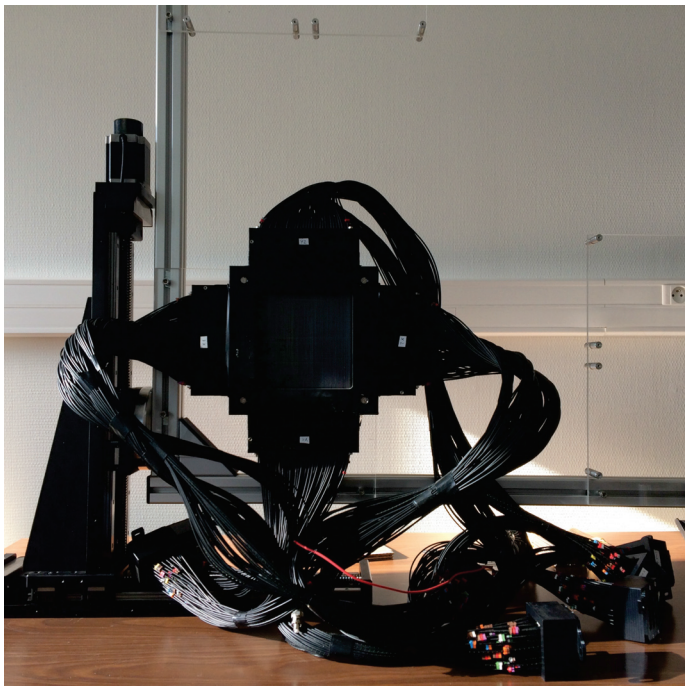

Figure 3.9: 128+128 scintillating fiber hodoscope on its 2-dimensional moving stand.

the ASIC gain can be tuned channel by channel, so that the response of each PM output channel can be fine tuned with respect to the others.

The second version of the ASIC includes all the features of the first version, with the addition of a TDC based on a 160 MHz clock for a more accurate time tagging of the detected events. Moreover, a Delay Locked Loop (DLL) is installed to divide the main clock in 32 intervals: for each event, the DLL state is stored in a 32 bit register and then encoded in a 5-bit Gray decoder. As a result, the TDC has a 6.25 ns dynamics, with a sampling step of 195 ps and a time resolution of 58.8 ps RMS, for a maximum accepted rate of 10^8 Hz (Deng 2012).

The third and final ASIC version, called HODOPIC, is adapted to the big size hodoscope (512 read-out channels), with the extension to 32 channels and with the TDC implemented on the second version. An external ADC is used for the charge measurement in test mode for a single channel, selected via slow control. All the ASIC outputs are sent to a FPGA installed on the card for the actual time measurement and data decoding. The FPGA finally handles the data transmission to the acquisition system, depending on the card version.

A first card has been developed to test the first ASIC version with the 32+32 fiber hodoscope. It is based on a FPGA Altera Cyclone III (Altera 2012) and on 9 ASICs, with a LabVIEW acquisition. A single card is enough for the read-out of the complete small hodoscope prototype. This first setup has been tested on beam at *Grand Accelerateur National d'Ions Lourds*, Caen, France (GANIL) and Heidelberg Ion Therapy Center, Germany (HIT), and a sub-ns time resolution has been verified, together with the expected 1 mm spatial resolution on the two fiber planes and an efficiency of more then 90 % at a 10^6 acquisition rate.

The second prototype of the card, shown in Figure 3.11a, has been adapted to the 512-channel hodoscope described in the previous section and to the gamma camera acquisition system

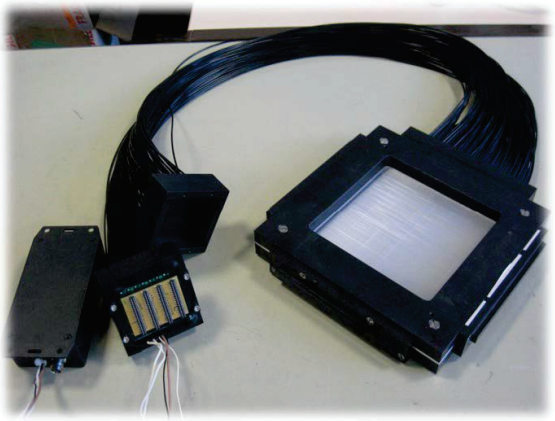

(a) Scintillating fiber hodoscope during mounting process.

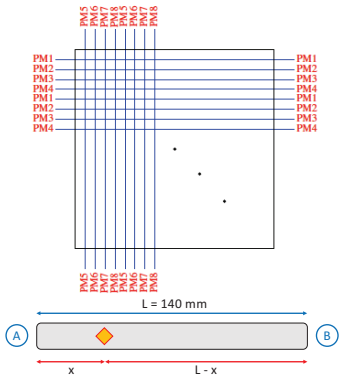

(b) Scheme of the scintillating fiber connection to the PMs (top) and of the double-sided fiber read-out (bottom).

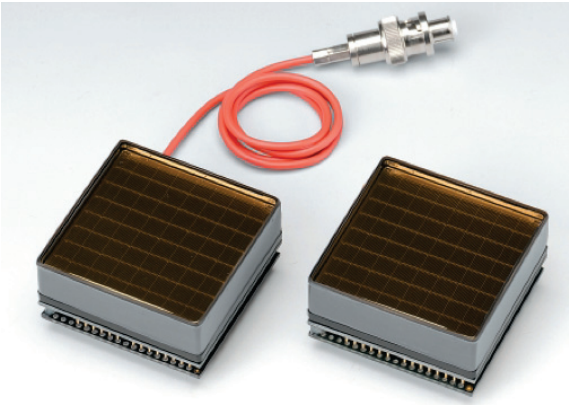

(c) Hodoscope read-out PMs Hamamatsu H8500.

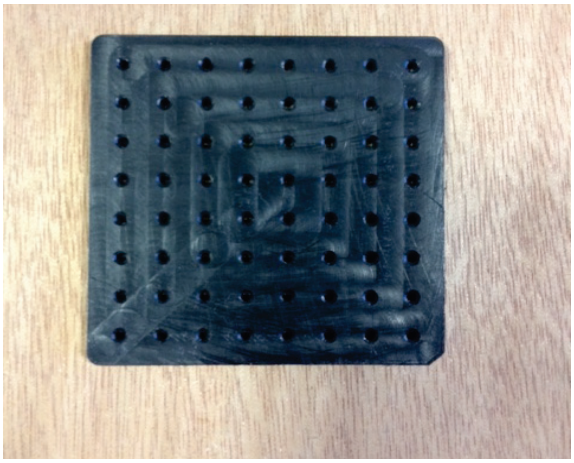

(d) PM plastic mask for optical fiber connection.

Figure 3.10: Details of the scintillating fiber hodoscope setup.

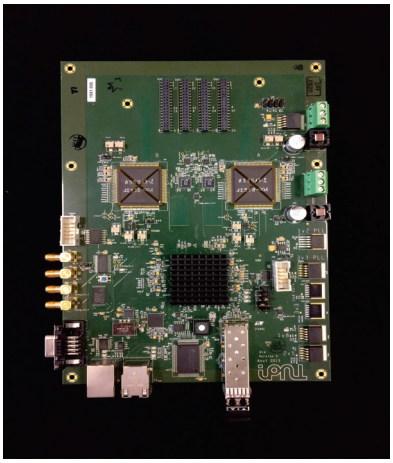

(a) Hodoscope FE card.

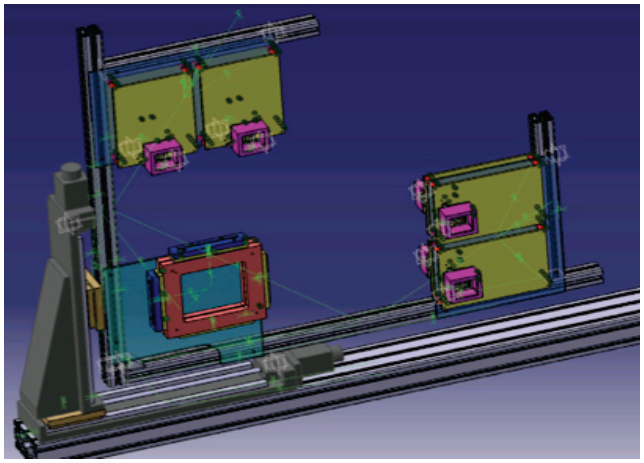

(b) Hodoscope mechanical support scheme.

Figure 3.11: HODOPIC board (a) and scheme of the beam-tagging hodoscope two-dimensional moving stand (b).

described in 3.1.5: each card has two HODOPIC ASICs, 32 channels each, so that it is designed for the read-out of a single 64-anode PM. 8 cards are then needed for the read-out of the whole hodoscope. This version is based on a FPGA Altera StratixII GX (Altera 2009), and the connection to the acquisition is ensured by a 3 Gbit/s optical link. 4 digital input-output channels are installed for test and validation purpose, together with an Ethernet port.

Further details about the different card versions and the applied validation tests can be found in Chen 2017.

The hodoscope card firmware has been developed in 2017 and tested in simplified versions on beam, as detailed in chapter 6.

3.1.4.2 Hodoscope mechanical support

The beam tagging hodoscope is set between the beam nozzle and the patient and requires a dedicated mechanical support. In order to profit from the large active area and to be able to remotely control the hodoscope position in the beam transverse plane, the detector is mounted on a 2-dimensional moving table (see the picture in Figure 3.9), which also supports the FE cards. Detector and FE cards are then integral and translate together. A scheme of the moving table is given in Figure 3.11b.

The 2-axis table is provided by Beijing Winner Optical Instruments; it is composed of two motorized linear stages, connected via a right angle bracket. The two stages have a moving range of 30 cm each and the stepper motors have a step resolution of 20 μm. The employed motor controller is a Newport XPS-Q8 (Newport 2017), equipped with 8 channels for the simultaneous control of a maximum of 8 motors. The movements are steered with an online interface or with a LabVIEW-based program, which will be integrated in the final setup of the slow control software under development with the cameras.

3.1.4.3 Small hodoscope prototypes

Before the production of the large active surface hodoscope prototype described in section 3.1.4, two smaller prototypes have been produced and tested in order to assess the potential of such a kind of detector for the required application. The first and simplest version consisted of one single scintillating fiber per plane, and the readout was performed with two PM tubes directly coupled to the scintillating fibers, without optical fibers. A picture of this prototype is given in Figure 3.12a. This simple version of the detector has been used as a demonstrator of the basic detection principle.

A second small size version of the final detector has been produced with almost the same features as the large area prototype but with simplified read-out logic. It is equipped with two perpendicular planes of 32 1 mm^2 scintillating fibers each (Saint Gobain BCF-10 (Saint Gobain 2017)), with a length of 4 cm and a total active area for a 2D read-out of 32×32 mm^2. As in the big hodoscope, the scintillating fibers are coupled to FORETEC optical fibers which transfer the scintillation light to 4 Hamamatsu H8500 PMs. 16 channels per PM are used, so

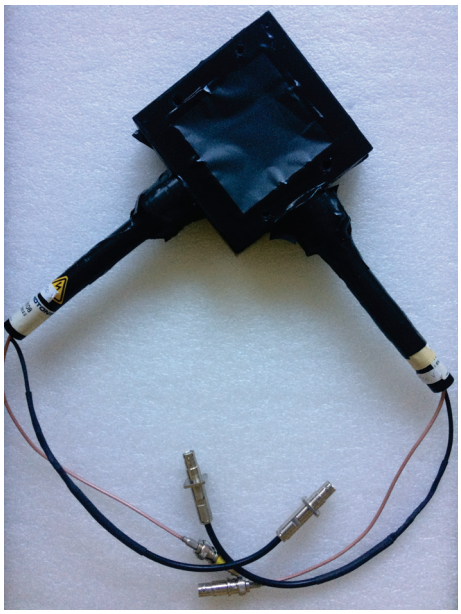

(a) Hodoscope small prototype, 1+1 scintillating fibers.

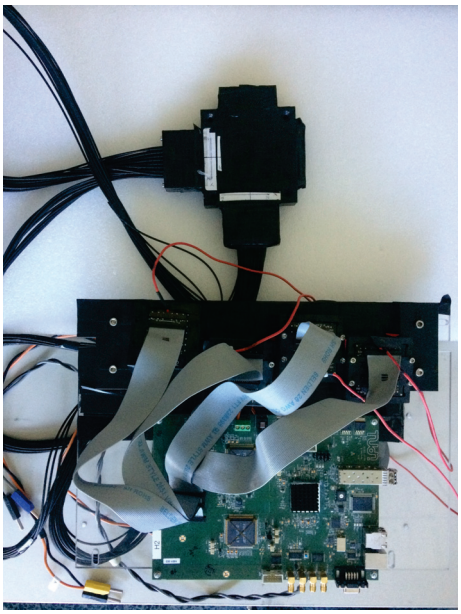

(b) Hodoscope small prototype, 32+32 scintillating fibers, connected to the HODOPIC FE board.

Figure 3.12: Hodoscope small prototypes.

that 2 PMs are dedicated to the horizontal fibers and 2 to the vertical ones, and the signal read-out is performed on a single side of the scintillating fibers (2 adjacent fibers are read by two different PMs). As the total number of read-out channels is 64, a single FE card is sufficient for the whole detector. In Figure 3.12b the 32+32-fiber hodoscope prototype is shown together with its FE card; 4 connections cables (16 channels each) are used to couple the PMs to the FE card.

The 32+32-fiber hodoscope prototype has been tested in 2014 on proton and carbon ion beams (at the GANIL - 75 MeV/u ^{13}C, HIT - protons and carbon ions at various energy, *Institut de Physique Nucléaire d'Orsay*, France (IPNO) - 25 MeV protons) with the first version of the FE card (see section 3.1.4.1): an efficiency of more than 90 % has been retrieved, with a time resolution of 1 ns FWHM (timing measurements performed with respect to the accelerator high frequency signal). Some more details about this beam tests results are given in chapter 6. The final version of the FE card has been also tested with this detector, and the test description and results are presented in chapter 6.

3.1.5 Camera acquisition system

The TOF gamma cameras developed by the CLaRyS collaboration are composed of various detection sections: beam tagging hodoscope and BGO absorber for the multi-slit collimated camera, with the addition of the silicon scatterer stack for the Compton camera. The acquisition system must be able to handle the data flux from the different components, for a total of 20 FE cards (7 for the silicon scatterer, 8 for the hodoscope and 5 for the absorber), select the events according to the chosen trigger logic and create and send the data packets with the right format to the acquisition PC.

The system is based on the μ-TCA standard; originally conceived as an adaptation of the Advanced Telecommunications Computing Architecture (ATCA) systems used in the telecommunication field for high-flux data transfers, it is employed for relatively simpler tasks and adopted in the particle physics domain since less than ten years (Abellan et al. 2013; Cachemiche et al. 2012). A standard μ-TCA crate equipped with a μ-TCA Carrier HUB (MCH) (shown in Figure 3.13a) is used as general purpose support for the Advanced Mezzanine Card (AMC), which is the section adapted for each specific application. An AMC40 has been developed for high energy physics applications, in particular for the Large Hadron Collider beauty (LHCb) experiment at *Conseil Européen pour la Recherche Nucléaire*, Geneva, Switzerland (CERN), and has been adapted for the gamma camera acquisition system by the CPPM research group (see Figure 3.13b). This card includes a FPGA Altera Stratix V (Altera 2016), 24 optical inputs at 4.8 Gbit/s and 12 at 9.6 Gbit/s, a 1 Gbit/s Ethernet output for the connection to the acquisition PC. In addition to the μ-TCA based components, two intermediate cards in VME format complete the acquisition system. The so-called THOR cards (see Figure 3.13c), developed in VME format at LPC in parallel to the ASM card, are used to generate and share the clock signal (40 MHz) common to the whole electronics cards for synchronization purpose (first card) and to govern the pre-trigger and trigger signals (second card) as explained in the following.

For both cameras, the acquisition starts in case the absorber section detects an interaction: the ASM involved card deals with the creation of a pre-trigger signal, which corresponds to the digital output signal and contains a time stamp (see the ASM card description in section 3.1.3.1). The pre-trigger is sent to the THOR card that governs its sending to the AMC40 card. To be noticed that the ASM card should in principle be able to handle both pre-trigger and data packets, but for this first prototype, the THOR card enables one to avoid conflicts in the ASM card signal handling. The acquisition process is easier and safer with the THOR card interaction.

In the multi-slit collimated camera, the pre-trigger signal directly operates as a trigger validating the data collection from absorber and hodoscope. In the Compton camera, the AMC40 receives the pre-trigger from the THOR card and sends it to the scatterer FE cards, which explore their buffer looking for events in the coincidence time window; if a coincidence is found, a trigger signal is generated by the scatterer FE card and sent to the acquisition system, which then starts the data read-out from all the detectors. A simplified graphical overview of the complete acquisition system and logic is given in Figure 3.14.

The AMC40 card makes use of a buffer for each FE card of the three detector sections, where the collected data are stored until the creation of packets of the selected size to be sent to the acquisition PC. The data transfer is achieved via a 1 Gbit/s Ethernet link, and the chosen standard is the User Datagram Protocol (UDP). The data format has been frozen at the camera conception stage and slightly modified following the electronics developments; it is deeply described in the appendix A, which also reports the expected data flow obtained in previous simulation studies.

In addition to the already explained functions, the μ-TCA is also in charge of handling the slow control signals for the configuration of the detector FE cards. The chosen format is in this case the Transmission Control Protocol (TCP), which is more reliable and ensures a feedback in case of communication failure. The possible slow control signals are detailed in appendix A.

(a) µ-TCA crate with the AMC40 board.

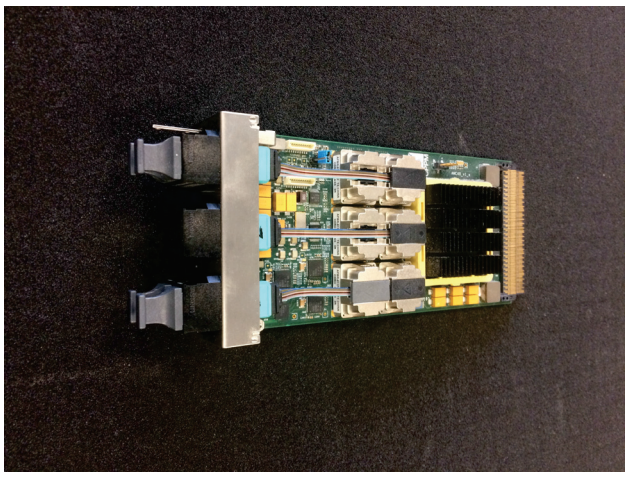

(b) AMC40 board.

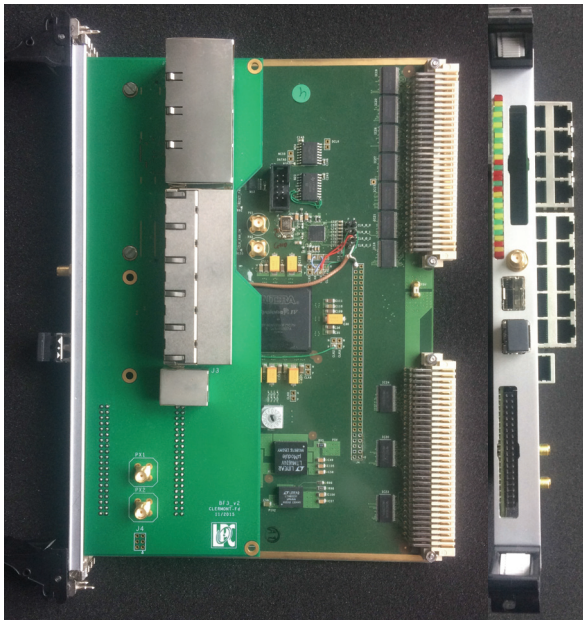

(c) THOR card.

Figure 3.13: Acquisition system components: µ-TCA crate (a), AMC40 board (b) and THOR card (c).

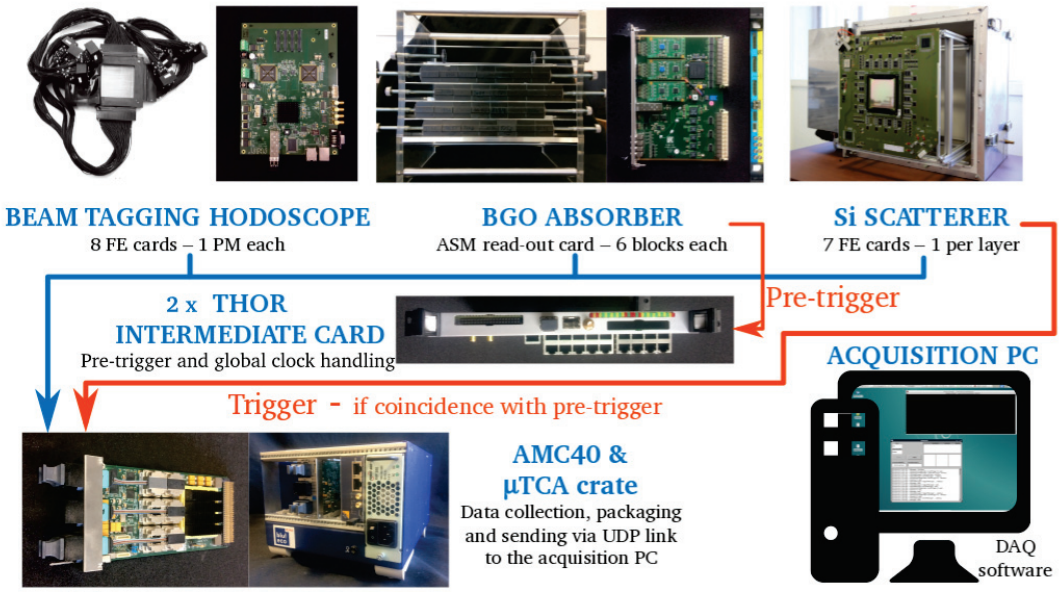

Figure 3.14: Schematic view of the Compton camera acquisition system. For the multi-collimated camera, the trigger and pre-trigger signals are the same.

3.1.6 Camera acquisition, monitoring and slow control software

The UDP data packets sent by the µ-TCA acquisition system via Ethernet link are received by the acquisition PC thanks to a C++ based acquisition software, developed at the IPNL. The software decodes the data packets and builds the events by grouping the data from the two (for the multi-slit collimated camera) or three (for the Compton camera) detection sections according to the time stamp. During the decoding process, the software also verifies the received data format and can highlight problems in the data encoding by the µ-TCA; this feature is used during the test phase to check the functionality of the AMC40 firmware. The reconstructed events are then stored in binary files with the structure presented in appendix A. The data file size can be selected by fixing the number of events stored per run in the acquisition run, knowing that each event can be composed by a slightly variable number of bits, according to the amount of detector modules involved. The file collection corresponding to the same run will be then grouped at the analysis stage. The number of events per file must be tuned taking care of the available Random Access Memory (RAM) (32 Gb), where the data are temporarily stored before the writing process on the hard-disk. In Figure 3.15a the minimal graphical interface developed for the acquisition software is shown.

A monitoring software has been developed in order to have a direct real-time feedback on the camera data acquisition. The software can show some information about the ongoing data collection, and it is at present designed to work on a single detector section (hodoscope, scatterer or absorber) or for the coupled acquisition of absorber and hodoscope (collimated camera). It is based on ROOT (Brun et al. 1997) with the following working logic: during the acquisition, it continuously searches for new data files in the storage folder, and analyses in the desired way a selected number of events per file, directly from the binary format. An example of the visualized output for an hodoscope monitoring is shown in Figure 3.15b. This picture corresponds to an acquisition performed during a beam test at the *Centre Antoine*

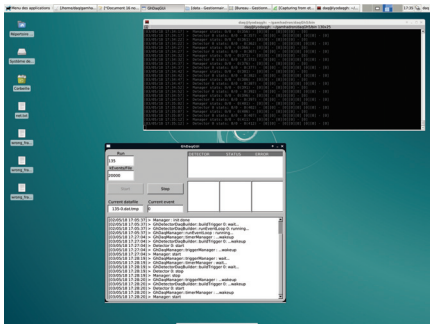

(a) Acquisition software user interface.

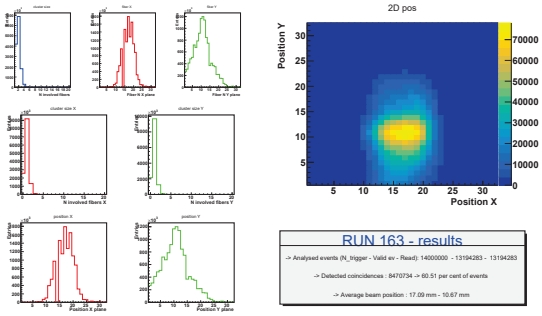

(b) Example of monitoring software visualization for the beam tagging hodoscope (applied to the 32+32 fiber prototype).

Figure 3.15: Software tools: user interface of the acquisition C++ software (a) and example of the ROOT (Brun et al. 1997) monitoring software visualization for the beam tagging hodoscope 32+32 fiber prototype.

Lacassagne, Nice, France (CAL), where the 32+32-fiber hodoscope has been tested, together with the monitoring software. More details about the beam tests are given in chapter 6.

As mentioned, the present version of the software is not yet adapted to the monitoring of the whole Compton camera, even if it can handle the three detector components with minor modifications. In addition to this, it is not automatically synchronized with the acquisition software, and not optimized in terms of needed calculation time. In the next future the planned upgrade will slightly modify the working logic by directly connecting the monitoring to the acquisition: the acquisition software will automatically send a selected fraction of events to the monitoring output during the acquisition, so that the search for data files would not be anymore necessary. This will drastically reduce the monitoring dead time and calculation time, achieving an actual online control.

Acquisition and monitoring software has been tested thanks to a data simulator developed in C++, which is able to create data UDP packets with the correct format and send them on the same Ethernet port used for the data collection, simulating a server-client communication.

As mentioned in section 3.1.5, the µ-TCA handles both the data collection and transfer and the slow-control of the whole system, including the configuration of all the electronics cards (discriminator thresholds, channel gains, ASIC reset signals, working mode, etc.) and the readout of the feedback signals. The development of the slow-control software is ongoing at the IPNL: it is designed in LabVIEW and includes all the needed controls in a single user interface. A dedicated PC is foreseen for this task, connected to the µ-TCA via TCP protocol. The slow-control software will also govern the high and low voltage suppliers for the detectors and acquisition electronics boards, the scatterer thermal box temperature setup and control, the steering of the 2D positioning table dedicated to the hodoscope, and the steering of the camera moving table, described in the next section. All the listed instruments will be connected to a patch panel, and a local network will be created for the camera equipment.

3.1.7 Camera integration and mechanical support

In order to setup the two camera configurations (multi-slit and Compton), the described components, together with the related mechanical supports, must be assembled in an integrated system, with the exception of the beam tagging hodoscope which has its own dedicated mechanical support, being placed between the beam nozzle and the target. A general mechanical structure is then needed to support the camera; it is required to be movable, as compact as possible but at the same time robust and large enough to support absorber and scatterer (or collimator), for a total maximum weight of about 100 kg. In addition to this, it should be possible to remotely control the position of the various camera components in order to adapt their position in 3D with respect to the beam line and to the target. The present system is not dedicated to clinical operation. However, it should cope with a versatile use with horizontal beams, including the use with anthropomorphic phantoms at clinical accelerators.

The realized solution is shown in Figure 3.16b. It is composed of two sections: a positioning table on wheels, designed and provided by Rose & Krieger, equipped with 4 telescopic feet, and a 4-axis moving table installed on it, developed by Kinetic System. The wheels allow to first position the camera, and the 4 telescopic feet are used to regulate with 1 mm precision the whole system height, in the range 630 – 1280 mm from the ground, to be adapted to the specific beam line. The feet are expected to be able to support a maximum weight of 150 kg. The telescopic feet are not connected to the slow-control but are controlled by a remote controller on the table itself. On the top surface of the table, 1200×750 mm^2, the 4-axis moving table is fixed and allows to adapt the camera position in 3D (distance camera-target, height, direction parallel to the beam line) with a 100 μm resolution and a range of 40 cm. In addition to this, a fourth axis allows to adjust the distance between the two detector components in the direction perpendicular to the beam line, in a range of 30 cm (to be noticed that this range is reduced by the size of the scatterer thermal box). The four axes are connected to the positioning table patch panel, which is directly controlled by the slow-control program in LabVIEW. Finally, a further manual control allows to rotate the whole system with respect to the table axis, in a range of $\pm$ 10 degrees.

In Figure 3.16a we present the mechanical scheme of the complete positioning table, with the Compton camera installed on it.

In Figure 3.17 we show a view of the three detectors composing the Compton camera, with one scatterer layer installed in the thermal box and the absorber mounted on the positioning table, and the beam tagging hodoscope on the right side on its dedicated mechanical support.

3.1.8 Data analysis and image reconstruction

All the data collected at the detector characterization stage (in standalone working mode) are analyzed via ROOT (Brun et al. 1997) and Python custom developed codes. Further details are given in section 3.2, where the performed characterization measurement on the three detector section are described. Concerning the data analysis for the complete systems (multi-collimated and Compton camera), automatic ROOT-C++ based programs will be developed in order to achieve an online data treatment for both tests and clinical application purposes.

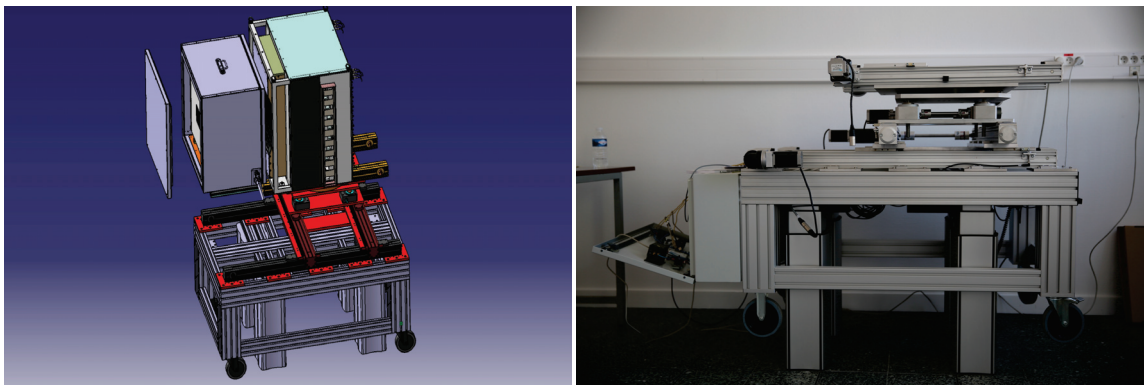

(a) Schematic view of the Compton camera integration on the positioning table.

(b) Gamma camera position table.

Figure 3.16: Details of the gamma camera integration and mechanical support.

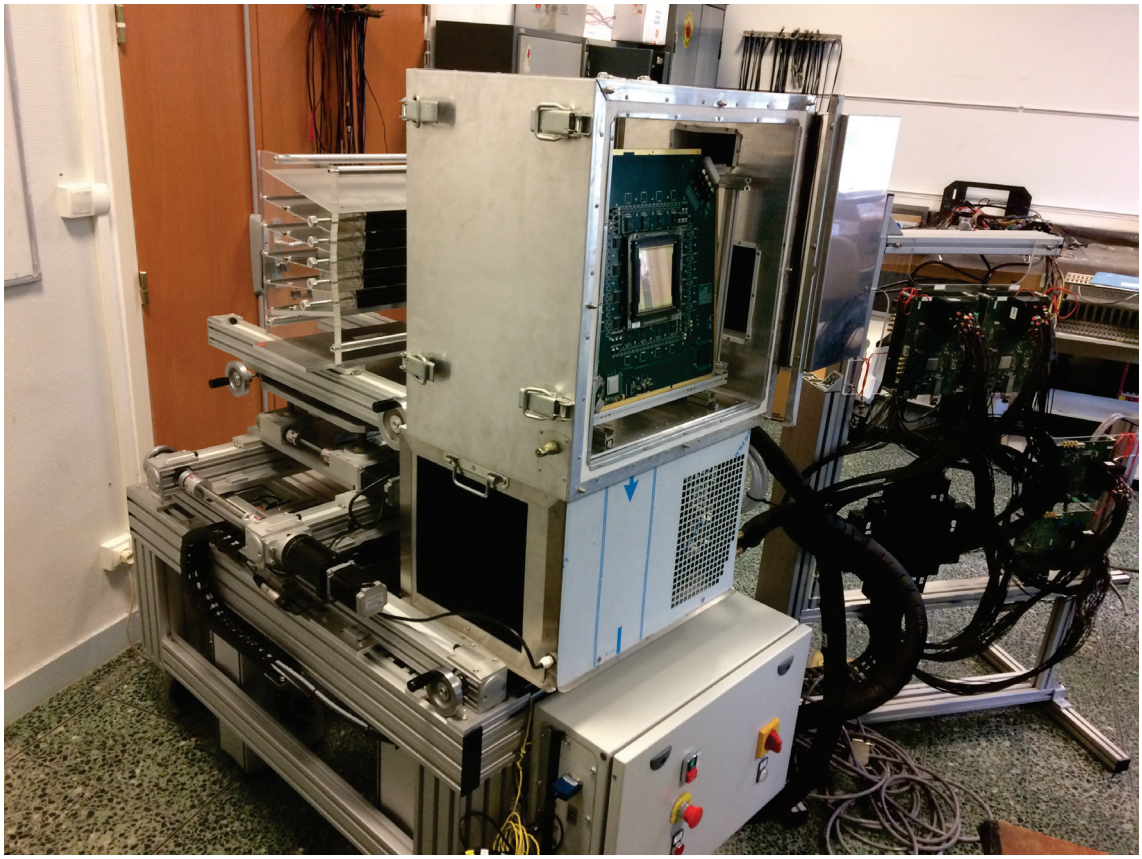

Figure 3.17: View of the Compton camera assembly with the beam tagging hodoscope on the developed mechanical supports.

The raw collected data samples must be adapted to the image reconstruction codes, needed to retrieve the final image for both camera configurations.

The multi-collimated camera is designed to provide 1-D information about the prompt-gamma emission distribution along the beam direction: the required data treatment is then relatively simple, and based on the chosen geometrical configuration of collimator and absorber. The detected events are spatially assigned to the BGO block pseudo-pixel where the gamma interaction took place, by means of center of gravity calculation with the four signals provided by the involved block and then with an automatic algorithm developed for test purposes and detailed in section 3.2.2.3. Knowing the block position within the whole absorber setup, the prompt-gamma emission profile can be reconstructed assuming a photon path perpendicular to the absorber entrance face. This simple approach can be refined thanks to the spatial information given by the beam tagging hodoscope. The detected beam position can constrain the reconstructed emission position to a point, so that a 3-D emission profile can be obtained. This solution is being explored to improve the reconstruction performance of the algorithm presently available for the camera.

Concerning the Compton camera, the image reconstruction requires the detection of coincidences in the scatterer and absorber sections: position and deposited energy information in the two detectors allow for the reconstruction of the emission cone via Compton kinematics, as explained in details in chapter 2. The photon emission profile (prompt-gamma for the ion beam therapy application, gamma emitted by the radio-tracer for the nuclear medicine approach) is then obtained via the overlap of several reconstructed cones. As described in chapter 2, analytic and iterative algorithms have been proposed and developed to reconstruct the final image given by a Compton camera, which intrinsically transport a 3-D information. In particular, the image reconstruction of the CLaRyS Compton camera relies on a line-cone analytic algorithm based on back-projection and on the code developed by the CREATIS group for the iterative method (Hilaire et al. 2014; Lojacono et al. 2013; Maxim 2014).

The analytic line-cone reconstruction is only applicable in ion beam therapy monitoring and is based on the intersection of each reconstructed emission cone with the beam direction information given by the beam tagging hodoscope. This method assumes that the prompt-gammas are generated along the beam path, considered as a straight line, and limits to two points the possible emission position for each detected event. The overlap of several events will then allow for the emission distribution definition in 3-D. The Compton camera performance has been tested for the application in ion beam therapy monitoring, and this reconstruction code has been employed to treat the simulated data: the results are given in chapter 4, where we usually refer to this reconstruction method as “line-cone”.

The iterative algorithm is called List Mode-Maximum Likelihood Expectation Maximization (LM-MLEM) and is able to include in the calculations the space and energy resolution of the involved detectors, leading to the reconstruction of a 3-D image. It requires the definition of a reconstruction volume, which is divided in a given number of voxels, and the list of coincidence events. Starting from the simple event back-projection, it defines the probability that a given photon detected in the Compton camera has been emitted from the voxels in the defined volume. For every iteration, this probability is re-computed taking into account the results of the previous iteration, converging to the most likely emission distribution. The number of iterations is fixed by the user and must be a trade-off between reconstruction accuracy and calculation time. This method has been used with ion beam therapy monitoring simulated

data (see chapter 4), as well as for the reconstruction of point-like sources simulated for the application of the camera in nuclear medicine, presented in chapter 5. To be noticed that, concerning the reconstruction of prompt-gamma emission distribution in ion beam therapy application, the spatial information about the beam given by the beam tagging hodoscope is still not included in the employed version of the code. An upgrade is under study and is at present at the preliminary test stage.

3.2 Camera component characterization and development status

As detailed in the previous sections, the CLaRyS TOF gamma cameras are equipped with various detector components with very different features. Each part must be separately studied in order to characterize its behavior and allow the final camera integration and operation.

I mostly worked on the beam tagging hodoscope and on the BGO absorber, and in the next paragraphs the performed measurements are described in details. Concerning the scatterer stack, the results achieved before the beginning of my PhD thesis are briefly described for the sake of completeness.

The results presented in this section also introduce the following one (3.3), where all the development steps still needed for a clinical implementation of the cameras are explained.

3.2.1 Scatterer silicon layer characterization

The 7 DSSDs selected for the application in the Compton camera system among the 10 provided by the producer have been characterized in terms of leakage current. The measurements have been performed by colleagues before the beginning of my PhD thesis. The extended description of the employed test-bench, the performed tests and the results are presented in Ley 2015.

The leakage current is an evaluation of the systematic uncertainty expected on each read-out channel, corresponding to a background current detected without an energy deposit in the depletion region. The 7 layers have been tested at the complete depletion voltage of –750 V with a test-bench developed at the IPNL specifically for these measurements. It is composed of a custom electronics card which is used to supply the detector with the depletion voltage and to the current read-out via the connection to a nano-ammeter (Nuclear Instrumentation Module (NIM) module with 0.1 nA resolution). Moreover, temperature variations in the range –40 – +40 °C have been applied with an automatic system, with the detectors and read-out card placed in a temperature programmable chamber Weiss WTL 64 (WeissTechnik 2017). The temperature variations, the channel selection and the data acquisition are handled by a Raspberry Pi. The temperature step has been fixed to 5 °C. Finally, temperature cycles have been carried out in order to study the detector response to rapid temperature variations and the time required to stabilize the leakage current at the working temperature, with temperature steps between –20 °C (working temperature) and +25 °C (room temperature).

The leakage currents measured at room temperature (+25 °C) are homogeneous on all the

strips, with some local exceptions. The average detected value is about 20 nA. Concerning the measurements at –40 °C, the average value for the n strips is close to 0 nA, while a current of 3 – 4 nA is still detected on the p strips. On each layer, a maximum of 3 strips show higher leakage current values; this is acceptable for the final application in the Compton camera. Moving from –40 °C to +40 °C, the leakage currents respect, on average, the expected trend defined by equation 3.1 (Spieler 1998).

$$I_p(T) \propto T^2 \times e^{-\frac{E}{2k_B T}} \tag{3.1}$$

where $I_p(T)$ is the leakage current as a function of the temperature, T is the temperature in Kelvin, E the silicon energy gap energy in eV, k_B the Boltzmann constant (8.617×10^5 eV K^{-1}).

The leakage current is generally stable or is slightly increasing for temperatures below 0 °C, with values always below 10 nA. Beyond 0 °C, it rapidly increases reaching some tens of nA at 40 °C, depending on the specific strip. This observation justifies the need of the described thermal regulated box, which is able to maintain a constant temperature of –20 °C during the detector operation, placing them in a minimum and stable leakage current regime.

The application of quick temperature variation steps between –20°C and +25°C allowed to estimate the time required by the detector to re-establish the working regime with minimal leakage current. When moving from –20 °C to +25 °C, the leakage current increases rapidly up to the values already detected during the slow temperature variations, with a transition time of the order of less than ten minutes. Approximately the same time is required to stabilize the leakage current after the cooling down to –20 °C.

In addition to the described leakage current measurements carried out with the 7 10×10 cm^2 DSSDs, a small silicon layer prototype (8+8 strips) has been tested with the first version of the FE card ASIC. The first version of the card allowed for the read-out of 8 channels, so that the 8 p strips have been characterized with this read-out system, while the n strip data have been collected with NIM modules. The data treatment has been performed thanks to VME modules.

The detector has been exposed to Sodium-22 (^{22}Na) and Cobalt-57 (^{57}Co) radioactive sources: the ^{22}Na source, producing two back-to-back 511 keV gammas as a result of the β^+ annihilation, has been used for timing measurements in coincidence with a Lanthanum Bromide ($LaBr_3$) crystal, while the 122 keV photons of the ^{57}Co source are used to characterize the energy response by photoelectric absorption.

The detected time resolution has been estimated to be in the range 13 – 23 ns FWHM for the p strips, and between 30 and 80 ns FWHM for the n strips (knowing that the “hole” drift time is about 3-4 times more than the electron one). The energy resolution is between 10 and 20 % FWHM for the tested strips. This test also allowed to verify the first version of the card and move forward with the development of the second and third version at present available for the final detector.

Thanks to the summarized measurements, a calibration database is available for the 7 silicon layers, which showed overall stable and acceptable performance. The final version of the card must be tested in order to check these results, validate the board behavior and move to the first

detector tests on beam. All the details concerning the next development steps are presented in section 3.3.1.

3.2.2 Absorber BGO blocks characterization

The BGO modules composing the Compton and multi-collimated camera absorber have been recovered from a SIEMENS PET system: they have been originally optimized for the detection of 511 keV photons from positron annihilation, and they have to be tested for the new gamma detection system, which must be able to deal with photons in the prompt-gamma energy range, i.e. from about 100 keV to approximately 10 MeV.

Each block must be characterized in terms of spatial and energy response, and the read-out PMs have to be calibrated to obtain a uniform response on the whole block surface (see section 3.1.3 for the detector description). The employed method relies on the work presented in J. G. Rogers et al. 1994 and Tornai et al. 1994 and on the calibration process described in Golnik 2015 and Hueso-González et al. 2015a, and has been extended with more refined features.

The measurements are performed with the irradiation by gamma sources, emitting photons at defined energies: in particular, we used 511 keV and 1275 keV photons from a ^{22}Na source, and the two photons emitted by a Cobalt-60 (^{60}Co) source, at energies of 1173 keV and 1332 keV.

The employed ^{22}Na source is a cylindrical source with an active diameter of 4 mm, and an activity of about 400 kBq: it has been placed at a distance of about 5 cm from the block entrance surface, with the center of the source facing the center of the block transverse surface. The ^{60}Co source has been installed in a lead cylindrical container (12 cm radius and 35 cm height), equipped with three different apertures: point-like (2×2 mm^2), linear (2×50 mm^2) and square (50×50 mm^2). The design of the lead container has been studied in simulation to ensure the proper radiation protection, and produced according to the specifications defined by the IPNL mechanics group. The activity of the ^{60}Co source is about 1.7 MBq, and the square shape has been used to obtain an homogeneous irradiation of the BGO block, with the block set with the center of the entrance surface corresponding to the source position, at a distance of 12 cm.

The signals produced by the four PMs of each block are collected via four analog outputs on the FE card (see Figure 3.6a). The four retrieved signals per event are treated via standard NIM modules in order to be adapted to the acquisition systems and measurement purposes.

Two different acquisition systems have been used for this characterization work. First, the PXIe described in section 3.2.3 with its two flash ADC read-out modules, 8 channels each, is used for the spatial and energy characterization and calibration of the tested blocks. A scheme of the acquisition setup for this part of the calibration is given in Figure 3.18. The raw signals coming from the four PMs are amplified and shaped via NIM modules (quad shaping bipolar amplifiers), which were fine-tuned via a pulse generator in order to adapt the amplification factor of each channel (an amplification factor of about 50 has been applied to the raw signals). The amplified signals are then split in order to be treated for trigger purpose. The trigger for the acquisition is based on the sum of the four signals, and a fixed threshold

is applied for background rejection. The employed discriminator provides the logical trigger signal, which is sent to the trigger input of the ADC modules on the PXI. The four amplified signals, conveniently delayed, are sent as inputs to the ADC modules on the PXI, together with the sum signal which is used for experimental verification of the acquisition setup. A LabVIEW-based acquisition software, developed for this particular application at the IPNL, provides real time event visualization together with a partial, on-line spatial reconstruction of the events, and stores them in text files for further analysis. A second threshold can be set at the software level in case particular selections are needed during the acquisition, otherwise the event selection is performed at the analysis stage.

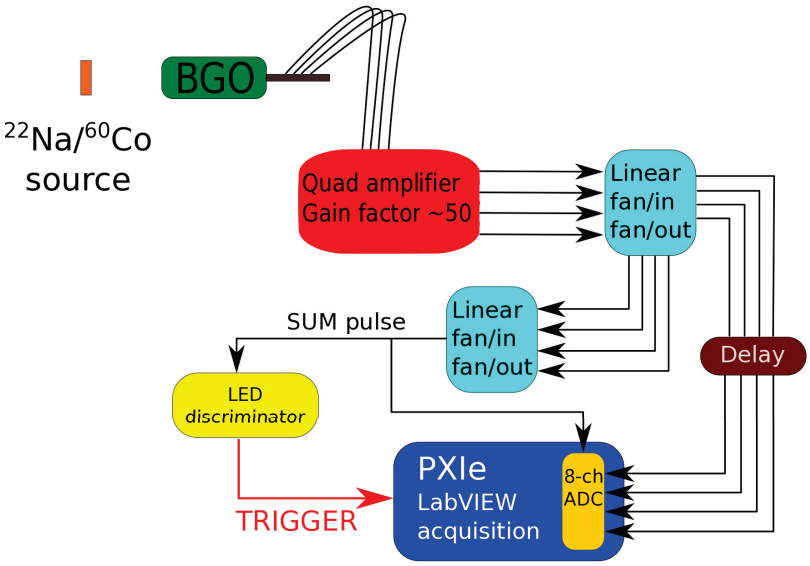

Figure 3.18: Scheme of the spatial and energy characterization test-bench.

Concerning the timing characterization measurements, an eight-channel signal digitizer at 3.2 GS/s has been employed for high time resolution acquisitions. The so-called WaveCatcher, shown in Figure 3.19a, has been developed by the *Laboratoire de l'Accélérateur Linéaire*, Paris, France (LAL) in Orsay and the *Institut de Recherche sur les lois Fondamentales de l'Univers*, Paris, France (IRFU) in CEA-Saclay, and its features are detailed in Breton et al. 2014. The digitizer is connected to the acquisition PC via Universal Serial Bus (USB) port, and the data read-out and storage are performed thanks to a custom acquisition software. The measurements are based on the coincidence detection of back-to-back 511 keV photons emitted by a ^{22}Na radioactive source, in order to be able to compare the time response of the tested BGO block to a reference fast timing scintillator. An external trigger is then provided to the WaveCatcher by treating the BGO block and reference scintillator signals with logic coincidence NIM modules, after proper discrimination. Further details are given in section 3.2.2.4, while a scheme of the acquisition setup is given in Figure 3.19b.

3.2.2.1 Space and energy calibration and characterization

The space and energy calibration process is mainly divided into three stages:

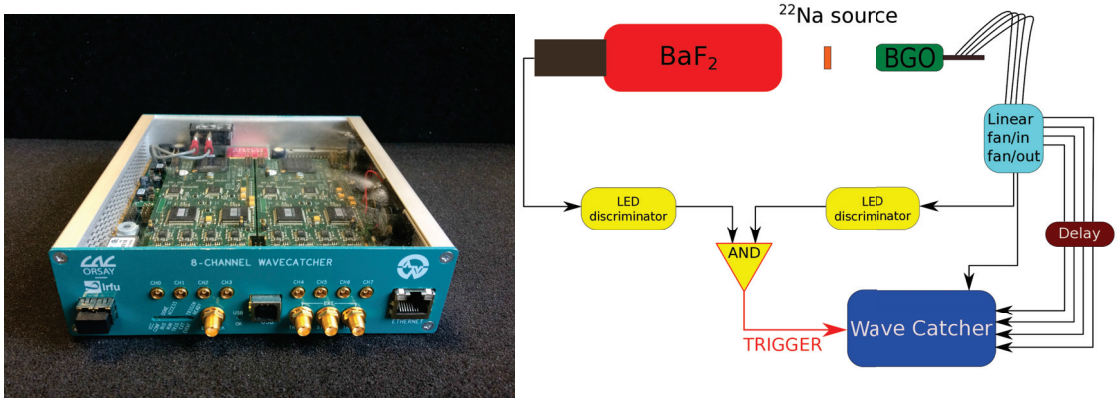

(a) Wave Catcher: 8-channel 3.2 GS/s signal digitizer.

(b) Scheme of the time response characterization test-bench.

Figure 3.19: Details about the BGO block time response characterization.

- PM gain equalization (^{22}Na): the block is irradiated with the ^{22}Na source and the raw ADC distributions for the four PMs are retrieved. The upper-energy falloff in the raw ADC spectra are taken as reference to equalize the distributions. Four energy calibration factors are extracted and used to the data correction; this correction corresponds to the PM gain equalization.

- Pixel identification (^{60}Co): once the calibration factors are extracted thanks to the ^{22}Na irradiation data, the block is exposed to the ^{60}Co source. The collected data are analyzed as in the previous step and calibrated according to the already calculated correction factors. The energy spectrum, the mono-dimensional spatial projections and the flood map are produced. The custom algorithm briefly described in the following section 3.2.2.3 has been developed to identify the pseudo-pixel positions on the flood map. It is applied to the ^{60}Co irradiation data and the pseudo-pixel position map is stored.

- Pixel energy calibration: the ^{22}Na irradiation data are re-analyzed in this last calibration step in order to assign each interaction to a single pseudo-pixel according to the pixel position map obtained with the ^{60}Co data. Then, the energy spectrum of each pixel can be produced and the two identified peaks (corresponding to the two photon energies emitted by the ^{22}Na source - 511 keV and 1275 keV) can be used to equalize the pseudo-pixel response. The sum of all the pixels spectra produces the block energy spectrum. At this stage, the ADC channel values are calibrated to obtain the absorbed energy values in keV.

It is worth noticing that the ^{60}Co irradiation is useful for the pixel identification given the high energy and narrow energy range of the emitted photons. The equalization factors obtained with the ^{22}Na source irradiation have been verified to be consistent with the ^{60}Co irradiation data, as expected. The whole method results to be robust.

3.2.2.2 Qualitative test of spatial reconstruction accuracy

Specific acquisitions have been devoted to the test of the block spatial accuracy potential. The detector is expected to be able to locate the collected interaction on the pseudo-pixel grid, but the possible sub-pixel accuracy can be tested with a collimated source scan of the block surface. The ^{60}Co source has been employed for this purpose, with the linear and point-like aperture. The block has been placed on a moving table with no distance between its entrance surface and the collimator aperture. The whole surface has been irradiated with horizontal and vertical movements of 1 and 2 mm per step with the linear collimator aperture. Concerning the point-like aperture test, only part of the block surface has been irradiated for further verification of the spatial accuracy results, with horizontal 1 mm step movements of the table in 1 mm vertically separated lines. The collected data have been calibrated with the factors obtained with the homogeneous ^{22}Na irradiation, as explained in the previous section. We present and qualitatively discuss the results in section 3.2.2.6.

3.2.2.3 Pixel identification and energy calibration algorithm

Subsequent to that gain equalization process, an automatic iterative algorithm has been developed to identify the block pseudo-pixel positions. Integrated mono-dimensional spatial projections are computed along rows and columns of the calibrated flood map in order to derive the peak and valley positions in the distributions with the ROOT (Brun et al. 1997) methods included in the TSpectrum class and simple analytic calculations. With the resulting valley positions, a first rectangular grid of pseudo-pixels is initialized. The projection of each identified pseudo-pixel row (respectively column) is re-analyzed using the same integrated 1-D spatial projections along columns (respectively rows) looking for peaks and valleys as before. A refined grid is then produced, distorted from the initial rectangular one, and this process is iterated until a complete 8×8 pseudo-pixel grid is obtained.

Once the pseudo-pixels grid is fixed, the maximum of each pseudo-pixel region is automatically identified with a bin per bin scan in the defined area and its position defines the pseudo-pixel center relative position in the map.

The event data are then assigned to the pseudo-pixels with the application of the following process, illustrated in Figure 3.20. The dual pseudo-pixel grid is created rows- and columns-wise to get the mid points on the pseudo-pixel edges. The even data assignment is then done by calculating the minimal distance between a column and a row average point with respect to the reconstructed event and then calculating two outer products, between the vector connecting the reconstructed point and closest column (row) average point and the vector connecting this average point to the previous or next one on the same column (row). The sign of the products defines the column (row) where to assign the interaction. Knowing the relative position of the interaction point with respect to the two minimal distance points on row and column, the correct pseudo-pixel is identified. A more simple approach could have been used, using the search of the minimal distance between the reconstructed event position and the pseudo-pixels centers, but it proved to be more liable to some assignment discrepancies due to the grid distortions. These distortions are mainly caused by the detection principle that relies on the pseudo-pixel separation via reflecting material, and can be corrected in event post-treatment with the *a priori* geometrical knowledge of the block pseudo-pixel structure.

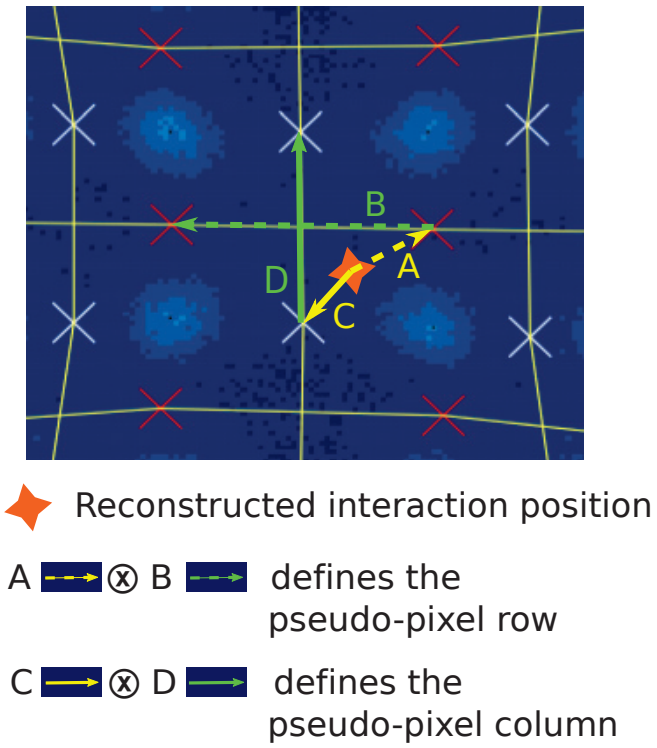

Figure 3.20: Logic for the event assignment to a single pixel. The dual pseudo-pixel grid is displayed: in white the mid points on the pseudo-pixel edges along rows (middle of lines in vertical direction), in red along columns (middle of lines in horizontal directions). The sign of the outer products detailed in the legend are used to define the column and row (so that the pseudo-pixel) where to assign the reconstructed event.

3.2.2.4 Time response characterization method

The test-bench for the time response characterization has been set as shown in Figure 3.19b. A Barium Fluoride (BaF_2) mono-block scintillator, read-out by a single photo-multiplier tube, has been used as reference detector. Its excellent time resolution makes it suitable for relative timing measurements in comparison to the BGO blocks. The reference scintillator and the BGO block under test have been set at arbitrary distances from the ^{22}Na source with the aim of detecting in coincidence the two 511 keV back-to-back photons resulting from the positron annihilation. The four raw signals coming out from the BGO block are summed with a NIM linear fan-in/fan-out module, and the resulting signal is sent to a leading edge discriminator and converted to a logic signal according to a fixed threshold. The single signal emerging from the reference detector passes through a selected threshold and is converted to logic signal. The two digital pulses, 100 ns width, are then sent to a coincidence module to create the trigger input for the WaveCatcher acquisition system described in section 3.2.2. The four BGO output raw signals, the reference scintillator raw output signal and the sum of the four raw BGO signals are sent to the WaveCatcher for digitization. An example of the collected raw signals from the studied BGO block is shown in Figure 3.21: the 4 output signals of each single PM are shown together with the resulting sum signal. The four signals exhibit a noisy feature that could be observed using the fast sampling acquisition, with a 80 – 100 MHz

oscillatory behavior. At the present stage we did not infer the sources of this noise, that would be canceled by appropriate lower frequency filtering.

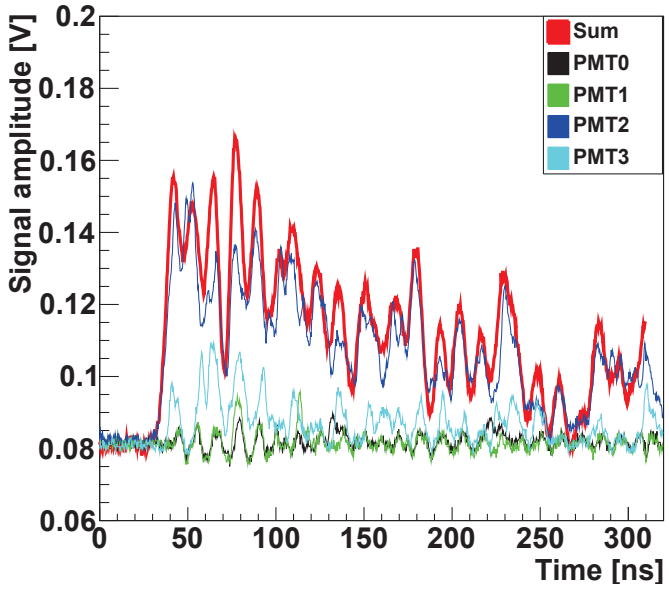

Figure 3.21: Reference BGO block raw signals collected with the Wave Catcher acquisition system. The four outputs of the single PMs are shown together with the sum signal.

For each coincidence event, the six collected signals are analyzed with focus on the signal rising edge. The time corresponding to the amplitude maximum and to 20, 30, 50 and 80 % of the maximum is retrieved for constant fraction discrimination tests. In addition to this, a fixed threshold is used for fixed value discrimination.

Different comparison methods have been tested in order to identify the more robust one for the definition of the time resolution of the blocks. The noisy structure of the single BGO raw signals (see Figure 3.21) leads to very variable results depending on the defined threshold, and the more stable results are given by the comparison of the sum of the four BGO signals and the reference scintillator with the arrival time identified by a fixed tuned threshold. With this method, the arrival time of each signal can be defined and the time difference distribution of the two signals can be produced.

The same analysis has been applied to a data set obtained with two identical BaF_2 detectors exposed to the ^{22}Na source in coincidence. This data set allowed for the definition of the reference scintillator time resolution.

The resulting BGO time resolution is defined as the FWHM of arrival time difference distribution between BGO block and reference scintillator, with the subtraction of the reference scintillator contribution via uncertainties composition calculation.

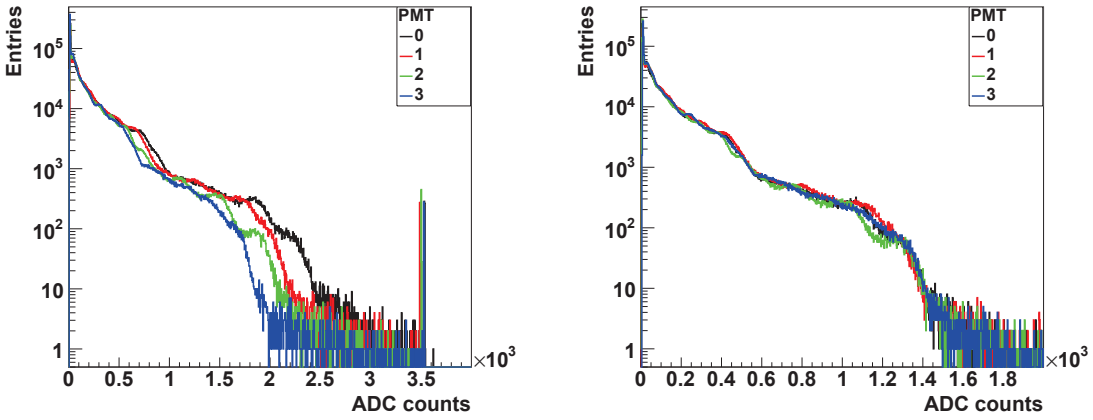

(a) Before gain equalization. **(b)** After gain equalization.

Figure 3.22: PM signal amplitude spectra before (a) and after (b) the PM gain equalization.

3.2.2.5 Results: PM gain equalization

Figures 3.22 and 3.23 show the effect of the PM gain equalization on the ADC count spectra and on the integrated mono-dimensional spatial distributions, while Figures 3.24 and 3.25 show the effect of the PM gain equalization on the block energy spectrum and two-dimensional spatial event distribution. All these results refer to the data collected with the reference BGO block irradiated with the ^{22}Na source.

In particular, Figures 3.22a and 3.22b show the raw and equalized ADC profiles of the four read-out photo-multipliers (the peaks above 3000 ADC counts in Figure 3.22a correspond to the saturation of the NIM linear fan-in/fan-out module used to handle the data read-out; these values are rejected during the equalization stage). Figures 3.23a and 3.23b show the projection on the two axes of the position of interaction reconstructed via Anger logic, before (left) and after (right) the PM gain equalization. Figures 3.24a and 3.24b show the ADC event spectrum, obtained by the sum of the ADC values of the four PMs, before (left) and after (right) the PM gain equalization. Figures 3.25a and 3.25b show the two dimensional event position map (this will be called “flood map” in the following) , before (left) and after (right) the PM gain equalization; the interaction position is reconstructed via Anger logic (see Figure 3.5d for details).

As shown by Figures 3.22 to 3.25, the PM gain equalization performed in this first calibration step is mandatory to optimize the spatial and energy response of the tested block. Figure 3.23b highlights the better definition of the pseudo-pixels ensured by the gain equalization: the peak-to-valley ratio is increased, in particular for the most external pixels. The spatial response improvement is also reflected in a better energy response (from about 46 % down to 35 % at 511 keV and from approximately 40 % down to 30 % at 1275 keV), as shown in Figure 3.24b, where the two energy peaks of the ^{22}Na source are narrower with respect to those obtained with the raw data. The obtained energy response is still not satisfactory, and the next steps of the calibration process are dedicated to its improvement. The flood map in Figure 3.25b shows how the gain equalization and the offset tuning allow to arrange the position map over the whole block surface; the borders are better defined and the pseudo-pixels on the block limits (especially on the corner) are better separated.

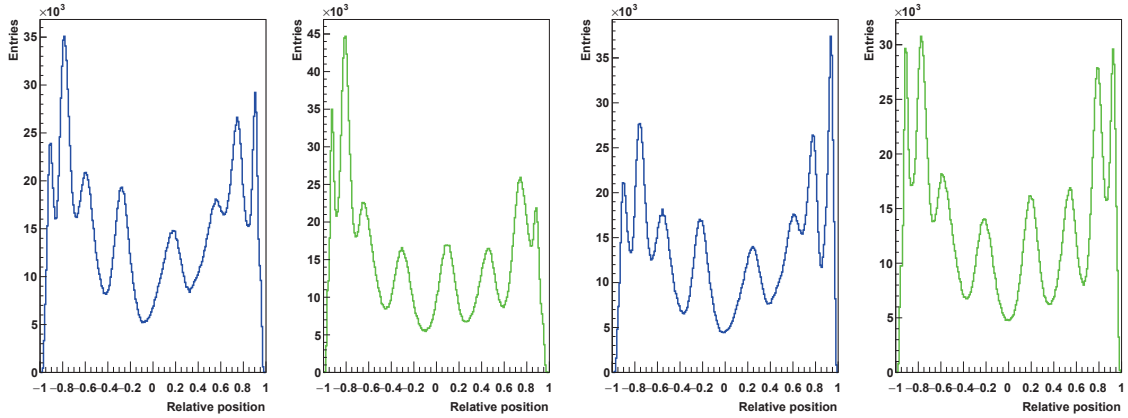

(a) Before gain equalization. **(b)** After gain equalization.

Figure 3.23: 1D integrated position distribution on the two transverse dimensions before (a) and after (b) the PM gain equalization. In the two sub-figures, left side for the horizontal dimension, right side for the vertical one.

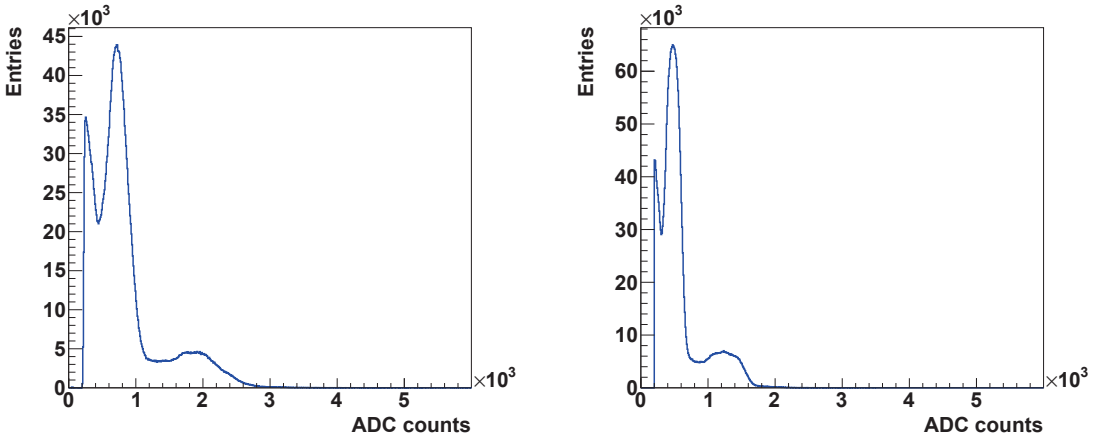

(a) Before gain equalization. **(b)** After gain equalization.

Figure 3.24: Block energy spectrum before (a) and after (b) the PM gain equalization.

3.2.2.6 Results: block spatial precision

Figure 3.26 shows four consecutive steps of the ^{60}Co source collimated irradiation, with a 2-mm step movement from left to right and the linear aperture (2×50 mm^2) set in vertical position. A qualitative analysis is enough to appreciate the block spatial precision limitation. The presented four points of the scan irradiated a total of three pseudo-pixel columns, moving from the left geometrical border of one column to the center of the next one. As shown by Figure 3.26b and 3.26d, as the collimator aperture position is in front of the center of a pixel column, the whole pseudo-pixel surface is reconstructed: no difference is observed with respect to the same column in Figure 3.25b, obtained with the homogeneous irradiation. In case the aperture faces the border between two pixel columns (Figure 3.26a and 3.26c), the events are shared between the two. This could show a possibility of sub-pixel resolution for integrated measurements, which is anyway not reproducible on a single event basis. The same behavior has been verified with a vertical scan (shown from Figure 3.27a to Figure 3.27d);

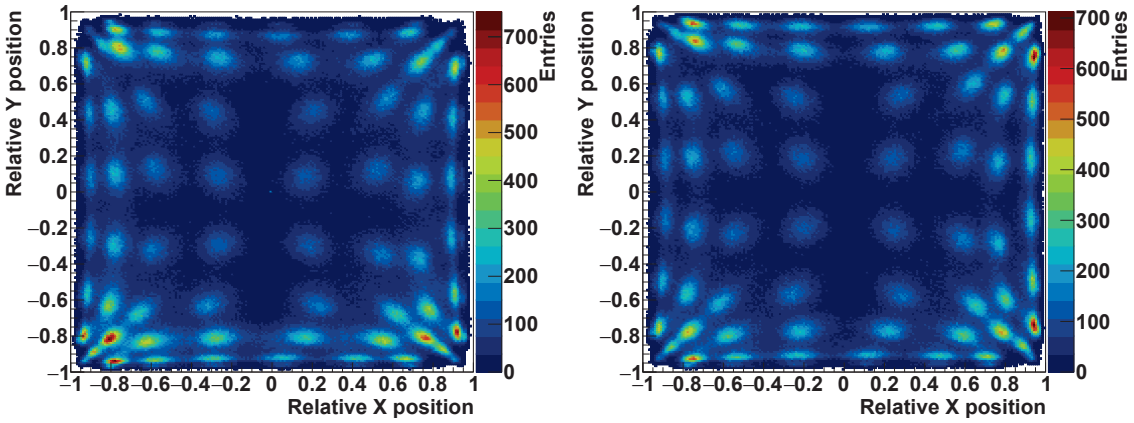

(a) Before gain equalization. **(b)** After gain equalization.

Figure 3.25: 2D reconstructed position map before (a) and after (b) the PM gain equalization.

the collimator and table configurations has been kept unchanged, while the block has been turned of 90 °. To be noticed that the slit position reported in the presented figures is the geometrical one, while the two-dimensional maps represent the response of the tested block: the spatial reconstruction distortions lead to the mismatch with respect to the real position, which will be corrected at the data treatment stage.

In order to further confirm these results and test the possibility of a sub-pixel resolution, a scan with reduced step size (1 mm) has been performed with the same collimator aperture, and no modifications are visually observed in the spatial distribution of events for the steps centered on the same pseudo-pixel column. As before, when the collimator aperture faces the limit between two pseudo-pixels columns, the events are equally distributed on the two. 9 measurement positions for this 1 mm scan are shown from Figure 3.28a to Figure 3.28i.

Figure 3.29 shows the superposition of the mono-dimensional position profiles integrated along the vertical axis for 5 positions of the 1-mm line-aperture scan: the differences between the distribution peaks related to neighboring positions of the aperture are of the order of 10 – 20 %, and demonstrate how a sub-pixel position accuracy is achievable for integrated measurements, even if it was not evident on the two-dimensional maps.

This result has been also tested with a point-like collimation scan of part of the studied block surface, with 1 mm step movements. The flood maps in Figure 3.30 show 6 reference points of the scan with the point-like aperture, during an horizontal movement from left to right of the table and the center of the aperture vertically centered on one pseudo-pixel line. The reported movement represents the transition from the center of a pseudo-pixel to the right limit of the next one. The aperture physical position is not highlighted on the maps in order to better show the event position distribution.

As for the linear aperture test, the mono-dimensional integrated distributions, reported in Figure 3.31, better show the differences between the various scanned point, approximately in the range 5 – 20 %. As before, these distributions verify how a millimeter accuracy is possible with the integrated analysis of sufficient event statistics.

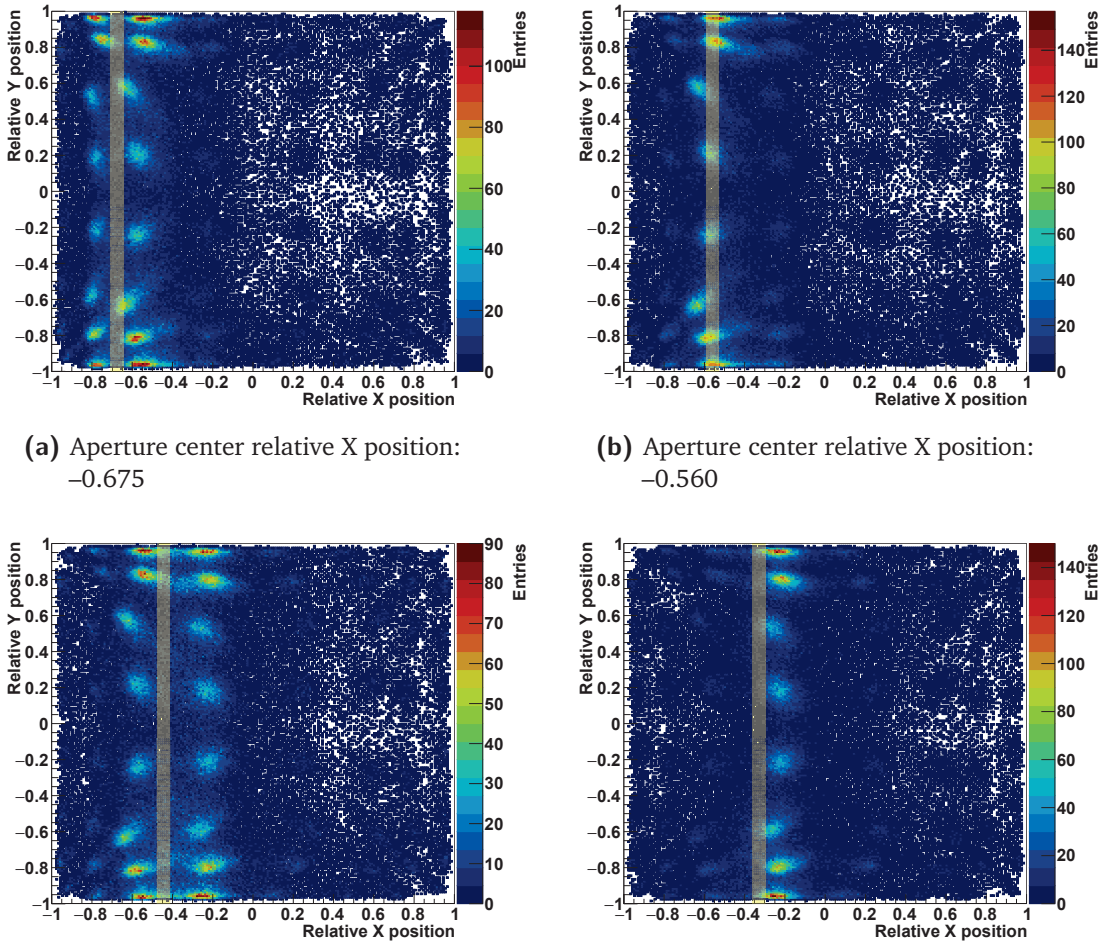

(a) Aperture center relative X position: –0.675

(b) Aperture center relative X position: –0.560

(c) Aperture center relative X position: –0.445

(d) Aperture center relative X position: –0.330

Figure 3.26: 2D reconstructed position maps during a 2-mm step scan performed with the ^{60}Co source with the line aperture from the left to the right size of the block surface. 4 reference measurements points, the position of the aperture is shown by the semi-transparent yellow band.

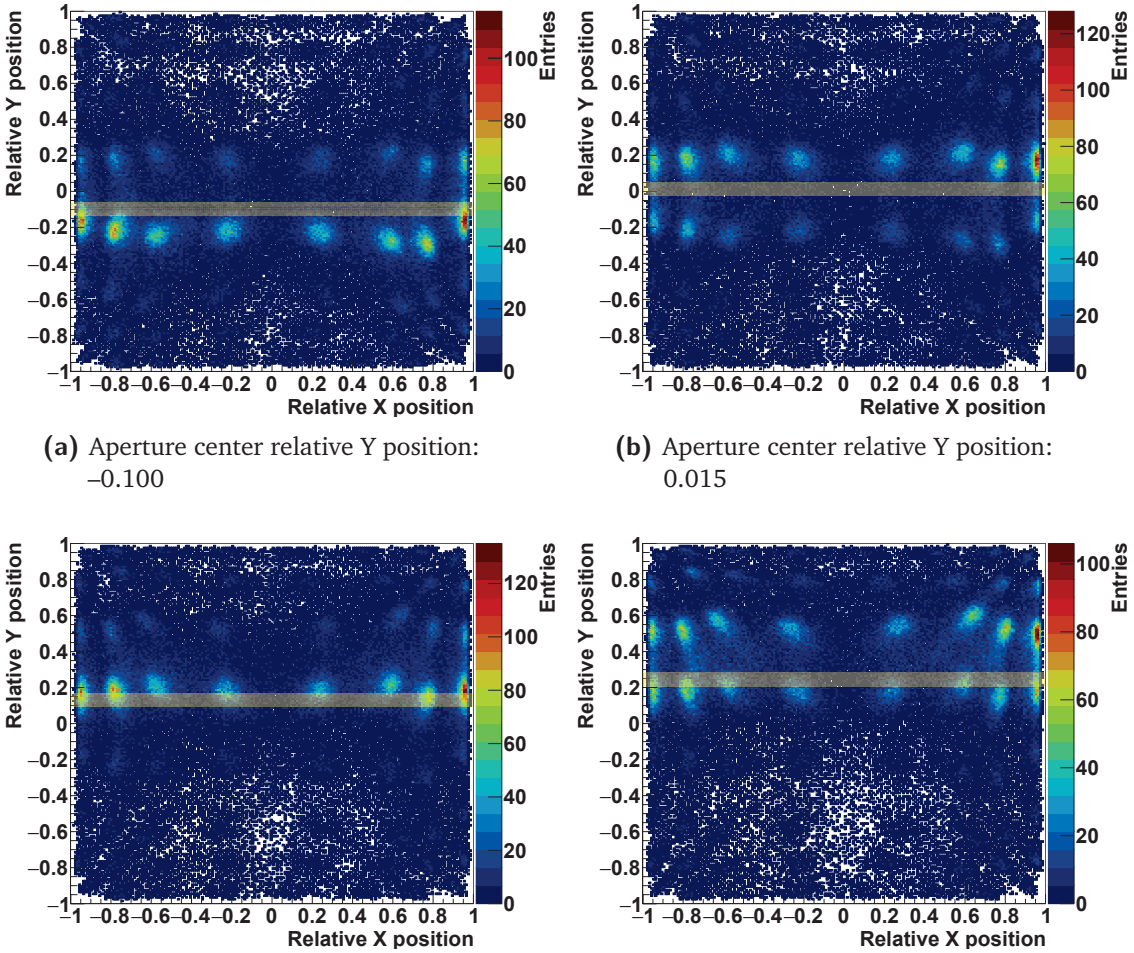

(a) Aperture center relative Y position: –0.100

(b) Aperture center relative Y position: 0.015

(c) Aperture center relative Y position: 0.130

(d) Aperture center relative Y position: 0.245

Figure 3.27: 2D reconstructed position maps during a 2-mm step scan performed with the ^{60}Co source with the line aperture from the bottom to the top side of the block surface. 4 reference measurements points, the position of the aperture is shown by the semi-transparent yellow band.

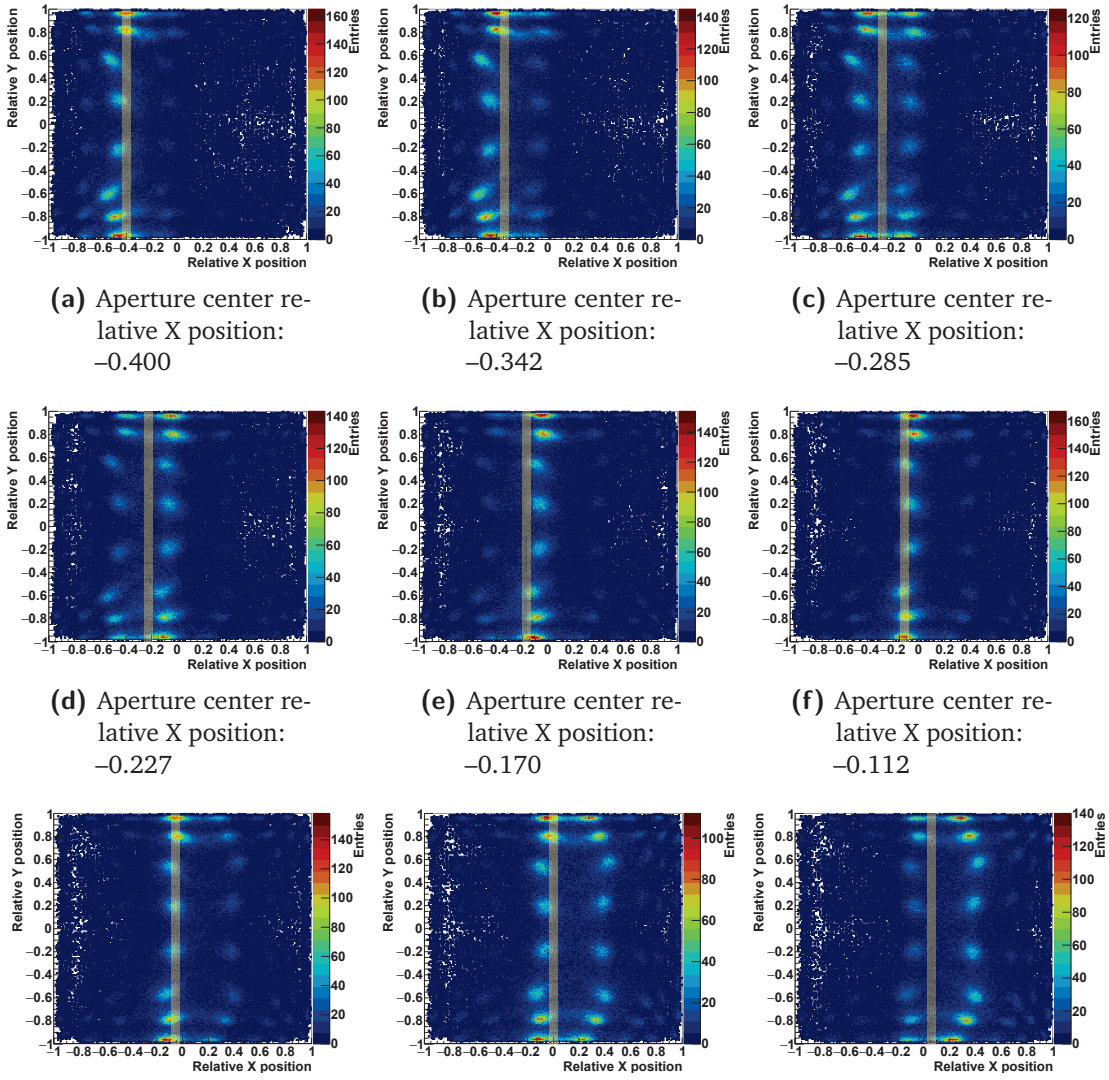

(a) Aperture center relative X position: –0.400

(b) Aperture center relative X position: –0.342

(c) Aperture center relative X position: –0.285

(d) Aperture center relative X position: –0.227

(e) Aperture center relative X position: –0.170

(f) Aperture center relative X position: –0.112

(g) Aperture center relative X position: –0.055

(h) Aperture center relative X position: 0.003

(i) Aperture center relative X position: 0.061

Figure 3.28: 2D reconstructed position maps during a 1-mm step scan performed with the ^{60}Co source with the line aperture. 9 reference measurements points, the position of the aperture is shown by the semi-transparent yellow band.

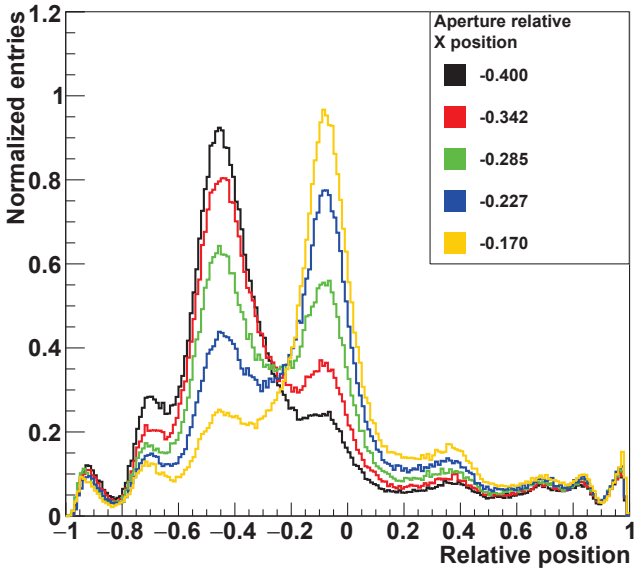

Figure 3.29: Superposition of the event reconstructed position profiles integrated along the vertical axis for 5 points of the 1-mm step scan performed with the ^{60}Co source with the line aperture. The 5 positions correspond to the two-dimensional maps in Figures 3.28a, 3.28b, 3.28c, 3.28d, and 3.28e.

In conclusion, all these sets of data verify that the spatial reconstruction accuracy of the employed blocks is limited by the pseudo-pixel size, and a sub-pixel resolution is not achievable on a single event basis. However, with integrated analysis a millimeter position accuracy can be obtained with both linear and point-like irradiation of the block.

3.2.2.7 Pixel identification

The results of the pixel identification algorithm described in section 3.2.2.3 are shown in Figure 3.32. Figure 3.32a shows the identified average values of the pseudo-pixels positions on the two transverse dimensions. As already detailed in the description section, starting from these average positions, the single pseudo-pixels positions in rows and columns are extracted and the “valleys” between neighboring pseudo-pixels are used to define the grid shown in Figure 3.32b together with the pseudo-pixel center position map.

3.2.2.8 Pixel energy calibration

Once the pseudo-pixel positions and the related grid are defined, each interaction can be assigned to a single pixel. The energy spectrum of each pixel is then separately studied in order to equalize the energy response on a pixel basis.

The assignation method described in section 3.2.2.3 makes use of the dual pseudo-pixel position map shown in Figure 3.33. The position assignment scheme to pseudo-pixels is shown in Figure 3.34: a color has been given to each reconstructed point according to the pseudo-pixel

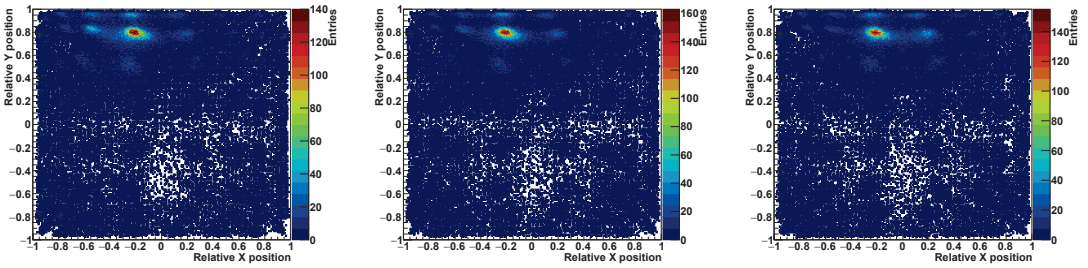

(a) Aperture center relative X position: –0.227

(b) Aperture center relative X position: –0.170

(c) Aperture center relative X position: –0.112

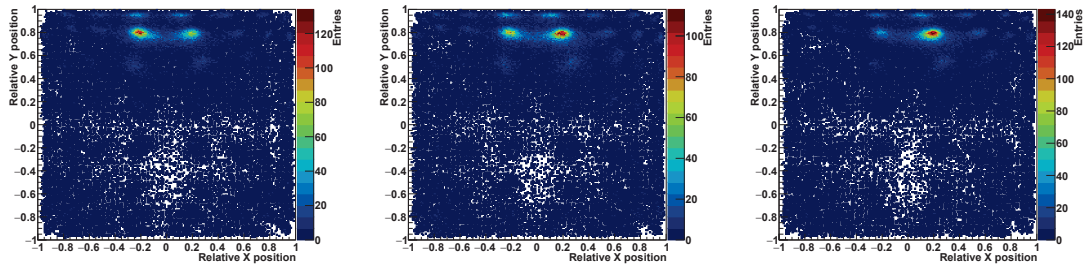

(d) Aperture center relative X position: –0.055

(e) Aperture center relative X position: 0.002

(f) Aperture center relative X position: 0.059

Figure 3.30: 2D reconstructed position maps during a 1-mm step scan performed with the ^{60}Co source with the point-like aperture. 6 reference measurements points, the relative X position of the aperture is reported in the caption of each figure. In the vertical dimension, the aperture is centered on the center of the pseudo-pixel line.

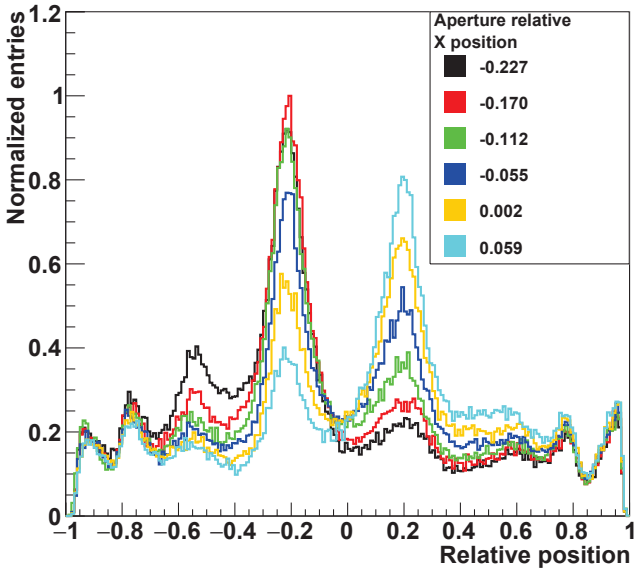

Figure 3.31: Superposition of the event reconstructed position profiles integrated along the vertical axis for 6 points of the 1-mm step scan performed with the ^{60}Co source with the point-like aperture. The 6 positions correspond to the two-dimensional maps in Figures 3.30a, 3.30b, 3.30c, 3.30d, 3.30e, and 3.30f.

region where it has been assigned by the described method. The method robustness is verified by the comparison of this map to the grid in Figure 3.32b and 3.33.

In Figure 3.35 the results of the pseudo-pixel energy calibration are shown. Figure 3.35a (left) shows the overlap of the energy spectra for 60 pseudo-pixels before the energy calibration and equalization. The 4 pseudo-pixels on the corners show a very different energy response and are not included in this picture. This is probably due to a non-complete light collection. The different response of each pixel to the two energy peaks is clearly visible. For each spectrum the low energy peak is assigned to 511 keV, and the high energy one to 1275 keV. In this way, the spectra are linearly calibrated and equalized, as shown in Figure 3.35a (right). For the 4 corner pseudo-pixels, the calibration is based only on the 1275 keV peak, while the 511 keV reference peak is substituted by the null ADC value.

Once the single pixel energy responses are equalized and calibrated, the whole block energy spectrum can be derived with the sum of all pixels. In Figure 3.35b (left) the ADC spectrum is shown before the equalization process, while in Figure 3.35b (right) the calibrated energy spectrum is presented. In Figure 3.35b (left) the energy spectra related to three reference positions on the block surface are reported: this makes possible to appreciate the different contributions to the non-calibrated spectrum and the behavior of different block sections. The block peripheral pixels show an overall lower light collection and a lower efficiency in detecting high energy photons (reduced peak integral with respect to the center and mid-center pseudo-pixels). Concerning the central pixels, the slight in-homogeneity is probably due to the streaked structure which guides less than on the borders the scintillation photons.

The two spectra are represented in logarithmic scale in order to better appreciate the calibration effect: it allows for the optimization of the energy response on the two spectroscopic lines

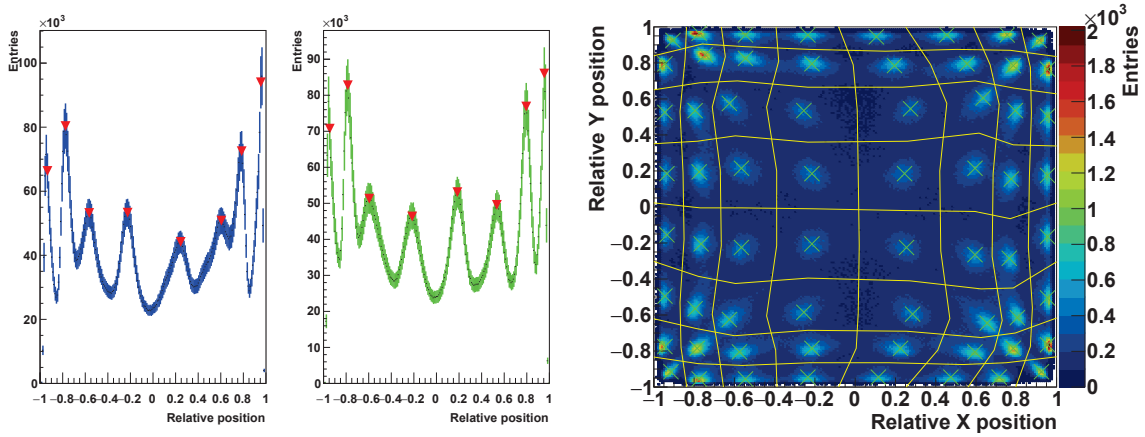

(a) 1D spatial integrated distributions with reconstructed peaks.

(b) 2D position map with reconstructed pseudo-pixel centers and areas.

Figure 3.32: 1D integrated position distributions on the two transverse dimensions with the retrieved position of the pseudo-pixel average center (a). Reconstructed 2D map with the identified pseudo-pixels positions and surfaces.

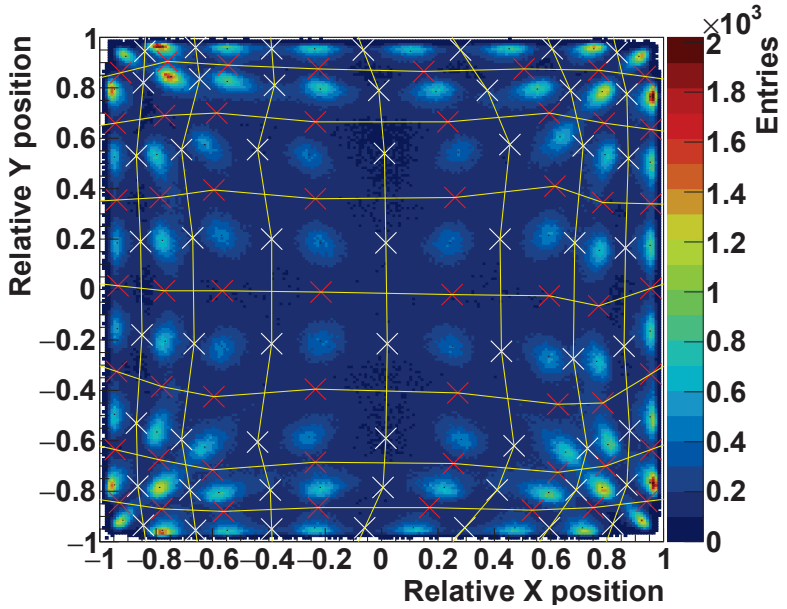

Figure 3.33: Auxiliary position map used for the assignment of the reconstructed events to a single pixel. The highlighted points represent the "valleys" between neighboring pixels on their separation borders.

of the ^{22}Na source. At this stage, the energy resolutions of the block can be defined as the FWHM of the two energy peaks.

In Table 3.1, the energy resolutions derived after the calibration process are compared to the raw ones, obtained by the non-calibrated data.

The results reported in Table 3.1 show the need for the implemented calibration process, which allows to optimize the BGO block spatial and energy response.

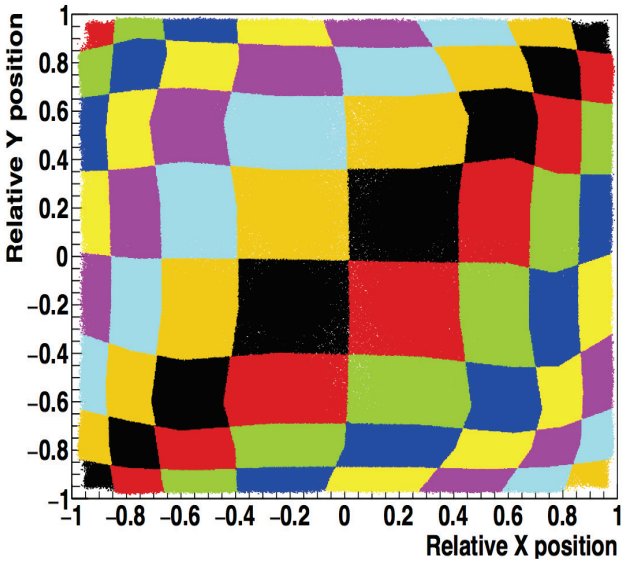

Figure 3.34: 2D map of the reconstructed event assignations to pseudo-pixels.

Table 3.1: Comparison of the block energy resolutions at the two reference energies of 511 keV and 1275 keV before and after the calibration process.

	Energy resolution @ 511 keV FWHM [%]	Energy resolution @ 1275 keV FWHM [%]
Before equalization	46.12	39.43
After equalization	23.03	18.04

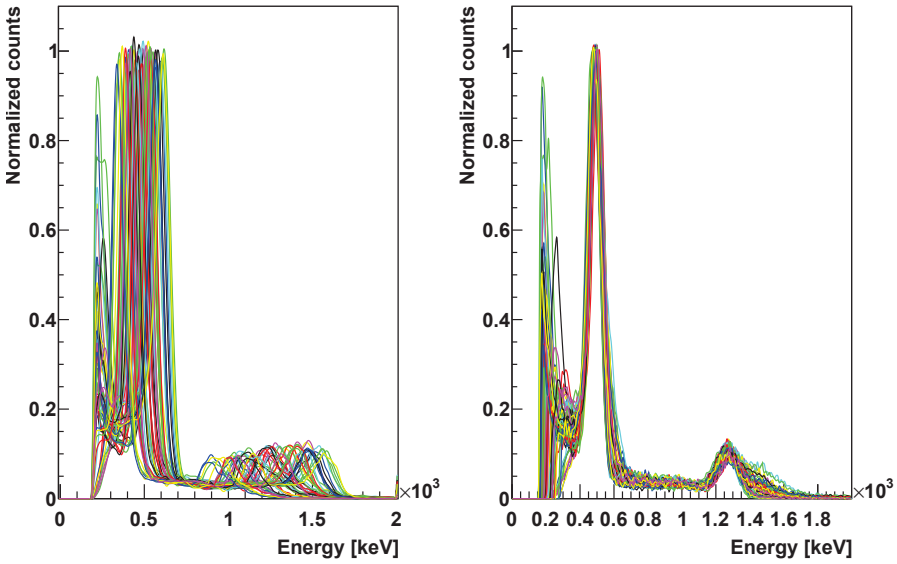

(a) Single pixel energy spectrum before (left) and after (right) equalization.

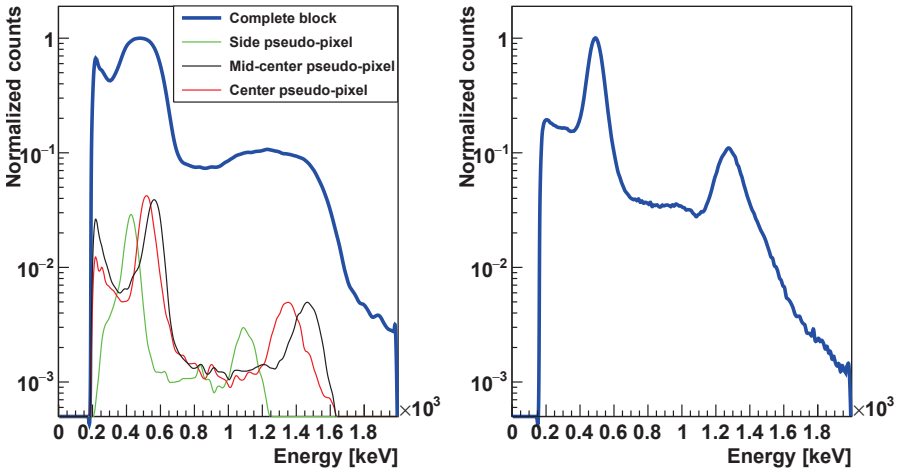

(b) Block energy spectrum before (left) and after (right) pixel response equalization.

Figure 3.35: Single pseudo-pixels (a) and whole block (b) energy spectra with the ^{22}Na source before (left) and after (right) the calibration process. The whole block spectra are reported in logarithmic scale. Three non calibrated spectra of pixels in reference positions (border, mid-center and center area) on the block are also reported with the non calibrated spectrum (a normalization factor has been applied for visualization purpose).

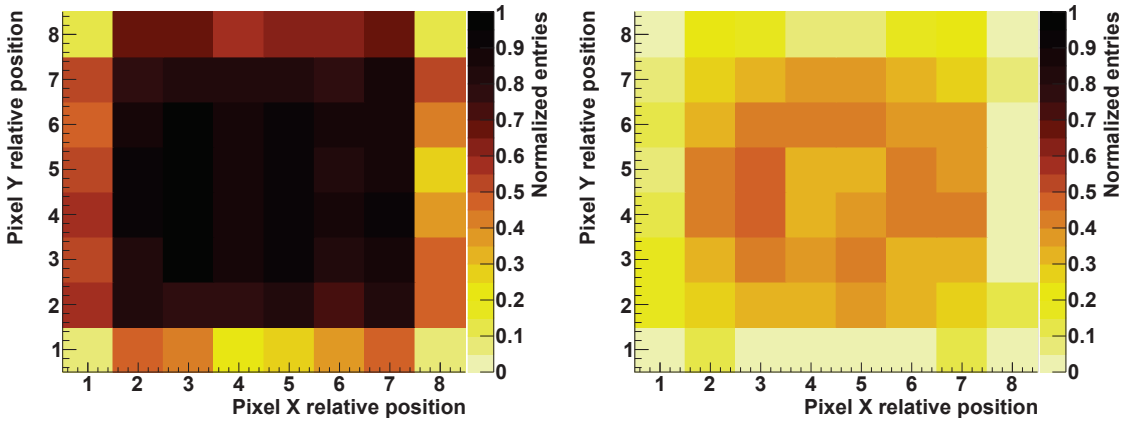

(a) 511 keV. **(b)** 1275 keV.

Figure 3.36: Relative number of entries for each pseudo-pixel as a function of the pixel relative position, represented by the row and column numbers (0 to 8 from left to right and bottom to top of the block surface). Figure(a) shows the entries in a selected energy window around 511 keV, Figure(b) in an energy window around 1275 keV. All the entries are normalized to the maximum collected number of entries, corresponding to 511 keV events in the central section of the block.

Thanks to the assignment of each reconstructed event to a single pseudo-pixel, the relative efficiency can be evaluated on a single pseudo-pixel basis. The two color maps in Figure 3.36 show the number of events collected by the 64 pseudo-pixels during the ^{22}Na source homogeneous irradiation, with an energy selection performed on the two photon energies emitted by the source (511 keV events in Figure 3.36a and 1275 keV events in Figure 3.36b). The entries are normalized to the maximum number of entries in a pseudo-pixel, detected for a 511 keV energy selection.

Figures 3.36a and 3.36b show that the expected homogeneous distribution of events over the whole block surface is confirmed for the central pseudo-pixels of central lines (2 to 7), while the block borders present a factor 2 – 3 lower detection efficiency. In particular, the pseudo-pixels on the 4 corners (line 1 and 8, pseudo-pixels 1 and 8), have an efficiency of a factor between 5 and 6 lower with respect to the center of the block surface. This effect is partially due to geometrical factors, given the fact that the side pseudo-pixels are slightly smaller with respect to the central ones (as also shown by the reconstructed 2D map in Figure 3.32b). In addition to this, the light collection is probably less performing in case of photons interacting on the block borders, causing the loss of events. Moreover, a solid angle effect is also possible given the limited distance between source and tested block (12 cm) with respect to the block size. By comparing the two maps, an overall reduced efficiency for the detection of photons beyond 1 MeV is verified. This is expected given the factor ∼2 difference in the photopeak efficiency of BGO at 511 keV and 1275 keV (Saint Gobain 2016). Moreover, the reduced efficiency in the central block area for 1275 keV photons can be related to the photo-multiplier tubes round geometry, which determines a dead space in the center of the block back surface (Uribe et al. 2003). The effect of the dead area is diminished by the light sharing effect at low energy, but it becomes considerable in case of deep-penetrating higher-energy photons. In order to fully understand the relative and absolute efficiency of each block section, an irradiation with a collimated source scanning the whole active area is foreseen. This will allow one to precisely define the detection rate variations on the block active area.

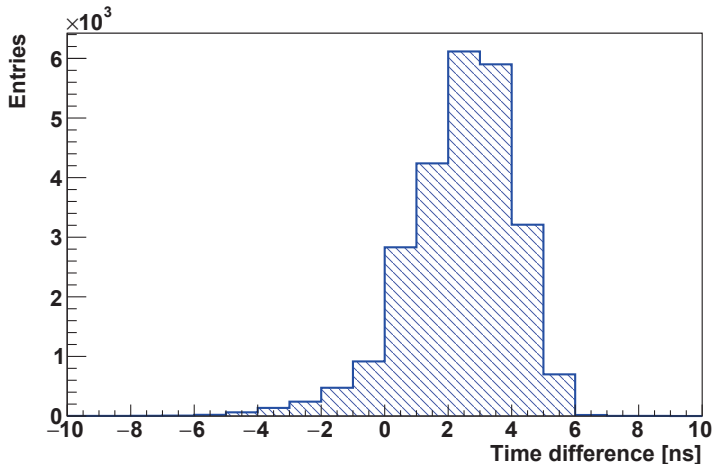

Figure 3.37: Distribution of arrival time differences between reference scintillator (a BaF_2 monoblock detector with 1 ns FWHM time resolution) and BGO block.

3.2.2.9 Time characterization

Figure 3.37 shows the distribution of arrival time differences between the reference BaF_2 detector and the tested BGO block. The time resolution is defined as the FWHM of this distribution.

3.2.2.10 Results for the 30 blocks

In Table 3.2 the results obtained for the calibration and characterization of a set of 30 blocks are listed. The characterized blocks show very uniform results, with an average energy resolution of 25 % FWHM at 511 keV and 20 % FWHM at 1275 keV and an average time resolution of 4.42 ns FWHM tested with coincidences of 511 keV photons. Both the energy and time resolutions are expected to be improved for the detection of photons in the prompt-gamma energy range, in particular above 1 MeV.

The last five blocks in the list of Table 3.2 showed detection problems, due to very low signal level on the read-out PMs or a poor spatial reconstruction accuracy with one missing pseudo-pixel on the two-dimensional map, probably due to crystal aging. The blocks with PMs issues will not be employed in the final absorber configuration, while the other two will be probably placed in the peripheral area in order to keep a wide active detection surface.

All the characterization measurements and tests described in the previous paragraphs have been performed with temporary acquisition system, because the final camera acquisition was still not optimized for the absorber blocks. The first tests with the final acquisition have been recently performed in order to characterize the BGO block response. In addition, 6 blocks have been tested on beam in a first configuration of multi-collimated cameras, coupled to the beam tagging hodoscope. The results are presented in chapter 6.

Table 3.2: Calibration and characterization results for the whole set of tested BGO blocks.

BGO block ID	Energy resolution @ 511 keV FWHM [%]	Energy resolution @ 1275 keV FWHM [%]	Time resolution FWHM [ns]
Ref. block 7627	**23**	**18**	**4.0**
3166	27	24	4.4
3171	23	18	4.4
3184	24	20	4.3
3232	24	20	3.6
3280	24	19	4.3
3322	25	20	4.2
3972	25	21	5.2
4368	25	20	5.3
5243	25	19	3.9
7130	24	21	4.9
7218	25	21	2.1
7240	25	20	6.7
7258	26	19	4.9
7369	23	19	4.3
7424	25	21	4.9
7581	26	23	4.1
7586	26	24	4.4
7601	24	19	4.1
7612	23	19	4.1
7624	22	19	3.9
7651	24	20	3.9
7657	24	19	2.7
14676	25	19	5.1
31210	25	21	4.8
3252	problem with PM 0		
3375	1 pseudo-pixel missing		6.4
6823	1 pseudo-pixel missing		1.7
7644	problem with PM 2		
7653	1 pseudo-pixel missing		2.3
21097	problem with PM 2		
Complete set	25 ± 1	20 ± 2	4.5 ± 0.9

3.2.3 Hodoscope PM characterization

The beam tagging hodoscope read-out is performed via 8 multi-anode PMs, Hamamatsu H8500 (Hamamatsu 2006), shown in Figure 3.10c. In order to guarantee a uniform response of the whole detector active area, composed of 256 scintillating fibers, the PMs must be previously characterized in terms of gain with a light source of fixed and known wave-length and intensity. The source selected for the measurements is a blue Light Emitting Diode (LED) (Hewlett-Packard HLMP-CB), installed on the test-bench shown in Figure 3.38a and described in the following. The test-bench has been developed by the LPC AVIRM group (see Gaglione 2013) and adapted at the IPNL to a different acquisition system.

The goal of the characterization measurements is to trace a gain map of the whole PM surface, with the aim of storing calibration data to be used to both tune the PM working parameters (supply voltage and threshold) and correct the collected data. This is achieved by scanning the PM photo-cathode surface with the LED. The LED is so mounted on a motorized double-axis table, controlled by two G203V stepper modules provided by GeckoDrive Motor Controls (GeckoDrive 2010). The two axes have a total range of 20 cm each, and the step resolution achieved by the controllers is 20 μm. A metal support is set on the table in order to fix the LED. It produces light pulses synchronized with a pulse generator, which is also used as trigger signal for the acquisition system, as detailed later. The light pulse produced by the LED is split into two pulses with a 45 °C mirror: one pulse is sent to the H8500 PM to be tested via optical fiber, in order to obtain a light beam perpendicular to the cathode surface (FWHM beam width estimated in 0.5 mm), the second one is detected by an Hamamatsu R5600 PM (Hamamatsu 1995), used as reference for the correction of temperature fluctuations. The PM under tests is fixed below the optical fiber output with a plastic support, not connected to the moving table. The whole described system is contained in a black box for external light shielding.

The output signals from the H8500 PM are initially amplified by custom pre-amplification cards: 8 cards are available and have been characterized in terms of amplification gain. Once amplified, the signals of the H8500 PM, together with the output of the reference PM, are sent to the acquisition system composed of a National Instrument PXI Express 1082 (National Instruments 2010) equipped with two 8-channel flash ADC modules (NI PXI-5105) and a two-channel ultra-fast digitizer (NI PXI-5154). The flash ADC modules have a maximum sampling rate of 60 MHz and are used for the read-out of the H8500 PM signals, while the ultra-fast digitizer, able to sample at a frequency up to 1 GHz, is used for the reference PM.

The acquisition and control software is developed with LabVIEW (2009) installed on the PXI; a picture of the software user interface is shown in Figure 3.38c. The PXI receives the signals from the two PMs and is also connected to the table stepper modules, so that the LabVIEW software can handle and synchronize data acquisition and table movements. The table movements can be automatized via LabVIEW macros, where step size, number and direction are stored and then used for the acquisition. The acquisition trigger, as mentioned, is given by the pulse generator which also controls the light pulses of the LED; in this way, a fixed number of pulses per table position can be recorded, and the measurement process is completely automatic. During the acquisition, the LabVIEW software automatically corrects the collected data according to the reference PM signal amplitude and to the pre-amplification card gain.

Given the limited number of flash ADC channels, only 16 PM pixels can be characterized per acquisition; four acquisitions are needed to scan the complete PM surface.

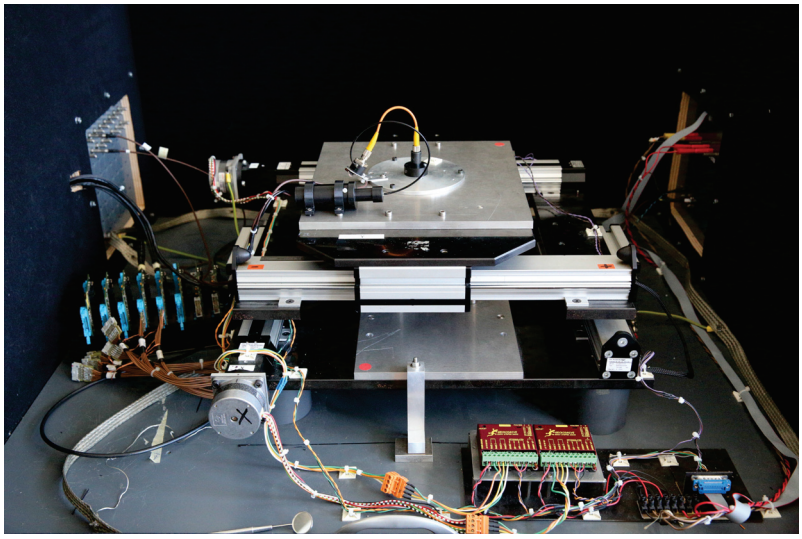

(a) Overview of the test-bench setup for the Hamamatsu PM characterization.

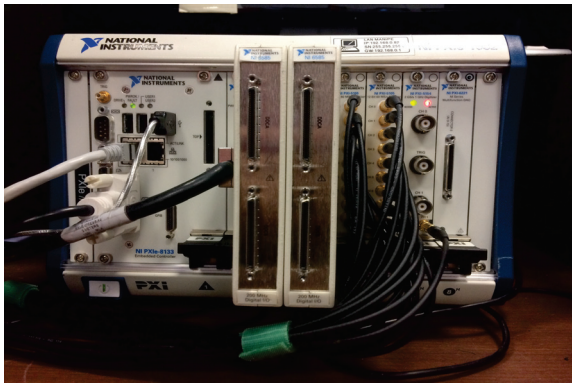

(b) National Instruments PXIe acquisition system.

(c) Example of LabVIEW software interface for the Hamamatsu PMs characterization.

Figure 3.38: Test-bench and tools for the characterization measurements performed on the Hamamatsu PMs of the beam tagging hodoscope.

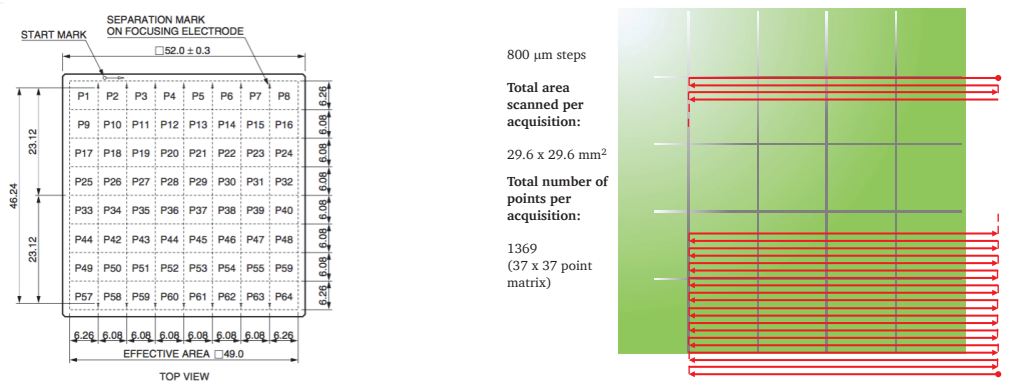

(a) Scheme and quotation of the Hamamatsu H8500 multi-anode PMs.

(b) Scheme of the scan performed for the Hamamatsu PM characterization measurements.

Figure 3.39: Details of the hodoscope PMs and of the performed characterization measurements.

Each performed acquisition is set to scan a matrix of 4×4 PM pixels, and safety margins are arranged on the PM sides in order to ensure a complete surface irradiation. As shown in the schematic view of the PM in Figure 3.39a, the total PM size is 52×52 mm^2, for an active area of about 49×49 mm^2. The active area of the pixels on the borders is slightly wider than the central ones. In order to optimize the measurement process, a preliminary analysis has been done for the definition of the needed step length, and the details are reported in Coudurier 2015. A trade-off between measurement accuracy, required time and stored data file size has been found with a step of 800 μm, so that each pixel is scanned with approximately 64 measurement points and the transition between neighboring pixels can be appreciated. A schematic of a table reference movement is presented in Figure 3.39b. To be noticed that for each irradiated point, 100 LED pulses are sent to the detector and the average amplitude value is calculated and collected.

The 8 Hamamatsu PMs have been completely scanned without the optical fiber mask used in the hodoscope and shown in Figure 3.10d, and the results are shown here for one reference PM. Some tests have been also performed with the fiber mask, in order to test the PM response mainly in terms of expected cross-talk between neighboring pixels. A complete result database has been created for calibration purpose.

Figure 3.40a shows the two-dimensional maps of a reference PM response for a complete irradiation, obtained with four separated acquisitions without the plastic fiber mask. Figure 3.40b shows the response of the same PM with the plastic fiber mask fixed on its surface. The reported signal amplitude has been normalized to the reference PM Hamamatsu R5600 for temperature oscillation correction.

In Figure 3.41 the two-dimensional response map for the 8 PMs are shown. In order to obtain a visual uniformity, the amplitude values have been normalized to the maximum value of each PM. We can observe response dis-uniformity on each PM surface, estimated in a factor ranging between 2 and 3. The retrieved response of each pixel will be useful for the calibration of the hodoscope final acquisition chain, in particular for what concerns the electronics FE settings (threshold and gain of each channel). In addition to this, these calibration measurements will allow for a proper data correction at the analysis stage.

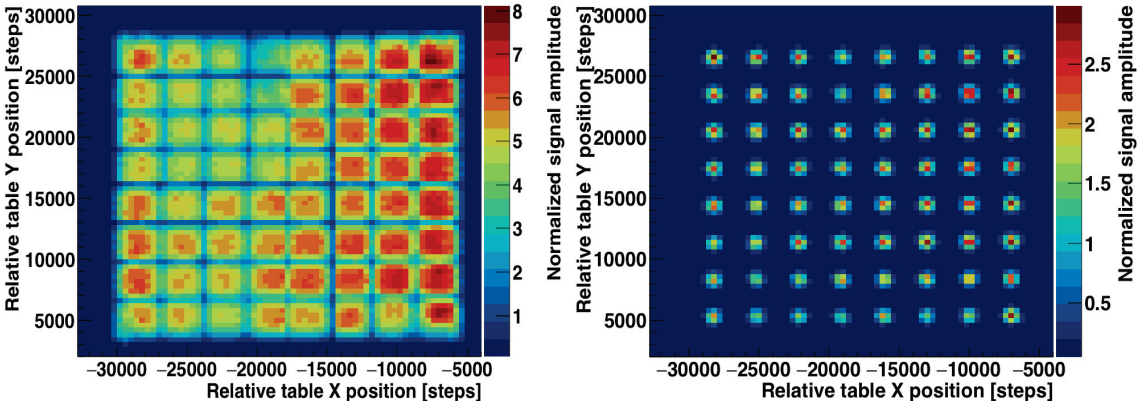

(a) 2D map without fiber mask. **(b)** 2D map with fiber mask.

Figure 3.40: Two-dimensional response maps of one of the Hamamatsu PMs for the scintillating fiber hodoscope readout, obtained with the irradiation with a blue LED. The signal amplitude is normalized to the reference PM response.

The irradiation performed with the fiber plastic mask is also used to study the signal cross-talk between neighboring pixels, which is expected to be negligible according to the provider specifications, given for similar measurements and shown in Figure 3.42a. The analysis results for one of the studied PMs are shown in Figure 3.42b as reference.

The retrieved cross-talk is more important with respect to the provider specifications (to be noticed that the measurement conditions are slightly different), but always below 3 % for the tested anodes. This cross-talk level is negligible and can be easily suppressed by a proper threshold setting.

3.2.4 Hodoscope fiber test with electron source

After the complete characterization of the Hamamatsu multi-anode PMs, they have been installed in the black boxes connected to the optical fibers of the hodoscope prototype, and the complete detection chain has been qualitatively tested to check the scintillating fiber light transmission to the optical fibers and to the read-out PMs. The observations have been performed by directly checking the pre-amplified PM output signal (with the same custom cards mentioned in the previous section) on an oscilloscope. A mechanical intervention has been necessary to fix some of the optical fibers not properly pasted to the plastic mask on the PM surface. In addition to this, a layer of black silicone has been added on the plastic mask surface to improve the light isolation on the only side where it is impossible to place the isolating black tape.

Then the hodoscope prototype has been tested with a beta source (^{90}Sr) for verification, and the obtained signal distributions (retrieved as before with an oscilloscope acquisition after signal pre-amplification) have been compared to simulation study performed by an internship Master 1 student (Vallois 2016). He tested by simulation the irradiation of the whole hodoscope surface with an equivalent ^{90}Sr source to retrieve the deposited energy distribution on the scintillating fibers. This distribution can be compared to the collected signals ampli-

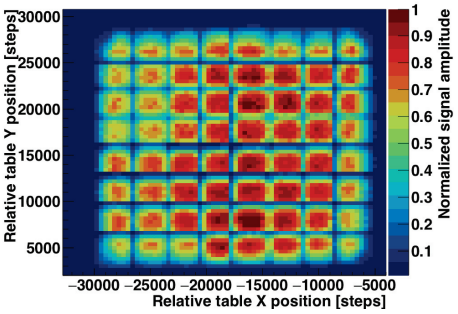

(a) PM 1 2D map without fiber mask.

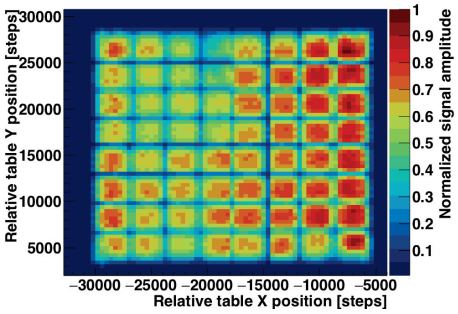

(b) PM 2 2D map without fiber mask.

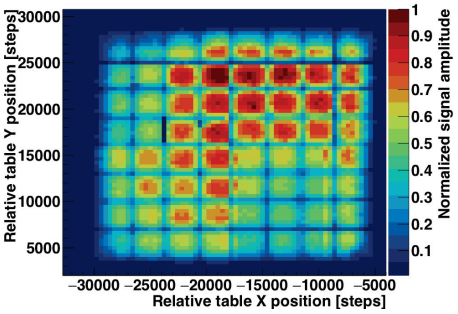

(c) PM 3 2D map without fiber mask.

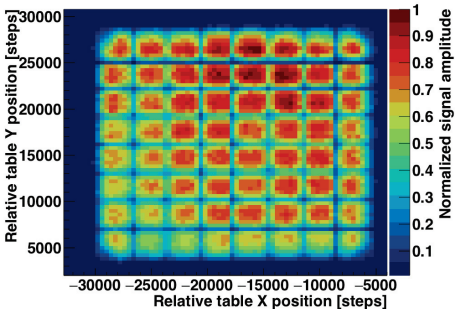

(d) PM 4 2D map without fiber mask.

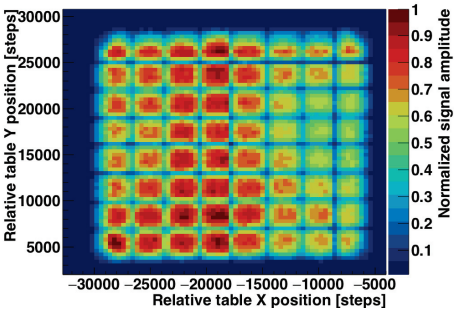

(e) PM 5 2D map without fiber mask.

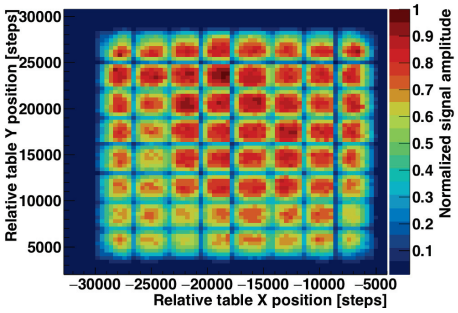

(f) PM 6 2D map without fiber mask.

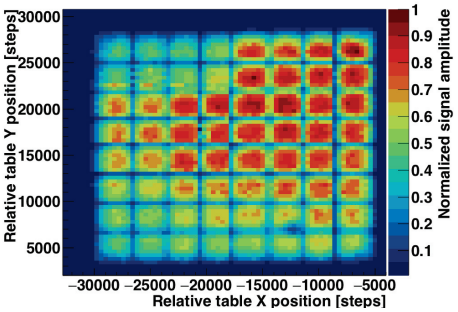

(g) PM 7 2D map without fiber mask.

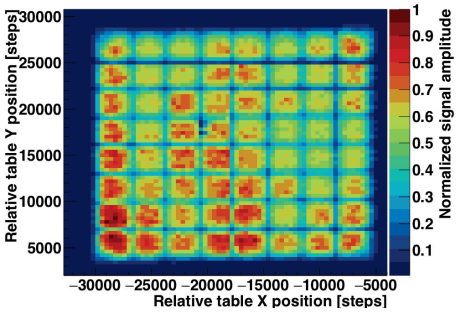

(h) PM 8 2D map without fiber mask.

Figure 3.41: Two-dimensional response maps of the Hamamatsu PMs for the scintillating fiber hodoscope readout, obtained with the irradiation with a blue LED. The signal amplitude is normalized to the reference PM response and then to each PM maximum detected amplitude.

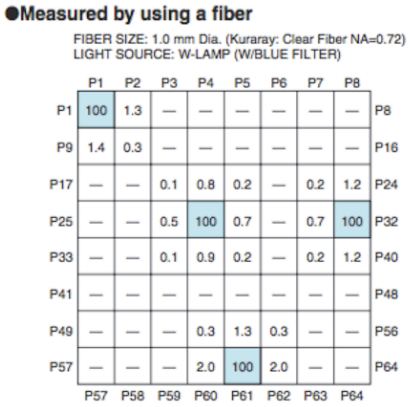

(a) Signal cross-talk provided by Hamamatsu for the PM H8500 (Hamamatsu 2006). The measurements have been performed with a 1 mm diameter optical fiber; the irradiated anode is in the light blue box, and the cross-talk on the neighboring ones is expressed in %.

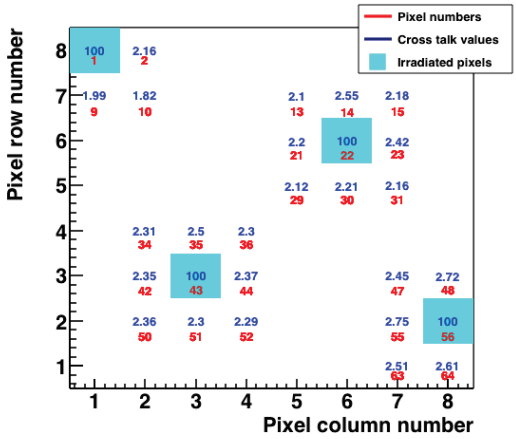

(b) Signal cross-talk on a reference PM measured with a blue LED irradiation through the plastic fiber mask. The irradiated anode is in the light blue box, and the cross-talk on the neighboring ones is expressed in %.

Figure 3.42: Cross-talk study on neighboring PM pixels. The experimental results obtained with the irradiation with a blue LED through the plastic fiber mask on a reference PM (right) are compared to the specifications provided by the producer, measured in similar conditions (left). The cross-talk is expressed in % with respect to the irradiated anode, which is represented by the light-blue cell with 100 % of the signal.

tude distribution obtained with the experimental tests, in order to calibrate the relationship signal amplitude-deposited energy. The distance between the source and the fiber was set to 3 mm in the simulation code, to reproduce the gap created by the plastic box of the real source, which was directly on the fiber for the experimental measurements. In Figure 3.43 the results for a reference fiber are shown. The distribution entries have been normalized to the total number of events for visualization purpose.

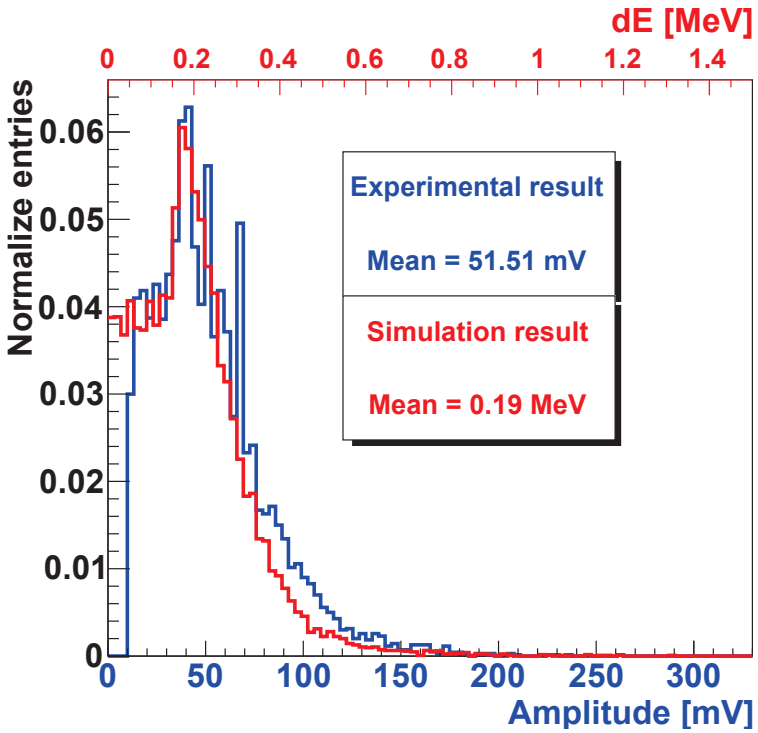

Figure 3.43: Comparison of the simulated distribution of energy deposited by electrons from the ^{90}Sr source on a single hodoscope fiber to the experimental signal amplitude distribution from a scintillating fiber irradiated with the ^{90}Sr source.

The comparison presented in Figure 3.43 can be useful as estimate of the expected signal for a given energy deposited by an ionizing particle (about 50 mV for about 200 keV of energy deposited). Knowing the applied amplification factor (given by the per-amplification card characterization) and the relative gain of each PM pixel, the expected raw signal integral can be estimated.

A complete characterization of the hodoscope acquisition chain will be necessary on proton and carbon beams in order to verify the beam primaries energy deposit in the scintillating fibers and tune the working parameters. In particular, the increased energy deposit expected for proton and carbons with respect to electrons should allow for a reduction of the high voltage applied to the PM. With reduced voltage, the detection rate capability would be improved. All these assumptions will be tested on beam soon.

A preliminary study of the hodoscope acquisition chain characterization has been performed by developing an automatic parameter scanning system, which has been tested for background characterization. The code is able to loop on each acquisition channel by testing its response to increasing threshold and gain values, in the range allowed by the electronics FE board. This work has been performed with the collaboration of a bachelor internship student, and

the results are presented in (Colléaux et al. 2018). Such a method will be applied during tests with proton and carbon beams to optimize the hodoscope acquisition parameters on a single channel basis.

3.3 Summary and perspectives

The CLaRyS collaboration is developing in parallel two gamma cameras for ion beam therapy monitoring and nuclear medicine applications. At present, the detector components are being tested separately for characterization purposes at the IPNL. I presented in this chapter a complete description of the detector components with the related FE electronics, mechanical support, acquisition system and software tools, together with all the characterization measurements I performed on the various detector sections. In the following, in addition to a short summary of the present status of the instrumental development of each camera component, I list the main tasks to be accomplished for the final integration a complete operation of the whole camera.

3.3.1 Silicon scatterer

Among the 10 DSSD layers provided by the seller, only 7 respected the design requirements and have been selected for the use in the Compton camera prototype. The 7 selected layer have been characterized in terms of leakage current with an acquisition system specifically developed for this purpose. Temperature cycles have been performed in order to precisely define the cooling performance needed to obtained the required noise level. These measurements allow to fix the working temperature to –20 °C and lead to the conception and production of a thermal regulated box, working with cold air and so adapted to the clinical use. A modular mechanical support has been fixed inside the camera to sustain the silicon layers with their FE cards. The FE card has been designed and tested at the IPNL, and includes a custom ASIC which has been optimized with three different developed versions. The final version of the whole board has been produced in 7 copies in 2017 and they are now available for the next test stages.

The development of the FE board firmware is at present ongoing at the IPNL, and the first tests of data collection with a temporary acquisition system and injected charges have been performed. A further verification and optimization of the code will be carried out in the next future, and the silicon layers will be tested with their FE cards by the end of 2018 with the μ-TCA acquisition system. The present AMC40 firmware performance has never been tested with the scatterer detectors before; some modifications can then be foreseen to optimize the data taking process, for what concerns both the stand-alone test mode and the operation within the complete system.

Moving to the thermal regulated box, its cooling performance has been tested without the detectors, so that a test with the power consumption of the seven operational detectors and boards has still to be performed. Dry air or nitrogen will be tested and used for the final setup. Additionally, the box has to be adapted to arrange the incoming and outgoing cables (power supply and data). Outside the box, a patch-panel will be also realized in order to properly

set all the needed connections. The patch panel will be conceived to be integral to the box and adapted to the camera moving table, where the box will be installed for the final camera integration.

Once the acquisition will be fully operational, laboratory measurements with gamma sources are foreseen to characterize the detector response. Low energy gammas will be employed to test the DSSD energy resolution with full gamma absorption on a single strip basis, on p and n sides, while higher energy gamma irradiation is foreseen to study realistic detection conditions and verify efficiency, time and spatial performance (time resolution, average cluster size as a function of the energy). In addition, we will also infer 3D position capability by comparing p and n signals. Once a full characterization of each channel of the 7 layer will be achieved, tests on beam with prompt-gammas are planned in stand-alone operation and, finally, with the complete Compton camera.

3.3.2 BGO absorber

As mentioned in the detector description section, the original camera design included 96 BGO blocks recovered from a dismantled SIEMENS PET system. The reconditioning process aimed to re-polish the crystal surfaces, test the PMs with a light source and group them in quartets with compatible gains. As reported, the reconditioned block prototypes didn't show the expected improved performance, but on the contrary an overall signal degradation has been observed, probably due to a worsened light collection. Several configurations have been tested with non satisfactory results, so that the present camera is set up with 30 original blocks, which have been deeply studied and characterized at the IPNL, as detailed in section 3.2.2. The calibration and characterization methods developed for the BGO block can be applied to similar detectors and represent an extension of previous studies (Golnik 2015; Hueso-González et al. 2015a; J. G. Rogers et al. 1994; Tornai et al. 1994). Some of the features developed for the characterization tests, such as the automatic research of the pseudo-pixel position and the pseudo-pixel assignation algorithm, will be used in the final camera at the data analysis stage, with simple adaptation to the camera acquisition system and data format. The complete set of characterization measurements described in this chapter has been performed with commercial acquisition systems and the required raw data treatment was performed with commercial NIM modules. The ASM read-out boards are at present under test at the IPNL, and their firmware must be optimized for the μ-TCA acquisition. A first, non-optimized version of the complete acquisition chain has been tested, including the pre-trigger logic with the THOR board, the μ-TCA data collection and communication to the acquisition PC, and used for the beam test described in chapter 6.

With a fully operational absorber, test with prompt-gammas (and so on proton and carbon beams) will be performed to test the block behavior in the prompt-gamma energy range, where an overall performance improvement is foreseen (in terms of space, time and energy resolution). Some tests performed at the GANIL in 2014, with an original block and an acquisition similar to the one employed for the characterization tests, showed promising results: in particular, a 2 ns FWHM time resolution was achieved with prompt-gammas (see Ley 2015). These results have to be confirmed with all the camera BGO blocks. In addition to this, with proton and carbon beams the absorber geometry (in terms of block arrangement in the mechanical support) will be tested to obtain the optimal configuration with the minimization of dead areas between the blocks. it is to be noticed that different geometrical setup can be foreseen for

Compton and multi-collimated camera, and for the desired measurement (detection of the all ion range, test of prompt-gamma distribution in the plane parallel to the beam line, etc.).

Concerning the mechanical support, it is finalized and already prepared for the integration on the moving table. As for the scatterer, a patch panel will be realized to arrange all the cables which have to be connected between FE and ASM cards. The 5 needed ASM cards will be placed in a dedicated VME crate, which will be integral to the table. Its setup will be fixed in order to minimize the interference with the table movements.

3.3.2.1 Absorber upgrade

One of the already identified main limitations of the Compton camera for the application in ion beam therapy monitoring at clinical beam intensity is the relevant background due to random coincidences. As already mentioned, the random coincidences can be created by secondary particles different from prompt-gammas, or, less likely, by two prompt-gammas in the same time window. The TOF solution has been verified to be efficient in reducing the first kind of random coincidences, and the background subtraction performance ensured by this method strongly relies on the detector time resolution. An improvement in the camera component time resolution would allow for a reduction of the coincidence window, further increasing the amount of rejected random coincidences. A challenge concerning the absorber, if we keep the actual architecture, would be an improvement of the timing and efficiency (with 3 cm thickness the probability of full absorption is reduced). An additional layer of LYSO would improve the performance; replace PMs by Silicon Photo-Multipliers (SiPMs), replace VME acquisition by on-board or μ-TCA dedicated cards, these would be necessary steps in view of a broader diffusion of a Compton camera for Single Photon Emission Computed Tomography (SPECT) application and Prompt-Gamma (PG) detection.

A possible change of the absorber architecture has already been considered for a second version of the Compton camera prototype, and involves a commercial detector provided by Damavan Imaging, called Temporal Delta Compton. It is based on a scintillation LYSO or Cerium Bromide ($CeBr_3$) crystals coupled to very fast Philips DPC3200 Tile sensors (based on SiPMs), with a Single Photon Time Resolution (SPTR) of the order of 100 ps (Brunner et al. 2016). This excellent time resolution allows for a direct measurement of the scintillation light shower development within the crystal, resulting in the possibility to retrieve a 3D spatial information in parallel to a time resolution in the hundred of ps scale. This solution will be further discussed in the future and can be applied for a second prototype of the Compton camera.

3.3.3 Scintillating fiber hodoscope

Three prototypes of scintillating fiber hodoscope are available at the IPNL: 1+1 fiber, 32+32 fibers and the large size version with two planes of 128 fibers. The 1+1 fiber has been studied at the beginning of the development process as proof of concept, and the employed technology has been transferred to the two final prototypes with the required improvements. The increased size of the 128+128 fiber one lead to the addition of the two-side fiber read-out, for efficiency optimization and improved timing performance. All the other features are common to the two, including the installed multi-anode PMs (Hamamatsu H8500) and the related FE

card. The advantage of the 32+32 hodoscope is the possibility to perform a complete read-out of the active surface with a single FE card, so that no synchronization features are required in the card and acquisition firmwares. This is the main reason why the first beam test performed on the hodoscope have been carried out with the small version (see chapter 6 for the description and the results of the beam tests). The FE card firmware is at present at the optimization stage, and the performed test allowed to define the needed improvements, mainly connected to the time measurements capabilities. In addition to this, the synchronization of the 8 cards used for the read-out of the 128+128 fiber prototype still has to be achieved. The first acquisition tests performed during the proton beam exposure allowed to validate the acquisition software and the μ-TCA firmware in a simple version, but additional trigger features must still be added to integrate the hodoscope in the final camera configuration. Concerning the detector performance, the optimization of the working parameters (gain and threshold of each read-out channel) required the development of an automatic measurement system, which will be employed on beam to perform similar characterization in presence of proton induced signals. Finally, the mechanical support is fully operational: the motor steering must be integrated in the slow-control software.

The overall development is at the final stage, and the integration of the 32+32-fiber hodoscope in a first multi-slit collimated camera configuration has been tested on beam in September 2018, in order to perform preliminary tests of TOF capabilities. The obtained results are shown in chapter 6.

Previous measurements with discrete electronics lead to counting rate capability up to 10^7 counts/s on a single multi-anode PM H8500. However, this count rate capability needs to be more systematically studied with the large hodoscope with the sharing of channels among PMs, as a function of the energy deposit (incident particles), PM bias and detection threshold. A larger size hodoscope may also be envisaged in order to cope with particle therapy irradiation fields. A more general issue concerns the use of additional > 2 mm water equivalent thick material upstream of the patient. A clinical integration of such a hodoscope would require the optimization of the material budget (possibly thinner fibers) and a redesign of the holder.

3.3.3.1 Hodoscope upgrade

As already explained concerning the absorber possible upgrade, the main direction for an improved camera prototype is the optimization of the detector timing capability. The LPSC group in Grenoble is developing high time resolution diamond detectors, which can be considered for a new version of the beam tagging hodoscope. The MoniDiam project aims to develop a diamond based hodoscope prototype with the related fast electronics to enable a time resolution of a few tens of ps. In addition to this, the diamond based detectors are intrinsically affected by a very low noise level and allow to overcome the radiation hardness limitation imposed by the present scintillating fiber prototype, together with further extending the rate capabilities to an expected 100 MHz acquisition rate without splitting the readout channels to several acquisition cards. Some tests of small diamond detector prototypes have already been performed with pulsed beams at the European Synchrotron Radiation Facility, Grenoble, France (ESRF) in Grenoble and with 95 MeV/u carbon beam at the GANIL, with promising results: a polycristalline detector, $5{\times}5{\times}0.3$ mm^3, exposed to the 95 MeV/u GANIL carbon beam, showed a time resolution of 37 ps RMS coupled to an energy resolution of the order of 7 % RMS for 25 MeV of deposited energy (see Gallin-Martel et al. 2016). Similar measure-

ments performed with diamond crystal with different sizes showed compatible results, with a time resolution between 20 and 90 ps RMS and an energy resolution between 7 and 9 % RMS (Gallin-Martel, M.-L. et al. 2018). Although sufficiently large area diamonds are not yet available, a mosaic assembly of several diamonds (with a total area of 15×15 cm^2) is expected to be tested in 2019-2020 and is a good candidate for a improved version of the Compton and multi-collimated cameras.

3.3.4 Acquisition and software

The acquisition μ-TCA based system development is managed by the CPPM research group, and frequent tests has been performed at the IPNL to verify and integrate its functionality to the read-out detector cards. As reported in the description, it should be able to receive and treat the trigger signal generated by the absorber for the multi-collimated camera or by the silicon scatterer for Compton one, collect the data flow from all the detectors, group them into UDP packets with the proper format and send them to the acquisition PC. The main tasks (data collection, packet creation and communication to the PC) have been already verified on beam for a single detector and a single FE board, so that now the trigger treatment capabilities and the ability to handle all the detectors components have to be developed in the AMC40 firmware and tested with the final system. Moreover, the μ-TCA must also be able to transfer the slow control signals sent by the LabVIEW software to the selected read-out cards; this feature is still at the debug stage.

Concerning the acquisition software, it has already been tested and validated with a data simulator, with a maximum achieved acquisition rate of about 300 Mb/s, sufficient to manage the data from the complete camera (see appendix A). It will be tested step by step with the increasing number of FE boards involved in the measurements. In parallel, the monitoring software is now available and operational for each single detection section, but an optimized version allowing for an on-line visualization of the whole camera acquisition must still be studied. Finally, the slow control software development is ongoing; all the required working parameters can already be controlled by various pieces of software, which must be integrated in a complete user interface and tested with the μ-TCA for what concerns the FE cards configuration. All the parameters related to the moving table motors (for camera and hodoscope), detector and card low and high voltage, have already been tested and do not require the μ-TCA intervention.

3.4 Conclusions

During the three years of my PhD thesis, the instrumentation development of the single detector components, as well as of the two cameras, saw an important advancement, thanks to the synchronized effort of the whole collaboration. In this chapter, the advancements achieved in the last years have been described in details, including, in addition to my personal contributions, results obtained before the beginning of my PhD thesis or in parallel by CLaRyS collaborators.

I personally characterized the hodoscope PMs as described in section 3.2.3, following the pre-

liminary internship work of a master student (Coudurier 2015) and using an instrumental setup already created by a previous PhD student (Gaglione 2013). During the first months of my work, I adapted the acquisition system in order to perform automatic scans of the hodoscope PM surfaces, I acquired data for the whole set of available PMs and I performed the complete data analysis to produce the results presented in the description section. In parallel, I studied in simulation the design of the lead collimator produced to host the ^{60}Co high activity source described in section 3.2.2. The source was originally foreseen to be employed for the characterization of the scatterer silicon layers, so that I optimized the design of the three apertures (point-like, linear and squared) in order to obtain the desired irradiation of the DSSDs layer surfaces. The collimator structure is designed, in collaboration with the radiation protection IPNL expert, to allow the source usage in a "public" area, so that the geometrical configuration is imposed by these constraints. The collimator production has been performed by an external company, and I directly participated in the source positioning inside the collimator, as well as to the radiation tests in its final location. Since the Spring 2016, I focused my efforts on the hodoscope, starting from the 128+128-fiber prototype mounting (I installed the characterized PMs) and testing with a simple acquisition, in order to verify the optical fiber and scintillating fiber connection. I identified the defective channels and participated in the fixing process with the mechanics IPNL group. After that, with the help of a master student, I performed a first characterization of the complete read-out chain for each channel, and compared the results of the irradiation with a beta source to simulation, for a preliminary detector calibration (see section 3.2.4 and Vallois 2016). In the following months I mainly focused on the simulation works presented in chapters 4 and 5, participating in parallel to the electronics development advancements. In particular, I collaborated with the IPNL electronics group to the characterization of the scatterer FE card in terms of electronic noise, by analyzing and discussing the collected data. Since the beginning of 2017, my attention was directed to the absorber components. As described in section 3.1.3, the whole set of original recovered block should have been "reconditioned" in order to be adapted and optimized to the new application in the CLaRyS gamma camera, and I directly worked on the test and characterization of the first reconditioned blocks received by the LPC group. With the help of a master student working for its internship, we developed an acquisition system based on the BGO block acquisition card, commercial NIM modules and the PXI described in section 3.2.3, and we tested several blocks reconditioned with different methods, in comparison to a reference original block. The test results are reported in Sandjong et al. 2017 and were not satisfactory, so that we decided to move to the application of original, "non-reconditioned" blocks, with a reduced size absorber configuration. The acquisition system we developed to characterize the reconditioned blocks has been used to test the original ones, which I completely characterized starting from September 2017. During the characterization process, I optimized, with the participation of a master student, the test method and developed the analysis and performance optimization process described in section 3.2.2 and published in Fontana et al. 2018. Concerning the mechanical supports, I participated in the design and realization of the reduced-size camera absorber support, in the final configuration of the hodoscope moving table, with particular focus on the setup of the patch panel for the cable connections, and to the first cooling tests involving the thermal regulated chamber to be employed with the scatterer layers. Moreover, I worked with IPNL colleagues to develop the LabVIEW based remote control of the camera moving table described in section 3.1.7 and shown in Figure 3.16b, which is still under test. Moving to my contribution to the camera software, I personally developed all the analysis code used to produce the results presented in this chapter, with the exception of the scatterer layer tests. Furthermore, I developed the camera monitoring software described in section 3.1.6, and I always participated in the optimization of the acquisition software, coded by the IPNL comput-

ing group, as well as in the design of the different acquisition card firmwares. Finally, I tested the hodoscope on beam during three tests campaigns, described in details in chapter 6.

The project is now reaching the final stage, where all the performed laboratory test and development studies will be transferred to the multi-collimated and to the Compton camera, which is foreseen to be tested on beam before the end of 2019. The next two years will be fundamental to estimate the potential of the developed detectors in realistic conditions and to plan the first clinical tests, final goal of the entire project.

4

Compton camera application for ion beam therapy monitoring

The results presented in this chapter will be submitted for publication on the journal *Physics in Medicine & Biology*.

Contents

4.1 Introduction

Ion beam therapy is a cancer treatment technique which is rapidly gaining importance in the global tumor therapy panorama. In addition to the already operational 70 clinical facilities, with more than 175000 patients already treated by the end of 2017, several new centers have been designed and approved for construction worldwide (Particle Therapy Cooperative Group 2017). The favorable feature of this treatment technique is connected to the characteristic energy deposition profile of charged particles as a function of depth in matter. As first observed by Bragg (Bragg et al. 1904), the depth-dose profile of charged particles shows a maximum close to the end of their range in matter; in addition to this, a strong enhancement of the Relative Biological Effectiveness (RBE) is observed for ions heavier than protons in the region of the Bragg peak (Elsässer et al. 2004; Weyrather et al. 1999), which further enhances the dose ratio between target and healthy tissues.

The maximum of the dose is deposited in the Bragg peak region in the patient and must be tuned to cover the target volume (defined via Computed Tomography (CT) scan) and, at the same time, spare the surrounding healthy tissues. Treatment planning and delivery uncertainties limit the tumour targeting capabilities, like uncertainties in the material composition determination, CT units conversion to ion stopping power, patient mis-positioning, organ motion or morphological changes between treatment fractions. These uncertainties force the clinicians to fix relatively large safety margins around the planned treatment volume, up to 3.5 % + 3 mm (Paganetti 2012b). Ion-range verification is one of the conditions required for a broader usage of ion beam therapy and for its further development. With the goal of fully exploiting the ion beam therapy dosimetric potential, the monitoring should be in real-time and ideally in 3 dimensions, in order to detect important deviations between the planned and delivered dose to the target volume or to surrounding organs, in particular in case of proximity to Organ At Risk (OAR). This capability would allow for a reduction of the above mentioned safety margins and for a better tumor targeting; in addition to this, it could permit the use of new irradiation fields with OAR downstream with respect to the tumor position (Knopf et al. 2013).

Several range verification techniques have been considered worldwide for twenty years. Most of them rely on the detection of secondary radiation generated during the slowing down process of incident ions, in particular during nuclear reactions. Among these secondary radiations, positron emitters have been deeply studied in order to exploit Positron Emission Tomography (PET) machines for treatment monitoring. The only available and functional range monitoring systems in a clinical center are based on this technique (Enghardt et al. 2004; Yamaya 2018), which is anyway affected by physical and technical limitations (Parodi 2015).

In addition to positron annihilation products, the relaxation of excited nuclei also produces secondary photons in a wide energy range, between some hundreds of keV till about 8 – 10 MeV. After the first idea proposal published in 2003 (Stichelbaut et al. 2003), these secondary products of particle treatment have been deeply investigated and the correlation of this gamma radiation to the ion depth-dose profile has been confirmed by several research groups, starting from Min et al. 2006 for protons and É. Testa et al. 2008 for carbon ions. The so-called Prompt-Gamma (PG)-rays have the advantage to be emitted almost instantaneously after the beam interaction in the tissue, making them more adapted than PET 511 keV gammas for real-time monitoring. Moreover, as shown in (Robert et al. 2013), the emission rate

is comparable or superior to the one of the annihilation gammas for both protons and carbon beams. Consequently, different techniques have been proposed to exploit this signal for treatment monitoring purpose, with the related detection systems. More details on PG monitoring can be found in chapter 2. In the same chapter, in section 2.2.3, the methods and devices developed for the detection of PG rays with the purpose of monitoring the ion range during particle therapy treatments are described. In particular, Compton camera prototypes have been studied and developed by several groups. Several sources of uncertainty and signal background are connected to the Compton camera detection method. The reported Compton kinematics formula (equation 2.10) assumes valid the relation in equation 4.1:

$$E_0 = E_1 + E_2. \tag{4.1}$$

where (E_0 is the energy of the incident photon, (E_1 and (E_2 are the energies deposited by the detected photon in scatterer and absorber, respectively. Since the initial photon energy is not known *a priori*, a complete photon energy absorption is needed for the cone calculation, or at least three photon interactions are required in a single event. An under-estimation of the total initial energy (caused by a photon non-complete absorption in the absorber section or by the Compton electron escape from the scatterer section), leads to a mis-estimation of the Compton angle, so to a Compton cone reconstruction uncertainty. If triple scattered photons are selected, the initial photon energy can be calculated analytically so that a complete absorption is not mandatory (Kurfess et al. 2000). In addition to this, the Compton formula considers the Compton scattering electron initially at rest, and its energy configuration creates a blur in the Compton angle reconstruction, resulting in the already cited Doppler broadening effect (Ordonez et al. 1997). Furthermore, the detection principle is based on time coincidences between the two detector sections, therefore the time structure of the incoming particles plays an important role. The final image accuracy suffers from random coincidences generated by two prompt gammas interacting within the same time window or by background contamination of secondaries, mainly neutrons and protons. The effect of random coincidences can be reduced by high detector time resolution or background rejection methods (Draeger et al. 2017). Energy selections can be applied to the collected coincidences (Hilaire et al. 2016; Polf et al. 2009a) or the homogeneous neutron background can be reduced via time-of-flight information (M. Testa et al. 2010).

Ortega and colleagues (Ortega et al. 2015) presented a detailed analysis of the noise sources for Compton imaging in proton therapy monitoring, and the clinical application of this method for detecting range shifts was tested for the setup under development in Valencia, Spain. The simulation study showed the relative expected rate of prompt gammas and neutrons, and the resulting rate of random coincidences ranging from 19 % to more than 60 % depending on the beam energy and the coincidence time window. This amount of fake events leads to complex reconstruction scenarios, where the identification of a 3 mm range shift is not clear for all cases.

Starting from these results, we studied with Monte Carlo simulations the Compton camera prototype developed by the CLaRyS collaboration based on semiconductor and scintillator detectors (see chapter 3 and Fontana et al. 2018; Krimmer et al. 2015). The camera performance is studied with respect to the gamma energy in the prompt gamma energy range. Furthermore, the feasibility of its clinical application as depth-dose profile monitor during ion beam therapy clinical treatment is analyzed. After a preliminary study with point-like gamma sources irradiation focused on detector efficiency measurements as a function of the source position and gamma energy, clinical proton and carbon beams impinging on an homogeneous Poly-Methyl-Metacrylate (PMMA) phantom are simulated to reproduce treatment conditions and analyze

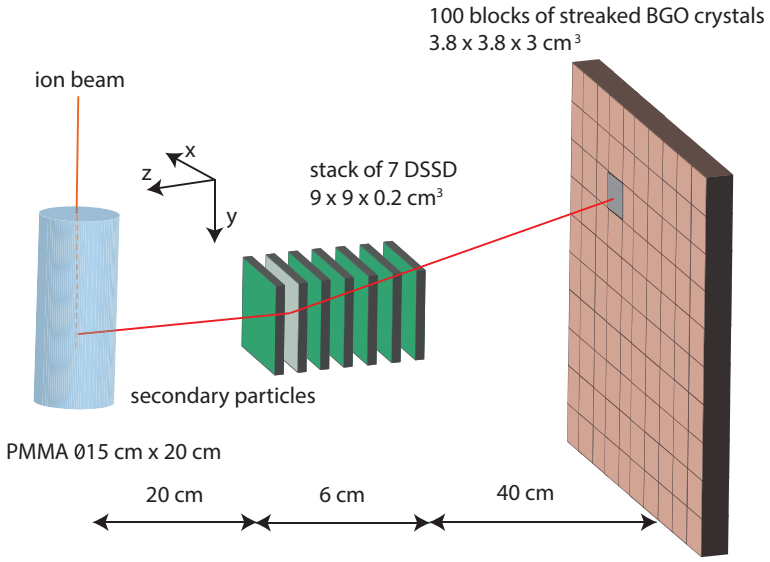

Figure 4.1: Scheme of the simulation setup (not at scale): a PMMA cylindrical phantom is set in front of the Compton camera prototype. The Compton camera is composed of a stack of 7 DSSDs (scatterer) and a plane of 100 single BGO blocks. The set distances are realistic for clinical conditions. This geometrical configuration has been used for all the simulations presented in this work.

the prompt gamma detection resulting scenario. The ratio between true and background coincidences is studied as a function of the beam intensity. Two kinds of reconstruction algorithms, a line-cone analytic method and a Maximum Likelihood Expectation Maximization (MLEM) iterative one, are applied to the collected data in order to compare the imaging results. Finally, the precision with which the dose profile fall-off can be detected with the Compton camera is reported for the line-cone reconstruction method.

4.2 Material and methods

4.2.1 Simulation setup

The monitoring system modeled in this simulation work is the Compton camera prototype under development within our collaboration. The detectors detailed characteristics can be found in chapter 3, and are here briefly recalled.
The scatterer consists of seven parallel planes of silicon detectors (Double-sided Silicon Strip Detectors (DSSDs)), $9\times9\times0.2$ cm^3, with 1 cm distance between the centers of two neighboring planes, while the absorber is composed of an array of 10 × 10 Bismuth Germanium Oxide - $Bi_{12}GeO_{20}$ (BGO) blocks ($3.5\times3.5\times3.0$ cm^3 each) placed behind the silicon layers at a distance which can be tuned according to the requirements.

The silicon detectors have a strip pitch of 1.4 mm, for a total of 64 strips per side (double-sided readout based on electron and hole pairs collection). Regarding the BGO blocks, their entrance surface is streaked in a 8×8 matrix of pseudo-pixels, 4.4 × 4.4 mm^2 size, and the readout is

performed via 4 Photo-Multiplier (PM) tubes. The position reconstruction is achieved via Anger logic.

A scheme of the simulation setup is given in Figure 4.1. The ion beam interacts with a cylindrical PMMA phantom (15 cm diameter and 20 cm length) placed in front of the Compton camera as target. It is placed 20 cm far from the first silicon plane (center-to-center distance) which seems a realistic distance in clinical conditions. The distance between the last silicon layer and the absorber array (center-to-center) is set to 40 cm in order to enable Time-Of-Flight (TOF) measurements (see section 4.2.4).

The silicon detector strips are not reproduced in the simulation code, and the spatial resolution in the detector plane is set to 0.9 mm Full Width at Half Maximum (FWHM) at the reference energy of 1 MeV, according to preliminary measurements performed on smaller detector prototypes. In the plane of the detectors (xy in Figure 4.1), interactions are defined as localized energy deposits, and the events presenting multiple hits separated by a distance beyond 3-strip equivalent are rejected. For the accepted multiple-hit interactions, the interaction position in the detector plane is defined as the center of gravity of the hits, weighted with the hit energy deposit. Concerning the direction perpendicular to the detector plane (z axis in Figure 4.1), the interaction position is set to the center of the involved silicon plane. A mono-block crystal is simulated for the absorber for simplicity. The events are selected to be limited to a single block component based on the interaction localization, and, as for the scatterer layers, the interaction position is reconstructed via center of gravity calculation if multiple interactions occur within the same block. An uncertainty contribution, randomly extracted from a Gaussian of 5 mm FWHM (corresponding to an overestimation of the geometrical resolution given by the pseudo-pixel matrix, set to reproduce not yet tested experimental conditions), is added to the reconstructed position to mimic the pseudo-pixel-based readout. Concerning the z direction, given the fact that the employed BGO blocks do not have Depth Of Interaction (DOI) reconstruction capabilities, the interaction position is fixed to the center of the mono-block crystal.

The energy resolution of the silicon detector is set to 5 keV FWHM for an energy deposit of 200 keV according to the design expectations, and linearly varies with $\sqrt{E_1}$ (see equation 5.1). The energy resolution of the BGO blocks was estimated in preliminary measurements and is accordingly set to 20 % FWHM at the reference energy of 667 keV (a ^{137}Cs source has been used for the measurements).

The time resolution is set to 15.0 ns FWHM for the silicon slabs and to 3.0 ns FWHM for the BGO blocks, according to preliminary measurements performed on test detector modules at the *Grand Accelerateur National d'Ions Lourds*, Caen, France (GANIL) center in France.

The detector spatial, energy and time resolutions play an important role in the Compton camera performances. The spatial and energy resolutions of scatterer and absorber influence the position of the axis orientation of the Compton cone and its aperture angle. The time resolution impacts the coincidence window between the absorber and the scatterer, and therefore the detectors ability to distinguish between true and background coincidences.

The CLaRyS project also includes the development of a beam tagging hodoscope, composed of scintillating fibers read out by multi-channel PMs. This detector is used to synchronize the beam time and space structure to the PM detection in order to tune the detection window

reducing the background contamination. In addition to this, the spatial localization of the impinging beam bunch can be included in the event reconstruction algorithm to add constraints to the obtained solutions (see section 4.2.5). The hodoscope is not included in the simulation, but its spatial and time resolution have to be taken into account for the TOF discrimination (see section 4.2.4) and events reconstruction. They are set to 1 ns and 1 mm FWHM, respectively. The detector's spatial, energy, and time resolutions are summarized in table 4.1.

Table 4.1: Estimations of reachable resolutions with the detectors. Those resolutions are applied during the simulations.

Resolution (FWHM) at 1 MeV	Scatterer	Absorber	Hodoscope
spatial [mm]	0.9	5	1
energy	5 keV	17 %	/
timing [ns]	15	3	1

The Monte Carlo simulation is performed with the Geant4 toolkit, version 9.6.02. The particle interactions in matter are described in this work by means of the models listed in table 4.2. Additionally, the Doppler broadening and the photon polarization effects are included.

4.2.2 Beam structure

4.2.2.1 Beam structure measurements at HIT

Our group performed a set of measurements to characterize the beam time structure of the synchrotron installed at Heidelberg Ion Therapy Center, Germany (HIT), Germany (Peters et al. 2008). This set of measurements extends the results reported in Peters et al. 2008 and is then used to reproduce a realistic beam in the simulation.
The beam characterization has been performed for 200 MeV/u and 400 MeV/u primary ion energy with a two-fiber hodoscope (basic prototype of the one at present under development - see chapter 3) and the spill signal was given by the accelerator. Figure 4.2 shows the results for carbon ions at 400 MeV/u. The pulses have a spill period of 150.2 ns (Δt) and each bunch has a width of approximately 21.5 ns FWHM. The mentioned measurements have shown that the spill phase changes during the extraction: this implies that the Radio-Frequency (RF) signal from the synchrotron can not be used to trigger the pulses, so that the use of an additional beam time stamp system like the hodoscope seems required for TOF background rejection purposes.

Table 4.2: Hadronic models used in the Geant4 simulations.

Process	Protons	Ions	Neutrons
Electromagnetic		$\text{standard}_{\text{option3}}$	
Inelastic	G4BinaryCascade	G4QMDReaction (G4IonsShenCrossSection)	G4BinaryCascade + G4NeutronHPInelastic (<19 MeV)
Elastic	G4LElastic	G4LElastic	G4LElastic + G4NeutronHPElastic (<19 MeV)
Fission	/	/	G4LFission + G4NeutronHPFission(<19 MeV)
Capture	/	/	G4LCapture + G4NeutronHPCapture (<19 MeV)
Radioactivedecay	/	G4Radioactivedecay	/

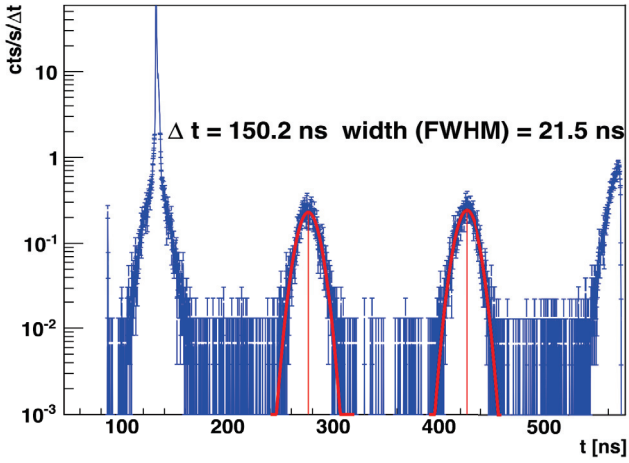

Figure 4.2: Beam time micro-structure measured from a carbon ion beam at 400 MeV/u delivered at HIT (time difference between two crossed-scintillating fibers). The pulses have an extraction period of 150.2 ns (Δt) and the bunches have a width of 21.5 ns FWHM. On the x axis the time has been measured with a two-scintillating-fiber hodoscope, with 1 ns FWHM time resolution.

4.2.2.2 Beam modeling

The two main beam particles used in clinics are considered in the simulation: protons and carbon ions. The beam range of interest is 15.2 cm in the PMMA phantom, and the associated energy is 160 MeV for protons and 305 MeV/u for carbon ions.
The beam transverse dimension is modeled with a Gaussian distribution with a standard deviation of 5 mm for protons at 160 MeV and 3.5 mm for carbon ions at 305 MeV/u. The number of incident ions for a spot in Pencil Beam Scanning (PBS) mode is 10^8 for protons (distal spot - upper intensity limit) and 10^5 for carbon ions (average spot intensity) (Grevillot et al. 2011; Krämer et al. 2000; Smeets et al. 2012). In the simulation, the beam intensity is modeled by an average number of particles per bunch. The exact number of particles in each bunch is given by a random extraction from a Poisson distribution, where the mean value is the selected beam intensity.
The beam time structure is applied at the data analysis stage. Two different time structures have been considered for this study, related to two kinds of accelerators used in clinical practice: the Ion Beam Applications, Belgium (IBA) C230 cyclotron for protons (used in 16 clinical centers worldwide) and the HIT synchrotron for carbon ions. For protons at 160 MeV, the primary particles are grouped in bunches of 2 ns (this value may vary also according to the distance between the cyclotron and the treatment room, and energy spread selection) at a frequency of 106 MHz (9.42 ns) (Roellinghoff et al. 2014). The clinical beam intensity is 3.2 nA which corresponds to about 200 protons per bunch. Concerning the carbon ion beam at 305 MeV/u, the simulated time structure refers to the measurements presented in section 4.2.2.1. We used 30 ns duration bunches at a frequency of 5.9 MHz (170 ns period). The clinical beam intensity for carbon ions is 5×10^7 ions/s during extraction, corresponding to about 9 ions per bunch. The macro-structure (50 % duty cycle with [1,5] ns period) is not considered.

The coincidence window (between scatterer and absorber events) is set to 40 ns, centered on each absorber detected interaction. This value is adapted to the detectors time resolutions. At the simulation stage, each interaction in the detector layers is collected with the related local time. The beam time structure is then applied to each single hit, and the selected coincidence window is used to retrieve scatterer-absorber coincidence events.
Table 4.3 summarizes the presented beam time structures and coincidence reconstruction features.

Table 4.3: Description of the two beam structures studied: the IBA cyclotron C230 for protons and the synchrotron installed at the HIT center in Germany for carbon ions. The macro-structure of the synchrotron, at the second time scale, is not considered here. The beam structures are applied to the simulation data.

		Protons	**Carbon ions**
Clinical features	Facility	IBA Cyclotron C230	Synchrotron at HIT
	Clinical intensity	2×10^{10} p/s	5×10^{7} ions/s
	Energy	160 MeV	305 MeV/u
Beam structure	Bunch time [ns]	3.2	30
	Period [ns]	9.4	170
	Primaries/bunch	217	9
Detectors	Coincidence window [ns]	40	40
	Time resolution (FWHM) [ns]	Si: 15 and BGO: 3	

4.2.3 Compton camera events

The Compton detection principle is based on the time coincidence of at least one scatterer and one absorber gamma interaction, where an interaction is defined as an energy deposit in a detector module, with the spatial selections detailed in section 4.2.1. As discussed in section 4.2.2, the coincidence reconstruction relies on a defined time window, fixed according to the detector resolution. In a simulation environment, different kinds of coincidence events can be distinguished and studied:

- true coincidences, created by a single photon first interacting in the scatterer stack and then in the absorber block array;

- quasi-simultaneous interaction of two secondary particles (photons – random coincidences – or massive particles), from the same incident ion of from different incident ions;

- double interaction of the same particle, not a photon (e.g. protons, neutrons).

A scheme representing the different kinds of Compton camera events is sketched in Figure 4.3. All the events not identified as true coincidences contribute to the signal background, and will be referred to background coincidences in the following.

Also in the single detector sections, different kinds of events can be identified in a simulation environment. As described in section 4.2.1, the simulation setup selects events with absorber

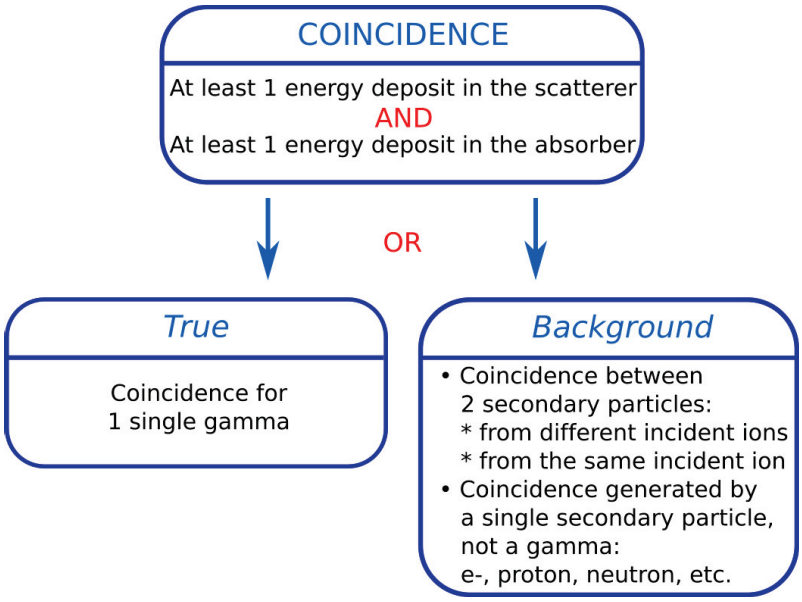

Figure 4.3: Diagram showing the different definitions of coincidences in the Compton camera. The energy deposits are selected in the silicon scatterer to be limited to neighboring strips (3 strips maximum), and in the absorber blocks the events are selected to be limited to a single block.

interactions limited to a single BGO block. Focusing on the scatterer section, among the true coincidences (same photon interacting in scatterer and absorber), three different kinds of events can be identified:

- gamma undergoing one or more interactions in a single silicon layer, with no other layers hit;

- gamma undergoing interactions in more than one silicon layer;

- Compton electron escape events: gamma undergoing Compton interaction in one layer and providing enough energy to the recoil electron to make it escape the layer where it has been created and interact in one or more of the next ones.

As mentioned in the introduction, events involving more than one photon interaction in the scatterer layers are advantageous since the total absorption of the detected prompt gamma is not required to reconstruct the Compton cone. However, the actual selection of such kind of events with respect to background interactions in real conditions is hardly achievable.

On the other hand, Compton electron escape events can be in principle identified and exploited. They are characterized by two or more scatterer layers involved: if the first Compton interaction in one layer provides enough energy to the recoil electron, it can escape the silicon plane and be detected by one (or more), neighboring planes. Thus, such events can be identified by the electron tracking, and carry additional information with respect to a Compton interaction with no electron escape. The electron tracking allows to reduce the reconstructed Compton cone to an arch of the cone, by the overlap of the cone with the electron tracking plane.

4.2.4 TOF and energy based data selection

In an experiment the collected data contain a certain number of the background coincidences (see Figure 4.3), which cannot be experimentally distinguished from true coincidences. Such a background level depends on the detector time resolutions, the fixed time coincidence window and the beam time structure, the phantom composition and the camera prototype setup. *Ad-hoc* filtering methods are applied to reduce the above described contamination.

- Time-Of-Flight: it has been demonstrated that a time-of-flight discrimination is possible and effective in reducing the background generated by massive particles interactions (M. Testa et al. 2010). The massive particles approach the detector at a lower speed with respect to photons. The time information provided by the hodoscope and the absorber can be combined to fix a detection time window and reject all the events outside the window. The time elapsed between the incident particle detection in the hodoscope and the secondary particle detection in the absorber is considered as the TOF. In order to define the appropriate time window, the TOF spectra of the collected events resulting from the irradiation of the PMMA target with 10^8 160 MeV protons have been produced for true gamma coincidences and background events, taking into account the detector resolutions. The result is shown in Figure 4.4. For this study, no time structure have been applied to the primary protons, thus only independent events have been considered. The TOF spectrum resulting from the simulation shows that:

  - the coincidences of interest (produced by prompt-gamma rays) are included in a window between 0 and 8 ns;

  - in the TOF window a comparable amount of true coincidences and background events is observed. Since we consider only independent events, this means that such background events are due to random coincidences between two prompt gammas directly or indirectly induced by the same incident ion. The background events outside the TOF window are due to massive particle interactions in the camera.

  It is worth to stress that the simulation results shown in Figure 4.4 do not include background coincidences created by prompt photons or massive particles emitted as a result of the interaction of different primary ions, and room background, mainly due to neutrons. Both components contribute to the background spectrum. In the case of the C230 cyclotron accelerator, the room background has been measured and showed a flat distribution in time (Pinto et al. 2014).

  When the beam time structure is applied to the simulated data (including the detector time resolutions), the lists of time-ordered interactions in hodoscope and absorber are produced. For each coincidence event, we look for the first hodoscope event in the 8 ns time window preceding the absorber interaction time. All events with no hodoscope coincidence in the time window are rejected.

- Energy selection: energy thresholds are defined for the event detection. 50 keV and 100 keV are set as lower threshold for the energy deposited in a single silicon layer and BGO block, respectively. For a complete event, a total absorbed energy lower limit is set to 1 MeV. In addition to the effect of background rejection, this selection also reduces the impact of partially absorbed photons.

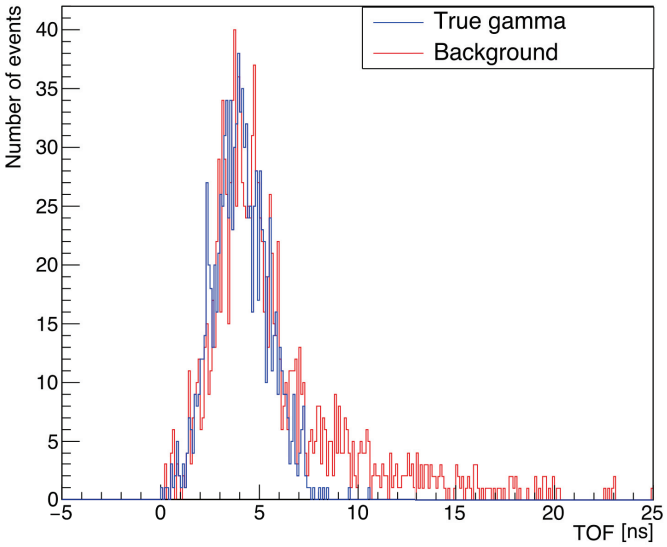

Figure 4.4: Time of flight spectra of true gamma coincidences (blue) and background events (red) obtained with 10^8 independent incident protons at an energy of 160 MeV.

Further energy selections, assuming for instance $E_1 + E_2$ equal to one of the strong gamma lines, have been applied by other authors (Draeger et al. 2017). Also, filters checking the possibility of reconstructing a Compton cone could be used. At this stage we did not consider such approaches in order to cope with simple considerations on signal to noise on raw data.

4.2.5 Reconstruction algorithms

Once the coincidences are defined and selected according to the fixed physical cuts, the distribution of the PG emission points has to be reconstructed. This can be done via analytic or iterative algorithms based on the Compton kinematics. Both are presented in the following sections.

4.2.5.1 Line-cone algorithm

The reconstruction via line-cone algorithm exploits the beam spatial information provided by the hodoscope in addition to the energy deposit and position information collected by the camera. The deposited energies in the detectors and the interaction positions define a cone surface via the Compton equation 2.10. Figure 4.5 shows a sketch of the reconstruction principle. The interaction position in the scatterer gives the cone apex and the line connecting the interaction positions in scatterer and absorber gives the cone axis. We assume that all the initial energy of the gamma ray is deposited in the camera. This assumption has been investigated and the results are shown in section 4.3.1. In order to constrain the reconstruction, the beam direction is used to limit the possible solutions (lying on the reconstructed cone surface) to two points (intersection of the beam direction and the reconstructed cone). At this stage we do not consider the lateral beam spread in the target, produced by multiple scattering. The

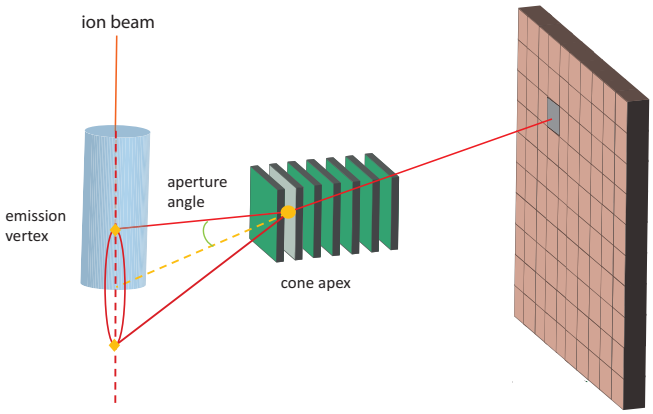

Figure 4.5: Scheme of the reconstruction principle for Compton events. For line-cone reconstruction methods, two points are extracted for each event (diamonds in the figure), provided by the intersection between the reconstructed Compton cone and the beam line. The result is a mono-dimensional profile.

set of all the reconstructed points gives the emission source distribution. The final result is an estimated of the mono-dimensional projection of the prompt gamma emission profile.

4.2.5.2 LM-MLEM algorithm

Iterative methods allow to get a three-dimensional image reconstruction, potentially by taking into account the spatial and the energy resolutions of the detectors. Several iterative algorithms have been developed for Compton image reconstruction (Andreyev et al. 2011; Gillam et al. 2011; Huang et al. 2018; Mackin et al. 2012; Schöne et al. 2017, 2010; Taya et al. 2017; Wilderman et al. 1998; Zoglauer et al. 2011).

The List Mode-Maximum Likelihood Expectation Maximization (LM-MLEM) algorithm is a MLEM version which enables one to reconstruct the image directly from the list of detected events. The features of the LM-MLEM algorithm used for this study are detailed in Hilaire et al. 2014.

4.2.6 Performance study

In this section the factors studied to assess the camera performance are explained. The study is mainly divided into four sections:

- the detection efficiency of the various types of true coincidences defined in section 4.2.3 is studied by means of mono-energetic irradiation with point-like sources as a function of the incident gamma energy;

- the absolute camera efficiency for the detection of events with a single scatterer layer

involved is studied by means of mono-energetic irradiation with point-like sources as a function of the incident gamma energy and the source position with respect to the camera. The absolute efficiency is defined as the ratio between the number of selected true coincidences and the total number of emitted gammas (see equation 4.2.6.2);

- the rate of background coincidences (for events with a single scatterer layer involved) is studied as a function of the beam intensity, with proton and carbon beams impinging on the PMMA phantom;

- the camera precision, defined as its capability of identifying the fall-off of the prompt-gamma emission profile, is tested (for events with a single scatterer layer involved) with the analytic line-cone reconstruction algorithm.

4.2.6.1 Detection efficiency of various types of true coincidences

The efficiency is crucial for the Compton camera performances and for its possible application in treatment monitoring. An efficient monitoring system should be ideally in real time, in order to allow for a treatment adaptation or interruption in case of severe issues detected in the delivered dose profile with respect to the planned treatment. In order to achieve an on-line detection of such deviations, given the limited prompt gamma emission rate per incident ion (Ortega et al. 2015), a high detection efficiency is required to perform a monitoring on, ideally, a beam spot basis. In addition to this, the absolute detection efficiency directly affects the image reconstruction quality, which is in general increased for increased statistics.

The efficiency in the detection of various kinds of true coincidence events (including the detector geometrical acceptance and detection efficiency), with specific interaction patterns in the scatterer section, detailed in section 4.2.3, has been studied with the irradiation from point-like mono-energetic gamma sources. The setup is the same as Figure 4.1, with the exception of the PMMA phantom which is removed to leave the gamma source in air. Different energies have been tested to mimic different prompt gamma lines: 300 and 500 keV, and 1, 2, 4 and 6 MeV. No time structure is reproduced for this part of the study. In addition, the rate of events with an almost full primary energy absorption has been studied for the various kinds of coincidences as a function of the primary gamma energy. The threshold for the energy absorption has been set to 90 % of the primary gamma energy. The results of this preliminary study (see section 4.3.1) determined the choice to limit the next investigations to events with a single scatterer plane involved; all events with more than one scatterer layer hit have been rejected for the analysis described from section 4.2.6.2 and the results presented from section 4.3.2.

4.2.6.2 Absolute detection efficiency

The absolute efficiency ϵ for the detection of coincidences with a single scatterer plane hit is defined as:

$$\epsilon = \frac{N\gamma_{\text{coinc}}}{N\gamma_{\text{total}}}, \tag{4.2}$$

with $N\gamma_{\text{coinc}}$ the number of gamma events corresponding to the selected true coincidences, $N\gamma_{\text{total}}$ the total number of emitted gammas.

In addition to its dependence on the gamma energy in the range 300 keV – 6 MeV (see section 4.2.6.1), the absolute efficiency has been also studied as a function of the point-like source position. The source is set in the range −300 mm to +300 mm (with the center of the camera transverse section set in the position 0), and moved with variable length steps, up to 1 cm. The movement followed the transverse axis of the camera.

4.2.6.3 Rate of background coincidences

As the Compton detection principle relies on time coincidences, in addition to the main importance played by the detectors energy resolutions, the beam intensity and time structure are important parameters to be studied in order to assess the possible clinical implementation of a Compton detection based monitoring of ion beam treatment. The ability of the detection system to distinguish between true and background coincidences, i.e. the resulting signal over noise ratio, strongly depends on the beam time structure. The number of true and background coincidences is studied as a function of the beam intensity, before and after data reconstruction via line-cone algorithm (see section 4.2.5). The events reconstructed outside the volume are indeed rejected. To be noticed that, following the results of the efficiency study (see section 4.3.1), only events with one single scatterer layer hit are selected.

The range of intensities is defined in order to cover a wide range of operation: from a very low beam intensity to a realistic clinical particle rate. Therefore, for proton and carbon ions, the lowest beam intensity is set to 0.1 particles per bunch on average, while the upper limit is set to 217 protons or 70 carbon ions per bunch. All the simulations are performed with a total of 10^8 primary protons and 2×10^5 primary carbon ions (see section 4.2.2.2). For the analysis of the results, the coincidence yields are scaled to the number of incident ions and the beam intensity to the average number of ions per bunch.

4.2.6.4 Camera precision

The camera precision is defined as the difference between the predicted PG Fall-Off Position (FOP) (according to the treatment planning) and the detected one. It has been studied with proton beams. A preliminary reconstruction test has been performed with the two algorithms (line-cone and LM-MLEM) and 10^8 incident protons, at two beam intensities: the clinical intensity – 200 protons per bunch – and a reduced intensity of 1 proton per bunch. For the LM-MLEM reconstruction, the volume is set to $20 \times 40 \times 1$ cm^3 around the expected FOP, with a $101 \times 201 \times 5$ voxel matrix. To be noticed that the two reconstruction methods produce different results: the line-cone method is based on the beam direction information, so that it naturally returns a mono-dimensional profile as result, while the LM-MLEM method is able to reconstruct the PG emission distribution in three dimensions. A mono-dimensional projection along the beam direction is used for the fall-off identification and for a direct comparison with the line-cone method. As shown in section 4.3.4, as a result of this preliminary evaluation, the camera precision is evaluated with a beam intensity of 1 proton per bunch, with the analysis described in the following paragraphs.

A reference profile has been defined as the line-cone reconstructed distribution of emission positions at high statistics (10^{10} incident protons). The *SmoothKern* method, with the Nadaraya-

Watson regression (Nadaraya 1964; Watson 1964), is used to smooth such a reference profile in order to reduce relative statistical fluctuations. A Region Of Interest (ROI) ranging from $y = 0$ mm to $y = +100$ mm is defined around the expected FOP, located at $y = +50$ mm in the phantom. The reference profile is modeled in the ROI by a linear combination of Non-Uniform Rational Basis Splines (NURBS) (D. F. Rogers 2001). The retrieved FOP is used as reference and compared to the ones at lower statistics: the reference profile is indeed normalized in order to obtain lower statistics distributions, in the range $1{\times}10^8$ to $5{\times}10^9$ incident protons. Statistical fluctuations, randomly extracted following a Poisson law, are generated on the obtained PG profiles to mimic realistic reconstructed distributions. This method is used to reduce the analysis time.

For each chosen incident proton statistics, 1000 PG profiles are generated and a custom minimization method is applied to deduce the minimal shift between the reference profile and the one at lower statistics. The minimization algorithm shifts the reference profile in a 60 mm range, between −30 mm and +30 mm with respect to the initial position, with a step of 0.1 mm, and for each position it compares its position to the low statistics profile by calculating the χ^2 as follows:

$$\chi^2 = \sum_{i=1}^{N_{bin}} (y_{\text{sample,i}} - y_{\text{NURBS,i}})^2, \tag{4.3}$$

where for every bin i, y_{sample} is the number of events in the low statistics profile, y_{NURBS} is the number of events for the reference profile NURBS (scaled at the same low statistic). The described approach is robust and allows to avoid artifacts at low statistics. The global minimum of all the calculated χ^2 is then retrieved and the shift associated to this value is added to the shift distributions. The standard deviation of the distribution resulting of the thousand results gives the precision of the camera for a given number of incident protons.

4.3 Results

The possible implementation of the CLaRyS Compton camera as a monitoring system for ion beam therapy has been investigated. The camera has been exposed to point-like gamma sources to study the detection efficiency. A PMMA cylindrical phantom has been simulated and exposed to proton and carbon beams at increasing intensities for an analysis of the prompt gamma detection environment (background, random coincidence contamination). The camera precision in the identification of the fall-off of the prompt gamma emission profile has been investigated. In this section we show the obtained results.

4.3.1 Detection efficiency of various types of true coincidences

Figure 4.6 shows the Compton camera efficiency in detecting the various kinds of true coincidence events described in section 4.2.3, as a function of the gamma energy in the prompt-gamma energy range (between 300 keV and 6 MeV). The results show how the single events, consisting in the coincidence between an energy deposit in a single scatterer layer and in one single absorber block, decreases at increasing energy, in favor of an increase in the number of

electron escape events (consisting in one primary photon Compton interaction in one scatterer layer, at least one interaction of the Compton escaped recoil electron in a different scatterer layer, and one primary photon interaction in one single absorber block). At the maximum investigated primary gamma energy, the amount of electron escape collected events is more than 35 %. However, the single events represent more than 60 % of the total amount of collected events in all the explored energy range, so that the results in the following paragraphs are focused on this kind of events (with the other kinds of events rejected at the analysis stage), as first approach for a feasibility study. The amount of 3 or more photon-interaction events is limited and negligible over the whole energy range.

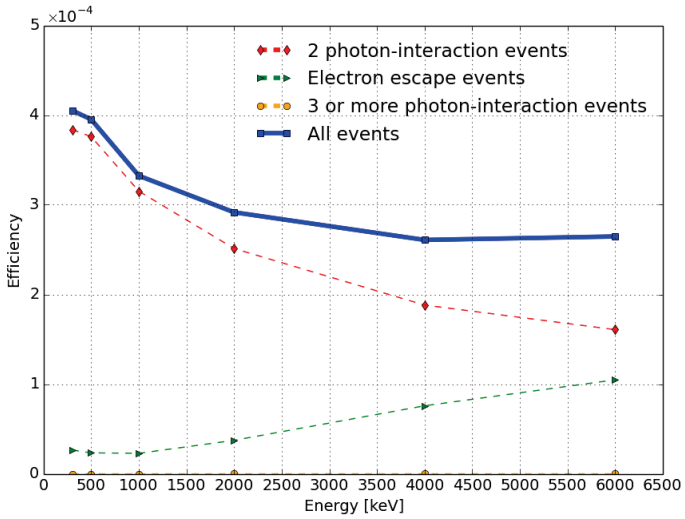

Figure 4.6: Compton camera efficiency as a function of the gamma energy for the different kind of possible coincidence events (see section 4.2.3), as a function of the gamma energy.

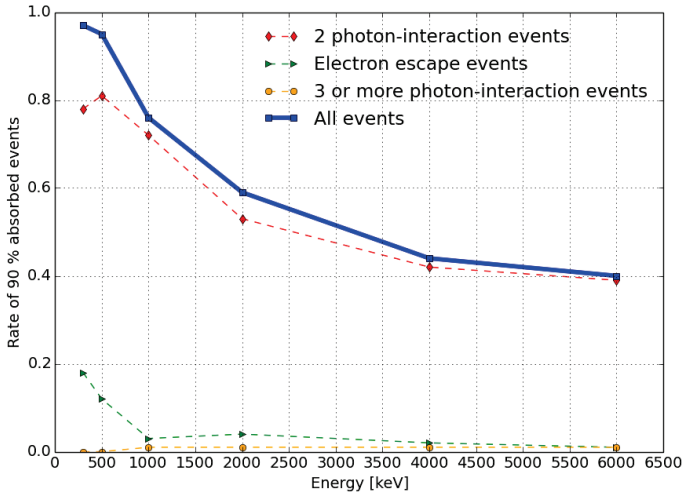

Figure 4.7: Ratio between coincidence events with more than 90 % of the primary photon energy absorbed in the detector layer and all detected coincidences as a function of the gamma energy. The curves shown the results for the different kind of possible coincidence events and for the all collected coincidences.

Figure 4.7 shows the rate of events with more than 90 % of the primary gamma energy deposited in the detector layers. The rate of 90 % absorbed events is reported for the different kinds of detected coincidences. As expected, the rate of almost fully absorbed events decreases as the energy increases, in a range between more than 80 % and 40 % for 300 keV

and 6 MeV primary photon energy, respectively. The most of the 90 % absorbed events are single events, with the electron escape and multiple ones negligible for primary gamma energies above 1 MeV. At lower energy, the Compton recoil electron is often able to exit the scatterer layer where the Compton interaction takes place, but can be lost without further interactions, so that this kind of events is considered as single with an energy absorption below 90 %. This can explain the decrease of single almost full absorption at 300 keV. If the electron interacts with a scatterer layer, it is generally absorbed at low energy, explaining the increasing electron escape absorbed events below 1 MeV. As mentioned, these results led to the choice of limiting the further analysis (from section 4.3.2) to events with a single scatterer layer involved, as first approach.

4.3.2 Absolute detection efficiency

Figure 4.8 shows the absolute gamma detection efficiency as a function of the gamma source position with respect to the center of the camera in the transverse plane. On the left side, we show the results achieved with an ideal detector (i.e. without energy detection threshold). On the right side realistic energy thresholds (50 keV for the scatterer layers and 100 keV for the absorber) are applied on each detector section.

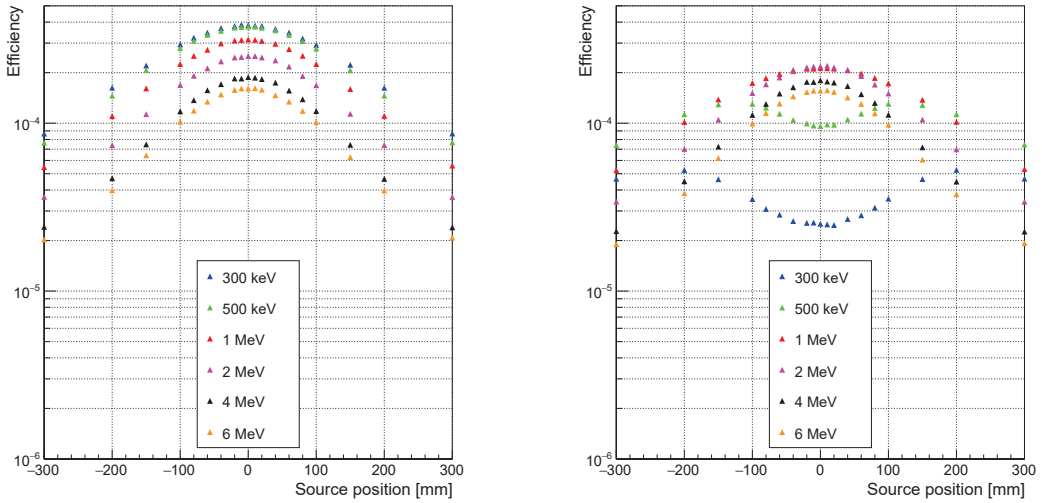

Figure 4.8: Absolute Compton camera efficiency as a function of the gamma source position for different gamma energies, in the range between 300 keV to 6 MeV. The left side shows the camera efficiency with no detection energy threshold. In the right side, detection energy thresholds are applied to reproduce a realistic scenario (lower limit of 50 keV for the scatterer, 100 keV for the absorber). These values can change for the final configuration, according to the detector energy resolutions achieved.

As expected according to the interaction probability energy dependency, the efficiency is higher for low gamma energies, and it lies in the range 4×10^{-4} at 300 keV and 1.5×10^{-4} at 6 MeV at the center of the camera. Moreover, it can be noticed how the efficiency drops as the point source is shifted away from the camera center: efficiency reductions of a factor approximately 4 and 8 at 500 keV and 4 MeV, respectively, are detected with the source

at 300 mm distance from the camera center, with respect to the value detected in central position. This effect is more important for high energies, for which the incident gamma is less deflected in the scatterer for the same energy deposited compared to a low energy gamma. Figure 4.8b shows the effect of realistic camera detection thresholds as opposed to ideal detection. The gamma detection efficiency drops of a factor ranging from about 1.25 to more than an order of magnitude for the central detection area for energies in the range 300 keV to 2 MeV respectively. The effect is reduced at increasing distance of the source from the center of the camera. Negligible effects are detected for positions with a distance greater than 200 mm from the center of the camera, and for any distance at energies above 2 MeV, while the efficiency is reduced in the central area of the camera for energies below 4 MeV.

4.3.3 Rate of background coincidences

In Figure 4.9, the different components of the signal resulting from the PMMA exposure to proton and carbon ion beams are shown as a function of the beam intensity. The true coincidences represent scatterer-absorber time coincidences generated by the same gamma ray (only events with hits in a single scatterer layer). All the other coincidence types compose the background (see section 4.2.3). The collected data sets are reported with and without the applied time-of-flight discrimination, mainly employed for neutron rejection, as mentioned in section 4.2.4.

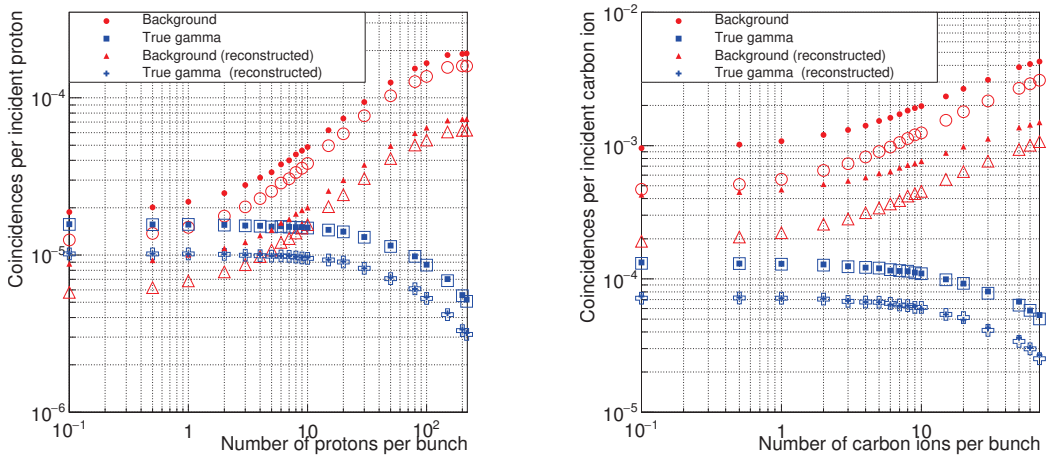

Figure 4.9: Coincidences yield for protons (left) and carbon ions (right) as a function of the beam intensity. The intensity is reported as number of incident particles per bunch. The filled markers correspond to the collected data without time-of-flight discrimination, while this cut is applied to the data reported with empty markers. Moreover, the yields are given before and after the profile reconstruction with the line-cone algorithm, which rejects events reconstructed out of the target volume.

In Figure 4.9(a) and (b) the amount of true gamma coincidences and background events are reported before and after reconstruction via line-cone algorithm as a function of the beam intensity for proton (a) and carbon ion (b) beams. In addition to this, for each curve realized with the complete collected data set, the related one obtained after time-of-flight selection of

events is sketched (empty symbols). All the curves have been normalized to the number of incident ions.

The amount of background events (mainly random coincidences – due to quasi-simultaneous interactions of different gammas) increases with the increasing beam intensity: a factor of about 30 with respect to true gamma events is obtained for proton beams at the intensity of 200 protons per bunch with no event selection, while a factor more than two times higher is reported for carbon ions in the same conditions. The TOF selection can slightly improve the Signal-to-Noise Ratio (SNR) by reducing the amount of background events. The amount of true gamma events and background events becomes similar at the intensity of about 1 proton per bunch. As expected by the observation of Figure 4.4, for intensity values below 1 proton per bunch, the ratio between true and background events remains stable.

4.3.4 Camera precision

The camera precision in the fall-off identification is investigated with proton beams. A data set corresponding to the irradiation of the PMMA phantom with a mono-energetic 160 MeV proton beam spot (10^8 protons) has been collected and analyzed at the clinical intensity of 200 protons per bunch and 1 proton per bunch on average (where we obtained a ratio between true and background coincidences of approximately 1). Figure 4.10 shows the results of the line-cone and LM-MLEM reconstructions of the simulated data for the two beam time structures applied at the analysis stage.

The results obtained for a clinical intensity of 200 protons per bunch qualitatively show how the fall-off of the PG profile cannot be retrieved with the two applied reconstruction methods, due to the contamination of background events. The fall-off can be identified at the reduced intensity of 1 proton per bunch for both line-cone and MLEM reconstructed data. The line-cone algorithm is able to give a prompt feedback on the ion range, and eventually trigger treatment emergency stop in case of major deviations of the retrieved range with respect to the treatment planning, while the LM-MLEM algorithm requires long calculation time. For these reasons, the camera precision is studied with the line-cone algorithm at the reduced intensity of 1 proton per bunch on average, at which a comparable rate of true and background events is expected, following the results shown in section 4.3.3. The iterative reconstruction method can in principle provide enhanced spatial response in the fall-off identification, so that the result obtained with the analytic approach can be considered as the lower limit for the camera precision. A total of 10^{10} protons has been simulated to define the reference PG profile, with a beam intensity of 1 proton per bunch on average, and then different low statistics profiles have been produced for the precision estimate as explained in section 4.2.6.4. The high statistics profile reconstructed via line-cone algorithm is shown in Figure 4.11a with the related NURBS fit. A NURBS fit of a low statistics sample (10^8 incident protons) is shown in Figures 4.11b. Poisson extracted fluctuations have been generated on the profile in the range 30 – 70 mm, where the fall-off position is expected to be located. The retrieved optimal shift distribution is shown in Figure 4.12 for 10^8 incident protons as well.

The analysis method described in section 4.2.6.4 is applied to the different PG obtained profiles to retrieve the camera precision in the fall-off identification. The results are shown in Figure 4.13.

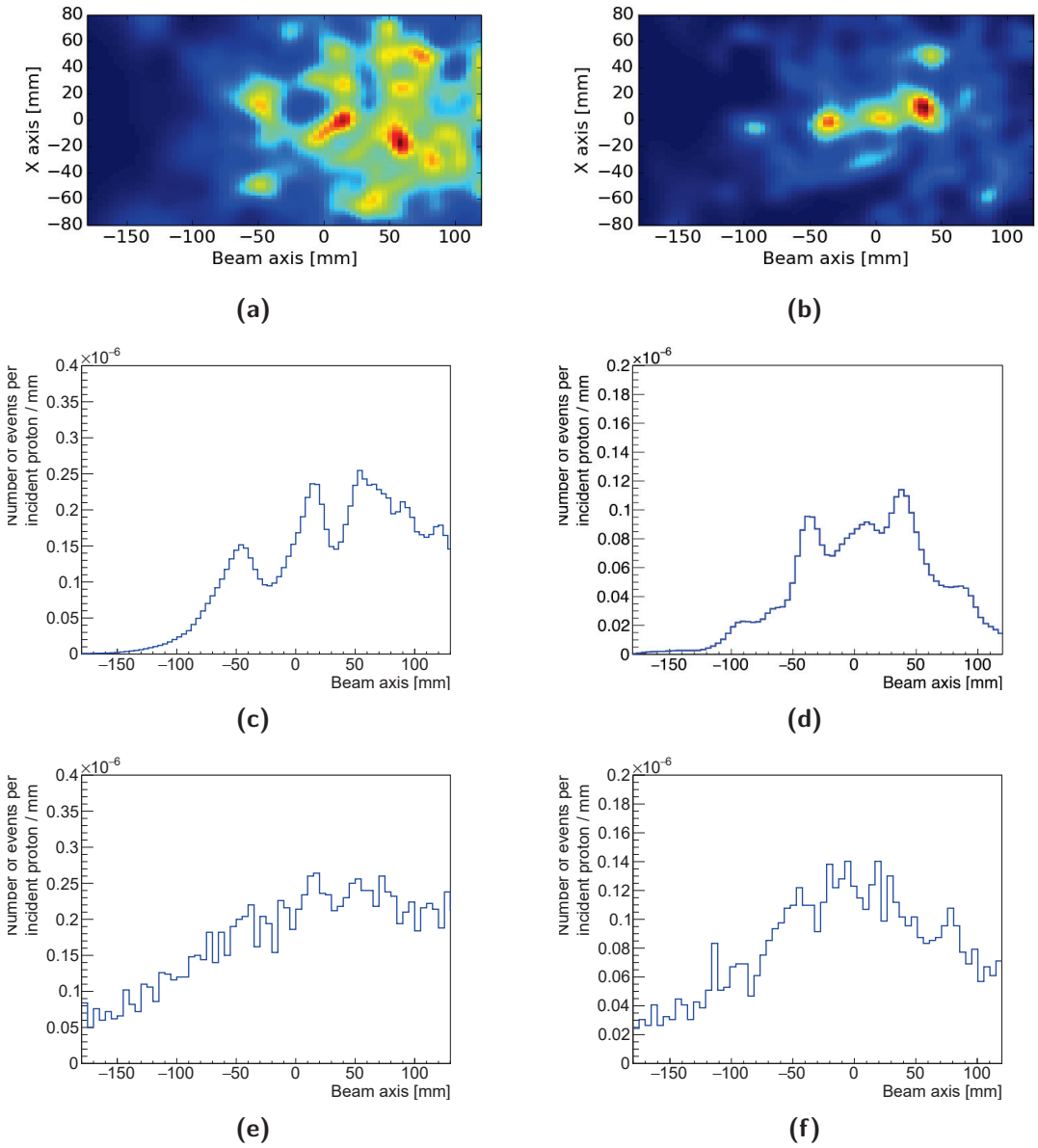

Figure 4.10: Line-cone and LM-MLEM reconstruction for a 160 MeV proton beam, 10^8 total incident protons. In the left column, the beam intensity is 200 proton per bunch on average; in the right one, the beam intensity is 1 proton per bunch on average. The Compton camera is centered at the expected Bragg peak position, $y = +50\,\text{mm}$. The time-of-flight event selection is applied on the collected data set. 20 iterations are performed for the MLEM reconstruction. The top row shows the MLEM reconstructed distribution two-dimensional projections in the plane (x, y), parallel to the camera entrance surface. The position $x = 0\,\text{mm}$ corresponds to the center of the PMMA phantom and the y direction corresponds to the beam axis, with the target entrance at $y = -100\,\text{mm}$ and the target end at $y = +100\,\text{mm}$. The center row shows the mono-dimensional profiles along the y axis. The expected profile fall-off is located at $y = +50\,\text{mm}$. The bottom row shows the profiles obtained by means of the line-cone algorithm for the same time-of-flight selected data.

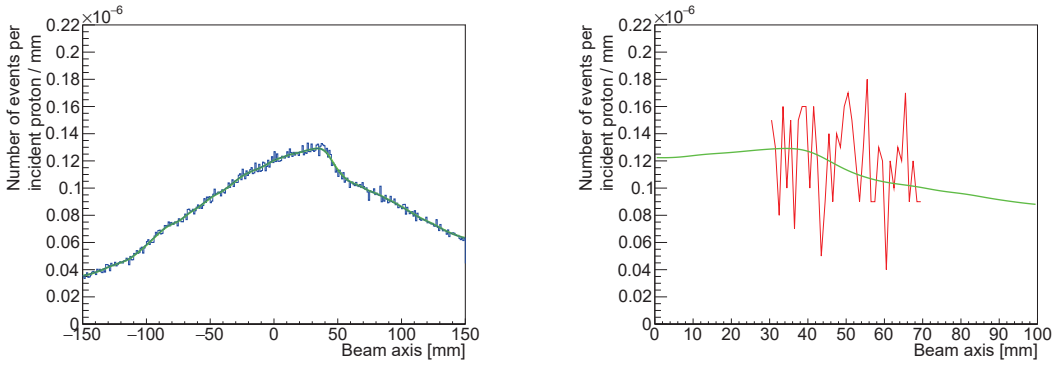

Figure 4.11: (a) Line-cone reconstructed reference profile (blue histogram) for 10^{10} incident protons, at a beam intensity of 1 proton per bunch, with the NURBS related curve (green solid line). (b) NURBS curve (green) obtained after the normalization to a 10^8 incident protons statistics and the profile realization with the Poisson generated statistical fluctuations (red); the curves are centered on the expected FOP at 50 mm.

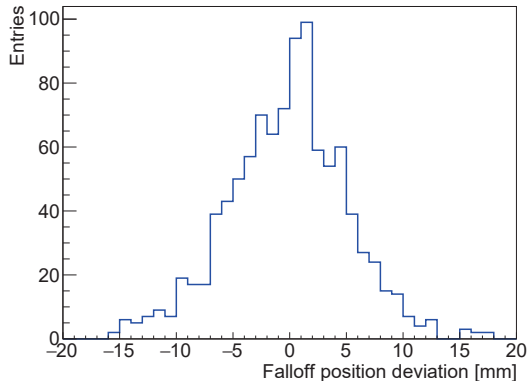

Figure 4.12: Distributions of the fall-off position deviation with respect to the fall-off position of the high statistics reference profile for 1000 realizations with 10^8 primary protons, obtained with line-cone reconstruction. The Root Mean Square (RMS) of these distributions represents the Compton camera precision for the selected statistics.

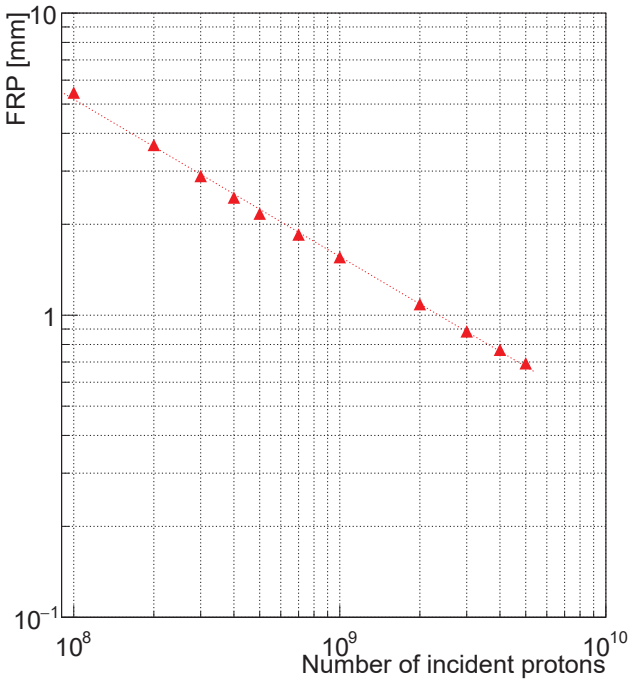

Figure 4.13: Fall-off Retrieval Position (FRP) with the line-cone reconstruction algorithm as a function of the total number of incident protons, in the range 1×10^8 to 5×10^9.

A linear behavior with a slope of –1/2 (in log-log scale), highlighted by the performed linear fit of the obtained curve, is verified with increasing number of primary protons, starting from the single spot scale of about 10^8 primaries, up to 5×10^9 protons, which can correspond to the monitoring of a group of spots with the same planned range. As expected, the retrieved precision increases for increasing statistics, in the range 5.5 – 0.7 mm.

4.4 Discussion

We studied in this simulation work the performance of the CLaRyS Compton camera prototype and its possible implementation as PG detector for ion beam therapy monitoring. The proposed analysis is focused on four main points: detection efficiency for various kind of coincidence events, and for events with a single scatterer layer hit absolute gamma detection efficiency, true and background coincidence rate and camera precision in the identification of the prompt-gamma emission profile fall-off.

The gamma detection efficiency has been measured with the detector exposed to gamma sources at six different energies, in the prompt-gamma energy range. The relative detection efficiency has been studied considering the three possible kinds of true coincidence events: single Compton interactions in the scatterer (2 photon interaction events), Compton recoil electron escape events and events with multiple gamma interactions in the scatterer (3 or more photon-interaction events). The coincidences composed of one single Compton interaction in one of the scatterer layers and an energy deposit in one single absorber blocks represent

the majority of the collected events in the whole explored energy range. However, for energies above 1 MeV the amount of electron escape events becomes significant. Such kind of events can be ideally exploited in the reconstruction, and the selection can be based on tracking analysis (if the escaped recoil electron interacts in more than one scatterer layer). In the camera performance evaluation study, only single events have been selected as first approach for a feasibility study of the Compton camera application in ion range monitoring. All the results discussed in the following have been obtained with such an event selection.

The absolute camera efficiency variation as a function of the source position has been reported, with an ideal detector and with the application of detection energy thresholds in scatterer (50 keV) and absorber (100 keV). For low energies, below 2 MeV, the increased efficiency in the central section of the camera active surface – shown in Figure 4.8a – is linked to the increased relative number of photons approaching the camera with small angles. These photons are more likely undergoing Compton scattering with a reduced energy deposition, which is recorded by an ideal detector and rejected by the fixed energy threshold. The effect is all the more important as the primary gamma energy is limited, creating the energy dependence of the efficiency reduction observed in the results in Figure 4.8a. Regarding the dependence of the efficiency on the Compton camera position, an accurate setup with respect to the expected Bragg peak position appears mandatory for the detection optimization.

The study of the signal-over-noise ratio as a function of beam intensity was performed (see Figure 4.9). The results show that, at clinical intensities, this ratio is very low. The TOF selection is effective in the case of carbon beams, where a significant proton and neutron contamination is expected. If we consider the case of proton beams, the amount of background and true coincidences is comparable at an intensity of about 1 proton per bunch, so that a clinical intensity reduction should be necessary to fit this configuration. The profile fall-off retrieval could not be achieved at clinical proton beam intensity for a single spot with the tested reconstruction methods. Even if a possible image reconstruction is not excluded by the low signal-over-noise ratio detected at realistic beam intensity with increased statistics (a group of spots with same expected range), given the fact that the background coincidences are distributed in an homogeneous way in the reconstructed volume, an intensity reduction can be an option in order to obtain more significant data sets. It must be noticed that the need for online check of Bragg peak position is all the more necessary for distal spots, which are in general the firsts to be treated, so that a beam intensity reduction at the beginning of the treatment can be foreseen in case an accurate monitoring is strictly needed. This would not affect the treatment delivery, nor the planned patient rate in the clinical work-flow; indeed, the spreading of the time duration for few spots is of the order of one second. In the case of carbon ions, the larger amount of secondary neutron produced during the patient treatment seems to require other background rejection methods in order to lead to an advantageous signal-over-noise ratio. Note also that online filtering strategies may be used to improve the quality of the data (see Figure 4.7): already in Figure 4.9, one can notice that the amount of reconstructed events is about half that of true gamma, which means that partial absorption in the absorber leads to events which cannot be reconstructed via the line-cone method. More refined pre-analysis could be used and have been proposed in Draeger et al. 2017. Note also that the line-cone reconstruction used here is quite rough: the two reconstruction points are systematically considered, although further selection may refine the procedure and improve the profile quality (for instance, rejecting points outside the planned treatment volume). Alternative approaches for the optimization of the signal-over-noise ratio should be focused on the camera geometrical design. In Fontana et al. 2017b we tested the same prototype with

two absorber configurations, showing an absolute efficiency reduction of a factor approximately two when reducing the absorber from a 8 × 6 block matrix to a 3 × 3 one. Such a significant absorber size reduction is expected to drastically reduce the background coincidence contamination, thus improving the signal-over-noise ratio, with not dramatic efficiency degradation for the FOP monitoring purpose. Moreover, to this efficiency reduction corresponds an increased spatial resolution, probably given by the selection of gamma scattered with small angles. This hypothesis is confirmed by the efficiency variation generated by the applied energy thresholds, as discussed before. The design optimization could also foresee the reduction of the number of silicon layers, with a further expected reduction of the background coincidence rate. In addition to the aforementioned advantages, a more compact configuration allows for the implementation of several detector heads, which can be set at different angles and provide additional spatial information, in particular in view of three-dimensional imaging. In case the highest possible efficiency is required, the distance between scatterer and absorber can also be modified, knowing that for reduced distances the efficiency is increased because a minimal amount of scattered photons escapes the absorber field of view. On the other hand, a reduction of the inter-detector distance is not recommended for accurate TOF measurements (for fixed target-scatterer distance), given the uncertainty added by the detectors time resolutions. In addition to this, also the spatial resolution is affected by a reduction of the scatterer-absorber distance, given the increased amount of photons scattered with large Compton angles included in the collected events. Indeed, large angle scatterings tend to degrade the spatial resolution. Dedicated design studies will be performed in the next future to address the proposed improvements.

The camera precision has been estimated with the line-cone reconstruction algorithm for proton beams at the reduced intensity of 1 proton per bunch on average. Starting from a reference prompt gamma emission profile obtained at high primary particle statistics (10^{10}), 1000 realizations per number of incident protons have been produced by normalizing the high-statistics profile and generating random statistical fluctuations. A robust minimization algorithm has been applied to define the shift of the identified profile fall-off with respect to the reference one. The camera precision in the fall-off identification rapidly increases for increasing primary particle statistics, with a slope of –1/2 in log-log scale, as already shown in Roellinghoff et al. 2014 and in accordance with statistical expectations. A sufficiently good precision is achieved on a spot basis for proton beams, where the precision is about 5.5 mm with the analytic reconstruction method: a qualitative monitoring of each spot seems then possible. In order to achieve millimeter precision, some spot grouping methods must be considered, or multiple-head detector configurations, e.g in a ring geometry. The LM-MLEM iterative algorithm, which is now the standard for this kind of image reconstruction, in principle guarantees a better fall-off identification precision, as qualitatively shown in Figure 4.10, at the expense of longer calculation time. The developed precision analysis process cannot be directly applied to profiles reconstructed via iterative algorithms, and long calculation time is required for the reconstruction of a number of profiles compatible to the one used for the line-cone reconstruction based analysis. Accelerated reconstruction solutions are being explored, and a dedicated study will be performed. The employed version of the LM-MLEM algorithm, used to reconstruct the data obtained with 10^8 protons, has been not able to reconstruct data sets analyzed at clinical intensities (200 protons/bunch on average). However, MLEM does not exploit the additional information provided by the knowledge of the beam position in the transverse plane. In future studies, such *a priori* information should be considered in order to improve the reconstruction rapidity and image quality. In addition to this, more restrictive data selection during reconstruction can in principle improve the image quality and speed up

the reconstruction process. At present, given the long calculation time required by the iterative algorithm and the presented precision performance, the line-cone reconstruction method can still be an option for on-line treatment check, when safety limit can be fixed in order to exclude severe deviation from the treatment planning and an interruption of the dose delivery in real time can be foreseen. Moreover, the TOF information can be included in the line-cone reconstruction method in order to constrain the emission on a single point, and improve its accuracy. Finally, it should be noticed that the presented study is focused on events involving one single scatterer layer: the inclusion of electron escape events can increase the reconstruction accuracy, given the constraint imposed on the reconstructed surface by the electron tracking information. Further study is needed to assess the gain in precision provided by such kind of events.

The Compton detection principle has already proven its potential in detecting prompt gammas for ion beam therapy monitoring purpose, and the CLaRyS Compton camera prototype shows promising results for this application. The detector is now at the final development stage, its components are being tested on beam in clinical facilities and a first beam test with a complete system is foreseen before the half of 2020. New simulation studies are to be carried out to benchmark the Compton camera device to other detection systems, like PET machines or collimated detectors, already used or tested in clinics for ion beam therapy monitoring. The proposed study verify the feasibility of range monitoring in particle therapy with the CLaRyS Compton camera with a minimal approach, and improved performance are expected after detector and reconstruction method optimization.

5

Compton camera application in nuclear medicine

Most of the results presented in this chapter have been published in (Fontana et al. 2017a) and (Fontana et al. 2017b).

Contents

5.1 Introduction

Single Photon Emission Computed Tomography (SPECT) is one of the most widespread techniques for nuclear medicine diagnostics examinations. In most clinical cases, a radiotracer is injected in the patient and the emitted γ-rays are collected by scintillating detectors coupled to physical collimation systems. This process leads to the reconstruction of a planar transmission image. Such a kind of imaging tool relies on the idea proposed by Hal Anger (Anger 1958, 1964), and it is now commercially available in different variants with specific features and applications. A complete system is often composed of at least two rotating detection heads, allowing a tomographic data acquisition and the reconstruction of a three-dimensional image of the radio-tracer distribution (see chapter 1 for further details).

The main consequence of the collimation system is a forced trade-off between sensitivity and spatial resolution: The spatial resolution is completely determined by the collimator geometry, and it can only be increased by reducing the collimator hole size, at the expense of a reduction in the detector sensitivity since fewer photons survive the mechanical selection. Moreover, the collimator thickness and septa limit the primary energy acceptance, and the performance of Anger cameras generally downgrades as the energy increases.

In order to overcome this mechanical collimator limitation, it is natural to move towards an "electronic collimation", where the emitted photons are tracked and the emission point is reconstructed via Compton kinematics, and so to the application of Compton cameras in this field (Everett et al. 1977; Singh 1983).

L. Han and colleagues (Han et al. 2008) have performed a simulation work comparing a standard Anger camera and a Compton camera prototype for a fixed source energy of 364 keV (Iodine-131 (^{131}I) gamma ray emission). The expected enhanced detection efficiency associated to the Compton camera with respect to the Anger system was estimated to a factor 20 at the tested energy, while the spatial resolution was compared for equal imaging time.

Starting from the results of Han and colleagues, we tested in simulation the performance of the CLaRyS Compton camera prototype (see chapter 3) for the application in SPECT. The aim of this simulation work consists in extending the aforementioned study to a wide energy range, with simplified analysis methods. The CLaRyS prototype is compared to the Infinia Anger camera delivered by General Electrics Healthcare (GE Healthcare 2006). The detector performances are compared in terms of efficiency and spatial response with the exposure to mono-energetic point-like radioactive sources at different energies, ranging from 245 keV to 2.614 MeV. The noise components related to the target (patient), such as photon attenuation, photon diffusion, patient movements, are common for both detectors and not considered in this context.

It should be noticed that the Compton detection principle requires coincidences between the two detector sections (scatterer and absorber), so that the random coincidence rate plays a fundamental role in the complete system performance, like in Positron Emission Tomography (PET) machines. The effect of these random coincidences will therefore be investigated. Moreover, a reliable Compton scattering cone reconstruction requires a precise energy resolution for the scatterer section of the detector. The influence of this parameter will be studied. Finally, the Doppler broadening effect will be quantified to give the physical limits of the Compton

imaging technique knowing that silicon corresponds to the lowest Z material available for gamma detection with precise energy resolution. A comparison with a different possible scatterer material is also performed for verification.

All the obtained results are discussed with direct reference to (Han et al. 2008), focusing on the possible advantages offered by the use of a Compton camera (in particular the CLaRyS prototype), which intrinsically introduce the possibility to update the clinical standards in terms of source kinds, energies and activities, examination duration, patient dose, imaging techniques.

5.2 Material and methods

In this section, the sources of gamma rays simulated for the study are presented and discussed and the two simulated systems are described in detail, as well as the proposed analysis techniques. In addition to this, some comments are given about the criteria chosen to represent a relevant comparison between the two investigated detectors.

5.2.1 Radioactive sources

Both simulated systems have been exposed to mono-chromatic point-like gamma sources in air. The performance of the two cameras has been studied in terms of spatial resolution and detection efficiency as a function of the gamma source energy, related to actual radioemitters, already used in clinical practice or suggested for this kind of application in previous works (Nurdan et al. 2015). The explored energy range was chosen having in mind the possible clinical usage of Compton systems like the one developed by the CLaRyS collaboration, to extend the present field of application of SPECT imaging.

In Table 5.1, the characteristics of the considered radioactive sources are given. Most of the sources do not emit gamma rays at a single energy, but only the ones selected for this study are presented in the table, together with the related branching ratio.

5.2.2 Compton camera simulation and data analysis

5.2.2.1 Simulation settings

The simulation code for the Compton camera was developed with GEometry And Tracking 4 (GEANT4) v.9.6 and the camera design is based on the specifications of the prototype at present under development by the CLaRyS collaboration, detailed in chapter 3. It should be noticed that the real size of the detector components slightly differs from the ones reproduced in simulation, which have been used in the code for simplicity. The geometric setting of the camera has initially been optimized for the application in ion therapy monitoring via prompt-gamma emission (see chapter 4) and has been adapted for SPECT for this study in order to maximize the similarities between the two systems (Compton and Anger camera) in terms

Table 5.1: Radioactive sources used in the comparison study. Decay mode list: EC for electron capture, $\beta-$ for electron emission, $\beta+$ for positron emission, IT for isomeric transition. Half-life expressed in days (d), hours (h) or minutes (m). Data extracted using the National Nuclear Data Center On-Line Data Service from the Evaluated Nuclear Structure Data File database, file revised as of (2017-05-17) (Bhat 1992).

Isotope	Gamma energy [keV]	Branching ratio [%]	Decay mode	Half-life
Indium 111	245	94.1	EC	2.8 d
Iodine 131	364	81.5	$\beta-$	8 d
Yttrium 91m	555	95.0	IT	50 m
Bismuth 212	727	6.7	$\beta-$	60 m
Iodine 132	773	75.6	$\beta-$	2.3 h
Iron 59	1099 – 1292	56.5 – 43.2	$\beta-$	45 d
Zinc 65	1116	50.0	EC / $\beta+$	244 d
Calcium 47	1297	67.0	$\beta-$	4.5 d
Magnesium 28	1342	54.0	$\beta-$	21 h
Sodium 24	1368	100.0	$\beta-$	25 h
Potassium 42	1524	18.1	$\beta-$	12 h
Thallium 208	2614	99.8	$\beta-$	3 m

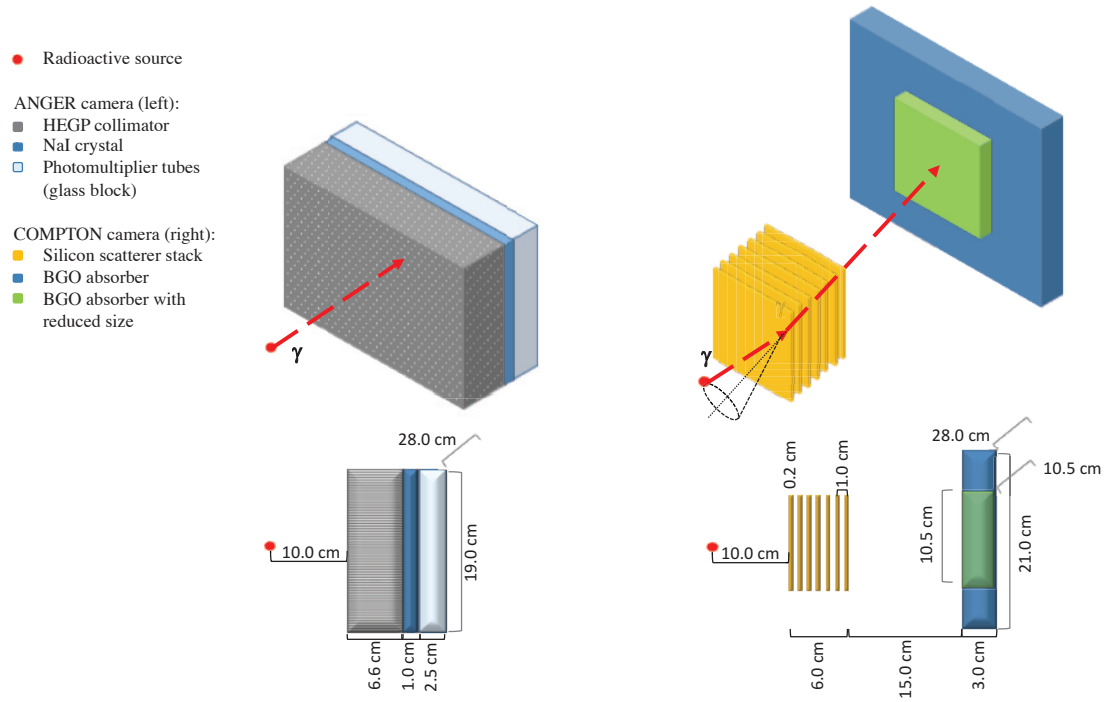

Figure 5.1: Sketch of the simulated geometry of the two systems: Anger camera (left) and Compton camera (right), in 3 dimensions (top line) and side projection (bottom line).

of detector acceptance, as detailed in the following. A SPECT specific optimization would depend on the choice of the particular gamma energy and it has not been studied yet.

The distance between the last silicon plane (center) and the center of the absorber is set to 15 cm (see Figure 5.1). Moreover, the absorber size has been adapted to be as close as possible to the Anger camera detector, maintaining the real Bismuth Germanium Oxide - $Bi_{12}GeO_{20}$ (BGO) block size. As a result, a matrix of 8×6 blocks has been arranged, for a total surface of 28×21 cm^2. In the work of Han and colleagues (Han et al. 2008) a Philips camera was described in GATE as Anger system and the same NaI absorber detector was adapted for the simulation of the Compton system with the introduction of silicon pad detectors as scatterer part. The two geometries compared in this study are slightly different but the common absorber size strategy has been maintained.

The values for energy and spatial resolution of the silicon and BGO detectors used in the simulation were derived from the first tests performed on the detector prototypes (see chapter 3). For the silicon planes, the energy resolution is obtained from the Equivalent Noise Charge (ENC):

$$\sigma_E = W_{Si}\sqrt{\mathrm{ENC}^2 + F_{Si}\frac{E_{dep}}{W_{Si}}}, \tag{5.1}$$

where F_{Si} =0.115 is the silicon Fano factor, E_{dep} is the energy released in the detector (in eV) and W_{Si} is the energy required to create an electron-hole pair in silicon (3.6 eV). The ENC strongly affects the detector performance and it will be analyzed in the following.

The spatial resolution was set according to the geometric parameters considering that the employed Double-sided Silicon Strip Detectors (DSSDs) have a total of 64 strips per side, with a pitch of 1.4 mm. The position of each interaction is set in the center of the strip where it is recorded in both detection planes. Charge sharing on neighbor strips can in principle allow for sub-pitch resolution, but according to preliminary characterization measurements the probability of such a kind of events is less than 10 %, and will be so neglected. The interaction depth is set as the center of the involved detector slab. The time resolution has been set to 20.0 ns Full Width at Half Maximum (FWHM) based on characterization measurements performed at the *Grand Accelerateur National d'Ions Lourds*, Caen, France (GANIL) accelerator in France and at the *Institut de Physique Nucléaire de Lyon*, France (IPNL) (see chapter 3 and Ley 2015).

The energy and timing resolution in the BGO blocks are set to 21 % FWHM and 3.0 ns FWHM respectively, also based on characterization measurements performed with a cesium-137 source (662 keV gamma ray emission) and at the GANIL with prototype blocks. Concerning the spatial resolution, it has been verified that a sub-pixel resolution is not achievable on a single event basis, it is therefore fixed to the size of a single pixel (see chapter 3). Each block surface is streaked with an 8×8 pixel matrix, 4.4 mm side, not reproduced in the simulation code. Each interaction is assigned to the center of the pixel where it is localized at the analysis stage, while the interaction depth is set at the center of the involved block.

5.2.2.2 Data collection and analysis

The radioactive source is placed at 10 cm distance from the first silicon detector, in the center of the scatterer stack transverse surface, and the number of simulated primaries is set to 10^7 gammas per energy step. To speed up the simulation, the primary gammas are emitted in a direction within the acceptance cone defined by the first Compton camera silicon plane. All results are then normalized to the full solid angle.

All the events with at least one interaction in a silicon plane or at least one interaction in a BGO block are stored during the simulation process in two data sets, one per detector section. A small fraction of events presents interactions in more than one scatterer plane ($<$ 1 % at 245 keV) and/or in more than one BGO block ($\sim$ 8 % at 245 keV). This kind of events leads to ambiguities in the cone reconstruction, because the cone vertex and axis are not univocally defined, and it is not treatable via List Mode-Maximum Likelihood Expectation Maximization (LM-MLEM) reconstruction. Alternative reconstruction algorithms (such as the one included in the Medium-Energy Gamma-ray Astronomy library (MEGAlib) (Zoglauer et al. 2006)) are able to estimate the most likely scenario for multiple interactions, at the expense of larger uncertainties and longer calculation time. The multiple interaction events, representing approximately 8 % of the total at 245 keV, are then refused in this study for simplicity. This choice reduces the detection efficiency, so that the value obtained here could be seen as the lower limit for this kind of detection system. Once the two lists of events are built, the time coincidences are defined according to the source activity, the detector geometry and the single detection section time resolution. Finally, the emission points are reconstructed with a LM-MLEM algorithm developed by the *Centre de Recherche en Acquisition et Traitement de l'Image pour la Santé*, Lyon, France (CREATIS) institute in Lyon (Lojacono et al. 2013). The iterative algorithm reconstructs the Compton cones from the position and energy deposited in the scatterer stack and in the absorber blocks. A reconstruction volume must be defined, as well as a voxel 3 dimensional matrix in this volume. For this study the reconstruction volume has been fixed to $5 \times 5 \times 5$ cm^3 around the source, with a matrix of $51 \times 51 \times 51$ voxels, and 15 algorithm iterations: this number is a compromise between reconstruction performance and calculation time.

5.2.2.3 Compton camera study for SPECT application

As already mentioned in the introduction, a critical parameter in the Compton camera performances is the scatterer detector energy resolution. The goal of the instrumental development is to obtain an energy resolution as close to 1 keV (σ_E) as possible. The silicon detectors composing the stack have been tested at various temperatures in order to understand the behavior of the electronic noise and of the leakage current, and the read-out electronics is being developed with the aim to reduce the electronic noise (see chapter 3). The first laboratory tests showed an energy resolution at 25 °C of approximately 10 – 15 keV FWHM with a first read-out card prototype. The new card has been tested with simulated signals and gives a noise level closer to the expectations. No data are yet available to determine the detector energy resolution at different temperatures and with the final card version. In the simulation two different resolutions have been considered in order to verify the influence of this parameter on the final reconstructed image. The two chosen values are $\sigma_{\mathrm{E}} = 2\,\mathrm{keV}$ and $\sigma_{\mathrm{E}} = 4\,\mathrm{keV}$, corresponding to about 5 keV and 9.5 keV FWHM, respectively, both calculated at 200 keV of released energy

using equation 5.1. The influence of Doppler broadening has also been studied by disabling the Doppler effect in the simulation with the energy resolution set to $\sigma_E = 2\,\text{keV}$. Finally, a different possible scatterer material, Cadmium Telluride (CdTe), has been tested at the same resolution in order to verify the expected advantage given by the choice of silicon.

A coincidence study is mandatory to define the source activity to be used in the simulations dedicated to the benchmark with the Anger camera. Timing information is not included in the simulation code and a time structure must be assigned to the simulated primaries at the data analysis stage. A reference time is chosen randomly from a uniform distribution between 0 s and the data acquisition time and assigned to a primary photon. The data acquisition time (T_{DAQ}) is calculated as the expected time needed for the emission of the desired number of primaries ($N_{primaries}$) according to the source activity A_{source}:

$$T_{DAQ} = \frac{N_{primaries}}{A_{source}}. \tag{5.2}$$

The source activity is not fixed at the simulation stage but only during data analysis afterwards. It can therefore be easily modified to perform a study of the camera performance with different kinds of sources. The scatterer and absorber interaction times are calculated with respect to the reference primary emission and included in the related data sets for the analysis.

Two sets of data are produced as output of this analysis, one for the scatterer and one for the absorber: Each element in the two sets corresponds to an interaction in the detector and includes the 3D interaction position, energy released, time with respect to the total data acquisition time and primary reference index provided by the simulation. The elements in the two data lists are ordered for increasing time. The detectors time resolution specified in section 5.2.2 and a time window set to 20 ns, corresponding to a 3 σ acceptance, are then used for the coincidence definition for different source activities. The time of each element in the absorber data set is compared to the time of the elements in the scatterer data set. A coincidence is defined when the scatterer event time is within the time window centered in the absorber event time. Each element is used only once, and the analysis continues until the end of the absorber data list. If the two elements (one from the scatterer data set and one from the absorber one) forming a coincidence have the same reference index, they correspond to interactions of the same primary photons and the coincidence is then a true one. If the reference index is different for the two elements, the coincidence is random. The number of true and random coincidences has been studied as a function of the source activity in a range of clinical interest between 1 MBq and 500 MBq, for a fixed energy value of 555 keV. The variation of the influence of random coincidences as a function of the energy was also investigated at a fixed source activity of 200 MBq.

The scatterer energy resolution and the source activity have been fixed for the benchmark study. The choice of their values is discussed in section 5.3.

Finally, with the same scatterer energy resolution, the design of the Compton camera has been tested for this specific application, in particular for what concerns the number of employed scatterer planes. In addition to the original design configuration with seven DSSDs, additional sets of simulations have been performed at four reference primary gamma energy reducing the number of layers in each set, in order to assess the camera optimal configuration as a func-

tion of the gamma energy. The analysis involved a study of the kind of events detected by the camera, with particular focus on the scatterer section, which can collect both single and multiple interaction (the benchmark study will be then focused on single Compton interactions for simplicity). The efficiency in detecting independent events (with no time structure applied) is estimated and compared in case of inclusion or rejection of multiple interaction events. With the selection of single events, the absolute camera efficiency after reconstruction is then studied for the selected source activity. The results are shown in section 5.3.3 and are expressed according to the figures of merit used for the benchmark study (see section 5.2.4).

5.2.3 Anger camera simulation and data analysis

5.2.3.1 Simulation settings

The Anger camera system is simulated with GEANT4 Application for Tomographic Emission (GATE) v.7.1 and it is based on the General Electrics Healthcare Infinia SPECT system (GE Healthcare 2006), a commercial clinical camera with parallel hole collimator and Sodium Iodide doped with Thallium (NaI(Tl)) scintillator. A single detection head is simulated in order to obtain a direct performance comparison to the Compton system.

The chosen configuration includes a High Energy General Purpose (HEGP) lead collimator, 6.6 cm thick, with a surface of 28×19 cm^2 (see Figure 5.1). The parallel hole grid is composed of hexagonal shaped holes, 0.2 cm radius, arranged in a quincunx structure, with a septal thickness of 1.8 mm. This collimator is optimized for energies below 364 keV, corresponding to the main gamma emission energy of ^{131}I. The NaI(Tl) crystal is simulated as a single block of 28×19×1 cm^3, in contact with the collimator back surface and read out by photo-multiplier tubes. The photo-multiplier grid is represented with a glass block of 2.5 cm thickness behind the crystal, with the same transverse surface (see Figure 5.1). The spatial and energy resolutions have been set according to the manufacturer specifications. Unless otherwise stated, their values correspond to one standard deviation. A lower detection energy threshold has been set to 80 keV.

The point-like source is placed at 10 cm distance from the collimator surface (the distance chosen in the Infinia data sheet), as for the Compton camera with respect to the first silicon layer, and its transverse position corresponds to the center of the central collimator hole. For each source energy, 10^8 primary photons are simulated in 4π. An event corresponds to single or multiple interaction of a photon (or secondary particle produced by the photon interaction in the collimator) in the NaI(Tl) crystal. All the detected interactions are computed and the gamma interaction position is calculated during the simulation as the center of gravity of the positions of all the hits (energy transfers of secondary electrons), with the deposited energy as weight for the calculation. The deposited energy corresponds to the sum of the energies released during each hit. A set of interaction points and energy deposited is then stored.

5.2.3.2 Data analysis

Four source primary energies have been chosen as references of the studied energy range and are used in the following to show the analysis method and the study results. The low energy range is represented by the Indium-111 (^{111}In) emission at 245 keV, the first energy above the Anger camera construction limit has been set to 555 keV Yttrium-91m (^{91m}Y), while Iron-59 (^{59}Fe) at 1099 keV and Potassium-42 (^{42}K) at 1524 keV have been chosen to represent the medium and high energy range respectively.

Figure 5.2 presents the raw radial event distributions for the four reference energies. Each distribution bin content is normalized according to the surface of the circular region corresponding to each radius. The first distribution bin always corresponds to the radius of the central collimator hole, with the partial inclusion of the surrounding septa. This choice is determined by the detector and collimator geometry and by the source position. It is possible to list three different kinds of events contributing to the radial distributions:

1. photons passing through the collimator holes without interactions,

2. photons traversing the collimator septa without interactions,

3. photons interacting in the collimator septa.

Only the first listed contribution transports true spatial information about the source location, and these photons generate the signal. All other kinds of events contribute to the background, which rapidly increases with the primary photon energy.

A background rejection is performed in order to extract the distribution corresponding to the signal. The complex background contribution cannot be determined analytically, we therefore approximated the background profile as a linear fit to the tail of the radial distribution. The fit limits have been defined as follows:

- the lower limit is calculated as the radial distance where the photon flux on the NaI(Tl) detector is reduced to a fraction $\frac{1}{e}$ by absorption effect in the collimator septa;

- the upper limit has been fixed to the half of the collimator smaller lateral side (95 mm), in order to avoid any kind of geometric effect due the binning choice or the normalization surface selection. The bin size creates artefacts in the radial distribution corresponding to the collimator limits, because three different geometries are involved: the circular surface covered by each distribution bin, the hexagonal shape of the collimator holes and the rectangular collimator geometry.

The estimated background profile is subtracted from the raw distribution and the result is used as reference of the image signal (Figure 5.2).

Three validation tests have been performed in order to check this analysis method.

First, according to the geometry of the collimator and to the mass attenuation coefficient of NaI(Tl) (Hubbell et al. 1987), we evaluated the expected number of entries in the first distribution bin (before normalization), corresponding to the central collimator hole in front

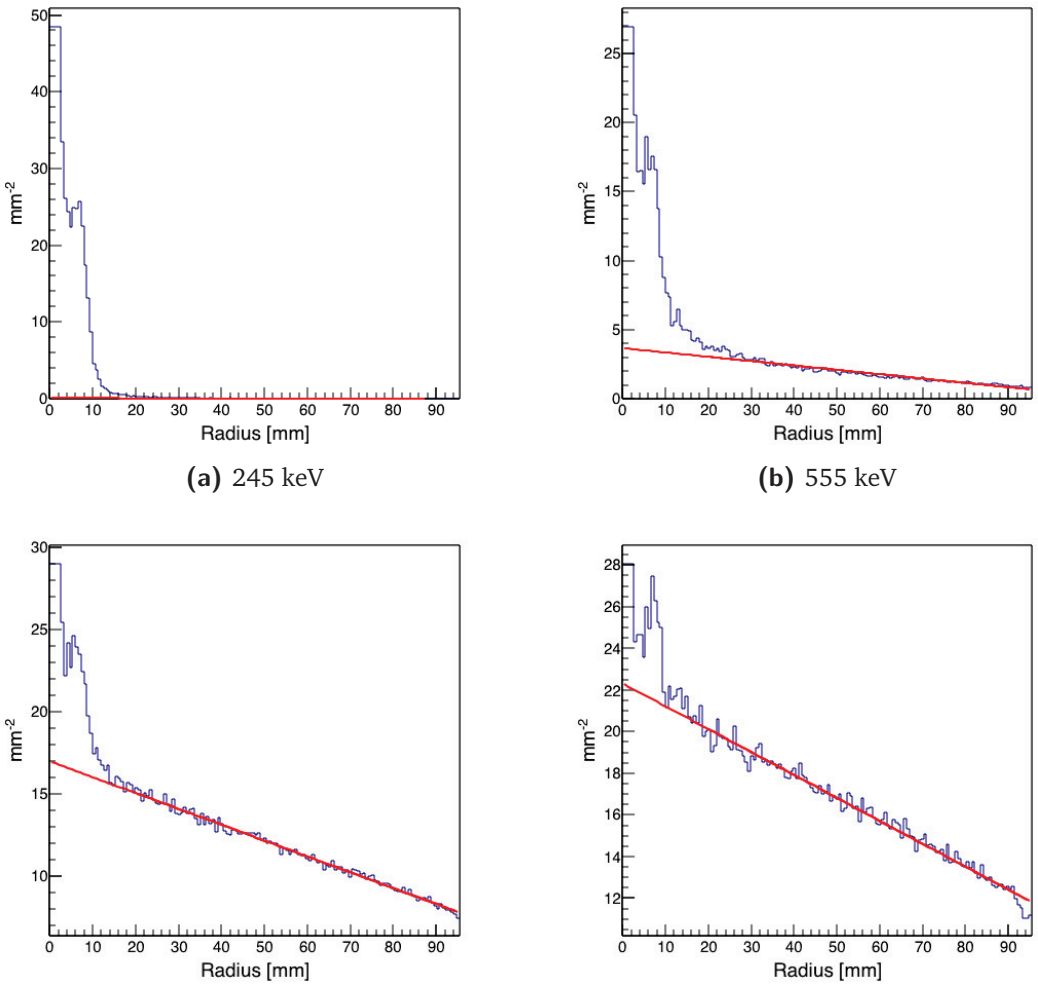

(a) 245 keV

(b) 555 keV

(c) 1099 keV

(d) 1524 keV

Figure 5.2: Radial event distribution normalized by the circular surface corresponding to each bin for 4 representative source energies, with the linear fit performed for background rejection. The total number of simulated primaries for each data set is 10^8.

of the source. The calculation is performed with the attenuation law of photons in 1 cm of NaI(Tl). A dedicated set of simulations has been performed equivalent to the ones for the Anger camera described in section 5.2.3.1, but using an ideal detector and a reduced number of photons of 10^7. No uncertainties are applied on the position of photon interactions to avoid resolution effects and the background is estimated via a linear fit as described above. The obtained entries in the first distribution bin after the fit selection are compared to the ones obtained with the theoretical calculation. In Figure 5.3 the results are shown as a function of the source energy.

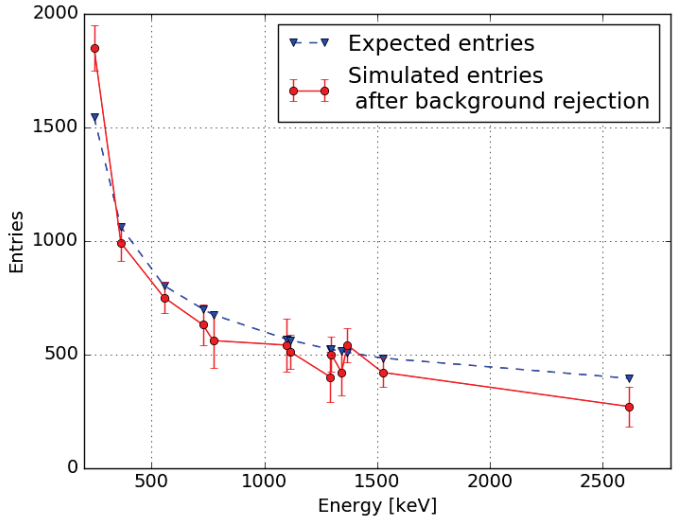

Figure 5.3: Comparison between expected entries in the central collimator hole (blue dashed curve) calculated according to pure geometrical factors and detector interaction cross section and simulated detected entries after background rejection (red solid curve) with null spatial resolution (ideal detector) to avoid resolution effects and lower energy threshold set to 80 keV.

There is a good agreement between the values calculated with the attenuation law and the simulation data selected with the fit-based background subtraction, and the detected variations from the ideal trend are within the statistical fluctuations. A slight overall effect of under-detection is observed (about 10 % on average), while the single value at 245 keV shows an opposite behavior (with a difference of less than 20 %). This is related to the chosen fit function.

As a second validation, an additional set of simulations has been performed with the same settings as defined in section 5.2.3.1 but with an infinitely dense collimator. This configuration removes the background contribution given by the photons deflected via Compton interaction on the collimator septa. The raw radial distributions obtained with this set of simulation is compared to the radial distribution "derived" by the simulations with nominal settings after the application of the fit-based background subtraction. The results are shown in Figure 5.4.

It can be noticed that the distribution overall trend is reproduced by the fit-based background rejection method, the main source of difference being probably the contribution of the scattering in the hole grid surrounding the central one.

The third validation test consisted in a set of simulation with a full lead collimator, with no holes. This configuration allows to estimate the distribution of events traversing the collimator

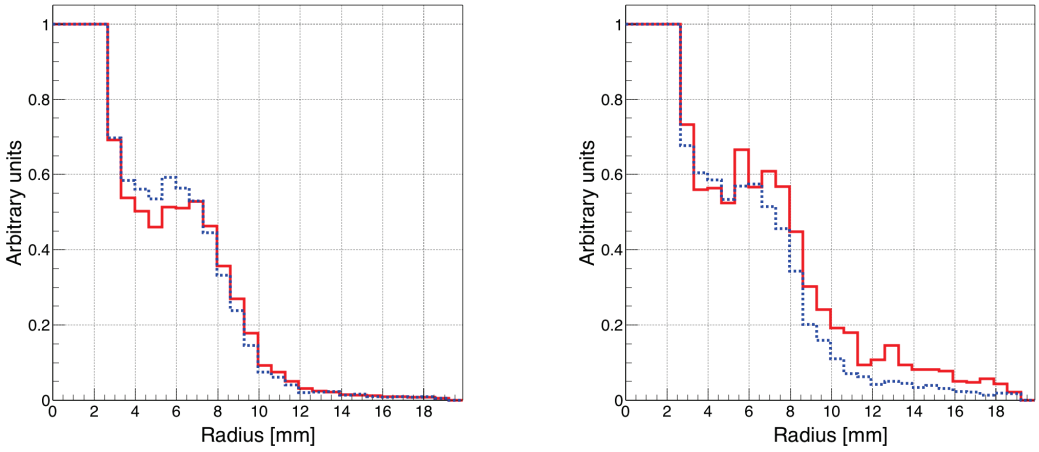

(a) 245 keV **(b)** 555 keV

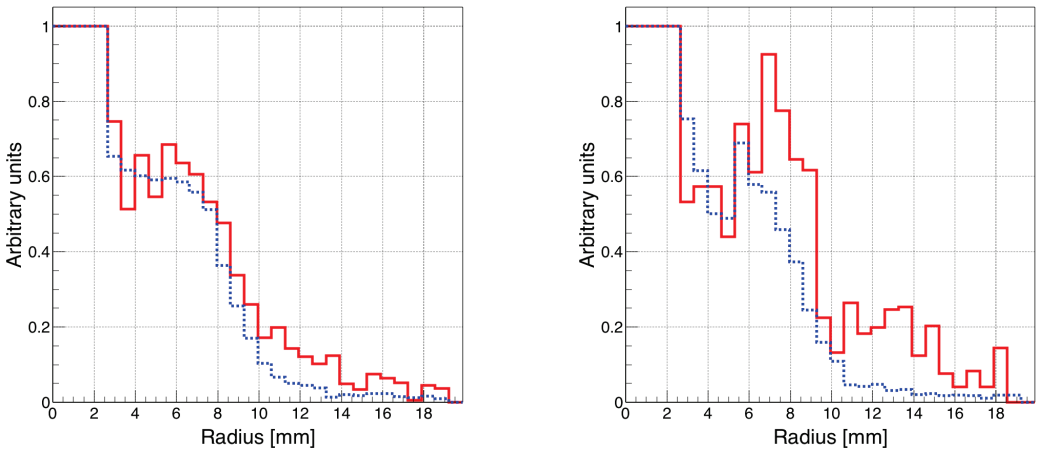

(c) 1099 keV **(d)** 1524 keV

Figure 5.4: Normalized radial distribution with background rejection (red solid lines) compared to normalized radial distribution for infinite density collimator (blue dashed lines).

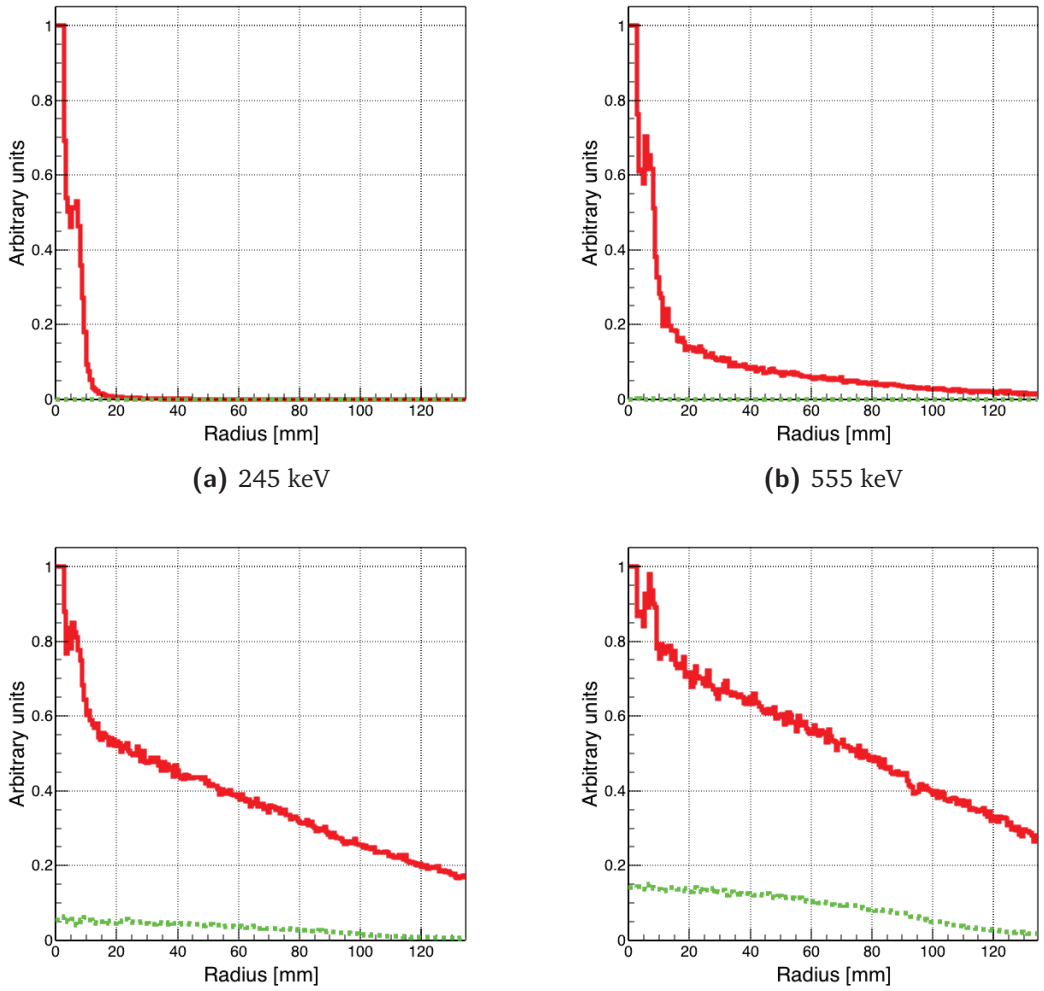

(a) 245 keV

(b) 555 keV

(c) 1099 keV

(d) 1524 keV

Figure 5.5: Normalized radial distribution with no event selection (red solid lines) compared to normalized radial distribution for full collimator (green dashed lines). Both curves are normalized to the maximum of the raw radial distribution.

with no interaction, with the aim of demonstrating the efficiency of the selection method to remove their contribution to the final image. Figure 5.5 shows the comparison between the raw distributions (no event selection is applied) obtained with the standard configuration and with the full collimator. The amount of photons able to traverse the lead block at low energy (245 and 555 keV) is totally negligible, while at higher energies this kind of events creates an offset which follows the raw event distribution. Anyway, by observing the selection functions obtained by the linear fit in Figure 5.2, the efficiency of the background employed rejection method in removing this contribution results clear.

The linear fit appears to be a robust way to select the signal transporting spatial information from the source and is applied with no modification for the entire energy range, giving to the analysis method the desired consistency.

5.2.4 Figures of merit for the comparison study

The two cameras are studied and compared according to three figures of merit which refer to their main detection parameters: spatial resolution, detection efficiency, and signal-to-background ratio. The definition of these three values must be adapted to the two detectors, keeping in mind their differences: on one side the Anger camera provides a transmission image through a mechanical collimator, with no need for a reconstruction process and with a single detector component; on the other side, the Compton camera relies on event time-coincidences and needs a reconstruction algorithm to obtain the final spatial distribution.

In this study, the imaging process of a point source was simulated. The three figures of merit are therefore evaluated based on the radial event distribution, in order to profit from the radial symmetry of the simulated system.

For the Compton camera, the standard deviation of the radial distribution is used to express the detector spatial resolution, the detection efficiency is defined as the ratio between reconstructed events (via LM-MLEM algorithm) and total simulated primaries, and the signal-to-background ratio corresponds to the ratio between the number of reconstructed events and the total number of coincidences selected before the reconstruction with the coincidence analysis.

For the Anger camera, it is difficult to define the spatial resolution, as shown in (Cecchin et al. 2015). Here, we use the standard deviation of the signal radial distribution in order to be consistent with the Compton camera definition already proposed (the "signal" substantive means entries after background rejection). The detection efficiency is defined as the ratio between the number of signal events and the total number of simulated primaries. Finally, the signal-to-background ratio is evaluated as the ratio between the signal events (the entries in the radial distribution after the fit-based background rejection) and the total number of events recorded by the detector (the entries in the raw radial distribution).

5.3 Results: Compton camera study for SPECT application

The results of the characterization of the CLaRyS Compton camera prototype for the application in SPECT are presented in the following sections, dedicated to the study of the scatterer detector energy resolution and of the Doppler broadening effect, and to the analysis of the rate of random coincidences, respectively.

5.3.1 Influence of Compton camera scatterer detector energy resolution

Figure 5.6 shows the standard deviation of the radial distribution obtained after the LM-MLEM reconstruction (see section 5.2.2.2) as a function of the source energy for the two different analyzed noise levels (ENC = 500 e^-, corresponding to $\sigma_E = 2$ keV, and ENC =1100 e^-, corresponding to $\sigma_E = 4$ keV). The maximum detected difference is about 35 %, but the influence of the silicon detectors' energy resolution rapidly reduces at increasing energy. In the same figure, the results for the simulation without the Doppler broadening for the lowest energy

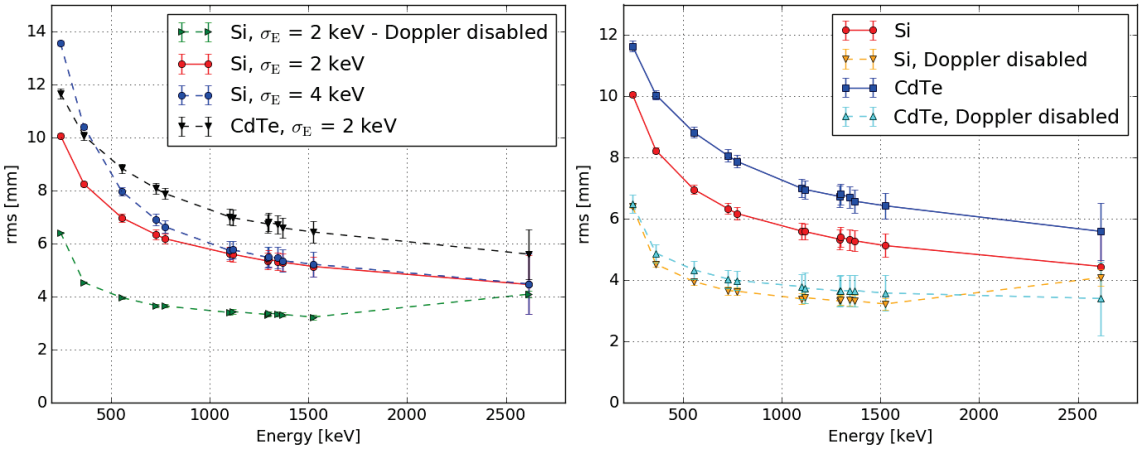

(a) Si with $\sigma_E = 2\,\text{keV}$ with and without Doppler effect, Si with $\sigma_E = 4\,\text{keV}$ and CdTe with $\sigma_E = 2\,\text{keV}$ with Doppler effect.

(b) Si and CdTe with $\sigma_E = 2\,\text{keV}$, with and without Doppler effect.

Figure 5.6: Compton camera-reconstructed radial distribution standard deviation as a function of the source energy. Two energy resolution values are set to the silicon detectors ($\sigma_E = 2\,\text{keV}$ - red dots solid line - and $\sigma_E = 4\,\text{keV}$ - blue dots dashed line), the Doppler broadening effect has been removed (green horizontal triangles dashed line) and the scatterer material has been changed with CdTe solid state detectors (black vertical triangles dashed line), for a fixed energy resolution of $\sigma_E = 2\,\text{keV}$.

resolution are shown. It is clear that this parameter has a strong influence for the Compton camera spatial resolution, at least for energies below 2.5 MeV. This result justifies the choice of silicon as scatterer material, because it is the lowest Z available detector and therefore minimizes the Doppler contribution. This is underlined by the black curve corresponding to a CdTe detector, i.e. a higher Z material than silicon (average value of Z=50 for CdTe). For this last study, the electronic noise level has been set for CdTe in order to have the same intrinsic resolution as for silicon ($\sigma_E = 2\,\text{keV}$ obtained with equation 5.1). Such a resolution for CdTe detectors seems realistic, at least for thin detectors (Alharbi 2018).

For the benchmark with the Anger camera, the ENC value of the Compton camera scatterer components has been fixed to 500 e^-, which corresponds to the expected average level of noise affecting the silicon detectors between –20 °C (identified as the ideal working temperature) and 0 °C (the silicon detectors are cooled down with a thermal-regulated box, see chapter 3 for a detailed description) and with the final acquisition card (about 2 keV σ_E). This value has to be experimentally verified.

5.3.2 Compton camera coincidence study

Figure 5.7 (left) shows the numbers of true and random coincidences as a function of the source activity, ranging between 1 and 500 MBq in order to explore the whole range potentially employed in real examinations. The energy is set to 555 keV.

At 200 MBq source activity, the same amount of true and random coincidences is observed at 555 keV gamma energy. With activities above this value, the ratio between true and random

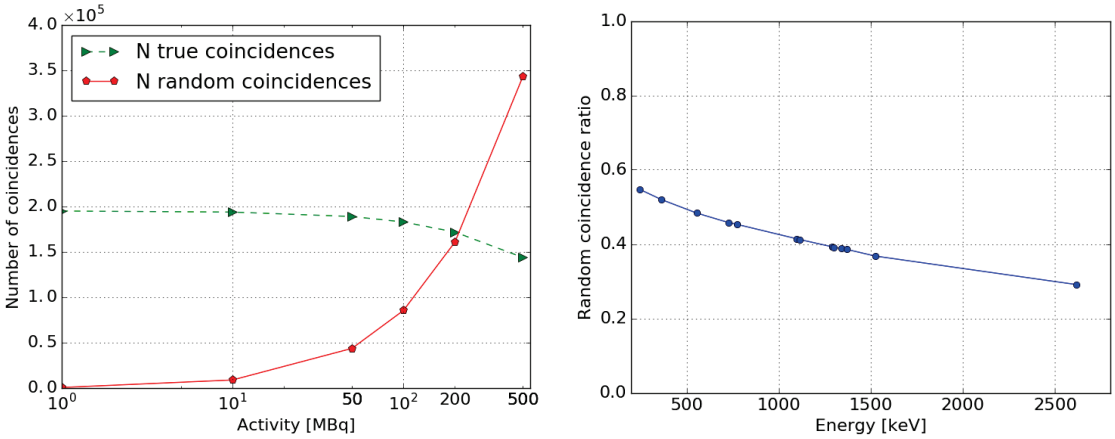

(a) Number of coincidences as a function of the source activity.

(b) Random coincidence ratio as a function of the gamma energy.

Figure 5.7: (a): number of true (green) and random (red) coincidences as a function of the source activity in the range 1 – 500 MBq, for the reference energy of 555 keV. (b): Percentage of random coincidences as a function of the source energy, with a fixed source activity of 200 MBq. Compton camera parameters: time resolution FWHM of 20 ns for silicon detectors, 3 ns for BGO and a coincidence window of 40 ns. The source branching ratio has been set to 100 % for all sources for simplicity in the comparison of results.

coincidences is less than one. In principle the reconstruction LM-MLEM program can partially reject this kind of events and if we consider the expected important increase in detection efficiency guaranteed by the "electronic collimation", it results clearly that it is not worth to employ high activity sources (or that a smaller camera can be considered at the expense of the examination time). Note also that filtering criteria, such as total energy detected or rejection of events that cannot be reconstructed, will certainly help decreasing the fraction of random coincidences. However, the efficiency for the detection of true coincidences clearly decreases with increasing activity, due to the camera occupancy fraction.

For the further analysis and the final detector comparison, the source activity has been then set to 200 MBq, and the number of random coincidences is studied as a function of the source energy. Figure 5.7 (right) shows the ratio of detected random coincidences over the total number of reconstructed coincidences (see Section 5.2.2.2) as a function of energy for a fixed activity of 200 MBq. The ratio decreases for increasing energies, because the product of independent interaction probabilities in two detectors decreases faster than the true coincidence one. Therefore, an increasing reconstruction efficiency with LM-MLEM is verified (see Section 5.4).

5.3.3 Compton camera design study

In order to test the Compton camera design for the application in SPECT, a preliminary investigation has been dedicated to the composition of the events collected by the camera, in particular by the scatterer section. As presented in chapter 4, a primary photon can undergo a single Compton interaction in one scatterer layer and be then, ideally, absorbed in the absorber blocks (single event), or multiple Compton interactions can occur in different scatterer layers before the absorption (multiple event). Finally, the Compton recoil electron can have

enough energy to exit the scatterer layer where the Compton interaction took place, and interact in a different layer (electron escape event). The raw efficiency (before reconstruction) of the Compton camera has been studied with the inclusion or rejection of multiple and electron escape events, as a function of the gamma energy for four reference primary gamma energies and for various scatterer configurations: starting from the original design with seven silicon layers, one layer has been removed for each simulation set, until a minimal scatterer stack composed of only one layer. The results are compared in Figure 5.8a, which shows the camera efficiency with no event selection, and Figure 5.8b, which shows the efficiency with the selection of single events.

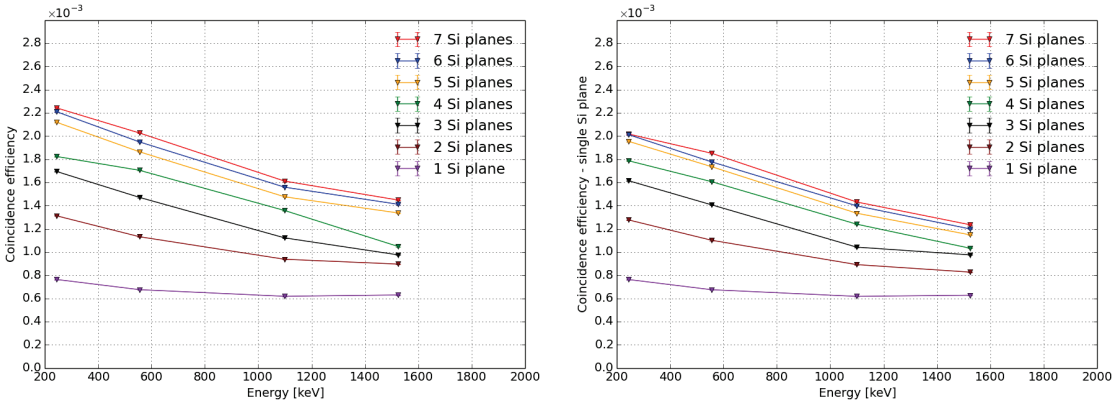

(a) Coincidence detection efficiency as a function of the source energy for seven configurations of the scatterer stack: one layer has been removed for each simulation set. No event selection applied. Compton camera silicon detector $\sigma_E = 2\,\text{keV}$.

(b) Coincidence detection efficiency as a function of the source energy for seven configurations of the scatterer stack: one layer has been removed for each simulation set. Selection of single Compton interaction events in the scatterer section has been applied. Compton camera silicon detector $\sigma_E = 2\,\text{keV}$.

Figure 5.8: Results of the Compton camera event composition study: the absolute Compton camera efficiency (before reconstruction) is shown without any event selection (a) and with the selection of event with single interaction in the scatterer section.

A slight reduction in the overall camera efficiency is verified when selecting single Compton interaction events. The amount of multiple and electron escape events is limited in the explored gamma energy range. This justifies the selection of single events for the benchmark study and the presented Compton camera analysis.

The reconstructed events efficiency for the four reference primary gamma energies is shown in Figure 5.9a for the different scatterer configurations. Figure 5.9b shows the results of the same sets of simulations for what concerns the reconstructed event radial distribution Root Mean Square (RMS).

An overall efficiency drop is observed for the scatterer configurations with more than four layers at 245 keV photon energy: this probably reveals an effect of total gamma absorption in the scatterer detector section, in parallel to an increased number of events deflected with large Compton angles which escape the absorber field of view. This effect is not confirmed at increasing gamma energy, already at 555 keV. In this energy range, the expected reduction of the overall efficiency for reduced number of scatterer layers (due to the diminished Comp-

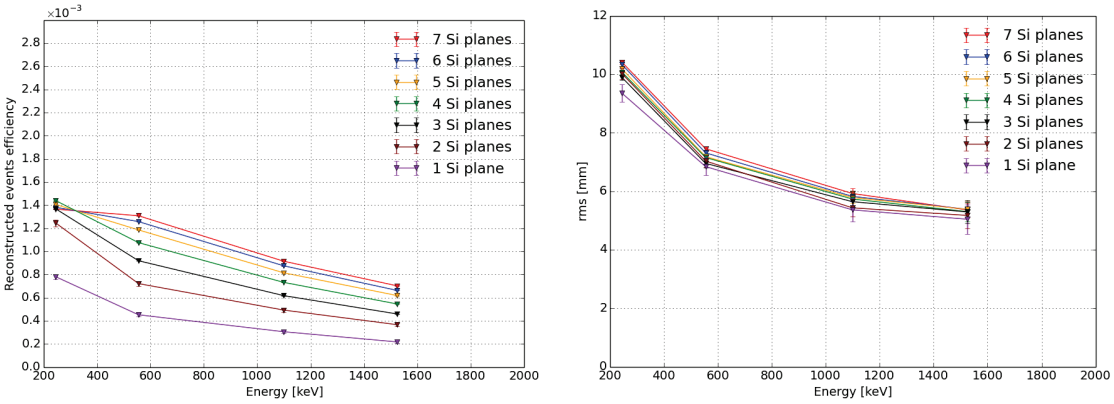

(a) Reconstructed efficiency as a function of the source energy for seven configurations of the scatterer stack: one layer has been removed for each simulation set. Selection of single Compton interaction events in the scatterer section has been applied. Source activity = 200 MBq, Compton camera silicon detector $\sigma_E = 2\,\text{keV}$.

(b) Standard deviation of the radial event distributions as a function of the source energy for seven configurations of the scatterer stack: one layer has been removed for each simulation set. Selection of single Compton interaction events in the scatterer section has been applied. Source activity = 200 MBq, Compton camera silicon detector $\sigma_E = 2\,\text{keV}$.

Figure 5.9: Results of the Compton camera design study: reconstructed events efficiency (left) and standard deviation of the radial event distribution (right) as a function of the primary gamma energies for four reference energies and seven scatterer stack configurations, with reduced number of scatterer layers.

ton effect probability) is verified. The radial distribution standard deviation shows minimal variations for the different tested configurations.

At very low gamma energy a scatterer configuration with four silicon scatterer planes appears to be the optimal solution. This is the energy range for which the Compton camera advantages with respect to the commercial Anger cameras are expected to be less remarkable, as explained and verified in the next sessions. At increasing energy, relevant to profit from the Compton camera advantageous features, the original CLaRyS camera design is verified to be the best configuration; this setup has been implemented for the benchmark study.

5.4 Results: Benchmark of Compton camera and Anger camera performance

The analysis methods presented in section 5.2.2.2 and section 5.2.3.2 for the Compton and Anger camera, respectively, have been applied to the simulated data sets of the two cameras at all energies.

The radial distributions for Anger and Compton camera at the different reference source energies and a source activity of 200 MBq are shown in Figure 5.10. The same reference energies selected in section 5.2.3.2 are included here. The radial range is limited to the smaller colli-

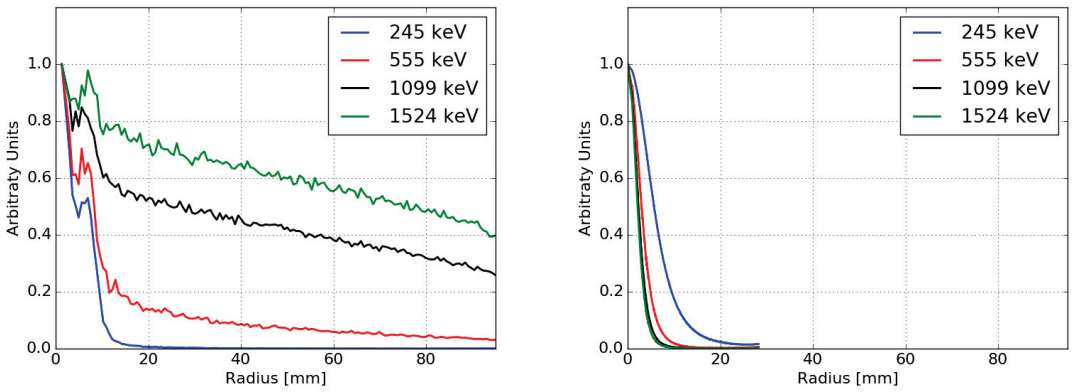

(a) Anger camera events.

(b) Compton camera reconstructed events.

Figure 5.10: Overlap of the normalized radial distributions for 4 selected source energies.

mator lateral size (95 mm), according to the fit limits imposed on the Anger camera data (see Section 5.2.3.2). The curves are normalized to 1 for an easier visual comparison.

In Figures 5.11, 5.12, and 5.13, the detection efficiency, the radial distribution standard deviation and the signal-over-noise ratio are respectively shown as a function of the source energy for the two sets of data. Uncertainties (one standard deviation) are reported for all the values and included in the data points when not visible.

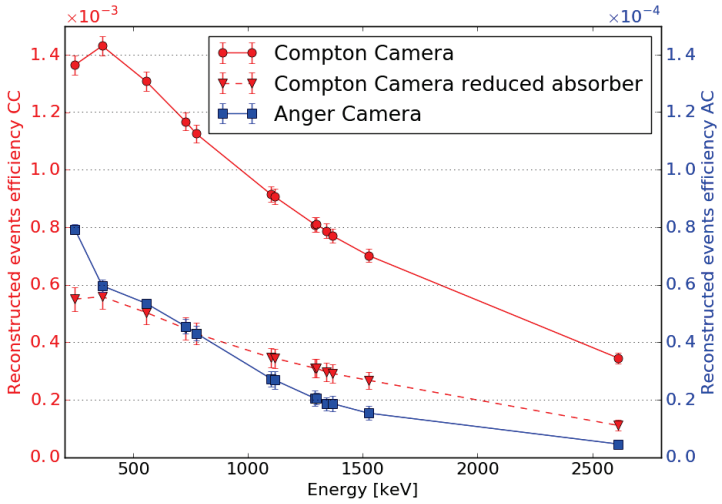

Figure 5.11: Detection efficiency as a function of the source energy. Source activity = 200 MBq, Compton camera silicon detector $\sigma_E = 2\,\text{keV}$. Note the factor 10 scale difference for the vertical axes.

From Figure 5.11 one can point out the advantage provided by the absence of a physical collimation system in terms of detector efficiency. It should be noticed that two different scales are applied to Figure 5.11 in order to show the two plots on the same figure and appreciate the variations with respect to the energy. The detection efficiency of the Compton camera is always more than a factor 20 higher than the one of the Anger camera. Although the images

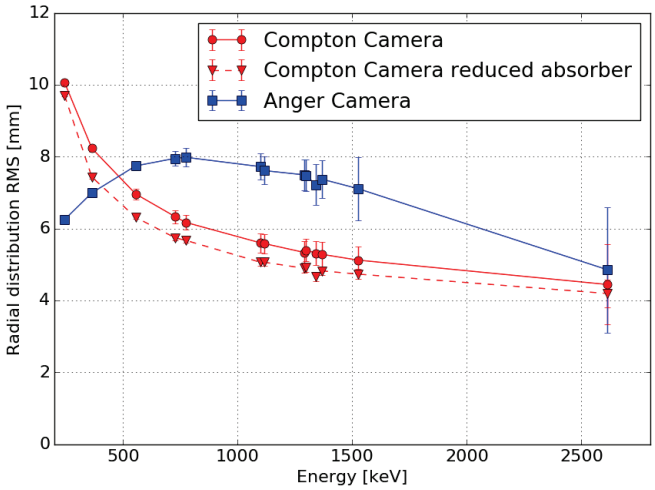

Figure 5.12: Standard deviation of the radial event distributions as a function of the source energy. Source activity = 200 MBq, Compton camera silicon detector $\sigma_E = 2\,\text{keV}$.

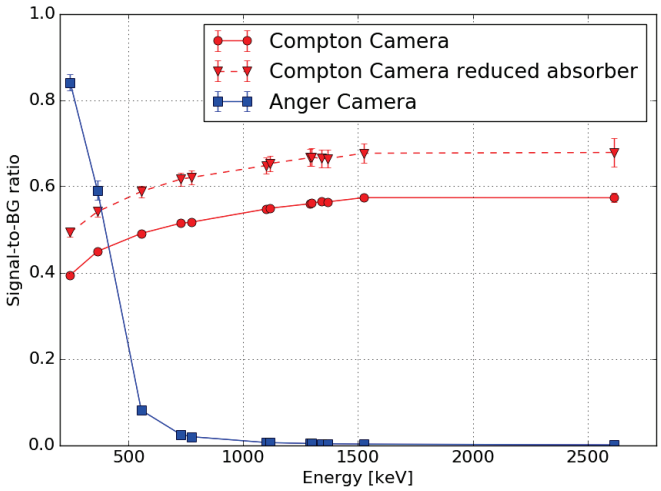

Figure 5.13: Signal-to-background ratio as a function of the source energy. Source activity = 200 MBq, Compton camera silicon detector $\sigma_E = 2\,\text{keV}$.

of the Anger and Compton cameras are based on different kinds of spatial information (a line and a cone, respectively), the Compton camera efficiency should allow a substantial reduction of the injected source activity and/or of the acquisition time. The efficiency of both cameras constantly decreases with increasing energy, because of the decreasing photon interaction probability. The only exception is found at the lowest considered energy of 245 keV in the Compton camera, due to an increased probability of photon absorption in the scatterer and, additionally, a larger fraction of events with wide Compton scattering angles at low gamma energy.

The standard deviation of the radial distribution, shown in Figure 5.12, confirms the optimization of the chosen collimator for the Anger camera for low energies (below 364 keV). With the *ad hoc* background subtraction operated here, which is not realistic for an extended source, the Anger camera outperforms the Compton one in terms of spatial resolution at low energies

(by > 3 mm at 245 keV and about 1.3 mm at 364 keV). However, above 500 keV, the Compton camera can provide a better spatial resolution with a difference ranging between a fraction of millimeter up to about 2 mm. For energies above 1.5 MeV, the two curves of standard deviation for the two cameras reach similar values (< 0.5 mm difference at 2614 keV), but Figure 5.13 shows how the background rejection for the Anger camera and the MLEM reconstruction for the Compton system (see Sections 5.2.3.2 and 5.2.2.2) affect this result. Above 364 keV, the selection for the background rejection of the Anger camera data drastically reduces the number of events contributing to the final image (the ratio between selected and detected events approaches zero). With an extreme selection, at very high energy the only events contributing to the final image are the events traversing the central hole of the collimator, resulting in an enhanced spatial resolution (see Figure 5.4d). The signal-to-background ratio of the Compton camera confirms the expectations concerning the reconstruction algorithm performance: if compared to Figure 5.7 (right), the curve in Figure 5.13 shows how the rejected events correspond approximately to the amount of random coincidences.

5.5 Summary and discussion

The Compton camera under development by the CLaRyS collaboration is now at the characterization stage. Originally designed and optimized for the application in ion beam therapy monitoring for the detection of prompt-gamma rays in a wide energy range (between some hundreds of keV until about 10 MeV), it is here studied as SPECT detector in comparison to a commercial system based on the Anger gamma camera design.

The expected significant enhancement in terms of detection efficiency, for comparable imaging performance in terms of spatial accuracy, has been already proven in simulation in (Han et al. 2008) with a silicon-sodium iodide based Compton camera prototype at a single primary energy of 364 keV. A factor 20 efficiency gain has been reported.

First of all, the present simulation study aimed to extend these results by testing the two detectors at increasing primary gamma energies, ranging from 245 keV to 2614 keV. A common analysis method has been defined in order to obtain comparable results, always keeping as reference the final image. The results were directly compared in terms of detection efficiency, spatial resolution (standard deviation of the radial event distribution) and event selection (background rejection for the Anger camera and LM-MLEM algorithm selection for the Compton camera) via the definition of three figures of merit.

A preliminary study has been performed on the simulated Compton camera data in order to fix the main parameters of the camera simulations, namely the energy resolution of the silicon scatterer detectors and the source activity determining the coincidence rate. Two ENC values have been studied, resulting in a maximum difference in spatial resolution of 35 % at the lowest energies, rapidly decreasing at increasing primary energy. A value of ENC = 500 e^- has been chosen as the closest to the instrumental development expectations and first tests. The influence of the Doppler broadening on the spatial resolution has been also estimated in a factor ∼1/3 at 500 keV, then reduced up to ∼0 at 2.5 MeV of primary gamma energy, with fixed energy resolution (σ_E = 2 keV – ENC = 500 e^-) in the silicon detectors. Moving to the coincidence rate analysis, at the reference energy of 555 keV and with detector time resolution set according to first characterization results, the simulated data have been analyzed by

reproducing a source activity in the range 1 – 500 MBq. The result shows the expected increase in the random coincidence rate at increasing source activity, with a ratio between true and random coincidences close to one at 200 MBq. This value has been chosen as clinical reference for the comparison analysis. In addition to this, the geometrical configuration of the scatterer stack has been studied in order to check alternative setups with reduced number of DSSDs; this study confirmed the choice of seven planes, as well as the choice of selecting events with one single interaction in the scatterer section, implemented for the benchmark analysis.

The results discussed in section 5.4 confirm the conclusion of Han et al. about the advantage given by the usage of a Compton system and show how the gain factor in the detector efficiency is maintained at increasing energy. Concerning the detector spatial resolution, the Compton camera outperforms the Anger system at energies above about 500 keV. The Anger camera spatial resolution can be boosted by aggressive background subtraction in the considered case (point-like source image), at the expense of a drastic signal suppression. However, this approach is not reproducible and exploitable in actual clinical conditions and the obtained results are not comparable to the Compton camera performance at the same energy.

The results of this work clearly show the potential of the Compton camera for the application in nuclear medicine examination, opening new possibilities for the clinical implementation. The studied detector has originally been designed and optimized for another application, and it has only been adapted for SPECT here, but not yet optimized in terms of detector geometry (size, position, and inter-detector distances). For an optimized detector, performance is therefore expected to be improved with respect to the presented results. In future development, the reconstruction LM-MLEM algorithm should be adapted to this application and the reconstruction parameters should be studied to further enhance the final performance, in particular for what concerns random coincidence rejection.

Anyway, these first evidences already allow one to investigate the possible modifications introduced by the clinical set of Compton detection systems. The enhanced detection efficiency in parallel with comparable spatial performances paves the way to the diffused usage of less active sources, or alternatively allows a substantial reduction of examination time: as a result, the dose delivered to the patient would be reduced. On the other side, the possible introduction of sources with higher primary emission energy will reduce the effect of photon attenuation in the patient (not studied in this simulation work), improving by definition the spatial information and further reducing the effective dose delivered to the patient. Simple analytic calculations can show how a photon attenuation of about 66 % is foreseen for 364 keV photons in 10 cm of water, while the effect is reduced, for example, to 49 % at photon energy of 1099 keV (Hubbell et al. 1987). Higher energies can be employed also with Anger cameras, at the expense of introducing thicker collimators with reduced holes size, with the result of a reduced efficiency with respect to the analyzed HEGP collimator. Furthermore, a possible implementation of Compton cameras is also foreseen for targeted radionuclide therapy, where the radionuclides used in clinics often have gamma radiation emission at relatively high energy. This signal is difficult to be detected and treated with conventional SPECT cameras, while the Compton detection technique could make it quantitatively exploitable in clinical practice, for both pre- and per- treatment images.

Even though Compton cameras intrinsically lead to 3 dimensional images with a single detector head, the spatial resolution associated to the direction normal to the detector planes has to

be more deeply studied, but this feature is an additional point in favor of the introduction of Compton systems in the clinical environment, moving beyond the tomographic concept and towards more compact detector solutions. Several studies are ongoing in order to improve the image reconstruction algorithms and, so, the 3 dimensional imaging performance (Kuchment et al. 2016). Different detection approaches can also, in principle, lead to improved image quality in 3 dimensions, such as the Compton electron tracking (Kabuki et al. 2007; Sonoda et al. 2015). Moreover, a further enhancement in image reconstruction should be given by the measurement of the photon depth of interaction: the photon is assumed to interact in the center of the detector components for our prototype, while perpendicularly segmented detectors can ensure an improved resolution in the third dimension and a resulting enhanced reconstruction accuracy, also involving better 3 dimensional imaging capabilities.

The advantages of the Compton detection principle are here shown thanks to a first detector prototype, but there is still wide room for improvement.

Once the CLaRyS Compton camera will be completed and characterized, tests in clinical environment are foreseen in the field of medical imaging. The actual potential of this kind of detector will be then quantified with experimental data.

6

Beam tests

Contents

As described in chapter 3, the components of the CLaRyS gamma cameras are in the characterization phase, and the related electronics and acquisition system are under debugging. The efforts of the collaboration are presently mainly focused on the optimization of the acquisition chain, including the electronics boards, the Micro Advanced Telecommunications Computing Architecture (μ-TCA) acquisition system and the associated acquisition, monitoring and slow control software. These tasks foresee several measurements campaigns, and three of them have been performed between the end of 2017 and the date of writing (September 2018). These campaigns are presented in this chapter. All the presented beam tests have been carried out at the *Centre Antoine Lacassagne*, Nice, France (CAL) with a 65 MeV proton beam.

The Nice hadrontherapy platform was the first site in France starting to treat patients in June 1991 with the MEDYCIC cyclotron proton beams. The cyclotron was designed to support regular neutron and proton therapy programs, as well as for the production of ^{18}F for Positron Emission Tomography (PET) applications (Mandrillon et al. 1992, 1989). The accelerator is a fixed frequency 25 MHz isochronous cyclotron with a peak voltage of 50 kV. Negative hydrogen ions are produced by an external source, axially injected and accelerated to 65 MeV. The extraction is performed by a 60×10^{-6} g/cm^2 carbon stripping foil and the exiting protons are transported down the beam line to the treatment room (Herault et al. 2005), or to the research nozzle used for the presented beam tests. The layout of the MEDICYC facility is shown in Figure 6.1. The details of the center layout are sketched in Figure 6.2, showing the cyclotron , the beam line, the proton therapy treatment room, and the research-dedicated line. The beam is bent by 90 ° to be sent to the treatment room, while it is extracted without deflection for research purpose.

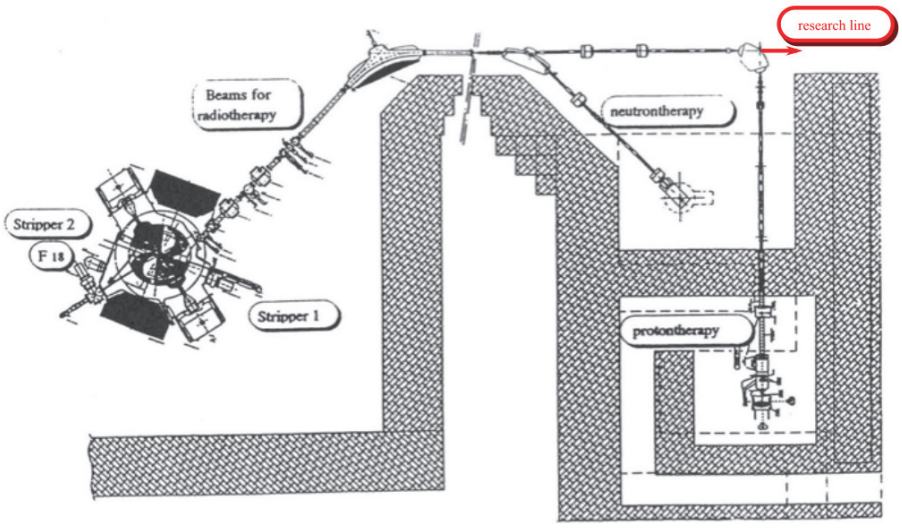

Figure 6.1: Layout of the Nice MEDICYC facility with the dedicated reserach line highlighted in the top right corner. Adapted from Mandrillon et al. 1992.

The CAL is at present equipped with a Proteus One Ion Beam Applications, Belgium (IBA) treatment facility, with an S2C2 cyclotron (Pearson et al. 2013), which has been finalized in June 2016. The MEDICYC low energy treatment line is dedicated to ocular tumors, while the new high-energy facility allows one to treat all other kinds of tumors.

The tests performed in the last year had been focused on the camera electronics and acquisi-

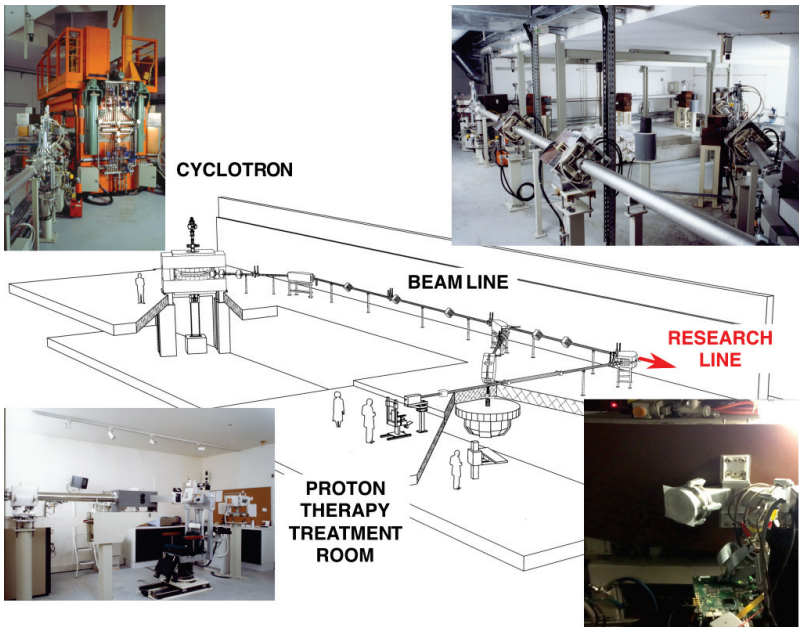

Figure 6.2: Layout of the Nice MEDICYC facility with pictures of the components: cyclotron, beam line, and treatment room. The beam nozzle dedicated to research activities is shown by the red arrow (also showing the beam direction) and shown in the picture in the bottom right corner of the scheme.

tion. The main objective was a first verification of the final camera acquisition chain, based on the custom Front-End (FE) cards developed for each detector section and on the μ-TCA acquisition system. All the reported results have been obtained with non-optimized electronics equipment and firmware, and have been used as reference to drive the improvements achieved after each test campaign. The tests presented in this chapter have been performed during single-day measurement campaigns, and further beam time is needed to validate the camera setup and acquisition as well as to evaluate the detector performance. In 2019, dedicated laboratory and beam tests will be focused the detector performance optimization, once a fully operational electronics and acquisition chain for the whole camera will be available.

We started testing the hodoscope stand-alone acquisition chain in December 2017. As a first minimal approach, the 32+32 fiber hodoscope has been used, given the fact that it can be read out by a single FE board, and no synchronization capabilities are required in the FE board firmware. The December test allowed to highlight the main limitations affecting the FE board, as well as the software governing the μ-TCA acquisition system. In the following months, an extensive revision work has been dedicated to the hodoscope FE board and to the μ-TCA firmware. The acquisition software has been also optimized for higher data throughput. A new beam test dedicated to the 32+32 fiber hodoscope has been carried out in May 2018, and it is detailed in section 6.1. This test allowed us to have a first characterization of the hodoscope with the final acquisition chain on beam, to evaluate the needed improvements and plan the test of a first multi-collimated camera configuration. In the following months, indeed, the attention has been focused on the Bismuth Germanium Oxide - $Bi_{12}GeO_{20}$ (BGO) absorber blocks, and the read-out through Analog Sampling Module (ASM) boards and μ-TCA system has been developed at the *Institut de Physique Nucléaire de Lyon*, France (IPNL). A minimal collimated camera setup, including the 32+32 fiber hodoscope (read-out with a single

hodoscope FE board) and 6 BGO blocks (read-out with a single ASM board) has been tested on beam in the second half of September 2018. The test details are given in section 6.2.

6.1 Hodoscope: May 2018

After the improvements implemented on the hodoscope FE board and μ-TCA firmware which followed the first preliminary test in December 2017, the 32+32 fiber hodoscope has been tested with the same configuration in May 2018. The acquisition logic allows to operate the hodoscope in triggered and stand-alone modes: in the first case, the trigger signal is given by the absorber in the collimated camera setup, or by the coincidence between absorber and scatterer in the Compton camera setup. For this test, an external trigger has been provided thanks to two 5×5 cm^2 plastic scintillators, read-out by a Photo-Multiplier (PM), placed on beam upstream and downstream with respect to the hodoscope. The plastic scintillators have been aligned to the hodoscope, in order to fully cover the hodoscope active area of 3.2×3.2 cm^2. The hodoscope was placed at a distance of 15 cm from the beam nozzle, the upstream plastic scintillator was approximately at 10 cm, the downstream one at 19 cm. A schematic view of the test setup is given in Figure 6.3, and two pictures of the system are shown in Figure 6.4.

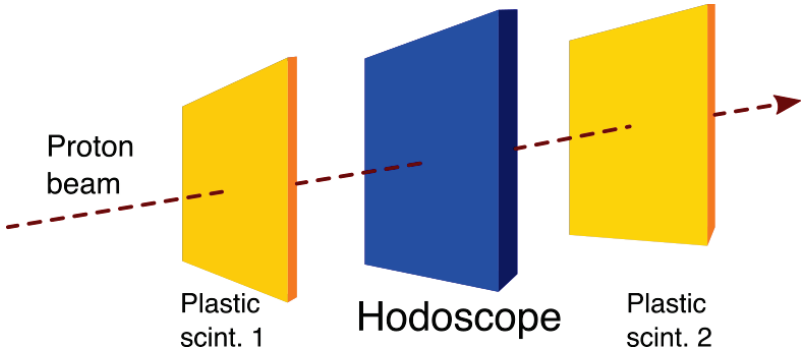

Figure 6.3: Schematic view of the hodoscope and plastic scintillator setup along the beam line.

The hodoscope and the two plastic scintillators have been mounted on the two-dimensional moving table described in chapter 3, to adjust the setup position with respect to the beam nozzle. The analog output of the two plastic scintillators was treated with standard Nuclear Instrumentation Modules (NIMs): each single signal was converted to logic via a fixed threshold discriminator (threshold set to 50 mV), and two output logic signals were sent as input in a logic coincidence module. The logic coincidence signal was converted to Transistor-Transistor Logic (TTL) and sent as trigger input to the hodoscope FE board. A third plastic scintillator (same kind and size as the two others) was installed outside the beam line approximately 1.5 m far from the beam exit. It is visible in the top left corner of Figure 6.4b. The purpose of this third detector is the measurement of high beam intensities through secondary particle detection. The detection rate acceptance of the plastic scintillator is indeed not able to directly follow the cyclotron beam intensity, which is measured by a Faraday cage used for quality assurance on the beam line. The third plastic scintillator is calibrated with the two detectors on beam at low beam intensities, and used to cross check the Faraday cage measurements and, at the same time, verify the acquisition rate reported by the hodoscope in stand-alone mode. An online beam intensity monitor is set up with a VERSABUS Module Eurocard (VME) based counting acquisition: the signals from the three independent plastic scintillators and the logic

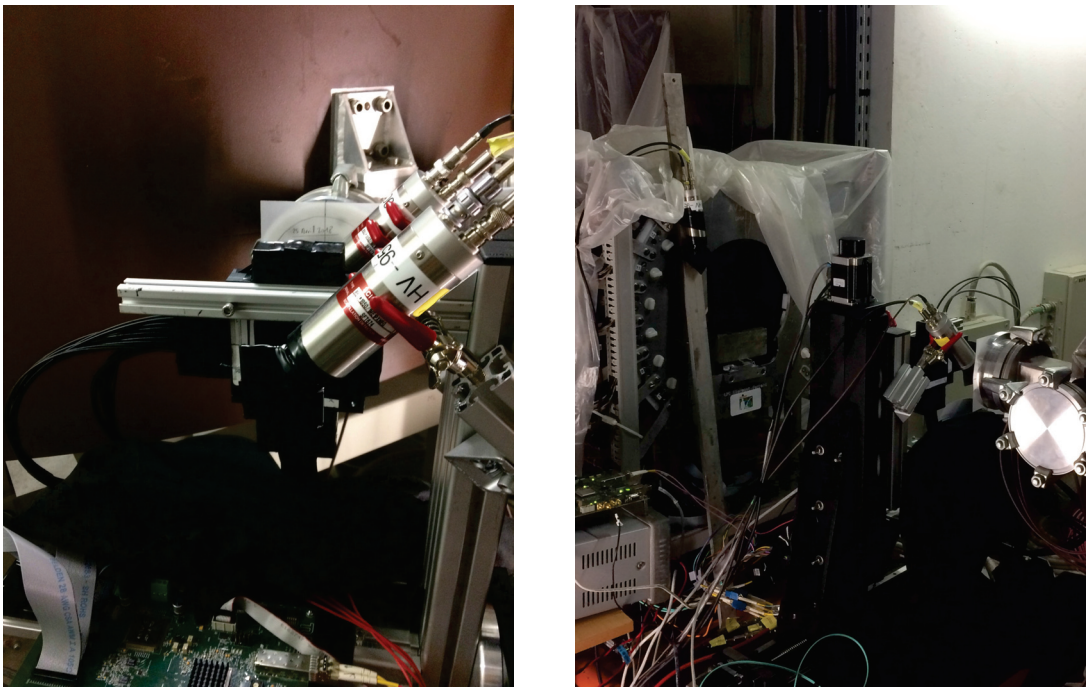

(a) (b)

Figure 6.4: Pictures of the hodoscope test setup. (a) From downstream the beam nozzle. The two 5 cm side plastic scintillators are set one upstream and one downstream with respect to the hodoscope. (b) Complete setup. Hodoscope and trigger scintillators are fixed to a two-dimensional moving table and set at approximately 15 cm from the nozzle (from the nozzle to the hodoscope center). A third plastic scintillator is fixed outside the beam line (top left corner) to provide intensity monitoring at the high rates not supported by the scintillators on beam.

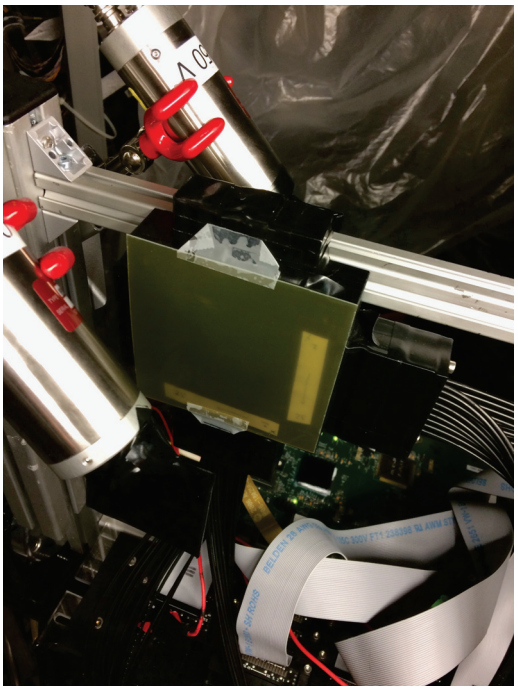

(a) GAFchromic film fixed on the entrance surface hodoscope to record the beam shape at the hodoscope position.

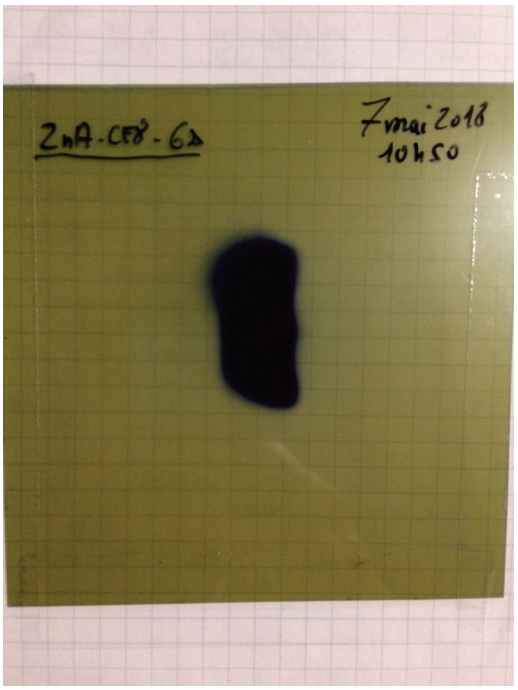

(b) Beam shape recorded with a 6 s irradiation at 2 nA beam intensity by a GAFchromic film fixed on the entrance surface of the hodoscope.

Figure 6.5: Setup and result of a preliminary irradiation performed to estimate the beam shape at the hodoscope position.

coincidence of the two scintillators on beam are sent to a VME scaler module, and the counting could be visualized during the acquition to estimate the beam intensity. As mentioned, the hodoscope can operate with an external trigger or in stand-alone auto-triggered mode. In both cases, the acquisition can be performed by selecting or not the coincidence of the two hodoscope fiber planes (horizontal and vertical). In the following, the coincidence acquisition will be referred to as AND acquisition, and the name OR acquisition will refer to data sets collected with no coincidence selection. The detector has been tested in all its possible working modes for various beam intensities, and we present here a selection of the obtained results, then discussed in section 6.1.2. Finally, at the end of the beam test, the trigger μ-TCA functionality has been first tested by using two hodoscope boards in order to simulate the trigger production by a different detector connected to the μ-TCA acquisition system.

A preliminary irradiation has been performed to estimate the beam shape and size at the hodoscope position. A GAFchromic film has been fixed to the hodoscope on the beam nozzle side, as shown in the picture of Figure 6.5a, and a 6 s irradiation at about 2 nA beam intensity (measured by the Faraday cage) was performed to record the beam transverse profile. The result is shown in Figure 6.5b. The recorded beam size is approximately 2×3.2 cm^2 with a rectangular shape.

6.1.1 Experimental results

After the tuning of the working parameters (plastic scintillators power supply and threshold, hodoscope PMs power supply, FE board threshold and gain of the two Application-Specific Integrated Circuits (ASICs)), our intensity monitoring system has been calibrated with the Faraday cage from very low intensities up to clinical intensities. In the following, we will refer to the intensity as a detection rate, measured by the hodoscope monitoring system based on the FE board read out, which has been verified to be consistent with this calibration. Several test runs have been performed to verify all the acquisition and monitoring features, and to tune the beam intensity, which has been fixed to obtain an initial rate of detected external trigger signals (given by the coincidence of the two plastic scintillators on beam) of about 23 kHz and a corresponding detection rate on the hodoscope of 17 kHz in AND configuration. As mentioned, the hodoscope detection efficiency has been tested at increasing beam intensity in the 23 – 280 kHz range of external trigger rate. The efficiency, expressed as percentage rate of recorded events with respect to the trigger counts, is reported as a function of the beam intensity in Figure 6.6. The efficiency has been evaluated for the two hodoscope working modes (AND and OR). Even though in AND configuration the hodoscope is supposed to record only events with a coincidence between horizontal (x) and vertical (y) fiber planes, single plane events are also recorded; this issue is discussed in section 6.1.2. For this reason, both the single plane and coincidence event detection efficiency are reported in Figure 6.6 for the two working modes of the hodoscope triggered by the external scintillator coincidence signal. In OR configuration, the horizontal-vertical plane coincidences are reconstructed at the analysis stage. Acquisition problems occurred at high trigger rate in hodoscope OR configuration, so that the data point at 280 kHz is missing for the OR configuration curves.

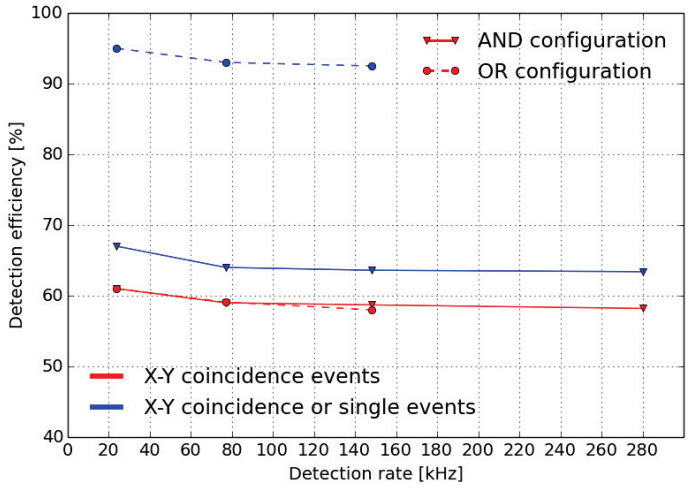

Figure 6.6: Hodoscope detection efficiency as a function of the trigger detected rate for the different acquisition modes. The solid lines corresponds to acquisitions with the hodoscope in AND configuration, the dashed lines to the OR configuration. Red curves represent events with coincidence of horizontal (X) and vertical (Y) fiber planes, while blue curves include single plane and coincidence events.

As expected, the detector efficiency slightly decreases for increasing beam intensity. The efficiency for events with coincidence of horizontal and vertical fiber planes ranges between 62 and 58 % and is compatible in AND and OR hodoscope working mode. An efficiency beyond

90 % over the whole beam intensity range has been obtained in OR configuration including both single plane and coincidence events. As mentioned, also in AND configuration single events are recorded and the efficiency for the detection of this kind of events is in the range 67 – 64 %.

The hodoscope spatial and time performance have been studied with acquisitions with external trigger and AND of horizontal and vertical fibers configuration, at the lowest beam intensity provided during the test, corresponding to 23 kHz of trigger detection rate. In Figure 6.7 the two-dimensional beam profile collected by the hodoscope is shown. To be noticed that each plot bin corresponds to a single 1 mm fiber in the two spatial directions. The collected beam profile perfectly fits with the expectation, with a vertical extension of 30 fibers (30 mm), by considering twice the distance between the profile maximum and the top irradiated bin, and a horizontal extension of about 20 fibers (20 mm). The mono-dimensional profiles shown in Figure 6.8 for the horizontal (left) and vertical (right) direction confirm the good spatial detection of the beam profile.

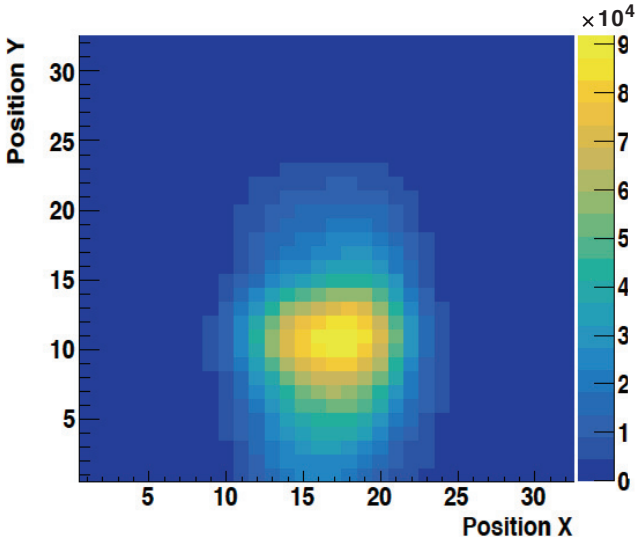

Figure 6.7: Two dimensional beam profile recorded by the hodoscope. The bin size corresponds to the hodoscope scintillating fiber size (1 mm).

The spatial performance of the hodoscope is also determined by the number of fibers involved in each interaction. This parameter has been studied and the results are shown in Figure 6.9 for the two axes. As expected, in most of the interactions one single fiber per axis is involved. However, a significant amount of events shows two or more fibers involved in at least one of the two axes. Moreover, since the acquisition was performed in hodoscope AND mode, at least one fiber per axis should be mandatory to validate the event and send it to the μ-TCA for the acquisition. The presence of events with no fibers hit in one of the two planes confirms the aforementioned problem, discussed in section 6.1.2.

The hodoscope timing performance has been also analyzed with this low beam intensity run. The absolute time (with respect to the board internal clock), is measured separately for the two fiber planes and for the trigger signal. Concerning the fiber plane time, it corresponds to the arrival time of the first event detected in the defined time coincidence window. The co-

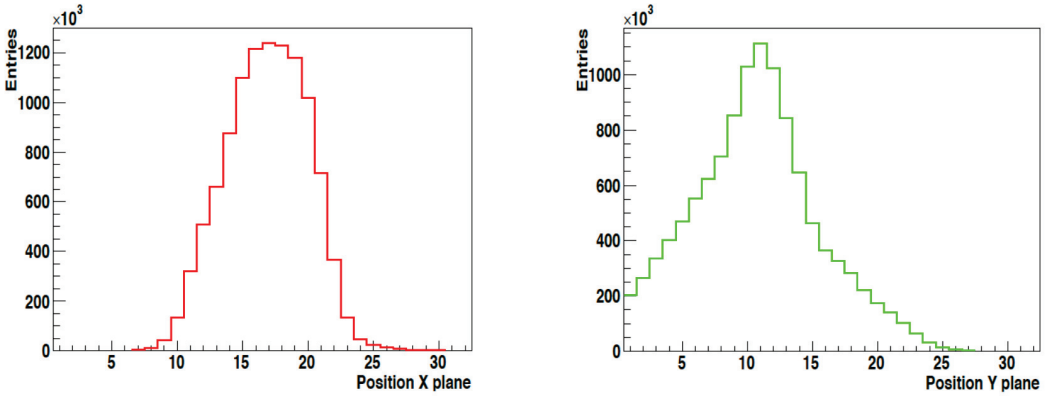

(a) Horizontal plane. **(b)** Vertical plane.

Figure 6.8: Mono-dimensional spatial profiles of the beam recorded by the hodoscope.

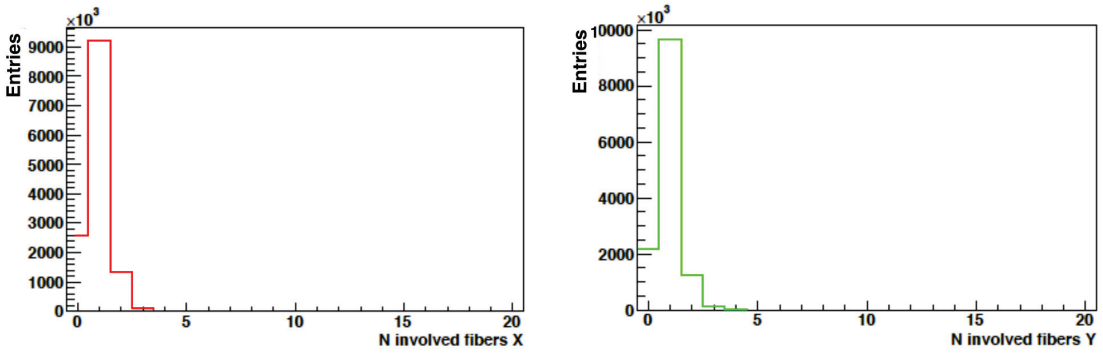

(a) Horizontal plane. **(b)** Vertical plane.

Figure 6.9: Number of involved fibers per event recorded by the hodoscope for the two planes (AND acquisition mode).

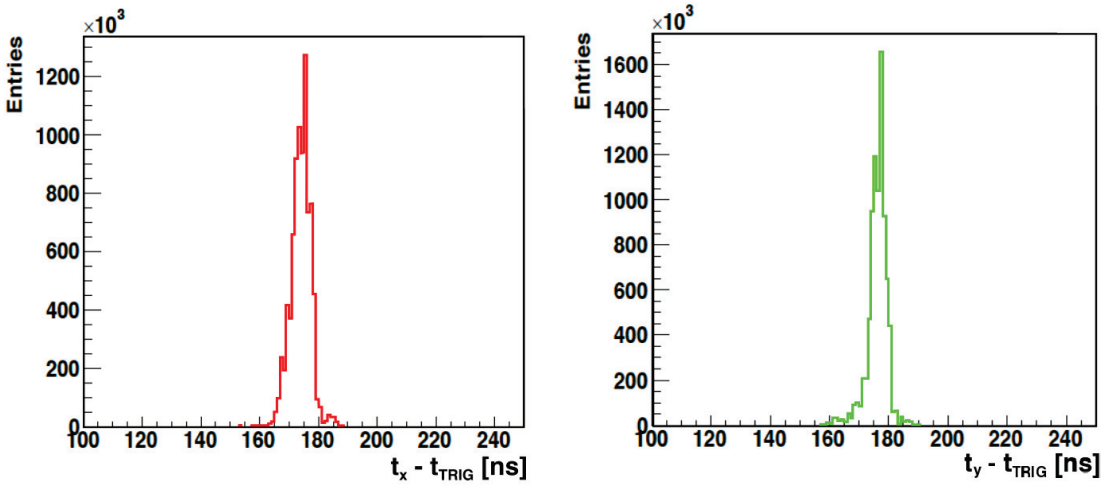

(a) Horizontal plane. **(b)** Vertical plane.

Figure 6.10: Distribution of the time difference between the trigger arrival time and the time measured by the two hodoscope fiber planes.

incidence window was fixed, for this test, to 3 board internal clock counts, corresponding to 24 ns. Given the problem detected in the previous analysis, the timing performance analysis is limited to coincidence events selected at the data processing stage. Figure 6.10 shows the distributions of the measured time for the two fiber planes (horizontal - left - and vertical - right). The distribution FWHM widths are 6.8 ns and 5.3 ns for the x and y plane, respectively.

The distribution of the measured absolute time difference between the two fiber planes has also been studied and is reported in Figure 6.11. The experimental distribution has a mean value of 2.4 ns and a width FWHM of 3.5 ns.

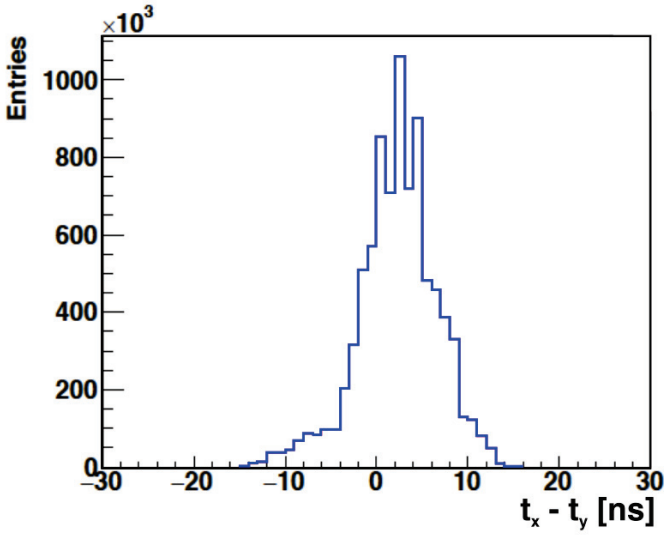

Figure 6.11: Distribution of the time difference between the two hodoscope fiber planes for horizontal-vertical plane coincidence events.

6.1.2 Discussion

After a preliminary test performed in December 2017, in May 2018 the 32+32 scintillating fiber hodoscope has been tested on beam for the first time with the final μ-TCA-based acquisition system. The promising results presented in the previous section allowed to estimate the hodoscope performance, highlight the main issues for what concerns the detector, the electronics boards and the acquisition system, and plan the development advancements. In particular, it has been shown that:

- a detection efficiency beyond 90 % can be achieved at the explored beam intensity;
- the hodoscope spatial response it satisfactory and the beam profile has been correctly recorded;
- in most of the events, 1 or 2 fibers per detection plane are involved;
- the time response is limited to a 6 – 7 ns time window.

Notwithstanding the encouraging results, the FE board and acquisition firmware and software showed some issues during this first test. In particular, the AND configuration showed an unexpected behavior. As mentioned, with this working mode, only events with time coincidence between the horizontal and the vertical fiber planes should be recorded, but also non-coincidence events have been collected. Some laboratory tests have been performed after the end of the beam test campaign, and a possible explanation has been found in the data processing at the hodoscope FE board level. The analog signals emerging from the hodoscope read-out PMs are collected on the board and converted to logic with the application of a fixed threshold. The logic signal time width depends on the time-over-threshold of the analog signal, so that low amplitude analog signals can trigger the acquisition but result in very short logic output. If the AND function implemented on the board to verify the coincidence takes more time than the logic signal width, the coincidence can be triggered but the logic signal related to the hit fiber can be lost. This effect could explain the presence of single plane interaction also in AND working mode. In addition, this effect could also be the cause of the low efficiency in AND configuration (below 60 %), and, in general, for the detection of coincidences between the two fiber perpendicular planes, shown in figure 6.6. The presented timing performance has been obtained with a preliminary time calculation method. The time measurement features implemented on the FE board was still under development at the moment of testing, and the trigger arrival time was measured according to the internal board clock (frequency 500 kHz). A dedicated clock with 250 ps resolution was already implemented on the FE board for the hodoscope fiber time measurement. The exploitation of a dedicated Time-to-Digital Converter (TDC) on the card or the trigger channel (not yet used in the tested version of the firmware) is foreseen for the final configuration, for which the Time-Of-Flight (TOF) between the absorber and the hodoscope interactions will be measured. The trigger time measurement method affected the time resolution which is below the expectations. The distribution of the time difference between the fibers in the two detection planes was expected to be centered in $t_x - t_y = 0$, and its width was expected to reflect the hodoscope time resolution, given the superior resolution of the reference clock (250 ps). The obtained results (3.5 ns FWHM width, mean value of 2.4 ns) are not satisfactory. This degraded performance is probably due to the time measurement method, which selects the first event in the time coincidence window as time reference. In case of background contamination, un-correlated

background events collected in the coincidence window degrades the time resolution. Background events are also the identified cause of events with more than one fiber hit per plane. The data analysis revealed a large amount of events with un-correlated fibers hit in coincidence (spatially separated by more than 2 mm), clear evidence of background contamination. The planned improvements to the firmware of the hodoscope FE boards and a fine tuning of the board working parameters are expected to solve the highlighted issues. In particular, a gain and a threshold are set on the hodoscope board ASIC; the gain can be set for each read-out channel (each fiber), while the threshold is common to the whole ASIC, thus for 32 fibers (one fiber plane). An appropriate calibration of the gain values will probably allow to obtain analog signals with sufficient amplitude to result in larger logic signal, able to trigger the coincidence read-out and, thanks to a tuning of the ASIC thresholds, be transferred to the data acquisition with non-zero values. This should improve the overall efficiency of the system and guarantee the correct functionality of the AND acquisition setting. Moreover, the proper threshold should reduce the background contamination, thus improving the timing and spatial performance. An automatic calibration method has been developed in the Summer 2018 in collaboration with an internship student, and applied to characterize the hodoscope board ASIC behavior for background measurements. The same strategy will be applied during a dedicated beam test before the end of 2018 to define the hodoscope optimal working parameters for the monitoring of proton beams. A second dedicated test will be then necessary for the characterization of the hodoscope with carbon ions, which are expected to induce different response due to an increased energy deposit in the scintillating fibers. The results obtained with an analog read-out and a VME-based acquisition, mentioned in section 3.1.4.1, showed that sub-ns time resolution and an efficiency beyond 90 % can be achieved, and are the reference objective for the needed electronics improvements. Finally, before the end of this first test, the μ-TCA trigger capabilities have been tested with two hodoscope cards to mimic the coupling of two camera components. This first attempt allowed to create the bases for the firmware and electronics development of the following months, which aimed to prepare the system for the test of a multi-collimated camera configuration, i.e. the coupling of hodoscope and absorber, performed in September 2018 and described in section 6.2.

6.2 Collimated camera: September 2018

As the main goal of May 2018 was to achieve data acquisition with the μ-TCA, we put our effort in the integration of the absorber block readout in this acquisition and on the validation of the trigger μ-TCA handling. The generation of trigger signals by the BGO blocks has been tested at the IPNL with gamma sources, and the final integration of hodoscope and absorber has been tested on beam in September 2018. 6 BGO blocks composed the minimal multi-collimated camera absorber, read-out by a single ASM board. As described in chapter 3, a FE card is connected to each block: it is in charge of splitting the power supply to the four PMs and sending the collected signals to the read-out ASM board. Each ASM board has 24 channels, so that it is designed for the read-out of a maximum of 6 blocks. The data are sampled at the selected frequency (up to 5 Giga Sample Per Second (Gsps) for 1024 samples). The integral of each signal (total collected charge) will be calculated on the card and directly sent to the acquisition system in the final camera acquisition configuration, while a test operating mode has been used for this preliminary beam measurements, with all the samples of each signal sent to the acquisition and stored (see section A.3.2). The selected sampling frequency has been 1 Gsps, with 1 μs signal width digitized. One of the two identical tungsten collimators

described in chapter 3 has been placed in front of the absorber blocks. One collimator slab (1.5 mm thick) is used for each slit, and the pitch between slits is 5.5 mm. This geometrical configuration leads to a spatial resolution (single slit Field Of View (FOV)) of about 6.5 mm. The 32+32 fiber hodoscope has been used for the trigger generation tests and the first TOF measurements. A schematic view of the measurement setup is shown in Figure 6.12 from top view.

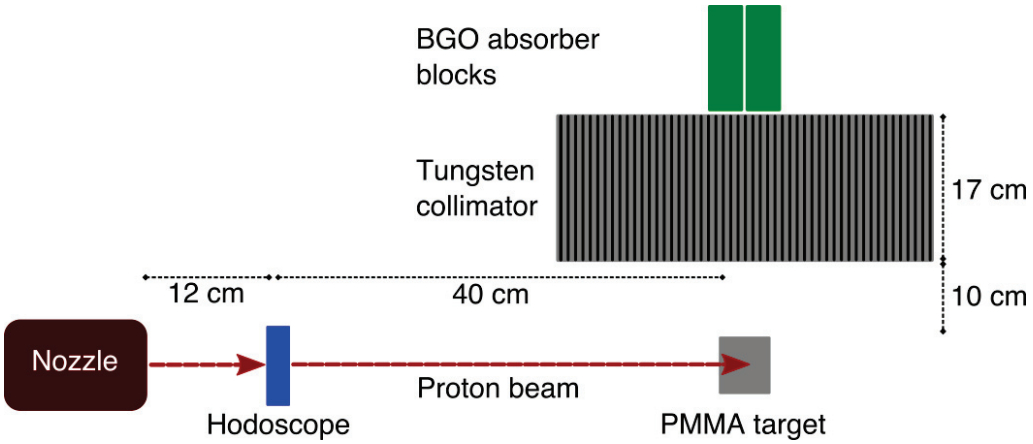

Figure 6.12: Schematic view of the hodoscope and the multi-collimated camera setup for the beam test at CAL.

The hodoscope, mounted on its remotely controlled support, has been set at a distance of 12 cm from the beam nozzle, and aligned to the beam exit. Two Poly-Methyl-Metacrylate (PMMA) 5 cm side cubes have been used as target, aligned along the beam line and set 40 cm far from the hodoscope center. The two targets have been disposed one on top of the other to completely stop the beam, which has a spot size increasing with the distance from the nozzle. GAFchromic films have been fixed at the hodoscope entrance surface and at the top target cube, and a 10 s irradiation at approximately 1 nA of beam current allowed to record the beam spot size in the two positions. The results are shown in Figure 6.13a. The beam size close to the nozzle (on the hodoscope surface) is approximately the same as in the previous test (see Figure 6.5b), with a 1.5×3 cm^2 rectangular shape. The beam spread is evident at the target position, where the spot has ellipsoidal shape, with axes of approximately 5 and 4 cm. The multi-collimated camera was set at 90 ° with respect to the beam direction, with the collimator entrance surface at a distance of 10 cm from the target. The 6 absorber blocks are in contact with the collimator back face, and disposed in two columns of three blocks each within the custom mechanical support built at IPNL, with the center of the column on the nozzle side approximately aligned with the target entrance face. A picture of the complete setup is shown in Figure 6.14a, while detailed side and front-views of the multi-collimated camera are given in Figure 6.14.

The absorber has been initially tested in stand-alone acquisitions to first characterize the BGO block response to beam-induced Prompt-Gammas (PGs). Various runs have been performed with and without the collimator, with the target fixed in the initial position. For the irradiation without collimator, the distance between the target and the absorber blocks has been kept unchanged, and corresponded to 27 cm (10 cm distance target-collimator entrance face + 17 cm collimator thickness). The trigger rate was monitored online, as well as the detection rate of each single block. A first set of measurements has been collected without the collimator with a beam current of approximately 150 pA, inducing a detection rate on each BGO block in

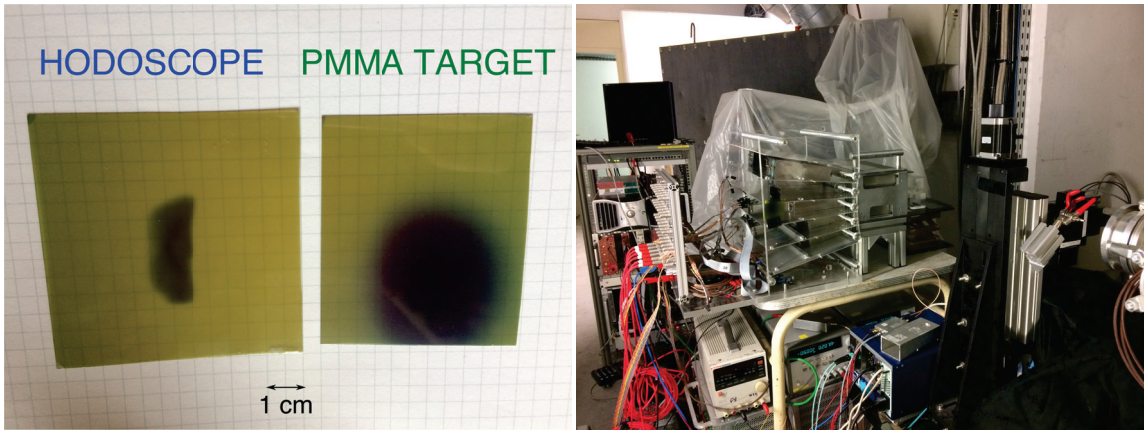

(a) (b)

Figure 6.13: (a) Beam size recorder with GAFchromic films on the hodoscope and PMMA target entrance surfaces. (b) Beam test setup including the beam tagging hodoscope 12 cm far from the beam nozzle, the PMMA cubes (40 cm far from the hodoscope) used as target and set on a support with adjustable height, and multi-collimated camera at 90 ° with respect to the beam direction. The tungsten collimator entrance face is at 10 cm from the target, and the 6 absorber blocks are in contact with the collimator back face.

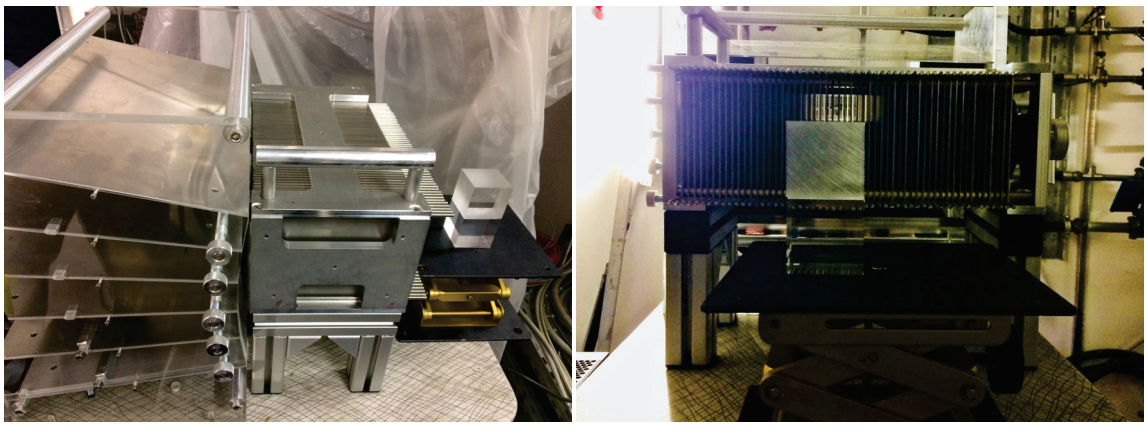

(a) Side view from the nozzle side.

(b) Front view. The beam direction is from left to right.

Figure 6.14: Detailed views of the multi-collimated camera setup with the PMMA target cubes.

the range 300 – 400 kHz. With the collimator, the beam current has been increased to obtain similar trigger rates, up to about 1 nA. In particular, two data sets have been collected with the collimator and with the target in two different positions: the initial one, and one shifted of 1 cm in the beam direction increasing the distance from the nozzle. A second phase of the test has been dedicated to the synchronization of absorber and hodoscope, with the trigger to the hodoscope acquisition given by the absorber blocks (as in the final multi-collimated camera configuration). With the setup including the collimator and the target in the initial position, the beam intensity has been tuned in order to obtain a trigger rate of a few kHz, corresponding to an hodoscope stand-alone detection rate of approximately 10 MHz, directly monitored by the hodoscope FE board, as done in the May 2018 test described in section 6.1. Such a stand-alone hodoscope detection rate represents an improvements with respect to the previous results, and will be verified in future hodoscope dedicated tests with optimized electronics configuration. Several data sets have been collected for different values of the coincidence window, and the TOF spectra have been produced. The beam tests allowed to verify on beam the new developed features of the acquisition system, as well as to test for the first time the BGO blocks with the final acquisition system, exposed to PGs. The main results of the test are presented in the next section and discussed in section 6.2.2.

6.2.1 Experimental results

Figure 6.15 shows the data collected by the 6 BGO absorber blocks without the collimator during the irradiation of the PMMA target, as visualized by the online monitoring tool mentioned in section 3.1.6. The left side panels show, from top to bottom, the histogram of the number of hit blocks per events, the integrated distribution of the reconstructed interaction positions along the horizontal and vertical axes. The right panel shows the two-dimensional map of the reconstructed interaction position in the 6 blocks. The beam direction is from left to right in the presented plots. The PM gain equalization step explained in section 3.2.2 is already included in the monitoring code. The calibration factors for each BGO block used in the beam test have been obtained during previous laboratory tests: the blocks have been exposed to a ^{22}Na source and the data have been collected with the final acquisition system.

The data set collected without the collimator has been used to fine tune the analysis and calibration parameters (calibration factors, data selection). The results of the complete calibration and analysis processes are shown in the following for one of the employed blocks.

The effect of the PM gain equalization are shown in Figure 6.16, where the signal integral spectra are presented for the four block PMs before (left) and after (right) the gain equalization. In the right panel, the calibrated energy spectrum (sum of the four PM signal integrals for each event) is also shown. The raw signals have been investigated to understand the origin of the peak in the spectra at the highest Analog-to-Digital Converter (ADC)/energy values (about 3200×10^3 ADC counts - left plot- and about 5800 keV - right plot) and more than 40 % of the events present signal amplitudes which are beyond the ASM board ADC saturation limit. Such events are rejected in the following analysis; in the case of saturation, indeed, the total energy deposition and interaction point estimate are not correct.

The whole block energy spectra before (left) and after (right) the PM gain equalization and event selection are sketched in Figure 6.17. The processed spectrum shows the spectroscopic gamma peaks expected for the irradiation of a PMMA target, corresponding to the

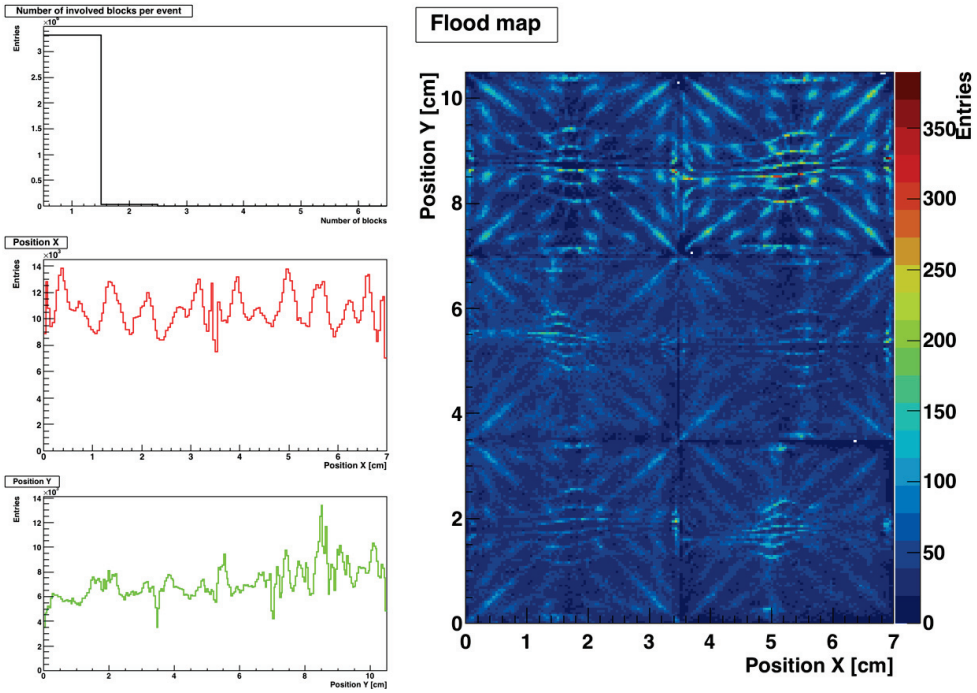

Figure 6.15: Raw data collected by the 6 absorber BGO blocks during an irradiation of the PMMA without the collimator. On the left side, the top histogram show the number of hit blocks per event, the central and bottom histograms show the projection of the reconstructed interaction positions on the horizontal and vertical direction, respectively (sum of the 6 blocks). The right side panel show the two-dimensional distribution of the reconstructed interaction positions. No data selection has been applied. The beam direction is from left to right.

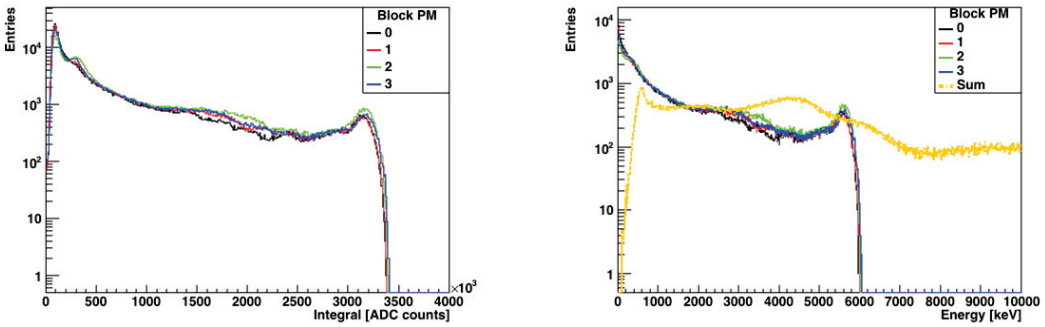

(a) Before gain equalization.

(b) After gain equalization.

Figure 6.16: PM signal integral spectra.

de-excitation of ^{12}C (4.44 MeV) and to the neutron capture by hydrogen (2.22 MeV - deuterium binding energy). In addition, the de-excitation of ^{16}O (6.13 MeV) creates the spectrum slope change visible at about 6000 keV. The energy spectrum shows the contamination of background events below 1 MeV, which will be rejected in the following analysis.

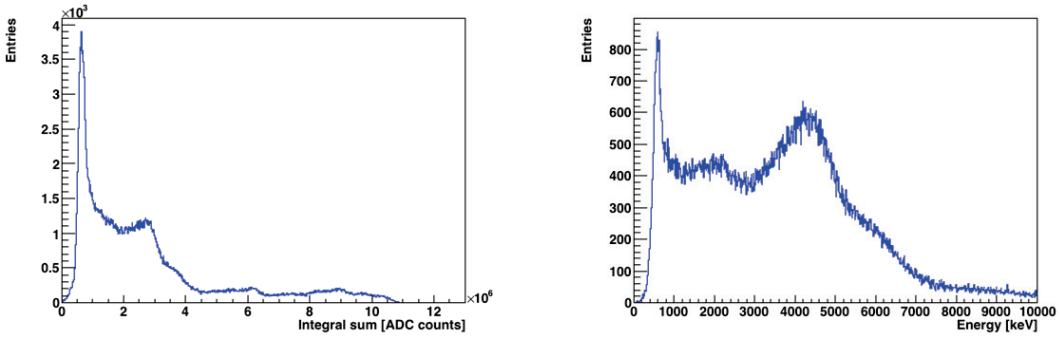

(a) (b)

Figure 6.17: Whole block energy spectrum before (a) and after (b) PM gain equalization and saturated events rejection.

The mono-dimensional integrated profiles and the two-dimensional maps of the reconstructed interaction positions are shown in Figure 6.18 and Figure 6.19, respectively, before (left) and after (right) the calibration and energy selection processes.

The described analysis steps have been applied to the data collected by the 6 blocks, and the resulting distributions are shown in Figure 6.20, to be compared to Figure 6.15.

Once properly calibrated and selected, the data obtained with the acquisition without collimator have been used to extract efficiency calibration factors to be used for the analysis of the data collected during irradiation with the collimator. The overall response of the blocks must be equalized to create an integrated profile along the beam direction (x); the equalization is based on the total integral of the mono-dimensional x position profiles (see Figure 6.18b - left). The mono-dimensional interaction position profile along the beam direction for two acquisitions (with collimator) with a target relative shift of 1 cm is shown in Figure 6.21. The response of each block has been normalized as just described, and the two resulting profiles have been normalized to their maximum. The bin size has been chosen to represent half of the BGO block pseudo-pixel size. The dashed vertical lines identify the entrance face of the target for the two positions.

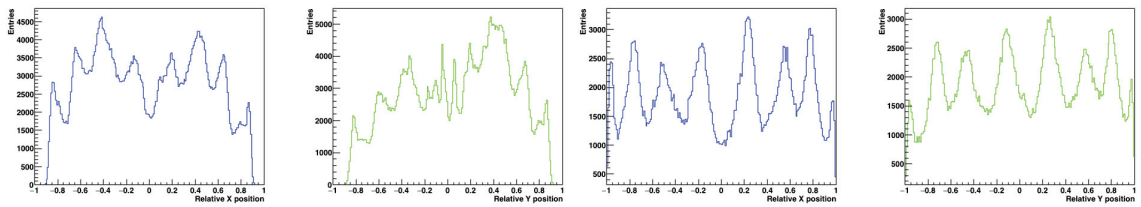

(a) (b)

Figure 6.18: 1D integrated position distribution on the two transverse dimensions before (a) and after (b) PM gain equalization and saturated events rejection. In the two sub-figures, left side for the horizontal dimension (x), right side for the vertical one (y).

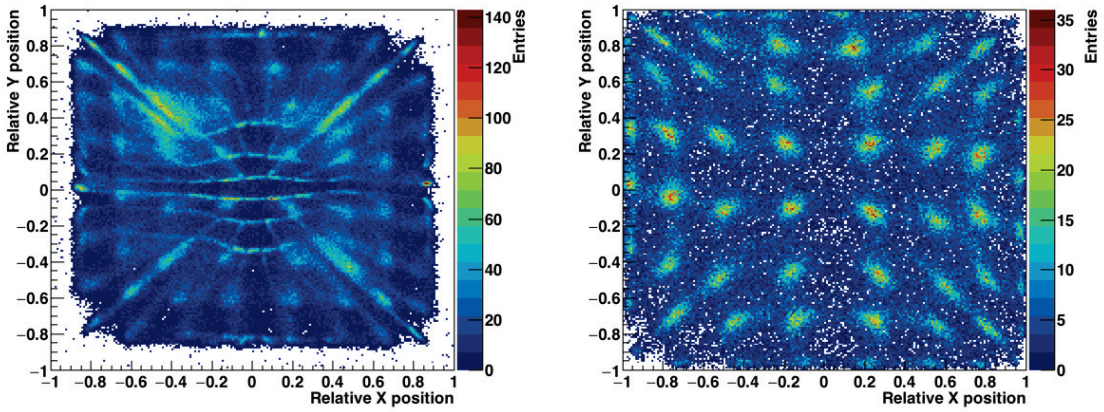

Figure 6.19: 2D maps of the reconstructed interaction positions before (a) and after (b) PM gain equalization, saturated events rejection, and selection of events with energy deposit higher than 1 MeV.

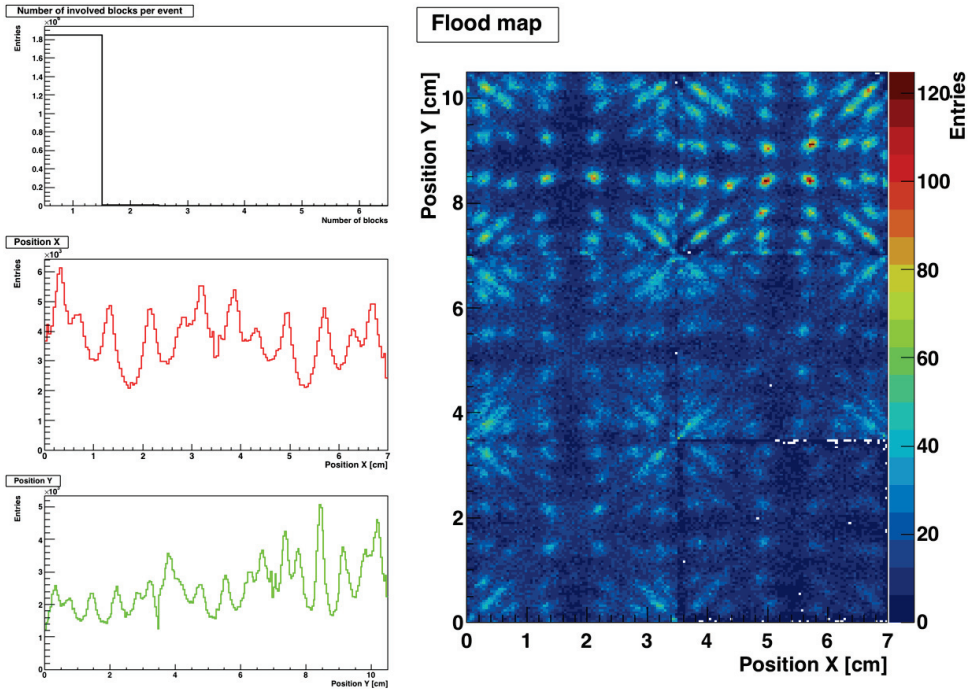

Figure 6.20: As for Figure 6.15, with the selection of events below the ASM board ADC saturation limit and with an deposited energy higher than 1 MeV. The beam direction is from left to right.

The PG profiles are not clearly visible from these position distributions, and information about the proton range cannot be retrieved. In particular, the profiles reflect the pseudo-pixel block structure and the separation between the two block columns is clearly visible in the region around 3.5 cm. As shown in section 3.2.2 for gamma energies below 1.3 MeV, the detection efficiency significantly varies on the surface of each block, so that the collected data must be further normalized according to the interaction position on the block surface to reconstruct

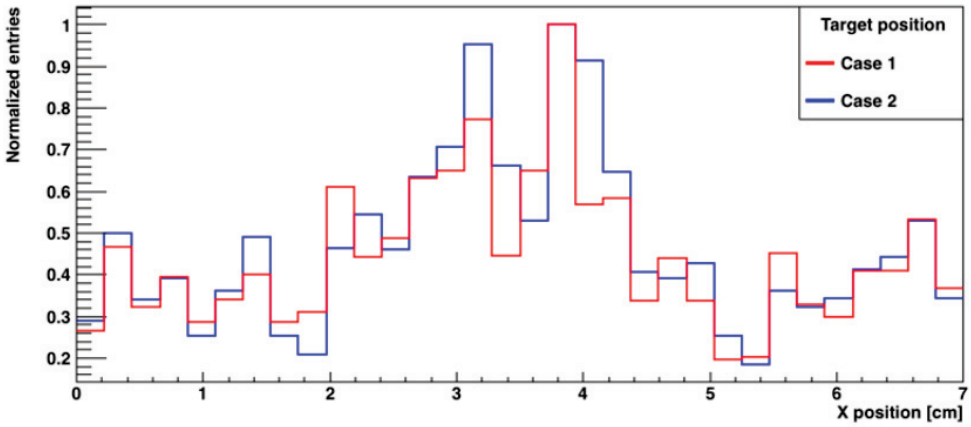

Figure 6.21: Mono-dimensional interaction position profile along the beam direction obtained for two acquisitions with the PMMA target set in two different positions. The red curve corresponds to the run with the target in its initial position (case 1), while the blue curve corresponds to a target shift of 1 cm in the beam direction (case 2). The beam direction is from left to right.

the PG profile. With the automatic algorithm developed for the BGO block calibration and presented in section 3.2.2, the regions corresponding to the pseudo-pixel columns have been identified for each block, and the integral of each pseudo-pixel column has been calculated from the mono-dimensional x position profiles (see Figure 6.18b - left). The obtained values have been used to normalize the collected statistics according to the reconstructed position in the block. The mono-dimensional profiles obtained as a result of this normalization are shown in Figure 6.22.

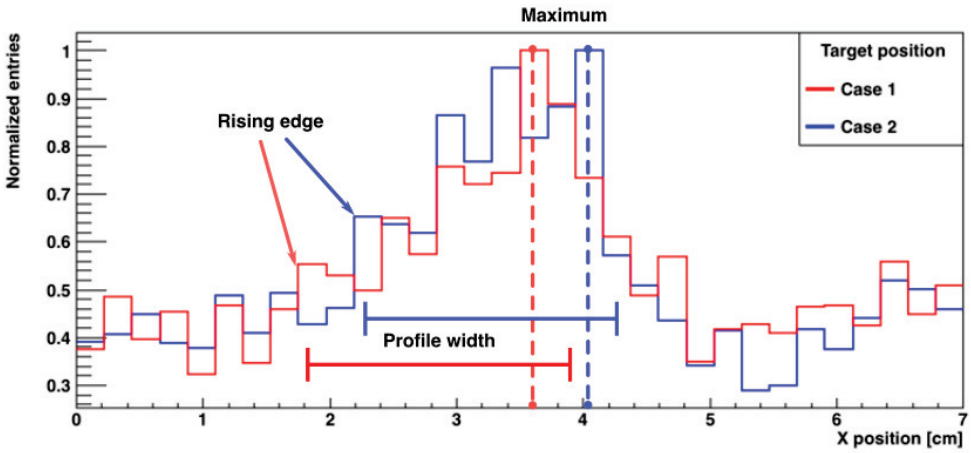

Figure 6.22: As Figure 6.21, after the normalization of the BGO block response according to the interaction position. For the two runs (case 1 and 2), the dashed lines highlight the distribution maximum, the arrows point to the distribution rising edges and the two segments show the profile widths. A shift of 2 – 3 bins is qualitatively visible between the two PG profiles. The beam direction is from left to right.

The proton expected range in the PMMA target is approximately 2.5 cm, considering the residual proton range after the interaction in the hodoscope. The PG profile fall-off position is expected to be located a few mm before the end of the proton range, leading to a profile

expected width of approximately 2 cm. Although the rising edges are slightly visible, the observed width of the two profiles is qualitatively estimated in 2 cm, and the associated shift is in agreement with the expectations. The maximum bins have been highlighted in the plot as further reference points for the profile overall position estimate.

As mentioned, in the second part of the beam test the synchronization and timing performance of the coupling of hodoscope and multi-collimated camera have been tested. In Figure 6.23 the TOF spectrum obtained with a 120 ns coincidence window is shown. The TOF is here defined as the difference between the trigger time and the arrival time of the first interaction recorded in the hodoscope, and the coincidence window starts at the trigger arrival time, with the coincidence research performed in the time window preceding the trigger. The coincidence between the two hodoscope fiber planes has been required.

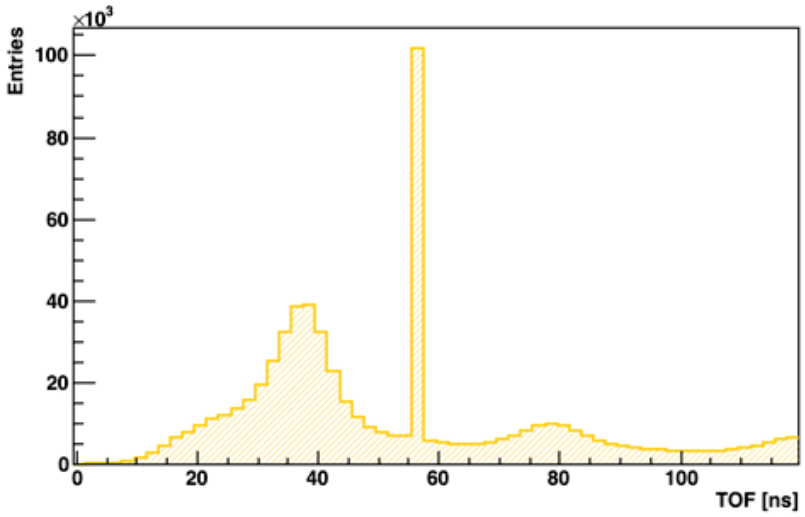

Figure 6.23: TOF spectrum obtained with hodoscope and multi-collimated camera with a coincidence window of 120 ns.

The TOF distributions shows the beam time structure, with bunches delivered each ∼40 ns. Two bunches are clearly visible in the presented distribution, and a third one is cut by the end of the coincidence window. The main peak (close to 40 ns) corresponds to the bunch which caused the emission of the PG inducing the trigger signal. The secondary peaks (at about 80 and 120 ns), represent the coincidence between the trigger signal and previous beam bunches; this effect is due to the approximately 60 % efficiency of the hodoscope in the selected working mode (coincidence of the two fiber planes), which causes a loss of information and the correlation of hodoscope and absorber events induced by different beam bunches. The peak at the center of the distribution is caused by a problem in the 250 ps resolution clock value conversion in the hodoscope FE board, discussed in section 6.2.2.

6.2.2 Discussion

The presented beam test followed the first measurement campaign performed in May 2018, with the aim to test and debug new features introduced in the electronics and acquisition system configuration. In particular, after the successful test of the hodoscope acquisition with

FE boards and μ-TCA-based acquisition, the main goal of this test was to verify the absorber read-out board functionality and its inclusion in the camera acquisition logic, as well as its synchronization to the hodoscope. A minimal multi-collimated camera configuration, composed of 6 BGO blocks and the tungsten collimator described in chapter 3, has been tested with the final μ-TCA-based acquisition system for the first time. In addition to this, the coupling between absorber and hodoscope has been tested for TOF measurements. The test provided encouraging outcomes: it allowed to obtain the first physics measurements, even if in a non-optimized version, and to plan the further development needed for both the electronics and the detector configuration. In particular, Figure 6.22 shows the potential of the camera in detecting range shifts in a homogeneous target. Even with a non-optimized electronics and absorber/collimator geometrical setup, for a 1 cm target shift, a 2 – 3 bin shift (bin size set to half the BGO pseudo-pixel size) is qualitatively estimated in the mono-dimensional PG interaction position profiles. For this test, the 6 employed blocks have been vertically aligned, but different solutions will be studied in future laboratory and beam tests to improve the spatial resolution by relatively shifting the block pseudo-pixel positions in a column. Moreover, the collimator multi-slit width can be varied to assess the best configuration according to the block spatial resolution. The retrieved performance is determined by the block calibration process developed with a preliminary acquisition system (see section 3.2.2) and for the first time adapted to the final acquisition logic, based on raw signal integrals. It must be noticed that the pixel-based energy calibration could not be performed due to the limited statistics. Extensive laboratory tests with the μ-TCA acquisition system, foreseen in the next months, will allow to optimize the block calibration process, and a performance improvement is expected. Moreover, the block and ASM card working parameters will be further studied to reduce the amount of events saturating the ADC limits. However, overall better performance has been verified with a signal amplification stage preceding the conversion to logic (as done with the preliminary acquisition system), so that the development of new FE cards including a shaping amplifier dedicated to each block PM can in principle significantly improve the detector performance. The proposed solutions will be evaluated in the next future and new tests focused on the absorber detector are already planned before the end of 2018. Concerning the TOF measurements, the beam time structure could be clearly identified, but a data TOF selection could not be verified due to the limited collected statistics. It will be tested in dedicated beam measurements. Improvements in the hodoscope FE board firmware, already discussed in section 6.1.2, are expected to improve the coincidence time resolution. In particular, the expected hodoscope increased efficiency (beyond 90 %) will allow to enhance the trigger-hodoscope coincidence efficiency, and correlate the PG-induced trigger signals to the correct beam bunch (which caused the PG emission). The amount PG-induced trigger signals correlated to bunches which preceded the generator one will be minimized, thus improving the resulting TOF selection accuracy. Furthermore, the time conversion artifacts highlighted in the comments to Figure 6.23 have been identified and will be corrected in a new version of the hodoscope FE card firmware developed by the IPNL electronics group. More generally, as mentioned in the discussion to the May 2018 test, the hodoscope has to be characterized to improve its working performance, with a proper evaluation of count rate capability, cross-talk, efficiency (> 90 % expected in AND working mode), and time resolution (expected < 1 ns). Finally, the camera timing performance will be also enhanced with the aforementioned optimization of the absorber block response.

The camera performance obtained during these tests are still not satisfactory when considering the design expectations and the monitoring objectives, but it must be noticed that the main objectives of the test were:

- the test of the acquisition coupling small-size collimated camera and beam hodoscope;
- a first test of the BGO response with the associated electronics.

These two objectives have been fulfilled, and all the proposed system improvements are expected to enhance the camera spatial and time response. As mentioned, new beam tests are already planned for the next months: a test will be dedicated to a detailed characterization of the available set of BGO blocks on beam and to fine tune the blocks and ASM board working parameters, as well as to optimize the collimator geometrical configuration.

Part III

Conclusion

The work presented in this thesis has been carried out within the CLaRyS collaboration, involving four French institutions with the common goal of developing gamma imaging solutions for the online monitoring of ion range in particle therapy. The project focuses on the detection of PGs, products of primary ion nuclear interactions in the patient body, and includes the parallel development of two gamma detection systems, which share some detector components. The multi-collimated camera consists of a multi-slit tungsten collimator to be set in front of an array of BGO blocks, working as absorber. The same absorber is part of the Compton camera, in addition to 7 DSSDs composing the scatterer section. A beam monitoring system (hodoscope) based on scintillating fibers and multi-anode PMs can be synchronized to the two cameras and provide spatial and time tagging information about the incident beam primary particles, thus allowing for TOF measurements. Such an additional information is used for background rejection and data reconstruction purposes.

The original objective of this thesis was the complete characterization of the camera components and of the hodoscope, and eventual tests in clinical conditions. As described in chapter 3, extensive work has been devoted to the experimental tests of the various detection sections. In particular, the development of hodoscope and absorber blocks saw a substantial advancement, as well as the related electronics and the camera acquisition system.

The hodoscope has been produced in three versions with increasing size and read-out complexity; the final prototype is composed of 256 scintillating fibers disposed on two perpendicular planes (128 fibers each), and is read out by 8 PMs, with a FE board each. All the PMs have been fully characterized, and first tests with radioactive sources have been performed with a National Instruments PXI-based acquisition system. In the last year, the IPNL electronics group advanced in the development of the FE card firmware, and the reduced size hodoscope (32 fibers per plane) has been tested on beam (see chapter 6) with the final acquisition system, based on the μ-TCA standard. The next instrumental development steps include:

- the debugging, optimization and validation of the acquisition chain, with FE boards and μ-TCA-based data handling;
- new tests in stand-alone mode to calibrate the detector response (ASIC gain and threshold, power supply, etc.) and estimate its performance (cross-talk, detection rate, space and time resolution);
- synchronization of the 8 FE boards and test of the 128+128 fiber prototype.

The absorber BGO blocks have been recovered from a dismantled SIEMENS PET scanner, and have been deeply studied during laboratory tests for the application to the detection of gamma rays in the PG energy range. The back surface of each block is glued to four identical PMs for the read-out, and the mono-block crystal is streaked in a matrix of 8×8 pseudo-pixels. Each interaction induces scintillation light which is shared among the four PMs according to the pseudo-pixel internal structure; the interaction position is retrieved with the center of gravity of the four collected signals. The original plan foresaw a reconditioning process for each block, consisting in separating the PM quartets from the crystals, polishing the crystal surface, testing each single PM and re-coupling the crystals to groups of four PMs with similar gain. Several tests have been performed, but the reconditioned blocks always showed degraded performance with respect to the original ones. For this reason, the attention has been focused on original blocks, which have been fully characterized with an acquisition system based on NIM

modules and the aforementioned National Instruments PXI equipment. A custom calibration method has been developed to optimize the block response. During the Summer 2018, after the first tests of the hodoscope with he camera final acquisition system, the absorber read-out boards developed in Clermont-Ferrand have been tested and the BGO block acquisition has been included in the μ-TCA-based data processing. A first test on beam has been performed in the second half of September 2018, and the obtained results have been exposed in chapter 6. During this test, the first synchronization between hodoscope and absorber has been also obtained. In the next months, the following development points will be addressed:

- debugging, optimization and validation of the acquisition chain, with ASM boards and μ-TCA-based data handling;
- new characterization tests to optimize the detector response with the final acquisition and assess the best block and collimator geometrical settings for improved spatial performance;
- synchronization of 5 ASM boards for the read-out of the complete 30-block array and new beam tests in stand-alone mode.

The silicon detectors composing the scatterer have been tested with a preliminary acquisition system before the beginning of my PhD thesis (see chapter 3), and I did not have the possibility to work on further characterization measurements due to the lack of functional read-out electronics. The IPNL electronics group focused the efforts on the hodoscope and the absorber acquisition in the last months, but the development of the firmware for the silicon layers is ongoing in parallel. A first preliminary version of such a firmware will be available before the end of 2019, and characterization measurements will start. The objectives to be achieved in the next months include:

- complete the development of the FE board firmware and validate its inclusion in the μ-TCA-based acquisition system;
- test at the IPNL (with radioactive sources) and on beam the detectors to properly set the working parameters and characterize the layer performance (cross-talk, spatial, energy and time resolution);
- synchronize the 7 FE boards for the read-out of the complete scatterer stack and test it on beam in stand-alone mode.

The measurement campaigns carried out in 2018 aimed to test the FE and read-out electronics for hodoscope and absorber and to debug the acquisition system and related software. This represented the first step towards the beam test of a fully operational multi-collimated camera, which is foreseen in Spring 2019. Once the three detector components will be fully characterized, the next development steps will be focused on the synchronization of the whole camera components, including 8 hodoscope FE cards, 5 absorber read-out boards and 7 FE boards for the silicon layers. A first configuration of Compton camera is expected to be tested on beam in the first half of 2020. The main points of the development planning are summarized in Figure 6.24.

In parallel, mechanical supports and software tools have been developed during the three

years of my PhD thesis. The multi-collimated and Compton cameras will be set on a multiple-axis remotely controlled table, described in chapter 3. The table has been designed and produced before the beginning of my thesis, and I participated in the development of the LabVIEW code for its remote control. In addition to this, a custom support for the absorber blocks has been designed and produced, and the cooling system (the thermal regulated box which also provides mechanical support) for the silicon layers has been tested. Concerning the software tools, the acquisition software for the camera has been completed in the last year and is being optimized according to the detector and acquisition test results. The camera data format has been defined and implemented in the whole acquisition system, and is presented in appendix A. I personally developed the ROOT-based monitoring software used during the hodoscope and multi-collimated camera tests presented in chapter 6: it allows for the online visualization of part of the collected data sets during the acquisition. As the acquisition software code, the monitoring code has been optimized according to the requirements emerged during the beam tests. The code is now available for the hodoscope and absorber data formats, but it can be easily adapted to the visualization of the silicon layer data, as well as to the requirements of the specific tests.

In addition to the instrumental development, part of my thesis work has been dedicated to simulation studies aiming to test the application of the Compton camera under development to the monitoring of ion range in particle therapy and to nuclear medicine examinations. The results, presented in chapters 4 and 5, are promising in both cases. In particular, the Compton camera prototype has been tested for the detection of PGs emerging from a PMMA target exposed to proton and carbon ion beams. Range shifts have been simulated, and the camera showed the capability of detecting such shift with millimeter precision with an analytic data reconstruction algorithm, even if at reduced beam intensity with respect to clinical conditions. The background contamination, mainly due to random coincidences, affects the camera performance, but improvements in the analytic reconstruction algorithms and the implementation of iterative reconstruction solutions are expected to guarantee substantial improvements. Further studies are already planned to investigate novel reconstruction solutions, towards the achievement of real-time, accurate range monitoring. A geometrically adapted version of the Compton camera has been compared to a commercial Anger camera for the application to SPECT-like examinations. The two cameras have been exposed to point-like radioactive gamma sources, in the gamma energy range 245 – 2614 keV, and their performance has been compared mainly according to detection efficiency and spatial resolution. The Compton camera outperforms the Anger system for gamma energies above 511 keV, with an efficiency gain of a factor 20 or more, and spatial resolution enhanced of few millimeters. At lower energies, the efficiency gain is still verified, but the spatial resolution is slightly worse with respect to the tested Anger camera. The implementation of Compton imaging solutions in nuclear medicine would open the possibility to high-accuracy and high-efficiency examinations thanks to the employment of gamma rays at higher energies with respect to the present clinical routine, limited by mechanically-collimated detectors. Higher gamma energy translates into reduced gamma attenuation in the patient, which means improved spatial accuracy with reduced absorbed dose. In parallel, the detection efficiency gain would allow for a reduction of the examination time for compatible source activities and required performance, or for a reduction of the injected activity for compatible examination time. Both solutions determine a further reduction in the patient dose. More realistic simulation studies are foreseen, including two and three-dimensional distributed gamma sources, and studies with phantoms with increasing complexity.

Even though the camera prototypes have not been clinically tested yet, the results obtained during the three years of my PhD thesis and presented in this document are promising. The next steps for the development of the two cameras have been clearly identified, and are summarized in the time-line in Figure 6.24. Moreover, the simulation studies opened new investigation directions which will be further explored in the next future.

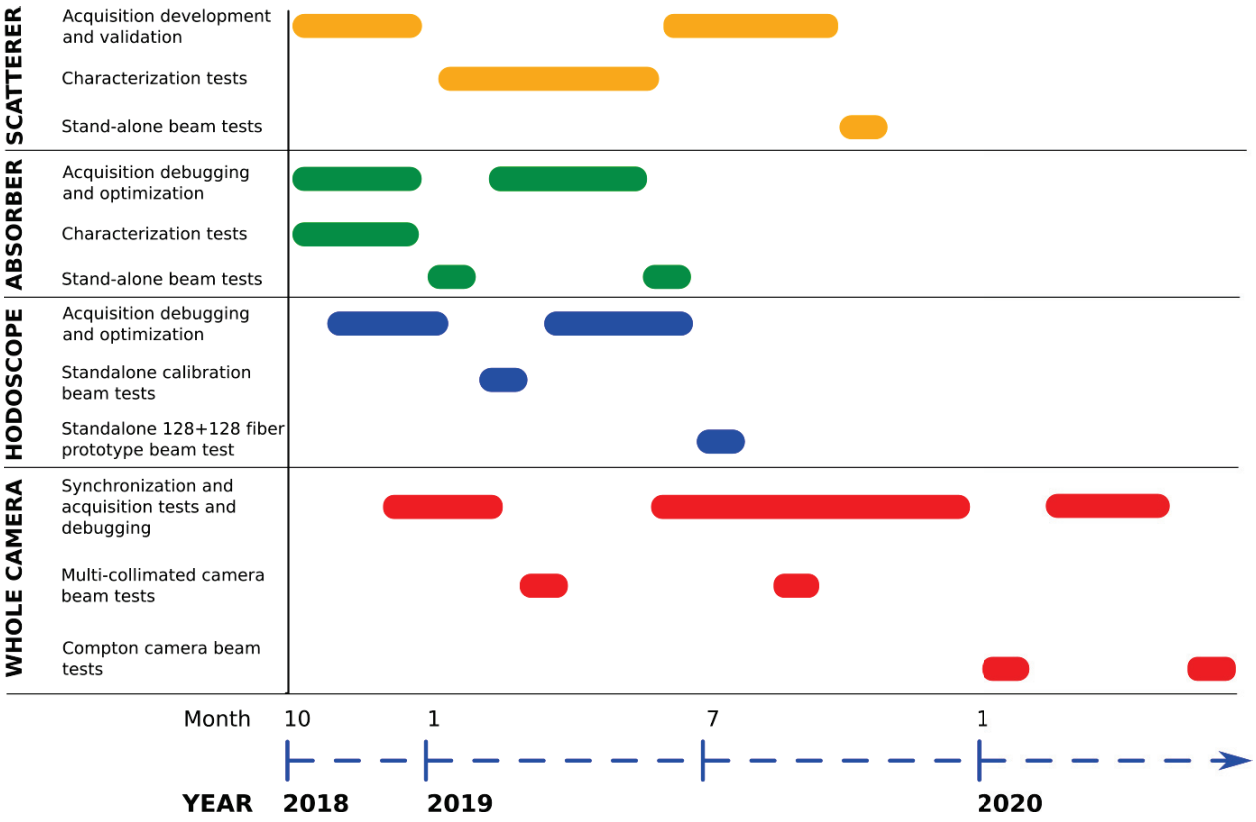

Figure 6.24: Gamma camera development timeline.

In the next two years, the development of the two CLaRyS gamma camera prototypes will be completed, and clinical tests are the final goal of the project. The only clinically-tested monitoring system based on PG detection is the IBA knife-edge camera, but non-imaging methods and alternative collimated and Compton prototypes have been developed by several research groups in the last years and are expected to provide clinical outcomes in the next future. Non-imaging solutions raised a significant interest: they produce a reliable (indirect) feedback about the ion range and, at the same time, minimize the footprint in the treatment room and the detection system complexity. Imaging approaches still seem more robust and are able to directly measure the ion range. In particular, the study and development of collimated systems is ongoing; the CLaRyS multi-collimated camera is well inserted in this context. Coupled

to the hodoscope, it is expected to provide millimeter precision in the identification of ion range shifts on a single spot basis, and represents a promising solution for real-time ion range verification. The CLaRyS Compton camera study advances in parallel to the development of other Compton imaging prototypes carried out by several research groups (e.g. in Munich, Germany and in Valencia, Spain). The foreseen clinical tests will assess its potential in the application for ion range monitoring, which seems at present mainly limited by the background coincidence contamination and by the required image reconstruction process. Iterative algorithms are not yet able to provide reliable results in real-time, but the advancements of the last years are encouraging. Moreover, dedicated studies are foreseen in order to optimize the geometrical setup of our Compton camera (size, number of silicon planes, absorber setting) in order to minimize the background effect and optimize the total detection efficiency. More generally, PG range monitoring techniques and detectors, such as collimated and Compton cameras, can be combined to alternative methods (PET, IVI) in hybrid systems, with the aim of fully profit from the complementary features of each technique.

A more direct clinical implementation of the Compton camera will be probably obtained in the nuclear medicine field, where the camera can allow for high-accuracy and high-efficiency examinations, bringing substantial advantages with respect to the established clinical routine, in terms of efficiency, energy acceptance and spatial resolution.

Compton imaging is still an active research field, which has the potential to enhance the performance of present solutions and detectors in several fields. In particular, Compton cameras can be employed outside the medical field, such as homeland security and nuclear site control. The realization and test of fully functional prototypes is of utmost importance for the further development of such an imaging technique, and our prototype is expected to give its contribution in the next future.

Appendices

A

Compton camera data format

A.1 Introduction

This document aims to formalize and fix the Compton camera data format. The structure of the data sent by each detector section (scatterer, absorber and beam hodoscope) to the acquisition card is detailed, as well as the structure of the events sent to the acquisition PC.

A.2 General features

A.2.1 Common information

The detector Front-End (FE) cards are connected to the Micro Advanced Telecommunications Computing Architecture (μ-TCA) via optical links, with a speed of 3.0 Gbit/s. The transfer frequency is 150 MHz.
All the FE card Time-to-Digital Converters (TDCs) share the same synchronized clock, at a 40 MHz frequency, which is sent to the cards through an external link.
Every data packet sent to the μ-TCA by the Front End cards starts with the following information:

- N° Front End (8 bits);
- N° Trigger (24 bits);
- N° Mode (8 bits);
- N° of element in the packet (8 bits).

A.2.1.1 Front End number

The FE number is the identification code of each FE card. A mechanical switch on the card defines the ID which is sent in the data packet header.
In Table A.1 the FE number IDs are listed with the corresponding cards.

Table A.1: Front End number associated to each Front End card.

FE number	FE card
0	All detectors
1	Silicon 1
2	Silicon 2
3	Silicon 3
4	Silicon 4
5	Silicon 5
6	Silicon 6
7	Silicon 7
8	Silicon 8
9	Silicon 9
10	Silicon 10
11	ASM 1
12	ASM 2
13	ASM 3
14	ASM 4
15	ASM 5
16	ASM 6
17	ASM 7
18	ASM 8
19	ASM 9
20	ASM 10
21	ASM 11
22	ASM 12
23	ASM 13
24	ASM 14
25	ASM 15
26	ASM 16
27	Hodoscope 1
28	Hodoscope 2
29	Hodoscope 3
30	Hodoscope 4
31	Hodoscope 5
32	Hodoscope 6
33	Hodoscope 7
34	Hodoscope 8
99	μ-TCA

A.2.1.2 Pre-trigger and trigger

The trigger number identifies each event, where an event is generated every time a coincidence is detected between a Bismuth Germanium Oxide - $Bi_{12}GeO_{20}$ (BGO) block and a silicon layer. Once an interaction is detected in a BGO block, the associated Analog Sampling Module (ASM) card generates a pre-trigger signal which is sent to the Trigger et HORloge (THOR) card. This intermediate card shares the pre-trigger signal with the silicon FE cards; if an interaction with a compatible time stamp is found in one of the silicon layer, a trigger signal is generated and sent to all the silicon FE card, as well as to the ASM and hodoscope cards via the THOR card. The trigger signal validates the event, and each FE card sends the collected data to the μ-TCA system. The trigger number allows for a complete event reconstruction by the event builder on the acquisition PC. In Figure A.1 the trigger generation process is sketched.
To be noticed that each FE cards sends the collected data independently from the others.

Trigger and pre-trigger encoding

Pre-trigger and trigger signals are used by all the detectors to select the collected data to be sent to the acquisition system. The data selection and transfer must be as fast as possible in order to minimize the trigger latency and camera dead time. In order to reduce the transmission time, pre-trigger and trigger signals have been encoded on 24 bits.
This same trigger number is sent at the beginning of each data packet and is used by the event builder to associate the interactions collected by the three detector sections. With a 24-bit encoding, the trigger number is reset every 1 ns $\times 2^{24} = 16{,}78$ ms. This time window is short for the event builder, so that for the physical data it is extended to 32 bits for all the FE cards in order to have a reset every 1 ns $\times 2^{32} = 4{,}2$ s, which is enough for the reconstruction of the events.

A.2.1.3 Mode number

The Compton camera detector components can work in different mode, according to the application requirements. At least two working modes are possible for every detector section: an “optimal” mode, corresponding to the final camera configuration; a “test” mode, allowing for the collection of more raw information. Every operating mode presents a peculiar data format, so that the data packets size is not fixed. In order to fix the acquisition tuning, the mode number is defined before its beginning.
The operating mode are identified as following:

- N° Mode = 1 : 1^{st} mode for silicon
- N° Mode = 2 : 2^{nd} mode for silicon
- N° Mode = 3 : 3^{rd} mode for silicon

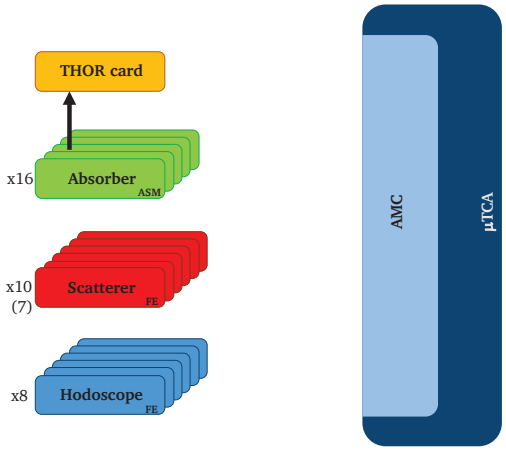

(a) An ASM card detects an interaction and sends a logical signal to the THOR card.

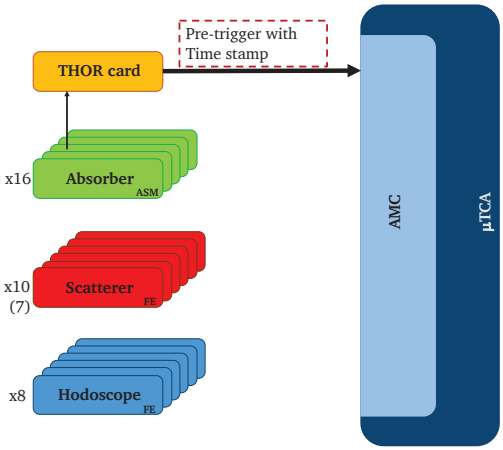

(b) The THOR card generates the pre-trigger signal.

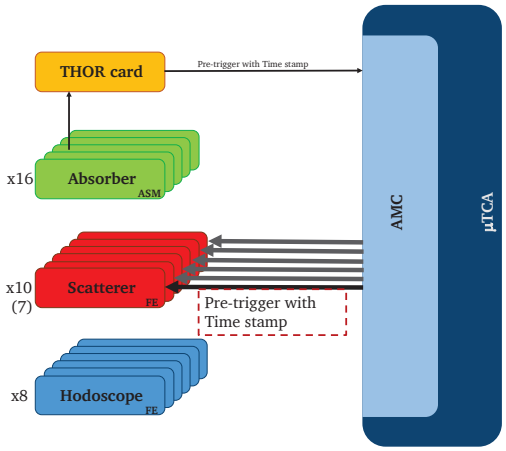

(c) The pre-trigger is sent to the 10 silicon FE cards.

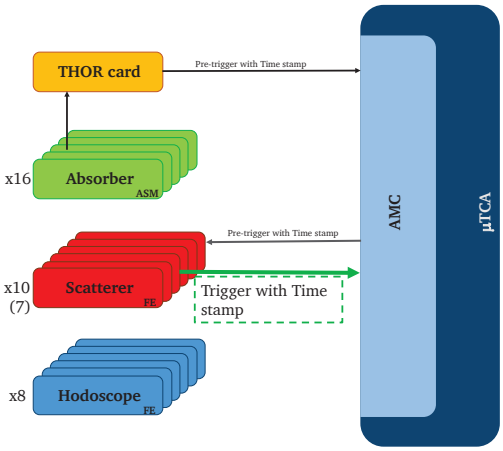

(d) A single silicon FE card generates the trigger.

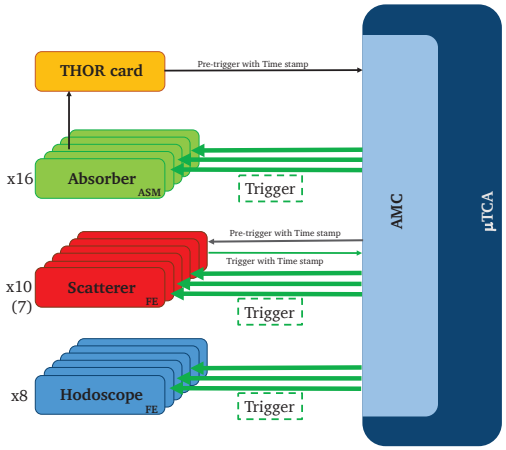

(e) The trigger signal is distributed to all the detectors.

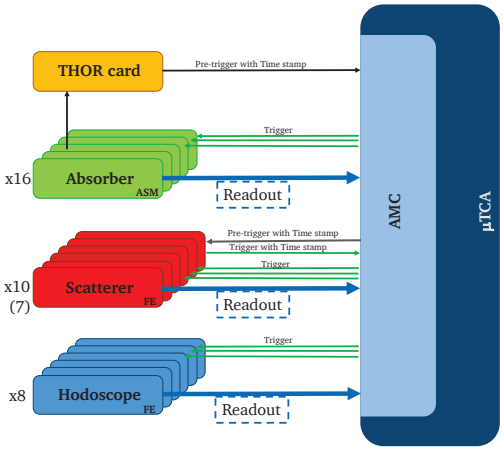

(f) The detectors send the collected data to the µ-TCA.

Figure A.1: Data acquisition logic: pre-trigger and trigger generation and readout process.

- N° Mode = 4 : 4^{th} mode for silicon
- N° Mode = 5 : 1^{st} mode for BGO
- N° Mode = 6 : 2^{nd} mode for BGO
- N° Mode = 7 : 1^{st} mode for hodoscope
- N° Mode = 8 : 2^{nd} mode for hodoscope.

A.3 Physical data format

A.3.1 Scatterer detector data format

Four different data formats, corresponding to four working modes, have been defined for the silicon scatterer operation (Figure A.2). For mode 1 and 2, the collected total charge is directly evaluated on the FE card via the slow shaper output and one Application-Specific Integrated Circuit (ASIC), while for mode 3 and 4 the ASIC pre-amplifier output directly sends a sampling of the raw signal. In this last case, the number of samples can be tuned and each sample corresponds to 10 ns. The complete sampling is stored in a dedicated buffer.

Modes 1 and 3
In mode 1 and 3, for each detector strip involved in the interaction, the strip ID, total collected charge and time are stored. The interaction position will be calculated via a center of gravity algorithm at the analysis stage. The raw information about the number of involved strips is useful for the evaluation of the signal dispersion in the detector.
Modes 2 and 4
In mode 2 and 4, the interaction is calculated on the FE card and the number of involved strip is then not stored.

A.3.2 Absorber detector data format

The BGO block readout is performed via the ASM cards. Each card is equipped with 24 input ports (signal Photo-Multiplier (PM)), corresponding to 6 BGO blocks. Two possible working modes have been defined for the BGO absorber: the collected total charge and time are evaluated on the card, or the PM raw signals are sampled and the sampling is sent to the acquisition (Figure A.3). Charge and time are then calculated at the analysis stage. This second operating mode can be useful in the test phase but it determines a low acquisition rate, so that it can be used only at low beam intensity.
The complete sampling is stored in a dedicated buffer.

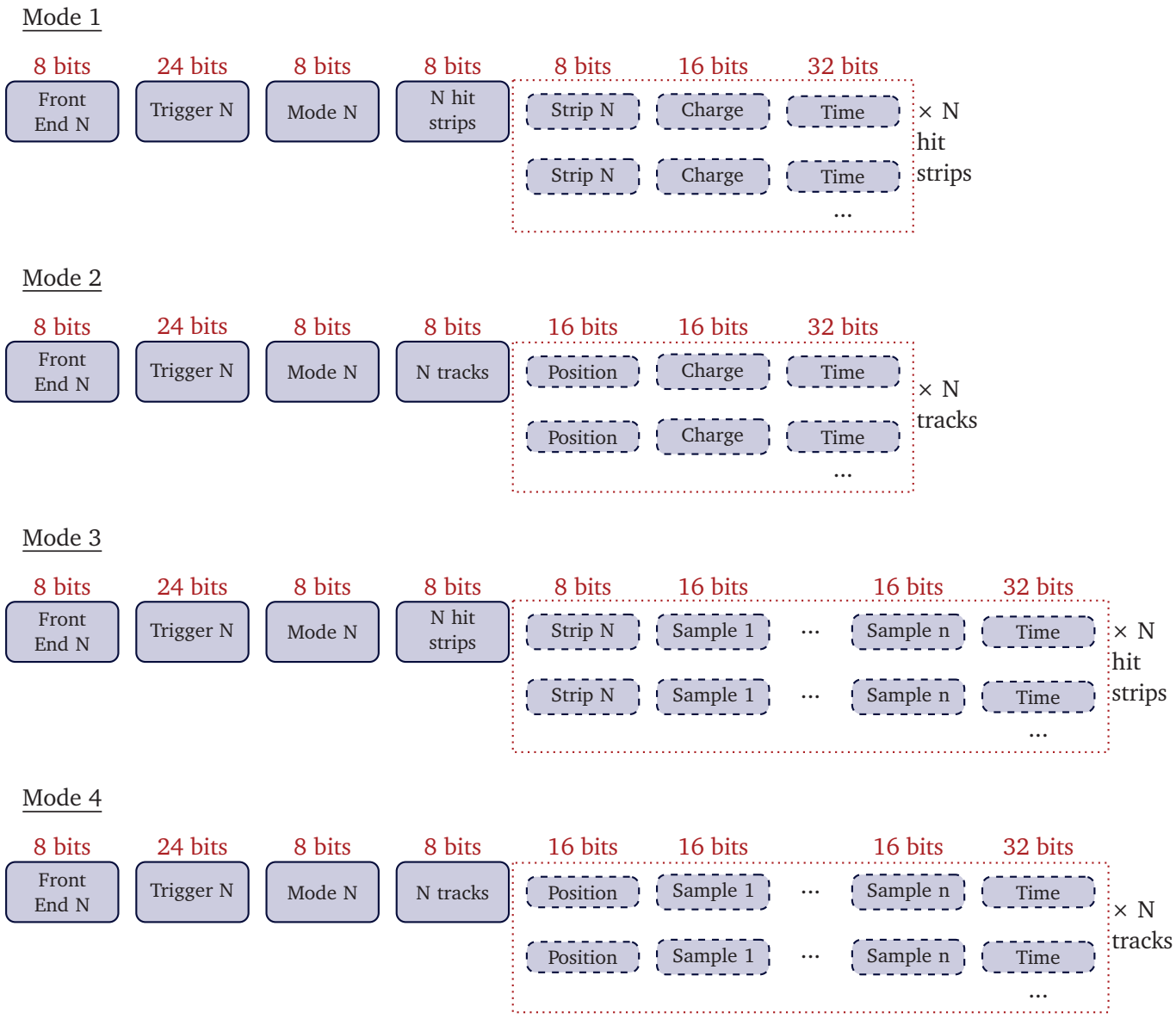

Figure A.2: Scatterer detector data format.

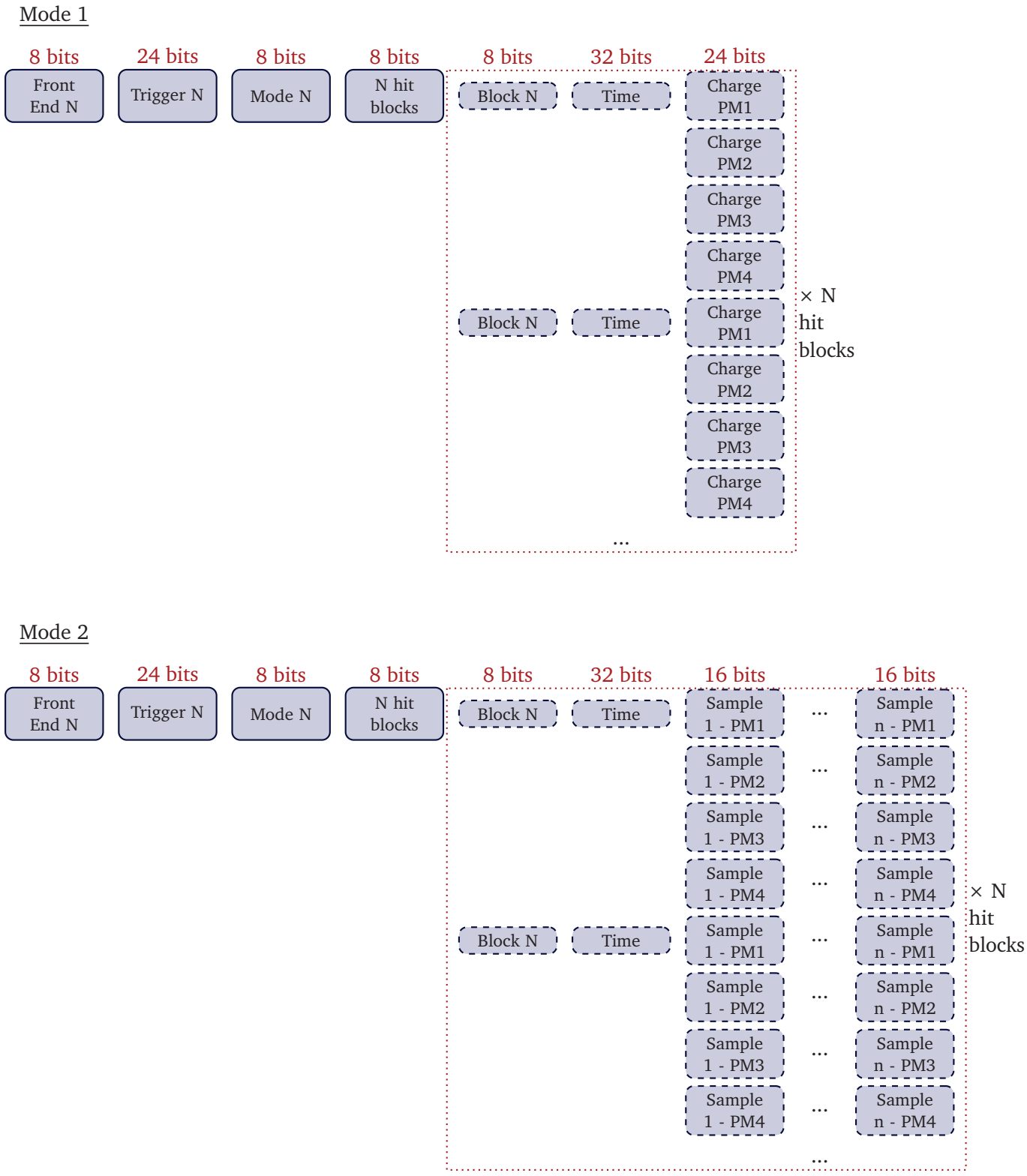

Figure A.3: Absorber detector data format.

A.3.3 Beam hodoscope data format

The beam tagging hodoscope is composed of two perpendicular planes of 128 scintillating fibers each. Each fiber is read-out on the two sides, for a total of 512 read-out channels. The output signals are send via optical fibers to 8 64-channel PMs H8500 by Hamamatsu. 8 FE cards have been developed for the signal collection, one per PM, and are equipped with two custom ASICs (32 channels each) and one Field Programmable Gate Array (FPGA).
Concerning the “optimal” mode (1st operating mode for the hodoscope), the only collected information are the ID of the involved fibers and the interaction time. The ASICs allow for a minimum time resolution of 10 ns; this means that if two particles interacts in the hodoscope within a 10 ns window, they will be considered as part of a single event.
In test mode, the total collected charge can be calculated. This feature is useful to evaluate the detector aging effect due to radiation exposure. The charge measurement is anyway limited to a single channel per ASIC, so to two channels per PM. The ASIC channel able to measure the charge is identified as "N° Fiber charge 1" and "N° Fiber charge 2".

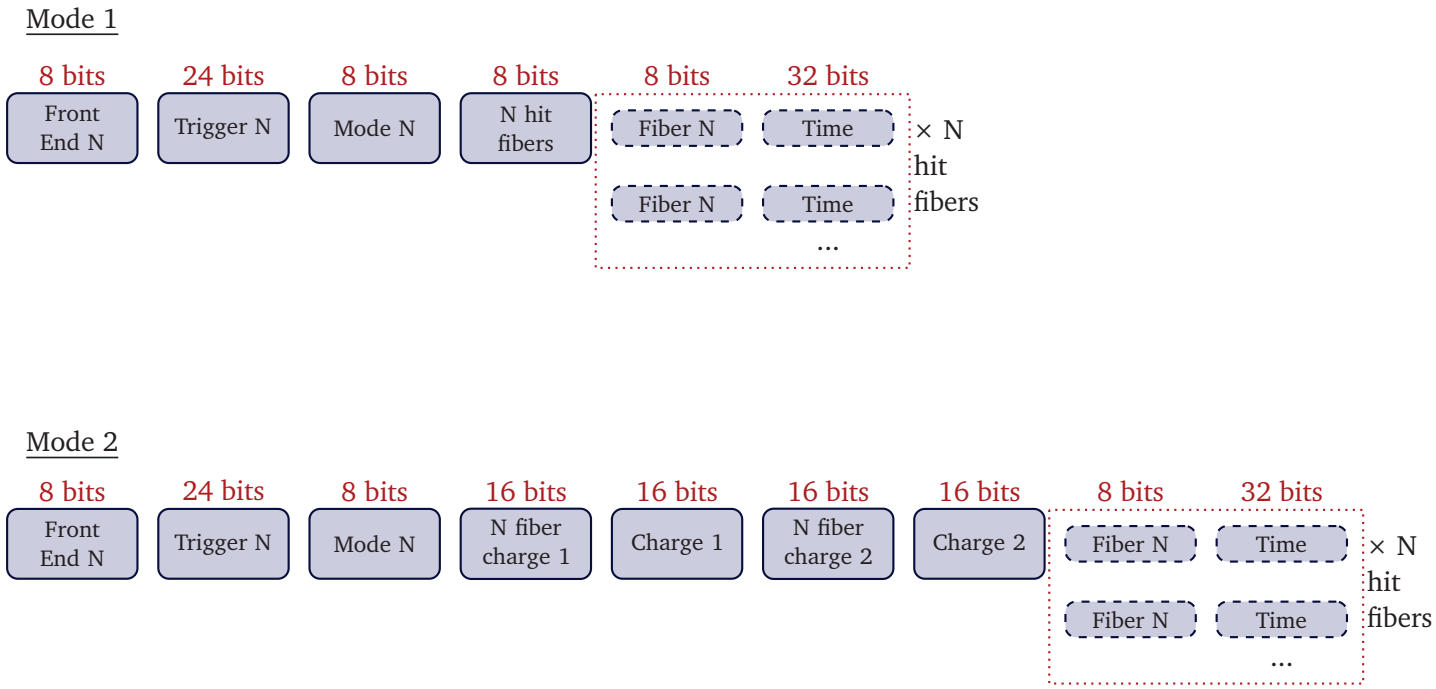

Figure A.4: Beam hodoscope data format.

A.4 Slow control, trigger and monitoring data format

A.4.1 Communication architecture

The Endpoint architecture is composed of three layers:

- application layer

- mac (or transport) layer/processor packet
- physical layer

Figure A.5: Architecture of communication between DAQ cards and μ-TCA.

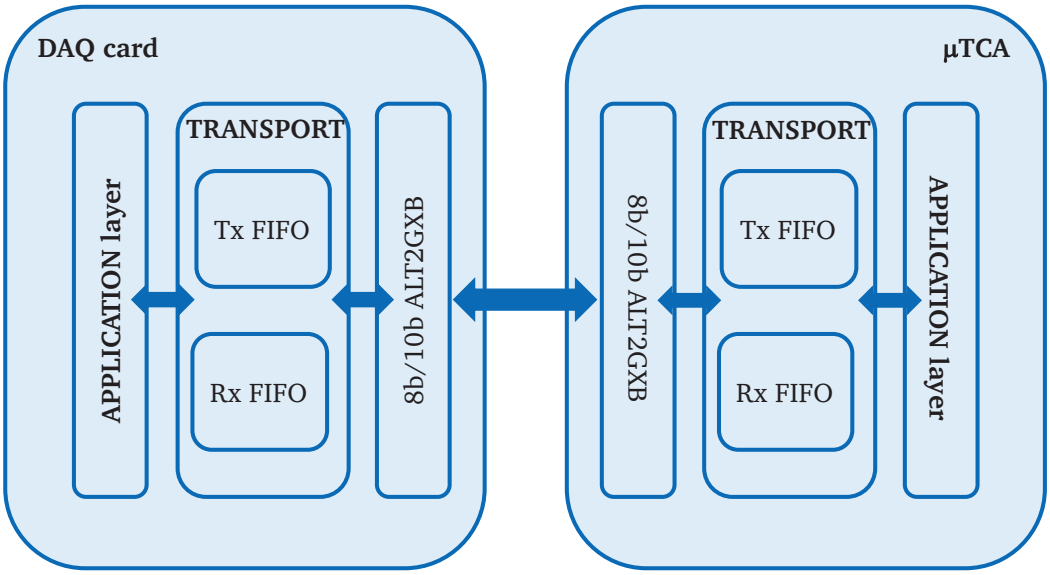

A.4.2 Transport protocol and processor packets

A.4.2.1 Definitions

It is worth to define some useful terms for the following part of the document:

- byte : 8 bits
- word : 16 bits
- K : control byte
- D : data byte
- cargo : data group
- terminator : packet end

- CRC : cyclic redundancy code

The CRC allows one to detect the transmission errors and the data transfer issues. A specific algorithm must be used, as CRC-16 : X16 + X15 + X2 + 1. In the present protocol, a “parity patter of 16 bits” have been used.

The transport layer ensures a proper packets exchange between two terminals via the data encapsulation. The data come from the application layer and are then sent to the physical layer.

A.4.2.2 Data encoding

For the transport layer, the data structure is created via the addition of a packet header, corresponding to a parity bit, of a 16 bit parity pattern and a bit for the end of the packet. The data are 8 bits/10 bits encoded. This standard 8 bits/10 bits encoding ensures sufficient data transitions for clock recovery.

A.4.2.3 Packets format

All the data packets have the same structure. A K byte (control symbol) is followed by the cargo to be sent. The end of the packets changes according to the cargo parity.
If the cargo contains an even number of bytes, the packet ends with K.28.6.

Table A.2: Packet with an even byte number cargo.

Item	Packet beginning	Cargo	Packet end
1	One K byte	0 - N D-bytes	K.28.6

If the cargo contains an odd number of bytes, the packet ends without any control symbol.

Table A.3: Packet with an odd byte number cargo.

Item	Packet beginning	Cargo	Packet end
1	One K byte	0 - N D-bytes	Beginning of a new packet

Remark :

- SYN packet is a special kind of packet starting with K.28.6 and ending with K.28.5. It is only composed of these two bytes (16 bits). It allows the receiver to find the beginning

and the end of the transmitted bytes with the aim to reconstruct the events in parallel. The synchronization speed is 44 Hz (defined by Carlos Abellan).

- In order to optimize the throughput, the control symbol at the beginning of the packet can probably be removed (further study needed).

A.4.2.4 Possible control symbols

In Table A.4, all the possible control symbols are listed (defined by Carlos Abellan).

Table A.4: Control symbol definition.

Item	Name	Control code	Comment
1	K.28.0	0x1C	Acknowledgement
2	K.28.1	0x3C	Ask for writing registers
3	K.28.2	0x5C	Ask for reading registers
4	K.28.3	0x7C	Special command
5	K.28.4	0x9C	Monitoring
6	K.28.5	0xBC	Default synchronization
7	K.28.6	0xDC	IDLE (default) and packet end
8	K.28.7	0xFC	Pre-trigger
9	K.23.7	0xF7	Trigger
10	K.27.7	0xFB	
11	K.29.7	0xFD	
12	K.30.7	0xFE	Physical data

A.4.3 Transport layer

A.4.3.1 Control packet

This kind of packet is used to check the link and for the control/command operations.

- For the link check, two kinds of packets are used: synchronization packet and IDLE packet.

- For the control/command operations, here are some examples: register configuration, FPGA dynamical programming, monitoring, etc.

Control symbol for control :

Acknowledgement packet (Front End cards → μ-TCA)

Table A.5: Control symbol definition.

Item	Name	Control code	Comment
1	K.28.0	0x1C	Acknowledgement
2	K.28.1	0x3C	Ask for writing registers
3	K.28.2	0x5C	Ask for reading registers
4	K.28.3	0x7C	Special command
5	K.28.4	0x9C	Monitoring
6	K.28.5	0xBC	Synchronization
7	K.28.6	0xDC	IDLE (default) and end of packet

This packet is sent by the FE cards and interpreted as an acknowledgement by the μ-TCA. If a part is missing, it is set to zero.

- If 0 = validation
- If 1 = problem detected

Table A.6: Definition of the acknowledgement packet.

Word	1st byte	2nd byte							
		7b	6b	5b	4b	3b	2b	1b	0b
1	K.28.0	0	Pb Front End number	Pb with packet beginning	Pb with packet end	Pb with CRC	Pb with number of received words	Pb with parity bit of byte 2	parity bit of the acknowledgement packet
2	Front End number								

A.4.3.2 Configuration packets

Writing register process (μ-TCA → Front End cards)

The process starts with a packet sent by the μ-TCA asking for the register writing. The receiver (FE card) sends back an acknowledgement packet to finish the process. In Table A.7 the format of this writing register packet is reported.

Reading register process (μ-TCA → Front End cards)

The process starts with a packet sent by the μ-TCA asking for the register reading. The receiver

Table A.7: Writing register packet.

Word	1st byte	2nd byte	Comment
1	K.28.1	Front End number + 1 parity bit	N/A
2	2 bytes with the number of words to be written		The length is word-based: max $2^{16} - 1 = 65535$ words
3	Register address		Address where the writing process starts
4..N+3	Data to be written		0000 0000
N+4	CRC composed of the "xor" of all bits in the same position, from word 2 to word (N+3)		

(FE card) sends back the "measure packet" if the command is correct, an acknowledgement packet if it is not.
At the beginning of the slow control, the physical addresses on the FE cards are read at the address 0.
In Table A.8 the format of this reading register packet is reported.

Table A.8: Reading register packet.

Word	1st byte	2nd byte	Comment
1	K.28.2	Front End number + 1 parity bit	N/A
2	2 bytes with the number of words to be read		The length is word-based: max $2^{16} - 1 = 65535$ words
3	Address of 1st data to be read		Address where the reading process starts
4	CRC composed of the "xor" of all bits in the same position, from word 2 to word 3		/

A.4.3.3 Monitoring process (Front End cards → μ-TCA)

In case of issues, for example when the temperature of a card go beyond a fixed threshold, the DAQ card sends a "monitoring" packet to the μ-TCA. There is not a corresponding acknowledgement from the μ-TCA.

Table A.9: Two special registers(μ-TCA → Front End cards)

Register address	Details	Comment
0	Front End number	No writing rights: register in read-only mode. Hard coded on DAQ card.
1	It defines the working modes	Optimal mode, test mode, collimated camera mode, Compton camera mode, individual detector section test. It is possible to write in the register.
2	It defines the detector to test (in single detector test mode)	Scatterer, absorber, hodoscope.
3	BGO number of sampling	For test mode with the BGO blocks signal sampling.
4	Silicon number of sampling	For test mode with the silicon layers signal sampling.

Table A.10: Measurement packet (Front End cards → μ-TCA)

Word	1st byte	2nd byte	Comment
1	K.28.1	Front End number + 1 parity bit	
2	2 bytes for the number of data words to send		The length is word-based: max $2^{16} - 1 = 65535$ words
3	Register address		Address where the writing process starts
4..N+3	Read data		0000 0000
N+4	CRC composed of the "xor" of all bits in the same position, from word 2 to word (N+3)		/

Table A.11: Monitoring packet.

Word	1st byte	2nd byte	Comment
1	K.28.4.	Front End number + 1 parity bit	Message in Table A.12.
2	15 bits for the message + 1 parity bit		Message in Table A.12.

Table A.12: Monitoring messages.

Item	Message	Bit[15]	...	Bit[7]	Bit[6]	Bit[5]	Bit[4]	Bit[3]	Bit[2]	Bit[1]	Comment
		Message type						Further information			
1	FPGA reconfiguration error	0	0	0	0	0	1	0	0	0	N/A
2	Temperature alarm	0	0	0	0	1	0	x	x	x	Bit "x" is 1 if the corresponding detector goes beyond the threshold (0 elsewhere)
3	Busy	0	0	0	1	0	0	0	0	0	Front End is not able to send data
...											

A.4.3.4 Special command process (μ-TCA → Front End cards)

This process is designed to allow the μ-TCA to send special commands to the FE cards.

Table A.13: Special command packets

Word	1st byte	2nd byte
1	K.28.3	Front End number + 1 parity bit
2	15 bits for the special command + 1 parity bit	

A register database (containing the operating mode identification) must be fixed and shared between all the detectors.

A.4.4 Data packets (Front End card → μ-TCA)

In the section the packets concerning trigger, pre-trigger and physical data are described. No acknowledgement is demanded for this kind of packets.

Pre-trigger format

This packet is sent to the μ-TCA by the THOR card. The μ-TCA then shares it with all the silicon FE cards.

Table A.14: Special commands examples

Item	Command name	Bit[15..1] of 2nd word	Comment
1	System reset	"0000 0000 0001 001"	Acknowledgement packet missing
2	Counter reset	"0000 0000 0001 000"	Acknowledgement packet needed
3	Start run	"0000 0000 0000 100"	Acknowledgement packet needed
4	Stop run	"0000 0000 0000 101"	Acknowledgement packet needed
5	Dynamical FPGA configuration	"0000 0000 0000 010"	Acknowledgement packet needed
6	Veto	"0000 0000 0000 011"	Example: μ-TCA cannot receive the data. Acknowledgement packet needed

Table A.15: Control symbol for pre-trigger, trigger and physical data.

Item	Name	Control code	Comment
1	K.28.7	0xFC	The pre-trigger is generated by the THOR card and sent to the μ-TCA who shares it with the silicon layers cards.
2	K.23.7	0xF7	The trigger is generated by a single silicon layer card and sent to the μ-TCA who shares it with all the FE cards.
5	K.30.7	0xFE	The FE cards send the data.

Table A.16: Pre-trigger packet

Item	1st byte	2nd - 4th bytes
1	K.28.7	24 bits for the trigger number

Trigger format

This packet is sent back to the μ-TCA if a silicon FE card finds an interaction in coincidence after the reception of the pre-trigger packet. The trigger is always sent before the physical data packets. The μ-TCA then sends the trigger packet to all the FE cards (scatterer, absorber, hodoscope).

Table A.17: Trigger packet

Item	1st byte	2nd - 4th bytes
1	K.23.7	24 bits for the trigger number

Physical data packet format

This packet sends the "useful" data to the μ-TCA. The data format (cargo) is defined in chapter 3.

Table A.18: Physical data packet

Item	1st byte	Cargo	End of packet
1	K.30.7.	From 0 to Nbr-1 words of D characters	K.28.6 or the beginning of a new packet.

A.5 UDP packets format

Once the μ-TCA receives the data from the FE cards, a physical event is generated and stored in dedicated buffers. The buffers are then sent to the acquisition PC via UDP packets. Each detector section has its own UDP socket, and three receiving ports are used for the three data fluxes: 60001 for the hodoscope, 60002 for the absorber, 60003 for the scatterer. The content of the data buffers are sent in order to avoid to divide events in different packets, so that each UDP packet is completely independent from the others and contains complete events. The maximum size of a packet is set to 1500 (UDP data = 1472), or to 9000 for the so called "jumbo frames", used for high speed acquisitions.
Each UDP packet has a custom defined header, composed of:

- 32 bits: packet number, starting from 0;
- 16 bits: number of data structures in the packet;

The data structures are then in a list one after the other with the already described format.

A.6 Data throughput expected in clinical conditions

A.6.1 Clinical intensities

In clinical standards, the beam maximum intensity is:

- protons : 10^{10} protons/s
- carbon ions : 5×10^{7} C ions/s

The Compton camera must be designed in order to be able to handle the whole range of clinical intensities. The design reference is then the maximum intensity, about 3.2 nA (2×10^{10} protons/s) delivered by the cyclotron C230 by IBA. The number of proton delivered per second is higher then the maximum considered rate (10^{10} protons/s).
As shown by the simulation results, the Compton camera can not be used for an online monitoring at the maximum beam intensity for both proton and carbon ion beams. The main limitation comes from the amount of random coincidences detected by the camera for high intensity beams. One possible solution is to deliver a lower intensity beam for the range monitoring before the beginning of the treatment. The results shown here relates to a reduced intensity, corresponding to the one selected via the simulation studies.

A.6.1.1 Review: detector and target sizes

Detectors sizes:

- Silicon scatterer : 7 silicon layers, 9.6×9.6×0.2 cm^3 (first layer 20 cm far from the beam line)
- BGO absorber: BGO block 3.5×3.8×3.0 cm^3 (67.5 cm far from the beam line - center of the block)

Poly-Methyl-Metacrylate (PMMA) target size: cylindrical shape, diameter 15 cm, 20 cm length along the beam direction.

A.6.2 Coincidence rate

In Table A.19 the coincidence and single (pre-trigger) rates expected for the different detector section are listed according to the beam kind and intensity. This values correspond the Compton camera, while for the collimated camera a reduced rate is expected for the absorber due to the presence of the physical collimator.

The application of the Compton camera at clinical intensity seems not feasible. The caemra distance with respect to the beam line should be increased to lower the rate to $1{\times}10^{5}$ Hz (which means to put the 1^{st} silicon layer 1 m far from the beam line). For a carbon ion beam at 5×10^{7} Hz, the estimated coincidence rate is 4×10^{4} Hz, with 1.4×10^{6} single rate on the

Table A.19: Coincidence and single rate as a function of the beam intensity. The BGO single rate corresponds to the pre-trigger rate.

	Clinical intensity		Reduced intensity		Collimated camera	
	Protons	Carbon ions	Protons	Carbon ions	Protons	Carbon ions
Intensity(ions/s)	2×10^{10}	5×10^{7}	1×10^{8}	5×10^{6}	2×10^{10}	5×10^{7}
Coincidence rate per incident ion	9×10^{-4}	8×10^{-4}	9×10^{-4}	8×10^{-4}	/	/
Coincidence rate (Hz)	1.8×10^{7}	4×10^{4}	9×10^{4}	4×10^{3}	/	/
Single rate BGO (Hz) - 96 blocks	7.8×10^{7}	1.4×10^{6}	3.9×10^{5}	1.4×10^{5}	/	/
Single rate BGO (Hz) - 1 block	8.1×10^{5}	1.5×10^{4}	4×10^{3}	1.5×10^{3}	/	/
Single rate BGO (Hz) - 1 ASM card (6 blocks)	6.5×10^{6}	1.2×10^{5}	3.2×10^{4}	1.2×10^{4}	/	/

absorber (measurements of coincidence rate on the HIT accelerator adapted to a real camera size with a 40 ns coincidence window, Krimmer ANIMMA 2013). The data flow between the μ-TCA and the acquisition PC corresponds to the coincidence rate, due to the fact that only coincidence events are stored.

A.6.3 Data flow (Front End cards → μ-TCA)

The data format previously described has been used to evaluate the data flow between each FE card and the μ-TCA. The calculation is performed according to the "optimal" mode of each detector. For the BGO, we only consider events where the 4 PMs are involved. For the silicon layers, two cases are considered:

- Case 1 : one single layer with 6 involved strips;
- Case 2 : all the 7 layers involved with 6 hit strips per layer.

Concerning the hodoscope, we considered an event with one hit fiber readout on the two sides.
The 8bits/10bits encoding in included in the calculation.

A.6.4 Acquisition data flow (μ-TCA → Acquisition PC)

The data flow from the μ-TCA to the acquisition PC is detailed here. The UDP encoding is included in the calculation.

Table A.20: Data flux between FE cards and μ-TCA.

	Clinical intensity		Reduced intensity	
	Protons	Carbon ions	Protons	Carbon ions
Intensity (ions/s)	2×10^{10}	5×10^{7}	1×10^{8}	5×10^{6}
Pre-trigger flux (Mbits/s)	2.5×10^{3}	47.6	13.3	4.76
Trigger flux (Mbits/s)	612	1.4	3.1	0.1
BGO data flux (Mbits/s) - 96 blocks	1.7×10^{5}	373	873	37.3
BGO data flux (Mbits/s)- 1 block	1.7×10^{3}	3.88	8.73	0.3
BGO data flux (Mbits/s) - 1 ASM card	1.4×10^{4}	31.1	69.9	3.1
Silicon data flux (Mbits/s) - case 1	2.3×10^{5}	522	1.2×10^{3}	52.2
Silicon data flux (Mbits/s) - case 2	1.6×10^{6}	3.7×10^{3}	8.2×10^{3}	366
Hodosocpe data flux (Mbits/s)	8.1×10^{4}	180	404	18

Table A.21: Data flow between μ-TCA and acquisition PC.

	Clinical intensity		Reduced intensity	
	Protons	Carbon ions	Protons	Carbon ions
Intensity (ions/s)	2×10^{10}	5×10^{7}	1×10^{8}	5×10^{6}
Coincidence rate per incident ion	9×10^{-4}	8×10^{-4}	9×10^{-4}	8×10^{-4}
Coincidence rate (Hz)	1.8×10^{7}	4×10^{4}	9×10^{4}	4×10^{3}
Data flow (Mbits/s) - case 1	2.2×10^{4}	46.7	112	5.0
Data flow (Mbits/s) - case 2	6×10^{4}	133	300	13.3

A.6.5 Conclusions

As already mentioned, the Compton camera application is not feasible at clinical beam intensities.
In order to have an online monitoring of the beam range, a reduced intensity must be foreseen. The main limitation is the rate of random coincidences detected at high intensity, while from the technological point of view no limitations are highlighted by this study. In the collimated camera configuration, where no coincidences are required and the random coincidences limitation is removed, we can then expect to be able to work at real clinical intensity.

Table A.22: Acquisition format of the Compton camera data.

COMPTON CAMERA ACQUISITION DATA FORMAT				
	Description	**Size (bytes)**	**Size (bits)**	**Details**
Beginning of file (10 bytes)	File start ID	2	16	F0F0 (hex) fixed ID
	Run number	4	32	Automatically increasing in DAQ software - it can be manually fixed
	Total number of events	4	32	Fixed at the beginning of the acquisition, it defines the file size
Event header (11 bytes) × total number of events	Event start ID	2	16	ABCD (hex) fixed ID
	Event number	4	32	Automatically increasing in μ-TCA data format
	Trigger number	3	24	Automatically increasing in μ-TCA data format
	Number of hits in trigger	2	16	
Data header (7 bytes) × number of hits in trigger	Hit start ID	1	8	EB (hex) fixed ID
	FE number	1	8	see Table A.1
	Trigger number	3	24	repeated from Event Header
	Mode number	1	8	see figure A.4 (7 or 8 for the hodoscope - 7 = optimal, 8 = test)
	Number of involved fibers	1	8	
Hit structure scatterer (7 bytes - mode 1, 9 bytes - mode 2, mode 3 and 4 with signal sampling) × number of involved strips (mode 1 and 3) or tracks (mode 2 and 4)	Strip number	1	8	mode 1 and 3
	Position	2	16	mode 2 and 4
	Time	4	32	all modes
	Charge	2	16	mode 1 and 2
	Signal samples	2	16	mode 3 and 4 - size per sample - n samples, with n selected in acquisition code
Hit structure absorber (17 bytes - mode 5, mode 6 with signal sampling) × number of involved blocks	Block number	1	8	both modes
	Time	4	32	both modes
	Charge PM 1-4	3	24	mode 5 - size per PM - 4 PMs per block
	Signal samples	2	16	mode 6 - size per sample per PM - n samples, with n selected in acquisition code, 4 PMs per block
Hit structure hodoscope (5 bytes - mode 7, 7 bytes - mode 8) × number of involved fibers	Fiber number	1	8	ranges from 0 to 128
	Time	4	32	in both modes 7 and 8
	Charge	2	16	only for mode 8
End of file (10 bytes)	File end ID	2	16	F1F1 (hex) fixed ID
	Number of events in file	4	32	for verification and debugging
	Number of octets in file	4	32	for verification and debugging

List of abbreviations

^{111}**In** Indium-111 203

^{123}**I** Iodine-123 99

^{131}**I** Iodine-131 6, 99, 196, 202

^{177}**Lu** Lutetium-177 99

^{22}**Na** Sodium-22 xii, 132–139, 148, 150, 151

^{42}**K** Potassium-42 203

^{57}**Co** Cobalt-57 132

^{59}**Fe** Iron-59 203

^{60}**Co** Cobalt-60 xi, xii, 133, 135, 136, 140, 142–147, 166

^{91m}**Y** Yttrium-91m 203

μ-TCA Micro Advanced Telecommunications Computing Architecture i, vi, xi, xvii, 72, 116, 124–127, 161–165, 220–222, 224, 226, 229, 230, 239, 243, 244, 251–254, 259, 261–267, 269, 270, 272

A.D.A.M. Advanced Oncotherapy 25

ADC Analog-to-Digital Converter xvi, 110, 112, 116, 120, 133–135, 139, 147, 154, 233, 236, 239

AMC Advanced Mezzanine Card xi, 124–126, 161, 165

ART Algebraic Reconstruction Technique 41

ASIC Application-Specific Integrated Circuit 110–112, 119, 120, 122, 127, 132, 161, 225, 230, 243, 255, 258

ASM Analog Sampling Module x, xvi, 114, 116, 117, 124, 162, 163, 221, 222, 230, 233, 236, 239, 240, 244, 252–255, 269, 270

ATCA Advanced Telecommunications Computing Architecture 124

AVIRM *Application et Valorisation des Interactions Rayonnements-Matière* 72, 114, 116, 117, 154

BaF_2 Barium Fluoride xii, 68, 75, 95, 137, 138, 152

BGO Bismuth Germanium Oxide - $Bi_{12}GeO_{20}$ i, x–xiii, xv–xvii, xix, 69, 70, 84, 89, 90, 94–96, 113–118, 123, 130, 131, 133–135, 137–139, 148, 151–153, 162, 166, 172, 173, 177, 178, 199, 200, 210, 221, 222, 230, 231, 233–235, 237, 239, 240, 243, 244, 253, 255, 264, 268–270

BIC Binary Intra-nuclear Cascade 17

BME Boltzmann-Master-Equation 14

BNCT Boron Neutron Capture Therapy 22

BNL Brookhaven National Laboratory 93

CAL *Centre Antoine Lacassagne*, Nice, France xvi, 18, 44, 72, 81, 84, 126, 220, 231

CAP Categorical Average Pattern 89

CCD Charge-Coupled Device 42

CdTe Cadmium Telluride xv, 45, 98, 201, 209

CdZnTe Cadmium Zinc Telluride 108

$CeBr_3$ Cerium Bromide 81, 163

CERN *Conseil Européen pour la Recherche Nucléaire*, Geneva, Switzerland 25, 124

CGDR Categorical Gaussian Distributed Replacement 89

CLaRyS *Contrôle en Ligne de l'hadronthérapie par Rayonnements Secondaires* i, ii, x, 43, 84, 89, 90, 100–102, 106–108, 118, 123, 130, 131, 161, 165, 166, 171, 173, 190, 193, 196, 197, 208, 212, 215, 217, 220, 243, 246, 247

CMOS Complementary Metal Oxide Semiconductor 43

CNAO *Centro Nazionale di Adroterapia Oncologica*, Italy vii, 24, 71

CPPM *Centre de Physique des Particules de Marseille*, France 106, 124, 165

CR-RC Capacitor Resistor - Resistor Capacitor 110

CREATIS *Centre de Recherche en Acquisition et Traitement de l'Image pour la Santé*, Lyon, France 101, 106, 130, 200

CRT Coincidence Resolution Time 71

CSA Charge Sensitive Amplifier 110

CSDA Continuous Slowing Down Approach 10, 11

CsF Cesium Fluoride 68, 95

CsI Cesium Iodide 41, 84

CT Computed Tomography i, viii, 29, 31, 36, 38–42, 47, 65–67, 70, 170

CTV Clinical Target Volume 34

CZT Cadmium Zinc Telluride 89–91

DLL Delay Locked Loop 120

DOI Depth Of Interaction 92–94, 173

DPGA *Détecteur Pixélisé de Grande Acceptance* 72, 106, 116

DRS Domino Ring Sampler 116

DSB Double-Strand Break 18, 19

DSSD Double-sided Silicon Strip Detector i, xiii, 89, 90, 98, 108–110, 131, 132, 161, 162, 166, 172, 199, 201, 216, 243

DWA Dielectric Wall Accelerator 25

EC Electron Capture 50

EM Electromagnetic 10, 12

ENC Equivalent Noise Charge 110, 199, 208, 209, 215

ESRF European Synchrotron Radiation Facility, Grenoble, France 164

FBP Filtered Back-Projection 41, 93

FDG Fluoro-Deoxy-Glucose 52, 72, 94, 99

FE Front-End i, x, 72, 109–112, 114, 116, 118, 119, 121–124, 132, 133, 156, 160, 161, 163–166, 221, 222, 225, 229, 230, 233, 238, 239, 243, 244, 251–255, 258, 262, 263, 265–267, 269, 270, 272

FFAG Fixed Field Alternating Gradient 24

FNAL Fermi National Accelerator Laboratory 41

FOP Fall-Off Position xiv, 182, 183, 189, 192

FOV Field Of View xix, 75, 76, 83, 97, 231

FPGA Field Programmable Gate Array 110–112, 116, 117, 120, 122, 124, 258, 261, 265, 266

FRP Fall-off Retrieval Position xiv, 190

FWHM Full Width at Half Maximum vii, xii, xiii, xv, 14, 68, 71, 89, 90, 92, 95, 96, 98, 110, 123, 132, 138, 148, 149, 152–154, 162, 173–175, 199, 200, 210, 228, 229

GAGG:Ce Cerium doped Gadolinium Aluminium Gallium Garnet ix, 78, 79, 88, 89

GANIL *Grand Accelerateur National d'Ions Lourds*, Caen, France ix, 17, 75, 83, 120, 123, 162, 164, 173, 199

GATE GEANT4 Application for Tomographic Emission 202

GE General Electric 94, 96

GEANT4 GEometry And Tracking 4 197

GEM Gas Electron Multiplier 41

GEVI Gamma Electron Vertex Imaging 90

GPU Graphics Processing Unit 77

GSI GSI Helmholtz Centre for Heavy Ion Research, Germany vii, viii, 17, 29, 31–33, 65, 67, 69, 71

GSO Gadolinium OxyorthoSilicate - Gd_2SiO_5 91

Gsps Giga Sample Per Second 116, 230

HEGP High Energy General Purpose 97, 202, 216

HIMAC Heavy Ion Medical Accelerator in Chiba, Japan 7, 17, 30, 33, 45, 65, 69, 70

HIT Heidelberg Ion Therapy Center, Germany vii–ix, xiii, xix, 7, 24, 30, 42, 43, 70, 72, 75, 76, 120, 123, 174–176

HSMC High-Speed Mezzanine Card 117

HU Hounsfield Units 31, 36, 39

IBA Ion Beam Applications, Belgium vii, xix, 24, 26, 80, 84, 85, 175, 176, 220, 246

IC Internal Conversion 51

IC Ionization Chamber 42, 44, 45

ICRP International Commission on Radiological Protection 17

IMPT Intensity-Modulated Particle Therapy 29, 34

IMRT Intensity-Modulated RadioTherapy 29, 34

INC Intra-nuclear Cascade 14, 17

INFN *Istituto Nazionale di Fisica Nucleare*, Italy 25

INSIDE Innovative Solutions for Dosimetry in Hadrontherapy 71

IPNL *Institut de Physique Nucléaire de Lyon*, France 81, 83–85, 101, 106, 109–111, 117, 119, 126, 127, 131, 133, 134, 154, 161–163, 165, 166, 199, 221, 230, 231, 239, 243, 244

IPNO *Institut de Physique Nucléaire d'Orsay*, France 123

IRFU *Institut de Recherche sur les lois Fondamentales de l'Univers*, Paris, France 134

IVI Interaction Vertex Imaging 43, 44, 247

$LaBr_3$ Lanthanum Bromide ix, 75, 80, 81, 83, 88, 89, 132

LAL *Laboratoire de l'Accélérateur Linéaire*, Paris, France 134

LAPD Large Area Pixelized Detector 72

LBL Lawrence Berkeley Laboratory 68

LED Light Emitting Diode xii, 154, 156–159

LEGP Low Energy General Purpose 97

LEHR Low Energy High Resolution 97

LEM Local Effect Model 33

LET Linear Energy Transfer vii, 19–21, 28, 33, 37

LFS Lutetium Fine Silicate 71

LHCb Large Hadron Collider beauty 124

LIGHT Linac for Image Guided HadronTherapy 25

LLNL Lawrence Livermore National Laboratory, USA 25

LLU Loma Linda University 41

LM-MLEM List Mode-Maximum Likelihood Expectation Maximization xiv, 101, 130, 180, 182, 187, 188, 192, 200, 208, 210, 215, 216

LOR Line Of Response x, 92, 93, 95

LPC *Laboratoire de Physique de Clermont*, France 72, 106, 114, 116, 117, 124, 154, 166

LPSC *Laboratoire de Physique Subatomique et Corpuscolaire*, Grenoble, France 106, 164

LQ Linear-Quadratic 19, 33

LSO Cerium-doped Lutetium OxyorthoSilicate - $Lu_2SiO_5(Ce)$ 85, 89, 94–96, 113

LVDS Low-Voltage Differential Signaling 110

LYSO Lutetium-Yttrium OxyorthoSilicate - $Lu_{2(1-x)}Y_{2x}SiO_5$ ix, 70–72, 75, 84, 85, 88, 95, 113, 116, 163

MC Monte Carlo 13, 77, 84, 98

MCH μ-TCA Carrier HUB 124

MCS Multiple Coulomb Scattering 13, 34–36, 41

MEGAlib Medium-Energy Gamma-ray Astronomy library 200

MEGP Medium Energy General Purpose 97

MGH Massachusetts General Hospital 70, 93

MICRHAU *Micro-électronique RHône AUvergne* 119

MIT Massachusetts Institute of Technology 99

MKM Microdosimetric Kinetic Model 33

MLEM Maximum Likelihood Expectation Maximization xiv, 86, 101, 172, 187, 188, 192

MLP Most Likely Path 39

MRI Magnetic Resonance Imaging 6, 31, 44, 66, 96

Msps Mega Sample Per Second 110

MWPC Multi Wire Proportional Chamber 41

NaI Sodium Iodide 41

NaI(Tl) Sodium Iodide doped with Thallium 75, 93–95, 98, 202, 203, 205

NIM Nuclear Instrumentation Module 131–134, 137, 139, 162, 166, 222, 243

NIRS National Institute of Radiological Sciences, Japan 29–31, 33, 42, 69

NIST National Institute of Standards and Technology 40, 64

NIU Northern Illinois University 41

NURBS Non-Uniform Rational Basis Splines xiv, 183, 187, 189

OAR Organ At Risk 8, 29, 31, 35, 37, 170

OER Oxygen Enhancement Ratio 21

PBS Pencil Beam Scanning 83, 85, 175

pCT proton Computed Tomography 31

PE Polyethylene 73, 74

PET Positron Emission Tomography i, viii–x, 6, 31, 42, 45–47, 50–53, 56, 64–72, 77, 91–96, 98–100, 106, 113, 116, 118, 133, 162, 170, 193, 196, 220, 243, 247

PG Prompt-Gamma i, ix, xvii, xix, 26, 39, 45, 64, 71–87, 89, 90, 100, 163, 170, 171, 179, 182, 183, 187, 190, 231, 233, 236–239, 243, 245–247

PGPI Prompt Gamma Peak Integral 74, 81

PGS Prompt Gamma Spectroscopy 74

PGT Prompt Gamma Timing 74, 80

PIDE Particle Radiation Data Ensemble 20

PM Photo-Multiplier i, ii, xi, xii, xvi, 68, 70, 72, 89, 91, 94–96, 113–117, 119–123, 133, 135, 137–141, 152–160, 162–166, 173, 222, 225, 229, 230, 233–236, 239, 243, 255, 258, 269, 272

PMMA Poly-Methyl-Metacrylate ix, xiii, xiv, xvi, 17, 43, 44, 65, 66, 69, 71–76, 78–81, 84, 85, 88, 90, 117, 171–173, 175, 178, 181, 183, 186–188, 231–234, 237, 245, 268

PRaVDA Proton Radiotherapy Verification and Dosimetry Application 42

PSF Point-Spread Function 92

PSI Paul Scherrer Institut, Villigen, Switzerland 29–31, 41, 116

PTCOG Particle Therapy Co-Operative Group 42

PTV Planned Target Volume 26–28, 31, 34, 35, 72, 76

QMD Quantum Molecular Dynamics 14, 17, 77

RAM Random Access Memory 126

RBE Relative Biological Effectiveness vii, viii, 20, 21, 32, 33, 37, 170

RF Radio-Frequency 80, 81, 174

RMS Root Mean Square xiv, 110, 120, 164, 165, 189, 211

ROI Region Of Interest 183

RPC Resistive Plate Chamber 72

RSP Relative Stopping Power 31

SHS Slow Shaper 110

SI Internation System of units 47

SiPM Silicon Photo-Multiplier 71, 84, 88, 95, 96, 163

SNR Signal-to-Noise Ratio 45, 187

SOBP Spread-Out Bragg Peak vii, 27, 28, 33, 35, 37

SOI Silicon-On-Insulator 89

SPECT Single Photon Emission Computed Tomography i, 42, 47, 53, 56, 77, 91, 95–100, 163, 196, 197, 199, 202, 208, 210, 215, 216, 245

SPTR Single Photon Time Resolution 163

TCP Tumor Control Probability 31

TCP Transmission Control Protocol 124, 127

TDC Time-to-Digital Converter 111, 120, 229, 251

THOR Trigger et HORloge xi, 116, 124, 125, 162, 253, 254, 265, 266

TOF Time-Of-Flight viii–x, xvii, 65, 67, 68, 71, 72, 74, 78–83, 95, 96, 107, 108, 118, 123, 131, 163, 164, 173, 174, 178, 187, 191–193, 229, 231, 233, 238, 239, 243

TOT Time-Over-Threshold 96

TPC Time Projection Chamber 45, 91

TPS Treatment-Planning System 31

TTL Transistor-Transistor Logic 222

UCSC University of California and Santa Cruz 41

UDP User Datagram Protocol 124, 126, 127, 165

USB Universal Serial Bus 134

VME VERSABUS Module Eurocard 72, 116, 124, 132, 163, 222, 224, 230

VRT Variance Reduction Technique 77

WEPL Water-Equivalent Path Length 31, 36

WPE West German Proton Therapy Center Essen 85

YAG:Ce Cerium-activated yttrium aluminum garnet 41

Bibliography

Abe, S., K. Nishimura, H. Sato, H. Muraishi, T. Inada, T. Tomida, T. Fujisaki, Y. Futami, T. Kanai, K. Kawachi, and S. Tazawa (2002). "Heavy ion CT system based on measurement of residual range distribution." In: *Igaku Butsuri* 22.1, pp. 39–47 (cit. on p. 42).

Abellan, C., J.-P. Cachemiche, F. Réthoré, and C. Morel (2013). "A data acquisition system for medical imaging". In: *2013 3rd International Conference on Advancements in Nuclear Instrumentation, Measurement Methods and their Applications (ANIMMA)*, pp. 1–7. DOI: 10.1109/ANIMMA.2013.6728028 (cit. on p. 124).

Adam, L.-E., J. Zaers, H. Ostertag, H. Trojan, M. E. Bellemann, and G. Brix (1997). "Performance evaluation of the whole-body PET scanner ECAT EXACT HR + following the IEC standard". In: *IEEE Transactions on Nuclear Science* 44.3, pp. 1172–1179. ISSN: 0018-9499. DOI: 10.1109/23.596983 (cit. on p. 113).

Agodi, C., G. Battistoni, F. Bellini, G. A. P. Cirrone, F. Collamati, G. Cuttone, E. De Lucia, M. De Napoli, A. Di Domenico, R. Faccini, F. Ferroni, S. Fiore, P. Gauzzi, E. Iarocci, M. Marafini, I. Mattei, S. Muraro, A. Paoloni, V. Patera, L. Piersanti, F. Romano, A. Sarti, A. Sciubba, E. Vitale, and C. Voena (2012). "Charged particle's flux measurement from PMMA irradiated by 80 MeV/u carbon ion beam". In: *Physics in Medicine & Biology* 57.18, p. 5667. URL: http://stacks.iop.org/0031-9155/57/i=18/a=5667 (cit. on pp. 43, 76).

Agodi, C., F. Bellini, G. A. P. Cirrone, F. Collamati, G. Cuttone, E. De Lucia, M. De Napoli, A. Di Domenico, R. Faccini, F. Ferroni, S. Fiore, P. Gauzzi, E. Iarocci, M. Marafini, I. Mattei, A. Paoloni, V. Patera, L. Piersanti, F. Romano, A. Sarti, A. Sciubba, and C. Voena (2013). "Erratum: Precise measurement of prompt photon emission from 80 MeV/u carbon ion beam irradiation". In: *Journal of Instrumentation* 8.11, E11002. URL: http://stacks.iop.org/1748-0221/8/i=11/a=E11002 (cit. on p. 76).

Ainsley, C. G. and C. M. Yeager (2014). "Practical considerations in the calibration of CT scanners for proton therapy". In: *Journal of Applied Clinical Medical Physics* 15.3, pp. 202–220. DOI: 10.1120/jacmp.v15i3.4721. URL: http://www.ncbi.nlm.nih.gov/pmc/articles/PMC5711046/ (cit. on p. 36).

Albertini, F., A. Bolsi, A. J. Lomax, H. P. Rutz, B. Timmerman, and G. Goitein (2008). "Sensitivity of intensity modulated proton therapy plans to changes in patient weight." In: *Radiotherapy and Oncology* 86.2, pp. 187–194 (cit. on p. 37).

Albertini, F., E. B. Hug, and A. J. Lomax (2011). "Is it necessary to plan with safety margins for actively scanned proton therapy?" In: *Physics in Medicine & Biology* 56.14, p. 4399. URL: http://stacks.iop.org/0031-9155/56/i=14/a=011 (cit. on p. 34).

Aldawood, S., P. G. Thirolf, A. Miani, M. Böhmer, G. Dedes, R. Gernhäuser, C. Lang, S. Liprandi, L. Maier, T. Marinsek, M. Mayerhofer, D. R. Schaart, I. I. Valencia Lozano, and K. Parodi (2017). "Development of a Compton camera for prompt-gamma medical imaging". In: *Radiation Physics and Chemistry* 140. 2nd International Conference on Dosimetry and its Applications

(ICDA-2) University of Surrey, Guildford, United Kingdom, 3-8 July 2016, pp. 190–197. ISSN: 0969-806X. DOI: https://doi.org/10.1016/j.radphyschem.2017.01.024. URL: http://www.sciencedirect.com/science/article/pii/S0969806X17300981 (cit. on p. 89).

Alharbi, T. (2018). "Energy resolution improvement of CdTe detectors by using the principal component analysis technique". In: *Nuclear Instruments and Methods in Physics Research Section A: Accelerators, Spectrometers, Detectors and Associated Equipment* 882, pp. 114–116. ISSN: 0168-9002. DOI: https://doi.org/10.1016/j.nima.2017.11.027. URL: http://www.sciencedirect.com/science/article/pii/S0168900217312251 (cit. on p. 209).

Alnaaimi, M. A., G. J. Royle, W. Ghoggali, E. Banoqitah, I. Cullum, and R. D. Speller (2011). "Performance evaluation of a pixellated Ge Compton camera." eng. In: *Physics in Medicine & Biology* 56.12. DOI: 10.1088/0031-9155/56/12/002 (cit. on p. 99).

Altera (2009). *Stratix II GX Device Handbook*. Volume 1. Altera Corporation (cit. on pp. 111, 122).

Altera (2012). *Cyclone III Device Handbook*. Volume 1. Altera Corporation (cit. on pp. 111, 120).

Altera (2015). *Stratix V Device Handbook*. Volume 3. Altera Corporation (cit. on p. 116).

Altera (2016). *Cyclone IV Device Handbook*. Volume 1. Altera Corporation (cit. on p. 124).

Alzahrani, A. S., O. AlShaikh, M. Tuli, A. Al-Sugair, R. Alamawi, and M. M. Al-Rasheed (2012). "Diagnostic value of recombinant human thyrotropin-stimulated ^{123}I whole-body scintigraphy in the follow-up of patients with differentiated thyroid cancer." In: *Clinical Nuclear Medicine* 37.3, pp. 229–234 (cit. on p. 99).

Amaldi, U. (2009). "Cyclinacs: Fast-Cycling Accelerators for Hadrontherapy". In: *Nuclear Instruments and Methods in Physics Research Section A: Accelerators, Spectrometers, Detectors and Associated Equipment* (cit. on p. 25).

Amaldi, U., P. Berra, K. R. Crandall, D. Toet, M. Weiss, R. Zennaro, E. Rosso, B. Szeless, M. Vretenar, C. Cicardi, C. De Martinis, D. Giove, D. Davino, M. R. Masullo, and V. Vaccaro (2004). "LIBO-a linac-booster for protontherapy: construction and tests of a prototype". In: *Nuclear Instruments and Methods in Physics Research Section A: Accelerators, Spectrometers, Detectors and Associated Equipment* 521.2, pp. 512–529. ISSN: 0168-9002. DOI: https://doi.org/10.1016/j.nima.2003.07.062. URL: http://www.sciencedirect.com/science/article/pii/S0168900203023994 (cit. on p. 25).

Amaldi, U., A. Bianchi, Y.-H. Chang, A. Go, W. Hajdas, N. Malakhov, J. Samarati, F. Sauli, and D. A. Watts (2011). "Construction, test and operation of a proton range radiography system". In: *Nuclear Instruments and Methods in Physics Research Section A: Accelerators, Spectrometers, Detectors and Associated Equipment* 629.1, pp. 337–344. ISSN: 0168-9002. DOI: https://doi.org/10.1016/j.nima.2010.11.096. URL: http://www.sciencedirect.com/science/article/pii/S0168900210026318 (cit. on p. 41).

Amaldi, U., R. Bonomi, S. Braccini, M. Crescenti, A. Degiovanni, M. Garlasché, A. Garonna, G. Magrin, C. Mellace, P. Pearce, G. Pittà, P. Puggioni, E. Rosso, S. Verdú Andrés, R. Wegner, M.

Weiss, and R. Zennaro (2010a). “Accelerators for hadrontherapy: From Lawrence cyclotrons to linacs”. In: *Nuclear Instruments and Methods in Physics Research Section A: Accelerators, Spectrometers, Detectors and Associated Equipment* 620.2, pp. 563–577. DOI: https://doi.org/10.1016/j.nima.2010.03.130. URL: http://www.sciencedirect.com/science/article/pii/S0168900210007357 (cit. on p. 24).

Amaldi, U., S. Braccini, and P. Puggioni (2009). “High Frequency Linacs for Hadrontherapy”. In: *Reviews of Accelerator Science and Technology* 02.01, pp. 111–131. DOI: 10.1142/S179362680900020X. URL: https://doi.org/10.1142/S179362680900020X (cit. on p. 25).

Amaldi, U., W. Hajdas, S. Iliescu, N. Malakhov, J. Samarati, F. Sauli, and D. A. Watts (2010b). “Advanced Quality Assurance for CNAO”. In: *Nuclear Instruments and Methods in Physics Research Section A: Accelerators, Spectrometers, Detectors and Associated Equipment* 617.1. 11th Pisa Meeting on Advanced Detectors, pp. 248–249. ISSN: 0168-9002. DOI: https://doi.org/10.1016/j.nima.2009.06.087. URL: http://www.sciencedirect.com/science/article/pii/S0168900209013424 (cit. on pp. 41, 43).

Andreyev, A., A. Sitek, and A. Celler (2011). “Fast image reconstruction for Compton camera using stochastic origin ensemble approach.” In: *Medical Physics* 38.1, pp. 429–438 (cit. on pp. 101, 180).

Anger, H. O. (1958). “Scintillation Camera”. In: *Review of Scientific Instruments* 29.1, pp. 27–33. DOI: 10.1063/1.1715998. URL: http://dx.doi.org/10.1063/1.1715998 (cit. on pp. 46, 96, 97, 196).

Anger, H. O. (1964). “Scintillation Camera with Multichannel Collimators”. In: *Journal of Nuclear Medicine* 5.7, pp. 515–531. URL: http://jnm.snmjournals.org/content/5/7/515.short (cit. on pp. 97, 196).

Anger, H. O. (1969). *Multiplane Tomographic Gamma-Ray Scanner*. International Atomic Energy Agency (IAEA): IAEA (cit. on p. 97).

Antoine, S., B. Autin, W. Beeckman, J. Collot, M. Conjat, F. Forest, J. Fourrier, E. Froidefond, J. L. Lancelot, J. Mandrillon, P. Mandrillon, F. Méot, Y. Mori, D. Neuvéglise, C. Ohmori, J. Pasternak, and T. Planche (2009). “Principle design of a protontherapy, rapid-cycling, variable energy spiral FFAG”. In: *Nuclear Instruments and Methods in Physics Research Section A: Accelerators, Spectrometers, Detectors and Associated Equipment* 602.2, pp. 293–305. DOI: https://doi.org/10.1016/j.nima.2009.01.025. URL: http://www.sciencedirect.com/science/article/pii/S0168900209000059 (cit. on p. 25).

Arena, C., V. Micco, E. Macaeva, and R. Quintens (2014). “Space radiation effects on plant and mammalian cells”. In: 104, pp. 419–431 (cit. on p. 20).

Aspen Aerogels (2011). *Spaceloft® - High performance Insulation for building envelopes. Data Sheet*. Aspen Aerogels Inc. (cit. on p. 111).

Attanasi, F., N. Belcari, M. Camarda, G. A. P. Cirrone, G. Cuttone, A. Del Guerra, F. Di Rosa, N. Lanconelli, V. Rosso, G. Russo, and S. Vecchio (2008). “Preliminary results of an in-beam PET prototype for proton therapy”. In: *Nuclear Instruments and Methods in Physics Research*

Section A: Accelerators, Spectrometers, Detectors and Associated Equipment 591.1. Radiation Imaging Detectors 2007, pp. 296–299. ISSN: 0168-9002. DOI: https://doi.org/10.1016/j.nima.2008.03.076. URL: http://www.sciencedirect.com/science/article/pii/S0168900208004610 (cit. on p. 71).

Attanasi, F., N. Belcari, A. Del Guerra, W. Enghardt, S. Moehrs, K. Parodi, V. Rosso, and S. Vecchio (2009). "Comparison of two dedicated 'in beam' PET systems via simultaneous imaging of 12 C-induced β + -activity". In: *Physics in Medicine & Biology* 54.2, N29. URL: http://stacks.iop.org/0031-9155/54/i=2/a=N01 (cit. on p. 71).

Barth, R. F., J. A. Coderre, M. G. H. Vicente, and T. E. Blue (2005). "Boron Neutron Capture Therapy of Cancer: Current Status and Future Prospects". In: *Clinical Cancer Research* 11.11, pp. 3987–4002. DOI: 10.1158/1078-0432.CCR-05-0035. URL: http://clincancerres.aacrjournals.org/content/11/11/3987 (cit. on p. 22).

Baskar, R., K. A. Lee, R. Yeo, and K.-W. Yeoh (2012). "Cancer and radiation therapy: current advances and future directions." eng. In: *International journal of medical sciences* 9.3, pp. 193–199. DOI: 10.7150/ijms.3635 (cit. on p. 7).

Basko, R., G. L. Zeng, and G. T. Gullberg (1998). "Application of spherical harmonics to image reconstruction for the Compton camera". In: *Physics in Medicine & Biology* 43.4, p. 887. URL: http://stacks.iop.org/0031-9155/43/i=4/a=016 (cit. on p. 101).

Bauer, J., D. Unholtz, F. Sommerer, C. Kurz, T. Haberer, K. Herfarth, T. Welzel, S. E. Combs, J. Debus, and K. Parodi (2013). "Implementation and initial clinical experience of offline PET/CT-based verification of scanned carbon ion treatment". In: *Radiotherapy and Oncology* 107.2, pp. 218–226. ISSN: 0167-8140. DOI: https://doi.org/10.1016/j.radonc.2013.02.018. URL: http://www.sciencedirect.com/science/article/pii/S0167814013001606 (cit. on pp. 67, 70).

Baum, R. P. and H. R. Kulkarni (2012). "THERANOSTICS: From Molecular Imaging Using Ga-68 Labeled Tracers and PET/CT to Personalized Radionuclide Therapy - The Bad Berka Experience." In: *Theranostics* 2.5, pp. 437–447 (cit. on p. 99).

Bazalova, M., J.-F. Carrier, L. Beaulieu, and F. Verhaegen (2008). "Dual-energy CT-based material extraction for tissue segmentation in Monte Carlo dose calculations". In: *Physics in Medicine & Biology* 53.9, p. 2439. URL: http://stacks.iop.org/0031-9155/53/i=9/a=015 (cit. on p. 36).

Bednarz, B., J. Daartz, and H. Paganetti (2010). "Dosimetric accuracy of planning and delivering small proton therapy fields." In: *Physics in Medicine & Biology* 55.24, pp. 7425–7438 (cit. on p. 38).

Belkić, D. (2010). "Review of theories on ionization in fast ion-atom collisions with prospects for applications to hadron therapy". In: *Journal of Mathematical Chemistry* 47.4, pp. 1366–1419. DOI: 10.1007/s10910-010-9662-x. URL: https://doi.org/10.1007/s10910-010-9662-x (cit. on p. 8).

Belli, M., D. T. Goodhead, F. Ianzini, G. Simone, and M. A. Tabocchini (1992). "Direct Comparison of Biological Effectiveness of Protons and Alpha/particles of the Same LET. II. Mutation Induction at the HPRT Locus in V79 Cells". In: *International Journal of Radiation Biology* 61.5, pp. 625–629. DOI: 10.1080/09553009214551431. URL: https://doi.org/10.1080/09553009214551431 (cit. on p. 19).

Bennett, G. W., A. C. Goldberg, G. S. Levine, J. Guthy, J. Balsamo, and J. O. Archambeau (1975). "Beam localization via ^{15}O activation in proton-radiation therapy". In: *Nuclear Instruments and Methods* 125.3, pp. 333–338. ISSN: 0029-554X. DOI: https://doi.org/10.1016/0029-554X(75)90246-3. URL: http://www.sciencedirect.com/science/article/pii/0029554X75902463 (cit. on pp. 42, 68).

Bentzen, S. M. (2006). "Preventing or reducing late side effects of radiation therapy: radiobiology meets molecular pathology." eng. In: *Nature reviews. Cancer* 6.9, pp. 702–713. DOI: 10.1038/nrc1950 (cit. on p. 7).

Berger, M. J., J. S. Coursey, M. Zucker, and J. Chang (2018). *ESTAR, PSTAR, and ASTAR: Computer Programs for Calculating Stopping-Power and Range Tables for Electrons, Protons, and Helium Ions*. URL: http://physics.nist.gov/Star (visited on 08/23/2018) (cit. on p. 40).

Bergstrom, P. M. and R. H. Pratt (1997). "An overview of the theories used in compton scattering calculations". In: *Radiation Physics and Chemistry* 50.1. Inelastic Scattering of X-Rays and Gamma Rays, pp. 3–29. ISSN: 0969-806X. DOI: https://doi.org/10.1016/S0969-806X(97)00022-4. URL: http://www.sciencedirect.com/science/article/pii/S0969806X97000224 (cit. on p. 60).

Bert, C., S. O. Grözinger, and E. Rietzel (2008). "Quantification of interplay effects of scanned particle beams and moving targets". In: *Physics in Medicine & Biology* 53.9, p. 2253. URL: http://stacks.iop.org/0031-9155/53/i=9/a=003 (cit. on p. 33).

Bert, C. and K. Herfarth (2017). "Management of organ motion in scanned ion beam therapy". In: *Radiation Oncology (London, England)* 12, p. 170. DOI: 10.1186/s13014-017-0911-z. URL: http://www.ncbi.nlm.nih.gov/pmc/articles/PMC5674859/ (cit. on p. 34).

Bertini, H. W., T. A. Gabriel, R. T. Santoro, O. W. Hermann, N. M. Larson, and J. M. Hunt (1974). "HIC-1: a first approach to the calculation of heavy-ion reactions at energies greater than or equal to 50 MeV/nucleon". In: *Office of Scientific & Technical Information Technical Reports* ORNL-TM-4134 (cit. on p. 14).

Bethe, H. (1930). "Zur Theorie des Durchgangs schneller Korpuskularstrahlen durch Materie". In: *Annalen der Physik* 397.3, pp. 325–400. DOI: 10.1002/andp.19303970303. URL: https://onlinelibrary.wiley.com/doi/abs/10.1002/andp.19303970303 (cit. on p. 10).

Bhat, M. R. (1992). *Evaluated Nuclear Structure Data File (ENSDF), Nuclear Data for Science and Technology, page 817, edited by S. M. Qaim (SpringerVerlag, Berlin, Germany, 1992)*. URL: https://www.nndc.bnl.gov/ (visited on 03/27/2017) (cit. on p. 198).

Bichsel, H. (2013). "Chapter One - Stochastics of Energy Loss and Biological Effects of Heavy Ions in Radiation Therapy". In: *Theory of Heavy Ion Collision Physics in Hadron Therapy*.

Vol. 65. Advances in Quantum Chemistry. Academic Press, pp. 1–38. DOI: https://doi.org/10.1016/B978-0-12-396455-7.00001-7. URL: http://www.sciencedirect.com/science/article/pii/B9780123964557000017 (cit. on p. 8).

Bischel, H. and T. Hiraoka (1992). "Energy loss of 70 MeV protons in elements". In: *Nuclear Instruments and Methods in Physics Research Section B: Beam Interactions with Materials and Atoms* 66.3, pp. 345–351. ISSN: 0168-583X. DOI: https://doi.org/10.1016/0168-583X(92)95995-4. URL: http://www.sciencedirect.com/science/article/pii/0168583X92959954 (cit. on p. 38).

Bisogni, M. G., A. Attili, G. Battistoni, N. Belcari, N. Camarlinghi, P. Cerello, S. Coli, A. Del Guerra, A. Ferrari, V. Ferrero, E. Fiorina, G. Giraudo, E. Kostara, M. Morrocchi, F. Pennazio, C. Peroni, M. A. Piliero, G. Pirrone, A. Rivetti, M. D. Rolo, V. Rosso, P. Sala, G. Sportelli, and R. Wheadon (2017). "INSIDE in-beam positron emission tomography system for particle range monitoring in hadrontherapy." In: *Journal of Medical Imaging (Bellingham)* 4.1, p. 011005 (cit. on p. 71).

Black, R. D., C. W. Scarantino, G. G. Mann, M. S. Anscher, R. D. Ornitz, and B. E. Nelms (2005). "An analysis of an implantable dosimeter system for external beam therapy." In: *International Journal of Radiation Oncology Biology Physics* 63.1, pp. 290–300 (cit. on p. 44).

Blahd, W. H. (1996). "Ben Cassen and the development of the rectilinear scanner." In: *Seminars on Nuclear Medicine* 26.3, pp. 165–170 (cit. on p. 46).

Blakely, E. A. and P. Y. Chang (2009). "Biology of charged particles." eng. In: *Cancer journal (Sudbury, Mass.)* 15.4, pp. 271–284. DOI: 10.1097/PPO.0b013e3181b666c5 (cit. on p. 7).

Blakely, E. A., F. Q. H. Ngo, S. B. Curtis, and C. A. Tobias (1984). "Heavy-Ion Radiobiology: Cellular Studies". In: *Advances in Radiation Biology*. Ed. by J. T. Lett. Vol. 11. Advances in Radiation Biology. Elsevier, pp. 295–389. DOI: https://doi.org/10.1016/B978-0-12-035411-5.50013-7. URL: http://www.sciencedirect.com/science/article/pii/B9780120354115500137 (cit. on pp. 19, 21).

Bloch, F. (1933). "Zur Bremsung rasch bewegter Teilchen beim Durchgang durch Materie". In: *Annalen der Physik* 408.3, pp. 285–320. DOI: 10.1002/andp.19334080303. URL: https://onlinelibrary.wiley.com/doi/abs/10.1002/andp.19334080303 (cit. on p. 10).

Bohlen, T. T., F. Cerutti, M. Dosanjh, A. Ferrari, I. Gudowska, A. Mairani, and J. M. Quesada (2010). "Benchmarking nuclear models of FLUKA and GEANT4 for carbon ion therapy." In: *Physics in Medicine & Biology* 55.19, pp. 5833–5847 (cit. on p. 77).

Bohr, N. (1915). "On the decrease of velocity of swiftly moving electrified particles in passing through matter". In: *The London, Edinburgh, and Dublin Philosophical Magazine and Journal of Science* 30.178, pp. 581–612. DOI: 10.1080/14786441008635432. URL: https://doi.org/10.1080/14786441008635432 (cit. on p. 12).

Boltwood, B. B. and E. Rutherford (1911). "LV. Production of helium by radium". In: *The London, Edinburgh, and Dublin Philosophical Magazine and Journal of Science* 22.130, pp. 586–604.

DOI: 10.1080/14786441008637154. URL: https://doi.org/10.1080/14786441008637154 (cit. on p. 48).

Bom, V., L. Joulaeizadeh, and F. Beekman (2012). "Real-time prompt gamma monitoring in spot-scanning proton therapy using imaging through a knife-edge-shaped slit". In: *Physics in Medicine & Biology* 57.2, p. 297. URL: http://stacks.iop.org/0031-9155/57/i=2/a=297 (cit. on p. 84).

Bothe, W. (1921). "Das allgemeine Fehlergesetz, die Schwankungen der Feldstärke in einem Dielektrikum und die Zerstreuung derα-Strahlen". In: *Zeitschrift für Physik* 5.1, pp. 63–69. DOI: 10.1007/BF01349687. URL: https://doi.org/10.1007/BF01349687 (cit. on p. 13).

Braccini, S. (2010). "Scientific and technological development of hadrontherapy". In: *Astroparticle, Particle and Space Physics, Detectors and Medical Physics Applications*, pp. 598–609. DOI: 10.1142/9789814307529_0099. URL: https://www.worldscientific.com/doi/abs/10.1142/9789814307529_0099 (cit. on p. 22).

Braccini, S., A. Ereditato, I. Kreslo, U. Moser, C. Pistillo, S. Studer, P. Scampoli, A. Coray, and E. S. Pedroni (2010). "First results on proton radiography with nuclear emulsion detectors". In: *Journal of Instrumentation* 5.09, P09001. URL: http://stacks.iop.org/1748-0221/5/i=09/a=P09001 (cit. on p. 42).

Bragg, W. H. M. A. and R. Kleeman (1904). "On the ionization curves of radium". In: *The London, Edinburgh, and Dublin Philosophical Magazine and Journal of Science* 8.48, pp. 726–738. DOI: 10.1080/14786440409463246. URL: https://doi.org/10.1080/14786440409463246 (cit. on pp. 8, 170).

Bragg, W. H. M. A. and R. Kleeman (1905). "On the α particles of radium, and their loss of range in passing through various atoms and molecules". In: *The London, Edinburgh, and Dublin Philosophical Magazine and Journal of Science* 10.57, pp. 318–340. DOI: 10.1080/14786440509463378. URL: https://doi.org/10.1080/14786440509463378 (cit. on pp. 8, 12).

Brahme, A. (2004). "Recent advances in light ion radiation therapy". In: *International Journal of Radiation Oncology Biology Physics* 58.2, pp. 603–616. DOI: 10.1016/j.ijrobp.2003.09.034. URL: http://dx.doi.org/10.1016/j.ijrobp.2003.09.034 (cit. on p. 7).

Braunn, B. (2010). "12C fragmentation at 95 MeV per nucleon for hadrontherapy. Experimental study and simulation with thick PMMA targets." PhD thesis. Université de Caen. URL: https://tel.archives-ouvertes.fr/tel-00536121 (cit. on p. 17).

Braunn, B., M. Labalme, G. Ban, M. Chevallier, J. Colin, D. Cussol, D. Dauvergne, J. M. Fontbonne, F. Haas, A. Guertin, D. Lebhertz, F. Le Foulher, C. Pautard, C. Ray, M. Rousseau, M. D. Salsac, L. Stuttge, É. Testa, and M. Testa (2011). "Nuclear reaction measurements of 95MeV/u 12C interactions on PMMA for hadrontherapy". In: *Nuclear Instruments and Methods in Physics Research Section B: Beam Interactions with Materials and Atoms* 269.22, pp. 2676–2684. ISSN: 0168-583X. DOI: https://doi.org/10.1016/j.nimb.2011.08.010. URL: http://www.sciencedirect.com/science/article/pii/S0168583X11007865 (cit. on p. 17).

Breton, D., E. Delagnes, J. Maalmi, and P. Rusquart (2014). "The WaveCatcher family of SCA-based 12-bit 3.2-GS/s fast digitizers". In: *2014 19th IEEE-NPSS Real Time Conference*, pp. 1–8. DOI: 10.1109/RTC.2014.7097545 (cit. on p. 134).

Brix, G., J. Zaers, L.-E. Adam, M. E. Bellemann, H. Ostertag, H. Trojan, U. Haberkorn, J. Doll, F. Oberdorfer, and W. Lorenz (1997). "Performance Evaluation of a Whole-Body PET Scanner Using the NEMA Protocol". In: *Journal of Nuclear Medicine* 38.10, pp. 1614–1623. URL: http://jnm.snmjournals.org/content/38/10/1614.short (cit. on p. 113).

Brun, R. and F. Rademakers (1997). "ROOT: An object oriented data analysis framework". In: *Nuclear Instruments and Methods in Physics Reasearch Section A: Accelerators, Spectrometers, Detectors and Associated Equipment* A389, pp. 81–86. DOI: 10.1016/S0168-9002(97)00048-X (cit. on pp. 126–128, 136).

Brunner, S. E., L. Gruber, A. Hirtl, K. Suzuki, J. Marton, and D. R. Schaart (2016). "A comprehensive characterization of the time resolution of the Philips Digital Photon Counter". In: *Journal of Instrumentation* 11.11, P11004. URL: http://stacks.iop.org/1748-0221/11/i=11/a=P11004 (cit. on p. 163).

Bucciantonio, M. (2015). "Development of an advanced Proton Range Radiography system for hadrontherapy". PhD thesis. Albert Einstein Center for Fundamental Physics - Laboratorium für Hochenergiephysik - Physikalisches Institut - Universität Bern (cit. on pp. 41, 43).

Bucciantonio, M., U. Amaldi, R. Kieffer, F. Sauli, and D. A. Watts (2013). "Development of a fast proton range radiography system for quality assurance in hadrontherapy". In: *Nuclear Instruments and Methods in Physics Research Section A: Accelerators, Spectrometers, Detectors and Associated Equipment* 732. Vienna Conference on Instrumentation 2013, pp. 564–567. ISSN: 0168-9002. DOI: https://doi.org/10.1016/j.nima.2013.05.110. URL: http://www.sciencedirect.com/science/article/pii/S0168900213007213 (cit. on p. 41).

Bucciantonio, M. and F. Sauli (2015). "Proton computed tomography". In: *Modern Physics Letters* A30.17, p. 1540024. DOI: 10.1142/S0217732315400246 (cit. on p. 39).

Buitenhuis, H. J. T., F. Diblen, K. W. Brzezinski, S. Brandenburg, and P. Dendooven (2017). "Beam-on imaging of short-lived positron emitters during proton therapy." In: *Physics in Medicine & Biology* 62.12, pp. 4654–4672 (cit. on p. 71).

Cachemiche, J.-P., P. Y. Duval, F. Hachon, R. Le Gac, and F. Réthoré (2012). "xTCA developments in Marseille for the LHCb Readout". In: *TWEPP 2012 Topical Workshop on Electronics for Particle Physics*. Oxford, United Kingdom. URL: http://hal.in2p3.fr/in2p3-00757616 (cit. on p. 124).

Camarlinghi, N., G. Sportelli, G. Battistoni, N. Belcari, M. Cecchetti, G. A. P. Cirrone, G. Cuttone, S. Ferretti, A. C. Kraan, A. Retico, F. Romano, P. Sala, K. Straub, A. Tramontana, A. Del Guerra, and V. Rosso (2014). "An in-beam PET system for monitoring ion-beam therapy: test on phantoms using clinical 62 MeV protons". In: *Journal of Instrumentation* 9.04, p. C04005. URL: http://stacks.iop.org/1748-0221/9/i=04/a=C04005 (cit. on p. 71).

Cambraia Lopes, P., J. Bauer, A. Salomon, I. Rinaldi, V. Tabacchini, T. Tessonnier, P. Crespo, K. Parodi, and D. R. Schaart (2016). “First in situ TOF-PET study using digital photon counters for proton range verification.” In: *Physics in Medicine & Biology* 61.16, pp. 6203–6230 (cit. on p. 72).

Cantor, D. (1988). “Pioneers and early years. A history of British radiology”. In: *Medical History* 32.2, pp. 224–224. URL: http://www.ncbi.nlm.nih.gov/pmc/articles/PMC1139872/ (cit. on p. 6).

Caporaso, G. J., Y.-J. Chen, and S. E. Sampayan (2009). “The Dielectric Wall Accelerator”. In: *Reviews of Accelerator Science and Technology* 02.01, pp. 253–263. DOI: 10.1142/S1793626809000235. URL: https://doi.org/10.1142/S1793626809000235 (cit. on p. 25).

Carnicer, A., V. Letellier, G. Rucka, G. Angellier, W. Sauerwein, and J. Herault (2012). “Study of the secondary neutral radiation in proton therapy: toward an indirect in vivo dosimetry.” In: *Medical Physics* 39.12, pp. 7303–7316 (cit. on p. 81).

Carnicer, A., V. Letellier, G. Rucka, G. Angellier, W. Sauerwein, and J. Hérault (2014). “An indirect in vivo dosimetry system for ocular proton therapy”. In: *Radiation protection dosimetry* 161.1-4, pp. 373–376. ISSN: 0144-8420. DOI: 10.1093/rpd/nct284. URL: https://doi.org/10.1093/rpd/nct284 (cit. on p. 17).

Castro, J. R. (1995). “Results of heavy ion radiotherapy.” eng. In: *Radiation and environmental biophysics* 34.1, pp. 45–48 (cit. on p. 21).

Catterall, M., C. Rogers, R. H. Thomlinson, and S. B. Field (1971). “An investigation into the clinical effects of fast neutrons”. In: *The British Journal of Radiology* 44.524. PMID: 4997649, pp. 603–611. DOI: 10.1259/0007-1285-44-524-603. URL: https://doi.org/10.1259/0007-1285-44-524-603 (cit. on p. 22).

Cecchin, D., D. Poggiali, L. Riccardin, P. Turco, F. Bui, and S. De Marchi (2015). “Analytical and experimental FWHM of a gamma camera: theoretical and practical issues.” In: *PeerJ - Life & Environment 3:e722* (cit. on p. 208).

Chatterjee, A., E. L. Alpen, C. A. Tobias, J. Llacer, and J. Alonso (1981). “High energy beams of radioactive nuclei and their biomedical applications”. In: *International Journal of Radiation Oncology Biology Physics* 7.4, pp. 503–507. ISSN: 0360-3016. DOI: https://doi.org/10.1016/0360-3016(81)90137-1. URL: http://www.sciencedirect.com/science/article/pii/0360301681901371 (cit. on p. 68).

Chen, X. (2017). “Développement de cartes Front-End avec leur firmware associé pour un hodoscope de faisceau et un diffuseur silicium utilisées pour le contrôle de dose en ligne en hadronthérapie.” Mémoire for CNAM engineer degree in Electronic Systems (cit. on pp. 111, 122).

Cherry, S. R., Y. Shao, R. W. Silverman, K. Meadors, S. Siegel, A. Chatziioannou, J. W. Young, W. Jones, J. C. Moyers, D. Newport, A. Boutefnouchet, T. H. Farquhar, M. Andreaco, M. J. Paulus, D. M. Binkley, R. Nutt, and M. E. Phelps (1997). “MicroPET: a high resolution PET scanner

for imaging small animals". In: *IEEE Transactions on Nuclear Science* 44.3, pp. 1161–1166. ISSN: 0018-9499. DOI: 10.1109/23.596981 (cit. on p. 94).

Chesler, D. A. (1971). "Three-dimensional activity distribution from multiple positron scintigraphs". In: *Journal of Nuclear Medicine* 12, pp. 347–348 (cit. on p. 93).

Chu, W. T., B. A. Ludewigt, and T. R. Renner (1993). "Instrumentation for treatment of cancer using proton and light-ion beams". In: *Review of Scientific Instruments* 64.8, pp. 2055–2122. DOI: 10.1063/1.1143946. URL: https://doi.org/10.1063/1.1143946 (cit. on p. 39).

Chvetsov, A. V. and S. L. Paige (2010). "The influence of CT image noise on proton range calculation in radiotherapy planning." In: *Physics in Medicine & Biology* 55.6, N141–9 (cit. on pp. 36, 38).

Cirrone, G. A. P., G. Cuttone, R. A. Lojacono, S. Lo Nigro, V. Mongelli, I. V. Patti, G. Privitera, L. Raffaele, D. Rifuggiato, M. G. Sabini, V. Salamone, C. Spatola, and L. M. Valastro (2003). "A 62 MeV proton beam for the treatment of ocular melanoma at Laboratori Nazionali del Sud-INFN (CATANIA)". In: *2003 IEEE Nuclear Science Symposium. Conference Record (IEEE Cat. No.03CH37515)*. Vol. 5, 3658–3662 Vol.5. DOI: 10.1109/NSSMIC.2003.1352701 (cit. on p. 71).

Colléaux, C. and É. Testa (2018). "Caractérisation d'un détecteur." Bachelor internship report (cit. on p. 161).

Compton, A. H. (1923). "A Quantum Theory of the Scattering of X-rays by Light Elements". In: *Physical Review* 21 (5), pp. 483–502. DOI: 10.1103/PhysRev.21.483. URL: https://link.aps.org/doi/10.1103/PhysRev.21.483 (cit. on p. 58).

Cookson, J. A. (1974). "Radiography with protons". In: *Naturwissenschaften* 61.5, pp. 184–191. ISSN: 1432-1904. DOI: 10.1007/BF00599915. URL: https://doi.org/10.1007/BF00599915 (cit. on p. 39).

Cormack, A. M. (1963). "Representation of a Function by Its Line Integrals, with Some Radiological Applications". In: *Journal of Applied Physics* 34.9, pp. 2722–2727. DOI: 10.1063/1.1729798. URL: https://doi.org/10.1063/1.1729798 (cit. on p. 39).

Cormack, A. M. and A. M. Koehler (1976). "Quantitative proton tomography: preliminary experiments". In: *Physics in Medicine & Biology* 21.4, p. 560. URL: http://stacks.iop.org/0031-9155/21/i=4/a=007 (cit. on p. 39).

Coudurier, V. (2015). "Caractérisation d'un hodoscope de faisceau pour l'hadronthérapie". Master internship report (cit. on pp. 156, 166).

Crandall, P. H. and B. Cassen (1966). "High speed section scanning of the brain." In: *Archives of Neurology* 15.2, pp. 163–171 (cit. on p. 97).

Cree, M. J. and P. J. Bones (1994). "Towards direct reconstruction from a gamma camera based on Compton scattering". In: *IEEE Transactions on Medical Imaging* 13.2, pp. 398–407. DOI: 10.1109/42.293932 (cit. on p. 101).

Crespo, P., G. Shakirin, and W. Enghardt (2006). “On the detector arrangement for in-beam PET for hadron therapy monitoring”. In: *Physics in Medicine & Biology* 51.9, p. 2143. URL: http://stacks.iop.org/0031-9155/51/i=9/a=002 (cit. on pp. 67, 68, 70).

Crespo, P., G. Shakirin, F. Fiedler, W. Enghardt, and A. Wagner (2007). “Direct time-of-flight for quantitative, real-time in-beam PET: a concept and feasibility study.” In: *Physics in Medicine & Biology* 52.23, pp. 6795–6811 (cit. on p. 67).

Cunha, M., C. Monini, É. Testa, and M. Beuve (2017). “NanOx, a new model to predict cell survival in the context of particle therapy.” In: *Physics in Medicine & Biology* 62.4, pp. 1248–1268 (cit. on p. 33).

Curie, P. and S. Curie (1898). “Sur une substance nouvelle radio-active, contenue dans la pechblende”. In: *Comptes Rendus Hebdomadaires des Séances de l’Académie des Sciences* 127, pp. 175–178 (cit. on p. 48).

Dahiya, M. (2016). “Brachytherapy: a review”. In: *Journal of Critical Reviews* 3, pp. 6–10 (cit. on p. 48).

Dahoumane, M., D. Dauvergne, J. Krimmer, J.-L. Ley, É. Testa, and Y. Zoccarato (2014). “A low noise and high dynamic range CMOS integrated Electronics associated with double sided Silicon Strip Detectors for a Compton camera gamma-ray detecting system”. In: *2014 IEEE Nuclear Science Symposium and Medical Imaging Conference (NSS/MIC)*, pp. 1–6. DOI: 10.1109/NSSMIC.2014.7431122 (cit. on p. 110).

Dahoumane, M., D. Dauvergne, J. Krimmer, H. Mathez, C. Ray, É. Testa, A. H. Walenta, and Y. Zoccarato (2012). “A low noise and high dynamic charge sensitive amplifier-shaper associated with Silicon Strip Detector for compton camera in hadrontherapy”. In: *2012 IEEE Nuclear Science Symposium and Medical Imaging Conference Record (NSS/MIC)*, pp. 1445–1451. DOI: 10.1109/NSSMIC.2012.6551351 (cit. on p. 111).

Dam, H. T. van, S. Seifert, R. Vinke, P. Dendooven, H. Lohner, F. J. Beekman, and D. R. Schaart (2011). “Improved Nearest Neighbor Methods for Gamma Photon Interaction Position Determination in Monolithic Scintillator PET Detectors”. In: *IEEE Transactions on Nuclear Science* 58.5, pp. 2139–2147. ISSN: 0018-9499. DOI: 10.1109/TNS.2011.2150762 (cit. on p. 89).

Dauvergne, D., M. Battaglia, G. Montarou, and É. Testa (2009). “New methods of real-time control imaging for ion therapy”. In: *NIRS-ETOILE Joint Symposium on Carbon Ion Therapy, March 2009, Lyon, France* (cit. on p. 43).

Dedes, G. and K. Parodi (2015). “Monte Carlo Simulations of Particle Interactions with Tissue in Carbon Ion Therapy”. In: *International Journal of Particle Therapy* 2.3, pp. 447–458. DOI: 10.14338/IJPT-15-00021. URL: https://doi.org/10.14338/IJPT-15-00021 (cit. on p. 77).

Dedes, G., M. Pinto, D. Dauvergne, N. Freud, J. Krimmer, J. M. Létang, C. Ray, and É. Testa (2014). “Assessment and improvements of Geant4 hadronic models in the context of prompt-gamma hadrontherapy monitoring.” In: *Physics in Medicine & Biology* 59.7, pp. 1747–1772 (cit. on p. 77).

Degenhardt, C., P. Rodrigues, A. Trindade, B. Zwaans, O. Mülhens, R. Dorscheid, A. Thon, A. Salomon, and T. Frach (2012). "Performance evaluation of a prototype Positron Emission Tomography scanner using Digital Photon Counters (DPC)". In: *2012 IEEE Nuclear Science Symposium and Medical Imaging Conference Record (NSS/MIC)*, pp. 2820–2824. DOI: 10.1109/NSSMIC.2012.6551643 (cit. on p. 72).

Degiovanni, A. and U. Amaldi (2015). "History of hadron therapy accelerators". In: *Physica Medica* 31.4, pp. 322–332. ISSN: 1120-1797. DOI: https://doi.org/10.1016/j.ejmp.2015.03.002. URL: http://www.sciencedirect.com/science/article/pii/S1120179715000629 (cit. on p. 22).

Dendooven, P., H. J. T. Buitenhuis, F. Diblen, P. N. Heeres, A. K. Biegun, F. Fiedler, M.-J. van Goethem, E. R. van der Graaf, and S. Brandenburg (2015). "Short-lived positron emitters in beam-on PET imaging during proton therapy." In: *Physics in Medicine & Biology* 60.23, pp. 8923–8947 (cit. on p. 71).

Deng, S.-M. (2012). "Etude de conception d'ASICs de lecture et d'étiquetage en temps associés à des photomultiplicateurs pour un hodoscope de faisceau en hadronthérapie". PhD thesis. École Doctorale EEA (Électronique, Électrontechnique et Automatique), Université Claude Bernard - Lyon 1 (cit. on p. 120).

Deng, S.-M., H. Mathez, D. Dauvergne, G.-N. Lu, and Y. Zoccarato (2012). "Front-end multi-channel PMT-associated readout chip for hodoscope application". In: *Nuclear Instruments and Methods in Physics Research Section A: Accelerators, Spectrometers, Detectors and Associated Equipment* 695. New Developments in Photodetection NDIP11, pp. 390–393. ISSN: 0168-9002. DOI: https://doi.org/10.1016/j.nima.2011.11.042. URL: http://www.sciencedirect.com/science/article/pii/S0168900211020845 (cit. on p. 119).

Deng, S.-M., H. Mathez, D. Dauvergne, Y. Zoccarato, and G.-N. Lu (2013). "Very fast front end ASIC associated with multi-anode PMTs for a scintillating-fibre beam hodoscope". In: *Journal of Instrumentation* 8, p. C01047. DOI: 10.1088/1748-0221/8/01/C01047. URL: https://hal.archives-ouvertes.fr/hal-00990850 (cit. on p. 119).

Despeignes, V. (1896). "Observations on a case of cancer of the stomach treated by Röntgen rays." In: *Lyon Medical Journal* 82, p. 428 (cit. on p. 6).

Dowdell, S., C. Grassberger, G. C. Sharp, and H. Paganetti (2013). "Interplay effects in proton scanning for lung: a 4D Monte Carlo study assessing the impact of tumor and beam delivery parameters". In: *Physics in Medicine & Biology* 58.12, p. 4137. URL: http://stacks.iop.org/0031-9155/58/i=12/a=4137 (cit. on p. 37).

Draeger, E., S. W. Peterson, D. S. Mackin, H. Chen, S. Beddar, and J. C. Polf (2017). "Feasibility Studies of a New Event Selection Method to Improve Spatial Resolution of Compton Imaging for Medical Applications." eng. In: *IEEE transactions on radiation and plasma medical sciences* 1.4, pp. 358–367. DOI: 10.1109/TRPMS.2017.2703095 (cit. on pp. 171, 179, 191).

Duck, F. A. (2014). "The origins of medical physics". In: *Physica Medica: European Journal of Medical Physics* 30.4, pp. 397–402. DOI: 10.1016/j.ejmp.2014.03.005. URL: http://dx.doi.org/10.1016/j.ejmp.2014.03.005 (cit. on p. 6).

DuMond, J. W. M. (1928). "The Structure of the Compton Shifted Line". In: *Proceedings of the National Academy of Sciences of the United States of America* 14.11, pp. 875–878. URL: http://www.jstor.org/stable/85639 (cit. on p. 60).

DuMond, J. W. M. (1929). "Compton Modified Line Structure and its Relation to the Electron Theory of Solid Bodies". In: *Physical Review* 33 (5), pp. 643–658. DOI: 10.1103/PhysRev.33.643. URL: https://link.aps.org/doi/10.1103/PhysRev.33.643 (cit. on p. 60).

Durante, M. and J. S. Loeffler (2009). "Charged particles in radiation oncology". In: *Nature Reviews Clinical Oncology* 7, p. 37. URL: http://dx.doi.org/10.1038/nrclinonc.2009.183 (cit. on pp. 7, 21).

Durante, M. and H. Paganetti (2016). "Nuclear physics in particle therapy: a review". In: *Reports on Progress in Physics* 79.9, p. 096702. URL: http://stacks.iop.org/0034-4885/79/i=9/a=096702 (cit. on pp. 7–9, 12, 14, 15, 20, 22, 27, 29, 37, 38).

Dyer, P., D. Bodansky, A. G. Seamster, E. B. Norman, and D. R. Maxson (1981). "Cross sections relevant to gamma-ray astronomy: Proton induced reactions". In: *Physical Review C* 23 (5), pp. 1865–1882. DOI: 10.1103/PhysRevC.23.1865. URL: https://link.aps.org/doi/10.1103/PhysRevC.23.1865 (cit. on p. 74).

El Kanawati, W., J. M. Létang, D. Dauvergne, M. Pinto, D. Sarrut, É. Testa, and N. Freud (2015). "Monte Carlo simulation of prompt gamma-ray emission in proton therapy using a specific track length estimator." In: *Physics in Medicine & Biology* 60.20, pp. 8067–8086 (cit. on p. 77).

Elftmann, R., J. Tammen, S. R. Kulkarni, C. Martin, S. Böttcher, and R. Wimmer-Schweingruber (2015). "Characterization of an LSO scintillator for space applications". In: *Journal of Physics: Conference Series* 632.1, p. 012006. URL: http://stacks.iop.org/1742-6596/632/i=1/a=012006 (cit. on p. 113).

Elsässer, T., W. K. Weyrather, T. Friedrich, M. Durante, G. Iancu, M. Krämer, G. Kragl, S. Brons, M. Winter, K.-J. Weber, and M. Scholz (2004). "Quantification of the Relative Biological Effectiveness for Ion Beam Radiotherapy: Direct Experimental Comparison of Proton and Carbon Ion Beams and a Novel Approach for Treatment Planning". In: *International Journal of Radiation Oncology Biology Physics* 78.4, pp. 1177–1183. DOI: 10.1016/j.ijrobp.2010.05.014. URL: http://dx.doi.org/10.1016/j.ijrobp.2010.05.014 (cit. on p. 170).

Engelsman, M., M. Schwarz, and L. Dong (2013). "Physics Controversies in Proton Therapy". In: *Seminars in Radiation Oncology* 23.2. Controversies in Proton Therapy, pp. 88–96. ISSN: 1053-4296. DOI: https://doi.org/10.1016/j.semradonc.2012.11.003. URL: http://www.sciencedirect.com/science/article/pii/S1053429612001063 (cit. on p. 33).

Enghardt, W., P. Crespo, F. Fiedler, R. Hinz, K. Parodi, J. Pawelke, and F. Pönisch (2004). "Charged hadron tumour therapy monitoring by means of PET". In: *Nuclear Instruments and Methods in Physics Research Section A: Accelerators, Spectrometers, Detectors and Associated Equipment* 525.1. Proceedings of the International Conference on Imaging Techniques in Subatomic Physics, Astrophysics, Medicine, Biology and Industry, pp. 284–288. ISSN: 0168-9002. DOI: https://doi.org/10.1016/j.nima.2004.03.128. URL: http://www.sciencedirect.com/science/article/pii/S0168900204004218 (cit. on pp. 69, 170).

Enghardt, W., W. D. Fromm, H. Geissel, H. Heller, G. Kraft, A. Magel, P. Manfrass, G. Munzenberg, F. Nickel, J. Pawelke, D. Schardt, C. Scheidenberger, and M. Sobiella (1992). "The spatial distribution of positron-emitting nuclei generated by relativistic light ion beams in organic matter". In: *Physics in Medicine & Biology* 37.11, p. 2127. URL: http://stacks.iop.org/0031-9155/37/i=11/a=009 (cit. on p. 69).

España, S. and H. Paganetti (2010). "The impact of uncertainties in the CT conversion algorithm when predicting proton beam ranges in patients from dose and PET-activity distributions." In: *Physics in Medicine & Biology* 55.24, pp. 7557–7571 (cit. on p. 38).

España, S. and H. Paganetti (2011a). "Uncertainties in planned dose due to the limited voxel size of the planning CT when treating lung tumors with proton therapy". In: *Physics in Medicine & Biology* 56.13, p. 3843. URL: http://stacks.iop.org/0031-9155/56/i=13/a=007 (cit. on p. 36).

España, S., X. Zhu, J. Daartz, G. El Fakhri, T. R. Bortfeld, and H. Paganetti (2011b). "Reliability of proton-nuclear interaction cross section data to predict proton-induced PET images in proton therapy". In: *Physics in Medicine & Biology* 56.9, pp. 2687–2698 (cit. on p. 64).

Essers, M. and B. Mijnheer (1999). "In vivo dosimetry during external photon beam radiotherapy". In: *International Journal of Radiation Oncology Biology Physics* 43, pp. 245–59 (cit. on p. 44).

Evans, T. C. (1951). "X-Ray Treatment-Its Origin, Birth and Early History. Emil H. Grubbe". In: *The Quarterly Review of Biology* 26.2, pp. 223–223. DOI: 10.1086/398163. URL: https://doi.org/10.1086/398163 (cit. on p. 6).

Everett, D. B., J. S. Fleming, R. W. Todd, and J. M. Nightingale (1977). "Gamma-radiation imaging system based on the Compton effect". In: *Proceedings of the Institution of Electrical Engineers* 124.11, p. 995. ISSN: 0020-3270. DOI: 10.1049/piee.1977.0203 (cit. on p. 196).

Fattori, G., M. Riboldi, E. Scifoni, M. Krämer, A. Pella, M. Durante, S. Ronchi, M. Bonora, R. Orecchia, and G. Baroni (2014). "Dosimetric effects of residual uncertainties in carbon ion treatment of head chordoma". In: *Radiotherapy and Oncology* 113.1, pp. 66–71. ISSN: 0167-8140. DOI: https://doi.org/10.1016/j.radonc.2014.08.001. URL: http://www.sciencedirect.com/science/article/pii/S0167814014003223 (cit. on p. 37).

Fermi, E. (1950). "High Energy Nuclear Events". In: *Progress of Theoretical Physics* 5.4, pp. 570–583. DOI: 10.1143/ptp/5.4.570. URL: http://dx.doi.org/10.1143/ptp/5.4.570 (cit. on p. 14).

Ferrero, V., E. Fiorina, M. Morrocchi, F. Pennazio, G. Baroni, G. Battistoni, N. Belcari, N. Camarlinghi, M. Ciocca, A. Del Guerra, M. Donetti, S. Giordanengo, G. Giraudo, V. Patera, C. Peroni, A. Rivetti, M. D. R. Rolo, S. Rossi, V. Rosso, G. Sportelli, S. Tampellini, F. Valvo, R. Wheadon, P. Cerello, and M. G. Bisogni (2018). "Online proton therapy monitoring: clinical test of a Silicon-photodetector-based in-beam PET". In: *Scientific Reports* 8.1, p. 4100 (cit. on p. 71).

Fiedler, F., D. Kunath, M. Priegnitz, and W. Enghardt (2012). "Online Irradiation Control by means of PET". In: *Ion Beam Therapy: Fundamentals, Technology, Clinical Applications, Biological and Medical Physics, Biomedical Engineering* (cit. on p. 66).

Fiedler, F., M. Priegnitz, R. Julich, J. Pawelke, P. Crespo, K. Parodi, F. Pönisch, and W. Enghardt (2008a). "In-beam PET measurements of biological half-lives of 12C irradiation induced β^+-activity." In: *Acta Oncologica* 47.6, pp. 1077–1086 (cit. on p. 65).

Fiedler, F., M. Priegnitz, D. Möckel, J. Pawelke, K. Parodi, F. Pönisch, W. Enghardt, and G. Shakirin (2008b). "Results of a 20 minutes decay measurement of a patient irradiation by the in-beam PET scanner". In: *GSI Scientific Report* 380 (cit. on p. 67).

Fiedler, F., G. Shakirin, J. Skowron, H. Braess, P. Crespo, D. Kunath, J. Pawelke, F. Pönisch, and W. Enghardt (2010). "On the effectiveness of ion range determination from in-beam PET data." In: *Physics in Medicine & Biology* 55.7, pp. 1989–1998 (cit. on p. 66).

Finck, C., Y. Karakaya, V. Reithinger, R. Rescigno, J. Baudot, J. Constanzo, D. Juliani, J. Krimmer, I. Rinaldi, M. Rousseau, É. Testa, M. Vanstalle, and C. Ray (2017). "Study for online range monitoring with the interaction vertex imaging method." In: *Physics in Medicine & Biology* 62.24, pp. 9220–9239 (cit. on p. 44).

Fontana, M., D. Dauvergne, J. M. Létang, R. Della Negra, F. Mounier, L. Zanetti, Y. Zoccarato, and É. Testa (2018). "Large surface gamma cameras for medical imaging: characterization of the bismuth germanate blocks". In: *Journal of Instrumentation* 13.08, P08018. URL: http://stacks.iop.org/1748-0221/13/i=08/a=P08018 (cit. on pp. 89, 90, 105, 166, 171).

Fontana, M., D. Dauvergne, J. M. Létang, J.-L. Ley, and É. Testa (2017a). "Compton camera study for high efficiency SPECT and benchmark with Anger system". In: *Physics in Medicine & Biology* 62.23, p. 8794. URL: http://stacks.iop.org/0031-9155/62/i=23/a=8794 (cit. on pp. 99, 195).

Fontana, M., D. Dauvergne, J.-L. Ley, J. M. Létang, V. Maxim, and É. Testa (2017b). "Versatile Compton camera for high energy gamma rays: Monte Carlo comparison with Anger camera for medical imaging". In: *2nd Jagiellonan Symposium on Fundamental and Applied Subatomic Physics*. Vol. 48. Krakow, Poland, pp. 1639–1645. DOI: 10.5506/APhysPolB.48.1639. URL: https://hal.archives-ouvertes.fr/hal-01609541 (cit. on pp. 99, 191, 195).

Foray, N. (2016). "Victor Despeignes, the Forgotten Pioneer of Radiation Oncology." eng. In: *International Journal of Radiation Oncology Biology Physics* 96.4, pp. 717–721. DOI: 10.1016/j.ijrobp.2016.07.019 (cit. on p. 6).

Fossati, P., S. Molinelli, N. Matsufuji, M. Ciocca, A. Mirandola, A. Mairani, J.-E. Mizoe, A. Hasegawa, R. Imai, T. Kamada, R. Orecchia, and H. Tsuji (2012). "Dose prescription in carbon ion radiotherapy: a planning study to compare NIRS and LEM approaches with a clinically-oriented strategy". In: *Physics in Medicine & Biology* 57.22, p. 7543. URL: http://stacks.iop.org/0031-9155/57/i=22/a=7543 (cit. on p. 33).

Francis, Z., E. Seif, S. Incerti, C. Champion, M. Karamitros, M. A. Bernal, V. N. Ivanchenko, A. Mantero, H. N. Tran, and Z. El Bitar (2014). "Carbon ion fragmentation effects on the nanometric level behind the Bragg peak depth." In: *Physics in Medicine & Biology* 59.24, pp. 7691–7702 (cit. on p. 17).

Frandes, M., A. Zoglauer, V. Maxim, and R. Prost (2010). “A Tracking Compton-Scattering Imaging System for Hadron Therapy Monitoring”. In: *IEEE Transactions on Nuclear Science* 57.1, pp. 144–150. ISSN: 0018-9499. DOI: 10.1109/TNS.2009.2031679 (cit. on p. 89).

Friedländer, E. M. and H. H. Heckman (1982). “Relativistic heavy ion collisions: experiment”. In: *LBL, Berkeley, Internal report* (cit. on p. 17).

Friedrich, T., U. Scholz, T. Elsässer, M. Durante, and M. Scholz (2012). “Calculation of the biological effects of ion beams based on the microscopic spatial damage distribution pattern”. In: *International Journal of Radiation Biology* 88.1-2, pp. 103–107. DOI: 10.3109/09553002.2011.611213. URL: https://doi.org/10.3109/09553002.2011.611213 (cit. on p. 7).

Gaglione, R. (2013). “Electronique d’acquisition d’une gamma-caméra.” PhD thesis. École Doctorale Sciences pour l’ingénieur de Clermont-Ferrand (cit. on pp. 154, 166).

Gallin-Martel, M.-L., Abbassi, L., Bes, A., Bosson, G., Collot, J., Crozes, T., Curtoni, S., Dauvergne, D., De Nolf, W., Fontana, M., Gallin-Martel, L., Hostachy, J.-Y., Krimmer, J., Lacoste, A., Marcatili, S., Morse, J., Motte, J.-F., Muraz, J.-F., Rarbi, F. E., Rossetto, O., Salomé, M., Testa, É., Vuiart, R., and Yamouni, M. (2018). “A large area diamond-based beam tagging hodoscope for ion therapy monitoring”. In: *European Physical Journal Web Conferences* 170, p. 09005. DOI: 10.1051/epjconf/201817009005. URL: https://doi.org/10.1051/epjconf/201817009005 (cit. on p. 165).

Gallin-Martel, M.-L., A. Bes, A. Boukhémiri, G. Bosson, J. Collot, D. Dauvergne, M. Fontana, L. Gallin-Martel, A. Gorecki, J.-Y. Hostachy, J. Krimmer, A. Lacoste, S. Marcatili, J. Morse, J.-F. Muraz, F. E. Rarbi, O. Rossetto, M. Salomé, É. Testa, and M. Yamouni (2016). “Large area polycrystalline diamond detectors for online hadron therapy beam tagging applications”. In: *2016 IEEE Nuclear Science Symposium, Medical Imaging Conference and Room-Temperature Semiconductor Detector Workshop (NSS/MIC/RTSD)*, pp. 1–5. DOI: 10.1109/NSSMIC.2016.8069398 (cit. on p. 164).

Gallo, G., D. Lo Presti, D. L. Bonanno, F. Longhitano, D. G. Bongiovanni, S. Reito, N. Randazzo, E. Leonora, V. Sipala, and F. Tommasino (2016). “QBeRT: an innovative instrument for qualification of particle beam in real-time”. In: *Journal of Instrumentation* 11.11, p. C11014. URL: http://stacks.iop.org/1748-0221/11/i=11/a=C11014 (cit. on p. 41).

Gariod, R., R. Allemand, E. Cormoreche, M. Laval, and M. Moszynski (1982). “The LETI positron tomograph architecture and time of flight improvements”. In: *Proceedings of The Workshop on Time of Flight Tomography. St Louis, USA* (cit. on p. 68).

GE Healthcare (2006). “Infinia”. In: Release 2.5 (cit. on pp. 196, 202).

GeckoDrive (2010). *G203V stepper drive - data sheet*. REV7. GeckoDrive Motor Controls Inc. (cit. on p. 154).

Gensheimer, M. F., T. I. Yock, N. J. Liebsch, G. C. Sharp, H. Paganetti, N. Madan, P. E. Grant, and T. R. Bortfeld (2010). “In vivo proton beam range verification using spine MRI changes.” In: *International Journal of Radiation Oncology Biology Physics* 78.1, pp. 268–275 (cit. on p. 44).

Gerard, S. K. and R. R. Cavalieri (2002). "I-123 diagnostic thyroid tumor whole-body scanning with imaging at 6, 24, and 48 hours." In: *Clinical Nuclear Medicine* 27.1, pp. 1–8 (cit. on p. 99).

Giantsoudi, D., C. Grassberger, D. Craft, A. Niemierko, A. Trofimov, and H. Paganetti (2013). "Linear energy transfer-guided optimization in intensity modulated proton therapy: feasibility study and clinical potential." eng. In: *International Journal of Radiation Oncology Biology Physics* 87.1, pp. 216–222. DOI: 10.1016/j.ijrobp.2013.05.013 (cit. on p. 21).

Giantsoudi, D., J. P. Schuemann, X. Jia, S. Dowdell, S. Jiang, and H. Paganetti (2015). "Validation of a GPU-based Monte Carlo code (gPMC) for proton radiation therapy: clinical cases study." eng. In: *Physics in Medicine & Biology* 60.6, pp. 2257–2269. DOI: 10.1088/0031-9155/60/6/2257 (cit. on p. 77).

Gillam, J. E., C. Lacasta, I. Torres-Espallardo, C. Candela Juan, G. Llosá, P. Solevi, J. Barrio, and M. Rafecas (2011). "A Compton imaging algorithm for on-line monitoring in hadron therapy". In: *Proceedings SPIE - Society of Photo-Optical Instrumentation Engineers* 7961, pp. 7961–8. DOI: 10.1117/12.877678. URL: https://doi.org/10.1117/12.877678 (cit. on pp. 101, 180).

Giovannini, G., T. T. Bohlen, G. Cabal, J. Bauer, T. Tessonnier, K. Frey, J. Debus, A. Mairani, and K. Parodi (2016). "Variable RBE in proton therapy: comparison of different model predictions and their influence on clinical-like scenarios." eng. In: *Radiation oncology (London, England)* 11, p. 68. DOI: 10.1186/s13014-016-0642-6 (cit. on p. 21).

Golnik, C. (2015). "Treatment verification in proton therapy based on the detection of prompt gamma-rays." PhD thesis. TU Dresden and Oncoray (cit. on pp. 133, 162).

Golnik, C., D. Bemmerer, W. Enghardt, F. Fiedler, F. Hueso-González, G. Pausch, K. Römer, H. Rohling, S. Schöne, L. Wagner, and T. Kormoll (2016). "Tests of a Compton imaging prototype in a monoenergetic 4.44 MeV photon field - a benchmark setup for prompt gamma-ray imaging devices". In: *Journal of Instrumentation* 11.06, P06009. URL: http://stacks.iop.org/1748-0221/11/i=06/a=P06009 (cit. on p. 89).

Golnik, C., F. Hueso-González, A. Muller, P. Dendooven, W. Enghardt, F. Fiedler, T. Kormoll, K. E. Römer, J. Petzoldt, A. Wagner, and G. Pausch (2014). "Range assessment in particle therapy based on prompt gamma-ray timing measurements." eng. In: *Physics in Medicine & Biology* 59.18. DOI: 10.1088/0031-9155/59/18/5399 (cit. on pp. 74, 78, 79).

Golovkov, M. S., D. V. Aleksandrov, L. V. Chulkov, G. Kraus, and D. Schardt (1997). "Fragmentation of 270 a MeV carbon ions in water". In: *1st International Week on Hadrontherapy : Advances in Hadrontherapy, Archamps, France, 20 - 24 Nov 1995* GSI-97-08, pp. 316–324. URL: https://cds.cern.ch/record/328169 (cit. on p. 17).

Goodman, G. B., G. K. Y. Lam, R. W. Harrison, P. M. Bergstrom, W. R. Martin, and B. D. Pate (1986). "The use of positron emission tomography in pion radiotherapy". In: *International Journal of Radiation Oncology Biology Physics* 12.10, pp. 1867–1871 (cit. on pp. 42, 68).

Gottschalk, B. (2006). "Neutron dose in scattered and scanned proton beams: in regard to Eric J. Hall (Int J Radiat Oncol Biol Phys 2006;65:1-7)." eng. In: *International Journal of*

Radiation Oncology Biology Physics 66.5, p. 1595. DOI: 10.1016/j.ijrobp.2006.08.014 (cit. on p. 18).

Gottschalk, B. (2010). "On the scattering power of radiotherapy protons." In: *Medical Physics* 37.1, pp. 352–367 (cit. on p. 13).

Gottschalk, B., A. M. Koehler, R. J. Schneider, J. M. Sisterson, and M. S. Wagner (1993). "Multiple Coulomb scattering of 160 MeV protons". In: *Nuclear Instruments and Methods in Physics Research Section B: Beam Interactions with Materials and Atoms* 74.4, pp. 467–490. ISSN: 0168-583X. DOI: https://doi.org/10.1016/0168-583X(93)95944-Z. URL: http://www.sciencedirect.com/science/article/pii/0168583X9395944Z (cit. on p. 13).

Gottschalk, B. and E. S. Pedroni (2008). "Treatment delivery systems". In: *Proton and charged particle radiotherapy*. Vol. 1 chap. 5. T. F. DeLaney, H. M. Kooy (Lippincott Williams, and Wilkins, Philadelphia), pp. 33–49 (cit. on p. 27).

Graeff, C., R. Lüchtenborg, J. G. Eley, M. Durante, and C. Bert (2013). "A 4D-optimization concept for scanned ion beam therapy". In: *Radiotherapy and Oncology* 109.3, pp. 419–424. DOI: 10.1016/j.radonc.2013.09.018. URL: https://doi.org/10.1016/j.radonc.2013.09.018 (cit. on p. 34).

Grassberger, C., S. Dowdell, G. C. Sharp, and H. Paganetti (2015). "Motion mitigation for lung cancer patients treated with active scanning proton therapy." In: *Medical Physics* 42.5, pp. 2462–2469 (cit. on p. 37).

Grassberger, C. and H. Paganetti (2011). "Elevated LET components in clinical proton beams". In: *Physics in Medicine & Biology* 56.20, p. 6677. URL: http://stacks.iop.org/0031-9155/56/i=20/a=011 (cit. on p. 17).

Grevillot, L., D. Bertrand, F. Dessy, N. Freud, and D. Sarrut (2011). "A Monte Carlo pencil beam scanning model for proton treatment plan simulation using GATE/GEANT4." eng. In: *Physics in Medicine & Biology* 56.16. DOI: 10.1088/0031-9155/56/16/008 (cit. on p. 175).

Grevillot, L., D. Bertrand, F. Dessy, N. Freud, and D. Sarrut (2012). "GATE as a GEANT4-based Monte Carlo platform for the evaluation of proton pencil beam scanning treatment plans." eng. In: *Physics in Medicine & Biology* 57.13, pp. 4223–4244. DOI: 10.1088/0031-9155/57/13/4223 (cit. on p. 76).

Guan, F., L. Bronk, U. Titt, S. H. Lin, D. Mirkovic, M. D. Kerr, X. R. Zhu, J. Dinh, M. Sobieski, C. Stephan, C. R. Peeler, R. Taleei, R. Mohan, and D. R. Grosshans (2015). "Spatial mapping of the biologic effectiveness of scanned particle beams: towards biologically optimized particle therapy". In: *Scientific Reports* 5. URL: http://dx.doi.org/10.1038/srep09850 (cit. on p. 21).

Gunter, D. L. (2004). "CHAPTER 8 - Collimator Design for Nuclear Medicine". In: *Emission Tomography*. Ed. by M. N. Wernick and J. N. Aarsvold. San Diego: Academic Press, pp. 153–168. ISBN: 978-0-12-744482-6. DOI: https://doi.org/10.1016/B978-012744482-6.50011-9. URL: http://www.sciencedirect.com/science/article/pii/B9780127444826500119 (cit. on p. 97).

Gunzert-Marx, K., H. Iwase, D. Schardt, and R. S. Simon (2008). "Secondary beam fragments produced by 200 MeV/u ^{12}C ions in water and their dose contributions in carbon ion radiotherapy". In: *New Journal of Physics* 10.7, p. 075003. URL: http://stacks.iop.org/1367-2630/10/i=7/a=075003 (cit. on pp. 18, 43).

Gwosch, K., B. Hartmann, J. Jakubek, C. Granja, P. Soukup, O. Jäkel, and M. Martisikova (2013). "Non-invasive monitoring of therapeutic carbon ion beams in a homogeneous phantom by tracking of secondary ions." In: *Physics in Medicine & Biology* 58.11, pp. 3755–3773 (cit. on p. 43).

Haberer, T., W. Becher, D. Schardt, and G. Kraft (1993). "Magnetic scanning system for heavy ion therapy". In: *Nuclear Instruments and Methods in Physics Research Section A: Accelerators, Spectrometers, Detectors and Associated Equipment* 330.1, pp. 296–305. ISSN: 0168-9002. DOI: https://doi.org/10.1016/0168-9002(93)91335-K. URL: http://www.sciencedirect.com/science/article/pii/016890029391335K (cit. on p. 29).

Haettner, E., H. Iwase, M. Krämer, G. Kraft, and D. Schardt (2013). "Experimental study of nuclear fragmentation of 200 and 400 MeV/u ^{12}C ions in water for applications in particle therapy". In: *Physics in Medicine & Biology* 58.23, p. 8265. URL: http://stacks.iop.org/0031-9155/58/i=23/a=8265 (cit. on p. 17).

Haettner, E., H. Iwase, and D. Schardt (2006). "Experimental fragmentation studies with ^{12}C therapy beams". In: *Radiation Protection Dosimetry* 122.1-4, pp. 485–487. DOI: 10.1093/rpd/ncl402. URL: http://dx.doi.org/10.1093/rpd/ncl402 (cit. on pp. 16, 17).

Hall, E. J. and A. J. Giaccia (2012). *Radiobiology for the radiologist*. URL: http://public.eblib.com/choice/publicfullrecord.aspx?p=2031840 (cit. on p. 19).

Halperin, E. C. (2006). "Particle therapy and treatment of cancer". In: *The Lancet Oncology* 7.8, pp. 676–685. DOI: 10.1016/S1470-2045(06)70795-1. URL: http://dx.doi.org/10.1016/S1470-2045(06)70795-1 (cit. on p. 7).

Hamamatsu (1995). *Metal Package Photomultiplier Tube R5600 Series*. TPMH1066E08. Hamamatsu Photonics K. K. (cit. on p. 154).

Hamamatsu (2006). *Flat Panel Type Multianode Photomultiplier Tube Assembly H8500, H8500B*. TPMH1282E09. Hamamatsu Photonics K. K. (cit. on pp. 119, 154, 159).

Hamm, R. W., K. R. Crandall, and J. M. Potter (1991). "Preliminary design of a dedicated proton therapy linac". In: *Conference Record of the 1991 IEEE Particle Accelerator Conference*. DOI: 10.1109/PAC.1991.165037 (cit. on p. 25).

Han, L., W. L. Rogers, S. S. Huh, and N. H. Clinthorne (2008). "Statistical performance evaluation and comparison of a Compton medical imaging system and a collimated Anger camera for higher energy photon imaging". In: *Physics in Medicine & Biology* 53.24, p. 7029. URL: http://stacks.iop.org/0031-9155/53/i=24/a=002 (cit. on pp. 196, 197, 199, 215).

Hayakawa, Y., J. Tada, N. Arai, K. Hosono, M. Sato, T. Wagai, H. Tsuji, and H. Tsuji (1995). "Acoustic pulse generated in a patient during treatment by pulsed proton radiation beam".

In: *Radiation Oncology Investigations* 3.1, pp. 42–45. DOI: 10.1002/roi.2970030107. URL: https://onlinelibrary.wiley.com/doi/abs/10.1002/roi.2970030107 (cit. on p. 44).

Hendee, W. R. and R. Ritenour E (2002). *Medical Imaging Physics*. John Wiley & Sons (cit. on p. 49).

Henriquet, P., É. Testa, M. Chevallier, D. Dauvergne, G. Dedes, N. Freud, J. Krimmer, J. M. Létang, C. Ray, M.-H. Richard, and F. Sauli (2012). "Interaction vertex imaging (IVI) for carbon ion therapy monitoring: a feasibility study." In: *Physics in Medicine & Biology* 57.14, pp. 4655–4669 (cit. on p. 43).

Herault, J., N. Iborra, B. Serrano, and P. Chauvel (2005). "Monte Carlo simulation of a protontherapy platform devoted to ocular melanoma." In: *Medical Physics* 32.4, pp. 910–919 (cit. on p. 220).

Hermanss, C. F. (2013). "X-ray absorption studies of metalloporphyrin molecules on surfaces". PhD thesis. Freie Universität Berlin (cit. on p. 62).

Hertz, B. (2016). "Dr. Saul Hertz (1905-1950) Discovers the Medical Uses of Radioactive Iodine: The First Targeted Cancer Therapy". In: *Thyroid Cancer*. Ed. by H. Ahmadzadehfar. Rijeka: IntechOpen. Chap. 1. DOI: 10.5772/64609. URL: https://doi.org/10.5772/64609 (cit. on p. 99).

Hertz, S. and A. Roberts (1942). "Radioactive iodine as an indicator in thyroid physiology. V. The use of radioactive iodine in the differential diagnosis of two types of graves' disease." In: *Journal of Clinical Investigation* 21.1, pp. 31–32 (cit. on p. 99).

Hettler, C., A. Zografos, Y. Parker, D. Pearson, V. Joshkin, C. Cohen-Jonathan, F. Huang, K. Leung, M. Rougieri, and T. Brown (2013). "Development of a dielectric wall accelerator proton therapy system". In: *2013 Abstracts IEEE International Conference on Plasma Science (ICOPS)*, pp. 1–1. DOI: 10.1109/PLASMA.2013.6635175 (cit. on p. 25).

Highland, V. L. (1975). "Some practical remarks on multiple scattering". In: *Nuclear Instruments and Methods* 129.2, pp. 497–499. DOI: https://doi.org/10.1016/0029-554X(75)90743-0. URL: http://www.sciencedirect.com/science/article/pii/0029554X75907430 (cit. on p. 13).

Hilaire, E., C. Robert, X. Lojacono, D. Sarrut, I. Buvat, F. Peyrin, and V. Maxim (2014). "Compton imaging in proton therapy: reconstructed image of the simulated prompt-γ distribution". In: *ICTR-PHE 2014*. Genève, Switzerland, S43. URL: https://hal.archives-ouvertes.fr/hal-01052717 (cit. on pp. 101, 130, 180).

Hilaire, E., D. Sarrut, F. Peyrin, and V. Maxim (2016). "Proton therapy monitoring by Compton imaging: influence of the large energy spectrum of the prompt-gamma radiation." eng. In: *Physics in Medicine & Biology* 61.8, pp. 3127–3146. DOI: 10.1088/0031-9155/61/8/3127 (cit. on p. 171).

Hirasawa, M. and T. Tomitani (Apr. 21, 2003). "An analytical image reconstruction algorithm to compensate for scattering angle broadening in Compton cameras." eng. In: *Physics in Medicine & Biology* 48.8, pp. 1009–1026 (cit. on p. 101).

Hishikawa, Y., K. Kagawa, M. Murakami, H. Sakai, T. Akagi, and M. Abe (2002). "Usefulness of positron-emission tomographic images after proton therapy". In: *International Journal of Radiation Oncology Biology Physics* 53.5, pp. 1388–1391. DOI: 10.1016/S0360-3016(02)02887-0. URL: http://dx.doi.org/10.1016/S0360-3016(02)02887-0 (cit. on p. 70).

Hoffmann, E. J., M. E. Phelps, N. A. Mullani, C. S. Higgins, and M. M. Ter-Pogossian (1976). "Design and performance characteristics of a whole-body positron transaxial tomograph." In: *Journal of Nuclear Medicine* 17.6, pp. 493–502 (cit. on pp. 47, 93).

Holley, W. R. and A. Chatterjee (1996). "Clusters of DNA induced by ionizing radiation: formation of short DNA fragments. I. Theoretical modeling." eng. In: *Radiation research* 145.2, pp. 188–199 (cit. on p. 19).

Hong, L., M. Goitein, M. Bucciolini, R. Comiskey, B. Gottschalk, S. Rosenthal, C. Serago, and M. Urie (1996). "A pencil beam algorithm for proton dose calculations". In: *Physics in Medicine & Biology* 41.8, p. 1305. URL: http://stacks.iop.org/0031-9155/41/i=8/a=005 (cit. on p. 35).

Hsi, W. C., D. J. Indelicato, C. Vargas, S. Duvvuri, Z. Li, and J. Palta (2009). "In vivo verification of proton beam path by using post-treatment PET/CT imaging." In: *Medical Physics* 36.9, pp. 4136–4146 (cit. on p. 70).

Huang, H.-M., C.-C. Liu, M.-L. Jan, and M.-W. Lee (2018). "A low-count reconstruction algorithm for Compton-based prompt gamma imaging". In: *Physics in Medicine & Biology* 63.8, p. 085013. URL: http://stacks.iop.org/0031-9155/63/i=8/a=085013 (cit. on pp. 101, 180).

Hubbell, J. H. and M. J. Berger (1987). *XCOM: Photon Cross Sections on a Personal Computer, Report NBSIR 87-3597 (1987), National Institute for Standards and Technology, U.S.A.* URL: http://physics.nist.gov/PhysRefData/XrayMassCoef/ (visited on 02/21/2017) (cit. on pp. 203, 216).

Hueso-González, F., A. K. Biegun, P. Dendooven, W. Enghardt, F. Fiedler, C. Golnik, K. Heidel, T. Kormoll, J. Petzoldt, K. E. Römer, R. Schwengner, A. Wagner, and G. Pausch (2015a). "Comparison of LSO and BGO block detectors for prompt gamma imaging in ion beam therapy". In: *Journal of Instrumentation* 10.09, P09015. URL: http://stacks.iop.org/1748-0221/10/i=09/a=P09015 (cit. on pp. 89, 90, 113, 133, 162).

Hueso-González, F., W. Enghardt, F. Fiedler, C. Golnik, G. Janssens, J. Petzoldt, D. Prieels, M. Priegnitz, K. E. Römer, J. Smeets, F. Vander Stappen, A. Wagner, and G. Pausch (2015b). "First test of the prompt gamma ray timing method with heterogeneous targets at a clinical proton therapy facility." In: *Physics in Medicine & Biology* 60.16, pp. 6247–6272 (cit. on p. 80).

Hueso-González, F., C. Golnik, M. Berthel, A. Dreyer, W. Enghardt, F. Fiedler, K. Heidel, T. Kormoll, H. Rohling, S. Schöne, R. Schwengner, A. Wagner, and G. Pausch (2014). "Test of Compton camera components for prompt gamma imaging at the ELBE bremsstrahlung beam". In: *Journal of Instrumentation* 9.05, P05002. URL: http://stacks.iop.org/1748-0221/9/i=05/a=P05002 (cit. on p. 89).

Hueso-González, F., M. Rabe, T. A. Ruggieri, T. R. Bortfeld, and J. M. Verburg (2018). "A full-scale clinical prototype for proton range verification using prompt gamma-ray spectroscopy." In: *Physics in Medicine & Biology* 63.18, p. 185019 (cit. on p. 83).

Hüfner, J., K. Schäfer, and B. Schürmann (1975). "Abrasion-ablation in reactions between relativistic heavy ions". In: *Physical Review C* 12 (6), pp. 1888–1898. DOI: 10.1103/PhysRevC.12.1888. URL: https://link.aps.org/doi/10.1103/PhysRevC.12.1888 (cit. on p. 14).

Huisman, B. F. B., J. M. Létang, É. Testa, and D. Sarrut (2016). "Accelerated prompt gamma estimation for clinical proton therapy simulations." In: *Physics in Medicine & Biology* 61.21, pp. 7725–7743 (cit. on p. 77).

Hünemohr, N., H. Paganetti, S. Greilich, O. Jäkel, and J. Seco (2014). "Tissue decomposition from dual energy CT data for MC based dose calculation in particle therapy". In: *Medical Physics* 41.6, p. 061714. DOI: 10.1118/1.4875976. URL: http://www.ncbi.nlm.nih.gov/pmc/articles/PMC4032427/ (cit. on p. 36).

ICRU (1980a). "ICRU Report 33 - Radiation Quantities and Units". In: *Journal of the International Commission on Radiation Units and Measurements, Bethesda, MD* (cit. on p. 19).

ICRU (1980b). "ICRU Report 49 - Stopping Powers and Ranges for Protons and Alpha Particles". In: *Journal of the International Commission on Radiation Units and Measurements, Bethesda, MD* (cit. on p. 38).

ICRU (1998). "ICRU Report 60 - Fundamental Quantities and Units for Ionising Radiation". In: *Journal of the International Commission on Radiation Units and Measurements, Bethesda, MD* (cit. on p. 19).

ICRU (2007). "ICRU Report 78 - Prescribing, recording, and reporting proton beam therapy". In: *Journal of the International Commission on Radiation Units and Measurements, Bethesda, MD* (cit. on p. 33).

Ido, T., C.-N. Wan, V. Casella, J. S. Fowler, A. P. Wolf, M. Reivich, and D. E. Kuhl (1978). "Labeled 2-deoxy-D-glucose analogs. 18F-labeled 2-deoxy-2-fluoro-D-glucose, 2-deoxy-2-fluoro-D-mannose and 14C-2-deoxy-2-fluoro-D-glucose". In: *Journal of Labelled Compounds and Radiopharmaceuticals* 14.2, pp. 175–183. DOI: 10.1002/jlcr.2580140204. URL: https://onlinelibrary.wiley.com/doi/abs/10.1002/jlcr.2580140204 (cit. on p. 94).

Inaniwa, T., N. Kanematsu, N. Matsufuji, T. Kanai, T. Shirai, K. Noda, H. Tsuji, T. Kamada, and H. Tsuji (2015). "Reformulation of a clinical-dose system for carbon-ion radiotherapy treatment planning at the National Institute of Radiological Sciences, Japan". In: *Physics in Medicine & Biology* 60.8, p. 3271. URL: http://stacks.iop.org/0031-9155/60/i=8/a=3271 (cit. on p. 33).

Inaniwa, T., H. Tashima, and N. Kanematsu (2018). "Optimum size of a calibration phantom for x-ray CT to convert the Hounsfield units to stopping power ratios in charged particle therapy treatment planning". In: *Journal of Radiation Research* 59.2, pp. 216–224. DOI: 10.1093/jrr/rrx059 (cit. on p. 31).

Iseki, Y., T. Kanai, M. Kanazawa, A. Kitagawa, H. Mizuno, T. Tomitani, M. Suda, and E. Urakabe (2004). "Range verification system using positron emitting beams for heavy-ion radiotherapy." In: *Physics in Medicine & Biology* 49.14, pp. 3179–3195 (cit. on p. 69).

Iwata, Y., K. Noda, T. Murakami, T. Shirai, T. Furukawa, T. Fujita, S. Mori, K. Mizushima, K. Shouda, T. Fujimoto, T. Ogitsu, T. Obana, N. Amemiya, T. Orikasa, S. Takami, and S. Takayama (2013). "Development of a superconducting rotating-gantry for heavy-ion therapy". In: *Nuclear Instruments and Methods in Physics Research Section B: Beam Interactions with Materials and Atoms* 317. XVIth International Conference on ElectroMagnetic Isotope Separators and Techniques Related to their Applications, December 2-7, 2012 at Matsue, Japan, pp. 793–797. DOI: https://doi.org/10.1016/j.nimb.2013.03.050. URL: http://www.sciencedirect.com/science/article/pii/S0168583X13003856 (cit. on p. 30).

Jäkel, O., C. Jacob, D. Schardt, C. P. Karger, and G. H. Hartmann (2001a). "Relation between carbon ion ranges and x-ray CT numbers." eng. In: *Medical Physics* 28.4, pp. 701–703. DOI: 10.1118/1.1357455 (cit. on pp. 31, 32).

Jäkel, O., M. Krämer, C. P. Karger, and J. Debus (2001b). "Treatment planning for heavy ion radiotherapy: clinical implementation and application". In: *Physics in Medicine & Biology* 46.4, p. 1101. URL: http://stacks.iop.org/0031-9155/46/i=4/a=314 (cit. on p. 33).

Jäkel, O. and P. Reiss (2007). "The influence of metal artefacts on the range of ion beams". In: *Physics in Medicine & Biology* 52.3, p. 635. URL: http://stacks.iop.org/0031-9155/52/i=3/a=007 (cit. on p. 36).

Jaszczak, R. J., L.-T. Chang, N. A. Stein, and F. E. Moore (1979). "Whole-body single-photon emission computed tomography using dual, large-field-of-view scintillation cameras". In: *Physics in Medicine & Biology* 24.6, p. 1123. URL: http://stacks.iop.org/0031-9155/24/i=6/a=003 (cit. on p. 98).

Jaszczak, R. J., P. H. Murphy, D. Huard, and J. A. Burdine (1977). "Radionuclide emission computed tomography of the head with 99mCc and a scintillation camera." In: *Journal of Nuclear Medicine* 18.4, pp. 373–380 (cit. on p. 98).

Jemal, A., M. M. Center, C. DeSantis, and E. M. Ward (2010). "Global Patterns of Cancer Incidence and Mortality Rates and Trends". In: *Cancer Epidemiology and Prevention Biomarkers* 19.8, pp. 1893–1907. ISSN: 1055-9965. DOI: 10.1158/1055-9965.EPI-10-0437. URL: http://cebp.aacrjournals.org/content/19/8/1893 (cit. on p. 6).

Johnson, R. P. (2017). "Review of medical radiography and tomography with proton beams". In: *Reports on Progress in Physics* 81.1, p. 016701. URL: http://stacks.iop.org/0034-4885/81/i=1/a=016701 (cit. on p. 40).

Johnson, R. P., V. Bashkirov, L. DeWitt, V. Giacometti, R. F. Hurley, P. Piersimoni, T. E. Plautz, H. F.-W. Sadrozinski, K. Schubert, R. Schulte, B. Schultze, and A. Zatserklyaniy (2016). "A Fast Experimental Scanner for Proton CT: Technical Performance and First Experience with Phantom Scans." In: *IEEE Trans Nucl Sci* 63.1, pp. 52–60 (cit. on p. 42).

Jones, B. (2015). "Towards Achieving the Full Clinical Potential of Proton Therapy by Inclusion of LET and RBE Models." eng. In: *Cancers (Basel)* 7.1, pp. 460–480. DOI: 10.3390/cancers7010460 (cit. on p. 21).

Kabuki, S., K. Hattori, R. Kohara, E. Kunieda, A. Kubo, H. Kubo, K. Miuchi, T. Nakahara, T. Nagayoshi, H. Nishimura, Y. Okada, R. Orito, H. Sekiya, T. Shirahata, A. Takada, T. Tanimori, and K. Ueno (2007). "Development of Electron Tracking Compton Camera using micro pixel gas chamber for medical imaging". In: *Nuclear Instruments and Methods in Physics Research Section A: Accelerators, Spectrometers, Detectors and Associated Equipment* 580.2. Imaging 2006, pp. 1031–1035. ISSN: 0168-9002. DOI: https://doi.org/10.1016/j.nima.2007.06.098. URL: http://www.sciencedirect.com/science/article/pii/S0168900207013186 (cit. on pp. 99, 217).

Kabuki, S., H. Kimura, H. Amano, Y. Nakamoto, H. Kubo, K. Miuchi, S. Kurosawa, M. Takahashi, H. Kawashima, M. Ueda, T. Okada, A. Kubo, E. Kunieda, T. Nakahara, R. Kohara, O. Miyazaki, T. Nakazawa, T. Shirahata, E. Yamamoto, K. Ogawa, K. Togashi, H. Saji, and T. Tanimori (2010). "Electron-tracking Compton gamma-ray camera for small animal and phantom imaging". In: *Nuclear Instruments and Methods in Physics Research Section A: Accelerators, Spectrometers, Detectors and Associated Equipment* 623.1. 1st International Conference on Technology and Instrumentation in Particle Physics, pp. 606–607. ISSN: 0168-9002. DOI: https://doi.org/10.1016/j.nima.2010.03.085. URL: http://www.sciencedirect.com/science/article/pii/S0168900210006492 (cit. on p. 99).

Kabuki, S., H. Kimura, H. Amano, Y. Nakamoto, H. Kubo, K. Miuchi, S. Kurosawa, M. Takahashi, H. Kawashima, M. Ueda, T. Okada, K. Ogawa, K. Togashi, H. Saji, and T. Tanimori (2009). "Imaging reagents study for nuclear medicine using an electron-tracking Compton gamma-ray camera". In: *2009 IEEE Nuclear Science Symposium Conference Record (NSS/MIC)*, pp. 2813–2816. DOI: 10.1109/NSSMIC.2009.5401649 (cit. on p. 99).

Kanai, T., K. Kawachi, H. Matsuzawa, and T. Inada (1983). "Three-dimensional beam scanning for proton therapy". In: *Nuclear Instruments and Methods in Physics Research* 214.2, pp. 491–496. ISSN: 0167-5087. DOI: https://doi.org/10.1016/0167-5087(83)90621-X. URL: http://www.sciencedirect.com/science/article/pii/016750878390621X (cit. on p. 29).

Kanazawa, M., A. Kitagawa, S. Kouda, T. Nishio, M. Torikoshi, K. Noda, T. Murakami, M. Suda, T. Tomitani, T. Kanai, Y. Futami, M. Shinbo, E. Urakabe, and Y. Iseki (2002). "Application of an RI-beam for cancer therapy: In-vivo verification of the ion-beam range by means of positron imaging". In: *Nuclear Physics A* 701.1. 5th International Conference on Radioactive Nuclear Beams, pp. 244–252. ISSN: 0375-9474. DOI: https://doi.org/10.1016/S0375-9474(01)01592-5. URL: http://www.sciencedirect.com/science/article/pii/S0375947401015925 (cit. on p. 69).

Kanematsu, N., N. Matsufuji, R. Kohno, S. Minohara, and T. Kanai (2003). "A CT calibration method based on the polybinary tissue model for radiotherapy treatment planning". In: *Physics in Medicine & Biology* 48.8, p. 1053. URL: http://stacks.iop.org/0031-9155/48/i=8/a=307 (cit. on p. 31).

Karp, J. S. and M. E. Daube-Witherspoon (1987). "Depth-of-interaction determination in NaI(Tl) and BGO scintillation crystals using a temperature gradient". In: *Nuclear Instruments and*

Methods in Physics Research Section A: Accelerators, Spectrometers, Detectors and Associated Equipment 260.2, pp. 509–517. ISSN: 0168-9002. DOI: https://doi.org/10.1016/0168-9002(87)90124-0. URL: http://www.sciencedirect.com/science/article/pii/0168900287901240 (cit. on p. 94).

Karp, J. S., S. Surti, M. E. Daube-Witherspoon, and G. Muehllehner (2008). "Benefit of time-of-flight in PET: experimental and clinical results." In: *Journal of Nuclear Medicine* 49.3, pp. 462–470 (cit. on p. 95).

Keevil, S. F. (2012). "Physics and medicine: a historical perspective". In: *The Lancet* 379.9825, pp. 1517–1524. ISSN: 0140-6736. DOI: https://doi.org/10.1016/S0140-6736(11)60282-1. URL: http://www.sciencedirect.com/science/article/pii/S0140673611602821 (cit. on p. 6).

Kelleter, L., A. Wronska, J. Besuglow, A. Konefal, K. Laihem, J. Leidner, A. Magiera, K. Parodi, K. Rusiecka, A. Stahl, and T. Tessonnier (2017). "Spectroscopic study of prompt-gamma emission for range verification in proton therapy." eng. In: *Physica Medica* 34, pp. 7–17. DOI: 10.1016/j.ejmp.2017.01.003 (cit. on p. 76).

Kereiakes, J. G. (1987). "The history and development of medical physics instrumentation: Nuclear medicine". In: *Medical Physics* 14.1, pp. 146–155. DOI: 10.1118/1.596105. URL: https://aapm.onlinelibrary.wiley.com/doi/abs/10.1118/1.596105 (cit. on p. 6).

Keyes, J. W. J., N. Orlandea, W. J. Heetderks, P. F. Leonard, and W. L. Rogers (1977). "The Humongotron–a scintillation-camera transaxial tomograph." In: *Journal of Nuclear Medicine* 18.4, pp. 381–387 (cit. on p. 98).

Kiener, J., M. Berheide, N. L. Achouri, A. Boughrara, A. Coc, A. Lefebvre, F. de Oliveira Santos, and C. Vieu (1998). "γ-ray production by inelastic proton scattering on O-16 and C-12". In: *Physical Review* C58, pp. 2174–2179. DOI: 10.1103/PhysRevC.58.2174 (cit. on p. 74).

Kim, C. H., H. J. Park, S. Hee, and R. L. Han (2012a). "Erratum: "Gamma electron vertex imaging and application to beam range verification in proton therapy"". In: *Medical Physics* 39.10, p. 1001. DOI: 10.1118/1.4749930. URL: https://aapm.onlinelibrary.wiley.com/doi/abs/10.1118/1.4749930 (cit. on p. 90).

Kim, C. H., H. J. Park, S. Hee, and R. L. Han (2012b). "Gamma electron vertex imaging and application to beam range verification in proton therapy". In: *Medical Physics* 39.2, pp. 1001–1005. DOI: 10.1118/1.3662890. URL: https://aapm.onlinelibrary.wiley.com/doi/abs/10.1118/1.3662890 (cit. on p. 90).

Kim, J.-W. (2009). "Pinhole Camera Measurements of Prompt Gamma-rays for Detection of Beam Range Variation in Proton Therapy". In: *Journal of Korean Physical Society* 55, p. 1673. DOI: 10.3938/jkps.55.1673 (cit. on p. 84).

Kim, S. M., H. Seo, J. H. Park, C. H. Kim, C. S. Lee, S.-J. Lee, D. S. Lee, and J. S. Lee (2013). "Resolution recovery reconstruction for a Compton camera." eng. In: *Physics in Medicine & Biology* 58.9, pp. 2823–2840. DOI: 10.1088/0031-9155/58/9/2823 (cit. on p. 87).

Kishimoto, A., J. Kataoka, T. Nishiyama, T. Taya, and S. Kabuki (2015). "Demonstration of three-dimensional imaging based on handheld Compton camera". In: *Journal of Instrumentation* 10.11, P11001. URL: http://stacks.iop.org/1748-0221/10/i=11/a=P11001 (cit. on p. 88).

Kitagawa, A., Y. Furusawa, T. Kanai, M. Kanazawa, H. Mizuno, M. Muramatsu, S. Sato, M. Suda, T. Tomitani, E. Urakabe, M. Yoshimoto, Q. Li, Z. Wei, K. Hanawa, Y. Iseki, and K. Sato (2006). "Medical application of radioactive nuclear beams at HIMAC". In: *Review of Scientific Instruments* 77.3, p. 03C105. DOI: 10.1063/1.2149309. URL: https://doi.org/10.1063/1.2149309 (cit. on p. 69).

Klein, O. and Y. Nishina (1929). "Über die Streuung von Strahlung durch freie Elektronen nach der neuen relativistischen Quantendynamik von Dirac". In: *Zeitschrift für Physik* 52.11, pp. 853–868. DOI: 10.1007/BF01366453. URL: https://doi.org/10.1007/BF01366453 (cit. on p. 60).

Knoll, G. F. (2000). *Radiation Detection and Measurement*. Third Edition. John Wiley & Sons Inc. (cit. on pp. 58, 61, 63, 108).

Knopf, A.-C. and A. J. Lomax (2013). "In vivo proton range verification: a review". In: *Physics in Medicine & Biology* 58.15, R131. URL: http://stacks.iop.org/0031-9155/58/i=15/a=R131 (cit. on pp. 35, 42, 170).

Knopf, A.-C., K. Parodi, H. Paganetti, T. R. Bortfeld, J. Daartz, M. Engelsman, N. J. Liebsch, and H. A. Shih (2011). "Accuracy of proton beam range verification using post-treatment positron emission tomography/computed tomography as function of treatment site." In: *International Journal of Radiation Oncology Biology Physics* 79.1, pp. 297–304 (cit. on p. 70).

Koehler, A. M. (1968). "Proton Radiography". In: *Science* 160.3825, pp. 303–304. ISSN: 0036-8075. DOI: 10.1126/science.160.3825.303. URL: http://science.sciencemag.org/content/160/3825/303 (cit. on pp. 36, 39, 41).

Komori, M., E. Sekihara, T. Yabe, R. Horita, T. Toshito, and S. Yamamoto (2018). "Luminescence imaging of water during uniform-field irradiation by spot scanning proton beams." In: *Physics in Medicine & Biology* 63.11, 11NT01 (cit. on p. 45).

Kormoll, T., F. Fiedler, S. Schöne, J. Wüstemann, K. Zuber, and W. Enghardt (2011). "A Compton imager for in-vivo dosimetry of proton beams. A design study". In: *Nuclear Instruments and Methods in Physics Research Section A: Accelerators, Spectrometers, Detectors and Associated Equipment* 626-627, pp. 114–119. ISSN: 0168-9002. DOI: https://doi.org/10.1016/j.nima.2010.10.031. URL: http://www.sciencedirect.com/science/article/pii/S0168900210022709 (cit. on p. 89).

Kraan, A. C. (2015). "Range Verification Methods in Particle Therapy: Underlying Physics and Monte Carlo Modeling." In: *Frontiers in Oncology* 5, p. 150 (cit. on p. 42).

Kraan, A. C., G. Battistoni, N. Belcari, N. Camarlinghi, F. Cappucci, M. Ciocca, A. Ferrari, S. Ferretti, A. Mairani, S. Molinelli, M. Pullia, A. Retico, P. Sala, G. Sportelli, A. Del Guerra, and V. Rosso (2015). "First tests for an online treatment monitoring system with in-beam PET for proton therapy". In: 10 (cit. on p. 71).

Kraan, A. C., G. Battistoni, N. Belcari, N. Camarlinghi, G. A. P. Cirrone, G. Cuttone, S. Ferretti, A. Ferrari, G. Pirrone, F. Romano, P. Sala, G. Sportelli, K. Straub, A. Tramontana, A. Del Guerra, and V. Rosso (2014). "Proton range monitoring with in-beam PET: Monte Carlo activity predictions and comparison with cyclotron data." In: *Physica Medica* 30.5, pp. 559–569 (cit. on p. 66).

Krämer, M., O. Jäkel, T. Haberer, G. Kraft, D. Schardt, and U. Weber (2000). "Treatment planning for heavy-ion radiotherapy: physical beam model and dose optimization." eng. In: *Physics in Medicine & Biology* 45.11, pp. 3299–3317 (cit. on pp. 33, 76, 175).

Kramer, S. L., R. L. Martin, D. R. Moffett, and E. P. Colton (1977). *Application of proton radiography to medical imaging*. Tech. rep. United States (cit. on p. 39).

Krimmer, J., G. Angellier, L. Balleyguier, D. Dauvergne, N. Freud, J. Hérault, J. M. L'etang, H. Mathez, M. Pinto, É. Testa, and Y. Zoccarato (2017a). "A cost-effective monitoring technique in particle therapy via uncollimated prompt gamma peak integration". In: *Applied Physics Letters* 110.15, p. 154102. DOI: 10.1063/1.4980103. URL: https://doi.org/10.1063/1.4980103 (cit. on pp. 74, 81).

Krimmer, J., L. Caponetto, X. Chen, M. Chevallier, D. Dauvergne, M. De Rydt, S.-M. Deng, J.-L. Ley, H. Mathez, C. Ray, V. Reithinger, É. Testa, and Y. Zoccarato (Feb. 1, 2014). "111: Real-time monitoring of the ion range during hadrontherapy: An update on the beam tagging hodoscope". In: *Radiotherapy and Oncology* 110, S54–S55. DOI: 10.1016/S0167-8140(15)34132-3. URL: http://dx.doi.org/10.1016/S0167-8140(15)34132-3 (cit. on pp. 89, 119).

Krimmer, J., D. Dauvergne, J. M. Létang, and É. Testa (2017b). "Prompt-gamma monitoring in hadrontherapy: A review". In: *Nuclear Instruments and Methods in Physics Research Section A: Accelerators, Spectrometers, Detectors and Associated Equipment* 878. Radiation Imaging Techniques and Applications, pp. 58–73. ISSN: 0168-9002. DOI: https://doi.org/10.1016/j.nima.2017.07.063. URL: http://www.sciencedirect.com/science/article/pii/S0168900217308380 (cit. on pp. 26, 73, 74, 76, 78, 82).

Krimmer, J., J.-L. Ley, C. Abellan, J.-P. Cachemiche, L. Caponetto, X. Chen, M. Dahoumane, D. Dauvergne, N. Freud, B. Joly, D. Lambert, L. Lestand, M. Magne, H. Mathez, V. Maxim, G. Montarou, C. Morel, M. Pinto, C. Ray, V. Reithinger, É. Testa, and Y. Zoccarato (2015). "Development of a Compton camera for medical applications based on silicon strip and scintillation detectors". In: *Nuclear Instruments and Methods in Physics Research Section A: Accelerators, Spectrometers, Detectors and Associated Equipment* 787, pp. 98–101. DOI: 10.1016/j.nima.2014.11.042. URL: https://hal.archives-ouvertes.fr/hal-01101334 (cit. on pp. 89, 171).

Kroniger, K., M. Herzog, G. Landry, E. Traneus, G. Dedes, and K. Parodi (2015). "A Fast Analytical Approach for Prompt Gamma and PET Predictions in a TPS for Proton Range Verification". In: *Medical Physics* 42.6Part2, pp. 3199–3199. DOI: 10.1118/1.4923825. URL: https://aapm.onlinelibrary.wiley.com/doi/abs/10.1118/1.4923825 (cit. on p. 77).

Kubiak, T. (2016). "Particle therapy of moving targets—the strategies for tumour motion monitoring and moving targets irradiation". In: *The British Journal of Radiology* 89.1066,

p. 20150275. DOI: 10.1259/bjr.20150275. URL: http://www.ncbi.nlm.nih.gov/pmc/articles/PMC5124789/ (cit. on p. 34).

Kuchment, P. and F. Terzioglu (2016). "3D Image Reconstruction from Compton camera data". In: *arXiv Cornell University Library* (cit. on pp. 87, 217).

Kuhl, D. E. and R. Q. Edwards (1963). "Image Separation Radioisotope Scanning". In: *Radiology* 80.4, pp. 653–662. DOI: 10.1148/80.4.653. URL: https://doi.org/10.1148/80.4.653 (cit. on p. 93).

Kuhl, D. E., R. Q. Edwards, A. R. Ricci, R. J. Yacob, T. J. Mich, and A. Alavi (1976). "The Mark IV system for radionuclide computed tomography of the brain." In: *Radiology* 121.2, pp. 405–413 (cit. on p. 97).

Kumazaki, Y., T. Akagi, T. Yanou, D. Suga, Y. Hishikawa, and T. Teshima (2007). "Determination of the mean excitation energy of water from proton beam ranges". In: *Radiation Measurements* 42.10, pp. 1683–1691. ISSN: 1350-4487. DOI: https://doi.org/10.1016/j.radmeas.2007.10.019. URL: http://www.sciencedirect.com/science/article/pii/S135044870700409X (cit. on p. 38).

Kurfess, J. D., W. N. Johnson, R. A. Kroeger, and B. F. Phlips (2000). "Considerations for the next Compton telescope mission". In: *AIP Conference Proceedings* 510.1, pp. 789–793. DOI: 10.1063/1.1303306. URL: https://aip.scitation.org/doi/abs/10.1063/1.1303306 (cit. on pp. 87, 171).

Kurosawa, S., H. Kubo, K. Ueno, S. Kabuki, S. Iwaki, M. Takahashi, K. Taniue, N. Higashi, K. Miuchi, T. Tanimori, D. Kim, and J. Kim (2012). "Prompt gamma detection for range verification in proton therapy". In: *Current Applied Physics* 12.2, pp. 364–368. ISSN: 1567-1739. DOI: https://doi.org/10.1016/j.cap.2011.07.027. URL: http://www.sciencedirect.com/science/article/pii/S1567173911004123 (cit. on p. 91).

Kwekkeboom, D. J., W. W. de Herder, B. L. Kam, C. H. van Eijck, M. van Essen, P. P. Kooij, R. A. Feelders, M. O. van Aken, and E. P. Krenning (2008). "Treatment with the radiolabeled somatostatin analog [177 Lu-DOTA 0,Tyr3]octreotate: toxicity, efficacy, and survival." In: *Journal of Clinical Oncology* 26.13, pp. 2124–2130 (cit. on p. 99).

La Tessa, C., T. Berger, R. Kaderka, D. Schardt, C. Korner, U. Ramm, J. Licher, N. Matsufuji, C. Vallhagen Dahlgren, A. J. Lomax, G. Reitz, and M. Durante (2012). "Out-of-field dose studies with an anthropomorphic phantom: comparison of X-rays and particle therapy treatments." In: *Radiotherapy and Oncology* 105.1, pp. 133–138 (cit. on p. 18).

Landau, L. (1944). "On the energy loss of fast particles by ionization". In: *Journal of Physics (USSR)* 8, pp. 201–205 (cit. on p. 12).

Landry, G., K. Parodi, J. E. Wildberger, and F. Verhaegen (2013). "Deriving concentrations of oxygen and carbon in human tissues using single- and dual-energy CT for ion therapy applications". In: *Physics in Medicine & Biology* 58.15, p. 5029. URL: http://stacks.iop.org/0031-9155/58/i=15/a=5029 (cit. on p. 66).

Lang, C., D. Habs, K. Parodi, and P. G. Thirolf (2014). "Sub-millimeter nuclear medical imaging with high sensitivity in positron emission tomography using $\beta + \gamma$ coincidences". In: *Journal of Instrumentation* 9.01, P01008. URL: http://stacks.iop.org/1748-0221/9/i=01/a=P01008 (cit. on pp. 45, 46).

Larsson, B. (1962). "On the application of a 185 MeV proton beam to experimental cancer therapy and neurosurgery: A biophysical study." PhD thesis. Acta Universitatis Upsaliensis (cit. on p. 23).

Larsson, S. A. (1980). "Gamma camera emission tomography. Development and properties of a multi-sectional emission computed tomography system." In: *Acta Radiologica Supplementum* 363, pp. 1–75 (cit. on p. 98).

Lawrence, E. O. and M. S. Livingston (1932). "The Production of High Speed Light Ions Without the Use of High Voltages". In: *Physical Review* 40 (1), pp. 19–35. DOI: 10.1103/PhysRev.40.19. URL: https://link.aps.org/doi/10.1103/PhysRev.40.19 (cit. on p. 22).

Lecoq, P. (2017). "Pushing the Limits in Time-of-Flight PET Imaging". In: *IEEE Transactions on Radiation and Plasma Medical Sciences* 1.6, pp. 473–485. ISSN: 2469-7311. DOI: 10.1109/TRPMS.2017.2756674 (cit. on p. 96).

Lee, C. Y., H. Song, C. W. Park, Y. H. Chung, J. S. Kim, and J. C. Park (2016). "Optimization of Proton CT Detector System and Image Reconstruction Algorithm for On-Line Proton Therapy". In: *PLOS ONE* 11.5, pp. 1–12. DOI: 10.1371/journal.pone.0156226. URL: https://doi.org/10.1371/journal.pone.0156226 (cit. on p. 42).

Lee, H. R., S. H. Kim, J. H. Park, W. G. Jung, H. Lim, and C. H. Kim (2017). "Prototype system for proton beam range measurement based on gamma electron vertex imaging". In: *Nuclear Instruments and Methods in Physics Research Section A: Accelerators, Spectrometers, Detectors and Associated Equipment* 857, pp. 82–97. ISSN: 0168-9002. DOI: https://doi.org/10.1016/j.nima.2017.03.022. URL: http://www.sciencedirect.com/science/article/pii/S0168900217303613 (cit. on p. 90).

Lehrack, S., W. Assmann, D. Bertrand, S. Henrotin, J. Herault, V. Heymans, F. V. Stappen, P. G. Thirolf, M. Vidal, J. Van de Walle, and K. Parodi (2017). "Submillimeter ionoacoustic range determination for protons in water at a clinical synchrocyclotron". In: *Physics in Medicine & Biology* 62.17, p. L20. URL: http://stacks.iop.org/0031-9155/62/i=17/a=L20 (cit. on p. 44).

Lennox, A. J. (1991). "Hospital-based proton linear accelerator for particle therapy and radioisotope production". In: *Nuclear Instruments and Methods in Physics Research Section B: Beam Interactions with Materials and Atoms* 56-57, pp. 1197–1200. ISSN: 0168-583X. DOI: https://doi.org/10.1016/0168-583X(91)95130-6. URL: http://www.sciencedirect.com/science/article/pii/0168583X91951306 (cit. on p. 25).

Leone, M. and N. Robotti (2010). "Frédéric Joliot, Irène Curie and the early history of the positron (1932-33)". In: *European Journal of Physics* 31.4, p. 975. URL: http://stacks.iop.org/0143-0807/31/i=4/a=027 (cit. on pp. 50, 51).

Levin, C., G. Glover, T. Deller, D. McDaniel, W. Peterson, and S. H. Maramraju (2013). "Prototype time-of-flight PET ring integrated with a 3T MRI system for simultaneous whole-body PET/MR imaging". In: *Journal of Nuclear Medicine* 54.supplement 2, p. 148. URL: http://jnm.snmjournals.org/content/54/supplement_2/148.abstract (cit. on p. 96).

Levy, R. P. (2007). "PET-CT: Evolving role in hadron therapy". In: *Nuclear Instruments and Methods in Physics Research Section B: Beam Interactions with Materials and Atoms* 261.1. The Application of Accelerators in Research and Industry, pp. 782–785. ISSN: 0168-583X. DOI: https://doi.org/10.1016/j.nimb.2007.04.039. URL: http://www.sciencedirect.com/science/article/pii/S0168583X07007975 (cit. on p. 31).

Lewellen, T. K., A. N. Bice, R. L. Harrison, M. D. Pencke, and J. M. Link (1988). "Performance measurements of the SP3000/UW time-of-flight positron emission tomograph". In: *IEEE Transactions on Nuclear Science* 35.1, pp. 665–669. ISSN: 0018-9499. DOI: 10.1109/23.12808 (cit. on p. 95).

Lewellen, T. K. and J. S. Karp (2004). "CHAPTER 10 - PET Systems". In: *Emission Tomography*. Ed. by M. N. Wernick and J. N. Aarsvold. San Diego: Academic Press, pp. 179–194. ISBN: 978-0-12-744482-6. DOI: https://doi.org/10.1016/B978-012744482-6.50013-2. URL: http://www.sciencedirect.com/science/article/pii/B9780127444826500132 (cit. on p. 93).

Lewis, H. W. (1950). "Multiple Scattering in an Infinite Medium". In: *Physical Review* 78 (5), pp. 526–529. DOI: 10.1103/PhysRev.78.526. URL: https://link.aps.org/doi/10.1103/PhysRev.78.526 (cit. on p. 13).

Ley, J.-L. (2015). "Mise en oeuvre d'un démonstrateur de caméra Compton pour l'imagerie en médecine nucléaire et pour le contrôle en temps réel de l'hadronthérapie à l'aide des rayonnements gamma prompts." PhD thesis. École Doctorale de Physique et d'Astrophysique de Lyon (cit. on pp. 109, 111, 131, 162, 199).

Liprandi, S., M. Mayerhofer, S. Aldawood, T. Binder, G. Dedes, A. Miani, D. R. Schaart, I. I. Valencia Lozano, K. Parodi, and P. G. Thirolf (2017). "Sub-3mm spatial resolution from a large monolithic LaBr3 (Ce) scintillator". In: *Current Directions in Biomedical Engineering* 3 (2), pp. 655–659. URL: https://doi.org/10.1515/cdbme-2017-0138 (cit. on p. 89).

Litzenberg, D. W., J. F. Bajema, F. D. Becchetti, J. A. Brown, R. S. Raymond, D. A. Roberts, J. Caraher, G. Hutchins, R. Ronningen, R. Smith, and M. Abbott (1992). "On-line monitoring and PET imaging of proton radiotherapy beams". In: *IEEE Conference on Nuclear Science Symposium and Medical Imaging*, pp. 954–956. DOI: 10.1109/NSSMIC.1992.301095 (cit. on p. 70).

Litzenberg, D. W., D. A. Roberts, M. Y. Lee, K. Pham, A. M. Vander Molen, R. Ronningen, and F. D. Becchetti (1999). "On-line monitoring of radiotherapy beams: experimental results with proton beams." In: *Medical Physics* 26.6, pp. 992–1006 (cit. on p. 70).

Liu, H., T. Omura, M. Watanabe, and T. Yamashita (2001). "Development of a depth of interaction detector for γ-rays". In: *Nuclear Instruments and Methods in Physics Research Section A: Accelerators, Spectrometers, Detectors and Associated Equipment* 459.1, pp. 182–190. ISSN:

0168-9002. DOI: https://doi.org/10.1016/S0168-9002(00)00939-6. URL: http://www.sciencedirect.com/science/article/pii/S0168900200009396 (cit. on p. 94).

Llacer, J., A. Chatterjee, E. L. Alpen, W. Saunders, S. Andreae, and H. C. Jackson (1984a). "Imaging by Injection of Accelerated Radioactive Particle Beams". In: *IEEE Transactions on Medical Imaging* 3.2, pp. 80–90. ISSN: 0278-0062. DOI: 10.1109/TMI.1984.4307660 (cit. on p. 69).

Llacer, J., A. Chatterjee, H. C. Jackson, J. C. Lin, and M. V. Zunzunegui (1979). "An Imaging Instrument for Positron Emitting Heavy Ion Beam Injection". In: *IEEE Transactions on Nuclear Science* 26.1, pp. 634–647. ISSN: 0018-9499. DOI: 10.1109/TNS.1979.4329701 (cit. on p. 68).

Llacer, J., J. B. Schmidt, and C. A. Tobias (1990). "Characterization of fragmented heavy-ion beams using a three-stage telescope detector: measurements of 670-MeV/amu 20Ne beams." In: *Medical Physics* 17.2, pp. 151–157 (cit. on p. 17).

Llacer, J., C. A. Tobias, W. R. Holley, and T. Kanai (1984b). "On-line characterization of heavy-ion beams with semiconductor detectors." In: *Medical Physics* 11.3, pp. 266–278 (cit. on p. 17).

Llosá, G., J. Barrio, J. Cabello, A. Crespo, C. Lacasta, M. Rafecas, S. Callier, C. de La Taille, and L. Raux (2012). "Detector characterization and first coincidence tests of a Compton telescope based on LaBr3 crystals and SiPMs". In: *Nuclear Instruments and Methods in Physics Research Section A: Accelerators, Spectrometers, Detectors and Associated Equipment* 695. New Developments in Photodetection NDIP11, pp. 105–108. ISSN: 0168-9002. DOI: https://doi.org/10.1016/j.nima.2011.11.041. URL: http://www.sciencedirect.com/science/article/pii/S0168900211020833 (cit. on p. 88).

Llosá, G., J. Bernabeu, D. Burdette, E. Chesi, V. Cindro, N. H. Clinthorne, K. Honscheid, H. Kagan, C. Lacasta, M. Mikuž, P. Modesto, W. L. Rogers, J. Steinberg, A. Studen, P. Weilhammer, L. Zhang, and D. Zontar (2006). "Results of a first demonstrator prototype of a Compton prostate probe". In: *Nuclear Instruments and Methods in Physics Research Section A: Accelerators, Spectrometers, Detectors and Associated Equipment* 569.2. Proceedings of the 3rd International Conference on Imaging Technologies in Biomedical Sciences, pp. 277–280. ISSN: 0168-9002. DOI: https://doi.org/10.1016/j.nima.2006.08.028. URL: http://www.sciencedirect.com/science/article/pii/S0168900206014525 (cit. on p. 98).

Llosá, G., J. Bernabeu, D. Burdette, E. Chesi, N. H. Clinthorne, K. Honscheid, H. Kagan, C. Lacasta, M. Mikuž, P. Modesto, W. L. Rogers, A. Studen, and P. Weilhammer (2008). "Last Results of a First Compton Probe Demonstrator". In: *IEEE Transactions on Nuclear Science* 55.3, pp. 936–941. ISSN: 0018-9499. DOI: 10.1109/TNS.2008.922817 (cit. on p. 98).

Llosá, G., J. Cabello, S. Callier, J. E. Gillam, C. Lacasta, M. Rafecas, L. Raux, C. Solaz, V. Stankova, C. de La Taille, M. Trovato, and J. Barrio (2013). "First Compton telescope prototype based on continuous LaBr3-SiPM detectors". In: *Nuclear Instruments and Methods in Physics Research Section A: Accelerators, Spectrometers, Detectors and Associated Equipment* 718. Proceedings of the 12th Pisa Meeting on Advanced Detectors, pp. 130–133. ISSN: 0168-9002. DOI: https://doi.org/10.1016/j.nima.2012.08.074. URL: http://www.sciencedirect.com/science/article/pii/S0168900212009771 (cit. on p. 88).

Llosá, G., M. Trovato, J. Barrio, A. Etxebeste, E. Muñoz, C. Lacasta, J. F. Oliver, M. Rafecas, C. Solaz, and P. Solevi (2016). "First Images of a Three-Layer Compton Telescope Prototype for Treatment Monitoring in Hadron Therapy". In: *Frontiers in Oncology* 6, p. 14. ISSN: 2234-943X. DOI: 10.3389/fonc.2016.00014. URL: https://www.frontiersin.org/article/10.3389/fonc.2016.00014 (cit. on p. 88).

Lo Presti, D., S. Aiello, D. L. Bonanno, G. A. P. Cirrone, E. Leonora, F. Longhitano, C. Pugliatti, N. Randazzo, F. Romano, G. V. Russo, M. Russo, C. Stancampiano, and V. Sipala (2014). "OFFSET: Optical Fiber Folded Scintillating Extended Tracker". In: *Nuclear Instruments and Methods in Physics Research Section A: Accelerators, Spectrometers, Detectors and Associated Equipment* 737, pp. 195–202. ISSN: 0168-9002. DOI: https://doi.org/10.1016/j.nima.2013.11.049. URL: http://www.sciencedirect.com/science/article/pii/S0168900213015908 (cit. on p. 41).

Lo Presti, D., D. L. Bonanno, F. Longhitano, D. G. Bongiovanni, G. V. Russo, E. Leonora, N. Randazzo, S. Reito, V. Sipala, and G. Gallo (2016). "Design and characterisation of a real time proton and carbon ion radiography system based on scintillating optical fibres." In: *Physica Medica* 32.9, pp. 1124–1134 (cit. on p. 41).

Lobrich, M., P. K. Cooper, and B. Rydberg (1996). "Non-random distribution of DNA double-strand breaks induced by particle irradiation". In: *International Journal of Radiation Biology* 70.5, pp. 493–503. DOI: 10.1080/095530096144680. URL: https://doi.org/10.1080/095530096144680 (cit. on p. 19).

Locher, G. L. (1936). "Biological effects and therapeutic possibilities of neutrons". In: *American Journal on Roentgenology Radium Therapy* 36.1, pp. 1–13 (cit. on p. 22).

Lojacono, X., M.-H. Richard, J.-L. Ley, É. Testa, C. Ray, N. Freud, J. M. Létang, D. Dauvergne, V. Maxim, and R. Prost (2013). "Low Statistics Reconstruction of the Compton Camera Point Spread Function in 3D Prompt-gamma Imaging of Ion Beam Therapy". In: *IEEE Transactions on Nuclear Science* 60.5, pp. 3355–3363. ISSN: 0018-9499. DOI: 10.1109/TNS.2013.2275200 (cit. on pp. 101, 130, 200).

Lomax, A. J. (2009). "Charged Particle Therapy: The Physics of Interaction". In: *The Cancer Journal* 15.4. URL: https://journals.lww.com/journalppo/Fulltext/2009/08000/Charged_Particle_Therapy___The_Physics_of.4.aspx (cit. on p. 8).

Lomax, A. J., T. Boehringer, A. Coray, E. Egger, G. Goitein, M. Grossmann, P. Juelke, S. Lin, E. S. Pedroni, B. Rohrer, W. Roser, B. Rossi, B. Siegenthaler, O. Stadelmann, H. Stauble, C. Vetter, and L. Wisser (2001). "Intensity modulated proton therapy: a clinical example." In: *Medical Physics* 28.3, pp. 317–324 (cit. on p. 37).

Lu, H.-M. (2008a). "A point dose method for in vivo range verification in proton therapy." In: *Physics in Medicine & Biology* 53.23, N415–22 (cit. on p. 44).

Lu, H.-M. (2008b). "A potential method for in vivo range verification in proton therapy treatment." In: *Physics in Medicine & Biology* 53.5, pp. 1413–1424 (cit. on p. 44).

Lu, H.-M., G. G. Mann, and E. Cascio (2010). "Investigation of an implantable dosimeter for single-point water equivalent path length verification in proton therapy." In: *Medical Physics* 37.11, pp. 5858–5866 (cit. on p. 44).

Lühr, A., C. von Neubeck, M. Krause, and E. G. C. Troost (2018). "Relative biological effectiveness in proton beam therapy –Current knowledge and future challenges". In: *Clinical and Translational Radiation Oncology* 9, pp. 35–41. DOI: 10.1016/j.ctro.2018.01.006. URL: http://www.ncbi.nlm.nih.gov/pmc/articles/PMC5862688/ (cit. on p. 33).

MacCabee, H. D. and M. A. Ritter (1974). "Fragmentation of High-Energy Oxygen-Ion Beams in Water". In: *Radiation Research* 60.3, pp. 409–421. DOI: 10.2307/3574021. URL: http://www.rrjournal.org/doi/abs/10.2307/3574021 (cit. on p. 17).

Mackin, D. S., S. W. Peterson, S. Beddar, and J. C. Polf (June 7, 2012). "Evaluation of a stochastic reconstruction algorithm for use in Compton camera imaging and beam range verification from secondary gamma emission during proton therapy." eng. In: *Physics in Medicine & Biology* 57.11, pp. 3537–3553. DOI: 10.1088/0031-9155/57/11/3537 (cit. on pp. 101, 180).

Mackin, D. S., J. C. Polf, S. W. Peterson, and S. Beddar (2013). "The effects of Doppler broadening and detector resolution on the performance of three-stage Compton cameras". In: *Medical Physics* 40.1, p. 012402. DOI: 10.1118/1.4767756. URL: https://aapm.onlinelibrary.wiley.com/doi/abs/10.1118/1.4767756 (cit. on p. 90).

Madsen, M. T. (2007). "Recent advances in SPECT imaging." eng. In: *Journal of Nuclear Medicine* 48.4, pp. 661–673 (cit. on p. 98).

Mandrillon, P., F. Farley, N. Brassart, J. Herault, A. Courdi, P. Chauvel, N. Fietier, and J. Y. Tang (1992). "Recent activities of the cyclotron laboratory in Nice". In: *Proceedings of the 13th International Conference on Cyclotrons and their Applications, Vancouver, Canada* (cit. on p. 220).

Mandrillon, P., F. Farley, N. Brassart, J. Herault, A. Susini, and R. Ostojic (1989). "Commissioning and implementation of the MEDiCYC cyclotron programme". In: *Proceedings of the 12th International Conference on Cyclotrons and their Applications, Berlin, Germany* (cit. on p. 220).

Manescu, P., H. Ladjal, J. Azencot, M. Beuve, and B. Shariat (2013). "Biomechanical-based respiratory motion-compensation for 4D dose calculation during hadron therapy". In: *27th International Congress and Exhibition, Computer Assisted Radiology*. Vol. 8. 1. Heidelberg, Germany, pp. 39–44. DOI: 10.1007/s11548-013-0849-z. URL: https://hal.archives-ouvertes.fr/hal-00850636 (cit. on p. 34).

Marafini, M., A. Attili, G. Battistoni, N. Belcari, M. G. Bisogni, N. Camarlinghi, F. Cappucci, M. Cecchetti, P. Cerello, F. Ciciriello, G. A. P. Cirrone, S. Coli, F. Corsi, G. Cuttone, E. De Lucia, S. Ferretti, R. Faccini, E. Fiorina, P. M. Frallicciardi, G. Giraudo, E. Kostara, A. Kraan, F. Licciulli, B. Liu, N. Marino, C. Marzocca, G. Matarrese, M. C. Morone, M. Morrocchi, S. Muraro, V. Patera, F. Pennazio, C. Peroni, L. Piersanti, M. A. Piliero, G. Pirrone, A. Rivetti, F. Romano, V. Rosso, P. Sala, A. Sarti, A. Sciubba, G. Sportelli, C. Voena, R. Wheadon, and A. Del Guerra (2015). "The INSIDE Project: Innovative Solutions for In-Beam Dosimetry in Hadrontherapy". English.

In: *Acta Physica Polonica A* 127.5, pp. 1465–1467. DOI: 10.12693/APhysPolA.127.1465 (cit. on p. 71).

Martin, J. B., N. Dogan, J. E. Gormley, G. F. Knoll, M. O'Donnell, and D. K. Wehe (1994). "Imaging multi-energy gamma-ray fields with a Compton scatter camera". In: *IEEE Transactions on Nuclear Science* 41.4, pp. 1019–1025. ISSN: 0018-9499. DOI: 10.1109/23.322851 (cit. on p. 88).

Matsufuji, N., A. Fukumura, M. Komori, T. Kanai, and T. Kohno (2003). "Influence of fragment reaction of relativistic heavy charged particles on heavy-ion radiotherapy". In: *Physics in Medicine & Biology* 48.11, p. 1605. URL: http://stacks.iop.org/0031-9155/48/i=11/a=309 (cit. on p. 17).

Matsufuji, N., T. Kanai, N. Kanematsu, T. Miyamoto, M. Baba, T. Kamada, H. Kato, S. Yamada, J.-E. Mizoe, and H. Tsuji (2007). "Specification of Carbon Ion Dose at the National Institute of Radiological Sciences (NIRS)." eng. In: *Journal of radiation research* 48 Suppl A, A81–6 (cit. on p. 33).

Matsufuji, N., M. Komori, H. Sasaki, K. Akiu, M. Ogawa, A. Fukumura, E. Urakabe, T. Inaniwa, T. Nishio, T. Kohno, and T. Kanai (2005). "Spatial fragment distribution from a therapeutic pencil-like carbon beam in water." In: *Physics in Medicine & Biology* 50.14, pp. 3393–3403 (cit. on p. 17).

Matsufuji, N., H. Tomura, Y. Futami, H. Yamashita, A. Higashi, S. Minohara, M. Endo, and T. Kanai (1998). "Relationship between CT number and electron density, scatter angle and nuclear reaction for hadron-therapy treatment planning." eng. In: *Physics in Medicine & Biology* 43.11, pp. 3261–3275 (cit. on pp. 31, 38).

Mattei, I., G. Battistoni, F. Bini, F. Collamati, E. De Lucia, M. Durante, R. Faccini, C. La Tessa, M. Marafini, L. Piersanti, M. Rovituso, A. Rucinski, A. Russomando, A. Sarti, C. Schuy, A. Sciubba, E. Solfaroli Camillocci, M. Toppi, G. Traini, M. Vanstalle, C. Voena, and V. Patera (2015). "Prompt-γ production of 220 MeV/u 12 C ions interacting with a PMMA target". In: *Journal of Instrumentation* 10.10, P10034. URL: http://stacks.iop.org/1748-0221/10/i=10/a=P10034 (cit. on p. 76).

Mattei, I., F. Bini, F. Collamati, E. De Lucia, P. M. Frallicciardi, E. Iarocci, C. Mancini-Terracciano, M. Marafini, S. Muraro, R. Paramatti, V. Patera, L. Piersanti, D. Pinci, A. Rucinski, A. Russomando, A. Sarti, A. Sciubba, E. Solfaroli Camillocci, M. Toppi, G. Traini, C. Voena, and G. Battistoni (2017). "Secondary radiation measurements for particle therapy applications: prompt photons produced by 4 He, 12 C and 16 O ion beams in a PMMA target". In: *Physics in Medicine & Biology* 62.4, p. 1438. URL: http://stacks.iop.org/0031-9155/62/i=4/a=1438 (cit. on p. 76).

Mattiazzo, S., D. Bisello, P. Giubilato, D. Pantano, N. Pozzobon, W. Snoeys, and J. Wyss (2015). "Advanced proton imaging in computed tomography". In: *Radiation Protection Dosimetry* 166.1-4, pp. 388–392 (cit. on p. 40).

Maxim, V. (2014). "Filtered Backprojection Reconstruction and Redundancy in Compton Camera Imaging". In: *IEEE Transactions on Image Processing* 23.1, pp. 332–341. ISSN: 1057-7149. DOI: 10.1109/TIP.2013.2288143 (cit. on p. 130).

Maxim, V., M. Frandes, and R. Prost (2009). "Analytical inversion of the Compton transform using the full set of available projections". In: *Inverse Problems* 25.9, p. 095001. URL: http://stacks.iop.org/0266-5611/25/i=9/a=095001 (cit. on p. 101).

McCleskey, M., W. Kaye, D. S. Mackin, S. Beddar, Z. He, and J. C. Polf (2015). "Evaluation of a multistage CdZnTe Compton camera for prompt γ imaging for proton therapy". In: *Nuclear Instruments and Methods in Physics Research Section A: Accelerators, Spectrometers, Detectors and Associated Equipment* 785, pp. 163–169. ISSN: 0168-9002. DOI: https://doi.org/10.1016/j.nima.2015.02.030. URL: http://www.sciencedirect.com/science/article/pii/S0168900215002193 (cit. on p. 90).

McKenzie, A. L., M. van Herk, and B. Mijnheer (2000). "The width of margins in radiotherapy treatment plans". In: *Physics in Medicine & Biology* 45.11, p. 3331. URL: http://stacks.iop.org/0031-9155/45/i=11/a=315 (cit. on p. 34).

McKisson, J. E., P. S. Haskins, G. W. Phillips, S. E. King, R. A. August, R. B. Piercey, and R. C. Mania (1994). "Demonstration of three-dimensional imaging with a germanium Compton camera". In: *IEEE Transactions on Nuclear Science* 41.4, pp. 1221–1224. ISSN: 0018-9499. DOI: 10.1109/23.322888 (cit. on pp. 87, 88).

McMillan, E. M. (1945). "The synchrotron - a proposed high energy accelerator." In: *Physical Review* 68.143 (cit. on p. 24).

McNamara, A. L., J. P. Schuemann, and H. Paganetti (2015). "A phenomenological relative biological effectiveness (RBE) model for proton therapy based on all published in vitro cell survival data". In: *Physics in Medicine & Biology* 60.21, p. 8399. URL: http://stacks.iop.org/0031-9155/60/i=21/a=8399 (cit. on p. 21).

Melcher, C. L. and J. S. Schweitzer (1992). "A promising new scintillator: cerium-doped lutetium oxyorthosilicate". In: *Nuclear Instruments and Methods in Physics Research Section A: Accelerators, Spectrometers, Detectors and Associated Equipment* 314.1, pp. 212–214. ISSN: 0168-9002. DOI: https://doi.org/10.1016/0168-9002(92)90517-8. URL: http://www.sciencedirect.com/science/article/pii/0168900292905178 (cit. on p. 94).

Miller, M., J. Zhang, K. Binzel, J. Griesmer, T. Laurence, M. Narayanan, D. Natarajamani, S. Wang, and M. Knopp (2015). "Characterization of the Vereos Digital Photon Counting PET System". In: *Journal of Nuclear Medicine* 56.supplement 3, p. 434. URL: http://jnm.snmjournals.org/content/56/supplement_3/434.abstract (cit. on p. 96).

Min, C.-H., C. H. Kim, M.-Y. Youn, and J.-W. Kim (2006). "Prompt-gamma measurements for locating the dose falloff region in the proton therapy". In: *Applied Physics Letters* 89.18, p. 183517. DOI: 10.1063/1.2378561. URL: https://doi.org/10.1063/1.2378561 (cit. on pp. 43, 83, 170).

Min, C.-H., J.-W. Kim, M.-Y. Youn, and C. H. Kim (2007). "Determination of distal dose edge location by measuring right-angled prompt-gamma rays from a 38MeV proton beam". In: *Nuclear Instruments and Methods in Physics Research Section A: Accelerators, Spectrometers, Detectors and Associated Equipment* 580.1. Proceedings of the 10 th International Symposium on Radiation Physics, pp. 562–565. ISSN: 0168-9002. DOI: https://doi.org/10.1016/j.nima.2007.05.235. URL: http://www.sciencedirect.com/science/article/pii/S0168900207011230 (cit. on p. 83).

Min, C.-H., H. R. Lee, C. H. Kim, and S. B. Lee (2012). "Development of array-type prompt gamma measurement system for in vivo range verification in proton therapy." In: *Medical Physics* 39.4, pp. 2100–2107 (cit. on p. 84).

Mizuno, H., T. Tomitani, M. Kanazawa, A. Kitagawa, J. Pawelke, Y. Iseki, E. Urakabe, M. Suda, A. Kawano, R. Iritani, S. Matsushita, T. Inaniwa, T. Nishio, S. Furukawa, K. Ando, Y. K. Nakamura, T. Kanai, and K. Ishii (2003). "Washout measurement of radioisotope implanted by radioactive beams in the rabbit." In: *Physics in Medicine & Biology* 48.15, pp. 2269–2281 (cit. on p. 65).

Moding, E. J., M. B. Kastan, and D. G. Kirsch (2013). "Strategies for optimizing the response of cancer and normal tissues to radiation." eng. In: *Nature reviews. Drug discovery* 12.7, pp. 526–542. DOI: 10.1038/nrd4003 (cit. on p. 7).

Moffett, D. R., E. P. Colton, G. A. Concaildi, E. W. Hoffman, R. D. Klem, M. J. Knott, S. L. Kramer, R. L. Martin, E. F. Parker, A. R. Passi, P. F. Schultz, R. L. Stockley, R. E. Timm, L. S. Skaggs, and V. W. Steward (1975). "Initial Test of a Proton Radiographic System". In: *IEEE Transactions on Nuclear Science* 22.3, pp. 1749–1751. ISSN: 0018-9499. DOI: 10.1109/TNS.1975.4327982 (cit. on pp. 40, 41).

Molière, G. (1948). "Theorie der Streuung schneller geladener Teilchen II. Mehrfach- und Vielfachstreuung". In: *Zeitschrift Naturforschung Teil A* 3, pp. 78–97. DOI: 10.1515/zna-1948-0203 (cit. on p. 13).

Monini, C., M. Cunha, É. Testa, and M. Beuve (2018). "Study of the Influence of NanOx Parameters". In: *Cancers* 10.4, p. 87 (cit. on p. 33).

Montarou, G., M. Bony, E. Busato, R. Chadelas, D. Donnarieix, P. Force, C. Guicheney, C. Insa, D. Lambert, L. Lestand, M. Magne, F. Martin, C. Millardet, M. Nivoix, F. Podlyski, and A. Rozes (2016). "Construction and tests of an in-beam PET-like demonstrator for hadrontherapy beam ballistic control". In: *Nuclear Instruments and Methods in Physics Research Section A: Accelerators, Spectrometers, Detectors and Associated Equipment* 845 (cit. on p. 72).

Morrocchi, M., S. Marcatili, N. Belcari, M. G. Bisogni, G. Collazuol, G. Ambrosi, F. Corsi, M. Foresta, C. Marzocca, G. Matarrese, G. Sportelli, P. Guerra, A. Santos, and A. Del Guerra (2012). "Timing performances of a data acquisition system for Time of Flight PET". In: *Nuclear Instruments and Methods in Physics Research Section A: Accelerators, Spectrometers, Detectors and Associated Equipment* 695. New Developments in Photodetection NDIP11, pp. 210–212. ISSN: 0168-9002. DOI: https://doi.org/10.1016/j.nima.2011.11.073. URL: http://www.sciencedirect.com/science/article/pii/S0168900211021413 (cit. on p. 71).

Moses, W. W. and S. E. Derenzo (1999). “Prospects for time-of-flight PET using LSO scintillator”. In: *IEEE Transactions on Nuclear Science* 46.3, pp. 474–478. ISSN: 0018-9499. DOI: 10.1109/23.775565 (cit. on p. 95).

Moteabbed, M., S. España, and H. Paganetti (2011). “Monte Carlo patient study on the comparison of prompt gamma and PET imaging for range verification in proton therapy.” eng. In: *Physics in Medicine & Biology* 56.4, pp. 1063–1082. DOI: 10.1088/0031-9155/56/4/012 (cit. on p. 76).

Moyers, M. F., D. W. Miller, D. A. Bush, and J. D. Slater (2001). “Methodologies and tools for proton beam design for lung tumors”. In: *International Journal of Radiation Oncology Biology Physics* 49.5, pp. 1429–1438. DOI: 10.1016/S0360-3016(00)01555-8. URL: https://doi.org/10.1016/S0360-3016(00)01555-8 (cit. on p. 36).

Muehllehner, G. and R. A. Wetzel (1971). “Section imaging by computer calculation”. In: *Journal of Nuclear Medicine* 12, pp. 76–84 (cit. on p. 98).

Muller, C., K. Zhernosekov, U. Koster, K. Johnston, H. Dorrer, A. Hohn, N. T. van der Walt, A. Turler, and R. Schibli (2012). “A unique matched quadruplet of terbium radioisotopes for PET and SPECT and for alpha- and beta- radionuclide therapy: an in vivo proof-of-concept study with a new receptor-targeted folate derivative.” In: *Journal of Nuclear Medicine* 53.12, pp. 1951–1959 (cit. on p. 99).

Mumot, M., C. Algranati, M. Hartmann, J. M. Schippers, E. B. Hug, and A. J. Lomax (2010). “Proton range verification using a range probe: definition of concept and initial analysis.” In: *Physics in Medicine & Biology* 55.16, pp. 4771–4782 (cit. on p. 44).

Murayama, H., I. Ishibashi, H. Uchida, T. Omura, and T. Yamashita (1998). “Depth encoding multicrystal detectors for PET”. In: *IEEE Transactions on Nuclear Science* 45.3, pp. 1152–1157. ISSN: 0018-9499. DOI: 10.1109/23.681994 (cit. on p. 94).

Nadaraya, E. A. (1964). “On Estimating Regression”. In: *Theory of Probability & Its Applications* 9.1, pp. 141–142. DOI: 10.1137/1109020. URL: https://doi.org/10.1137/1109020 (cit. on p. 183).

Naimuddin, M., G. Coutrakon, G. Blazey, S. Boi, A. Dyshkant, B. Erdelyi, D. Hedin, E. Johnson, J. Krider, V. Rukalin, S. A. Uzunyan, V. Zutshi, R. Fordt, G. Sellberg, J. E. Rauch, M. Roman, P. Rubinov, and P. Wilson (2016). “Development of a proton Computed Tomography detector system”. In: *Journal of Instrumentation* 11.02, p. C02012. URL: http://stacks.iop.org/1748-0221/11/i=02/a=C02012 (cit. on p. 41).

National Instruments (2010). *PXI Express - NI PXIe-1082 User Manual*. 372752B-01. National Instruments (cit. on p. 154).

Nedunchezhian, K., N. Aswath, M. Thiruppathy, and S. Thirugnanamurthy (2016). “Boron Neutron Capture Therapy - A Literature Review”. In: *Journal of Clinical and Diagnostic Research : JCDR* 10.12, ZE01–ZE04. DOI: 10.7860/JCDR/2016/19890.9024 (cit. on p. 22).

Nestor, O. H. and C. Y. Huang (1975). “Bismuth Germanate: A High-Z Gamma-Ray and Charged Particle Detector”. In: *IEEE Transactions on Nuclear Science* 22.1, pp. 68–71. ISSN: 0018-9499. DOI: 10.1109/TNS.1975.4327617 (cit. on p. 94).

Newhauser, W. D. and M. Durante (2011). “Assessing the risk of second malignancies after modern radiotherapy”. In: *Nature Reviews Cancer* 11, p. 438. URL: http://dx.doi.org/10.1038/nrc3069 (cit. on p. 18).

Newhauser, W. D., J. Fontenot, N. Koch, L. Dong, K. A. Lee, Y. Zheng, L. Waters, and R. Mohan (2007). “Monte Carlo simulations of the dosimetric impact of radiopaque fiducial markers for proton radiotherapy of the prostate”. In: *Physics in Medicine & Biology* 52.11, p. 2937. URL: http://stacks.iop.org/0031-9155/52/i=11/a=001 (cit. on p. 36).

Newhauser, W. D., U. Titt, D. Dexheimer, X. Yan, and S. Nill (2002). “Neutron shielding verification measurements and simulations for a 235-MeV proton therapy center”. In: *Nuclear Instruments and Methods in Physics Research Section A: Accelerators, Spectrometers, Detectors and Associated Equipment* 476.1. Int. Workshop on Neutron Field Spectrometry in Science, Technology and Radiation Protection, pp. 80–84. ISSN: 0168-9002. DOI: https://doi.org/10.1016/S0168-9002(01)01400-0. URL: http://www.sciencedirect.com/science/article/pii/S0168900201014000 (cit. on p. 18).

Newhauser, W. D. and R. Zhang (2015). “The physics of proton therapy”. In: *Physics in Medicine & Biology* 60.8, R155. URL: http://stacks.iop.org/0031-9155/60/i=8/a=R155 (cit. on pp. 8, 10, 16, 77).

Newport (2017). *XPS-Q8 Universal High-Performance Motion Controller/Driver*. v.1.4.x. Newport Corporation (cit. on p. 122).

Niedźwiecki, S., P. Bialas, C. Curceanu, E. Czerwiński, K. Dulski, A. Gajos, B. Glowacz, M. Gorgol, B. Hiesmayr, B. Jasińska, L. Kaplon, D. Kisielewska-Kamińska, G. Korcyl, P. Kowalski, T. Kozik, N. Krawczyk, W. Krzemień, E. Kubicz, M. Mohammed, M. Pawlik-Niedźwiecka, M. Packa, L. Raczyński, Z. Rudy, N. G. Sharma, S. Sharma, R. Y. Shopa, M. Silarski, M. Skurzok, A. Wieczorek, W. Wiślicki, B. Zgardzińska, M. Zieliński, and P. Moskal (2017). “J-PET: a new technology for the whole-body PET imaging”. In: *Acta Physica Polonica* B48, p. 1567. DOI: 10.5506/APhysPolB.48.1567 (cit. on p. 96).

Nishio, T., A. Miyatake, T. Ogino, K. Nakagawa, N. Saijo, and H. Esumi (2010). “The development and clinical use of a beam ON-LINE PET system mounted on a rotating gantry port in proton therapy.” In: *International Journal of Radiation Oncology Biology Physics* 76.1, pp. 277–286 (cit. on p. 70).

Nishio, T., T. Ogino, K. Nomura, and H. Uchida (2006). “Dose-volume delivery guided proton therapy using beam on-line PET system.” In: *Medical Physics* 33.11, pp. 4190–4197 (cit. on p. 70).

NuPECC (2014). “Nuclear Physics for Medicine”. In: *Strasbourg: European Science Foundation*. URL: http://www.nupecc.org (cit. on p. 8).

Nurdan, T. C., K. Nurdan, A. B. Brill, and A. H. Walenta (2015). "Design criteria for a high energy Compton Camera and possible application to targeted cancer therapy". In: *Journal of Instrumentation* 10.07, p. C07018. URL: http://stacks.iop.org/1748-0221/10/i=07/a=C07018 (cit. on p. 197).

Oelfke, U., G. K. Y. Lam, and M. S. Atkins (1996). "Proton dose monitoring with PET: quantitative studies in Lucite". In: *Physics in Medicine & Biology* 41.1, p. 177. URL: http://stacks.iop.org/0031-9155/41/i=1/a=013 (cit. on pp. 64, 70).

Oger, T., W.-T. Chen, J.-P. Cussonneau, J. Donnard, S. Duval, J. Lamblin, O. Lemaire, A. F. M. Hadi, P. Leray, E. Morteau, L. L. Scotto, J.-S. Stutzmann, and D. Thers (2012). "A liquid xenon TPC for a medical imaging Compton telescope". In: *Nuclear Instruments and Methods in Physics Research Section A: Accelerators, Spectrometers, Detectors and Associated Equipment* 695. New Developments in Photodetection NDIP11, pp. 125–128. ISSN: 0168-9002. DOI: https://doi.org/10.1016/j.nima.2011.12.004. URL: http://www.sciencedirect.com/science/article/pii/S0168900211021632 (cit. on p. 45).

Oliphant, M. O. (1943). "The acceleration of particles to very high energies". In: *Classified memo submitted to DSIR, United Kingdom, Sept. 1943* (cit. on p. 24).

Ordonez, C. E., A. Bolozdynya, and W. Chang (1997). "Doppler broadening and energy uncertainties in Compton cameras". In: *IEEE Nucl. Sci. Symp. Conf. Rec. 2 1361-65* (cit. on pp. 86, 171).

Ortega, P. G., I. Torres-Espallardo, F. Cerutti, A. Ferrari, J. E. Gillam, C. Lacasta, G. Llosá, J. F. Oliver, P. Sala, P. Solevi, and M. Rafecas (Mar. 7, 2015). "Noise evaluation of Compton camera imaging for proton therapy". eng. In: *Physics in Medicine & Biology* 60.5, pp. 1845–1863. DOI: 10.1088/0031-9155/60/5/1845 (cit. on pp. 113, 171, 181).

Owen, H. L., D. Holder, J. Alonso, and R. MacKay (2014). "Technologies for Delivery of Proton and Ion Beams for Radiotherapy". In: *International Journal of Modern Physics* A29, p. 1441002. DOI: 10.1142/S0217751X14410024 (cit. on p. 30).

Paans, A. M. J. and J. M. Schippers (1993). "Proton therapy in combination with PET as monitor: a feasibility study". In: *IEEE Transactions on Nuclear Science* 40.4, pp. 1041–1044. ISSN: 0018-9499. DOI: 10.1109/23.256709 (cit. on p. 70).

Paganetti, H. (2012a). *Proton Therapy Physics*. Boca Raton: CRC Press (cit. on pp. 9, 23).

Paganetti, H. (2012b). "Range uncertainties in proton therapy and the role of Monte Carlo simulations". In: *Physics in Medicine & Biology* 57.11, R99–R117. DOI: 10.1088/0031-9155/57/11/R99. URL: http://www.ncbi.nlm.nih.gov/pmc/articles/PMC3374500/ (cit. on pp. 34, 37, 170).

Paganetti, H. (2014). "Relative biological effectiveness (RBE) values for proton beam therapy. Variations as a function of biological endpoint, dose, and linear energy transfer." eng. In: *Physics in Medicine & Biology* 59.22, R419–72. DOI: 10.1088/0031-9155/59/22/R419 (cit. on p. 33).

Paganetti, H. and M. Goitein (2000). “Radiobiological significance of beamline dependent proton energy distributions in a spread-out Bragg peak.” In: *Medical Physics* 27.5, pp. 1119–1126 (cit. on pp. 37, 38).

Paganetti, H., A. Niemierko, M. Ancukiewicz, L. E. Gerweck, M. Goitein, J. S. Loeffler, and H. Suit (2002). “Relative biological effectiveness (RBE) values for proton beam therapy.” eng. In: *International Journal of Radiation Oncology Biology Physics* 53.2, pp. 407–421 (cit. on p. 33).

Paganetti, H. and P. Van Luijk (2013). “Biological Considerations When Comparing Proton Therapy With Photon Therapy”. In: *Seminars in Radiation Oncology* 23.2, pp. 77–87. DOI: 10.1016/j.semradonc.2012.11.002. URL: http://dx.doi.org/10.1016/j.semradonc.2012.11.002 (cit. on pp. 18, 33).

Parodi, K. (2014). “Heavy ion radiography and tomography”. In: *Physica Medica* 30.5. Particle Radiosurgery Conference, pp. 539–543. ISSN: 1120-1797. DOI: https://doi.org/10.1016/j.ejmp.2014.02.004. URL: http://www.sciencedirect.com/science/article/pii/S1120179714000271 (cit. on pp. 41, 42).

Parodi, K. (2015). “On- and off-line monitoring of ion beam treatment”. In: *Nuclear Instruments and Methods in Physics Research Section A: Accelerators, Spectrometers, Detectors and Associated Equipment* 809. Advances in detectors and applications for medicine, pp. 113–119. DOI: https://doi.org/10.1016/j.nima.2015.06.056. URL: http://www.sciencedirect.com/science/article/pii/S0168900215008062 (cit. on pp. 39, 67, 170).

Parodi, K. (2018). “On the feasibility of dose quantification with in-beam PET data in radiotherapy with 12C and proton beams”. PhD thesis (cit. on p. 65).

Parodi, K. and W. Assmann (2015). “Ionoacoustics: A new direct method for range verification”. In: *Modern Physics Letters A* 30.17, p. 1540025. DOI: 10.1142/S0217732315400258. URL: https://doi.org/10.1142/S0217732315400258 (cit. on pp. 44, 46).

Parodi, K. and T. R. Bortfeld (2006). “A filtering approach based on Gaussian-powerlaw convolutions for local PET verification of proton radiotherapy.” In: *Physics in Medicine & Biology* 51.8, pp. 1991–2009 (cit. on p. 65).

Parodi, K., T. R. Bortfeld, and T. Haberer (2008). “Comparison between in-beam and offline positron emission tomography imaging of proton and carbon ion therapeutic irradiation at synchrotron- and cyclotron-based facilities.” In: *International Journal of Radiation Oncology Biology Physics* 71.3, pp. 945–956 (cit. on p. 70).

Parodi, K., S. Brons, F. Cerutti, A. Ferrari, A. Mairani, H. Paganetti, and F. Sommerer (2010). “The FLUKA code for application of Monte Carlo methods to promote high precision ion beam therapy”. In: *12th International Conference on Nuclear Reaction Mechanisms, Villa Monastero, Varenna, Italy, 15 - 19 Jun 2009*, pp. 509–516. URL: https://cds.cern.ch/record/1238366 (cit. on p. 65).

Parodi, K., P. Crespo, H. Eickhoff, T. Haberer, J. Pawelke, D. Schardt, and W. Enghardt (2005). “Random coincidences during in-beam PET measurements at microbunched therapeutic

ion beams". In: *Nuclear Instruments and Methods in Physics Research Section A: Accelerators, Spectrometers, Detectors and Associated Equipment* 545.1, pp. 446–458. ISSN: 0168-9002. DOI: https://doi.org/10.1016/j.nima.2005.02.002. URL: http://www.sciencedirect.com/science/article/pii/S0168900205005759 (cit. on p. 42).

Parodi, K., H. Paganetti, H. A. Shih, S. Michaud, J. S. Loeffler, T. F. DeLaney, N. J. Liebsch, J. E. Munzenrider, A. J. Fischman, A.-C. Knopf, and T. R. Bortfeld (2007). "Patient Study of *In Vivo* Verification of Beam Delivery and Range, Using Positron Emission Tomography and Computed Tomography Imaging After Proton Therapy". In: *International Journal of Radiation Oncology Biology Physics* 68.3, pp. 920–934. DOI: 10.1016/j.ijrobp.2007.01.063. URL: http://dx.doi.org/10.1016/j.ijrobp.2007.01.063 (cit. on pp. 65, 70).

Parra, L. C. (2000). "Reconstruction of cone-beam projections from Compton scattered data". In: *IEEE Transactions on Nuclear Science* 47.4, pp. 1543–1550. DOI: 10.1109/23.873014 (cit. on p. 101).

Particle Therapy Cooperative Group, P. (2017). "PTCOG stats". In: *www.ptcog.ch* (cit. on p. 170).

Pausch, G., J. Petzoldt, M. Berthel, W. Enghardt, F. Fiedler, C. Golnik, F. Hueso-González, R. Lentering, K. Römer, K. Ruhnau, J. Stein, A. P. Wolf, and T. Kormoll (2016). "Scintillator-Based High-Throughput Fast Timing Spectroscopy for Real-Time Range Verification in Particle Therapy". In: *IEEE Transactions on Nuclear Science* 63.2, pp. 664–672. ISSN: 0018-9499. DOI: 10.1109/TNS.2016.2527822 (cit. on p. 81).

Pawelke, J., L. Byars, W. Enghardt, W. D. Fromm, H. Geissel, B. G. Hasch, K. Lauckner, P. Manfrass, D. Schardt, and M. Sobiella (1996). "The investigation of different cameras for in-beam PET imaging." In: *Physics in Medicine & Biology* 41.2, pp. 279–296 (cit. on p. 69).

Peach, K. J., J. H. Cobb, S. L. Sheehy, H. Witte, T. Yokoi, M. Aslaninejad, M. J. Easton, J. Pasternak, R. Barlow, H. L. Owen, S. C. Tygier, C. D. Beard, P. A. McIntosh, S. M. Pattalwar, S. L. Smith, S. I. Tzenov, N. Bliss, T. J. Jones, J. Strachan, R. Edgecock, J. K. Pozimski, R. J. L. Fenning, A. Khan, I. S. K. Gardner, D. J. Kelliher, S. Machida, M. A. Hill, C. Johnstone, B. Jones, B. Vojnovic, and R. Seviour (2010). "PAMELA : overview and status". In: *Proceedings of the 1st International Particle Accelerator Conference IPAC 2010*. Kyoto, Japan: JACoW, pp. 112–114. URL: http://eprints.hud.ac.uk/id/eprint/15286/ (cit. on p. 25).

Pearson, E., M. Abs, S. Henrotin, W. Kleeven, J. Van de Walle, P. Verbruggen, and S. Zaremba (2013). "The New IBA Superconducting Synchrocyclotron (S2C2): From Modelling to Reality". In: *XI International Topical Meeting or Nuclear Applications of Accelerators* (cit. on p. 220).

Pedroni, E. S., R. Bacher, H. Blattmann, T. Bohringer, A. Coray, A. J. Lomax, S. Lin, G. Munkel, S. Scheib, and U. Schneider (1995). "The 200-MeV proton therapy project at the Paul Scherrer Institute: conceptual design and practical realization." In: *Medical Physics* 22.1, pp. 37–53 (cit. on pp. 29, 30).

Pedroni, E. S., S. Scheib, T. Bohringer, A. Coray, M. Grossmann, S. Lin, and A. J. Lomax (2005). "Experimental characterization and physical modelling of the dose distribution of scanned proton pencil beams." eng. In: *Physics in Medicine & Biology* 50.3, pp. 541–561 (cit. on pp. 13, 16).

Pemler, P., J. Besserer, J. de Boer, M. Dellert, C. Gahn, M. Moosburger, U. Schneider, E. S. Pedroni, and H. Stäuble (1999). "A detector system for proton radiography on the gantry of the Paul-Scherrer-Institute". In: *Nuclear Instruments and Methods in Physics Research Section A: Accelerators, Spectrometers, Detectors and Associated Equipment* 432.2, pp. 483–495. ISSN: 0168-9002. DOI: https://doi.org/10.1016/S0168-9002(99)00284-3. URL: http://www.sciencedirect.com/science/article/pii/S0168900299002843 (cit. on p. 41).

Penfold, S. N., A. B. Rosenfeld, R. Schulte, and K. Schubert (2009). "A more accurate reconstruction system matrix for quantitative proton computed tomography." In: *Medical Physics* 36.10, pp. 4511–4518 (cit. on p. 41).

Pennazio, F., G. Battistoni, M. G. Bisogni, N. Camarlinghi, A. Ferrari, V. Ferrero, E. Fiorina, M. Morrocchi, P. Sala, G. Sportelli, R. Wheadon, and P. Cerello (2018). "Carbon ions beam therapy monitoring with the INSIDE in-beam PET". In: *Physics in Medicine & Biology* 63.14, p. 145018. URL: http://stacks.iop.org/0031-9155/63/i=14/a=145018 (cit. on p. 71).

Perali, I., A. Celani, L. Bombelli, C. Fiorini, F. Camera, E. Clementel, S. Henrotin, G. Janssens, D. Prieels, F. Roellinghoff, J. Smeets, F. Stichelbaut, and F. Vander Stappen (2014). "Prompt gamma imaging of proton pencil beams at clinical dose rate". In: *Physics in Medicine & Biology* 59.19, p. 5849. URL: http://stacks.iop.org/0031-9155/59/i=19/a=5849 (cit. on pp. 77, 84).

Peters, A., R. Cee, T. Hoffmann, A. Reiter, M. Schwickert, and T. Winkelmann (2008). "Spill structure measurements at the Heidelberg Ion Therapy center". In: *Proceedings of EPAC08, Genoa, Italy* (cit. on p. 174).

Peterson, S. W., D. Robertson, and J. C. Polf (2010). "Optimizing a three-stage Compton camera for measuring prompt gamma rays emitted during proton radiotherapy". In: *Physics in Medicine & Biology* 55.22, p. 6841. URL: http://stacks.iop.org/0031-9155/55/i=22/a=015 (cit. on p. 90).

Petzoldt, J., K. E. Römer, W. Enghardt, F. Fiedler, C. Golnik, F. Hueso-González, S. Helmbrecht, T. Kormoll, H. Rohling, J. Smeets, T. Werner, and G. Pausch (2016). "Characterization of the microbunch time structure of proton pencil beams at a clinical treatment facility." In: *Physics in Medicine & Biology* 61.6, pp. 2432–2456 (cit. on p. 80).

Phillips, M. H., E. S. Pedroni, H. Blattmann, T. Boehringer, A. Coray, and S. Scheib (1992). "Effects of respiratory motion on dose uniformity with a charged particle scanning method." eng. In: *Physics in Medicine & Biology* 37.1, pp. 223–234 (cit. on p. 33).

Piersanti, L., F. Bellini, F. Bini, F. Collamati, E. De Lucia, M. Durante, R. Faccini, F. Ferroni, S. Fiore, E. Iarocci, C. La Tessa, M. Marafini, I. Mattei, V. Patera, P. G. Ortega, A. Sarti, C. Schuy, A. Sciubba, M. Vanstalle, and C. Voena (2014). "Measurement of charged particle yields from PMMA irradiated by a 220 MeV/u (12)C beam." In: *Physics in Medicine & Biology* 59.7, pp. 1857–1872 (cit. on p. 43).

Pinto, M., M. Bajard, S. Brons, M. Chevallier, D. Dauvergne, G. Dedes, M. De Rydt, N. Freud, J. Krimmer, C. La Tessa, J. M. Létang, K. Parodi, R. Pleskac, D. Prieels, C. Ray, I. Rinaldi, F. Roellinghoff, D. Schardt, É. Testa, and M. Testa (2015). "Absolute prompt-gamma yield

measurements for ion beam therapy monitoring." eng. In: *Physics in Medicine & Biology* 60.2, pp. 565–594. DOI: 10.1088/0031-9155/60/2/565 (cit. on pp. 74–76).

Pinto, M., D. Dauvergne, N. Freud, J. Krimmer, J. M. Létang, C. Ray, F. Roellinghoff, and É. Testa (2014). "Design optimisation of a TOF-based collimated camera prototype for online hadrontherapy monitoring". In: *Physics in Medicine & Biology* 59.24, p. 7653. URL: http://stacks.iop.org/0031-9155/59/i=24/a=7653 (cit. on pp. 84, 85, 112, 178).

Pinto, M., D. Dauvergne, N. Freud, J. Krimmer, J. M. Létang, and É. Testa (2016). "Assessment of Geant4 Prompt-Gamma Emission Yields in the Context of Proton Therapy Monitoring." In: *Frontiers in Oncology* 6, p. 10 (cit. on p. 77).

Plautz, T. E., V. Bashkirov, V. Feng, R. F. Hurley, R. P. Johnson, C. Leary, S. Macafee, A. Plumb, V. Rykalin, H. F.-W. Sadrozinski, K. Schubert, R. Schulte, B. Schultze, D. Steinberg, M. Witt, and A. Zatserklyaniy (2014). "200 MeV Proton Radiography Studies with a Hand Phantom Using a Prototype Proton CT Scanner". In: *IEEE transactions on medical imaging* 33.4, pp. 875–881 (cit. on p. 40).

Podgorsak, E. B. (2010). *Radiation Physics for Medical Physicists*. Springer (cit. on pp. 57, 60, 62).

Polf, J. C., S. Avery, D. S. Mackin, and S. Beddar (2015). "Imaging of prompt-gamma rays emitted during delivery of clinical proton beams with a Compton camera: feasibility studies for range verification". In: *Physics in Medicine & Biology* 60.18, p. 7085. URL: http://stacks.iop.org/0031-9155/60/i=18/a=7085 (cit. on pp. 90, 91).

Polf, J. C., R. Panthi, D. S. Mackin, M. McCleskey, A. Saastamoinen, B. T. Roeder, and S. Beddar (2013). "Measurement of characteristic prompt gamma rays emitted from oxygen and carbon in tissue-equivalent samples during proton beam irradiation." In: *Physics in Medicine & Biology* 58.17, pp. 5821–5831 (cit. on p. 81).

Polf, J. C., S. W. Peterson, G. Ciangaru, M. T. Gillin, and S. Beddar (2009a). "Prompt-gamma-ray emission from biological tissues during proton irradiation: a preliminary study." eng. In: *Physics in Medicine & Biology* 54.3, pp. 731–743. DOI: 10.1088/0031-9155/54/3/017 (cit. on pp. 81, 171).

Polf, J. C., S. W. Peterson, M. McCleskey, B. T. Roeder, A. Spiridon, S. Beddar, and L. Trache (2009b). "Measurement and calculation of characteristic prompt gamma ray spectra emitted during proton irradiation." In: *Physics in Medicine & Biology* 54.22, N519–27 (cit. on p. 81).

Poludniowski, G., N. M. Allinson, and P. M. Evans (2015). "Proton radiography and tomography with application to proton therapy." In: *British Journal of Radiology* 88.1053, p. 20150134 (cit. on p. 39).

Pönisch, F., K. Parodi, B. G. Hasch, and W. Enghardt (2004). "The modelling of positron emitter production and PET imaging during carbon ion therapy." In: *Physics in Medicine & Biology* 49.23, pp. 5217–5232 (cit. on p. 65).

Powsner, R. A., R. P. Matthew, and E. R. Powsner (2013). *Essentials of Nuclear Medicine Physics and Instrumentation*. John Wiley & Sons (cit. on p. 49).

Priegnitz, M., S. Helmbrecht, G. Janssens, I. Perali, J. Smeets, F. Vander Stappen, E. Sterpin, and F. Fiedler (2015). "Measurement of prompt gamma profiles in inhomogeneous targets with a knife-edge slit camera during proton irradiation". In: *Physics in Medicine & Biology* 60.12, p. 4849. URL: http://stacks.iop.org/0031-9155/60/i=12/a=4849 (cit. on pp. 84, 85).

Priegnitz, M., S. Helmbrecht, G. Janssens, I. Perali, J. Smeets, F. Vander Stappen, E. Sterpin, and F. Fiedler (2016). "Detection of mixed-range proton pencil beams with a prompt gamma slit camera". In: *Physics in Medicine & Biology* 61.2, p. 855. URL: http://stacks.iop.org/0031-9155/61/i=2/a=855 (cit. on p. 84).

Qin, N., M. Pinto, Z. Tian, G. Dedes, A. Pompos, S. B. Jiang, K. Parodi, and X. Jia (2017). "Initial development of goCMC: a GPU-oriented fast cross-platform Monte Carlo engine for carbon ion therapy." eng. In: *Physics in Medicine & Biology* 62.9, pp. 3682–3699. DOI: 10.1088/1361-6560/aa5d43 (cit. on p. 77).

Radon, J. (1917). "Über die Bestimmung von Funktionen durch ihre Integralwerte längs gewisser Mannigfaltigkeiten". In: *Akademie der Wissenschaften - Journal of Mathematical Physics* 69, pp. 262–277 (cit. on p. 47).

Ready, J. (2016). "Development of a multi-knife-edge slit collimator for prompt gamma ray imaging during proton beam cancer therapy". PhD thesis. University of California, Berkeley. URL: https://escholarship.org/uc/item/14d0r6zb (cit. on p. 85).

Ready, J., V. Negut, L. Mihailescu, and K. Vetter (2016). "Prompt Gamma Imaging with a Multi-Knife-Edge Slit Collimator: Evaluation for Use in Proton Beam Range Verification". In: *Medical Physics* 43.6Part31, pp. 3717–3717. DOI: 10.1118/1.4957338. URL: https://aapm.onlinelibrary.wiley.com/doi/abs/10.1118/1.4957338 (cit. on p. 85).

Richard, M.-H. (2012). "Design study of a Compton camera for prompt-gamma imaging during ion beam therapy". PhD thesis. Université Claude Bernard - Lyon I (cit. on p. 108).

Richter, C., G. Pausch, S. Barczyk, M. Priegnitz, I. Keitz, J. Thiele, J. Smeets, F. Vander Stappen, L. Bombelli, C. Fiorini, L. Hotoiu, I. Perali, D. Prieels, W. Enghardt, and M. Baumann (2016). "First clinical application of a prompt gamma based in vivo proton range verification system". In: *Radiotherapy and Oncology* 118.2, pp. 232–237. DOI: 10.1016/j.radonc.2016.01.004. URL: https://doi.org/10.1016/j.radonc.2016.01.004 (cit. on pp. 85, 86).

Rietzel, E., D. Schardt, and T. Haberer (2007). "Range accuracy in carbon ion treatment planning based on CT-calibration with real tissue samples". In: *Radiation Oncology (London, England)* 2, pp. 14–14. DOI: 10.1186/1748-717X-2-14. URL: http://www.ncbi.nlm.nih.gov/pmc/articles/PMC1858700/ (cit. on pp. 31, 32, 36).

Rinaldi, I., S. Brons, J. Gordon, R. Panse, B. Voss, O. Jäkel, and K. Parodi (2013). "Experimental characterization of a prototype detector system for carbon ion radiography and tomography." In: *Physics in Medicine & Biology* 58.3, pp. 413–427 (cit. on p. 42).

Ritt, S. (2009). *9 Channel, 5 GSPS Switched Capacitor Array DRS4*. Revision 0.9. Paul Scherrer Institut (cit. on p. 116).

Robert, C., G. Dedes, G. Battistoni, T. T. Böhlen, I. Buvat, F. Cerutti, M. P. W. Chin, A. Ferrari, P. Gueth, C. Kurz, L. Lestand, A. Mairani, G. Montarou, R. Nicolini, P. G. Ortega, K. Parodi, Y. Prezado, P. Sala, D. Sarrut, and É. Testa (2013). "Distributions of secondary particles in proton and carbon-ion therapy: a comparison between GATE/Geant4 and FLUKA Monte Carlo codes". In: *Physics in Medicine & Biology* 58.9, p. 2879. URL: http://stacks.iop.org/0031-9155/58/i=9/a=2879 (cit. on pp. 76, 77, 170).

Robertson, D., J. C. Polf, S. W. Peterson, M. T. Gillin, and S. Beddar (2011). "Material efficiency studies for a Compton camera designed to measure characteristic prompt gamma rays emitted during proton beam radiotherapy". In: *Physics in Medicine & Biology* 56.10, p. 3047. URL: http://stacks.iop.org/0031-9155/56/i=10/a=010 (cit. on p. 90).

Robertson, J. B., J. R. Williams, R. A. Schmidt, J. B. Little, D. F. Flynn, and H. Suit (1975). "Radiobiological studies of a high-energy modulated proton beam utilizing cultured mammalian cells." In: *Cancer* 35.6, pp. 1664–1677 (cit. on pp. 37, 38).

Robertson, J. S., R. B. Marr, M. Rosenblum, V. Radeka, and Y. L. Yamamoto (1972). *32-crystal positron transverse section detector*. Tech. rep. United States (cit. on p. 93).

Roellinghoff, F., A. Benilov, D. Dauvergne, G. Dedes, N. Freud, G. Janssens, J. Krimmer, J. M. Létang, M. Pinto, D. Prieels, C. Ray, J. Smeets, F. Stichelbaut, and É. Testa (2014). "Real-time proton beam range monitoring by means of prompt-gamma detection with a collimated camera". In: *Physics in Medicine & Biology* 59.5, p. 1327. URL: http://stacks.iop.org/0031-9155/59/i=5/a=1327 (cit. on pp. 175, 192).

Roellinghoff, F., M.-H. Richard, M. Chevallier, J. Constanzo, D. Dauvergne, N. Freud, P. Henriquet, F. Le Foulher, J. M. Létang, G. Montarou, C. Ray, É. Testa, M. Testa, and A. H. Walenta (2011). "Design of a Compton camera for 3D prompt-γ imaging during ion beam therapy". In: *Nuclear Instruments and Methods in Physics Research Section A: Accelerators, Spectrometers, Detectors and Associated Equipment* 648. NIMA 4th International Conference on Imaging techniques in Subatomic Physics, Astrophysics, Medicine, Biology and Industry, S20–S23. ISSN: 0168-9002. DOI: https://doi.org/10.1016/j.nima.2011.01.069. URL: http://www.sciencedirect.com/science/article/pii/S0168900211001471 (cit. on p. 88).

Rogers, D. F. (2001). *An Introduction to NURBS: With Historical Perspective*. San Francisco, CA, USA: Morgan Kaufmann Publishers Inc. ISBN: 1-55860-669-6 (cit. on p. 183).

Rogers, J. G., R. Nutt, M. Andreaco, and C. W. Williams (1994). "Testing 144- and 256-crystal BGO block detectors". In: *IEEE Transactions on Nuclear Science* 41.4, pp. 1423–1429. DOI: 10.1109/23.322926 (cit. on pp. 133, 162).

Rogers, W. L., N. H. Clinthorne, L. Shao, P. Chiao, Y. Ding, J. A. Stamos, and K. F. Koral (1988). "SPRINT II: a second generation single photon ring tomograph." In: *IEEE Transactions on Medical Imaging* 7.4, pp. 291–297 (cit. on p. 98).

Rolo, M. D., R. Bugalho, F. Goncalves, G. Mazza, A. Rivetti, J. C. Silva, R. Silva, and J. Varela (2013). "TOFPET ASIC for PET applications". In: *Journal of Instrumentation* 8.02, p. C02050. URL: http://stacks.iop.org/1748-0221/8/i=02/a=C02050 (cit. on p. 71).

Ronsivalle, C., M. Carpanese, C. Marino, G. Messina, L. Picardi, S. Sandri, E. Basile, B. Caccia, D. M. Castelluccio, E. Cisbani, S. Frullani, F. Ghio, V. Macellari, M. Benassi, M. D'Andrea, and L. Strigari (2011). "The TOP-IMPLART project". In: *The European Physical Journal Plus* 126.7, p. 68. DOI: 10.1140/epjp/i2011-11068-x. URL: https://doi.org/10.1140/epjp/i2011-11068-x (cit. on p. 25).

Rossi, B. B. (1952). *High-energy particles*. Prentice-Hall physics. New York, NY: Prentice-Hall. URL: https://cds.cern.ch/record/99081 (cit. on p. 12).

Rosso, V., G. Battistoni, N. Belcari, N. Camarlinghi, A. Ferrari, S. Ferretti, A. C. Kraan, A. Mairani, N. Marino, J. E. Ortuño, M. Pullia, P. Sala, A. Santos, G. Sportelli, K. Straub, and A. Del Guerra (2013). "A new PET prototype for proton therapy: comparison of data and Monte Carlo simulations". In: *Journal of Instrumentation* 8.03, p. C03021. URL: http://stacks.iop.org/1748-0221/8/i=03/a=C03021 (cit. on p. 71).

Russo, G., A. Attili, G. Battistoni, D. Bertrand, F. Bourhaleb, F. Cappucci, M. Ciocca, A. Mairani, F. M. Milian, S. Molinelli, M. C. Morone, S. Muraro, T. Orts, V. Patera, P. Sala, E. Schmitt, G. Vivaldo, and F. Marchetto (2016). "A novel algorithm for the calculation of physical and biological irradiation quantities in scanned ion beam therapy: the beamlet superposition approach." In: *Physics in Medicine & Biology* 61.1, pp. 183–214 (cit. on p. 77).

Ruth, T. J. (2009). "The Production of Radionuclides for Radiotracers in Nuclear Medicine". In: *Reviews of Accelerator Science and Technology* 02.01, pp. 17–33. DOI: 10.1142/S1793626809000314. URL: https://doi.org/10.1142/S1793626809000314 (cit. on p. 51).

Rutherford, E. (1899). "Uranium radiation and the electrical conduction produced by it". In: *Philos. Mag.* 47, p. 109. URL: http://cds.cern.ch/record/261896 (cit. on p. 48).

Rutherford, E. (1911). "The scattering of α and β particles by matter and the structure of the atom". In: *Philosophical Magagazine Series 6* 21, pp. 669–688. DOI: 10.1080/14786440508637080 (cit. on p. 13).

Rydberg, B. (1996). "Clusters of DNA damage induced by ionizing radiation: formation of short DNA fragments. II. Experimental detection." eng. In: *Radiation research* 145.2, pp. 200–209 (cit. on p. 19).

Sadrozinski, H. F.-W., V. Bashkirov, B. Colby, G. Coutrakon, B. Erdelyi, D. Fusi, R. F. Hurley, R. P. Johnson, S. Kashiguine, S. McAllister, F. Martinez-McKinney, J. Missaghian, M. Scaringella, S. N. Penfold, V. Rykalin, R. Schulte, K. Schubert, D. Steinberg, and A. Zatserklaniy (2011). "Detector development for Proton Computed Tomography (pCT)". In: *2011 IEEE Nuclear Science Symposium Conference Record*, pp. 4457–4461. DOI: 10.1109/NSSMIC.2011.6152494 (cit. on p. 41).

Saint Gobain (2016). *BGO Bismuth Germanate Scintillation material - Datasheet*. Saint Gobain Ceramics & Plastics (cit. on p. 151).

Saint Gobain (2017). *Plastic Scintillating Fibers - Product brochure*. Saint Gobain Ceramics & Plastics (cit. on pp. 119, 122).

Sandjong, S., M. Fontana, and É. Testa (2017). "Compton camera prototype for ion beam therapy monitoring: characterization of the BGO scintillators and simulation of the scintillating fiber beam hodoscope". Master internship report (cit. on pp. 114, 166).

Saraya, Y., T. Izumikawa, J. Goto, T. Kawasaki, and T. Kimura (2014). "Study of spatial resolution of proton computed tomography using a silicon strip detector". In: *Nuclear Instruments and Methods in Physics Research Section A: Accelerators, Spectrometers, Detectors and Associated Equipment* 735, pp. 485–489. ISSN: 0168-9002. DOI: https://doi.org/10.1016/j.nima.2013.09.051. URL: http://www.sciencedirect.com/science/article/pii/S0168900213012850 (cit. on p. 42).

Sauli, F. (1997). "GEM: A new concept for electron amplification in gas detectors". In: *Nuclear Instruments and Methods in Physics Research Section A: Accelerators, Spectrometers, Detectors and Associated Equipment* 386.2, pp. 531–534. ISSN: 0168-9002. DOI: https://doi.org/10.1016/S0168-9002(96)01172-2. URL: http://www.sciencedirect.com/science/article/pii/S0168900296011722 (cit. on p. 41).

Sawakuchi, G. O., U. Titt, D. Mirkovic, and R. Mohan (2008). "Density heterogeneities and the influence of multiple Coulomb and nuclear scatterings on the Bragg peak distal edge of proton therapy beams." In: *Physics in Medicine & Biology* 53.17, pp. 4605–4619 (cit. on p. 38).

Scarantino, C. W., B. R. Prestidge, M. S. Anscher, C. R. Ferree, W. T. Kearns, R. D. Black, N. G. Bolick, and G. P. Beyer (2008). "The observed variance between predicted and measured radiation dose in breast and prostate patients utilizing an in vivo dosimeter." In: *International Journal of Radiation Oncology Biology Physics* 72.2, pp. 597–604 (cit. on p. 44).

Scaringella, M., M. Brianzi, M. Bruzzi, M. Bucciolini, M. Carpinelli, G. A. P. Cirrone, C. Civinini, G. Cuttone, D. Lo Presti, S. Pallotta, C. Pugliatti, N. Randazzo, F. Romano, V. Sipala, C. Stancampiano, C. Talamonti, M. Tesi, E. Vanzi, and M. Zani (2013). "The PRIMA (PRoton IMAging) collaboration: Development of a proton Computed Tomography apparatus". In: *Nuclear Instruments and Methods in Physics Research Section A: Accelerators, Spectrometers, Detectors and Associated Equipment* 730. Proceedings of the 9th International Conference on Radiation Effects on Semiconductor Materials Detectors and Devices, pp. 178–183. ISSN: 0168-9002. DOI: https://doi.org/10.1016/j.nima.2013.05.181. URL: http://www.sciencedirect.com/science/article/pii/S0168900213008036 (cit. on p. 41).

Schaffner, B. (1998). "Range precision of therapeutic proton beams". In: *Medical Physics* 25.8, pp. 1555–1555. DOI: 10.1118/1.598334. URL: https://aapm.onlinelibrary.wiley.com/doi/abs/10.1118/1.598334 (cit. on p. 36).

Schaffner, B. and E. S. Pedroni (1998). "The precision of proton range calculations in proton radiotherapy treatment planning: experimental verification of the relation between CT-HU and proton stopping power". In: *Physics in Medicine & Biology* 43.6, p. 1579. URL: http://stacks.iop.org/0031-9155/43/i=6/a=016 (cit. on pp. 31, 38).

Schall, I., D. Schardt, H. Geissel, H. Irnich, E. Kankeleit, G. Kraft, A. Magel, M. F. Mohar, G. Münzenberg, F. Nickel, C. Scheidenberger, and W. Schwab (1996). "Charge-changing nuclear reactions of relativistic light-ion beams ($5 \leq Z \leq 10$) passing through thick absorbers". In: *Nuclear Instruments and Methods in Physics Research Section B: Beam Interactions with Materials and Atoms* 117.3, pp. 221–234. ISSN: 0168-583X. DOI: https://doi.org/10.1016/0168-583X(96)00325-4. URL: http://www.sciencedirect.com/science/article/pii/0168583X96003254 (cit. on pp. 15, 17).

Schardt, D., T. Elsässer, and D. Schulz-Ertner (2010). "Heavy-ion tumor therapy: Physical and radiobiological benefits". In: *Rev. Mod. Phys.* 82 (1), pp. 383–425. DOI: 10.1103/RevModPhys.82.383. URL: https://link.aps.org/doi/10.1103/RevModPhys.82.383 (cit. on pp. 7, 8, 21, 28, 30, 34).

Schardt, D., P. Steidl, M. Krämer, U. Weber, K. Parodi, and S. Brons (2008). "Precision Bragg-curve measurements for light-ion beams in water" (cit. on pp. 15, 16).

Schimmerling, W., J. Miller, M. Wong, M. Rapkin, J. Howard, G. H. Spieler, and V. B. Jarret (1989). "The Fragmentation of 670A MeV Neon-20 as a Function of Depth in Water: I. Experiment". In: 120, pp. 36–71 (cit. on p. 17).

Schimmerling, W., T. S. Subramanian, W. J. McDonald, S. N. Kaplan, A. Sadoff, and G. Gabor (1983). "Beam analysis spectrometer for relativistic heavy ions". In: *Nuclear Instruments and Methods in Physics Research* 205.3, pp. 531–543. ISSN: 0167-5087. DOI: https://doi.org/10.1016/0167-5087(83)90021-2. URL: http://www.sciencedirect.com/science/article/pii/0167508783900212 (cit. on p. 17).

Schlegel, W., T. R. Bortfeld, A. Grosu, T. Pan, and D. Luo (2008). "New Technologies in Radiation Oncology". In: *Journal of Nuclear Medicine* 49, pp. 683–684 (cit. on p. 35).

Schneider, U., J. Besserer, P. Pemler, M. Dellert, M. Moosburger, E. S. Pedroni, and B. Kaser-Hotz (2004). "First proton radiography of an animal patient." In: *Medical Physics* 31 5, pp. 1046–51 (cit. on pp. 40, 41).

Schneider, U. and R. Hälg (2015). "The Impact of Neutrons in Clinical Proton Therapy". In: *Frontiers in Oncology* 5, p. 235. DOI: 10.3389/fonc.2015.00235. URL: http://www.ncbi.nlm.nih.gov/pmc/articles/PMC4617104/ (cit. on p. 18).

Schneider, U. and E. S. Pedroni (1995). "Proton radiography as a tool for quality control in proton therapy". In: *Medical Physics* 22.4, pp. 353–363. DOI: 10.1118/1.597470. URL: https://aapm.onlinelibrary.wiley.com/doi/abs/10.1118/1.597470 (cit. on pp. 36, 40, 41).

Schneider, U., E. S. Pedroni, and A. J. Lomax (1996). "The calibration of CT Hounsfield units for radiotherapy treatment planning". In: *Physics in Medicine & Biology* 41.1, p. 111. URL: http://stacks.iop.org/0031-9155/41/i=1/a=009 (cit. on pp. 31, 36).

Schneider, W., T. R. Bortfeld, and W. Schlegel (2000). "Correlation between CT numbers and tissue parameters needed for Monte Carlo simulations of clinical dose distributions". In: *Physics in Medicine & Biology* 45.2, p. 459. URL: http://stacks.iop.org/0031-9155/45/i=2/a=314 (cit. on p. 36).

Schöne, S., W. Enghardt, F. Fiedler, C. Golnik, G. Pausch, H. Rohling, and T. Kormoll (2017). "An Image Reconstruction Framework and Camera Prototype Aimed for Compton Imaging for In-vivo Dosimetry of Therapeutic Ion Beams". In: *IEEE Transactions on Radiation and Plasma Medical Sciences* 1.1, pp. 96–107. ISSN: 2469-7311. DOI: 10.1109/TNS.2016.2623220 (cit. on pp. 101, 180).

Schöne, S., G. Shakirin, T. Kormoll, C. M. Herbach, G. Pausch, and W. Enghardt (2010). "A common approach to image reconstruction for different applications of Compton cameras". In: *IEEE Nuclear Science Symposuim Medical Imaging Conference*, pp. 2292–2293. DOI: 10.1109/NSSMIC.2010.5874192 (cit. on pp. 101, 180).

Schuemann, J. P., S. Dowdell, C. Grassberger, C.-H. Min, and H. Paganetti (2014). "Site-Specific Range Uncertainties Due to by Dose Calculation Algorithms for Proton Therapy". In: *International Journal of Radiation Oncology Biology Physics* 90.1, S26. DOI: 10.1016/j.ijrobp.2014.05.125. URL: https://doi.org/10.1016/j.ijrobp.2014.05.125 (cit. on p. 36).

Schulz-Ertner, D., O. Jäkel, and W. Schlegel (2006). "Radiation therapy with charged particles." In: *Seminars in radiation oncology* 16.4, pp. 249–259. DOI: 10.1016/j.semradonc.2006.04.008 (cit. on p. 29).

Schumann, A., J. Petzoldt, P. Dendooven, W. Enghardt, C. Golnik, F. Hueso-González, T. Kormoll, G. Pausch, K. E. Römer, and F. Fiedler (2015). "Simulation and experimental verification of prompt gamma-ray emissions during proton irradiation." eng. In: *Physics in Medicine & Biology* 60.10, pp. 4197–4207. DOI: 10.1088/0031-9155/60/10/4197 (cit. on p. 77).

Seltzer, S. M. (1993). "Calculation of Photon Mass Energy-Transfer and Mass Energy-Absorption Coefficients". In: *Radiation Research* 136.2, pp. 147–170. DOI: 10.2307/3578607. URL: http://www.rrjournal.org/doi/abs/10.2307/3578607 (cit. on p. 64).

Seo, H., S. H. An, J. K. Kim, and C. H. Kim (2007). "Monte Carlo study of a double-scattering Compton camera with GEANT4". In: *Nuclear Instruments and Methods in Physics Research Section A: Accelerators, Spectrometers, Detectors and Associated Equipment* 580.1. Proceedings of the 10 th International Symposium on Radiation Physics, pp. 314–317. ISSN: 0168-9002. DOI: https://doi.org/10.1016/j.nima.2007.05.164. URL: http://www.sciencedirect.com/science/article/pii/S0168900207010388 (cit. on p. 98).

Seo, H., C. H. Kim, J. H. Park, J. H. Kim, J. H. Lee, C. S. Lee, and J. S. Lee (2010). "Development of double-scattering-type Compton camera with double-sided silicon strip detectors and NaI(Tl) scintillation detector". In: *Nuclear Instruments and Methods in Physics Research Section A: Accelerators, Spectrometers, Detectors and Associated Equipment* 615.3, pp. 333–339. ISSN: 0168-9002. DOI: https://doi.org/10.1016/j.nima.2010.02.060. URL: http://www.sciencedirect.com/science/article/pii/S0168900210002585 (cit. on pp. 87, 98).

Seo, H., J. H. Park, A. Ushakov, C. H. Kim, J. K. Kim, J. H. Lee, C. S. Lee, and J. S. Lee (2011). "Experimental performance of double-scattering Compton camera with anthropomorphic phantom". In: *Journal of Instrumentation* 6.01, p. C01024. URL: http://stacks.iop.org/1748-0221/6/i=01/a=C01024 (cit. on p. 99).

Serber, R. (1947). “Nuclear Reactions at High Energies”. In: *Physical Review* 72 (11), pp. 1114–1115. DOI: 10.1103/PhysRev.72.1114. URL: https://link.aps.org/doi/10.1103/PhysRev.72.1114 (cit. on p. 14).

Sethi, R. V., D. Giantsoudi, M. Raiford, I. Malhi, A. Niemierko, O. Rapalino, P. Caruso, T. I. Yock, N. J. Tarbell, H. Paganetti, and S. M. MacDonald (2014). “Patterns of Failure After Proton Therapy in Medulloblastoma; Linear Energy Transfer Distributions and Relative Biological Effectiveness Associations for Relapses”. In: *International Journal of Radiation Oncology Biology Physics* 88.3, pp. 655–663. DOI: 10.1016/j.ijrobp.2013.11.239. URL: https://doi.org/10.1016/j.ijrobp.2013.11.239 (cit. on p. 21).

Shakirin, G., H. Braess, F. Fiedler, D. Kunath, K. Laube, K. Parodi, M. Priegnitz, and W. Enghardt (2011). “Implementation and workflow for PET monitoring of therapeutic ion irradiation: a comparison of in-beam, in-room, and off-line techniques.” In: *Physics in Medicine & Biology* 56.5, pp. 1281–1298 (cit. on pp. 67, 69).

Sheehy, S. L. (2017). “Fixed-Field Alternating-Gradient Accelerators”. In: *Proceedings, CAS-CERN Accelerator School: Accelerators for Medical Applications: Vösendorf, Austria, May 26 - June 5, 2015*, pp. 321–336. URL: https://inspirehep.net/record/1448340/files/arXiv:1604.05221.pdf (cit. on p. 24).

Shinoda, H., T. Kanai, and T. Kohno (2006). “Application of heavy-ion CT.” In: *Physics in Medicine & Biology* 51.16, pp. 4073–4081 (cit. on p. 42).

Shirato, H., R. L. Harrison, R. O. Kornelsen, G. K. Y. Lam, C. C. Gaffney, G. B. Goodman, E. Grochowski, and B. D. Pate (1989). “Detection of pion-induced radioactivity by autoradiography and positron emission tomography (PET)”. In: *Medical Physics* 16.3, pp. 338–345. DOI: 10.1118/1.596426. URL: https://aapm.onlinelibrary.wiley.com/doi/abs/10.1118/1.596426 (cit. on p. 68).

Singh, M. (1983). “An electronically collimated gamma camera for single photon emission computed tomography. Part I: theoretical considerations and design criteria”. In: *Medical Physics* 10.4, pp. 421–427. ISSN: 2473-4209. DOI: 10.1118/1.595313. URL: http://dx.doi.org/10.1118/1.595313 (cit. on pp. 86, 98, 196).

Singh, M. and D. Doria (1981). “Computer Simulation Of Image Reconstruction With A New Electronically Collimated Gamma Tomography System”. In: *Proceedings SPIE - Society of Photo-Optical Instrumentation Engineers* 0273, pp. 273–279. DOI: 10.1117/12.931803. URL: https://doi.org/10.1117/12.931803 (cit. on p. 98).

Singh, M. and D. Doria (1983). “An electronically collimated gamma camera for single photon emission computed tomography. Part II: Image reconstruction and preliminary experimental measurements.” In: *Medical Physics* 10.4, pp. 428–435 (cit. on p. 98).

Smeets, J., F. Roellinghoff, G. Janssens, I. Perali, A. Celani, C. Fiorini, N. Freud, É. Testa, and D. Prieels (2016). “Experimental Comparison of Knife-Edge and Multi-Parallel Slit Collimators for Prompt Gamma Imaging of Proton Pencil Beams”. In: *Frontiers in Oncology* 6, p. 156. ISSN: 2234-943X. DOI: 10.3389/fonc.2016.00156. URL: https://www.frontiersin.org/article/10.3389/fonc.2016.00156 (cit. on p. 85).

Smeets, J., F. Roellinghoff, D. Prieels, F. Stichelbaut, A. Benilov, P. Busca, C. Fiorini, R. Peloso, M. Basilavecchia, T. Frizzi, J. C. Dehaes, and A. Dubus (2012). "Prompt gamma imaging with a slit camera for real-time range control in proton therapy". In: *Physics in Medicine & Biology* 57, pp. 3371–405 (cit. on pp. 84, 175).

Solevi, P., E. Munoz, C. Solaz, M. Trovato, P. Dendooven, J. E. Gillam, C. Lacasta, J. F. Oliver, M. Rafecas, I. Torres-Espallardo, and G. Llosá (2016). "Performance of MACACO Compton telescope for ion-beam therapy monitoring: first test with proton beams." eng. In: *Physics in Medicine & Biology* 61.14, pp. 5149–5165. DOI: 10.1088/0031-9155/61/14/5149 (cit. on p. 88).

Sommerer, F., F. Cerutti, K. Parodi, A. Ferrari, W. Enghardt, and H. Aiginger (2009). "In-beam PET monitoring of mono-energetic (16)O and (12)C beams: experiments and FLUKA simulations for homogeneous targets." In: *Physics in Medicine & Biology* 54.13, pp. 3979–3996 (cit. on pp. 70, 77).

Sonoda, S., Y. Ichimura, H. Kimura, S. Kabuki, A. Takada, T. Mizmoto, H. Kubo, S. Miyamoto, S. Komura, T. Takemura, T. Sawano, T. Kishimoto, Y. Matsuoka, Y. Mizumura, and T. Tanimori (2015). "Application of Electron Tracking Compton Camera (ETCC) in medical imaging". In: *2015 IEEE Nuclear Science Symposium and Medical Imaging Conference (NSS/MIC)*, pp. 1–3. DOI: 10.1109/NSSMIC.2015.7582015 (cit. on p. 217).

Spieler, H. (1998). "Semiconductor Detectors Part 2". Lectures on Detector Techniques, Stanford Linear Accelerator Center , September 1998 - February, 1999 (cit. on p. 132).

Sportelli, G., N. Belcari, N. Camarlinghi, G. A. P. Cirrone, G. Cuttone, S. Ferretti, A. C. Kraan, J. E. Ortuño, F. Romano, A. Santos, K. Straub, A. Tramontana, A. Del Guerra, and V. Rosso (2014). "First full-beam PET acquisitions in proton therapy with a modular dual-head dedicated system". In: *Physics in Medicine & Biology* 59.1, p. 43. URL: http://stacks.iop.org/0031-9155/59/i=1/a=43 (cit. on p. 71).

Srivastava, R., B. Jyoti, M. Gupta, and N. Singh (2015). "CyberKnife: The cutting edge technology in precision surgery". In: *SRM Journal of Research in Dental Sciences* 6.2, pp. 106–115. DOI: 10.4103/0976-433X.155469. URL: http://www.srmjrds.in/article.asp?issn=0976-433X;year=2015;volume=6;issue=2;spage=106;epage=115;aulast=Srivastava;t=6 (cit. on p. 29).

Steinsträter, O., R. Grün, U. Scholz, T. Friedrich, M. Durante, and M. Scholz (2012). "Mapping of RBE-Weighted Doses Between HIMAC- and LEM-Based Treatment Planning Systems for Carbon IonvTherapy". In: *International Journal of Radiation Oncology Biology Physics* 84.3, pp. 854–860. DOI: 10.1016/j.ijrobp.2012.01.038. URL: https://doi.org/10.1016/j.ijrobp.2012.01.038 (cit. on p. 33).

Sterpin, E., G. Janssens, J. Smeets, F. Vander Stappen, D. Prieels, M. Priegnitz, I. Perali, and S. Vynckier (2015). "Analytical computation of prompt gamma ray emission and detection for proton range verification." In: *Physics in Medicine & Biology* 60.12, pp. 4915–4946 (cit. on p. 77).

Steward, V. W. and A. M. Koehler (1973). “Proton Beam radiography in tumor detection”. In: *Science* 179, p. 913 (cit. on p. 39).

Stichelbaut, F. and Y. Jongen (2003). “Verification of the proton beam position in the patient by the detection of prompt gamma-ray emission”. In: *Proceedings of the 39th Meeting of the Particle Therapy Co-Operative Group* (cit. on pp. 43, 77, 170).

Stone, R. S. (1948). “Neutron therapy and specific ionization.” eng. In: *The American journal of roentgenology and radium therapy* 59.6, pp. 771–785 (cit. on p. 22).

Stone, R. S., J. H. Lawrence, and P. C. Aebersold (1940). “A Preliminary Report on the Use of Fast Neutrons in the Treatment of Malignant Disease”. In: *Radiology* 35.3, pp. 322–327. DOI: 10.1148/35.3.322. URL: https://doi.org/10.1148/35.3.322 (cit. on p. 22).

Strosberg, J., G. El-Haddad, E. Wolin, A. Hendifar, J. Yao, B. Chasen, E. Mittra, P. L. Kunz, M. H. Kulke, H. Jacene, D. Bushnell, T. M. O’Dorisio, R. P. Baum, H. R. Kulkarni, M. Caplin, R. Lebtahi, T. Hobday, E. Delpassand, E. Van Cutsem, A. Benson, R. Srirajaskanthan, M. Pavel, J. Mora, J. Berlin, E. Grande, N. Reed, E. Seregni, K. Oberg, M. Lopera Sierra, P. Santoro, T. Thevenet, J. L. Erion, P. Ruszniewski, D. J. Kwekkeboom, and E. Krenning (2017). “Phase 3 Trial of (177)Lu-Dotatate for Midgut Neuroendocrine Tumors.” In: *New England Journal of Medicine* 376.2, pp. 125–135 (cit. on p. 99).

Suit, H., T. F. DeLaney, S. Goldberg, H. Paganetti, B. Clasie, L. Gerweck, A. Niemierko, E. J. Hall, J. Flanz, J. Hallman, and A. Trofimov (2010). “Proton vs carbon ion beams in the definitive radiation treatment of cancer patients.” In: *Radiotherapy and Oncology* 95.1, pp. 3–22 (cit. on p. 32).

Suntharalingam, N., E. B. Podgorsak, and H. Tölli (2005). “Brachytherapy: Physical and clinical aspects”. In: *Radiation Oncology Physics: A Handbook for Teachers and Students* (cit. on p. 48).

Surti, S. and J. S. Karp (2016). “Advances in time-of-flight PET.” In: *Physica Medica* 32.1, pp. 12–22 (cit. on p. 96).

Surti, S., A. Kuhn, M. E. Werner, A. E. Perkins, J. Kolthammer, and J. S. Karp (2007). “Performance of Philips Gemini TF PET/CT scanner with special consideration for its time-of-flight imaging capabilities.” In: *Journal of Nuclear Medicine* 48.3, pp. 471–480 (cit. on p. 68).

Surti, S., W. Zou, M. E. Daube-Witherspoon, J. McDonough, and J. S. Karp (2011). “Design Study of an In-Situ PET Scanner for Use in Proton Beam Therapy”. In: *Physics in Medicine & Biology* 56.9, pp. 2667–2685 (cit. on p. 67).

Suzuki, Y., M. Yamaguchi, H. Odaka, H. Shimada, Y. Yoshida, K. Torikai, T. Satoh, K. Arakawa, N. Kawachi, S. Watanabe, S. Takeda, S. Ishikawa, H. Aono, S. Watanabe, T. Takahashi, and T. Nakano (2013). “Three-dimensional and multienergy gamma-ray simultaneous imaging by using a Si/CdTe Compton camera.” In: *Radiology* 267.3, pp. 941–947 (cit. on p. 98).

Sweet, W. H. (1951). “The Uses of Nuclear Disintegration in the Diagnosis and Treatment of Brain Tumor”. In: *New England Journal of Medicine* 245.23. PMID: 14882442, pp. 875–878. DOI:

10.1056/NEJM195112062452301. URL: https://doi.org/10.1056/NEJM195112062452301 (cit. on p. 93).

Tada, J., Y. Hayakawa, K. Hosono, and T. Inada (1991). "Time resolved properties of acoustic pulses generated in water and in soft tissue by pulsed proton beam irradiation–a possibility of doses distribution monitoring in proton radiation therapy." In: *Medical Physics* 18.6, pp. 1100–1104 (cit. on p. 44).

Tajima, T., D. Habs, and X. Yan (2009). "Laser Acceleration of Ions for Radiation Therapy". In: *Reviews of Accelerator Science and Technology* 02.01, pp. 201–228. DOI: 10.1142/S1793626809000296. URL: https://doi.org/10.1142/S1793626809000296 (cit. on p. 25).

Takada, A., H. Kubo, H. Nishimura, K. Ueno, K. Hattori, S. Kabuki, S. Kurosawa, K. Miuchi, E. Mizuta, T. Nagayoshi, N. Nonaka, Y. Okada, R. Orito, H. Sekiya, A. Takeda, and T. Tanimori (2011). "Observation of Diffuse Cosmic and Atmospheric Gamma Rays at Balloon Altitudes with an Electron-tracking Compton Camera". In: *The Astrophysical Journal* 733.1, p. 13. URL: http://stacks.iop.org/0004-637X/733/i=1/a=13 (cit. on p. 91).

Takeda, S., H. Aono, S. Okuyama, S. Ishikawa, H. Odaka, S. Watanabe, M. Kokubun, T. Takahashi, K. Nakazawa, H. Tajima, and N. Kawachi (2009). "Experimental Results of the Gamma-Ray Imaging Capability With a Si/CdTe Semiconductor Compton Camera". In: *IEEE Transactions on Nuclear Science* 56.3, pp. 783–790. ISSN: 0018-9499. DOI: 10.1109/TNS.2008.2012059 (cit. on p. 98).

Takeda, S., S. Ishikawa, H. Odaka, S. Watanabe, T. Takahashi, K. Nakazawa, H. Tajima, Y. Kuroda, M. Onishi, Y. Fukazawa, and H. Yasuda (2007). "A new Si/CdTe semiconductor Compton camera developed for high-angular resolution". In: *Proceedings SPIE - Society of Photo-Optical Instrumentation Engineers*, pp. 6706–6711. DOI: 10.1117/12.733840. URL: https://doi.org/10.1117/12.733840 (cit. on p. 98).

Takeda, S., H. Odaka, S. Ishikawa, S. Watanabe, H. Aono, T. Takahashi, Y. Kanayama, M. Hiromura, and S. Enomoto (2012). "Demonstration of in-vivo Multi-Probe Tracker Based on a Si/CdTe Semiconductor Compton Camera". In: *IEEE Transactions on Nuclear Science* 59.1, pp. 70–76. ISSN: 0018-9499. DOI: 10.1109/TNS.2011.2178432 (cit. on p. 98).

Takeda, S., T. Takahashi, S. Watanabe, H. Tajima, T. Tanaka, K. Nakazawa, and Y. Fukazawa (2008). "Double-sided silicon strip detector for x-ray imaging". In: *SPIE - Society of Photo-Optical Instrumentation Engineers - Newsroom* (cit. on p. 109).

Tashima, H., T. Yamaya, E. Yoshida, S. Kinouchi, M. Watanabe, and E. Tanaka (2012). "A single-ring OpenPET enabling PET imaging during radiotherapy". In: *Physics in Medicine & Biology* 57.14, p. 4705. URL: http://stacks.iop.org/0031-9155/57/i=14/a=4705 (cit. on pp. 68, 70).

Tashima, H., E. Yoshida, N. Inadama, F. Nishikido, Y. Nakajima, H. Wakizaka, T. Shinaji, M. Nitta, S. Kinouchi, M. Suga, H. Haneishi, T. Inaniwa, and T. Yamaya (2016). "Development of a small single-ring OpenPET prototype with a novel transformable architecture." In: *Physics in Medicine & Biology* 61.4, pp. 1795–1809 (cit. on p. 70).

Taya, T., J. Kataoka, A. Kishimoto, Y. Iwamoto, A. Koide, T. Nishio, S. Kabuki, and T. Inaniwa (2016). "First demonstration of real-time gamma imaging by using a handheld Compton camera for particle therapy". In: *Nuclear Instruments and Methods in Physics Research Section A: Accelerators, Spectrometers, Detectors and Associated Equipment* 831. Proceedings of the 10th International "Hiroshima" Symposium on the Development and Application of Semiconductor Tracking Detectors, pp. 355–361. ISSN: 0168-9002. DOI: https://doi.org/10.1016/j.nima.2016.04.028. URL: http://www.sciencedirect.com/science/article/pii/S0168900216301929 (cit. on p. 88).

Taya, T., J. Kataoka, A. Kishimoto, L. Tagawa, S. Mochizuki, T. Toshito, M. Kimura, Y. Nagao, K. Kurita, M. Yamaguchi, and N. Kawachi (2017). "Optimization and verification of image reconstruction for a Compton camera towards application as an on-line monitor for particle therapy". In: *Journal of Instrumentation* 12.07, P07015. URL: http://stacks.iop.org/1748-0221/12/i=07/a=P07015 (cit. on pp. 101, 180).

Taylor, J. T., P. P. Allport, G. L. Casse, N. A. Smith, I. Tsurin, N. M. Allinson, M. Esposito, A. Kacperek, J. Nieto-Camero, T. Price, and C. Waltham (2015). "Proton tracking for medical imaging and dosimetry." In: *Journal of Instrumentation* 10 (cit. on p. 42).

Taylor, J. T., G. Poludniowski, T. Price, C. Waltham, P. P. Allport, G. L. Casse, M. Esposito, P. M. Evans, S. Green, S. Manger, S. Manolopoulos, J. Nieto-Camero, D. J. Parker, J. Symons, and N. M. Allinson (2016). "An experimental demonstration of a new type of proton computed tomography using a novel silicon tracking detector." In: *Medical Physics* 43.11, p. 6129 (cit. on p. 42).

Telsemeyer, J., O. Jäkel, and M. Martisikova (2012). "Quantitative carbon ion beam radiography and tomography with a flat-panel detector." In: *Physics in Medicine & Biology* 57.23, pp. 7957–7971 (cit. on p. 42).

Ter-Pogossian, M. M. (1983). "Positron Emission Tomography (PET)". In: *Diagnostic Imaging in Medicine*. Ed. by R. C. Reba, D. J. Goodenough, and H. F. Davidson. Dordrecht: Springer Netherlands, pp. 273–277. ISBN: 978-94-009-6810-3. DOI: 10.1007/978-94-009-6810-3_12. URL: https://doi.org/10.1007/978-94-009-6810-3_12 (cit. on p. 47).

Ter-Pogossian, M. M., D. C. Ficke, M. Yamamoto, and J. T. Hood (1982). "Super PETT I: A Positron Emission Tomograph Utilizing Photon Time-of-Flight Information". In: *IEEE Transactions on Medical Imaging* 1.3, pp. 179–187 (cit. on p. 95).

Ter-Pogossian, M. M., M. E. Phelps, E. J. Hoffmann, and N. A. Mullani (1975). "A positron-emission transaxial tomograph for nuclear imaging (PETT)." In: *Radiology* 114.1, pp. 89–98 (cit. on p. 47).

Terasic (2009). *SFP HSMC Terasic Board User Manual*. Revision 1. Terasic Technologies Inc. (cit. on p. 117).

Terasic (2015). *SoCKit User Manual*. Revision F. Terasic Technologies Inc. (cit. on p. 117).

Testa, É., M. B. Bajard, M. Chevallier, D. Dauvergne, F. Le Foulher, N. Freud, J. M. Létang, J.-C. Poizat, C. Ray, and M. Testa (2009). "Dose profile monitoring with carbon ions by means

of prompt-gamma measurements". In: *Nuclear Instruments and Methods in Physics Research Section B: Beam Interactions with Materials and Atoms* 267.6. Proceedings of the Seventh International Symposium on Swift Heavy Ions in Matter, pp. 993–996. ISSN: 0168-583X. DOI: https://doi.org/10.1016/j.nimb.2009.02.031. URL: http://www.sciencedirect.com/science/article/pii/S0168583X09002468 (cit. on p. 83).

Testa, É., M. Bajard, M. Chevallier, D. Dauvergne, F. Le Foulher, N. Freud, J. M. Létang, J.-C. Poizat, C. Ray, and M. Testa (2008). "Monitoring the Bragg peak location of 73 MeV/u carbon ions by means of prompt γ-ray measurements". In: *Applied Physics Letters* 93.9, p. 093506. DOI: 10.1063/1.2975841. URL: https://doi.org/10.1063/1.2975841 (cit. on pp. 43, 83, 170).

Testa, M., M. Bajard, M. Chevallier, D. Dauvergne, N. Freud, P. Henriquet, S. Karkar, F. Le Foulher, J. M. Létang, R. Pleskac, C. Ray, M.-H. Richard, D. Schardt, and É. Testa (2010). "Real-time monitoring of the Bragg-peak position in ion therapy by means of single photon detection." eng. In: *Radiation and environmental biophysics* 49.3, pp. 337–343. DOI: 10.1007/s00411-010-0276-2 (cit. on pp. 17, 171, 178).

Thirolf, P. G., S. Aldawood, M. Böhmer, J. Bortfeldt, I. Castelhano, G. Dedes, F. Fiedler, R. Gernhäuser, C. Golnik, S. Helmbrecht, F. Hueso-González, H. v. Kolff, T. Kormoll, C. Lang, S. Liprandi, R. Lutter, T. Marinsek, L. Maier, G. Pausch, J. Petzoldt, K. E. Römer, D. R. Schaart, and K. Parodi (2016). "A Compton camera prototype for prompt gamma medical imaging". In: *EPJ Web of Conferences* 117, p. 05005. DOI: 10.1051/epjconf/201611705005. URL: https://doi.org/10.1051/epjconf/201611705005 (cit. on pp. 89, 90).

Thörnqvist, S., L. P. Muren, L. Bentzen, L. B. Hysing, M. Hoyer, C. Grau, and J. B. B. Petersen (2013). "Degradation of target coverage due to inter-fraction motion during intensity-modulated proton therapy of prostate and elective targets". In: *Acta Oncologica* 52.3, pp. 521–527. DOI: 10.3109/0284186X.2012.752860. URL: https://doi.org/10.3109/0284186X.2012.752860 (cit. on p. 33).

Thun, M. J., J. O. DeLancey, M. M. Center, A. Jemal, and E. M. Ward (2010). "The global burden of cancer: priorities for prevention". In: *Carcinogenesis* 31.1, pp. 100–110. DOI: 10.1093/carcin/bgp263. URL: http://www.ncbi.nlm.nih.gov/pmc/articles/PMC2802672/ (cit. on p. 6).

Tobias, C. A., E. V. Benton, M. P. Capp, A. Chatterjee, M. R. Cruty, and R. P. Henke (1977). "Particle radiography and autoactivation". In: *International Journal of Radiation Oncology Biology Physics* 3. Particles and Radiation Therapy Second International Conference, pp. 35–44. ISSN: 0360-3016. DOI: https://doi.org/10.1016/0360-3016(77)90224-3. URL: http://www.sciencedirect.com/science/article/pii/0360301677902243 (cit. on p. 39).

Tobias, C. A., E. A. Blakely, E. L. Alpen, J. R. Castro, E. J. Ainsworth, S. B. Curtis, F. Q. H. Ngo, A. Rodriguez, R. J. Roots, T. Tenfordf, and T. C. H. Yang (1982). "Molecular and cellular radiobiology of heavy ions". In: *International Journal of Radiation Oncology Biology Physics* 8.12. Particle Accelerators in Radiation Therapy, pp. 2109–2120. ISSN: 0360-3016. DOI: https://doi.org/10.1016/0360-3016(82)90554-5. URL: http://www.sciencedirect.com/science/article/pii/0360301682905545 (cit. on pp. 7, 19).

Tobias, C. A., A. Chatterjee, and A. R. Smith (1971). "Radioactive fragmentation of N7+ ion beam observed in a beryllium target". In: *Physics Letters A* 37.2, pp. 119–120. ISSN: 0375-9601. DOI: https://doi.org/10.1016/0375-9601(71)90086-7. URL: http://www.sciencedirect.com/science/article/pii/0375960171900867 (cit. on p. 69).

Tobias, C. A., J. H. Lawrence, J. L. Born, R. K. McCombs, J. E. Roberts, H. O. Anger, B. V. A. Low-Beer, and C. B. Huggins (1958). "Pituitary Irradiation with High-Energy Proton Beams. A Preliminary Report". In: *Cancer Research* 18.2, pp. 121–134. URL: http://cancerres.aacrjournals.org/content/18/2/121 (cit. on pp. 7, 22).

Tobias, C. A., J. E. Roberts, J. H. Lawrence, B. V. A. Low-Beer, H. O. Anger, and J. L. Born (1955). "Irradiation Hypophysectomy and related studies using 340 MeV protons an 190 MeV deuterons". In: *Lawrence Berkeley National Laboratory. LBNL Report* UCRL-2907 (cit. on pp. 7, 22).

Todd, R. W., J. M. Nightingale, and D. B. Everett (1974). "A proposed γ camera". In: *Nature* 251, 132 EP (cit. on pp. 86, 98).

Toltz, A., M. Hoesl, J. P. Schuemann, J. Seuntjens, H.-M. Lu, and H. Paganetti (2017). "Time-resolved diode dosimetry calibration through Monte Carlo modeling for in vivo passive scattered proton therapy range verification." In: *Journal of Applied Clinical Medical Physics* 18.6, pp. 200–205 (cit. on p. 44).

Tomitani, T., J. Pawelke, M. Kanazawa, K. Yoshikawa, K. Yoshida, M. Sato, A. Takami, M. Koga, Y. Futami, A. Kitagawa, E. Urakabe, M. Suda, H. Mizuno, T. Kanai, H. Matsuura, I. Shinoda, and S. Takizawa (2003). "Washout studies of 11C in rabbit thigh muscle implanted by secondary beams of HIMAC." In: *Physics in Medicine & Biology* 48.7, pp. 875–889 (cit. on p. 65).

Tornai, M. P., G. Germano, and E. J. Hoffmann (1994). "Positioning and energy response of PET block detectors with different light sharing schemes". In: *IEEE Transactions on Nuclear Science* 41.4, pp. 1458–1463. ISSN: 0018-9499. DOI: 10.1109/23.322931 (cit. on pp. 133, 162).

Tsai, Y.-S. (1974). "Pair Production and Bremsstrahlung of Charged Leptons". In: *Review of Modern Physics* 46. [Erratum: Rev. Mod. Phys.49,521(1977)], p. 815. DOI: 10.1103/RevModPhys.46.815,10.1103/RevModPhys.49.421 (cit. on p. 13).

Unkelbach, J. and H. Paganetti (2018). "Robust Proton Treatment Planning: Physical and Biological Optimization". In: *Seminars in Radiation Oncology* 28.2. Proton Radiation Therapy, pp. 88–96. ISSN: 1053-4296. DOI: https://doi.org/10.1016/j.semradonc.2017.11.005. URL: http://www.sciencedirect.com/science/article/pii/S1053429617301078 (cit. on p. 33).

Urakabe, E., T. Kanai, M. Kanazawa, A. Kitagawa, K. Noda, T. Tomitani, M. Suda, Y. Iseki, K. Hanawa, K. Sato, M. Shimbo, H. Mizuno, Y. Hirata, Y. Futami, Y. Iwashita, and A. Noda (2001). "Spot Scanning Using Radioactive 11 C Beams for Heavy-Ion Radiotherapy". In: *Japanese Journal of Applied Physics* 40.4R, p. 2540. URL: http://stacks.iop.org/1347-4065/40/i=4R/a=2540 (cit. on p. 69).

Uribe, J., H. Li, T. Xing, Y. Liu, H. Baghaei, Y. Wang, M. Aykac, R. Ramirez, and W.-H. Wong (2003). "Signal characteristics of individual crystals in high resolution BGO detector designs

using PMT-quadrant sharing". In: *IEEE Transactions on Nuclear Science* 50.3, pp. 355–361. DOI: 10.1109/TNS.2003.812478 (cit. on p. 151).

Urie, M., M. Goitein, W. R. Holley, and G. T. Y. Chen (1986). "Degradation of the Bragg peak due to inhomogeneities". In: *Physics in Medicine & Biology* 31.1, p. 1. URL: http://stacks.iop.org/0031-9155/31/i=1/a=001 (cit. on pp. 36, 38).

Uzawa, A., K. Ando, S. Koike, Y. Furusawa, Y. Matsumoto, N. Takai, R. Hirayama, M. Watanabe, M. Scholz, T. Elsässer, and P. Peschke (2009). "Comparison of Biological Effectiveness of Carbon-Ion Beams in Japan and Germany". In: *International Journal of Radiation Oncology Biology Physics* 73.5, pp. 1545–1551. ISSN: 0360-3016. DOI: https://doi.org/10.1016/j.ijrobp.2008.12.021. URL: http://www.sciencedirect.com/science/article/pii/S0360301608039175 (cit. on p. 33).

Vallois, Y. (2016). "Test d'un hodoscope de faisceau à fibres scintillantes". Master internship report (cit. on pp. 157, 166).

Vandenberghe, S., E. Mikhaylova, E. D'Hoe, P. Mollet, and J. S. Karp (2016). "Recent developments in time-of-flight PET". In: *EJNMMI Physics* 3, p. 3 (cit. on p. 65).

Vaquero, J. J. and P. Kinahan (2015). "Positron Emission Tomography: Current Challenges and Opportunities for Technological Advances in Clinical and Preclinical Imaging Systems." In: *Annual Review of Biomedical Engineering* 17, pp. 385–414 (cit. on pp. 92, 95).

Vavilov, P. V. (1957). "Ionization losses of high-energy heavy particles". In: *Sov. Phys. JETP* 5. [Zh. Eksp. Teor. Fiz.32,920(1957)], pp. 749–751 (cit. on p. 12).

Vecchio, S., F. Attanasi, N. Belcari, M. Camarda, G. A. P. Cirrone, G. Cuttone, F. Di Rosa, N. Lanconelli, S. Moehrs, V. Rosso, G. Russo, and A. Del Guerra (2009). "A PET Prototype for "In-Beam" Monitoring of Proton Therapy". In: *IEEE Transactions on Nuclear Science* 56.1, pp. 51–56. ISSN: 0018-9499. DOI: 10.1109/TNS.2008.2008306 (cit. on p. 71).

Veksler, V. I. (1944). "A new method of accelerating relativistic particles." In: *Comptes Rendus (Dokaldy) de l'Academie Sciences de l'URSS* 43.8, pp. 329–331 (cit. on p. 23).

Verburg, J. M., K. Riley, T. R. Bortfeld, and J. Seco (2013). "Energy- and time-resolved detection of prompt gamma-rays for proton range verification." eng. In: *Physics in Medicine & Biology* 58.20, pp. L37–49. DOI: 10.1088/0031-9155/58/20/L37 (cit. on pp. 76, 81, 82).

Verburg, J. M. and J. Seco (2014). "Proton range verification through prompt gamma-ray spectroscopy." In: *Physics in Medicine & Biology* 59.23, pp. 7089–7106 (cit. on pp. 74, 76, 81, 82).

Verburg, J. M., H. A. Shih, and J. Seco (2012). "Simulation of prompt gamma-ray emission during proton radiotherapy." In: *Physics in Medicine & Biology* 57.17, pp. 5459–5472 (cit. on pp. 77, 81).

Vynckier, S., F. Vanneste, F. Richard, A. Bol, C. Michel, and A. Wambersie (1989). "Control of patient positioning for fast neutron therapy using positron emission tomography." In: *British Journal of Radiology* 62.743, pp. 1031–1032 (cit. on p. 68).

Watson, G. S. (1964). "Smooth Regression Analysis". In: *Sankhyā: The Indian Journal of Statistics, Series A (1961-2002)* 26.4, pp. 359–372. URL: http://www.jstor.org/stable/25049340 (cit. on p. 183).

Watts, D. A., U. Amaldi, A. Go, Y.-H. Chang, W. Hajdas, S. Iliescu, N. Malakhov, J. Samarati, and F. Sauli (2009). "A proton range telescope for quality assurance in hadrontherapy". In: *2009 IEEE Nuclear Science Symposium Conference Record (NSS/MIC)*, pp. 4163–4166. DOI: 10.1109/NSSMIC.2009.5402303 (cit. on p. 44).

Watts, D. A., G. Borghi, F. Sauli, and U. Amaldi (2013). "The use of multi-gap resistive plate chambers for in-beam PET in proton and carbon ion therapy". In: *Journal of Radiation Research* 54.Suppl 1, pp. i136–i142 (cit. on p. 72).

Webb, S. (2009). "The contribution, history, impact and future of physics in medicine". In: *Acta Oncologica* 48, pp. 169–177. DOI: 10.1080/02841860802244158 (cit. on p. 6).

Weber, M. J. and R. R. Monchamp (1973). "Luminescence of Bi4 Ge3 O12 : Spectral and decay properties". In: *Journal of Applied Physics* 44.12, pp. 5495–5499. DOI: 10.1063/1.1662183. URL: https://doi.org/10.1063/1.1662183 (cit. on p. 94).

Weisskopf, V. (1937). "Statistics and Nuclear Reactions". In: *Physical Review* 52 (4), pp. 295–303. DOI: 10.1103/PhysRev.52.295. URL: https://link.aps.org/doi/10.1103/PhysRev.52.295 (cit. on p. 14).

WeissTechnik (2017). *Products brochure*. rev. Jan 2017. Weiss Technik North America, Inc. (cit. on p. 131).

Weyrather, W. K., S. Ritter, M. Scholz, and G. Kraft (1999). "RBE for carbon track-segment irradiation in cell lines of differing repair capacity". eng. In: *International journal of radiation biology* 75.11, pp. 1357–1364 (cit. on p. 170).

Wideröe, R. (1928). "Über ein neues Prinzip zur Herstellung hoher Spannungen". In: *Archiv für Elektrotechnik* 21.4, pp. 387–406. ISSN: 1432-0487. DOI: 10.1007/BF01656341. URL: https://doi.org/10.1007/BF01656341 (cit. on p. 22).

Wilderman, S. J., N. H. Clinthorne, J. A. Fessler, and W. L. Rogers (1998). "List-mode maximum likelihood reconstruction of Compton scatter camera images in nuclear medicine". In: *1998 IEEE Nuclear Science Symposium Conference Record. 1998 IEEE Nuclear Science Symposium and Medical Imaging Conference (Cat. No.98CH36255)* 3, pp. 1716–1720. ISSN: 1082-3654. DOI: 10.1109/NSSMIC.1998.773871 (cit. on pp. 87, 180).

Wilkens, J. J. and U. Oelfke (2008). "Direct comparison of biologically optimized spread-out bragg peaks for protons and carbon ions." In: *International Journal of Radiation Oncology Biology Physics* 70.1, pp. 262–266 (cit. on p. 21).

Willers, H., A. Allen, D. R. Grosshans, S. J. McMahon, C. von Neubeck, C. Wiese, and B. Vikram (2018). "Toward A variable RBE for proton beam therapy". In: *Radiotherapy and Oncology* 128.1, pp. 68–75. ISSN: 0167-8140. DOI: https://doi.org/10.1016/j.radonc.2018.05.019. URL: http://www.sciencedirect.com/science/article/pii/S0167814018302780 (cit. on p. 33).

Wilson, R. (2004). *A brief history of the Harvard cyclotrons.* Harvard University Press (cit. on p. 23).

Wilson, R. R. (1946). "Radiological Use of Fast Protons". In: *Radiology* 47.5. PMID: 20274616, pp. 487–491. DOI: 10.1148/47.5.487. URL: https://doi.org/10.1148/47.5.487 (cit. on pp. 7, 22).

Wohlfahrt, P., C. Möhlerm, C. Richter, and S. Greilich (2018). "Evaluation of Stopping-Power Prediction by Dual- and Single-Energy Computed Tomography in an Anthropomorphic Ground-Truth Phantom". In: *International Journal of Radiation Oncology Biology Physics* 100.1, pp. 244–253. ISSN: 0360-3016. DOI: https://doi.org/10.1016/j.ijrobp.2017.09.025. URL: http://www.sciencedirect.com/science/article/pii/S0360301617338920 (cit. on pp. 36, 83).

Wouters, B. G., G. K. Y. Lam, U. Oelfke, K. Gardey, R. E. Durand, and L. D. Skarsgard (1996). "Measurements of relative biological effectiveness of the 70 MeV proton beam at TRIUMF using Chinese hamster V79 cells and the high-precision cell sorter assay." In: *Radiation Research* 146.2, pp. 159–170 (cit. on pp. 37, 38).

Wrenn, F. R., M. L. Good, and P. Handler (1951). "The Use of Positron-emitting Radioisotopes for the Localization of Brain Tumors". In: *Science* 113.2940, pp. 525–527. ISSN: 0036-8075. DOI: 10.1126/science.113.2940.525. URL: http://science.sciencemag.org/content/113/2940/525 (cit. on p. 93).

Wroe, A. J., I. M. Cornelius, and A. B. Rosenfeld (2005). "The role of nonelastic reactions in absorbed dose distributions from therapeutic proton beams in different medium". In: *Medical Physics* 32.1, pp. 37–41. DOI: 10.1118/1.1824194. URL: https://aapm.onlinelibrary.wiley.com/doi/abs/10.1118/1.1824194 (cit. on p. 17).

Xie, Y., E. H. Bentefour, G. Janssens, J. Smeets, F. Vander Stappen, L. Hotoiu, L. Yin, D. Dolney, S. Avery, F. O'Grady, D. Prieels, J. McDonough, T. D. Solberg, R. A. Lustig, A. Lin, and B.-K. K. Teo (2017). "Prompt Gamma Imaging for In-Vivo Range Verification of Pencil Beam Scanning Proton Therapy". In: *International Journal of Radiation Oncology Biology Physics* 99.1, pp. 210–218. DOI: 10.1016/j.ijrobp.2017.04.027. URL: https://doi.org/10.1016/j.ijrobp.2017.04.027 (cit. on p. 85).

Yamaguchi, M., Y. Nagao, K. Ando, S. Yamamoto, M. Sakai, R. K. Parajuli, K. Arakawa, and N. Kawachi (2018). "Imaging of monochromatic beams by measuring secondary electron bremsstrahlung for carbon-ion therapy using a pinhole x-ray camera". In: *Physics in Medicine & Biology* 63.4, p. 045016. URL: http://stacks.iop.org/0031-9155/63/i=4/a=045016 (cit. on p. 45).

Yamaguchi, M., K. Torikai, N. Kawachi, H. Shimada, T. Satoh, Y. Nagao, S. Fujimaki, M. Kokubun, S. Watanabe, T. Takahashi, K. Arakawa, T. Kamiya, and T. Nakano (2012). "Beam range

estimation by measuring bremsstrahlung". In: *Physics in Medicine & Biology* 57.10, p. 2843. URL: http://stacks.iop.org/0031-9155/57/i=10/a=2843 (cit. on p. 45).

Yamaya, T. (2017). "OpenPET: a novel open-type PET system for 3D dose verification in particle therapy". In: *Journal of Physics: Conference Series* 777.1, p. 012023. URL: http://stacks.iop.org/1742-6596/777/i=1/a=012023 (cit. on pp. 68, 70).

Yamaya, T. (2018). "Development of the OpenPET for in-beam carbon ion therapy imaging". In: *MediNet collaboration Midterm meeting - Belgrade, March 2018* (cit. on pp. 68, 72, 170).

Yamaya, T., T. Inaniwa, S. Minohara, E. Yoshida, N. Inadama, F. Nishikido, K. Shibuya, C. F. Lam, and H. Murayama (2008). "A proposal of an open PET geometry". In: *Physics in Medicine & Biology* 53.3, p. 757. URL: http://stacks.iop.org/0031-9155/53/i=3/a=015 (cit. on pp. 68, 70).

Yamaya, T., T. Inaniwa, S. Mori, T. Furukawa, S. Minohara, E. Yoshida, F. Nishikido, K. Shibuya, N. Inadama, and H. Murayama (2009). "Imaging simulations of an "OpenPET" geometry with shifting detector rings." In: *Radiological Physics and Technology* 2.1, pp. 62–69 (cit. on p. 70).

Yamaya, T., E. Yoshida, H. Tashima, A. Tsuji, K. Nagatsu, M. Yamaguchi, N. Kawachi, Y. Okumura, M. Suga, and K. Parodi (2017). "Whole gamma imaging (WGI) concept: simulation study of triple-gamma imaging". In: *Journal of Nuclear Medicine* 58.supplement 1, p. 152. URL: http://jnm.snmjournals.org/content/58/supplement_1/152.abstract (cit. on p. 45).

Yan, X., U. Titt, A. M. Koehler, and W. D. Newhauser (2002). "Measurement of neutron dose equivalent to proton therapy patients outside of the proton radiation field". In: *Nuclear Instruments and Methods in Physics Research Section A: Accelerators, Spectrometers, Detectors and Associated Equipment* 476.1. Int. Workshop on Neutron Field Spectrometry in Science, Technology and Radiation Protection, pp. 429–434. ISSN: 0168-9002. DOI: https://doi.org/10.1016/S0168-9002(01)01483-8. URL: http://www.sciencedirect.com/science/article/pii/S0168900201014838 (cit. on p. 18).

Yang, M., G. Virshup, J. Clayton, X. R. Zhu, R. Mohan, and L. Dong (2010). "Theoretical variance analysis of single- and dual-energy computed tomography methods for calculating proton stopping power ratios of biological tissues". In: *Physics in Medicine & Biology* 55.5, p. 1343. URL: http://stacks.iop.org/0031-9155/55/i=5/a=006 (cit. on pp. 31, 36).

Yordanova, A., E. Eppard, S. Kürpig, R. A. Bundschuh, S. Schönberger, M. Gonzalez-Carmona, G. Feldmann, H. Ahmadzadehfar, and M. Essler (2017). "Theranostics in nuclear medicine practice". In: *OncoTargets and therapy* 10, pp. 4821–4828 (cit. on pp. 52, 100).

Yoshihara, Y., K. Shimazoe, Y. Mizumachi, H. Takahashi, K. Kamada, A. Takeda, T. Tsuru, and Y. Arai (2017). "Development of electron-tracking Compton imaging system with 30-μm SOI pixel sensor". In: *Journal of Instrumentation* 12.01, p. C01045. URL: http://stacks.iop.org/1748-0221/12/i=01/a=C01045 (cit. on p. 89).

Zeng, G. L., J. R. Galt, M. N. Wernick, R. A. Mintzer, and J. N. Aarsvold (2004). "CHAPTER 7 - Single-Photon Emission Computed Tomography". In: *Emission Tomography*. Ed. by M. N.

Wernick and J. N. Aarsvold. San Diego: Academic Press, pp. 127–152. ISBN: 978-0-12-744482-6. DOI: https://doi.org/10.1016/B978-012744482-6.50010-7. URL: http://www.sciencedirect.com/science/article/pii/B9780127444826500107 (cit. on p. 97).

Zhu, X., S. España, J. Daartz, N. J. Liebsch, J. Ouyang, H. Paganetti, T. R. Bortfeld, and G. El Fakhri (2011). "Monitoring proton radiation therapy with in-room PET imaging". In: *Physics in Medicine & Biology* 56.13, pp. 4041–4057 (cit. on p. 70).

Zhu, X. and G. E. Fakhri (2013). "Proton Therapy Verification with PET Imaging". In: *Theranostics* 3.10, pp. 731–740 (cit. on p. 69).

Zoglauer, A., R. Andritschke, and F. Schopper (2006). "MEGAlib The Medium Energy Gamma-ray Astronomy Library". In: *New Astronomy Reviews* 50, pp. 629–632. DOI: 10.1016/j.newar.2006.06.049 (cit. on p. 200).

Zoglauer, A., E. S. Boggs, M. Galloway, M. Amman, N. P. Luke, and R. Kippen (2011). "Design, implementation, and optimization of MEGAlib's image reconstruction tool Mimrec". In: 652, pp. 568–571 (cit. on pp. 101, 180).

Zografos, A., T. Brown, C. Cohen-Jonathan, C. Hettler, F. Huang, V. Joshkin, K. Leung, M. F. Moyers, Y. Parker, D. Pearson, M. Rougieri, and R. W. Hamm (2013). "Development of the Dielectric Wall Accelerator". In: *Proceedings, 4th International Particle Accelerator Conference (IPAC 2013): Shanghai, China, May 12-17, 2013*, THOAB201. URL: http://JACoW.org/IPAC2013/papers/thoab201.pdf (cit. on p. 25).

Index

Acknoledgements

This work was supported by the LABEX PRIMES (ANR-11-LABX-0063) of Université de Lyon and by France HADRON (ANR-11-INBS-0007), within the program "Investissements d'Avenir" (ANR-11-IDEX-0007) operated by the French National Research Agency (ANR).